eman ta zabal zazu

Universidad del País Vasco
Euskal Herriko Unibertsitatea

FACULTY
OF SCIENCE
AND TECHNOLOGY
UNIVERSITY
OF THE BASQUE
COUNTRY

# Petrology of cordierite-bearing monzogranites and related mesocratic rocks from the Sierra Bermeja Pluton (southern Iberian Massif)

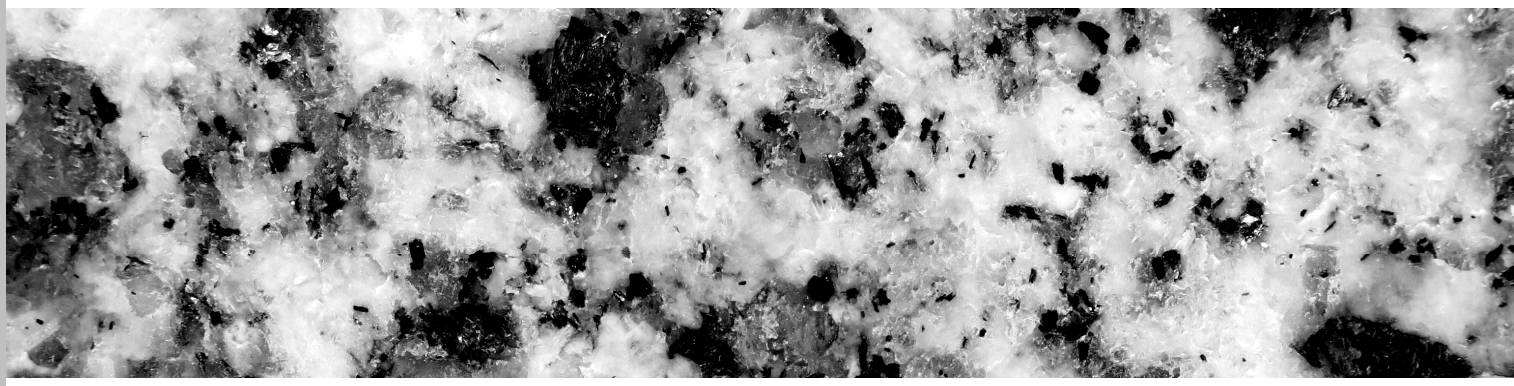

**Jon Errandonea Martin**

PhD Thesis
Mineralogy and Petrology Department
2019

eman ta zabal zazu

Universidad del País Vasco
Euskal Herriko Unibertsitatea

FACULTY
OF SCIENCE
AND TECHNOLOGY
UNIVERSITY
OF THE BASQUE
COUNTRY

# Petrology of cordierite-bearing monzogranites and related mesocratic rocks from the Sierra Bermeja Pluton (southern Iberian Massif)

**Supervisors**

Fernando Sarrionandia-Ibarra Eguidazu

José Ignacio Gil Ibarguchi

**PhD student**

Jon Errandonea Martin

2019

Universidad del País Vasco | Euskal Herriko Unibertsitatea

NAZIOARTEKO BIKAINTASUN CAMPUSA
CAMPUS DE EXCELENCIA INTERNACIONAL

**AUTORIZACION DEL DIRECTOR DE TESIS**

**PARA SU PRESENTACION**

Dr. Fernando Sarrionandia-Ibarra Eguidazu, con N.I.F. 44671849-F, como Director de la Tesis Doctoral '*Petrology of cordierite-bearing monzogranites and related mesocratic rocks from the Sierra Bermeja Pluton (southern Iberian Massif)*' realizada en el Programa de Doctorado 'Cuaternario: Cambios Ambientales y Huella Humana' por el Doctorando Don Jon Errandonea Martin, autorizo la presentación de la citada Tesis Doctoral, dado que reúne las condiciones necesarias para su defensa.

En Leioa a 12 de junio de 2019

EL DIRECTOR DE LA TESIS

Fdo.: Fernando Sarrionandia-Ibarra Eguidazu

Universidad del País Vasco | Euskal Herriko Unibertsitatea

NAZIOARTEKO BIKAINTASUN CAMPUSA
CAMPUS DE EXCELENCIA INTERNACIONAL

**AUTORIZACION DEL DIRECTOR DE TESIS**

**PARA SU PRESENTACION**

Dr. José Ignacio Gil Ibarguchi, con N.I.F. 11365743-V, como Director de la Tesis Doctoral '*Petrology of cordierite-bearing monzogranites and related mesocratic rocks from the Sierra Bermeja Pluton (southern Iberian Massif)*' realizada en el Programa de Doctorado 'Cuaternario: Cambios Ambientales y Huella Humana' por el Doctorando Don Jon Errandonea Martin, autorizo la presentación de la citada Tesis Doctoral, dado que reúne las condiciones necesarias para su defensa.

En Leioa a 12 de junio de 2019

EL DIRECTOR DE LA TESIS

Fdo.: José Ignacio Gil Ibarguchi

Universidad del País Vasco Euskal Herriko Unibertsitatea | NAZIOARTEKO BIKAINTASUN CAMPUSA CAMPUS DE EXCELENCIA INTERNACIONAL

# AUTORIZACIÓN DE LA COMISIÓN ACADÉMICA DEL PROGRAMA DE DOCTORADO

La Comisión Académica del Programa de Doctorado en Cuaternario: Cambios Ambientales y Huella Humana, en reunión celebrada el 12 de junio de 2019, ha acordado dar la conformidad a la presentación de la Tesis Doctoral titulada *Petrology of cordierite-bearing monzogranites and related mesocratic rocks from the Sierra Bermeja Pluton (southern Iberian Massif),* dirigida por el Dr. Fernando Sarrionandia-Ibarra Eguidazu y el Dr. José Ignacio Gil Ibarguchi, y presentada por Don Jon Errandonea Martin, adscrito al Departamento Mineralogía y Petrología.

En Leioa a 12 de junio de 2019

EL RESPONSABLE DEL PROGRAMA DE DOCTORADO

Fdo.: Alejandro Cearreta Bilbao

# AUTORIZACION DEL DEPARTAMENTO

El Consejo del Departamento de Mineralogía y Petrología en reunión celebrada el día 5 de junio de 2019 ha acordado dar la conformidad a la admisión a trámite de presentación de la Tesis Doctoral titulada: *Petrology of cordierite-bearing monzogranites and related mesocratic rocks from the Sierra Bermeja Pluton (southern Iberian Massif)*, dirigida por el Dr. Fernando Sarrionandia-Ibarra Eguidazu y el Dr. José Ignacio Gil Ibarguchi, y presentada por Don Jon Errandonea Martin ante este Departamento.

En Leioa a 12 de junio de 2019

VºBº DIRECTOR DEL DEPARTAMENTO

Fdo.: José Miguel Herrero Rubio

SECRETARIO DEL DEPARTAMENTO

Fdo.: José Francisco Santos Zalduegui

# ACTA DE GRADO DE DOCTOR O DOCTORA
# ACTA DE DEFENSA DE TESIS DOCTORAL

DOCTORANDO: Don Jon Errandonea Martin

TITULO DE LA TESIS: Petrology of cordierite-bearing monzogranites and related mesocratic rocks from the Sierra Bermeja Pluton (southern Iberian Massif)

El Tribunal designado por la Comisión de Postgrado de la UPV/EHU para calificar la Tesis Doctoral arriba indicada y reunido en el día de la fecha, una vez efectuada la defensa por el doctorando y contestadas las objeciones y/o sugerencias que se le han formulado, ha otorgado por_____la calificación de:

*unanimidad ó mayoría*

| |
|---|
| |

*SOBRESALIENTE / NOTABLE / APROBADO / NO APTO*

Idioma/s de defensa (en caso de más de un idioma, especificar porcentaje defendido en cada idioma):

Castellano _____

Euskera _____

Otros Idiomas (especificar cuál/cuales y porcentaje) _____

En Leioa a _____ de septiembre de 2019

| | |
|---|---|
| EL PRESIDENTE, | LA SECRETARIA, |
| Fdo.: | Fdo.: |
| Dr. Carlos Villaseca González | Dra. Ainhoa Alonso Olazabal |
| VOCAL 1º, | EL DOCTORANDO, |
| Fdo.: | Fdo.: |
| Dra. Patrizia Fiannacca | Jon Errandonea Martin |

*'We must not forget that when radium was discovered no one knew that it would prove useful in hospitals. The work was one of pure science. And this is a proof that scientific work must not be considered from the point of view of the direct usefulness of it. It must be done for itself, for the beauty of science, and then there is always the chance that a scientific discovery may become like the radium a benefit for humanity'*

Maria Salomea Sklodowska-Curie (Marie Curie)
Vassar College Conference
14 May 1921

# ACKNOWLEDGEMENTS
# ESKER ONAK
# AGRADECIMIENTOS

Urte asko dira geologia ikasi eta ikerketan ari nahi nuela garbi ikusi nuenetik, beraz ez dut beste modu hoberik ikusten memoria hau hasteko, ordutik lerro hauek idatzi arte nire ondoan egon zaretenei eskertzen baino.

Hasteko, Euskal Herriko Unibertsitatea eta Mineralogia eta Petrologia saila eskertu beharrean nago, bertako partaide gisa onartuz proiektu hau ahalbidetzeagatik. Mila esker saileko kide zaraten guztioi. Modu berean, barne hartu nauen ikerketa taldea eta bertako kideak ere eskertu nahi nituzke, beti esku bat botatzeko prest egoteagatik.

Proiektu honen egunerokotasunean nire gainean izan ditudan “3” zuzendariak eskertu nahi nituzke bereziki: Fernando, Iñaki eta Manu. Lehenik zuri Fernando, zuzendari, lankide, adiskide. Mila esker urte guzti hauetan elkarlanean arituz erakutsi didazun guztiagatik, gaur egun naizen geologoak asko du ikusteko zurekin landan eta laborategian pasa ditudan ordu guztiekin. Plazer bat izan da zu bezalako zuzendari bat izatea.

De igual modo, no puedo estar más agradecido de haberte tenido como director, Iñaki. Mil gracias por las facilidades brindadas a lo largo de estos años y por los conocimientos que me has transmitido, que no han sido pocos. Y a ti también Manu, todavía me acuerdo del primer día que entré en tu despacho para pedirte consejo sobre la tesis... He sido muy afortunado al poder aprender de ti durante los años que hemos coincidido, espero que estés disfrutando de una más que merecida jubilación.

No llevo la cuenta de la de apuros que me has sacado y de todas las veces que me has ayudado sin pedir nada a cambio Sonia, millones de gracias. Aprovecho también para agradecer a Luis y a Josu, por la ayuda recibida durante los trabajos de campo y de cartografía, eres un artista con los mapas Josu.

Urte hauetan laborategian topo egin dudan jendeaz ere ezin naiz ahaztu. Mila esker Aratz eta Maruri hasiberri nintzenean emandako aholkuengatik eta tesian zehar jasotako laguntzagatik, baita Iranzu, Graciela eta Haizeari ere elkarbanatutako elkarrizketa filosofikoengatik. Burutan ditut ere urte hauetan unibertsitatean kointziditutako beste hainbat kide eta lagun… Baita unibertsitatera kotxean elkarrekin joan garenak: Esther,

Miren, Iraia… Batzuetan eskertzen da tesi bat aurrera ateratzeak suposatzen duen guztiari buruz hitz egitean benetan ulertzen duen jendearekin egitea.

Fuera de la Universidad del País Vasco, no puedo olvidarme de la gente de la Universidad Complutense de Madrid, por todo lo que aprendí durante el año que estuve con ellos y por el buen recuerdo que guardo. Especialmente quiero agradecer a Carlos Villaseca y a David Orejana, fue un placer teneros como directores de TFM y poder trabajar con vosotros. Gracias Carlos por tus sabios consejos que me han guiado acertadamente en el mundo de los granitos, eres todo un referente para mí.

I would like to thank also colleagues from the Institute of Petrology and Structural Geology of Charles University in Prague, thank you for kindly accepting me during the stay. Thanks a mil very particularly to you Vojtěch, it has been an immense privilege to learn from you. My sincere thanks for your supervision, patience and wise advices. 'Grazie mille' also to my office colleague Alessandro Fabbrizio.

I really appreciate willingness and effort of Patrizia Fiannacca and Christian Pin for the external report of the present PhD dissertation, as well as disposition of other candidates of the PhD examination panel. Zentzu honetan, epaimahaiko kide izateaz gain, bereziki eman nahi dizkizut eskerrak Ainhoa, landu ditudan granitoen inguruko zure ezagutza eta aholkuak lagungarriak izan baitzaizkit.

Bukatzen hasteko, bide luze honetan denbora gehien sufritu nauen jendeaz nola ahantzi… Ez dut hitzik behar bezainbertze eskertzeko ttikitatik inolako baldintzarik gabe emandako guziagatik, eskerrikasko barren barrenetik atta ta ama. Eskerrikasko Julen, beti hor egoteagatik eta aunitzetan bizitza bertze modu batean ikusten laguntzeagatik. Eskerrikasko Ali, Ezti, lehengusu-izeba-osaba, Eibarko familia… Eta nola ez, nire lagun minei, eskerrikasko kuadrilla, aupa Eztabat!

Azken hitzak zuretzat, Idoia. Momentu onetan egotea erraza den bezala momentu txarrak dira benetan hurbilean nor dagoen erakusten dutenak. Hor lehendabiziko postuan zaude dudarik gabe. Bizitzan bidelagun hoberik ezin izango nuke aurkitu, beraz, mila esker bihotz bihotzez.

# FOREWORD

The present PhD project has been performed at the Mineralogy and Petrology Department of the University of the Basque Country. This work was financially supported by the Spanish Ministerio de Economía y Competitividad and the European Regional Development Fund, project CGL2015-63530-P (MINECO/FEDER, EU) 'Applied Petrochronology and Petrofabrics: study of igneous and metamorphic rocks from the pre-Alpine Orogens of the Iberian Peninsula', and by the University of the Basque Country UPV/EHU (Grupo Consolidado project GIU15/05) 'Basement Petrochronology and Petrofabrics'. The PhD student benefited from a 'Personal Investigador en Formación' (PIF) grant of the University of the Basque Country UPV/EHU 2014 program.

This PhD aims for the 'International Doctor' distinction, for which a stay of three months, from 21st September until 21st December 2017, has been done at the Institute of Petrology and Structural Geology of Charles University in Prague.

Concurrently to the writing of the PhD dissertation, the obtained results have been published in SCI journals. These papers are the result of collaboration with other co-authors, who have approved the publication of the results in this memory. Nevertheless, this memory includes new unpublished data that will be part of forthcoming works. In this sense, the most relevant contributions related to the present PhD project are those listed below:

Errandonea-Martin, J., Sarrionandia, F., Carracedo-Sánchez, M., Gil Ibarguchi, J.I., Eguíluz, L., 2018. Petrography and geochemistry of late- to post-Variscan vaugnerite series rocks and calc-alkaline lamprophyres within a cordierite-bearing monzogranite (the Sierra Bermeja Pluton, southern Iberian Massif). Geologica Acta 16 (3), 237–255. https://doi.org/10.1344/GeologicaActa2018.16.3.1

Errandonea-Martin, J., Sarrionandia, F., Junguitu, J., Carracedo-Sánchez, M., Eguíluz, L., Gil Ibarguchi, J.I., 2018. The composite Sierra Bermeja Pluton (southern Iberian Massif): science, heritage and geoconservation. Journal of Maps 15 (2), 101–111. https://doi.org/10.1080/17445647.2018.1548981

Errandonea-Martin, J., Janoušek, V., Sarrionandia, F., Carracedo-Sánchez, M., Gil Ibarguchi, J.I., 2018. The nested Sierra Bermeja Pluton (SW Iberian Massif): likely sources and magma evolution. European General Union Assembly, Geophysical Research Abstracts 20, 1709.

https://meetingorganizer.copernicus.org/EGU2018/EGU2018-1709.pdf

Errandonea-Martin, J., Sarrionandia, F., Janoušek, V., Carracedo-Sánchez, M., Gil Ibarguchi, J.I., 2019. Origin of cordierite-bearing monzogranites from the southern Central Iberian Zone – inferences from the zoned Sierra Bermeja Pluton (Extremadura, Spain). Lithos, 342–343, 440–462. https://doi.org/10.1016/j.lithos.2019.06.009

In addition, two other contributions have been published in meetings of the Spanish Mineralogical Society:

Errandonea-Martin, J., Sarrionandia, F., Carracedo-Sánchez, M., Gil Ibarguchi, J.I., 2016. Pasillos de Enclaves Máficos en el Plutón Granítico de Sierra Bermeja (Zona Centro Ibérica). Macla 21, 32–34. http://www.ehu.eus/sem/macla_pdf/macla21/Macla21_032.pdf

Errandonea-Martin, J., Sarrionandia, F., Carracedo-Sánchez, M., Eguíluz, L., Gil Ibarguchi, J.I., 2017. Vaugneritas en el Plutón de Sierra Bermeja (Área de Mérida; Zona Centro Ibérica). Macla 22, 37–38. http://www.ehu.eus/sem/macla_pdf/macla22/Macla22_037.pdf

*Geologica Acta, Vol.16, Nº 3, September 2018, 237-255*
DOI: 10.1344/GeologicaActa2018.16.3.1


geologica acta

# Petrography and geochemistry of late- to post-Variscan vaugnerite series rocks and calc-alkaline lamprophyres within a cordierite-bearing monzogranite (the Sierra Bermeja Pluton, southern Iberian Massif)

**J. ERRANDONEA-MARTIN[1] F. SARRIONANDIA[2] M. CARRACEDO-SÁNCHEZ[1] J.I. GIL IBARGUCHI[1] L. EGUÍLUZ[2]**

**[1]Department of Mineralogy and Petrology, Faculty of Science and Technology, University of the Basque Country (UPV/EHU)**
Sarriena n/n, 48940 Leioa, Spain

**[2]Department of Geodynamics, Faculty of Pharmacy, University of the Basque Country (UPV/EHU)**
Paseo de la Universidad 7, 01006 Vitoria-Gasteiz, Spain

## ABSTRACT

The Sierra Bermeja Pluton (southern Central Iberian Zone, Iberian Massif) is a late-Variscan intrusive constituted by cordierite-bearing peraluminous monzogranites. Detailed field mapping has allowed to disclose the presence of several NE–SW trending longitudinal composite bodies, formed by either aphanitic or phaneritic mesocratic rocks. According to their petrography and geochemistry these rocks are categorised as calc-alkaline lamprophyres and vaugnerite series rocks. Their primary mineralogy is characterised by variable amounts of plagioclase, amphibole, clinopyroxene, biotite, K-feldspar, quartz and apatite. Broadly, they show low $SiO_2$ content (49–56wt.%), and high $MgO+FeO_t$ (10–17wt.%), $K_2O$ (3–5wt.%), Ba (963–2095ppm), Sr (401–1149ppm) and Cr (87–330ppm) contents. Field scale observations suggest that vaugneritic rocks and lamprophyres would constitute two independent magma pulses. Vaugneritic dioritoids intruded as syn-plutonic dykes, whereas lamprophyres were emplaced after the almost complete consolidation of the host monzogranites. In this way, vaugnerite series rocks would be an evidence for the contemporaneity of crustal- and mantle-melting processes during a late-Variscan stage, while lamprophyres would represent the ending of this stage.

***KEYWORDS*** **Calc-alkaline lamprophyre. Vaugnerite series. Redwitzite. Cordierite-bearing granite. Iberian Massif.**

## INTRODUCTION

Mg-rich ultrapotassic igneous rocks are generally related to volcanic and hypabyssal settings and, among them, lamprophyres are some of the most representative, which usually form subvolcanic dykes, sills, plugs or stocks (Rock, 1991). Calc-alkaline lamprophyres (minettes, kersantites, spessartites and vogesites) constitute a group of rocks enriched in volatiles, Large Ion Lithophile Elements (LILE), alkaline earth and some transition metals (Rock, 1991). Plutonic equivalents of these calc-alkaline types are found across the Variscan Orogeny being referred to with local names such as 'durbachites' (Sauer, 1893), 'vaugnerites' (Fournet, 1837) and 'redwitzites' (Willmann, 1920). Nevertheless, in orogenic areas elsewhere these rocks are known as 'appinites', 'high Sr-Ba granitoids' and 'sanukitoids' (*e.g.* von Raumer *et al.*, 2014 and references therein; Moyen *et al.*, 2017 and references therein).

JOURNAL OF MAPS
2018, VOL. 15, NO. 2, 101–111
https://doi.org/10.1080/17445647.2018.1548981

Science

OPEN ACCESS Check for updates

# The composite Sierra Bermeja Pluton (southern Iberian Massif): science, heritage and geoconservation

Jon Errandonea-Martin [a], Fernando Sarrionandia[b,c], Josu Junguitu[b,c], Manuel Carracedo-Sánchez[a], Luis Eguíluz[b,c] and José Ignacio Gil Ibarguchi[a]

[a]Department of Mineralogy and Petrology, Faculty of Science and Technology, University of the Basque Country UPV/EHU, Leioa, Spain; [b]Department of Geodynamics, Faculty of Pharmacy, University of the Basque Country UPV/EHU Vitoria-Gasteiz, Spain; [c]General Cartography and Geographic Information Systems Service (SGIKER), Lascaray Research Center, University of the Basque Country UPV/EHU Vitoria-Gasteiz, Spain

**ABSTRACT**

The Sierra Bermeja Pluton (~60 km$^2$ surface area) exemplifies a type of controversial granites of the Iberian Massif (European Variscan Belt), the cordierite-bearing 'Serie Mixta' (mixed series) monzogranites. The pluton is included almost completely in the Cornalvo Natural Park (Badajoz, Spain), a relevant target area in Roman times. The geological mapping summarised in the presented map at 1:10,000 scale has revealed a complex intrusive assemblage. Three main cordierite-bearing monzogranite types that show local varieties constitute most of the massif. Monzogranite intrusions are younger towards the centre of the pluton and gave rise to outstanding mappable mingling/mixing zones in some areas. A NE–SW trending reduced dyke complex composed by vaugnerite series rocks, lamprophyres, aplites and quartz dykes, completes the lithological assemblage of the pluton. An inventory of Geologic Points of Interest to promote the geological knowledge of this remarkable protected area and its geoconservation is also presented.

**ARTICLE HISTORY**
Received 12 September 2018
Revised 8 November 2018
Accepted 13 November 2018

**KEYWORDS**
Granite mapping; cordierite-bearing monzogranite; vaugnerite series rocks; lamprophyre; Iberian Massif; geoconservation

## 1. Introduction

Precise geological maps constitute the basis of studies such as those applied in resources exploration, civil engineering, environmental geosciences and natural hazards (Lisle, Brabham, & Barnes, 2011). Indeed, their accuracy is decisive to prevent severe economic and/or human losses, and the progress of the scientific knowledge requires as well accurate maps. This is the case of the Igneous Petrology, where detailed mapping of granitic areas is essential. Granitic rocks dominate the upper continental crust and, since the crust records the evolution of the Earth through time, their study provides essential information about major geological processes (Bonin, Azzouni-Sekkal, Bussy, & Ferrag, 1998; Hawkesworth et al., 2010; Rudnick & Gao, 2014). Igneous intrusions often form large adjacent arrays of multiple plutons (batholiths), in many cases up to several thousands of km$^2$ in surface area (e.g. Strathbogie Batholith in the Lachlan Fold Belt, Sierra Nevada Batholith in the Cordilleran Belt, Gangdese Batholith of Himalaya, Spanish Central System in the Iberian Variscan Belt, etc.), where the study of discrete magma batches is feasible (Pitcher, 1997; Villaseca & Herreros, 2000). In such extensive batholiths, a regional scale mapping could be the best initial approach (e.g. Casini et al., 2015; Martínez Catalán et al., 2007; Porquet et al., 2017). However, as a result of the usual complex assemblage of different magma pulses, detailed maps are mandatory for specific researches (e.g. Cobbing, 2000; Díez Fernández, Martín Parra, & Rubio Pascual, 2017; Díez Fernández, Rubio Pascual, & Martín Parra, 2018, in press; Sarrionandia et al., 2013).

The interest of mapping granitic areas furthermore transcends the purely scientific realms. Granitoids have been highly exploited through History (e.g. Barral I Altet, 1991; Sureda, 1991). In the Egyptian, Greek and Roman Civilisations, granites represented an essential construction material in dams, aqueducts, temples, circuses and other monumental buildings due to their durability (Barral I Altet, 1991; Sureda, 1991; Wilson Jones, 2000). While this use as building or dimension stone still remains, granites are currently prospective targets of maximum interest since modern technologies require granite-related ore deposits for the increasing demand of Rare Earth Elements (REE), precious and critical metals (Chakhmouradian & Zaitsev, 2012; Linnen, Lichtervelde, & Černý, 2012; Sial, Bettencourt, De Campos, & Ferreira, 2011).

Since geology is part of all natural systems, the care for geological heritage is undeniably essential for an

CONTACT Jon Errandonea-Martin jon.errandonea@ehu.eus Department of Mineralogy and Petrology, Faculty of Science and Technology, University of the Basque Country UPV/EHU, Sarriena street N/N, Leioa, Bizkaia 48940, Spain

Lithos 342–343 (2019) 440–462

Contents lists available at ScienceDirect

Lithos

journal homepage: www.elsevier.com/locate/lithos

# Origin of cordierite-bearing monzogranites from the southern Central Iberian Zone – Inferences from the zoned Sierra Bermeja Pluton (Extremadura, Spain)

Jon Errandonea-Martin [a,*], Fernando Sarrionandia [b], Vojtěch Janoušek [c,d], Manuel Carracedo-Sánchez [a], José Ignacio Gil Ibarguchi [a]

[a] Department of Mineralogy and Petrology, Faculty of Science and Technology, University of the Basque Country UPV/EHU, 48940 Leioa, Spain
[b] Department of Geodynamics, Faculty of Pharmacy, University of the Basque Country UPV/EHU, 01006 Vitoria-Gasteiz, Spain
[c] Czech Geological Survey, Klárov 3, 118 21 Prague 1, Czech Republic
[d] Institute of Petrology and Structural Geology, Faculty of Science, Charles University, Albertov 6, 128 43 Prague 2, Czech Republic

ARTICLE INFO

*Article history:*
Received 3 April 2019
Received in revised form 5 June 2019
Accepted 7 June 2019
Available online 12 June 2019

*Keywords:*
Cordierite-bearing monzogranites
Crustal sources
Peraluminous
Late-Variscan
Central Iberian Zone
Iberian Massif

ABSTRACT

Voluminous peraluminous (biotite, biotite–cordierite and cordierite–muscovite-bearing) granitic plutons were emplaced in the southern part of the Central Iberian Zone (Iberian Massif) during the waning stages of the Variscan Orogeny. The role of the mantle and the nature of the crustal sources involved in the generation of these remarkable granites are still a matter of discussion. To address these issues, a detailed study of the Sierra Bermeja Pluton, a ~60 km$^2$ cordierite-bearing monzogranite intrusion representative of the regional Nisa–Alburquerque–Los Pedroches Magmatic Alignment, has been carried out. This pluton was formed by an inward sequence of three distinct but near contemporaneous magma pulses: Outer Unit (OU), Middle Unit (MU) and Inner Unit (IU). The nested pluton is cut by a number of syn-plutonic vaugneritic dykes, while lamprophyres were distinctly later.

The age of the Pluton has been established at ca. 306 Ma (309 ± 3 to 304 ± 3 Ma) by LA-ICP-MS U–Pb dating of zircon and monazite. The peraluminosity (A/CNK = 1.01–1.33) and $P_2O_5$ contents (0.19–0.35 wt%) of the monzogranitic units increase inwards (OU → MU → IU). This is accompanied by an overall decrease in $TiO_2$, MgO, CaO, and $FeO^t$, and most trace-elements, including REE. The three units display similarly low $^{87}Sr/^{86}Sr_{306Ma}$ ratios (0.7033–0.7046) but decreasing $\varepsilon Nd_{306Ma}$ (OU: ~ −2.7, MU: ~ −3.8, IU: −7.5 to −4.7). Vaugneritic rocks have homogeneous composition with similar $^{87}Sr/^{86}Sr_{306Ma}$ ratios (~0.7043) to those of the monzogranites but higher $\varepsilon Nd_{306Ma}$ (~ +1.1) values. Whole-rock geochemical data imply a partial melting of mainly Cambro–Ordovician felsic metaigneous rocks (OU) with increasing proportion of Neoproterozoic–Lower Cambrian metasediments of the Schist–Greywacke Complex (MU) that formed, almost exclusively, the source of the IU. Thermobarometric data suggest that melting processes progressed upward through the geological record and magma emplacement took place at <3 kbar, with crystallization temperatures of 710–810 °C. Geochemical modelling implies that each monzogranitic unit could have evolved independently at the emplacement level by a 20–26% fractional crystallization of a mineral assemblage constituted by Kfs + Pl > Bt >> Ap + Mnz + Xtm. The present results could be extensible to other cordierite-bearing granites of the southern Central Iberian Zone although forthcoming experimental work and detailed comparisons are required to confirm such extrapolation.



## 1. Introduction

Because of the abundance of granitoids in the upper crust, granite petrology constitutes an essential tool to unravel the evolution of continental crust and its recycling in orogenic belts (Hawkesworth et al., 2010; Moyen et al., 2017; Villaseca et al., 2012). Nevertheless, the nature of granitic melts could be controversial since they can result from the extreme fractionation of mantle-derived magmas (e.g. Whalen, 1985), partial melting of crustal sources (metasedimentary/metaigneous; e.g. Chappell and White, 1992; Clemens, 2012), or hybridization of mantle- and crustal-derived magmas (e.g. Annen and Sparks, 2002; Castro et al., 1999; Patiño Douce, 1999). Thus, the partial melting of a variety of magma sources followed by variable magma differentiation mechanisms (e.g. Clemens and Stevens, 2012; Wilson, 1993) results in generation of compositionally diverse granitic magmas. This is the

* Corresponding author.
*E-mail address:* jon.errandonea@ehu.eus (J. Errandonea-Martin).

https://doi.org/10.1016/j.lithos.2019.06.009
0024-4937/

# ABSTRACT

Voluminous peraluminous (biotite, biotite–cordierite and cordierite–muscovite-bearing) granitic plutons were emplaced in the southern part of the Central Iberian Zone (Iberian Massif) during the waning stages of the Variscan Orogeny. The role of the mantle and the nature of the crustal sources involved in the generation of these remarkable granites are still a matter of discussion. To address these issues, a detailed study of the Sierra Bermeja Pluton, a ~60 $km^2$ cordierite-bearing monzogranite intrusion representative of the regional Nisa–Alburquerque–Los Pedroches Magmatic Alignment, has been carried out. This pluton was formed by an inward sequence of three distinct but near contemporaneous magma pulses: Outer Unit (OU; K-feldspar phenocryst-bearing porphyritic monzogranites) → Middle Unit (MU; cordierite-rich monzogranites) → Inner Unit (IU; two-mica leucogranites). Besides, the nested pluton is intruded by a number of syn-plutonic dykes of dioritoids (vaugnerite series rocks) and later calc-alkaline lamprophyres.

The age of the Pluton has been established at *ca*. 306 Ma (309 ± 3 to 304 ± 3 Ma) by LA-ICP-MS U–Pb dating of zircon and monazite. In the same vein, the obtained LA-ICP-MS U–Pb ages on apatite yields an age of 305 ± 17 Ma for the emplacement of the studied vaugnerite series rocks. The peraluminosity (A/CNK = 1.01–1.33) and $P_2O_5$ contents (0.19–0.35 wt. %) of the monzogranitic units increase inwards (OU → MU → IU). This is accompanied by an overall decrease in $TiO_2$, MgO, CaO, and $FeO^t$, and most trace-elements, including REE. The three monzogranite units display similarly low $^{87}Sr/^{86}Sr_{306Ma}$ ratios (0.7033–0.7046) but decreasing $\varepsilon Nd_{306Ma}$ (OU: ~ –2.7, MU: ~ –3.8, IU: –7.5 to –4.7). Studied dioritoids and calc-alkaline lamprophyres show basic to intermediate, metaluminous (A/CNK = 0.71–0.79) compositions, with high $MgO+FeO^t$ values (9.53–16.69 wt. %) and high $K_2O$, Ba, Cr, Sr and Zr contents. Vaugneritic rocks have similar $^{87}Sr/^{86}Sr_{306Ma}$ ratios (~0.7043) to those of the monzogranites but higher $\varepsilon Nd_{306Ma}$ (~ +1.1) values, whereas lamprophyres show Sr–Nd isotopic compositions ($^{87}Sr/^{86}Sr_{306Ma}$: 0.7056; $\varepsilon Nd_{306Ma}$: –2.0 to –2.6) that point to a distinct provenance.

Whole-rock geochemical data imply partial melting of mainly Cambro–Ordovician felsic metaigneous rocks (OU) with increasing input of Neoproterozoic–Lower Cambrian metasediments of the Schist–Greywacke Complex (MU) that formed, almost exclusively, the source of the IU monzogranites. Additionally, these data suggest that hybridization of

vaugneritic magmas did not play a considerable role in the genesis of the studied monzogranites. Thermobarometric data suggest that melting processes progressed upward through the geological record and magma emplacement took place at < 3 kbar, with crystallization temperatures of 710–810 ºC. Geochemical modelling implies that each monzogranitic unit could have evolved independently at the emplacement level by a 20–26 % fractional crystallization of a mineral assemblage constituted by Kfs + Pl > Bt >> Ap + Mnz + Xtm.

The present results could be extensible to other cordierite-bearing granites of the southern Central Iberian Zone although forthcoming experimental work and detailed comparisons are required. At first glance, it seems that the most suitable intrusives are those of the central and eastern areas of the Nisa–Alburquerque–Los Pedroches Magmatic Alignment.

# RESUMEN

Durante las etapas tardías de la Orogenia Varisca grandes volúmenes de plutones graníticos peralumínicos (con biotita, biotita–cordierita, y cordierita–moscovita) se emplazaron en las áreas meridionales de la Zona Centro Ibérica (Macizo Ibérico). El papel que pudo haber jugado el manto y la naturaleza de las fuentes corticales implicadas en la generación de estos granitos singulares es todavía objeto de discusión. Con el fin de avanzar en el conocimiento del origen de estos granitos se ha abordado el estudio detallado del plutón de Sierra Bermeja, una intrusión de ~60 $km^2$ formada por monzogranitos con cordierita, representativa de la Alineación Magmática Nisa–Alburquerque–Los Pedroches. Este plutón se generó por una secuencia de tres pulsos magmáticos principales emplazados próximos en el tiempo: Unidad Externa (OU; monzogranitos porfídicos con fenocristales de feldespato potásico) → Unidad Intermedia (MU; monzogranitos ricos en cordierita) → Unidad Interna (IU; leucogranitos de dos micas). Estas unidades además están intruidas por varios diques sin-plutónicos de dioritoides (rocas de la serie vaugnerítica) y lamprófidos calcoalcalinos tardíos.

La edad del plutón, determinada mediante U–Pb en circón y monacita (LA-ICP-MS), se ha establecido en ~306 Ma (309 ± 3 a 304 ± 3 Ma). De la misma manera, la edad U–Pb obtenida por LA-ICP-MS en apatitos arroja una edad de 305 ± 17 Ma para el emplazamiento de las rocas de la serie vaugnerítica estudiadas. Los índices de peraluminosidad (A/CNK = 1,01–1,33) y los contenidos en $P_2O_5$ (0,19–0,35 wt. %) de las unidades monzograníticas aumentan hacia el interior del plutón (OU → MU → IU). Paralelamente, se observa una disminución general en $TiO_2$, MgO, CaO, y $FeO^t$, así como en la mayoría de los elementos traza, incluyendo las tierras raras. Las tres unidades monzograníticas exhiben similares bajos ratios de $^{87}Sr/^{86}Sr_{306Ma}$ (0,7033–0,7046), mientras que los valores de $\varepsilon Nd_{306Ma}$ descienden hacia el interior del plutón (OU: ~ –2,7; MU: ~ –3,8; IU: –7,5 a –4,7). Los dioritoides y lamprófidos estudiados presentan composiciones básicas-intermedias metalumínicas (A/CNK = 0,71–0,79), con valores altos de $MgO+FeO^t$ (9,53–16,69 wt. %) y contenidos elevados en $K_2O$, Ba, Cr, Sr y Zr. Las rocas vaugneríticas muestran ratios de $^{87}Sr/^{86}Sr_{306Ma}$ similares (~0,7043) a los monzogranitos, pero valores más altos de $\varepsilon Nd_{306Ma}$ (~ +1,1). Por otra parte, los lamprófidos presentan composiciones isotópicas de Sr–Nd ($^{87}Sr/^{86}Sr_{306Ma}$: 0,7056; $\varepsilon Nd_{306Ma}$: –2,0 a –2,6) que sugieren una procedencia distinta a la de los dioritoides.

Los datos de roca total indican la fusión parcial de principalmente rocas Cambro-Ordovícicas félsicas para la formación de la OU, con un mayor aporte de metasedimentos Neoproterozoicos-Cámbricos Inferiores del Complejo Esquisto-Grauváquico en la formación de la MU, que representarían casi por completo la fuente de los monzogranitos de la IU. Adicionalmente, estos datos apuntan a que los procesos de hibridación de los magmas vaugneríticos no jugaron un papel considerable en la génesis de los granitos estudiados. Los datos termobarométricos sugieren que los procesos de fusión progresaron hacia arriba siguiendo el registro geológico, y que el emplazamiento de los magmas se produjo a < 3 kbar, con temperaturas de cristalización de entre 710 y 810 ºC. La modelización geoquímica implica que cada pulso monzogranítico pudo haber evolucionado independientemente, en el nivel de emplazamiento, por un 20–26 % de fraccionación de un conjunto mineral formado por Kfs + Pl > Bt >> Ap + Mnz + Xtm.

Los resultados del presente trabajo podrían ser extrapolables a otros granitos con cordierita de la Zona Centro Ibérica meridional, aunque serían indispensables futuros trabajos experimentales y comparativas más detalladas. A primera vista parece que las intrusiones más apropiadas son aquellas ubicadas en las áreas central y oriental de la Alineación Magmática Nisa–Alburquerque–Los Pedroches.

# LABURPENA

Orogenia Variskarraren azken estaietan plutoi granitiko peraluminikoen (biotita, biotita-kordierita, eta kordierita-muskobitadun) bolumen handiak lekutu ziren Erdialdeko Iberiar Zonan (Iberiar Mazizoa). Granito aipagarri hauen jatorrian mantuak izandako papera eta lurrazaleko iturrien izaera eztabaidagai dira oraindik ere. Gai hauek jorratzeko Nisa–Alburquerque–Los Pedroches Lerrokadura Magmatikoko intrusio adierazgarri baten azterketa zehatza burutu da, kordieritadun monzogranitoz osaturiko ~60 $km^2$-ko azalerako Sierra Bermeja plutoiarena. Intrusio hau hiru pultsu magmatiko desberdin baina ia garaikidez eraikitako barruranzko sekuentzia batez osaturik dago: Kanpoaldeko Unitatea (OU; feldespato potasikozko fenokristaldun monzogranito porfidikoak) → Erdialdeko Unitatea (MU; kordieritan aberatsak diren monzogranitoak) → Barrualdeko Unitatea (IU; bi-mikako leukogranitoak). Bestalde, plutoi hau dioritoidez osatutako dike sin-plutonikoz (vaugnerita serieko arrokak) eta dike lanprofidiko kalkoalkalino berantiarrez intruituta ageri da.

Plutoiaren adina ~306 Ma-tan zehaztu da (309 ± 3-tik 304 ± 3 Ma-ra) zirkoi eta monazitan U–Pb datazioz (LA-ICP-MS). Era berean, LA-ICP-MS bidez apatitoetan lorturiko U–Pb datuek 305 ± 17 Ma-ko enplazamendu adina ematen dute aztertutako vaugnerita serieko arrokentzat. Unitate monzogranitikoen peraluminositatea (A/CNK = 1,01–1,33) eta $P_2O_5$ edukiak (0,19–0,35 wt. %) plutoiaren barrurantz areagotu egiten dira (OU → MU → IU). Hau $TiO_2$, MgO, CaO, $FeO^t$ eta aztarna elementu gehienen (lur arraroak barne) gutxitze orokor batekin ematen da. Hiru unitate monzogranitikoek antzeko $^{87}Sr/^{86}Sr_{306Ma}$ ratio baxuak (0,7033–0,7046) eta geroz eta txikiagoak diren $\varepsilon Nd_{306Ma}$ balioak (OU: ~ –2,7; MU: ~ –3,8; IU: –7,5-tik –4,7-ra) erakusten dituzte. Aztertutako dioritoideek eta lanprofido kalkoalkalinoek konposizio basiko-bitarteko metaluminikoak (A/CNK = 0,71–0,79) dituzte, MgO+$FeO^t$ balio (9,53–16,69 wt. %) eta $K_2O$, Ba, Cr, Sr eta Zr eduki altuekin. Arroka vaugneritikoek monzogranitoen $^{87}Sr/^{86}Sr_{306Ma}$ ratio berdintsuak (~0.7043) baina $\varepsilon Nd_{306Ma}$ balore (~ +1.1) altuagoak dituzte. Era berean, lanprofidoen Sr–Nd konposizio isotopikoek ($^{87}Sr/^{86}Sr_{306Ma}$: 0,7056; $\varepsilon Nd_{306Ma}$: –2,0-tik –2,6-ra) dioritoideen bestelako jatorri bat islatuko lukete.

Datu geokimikoek Kanbriar–Ordobiziarreko arroka metaigneo feltsikoen urtze partziala adierazten dute nagusiki OU-rako, eta Konplexu Eskisto Graubakatsuko Neoproterozoiko–Behe Kanbriarreko metasedimentuen ekarpen handiagoa MU-ren

kasuan, azken iturri honek osatuko lukeelarik funtsean IU-ko monzogranitoen jatorria. Lortutako datuek agerian uzten dute magma vaugneritikoen hibridazioak ez zuela zerikusi aipagarririk izan ikertutako monzogranitoen jatorrian. Datu termobarometrikoek iradokitzen dutenez, urtze prozesua erregistro geologikoan gora eman zen, magmen lekutzea < 3 kbar-etan izanik 710–810 ºC bitarteko kristaltze tenperaturekin. Modelizazio geokimikoak adierazten du hiru unitate monzogranitikoak modu independentean garatu ahal izan zirela lekutze-mailan, Kfs + Pl > Bt >> Ap + Mnz + Xtm mineral elkartearen % 20–26 kristaltze frakzionatu bidez.

Lan honetan lorturiko emaitzak hedagarriak izan litezke Erdialdeko Iberiar Zonaren hegoaldeko beste kordieritadun granitoetara, nahiz eta horretarako etorkizuneko lan esperimentalak eta zehaztasunezko alderaketak nahitaezkoak izan. Lehen begiratuan esan daiteke Nisa–Alburquerque–Los Pedroches Lerrokadura Magmatikoko ekialde eta erdialdeko intrusioak izango liratekela egokienak.

# TABLE OF CONTENTS

# LIST OF TABLES

# LIST OF FIGURES

# CHAPTER 1
# GRANITE MAGMATISM – CURRENT STATE OF THE ART

## 1.1. GRANITE MAGMATISM

Granitic rocks are the most abundant and enigmatic rock-type in the upper continental crust, and have helped over geological time to uphold the landmasses of the Earth stable and elevated at the surface (Bonin *et al.*, 2002; Hawkesworth *et al.*, 2010; Rudnick and Gao, 2014). These common rocks crop out worldwide, often giving rise to impressive landscapes with a characteristic assemblage of landforms that constitute natural protected areas (Fig. 1; Campbell, 1997; Twidale and Vidal Romaní, 2005).

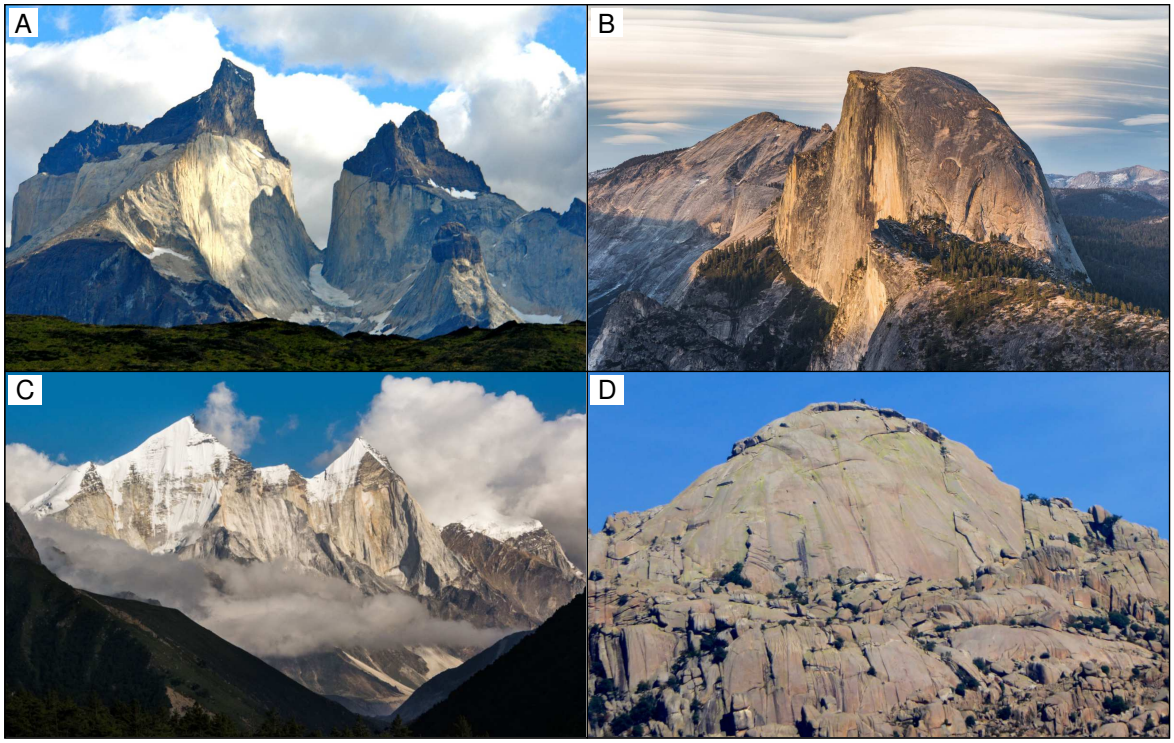


**Figure 1.** A) Cuernos del Paine in the Torres del Paine National Park (Torres del Paine Intrusive Complex, Chile). B) Half Dome in the Yosemite National Park (Tuolumne Batholith; U.S.A.). C) Bhagirathi Peaks in the Garhwal Himalayas (High Himalayan Leucogranite Belt, India). D) El Yelmo Dome in the Sierra de Guadarrama National Park (Spanish Central System Batholith, Spain). Images taken from https://commons.wikimedia.org (A: Proimos, 2011; under license CC-by-2.0; B: Iliff, 2013; under GNU Free Documentation License; C: Prasad, 2014; under the license CC-by-2.0; D: unknown author, 2016; under the Creative Commons Attribution-Share Alike 4.0 International license).

Granitoids (granites–granodiorites–tonalites) are igneous plutonic rocks constituted mainly by quartz, alkali feldspar and plagioclase, accompanied usually by a ferromagnesian mineral phase (Fig. 2; Glazner *et al.*, 2019; Le Maitre *et al.*, 2002; Streckeisen, 1976). The mentioned essential mineral assemblage results from the interaction between many processes, related with melt generation and segregation, magma transport and differentiation, and final emplacement conditions (Barbarin, 1999; Bonin, 2007; Brown, 1977, 2013; Chappel and Stephens, 1988; Chappell and White, 1974, 1992; Clemens, 2003; Clemens *et al.*, 2011; Loiselle and Wones, 1979; Miller, 1985; Sylvester, 1998; Villaseca *et al.*, 1998a).

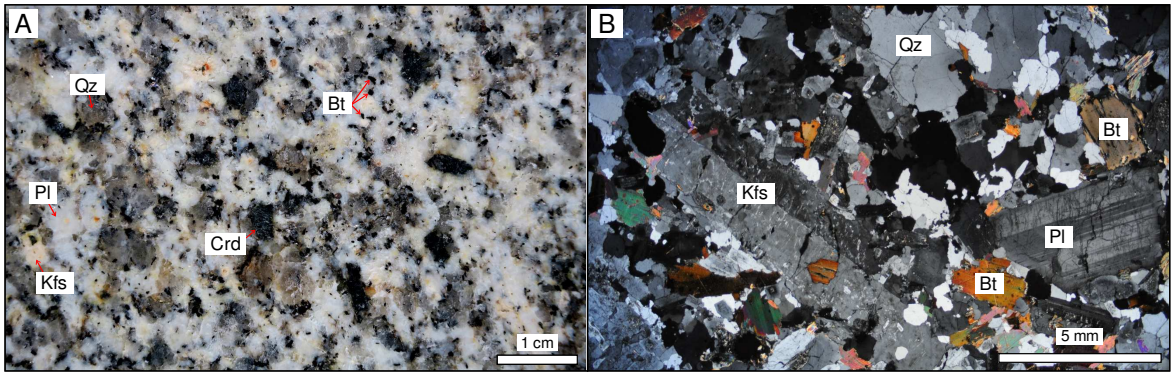


**Figure 2.** A) Scanned polished section of a granite sample, showing the essential mineral assemblage plus cordierite and biotite crystals. B) Optical microphotograph in cross-polarized light showing the essential mineral assemblage plus biotite. Mineral abbreviations from Whitney and Evans (2010).

Since Read (1957) and other early workers (*e.g.* Peacock, 1931), petrologist have attempted to classify the wide granite varieties into specific granitoid series to reveal the crustal processes behind their genesis (*e.g.* Barbarin, 1999; Batchelor and Bowden, 1985; Chappell and White, 1992; De la Roche *et al.*, 1980; Debon and Le Fort, 1983; Frost *et al.*, 2001; Miyashiro, 1970; Pearce *et al.*, 1984; Shand, 1943; Villaseca *et al.*, 1998a). In these sense, these felsic rocks have been related fundamentally to geodynamic environments in which the continental crust has been involved in orogeny, either continental-arc subduction zones or continental-collision settings (Barbarin, 1990, 1999; Bonin *et al.*, 1998; Pitcher,

1987, 1997; Sylvester, 1998). Nevertheless, granites could be also related to continental rifting processes and, in a lesser extent, to mid-ocean ridges and oceanic island arcs (Fig. 3; Barbarin, 1990, 1999; Pitcher, 1987, 1997). Thus, granitoids are polygenetic, and depending on the geodynamic environment, the melts from which are crystallized could result from extreme fractionation of mantle-derived magmas, partial melting of crustal metasedimentary/metaigneous rocks, or mixing/hybridization of mantle- and crustal-derived magmas (Fig. 3; Annen *et al.*, 2006; Barbarin, 1996, 1999; Brown, 1977, 2013; Chappell and White, 1974; Clemens, 2012; Clemens *et al.*, 2011; Didier *et al.*, 1982; Healy, *et al.*, 2004; Miller, 1985; Villaseca *et al.*, 1998a, 2012; Whalen, 1985). The consequence of these igneous processes is that throughout time the continental crust has been differentiated from the mantle, resulting on a lower part constituted by residue or cumulate and/or new mafic crust, and an upper part dominated by granitic to granodioritic rocks (Hawkesworth *et al.*, 2010; Moyen *et al.*, 2017; Rudnick and Gao, 2003, 2014; Spencer *et al.*, 2017).

| | OROGENIC | | | TRANSITIONAL | ANOROGENIC | |
|---|---|---|---|---|---|---|
| granitoid magma / underplated mantle melts | Oceanic Island Arc | Continental Arc | Continental Collision | Post-Orogenic Uplift/Collapse | Continental Rifting, Hot Spot | Mid-Ocean Ridge, Ocean Islands |
| | 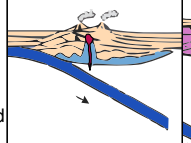 | 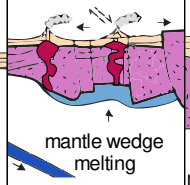 | 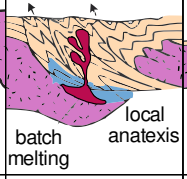 | 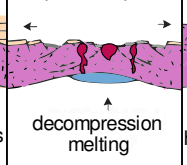 | 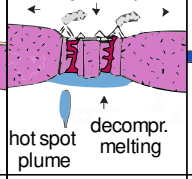 | 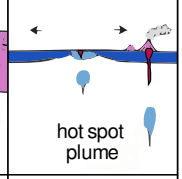 |
| | | mantle wedge melting | batch melting / local anatexis | decompression melting | hot spot plume / decompr. melting | hot spot plume |
| **Chemistry** | calc-alkaline > thol. M-type & I-M hybrid metaluminous | calc-alkaline I-type > S-type metalum. to ± peral. | calc-alkaline S-type peraluminous | calc-alkaline I- S-type (A-type) metalum. to peral. | alkaline A-type peralkaline | tholeiitic M-type metaluminous |
| **Associated minerals** | Hbl > Bt | Hbl, Bt | Bt, Ms, Hbl, Grt, Als, Crd | Hbl > Bt | Hbl, Bt, aegirine fayalite, Rbk, arfved. | Hbl |
| **Origin** | mantle-derived mafic underplate | mantle-deriv. mafic underplate + crustal contribution | recycled crustal material | lower crust + mantle & mid-crust contrib. | mantle and/or lower crust (anhydrous) | mantle + fractional crystallisation |

**Figure 3.** Classification scheme for granitoids based on their tectonic setting (after Barbarin, 1990, 1999; Pitcher, 1987,1997).

## 1.2. MELT GENERATION, SEGREGATION AND ASCENT

Petrogenetic studies of granitic plutons require the understanding of diverse processes that operate on different temporal and spatial scales during melt generation, melt segregation,

magma transport and final emplacement (Brown, 1994; Petford *et al.*, 2000; Pitcher, 1979). The two former processes are usually controlled by external factors (tectonic regime, pre-existing anisotropies), while the last two depend mainly on intrinsic properties of the granitic magma (Belcher and Kisters, 2006).

Experimental data provide quantitative evaluation of P–T–$H_2O$ conditions in the generation of granitic melts. Since Tuttle and Bowen (1958), who dealt with the chemical $NaAlSi_3O_8$ (Ab) – $KAlSi_3O_8$ (Or) – $SiO_2$ (Qz) ternary 'granite system' that simplifies natural granitic melts, numerous experimental studies have been performed to explain the generation of such melts. The formation of granitic magma in the anhydrous lower-crust involves high metamorphic temperatures (T > 650 ºC) to promote the partial melting of the rocks located at high depths (Fig. 4; Clark *et al.*, 2011; Sawyer *et al.*, 2011).

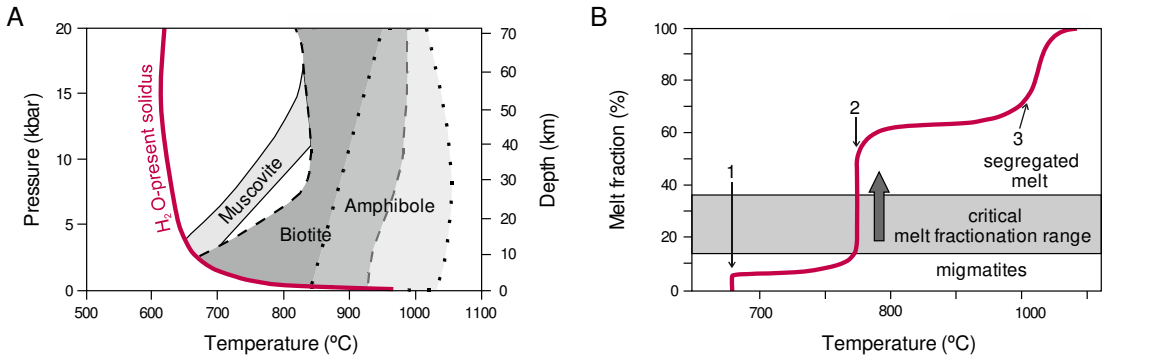


**Figure 4.** A) Simplified P-T phase diagram that shows breakdown fields of different hydrated minerals for thickened continental crust (based on Sawyer *et al.*, 2011). B) Temperature *vs.* melt fraction diagram. 1: muscovite breakdown; quantity of melt depends on modal % of muscovite. 2: biotite breakdown; rapid production of melt. 3: melting of anhydrous phases; gradual increase of melt fraction with T (based on Winter, 2014).

Since the natural state of rocks in the middle-lower crust is solid, an increase of temperature is required to start such melting processes. The temperature increase could be resolved by two main mechanisms of heat production: 1) radioactive decay of heat producing elements (Th, U, K) that are concentrated in crustal rocks (*e.g.* Artemieva *et al.*, 2017; Bea, 2012; Clark *et al.*, 2011; England and Thompson, 1984), or 2) heat transfer by underplating and/or emplacement in the crust of mantle-derived magmas (*e.g.* Annen and Sparks, 2002;

Blundy and Annen, 2016; Bonin, 2004; Patiño Douce, 1999). Another alternative could be the strain heating produced by ductile deformation and friction into shear zones at middle to lower crustal depths (Devès *et al.*, 2014; Nabelek *et al.*, 2010). Under anhydrous conditions, the temperature increase promotes the breakdown of mica and amphibole at 750–800 °C and 850–900 °C temperature ranges, respectively, producing melting reactions that involve these minerals (Fig. 4). Depending on the nature of the source, such melting reactions can generate different melt fractions (Clemens, 2006; Patiño Douce, 1999; Sawyer *et al.*, 2011). In the same way, depending on the availability of free $H_2O$ in the system (fluid-present or fluid-absent melting) the melting temperature varies (lower if it is present) and also the generated melt fraction (larger fraction by fluid-absent incongruent melting; Holtz *et al.*, 2001; Patiño Douce, 1996, 1999; Sawyer *et al.*, 2011).

Under fluid-absent conditions, as occurs at lower crustal levels, a crucial consequence of melting reactions is the volume change of the adjacent rocks. This volume variation generates a local deformation that, coupled with tectonic stress, may originate an increase of permeability in the melting area, allowing the magma segregation (Bons *et al.*, 2004; Petford *et al.*, 2000). The ability of the newly generated melt to segregate depends basically on its density and viscosity, which is a function of its composition, temperature and $H_2O$ content (Brown, 2013; Petford *et al.*, 2000). Deformation is the main acting mechanism during melt segregation, what implies that operating at reduced geological time-scales is unlikely to form large magmatic chambers in the source regions (Brown, 2010; Petford *et al.*, 2000; Petford and Koenders, 1998). As the melt volume increases, the melt fraction connectivity rises, and once reached a minimum of ~ 7 vol.% of melt fraction (commonly around 10–40 vol.%) the melt may escape from the melting area (Fig. 4; Brown, 2010; Petford *et al.*, 2000), leaving the remaining solid refractory material, 'restite', in the source region. Additionally, Brown (2010) suggests that in general terms, 80–90 vol.% of

the available melt is potentially extractable. In these sense, under fluid absent conditions, metapelites, metagreywackes, meta-andesites, and some amphibolites may generate 10–50 vol.% of $H_2O$-undersaturated melts at feasible crustal temperatures (Brown, 2010; Clemens and Vielzeuf, 1987; Montel and Vielzeuf, 1997; Patiño Douce, 1999; Patiño Douce and Beard, 1995; Patiño Douce and Harris, 1998; Patiño Douce and Jhonston, 1991; Vielzeuf and Montel, 1994). If the amount of the newly generated melt is less than the critical fraction to segregate, this may be retained in the source region. At this point, under high-grade metamorphism conditions, composite silicate rocks, known as 'migmatites', are generated, which consist on an ensemble of metamorphic and igneous fraction of rocks (Fig. 4). The newly generated granitic melt will define the leucosome of the migmatite, whereas the restitic material will constitute the melanosome; the mesosome would represent the preserved fraction of the source rock that has endured to the melting process (Pitcher, 1997; Winter, 2014).

During magma ascent, gravity is the main driving force for large-scale vertical transport process (Petford *et al*., 2000). Traditional models that support magma ascent by diapirism, ballooning, stoping, doming or cauldron subsidence (Castro, 1987; Hutton, 1988; Pitcher, 1979) have been replaced by new models that consider narrow conduits, either as self-propagating dykes along pre-existing faults or as an interconnected network of active shear zones (Petford *et al*., 2000 and references therein; Ferre and Galland, 2012).

## 1.3. MAGMA EMPLACEMENT AND EVOLUTION

Magma emplacement occurs when a principally vertical flow switches to a mainly horizontal one, producing the accumulation, inflation and crystallization of the granitic magma (Brown, 2013, Petford *et al*., 2000). Traditionally two emplacement mechanisms have been

distinguished considering regional stress-regime: "forceful" mechanisms that deform the host rocks and "passive" or "permissive" mechanisms that leverage the space generated by regional deformation (Hutton, 1988). Whether forceful or passive mechanism, the so-called 'space problem' or 'room problem' for the incoming magma has led to new emplacement models, which increase the role of tectonics in the space generation, suggesting that emplacement is an episodic process with discrete magma pulses (Brown, 2013; Coleman *et al.*, 2016; Petford *et al.*, 2000). This space-problem may seem easy to solve in stocks, consisting usually of a single intrusion smaller than 100 $km^2$, but it becomes complex for batholiths (> 100 $km^2$ in extent), commonly composed by a number of plutons. Batholiths can be multiple, if all intrusions are of the same composition, and composite if the composition varies. In any case, plutons rarely constitute truly homogeneous bodies in composition, and their internal heterogeneity results on compositionally and/or texturally distinguishable parts, producing a pluton-scale zonation (Paterson and Vernon, 1995; Pitcher, 1997). Mentioned new ascent models that consider narrow conduits and multiple magma pulses, point to geologically short timescales of about tens to hundreds of thousands of years (< 1 Ma) for the emplacement process (*e.g.* Cruden, 1998; Petford *et al.*, 2000).

In collisional settings, since intrusions may occur before, during or after a deformation/metamorphic episode, the structure and textural characteristics of a pluton may differ depending on the timing and depth of emplacement (Pitcher, 1997). Plutons that intrude in the catazone (> 10 km of depth, approximately) are usually syn-tectonic and show gradational contacts with the host rocks (*e.g.* Winter, 2014), which endure high-grade regional metamorphic conditions (450–600 °C). In the mesozone (5–15 km) the country rocks are under low-grade regional metamorphism (300–500 °C), and intrusions may be either syn- or post-tectonic (*e.g.* Winter, 2014). In this context, the existence of a well-developed contact metamorphic aureole is common, and the contact between plutons and

host rocks may be sharp or gradational. Rocks of the contact aureole commonly have a foliated fabric, being common the formation of 'spotted' slates and phyllites. Granitoids emplaced in the epizone (< 8 km, approximately) intrude in a relatively cool (< 300°C) country rock, showing sharp discordant contacts with the host rocks. In these mainly post-tectonic intrusions, hydrothermal alteration and ore mineralization are common, and the development of a contact metamorphism aureole is limited to the size of the intrusion (*e.g.* Winter, 2014).

Before the complete crystallization of the granitic magma at the final emplacement level, several processes may occur leading to magmatic differentiation (Wilson, 1993). Although some authors suggest that processes that might cause magmatic differentiation have not the first-order importance to generate the observed chemical variation within granitoid series (*e.g.* Clemens *et al.*, 2010; Clemens and Stevens, 2012), it is widely accepted that these processes occur and affect the nature of the primary magma at different extent (*e.g.* Bea *et al.*, 1994a; Castro *et al.*, 1999; Garate-Olave *et al.*, 2017; Janoušek *et al.*, 2004; Rodríguez and Castro, 2017; Ugidos *et al.*, 2008). Magma mixing and mingling are one of the most common differentiation processes that petrologists have often resorted to explain the generation of 'hybrid' granitoids, suggesting the interaction of coeval mafic and felsic magmas (*e.g.* Barbarin, 2005; Bonin, 2004; Castro *et al.*, 1999; Gerdes *et al.*, 2000; Janoušek *et al.*, 2004). Evidences of this open-system scenario are the syn-plutonic mafic dykes and mafic microgranular enclaves or mafic magmatic enclaves enclosed in granites, which would represent blobs of coeval mafic magmas (Barbarin, 2005; Bonin, 2004; Castro *et al.*, 1999; Gerdes *et al.*, 2000; Janoušek *et al.*, 2004). Depending on the mixing degree between the felsic and mafic melts, schlieren layers may be formed by disruption of mafic aggregates, or autoliths if they show cumulate textures (Barbarin, 2005; Didier and Barbarin, 1991, Pitcher, 1997). Bulk assimilation of wall rock is another open-system process of differentiation,

accomplished by mechanical disaggregation of absorbed country rock fragments (xenoliths) or by reactive dissolution and precipitation of crystals (*e.g.* Beard *et al.*, 2005; Ugidos *et al.*, 2008). On the other hand, fractional crystallization would constitute the main differentiation mechanism in closed systems. This mechanism consists in the separation or isolation of one or several mineral phases from their coexisting primitive melt, producing an evolved remaining liquid (Bowen, 1928; Wilson, 1993). Crystal entrainment and unmixing (as summarized in Clemens and Stevens, 2012), considers that magmas may contain components from the residual solid of the melting stage, as restites (surmicaceous residues), accessory isolated foreign crystals (xenocryst) and new anhydrous minerals co-formed with the hydrous melt (peritectic phases). Peritectic assemblage entrainment and restite unmixing processes would explain the mixing between melts and above mentioned components (Clemens and Stevens, 2012). Other less widespread processes that cause chemical variation in granitic magmas during ascent and emplacement would be the progressive partial melting, liquid immiscibility, vapour-phase alkali leaching, double-diffusive convection and Soret diffusion, deep-seated magma hybridization in MASH or 'hot' zones, and progressive partial melting (*e.g.* Clemens and Stevens, 2012).

## 1.4. PERALUMINOUS GRANITES

Peraluminous granitoids are defined chemically as rocks with molar $Al_2O_3$ / (CaO + $Na_2O$ + $K_2O$) ratios (expressed as A/CNK) greater than unity, parameter that often is also referred to as Aluminium Saturation Index (ASI; Clarke, 1981; Shand, 1943; Zen, 1988). Thus, if the A/CNK calculation is first corrected for CaO in apatite, these rocks contain more aluminium than that feasible to accommodate by feldspars in a CIPW norm calculation, implying the existence of normative corundum (Zen, 1988). Besides mandatory A/CNK > 1 ratios, a discernible feature of peraluminous granitoids is the presence of characteristic mineral

phases such as cordierite, almandine-rich garnet, muscovite, andalusite, sillimanite, topaz, and tourmaline (the last two require also fluorine and boron, respectively; Zen, 1988; Fig. 5). If the A/CNK ratio is greater than 1.1 and if any of the mentioned characteristic mineral phase is present in the rock, the granitoid must be termed 'strongly' peraluminous (Sylvester, 1998; Zen, 1988). On the contrary, granites that show A/CNK values < 1.1 are denoted 'weakly' to 'moderately' peraluminous. Besides the mentioned characteristic minerals, peraluminous granitoids usually contain biotite, mullite, spinel, and corundum (Clarke, 1981), accompanied by accessory phases as monazite, xenotime, ilmenite, apatite and zircon (Bea, 1996b). Scaillet *et al.* (2016) summarized the crystallization pressures of some mineral phases in peraluminous magmas. According to these authors, in those iron-rich peraluminous magmas, crystallization of garnet at 4–5 kbar occurs at near-liquidus temperatures, forcing the crystallization of cordierite to near-solidus ones, while at low pressures (< 2 kbar) cordierite crystallises at near-liquidus temperatures. Muscovite, often a late-magmatic mineral, is the indicative phase of peraluminous magmas in leucogranites, and although magmatic muscovite is only expected at pressures higher than 3.5 kbar, under high oxygen fugacities, this phase could crystallize at higher temperatures (*e.g.* Scaillet *et al.*, 2016).

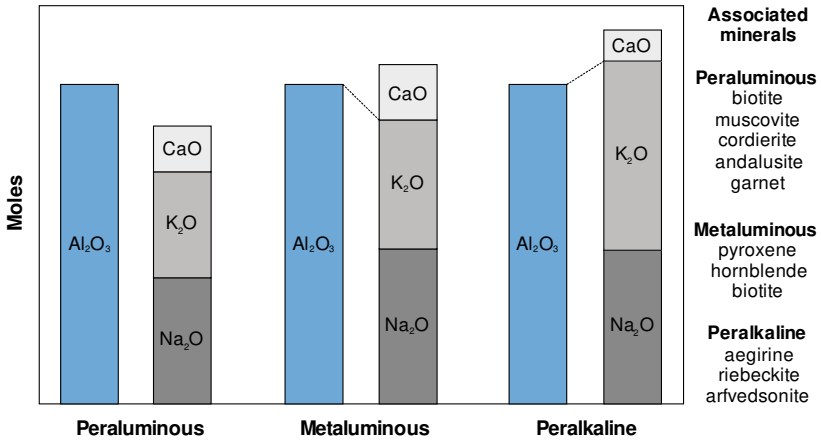


**Figure 5.** Types of alumina saturation based on the A/CNK (molar %) ratio and associated distinctive minerals (after Clarke, 1992).

Peraluminous granitoids are common in orogenic belts, and they constitute one of the major groups of collision-related granitoids (Barbarin, 1996, 1999; Bea *et al*., 1994a; Pitcher, 1987; Sylvester, 1998; Villaseca *et al*., 1998a). Within the different varieties of collision-related granitoids, the strongly peraluminous granites are broadly related to post-collisional settings (*e.g*. Sylvester, 1998). Peraluminous granites can be derived from partial melting of metasedimentary rocks (pelites and greywackes; S-type) or felsic (quartz-feldspathic) metaigneous rocks (I-type), from the fractional crystallization of mafic and metaluminous magmas (amphibolites; I-type), and in a lesser extent from late-stage metasomatic loss of alkalis (*e.g*. Villaseca *et al*., 1998a; Zen 1988). Thus, peraluminous melts are commonly produced by melting of pre-existing crustal materials (Barbarin, 1999; Chappell and White, 1992; Clemens, 2003; Moyen *et al*., 2017; Villaseca *et al*., 2012). Notwithstanding, they display a wide range of petrological and geochemical varieties, and petrologists have resorted frequently to crustal assimilation accompanied by fractional crystallization (AFC) of mafic magmas, or mixing and hybridization of mantle- and crustal-derived magmas to explain the observed differences between these granitoids (Castro *et al*., 1999; García-Moreno *et al*., 2006; Healy, *et al*., 2004; Patiño Douce, 1999).

Some authors have suggested that S- and I-type granites show contrasting whole-rock major element characteristics, although severe overlaps are observed towards high silica contents (*e.g*. Chappell, 1999; Clemens and Stevens, 2012). Among these characteristics stands out the behaviour of $P_2O_5$, which differs in these two types of granitoids with the $SiO_2$ content and A/CNK values (Champion and Bultitude, 2013; Chappell, 1999). Overall, in I-type granitoids $P_2O_5$ shows negative correlation with the $SiO_2$ content and the A/CNK values, reaching up to ~ 0.3 wt.% in $P_2O_5$ for the lowest silica contents and ASI values (*e.g*. Gao *et al*., 2016). On the contrary, these correlations in S-type granites are diffuse, although it seems that $P_2O_5$ may show a positive correlation with

A/CNK ratios, reaching to clearly greater proportions (up to ~ 0.6 wt.%) in the most peraluminous terms (*e.g.* Roda-Robles *et al.*, 2018). Even though the discrimination of the above mentioned S- and I-type peraluminous granites is uncertain, recent studies have shown that in situ zircon O isotope analysis, coupled with the identification of inherited zircons, is a powerful method to unravel the source nature of granitoids (*e.g.* Gao *et al.*, 2016). Despite that some authors have argued in favor of the strong source control in granite genesis (*e.g.* Clemens and Stevens, 2012), the action of the aforementioned magmatic differentiation mechanisms, sometimes undoubtedly significant, produces a wide geochemical variability that makes difficult the identification of the source composition. This identification becomes more complex as peraluminous magmas approach to haplogranitic compositions or highly fractionated terms. Thus, the origin of several peraluminous granites remains controversial.

# CHAPTER 2
# VARISCAN MAGMATISM AND PERALUMINOUS GRANITOIDS IN THE CENTRAL IBERIAN ZONE

## 2.1. VARISCAN COLLISIONAL MAGMATISM IN THE IBERIAN MASSIF

The formation of the Variscan Orogen in Europe is not a continuous process but it resulted from a number of major orogenic cycles developed in the Late Cambrian–Middle Ordovician, Early Silurian–Late Devonian and Carboniferous–Early Permian times (*e.g.* Martínez Catalán *et al.*, 2007; Schulmann *et al.*, 2014). The last episode, that of the Carboniferous–Early Permian, corresponds to the collisional event between Gondwana and Laurussia, and led to the generation of the Variscan Belt and culmination of the ensemble of Pangea (*e.g.* Lefort, 1989; Martínez Catalán *et al.*, 2007; Matte, 2001). The Variscan Belt defines a linear and sinuous trend, with several oroclines that extend along Europe between two main arched segments, the Bohemian Massif and the Ibero-Armorican Arc (*e.g.* Martínez Catalán, 2012; Martínez Catalán et *al.*, 2014). Furthermore, this orogenic belt exhibits different pictures along Europe (*e.g.* Schulmann *et al.*, 2014). The most complete representation of the Variscan European Belt is recorded in the Iberian Massif, located in the southern branch of the Ibero-Armorican Arc (Fig. 6). This massif has been classically divided into distinct tectonostratigraphic zones that, from the Northeast to Southwest, have been termed as Cantabrian, West Asturian-Leonese, Galicia-Trás-os-Montes, Central Iberian, Ossa-Morena and South-Portuguese (Fig. 7; after Farias *et al.*, 1987; Julivert *et al.*, 1972; Lotze, 1945). In the Northwest and Central Iberia a Barrovian gradient, result of the crustal thickening, was followed by a low-pressure/high-temperature (LP/HT)

metamorphism, which promoted an extensive granitic magmatism that occurred during a thermal relaxation stage (*e.g.* Martínez Catalán et *al.*, 2014).

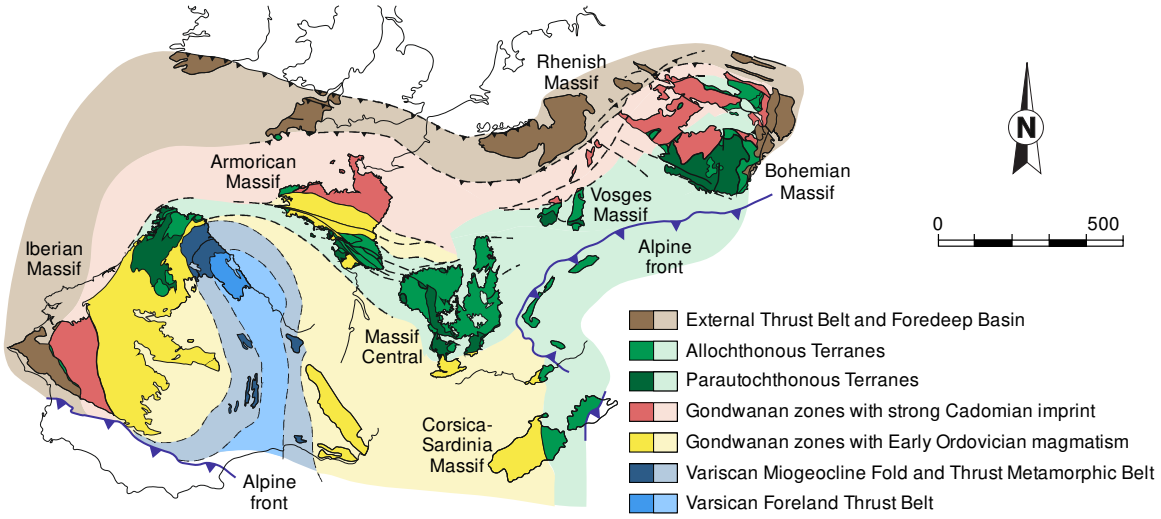


**Figure 6.** Subdivision of the European Variscan Belt that shows the main massifs (simplified from Martínez Catalán *et al.*, 2007).

The mentioned extensive granitic magmatism is one of the distinctive features of the Iberian Massif and is represented by substantial amount of intrusions that occur in all tectonostratigraphic domains apparently without any chronological distribution (Fig. 7; Bea *et al.*, 1999, 2003; Capdevila *et al.*, 1973; Dias *et al.*, 2002; Villaseca *et al.*, 1998b). This Variscan segment recorded a relevant magmatic event that generated large volumes of granitic (*sensu lato*) magmas over 120 Ma, developed mainly in the age range of 330–290 Ma, (*e.g.* Bea *et al.*, 1999, 2003; Carracedo *et al.*, 2005, 2009; Castro *et al.*, 2002; Dias *et al.*, 1998; Gutiérrez-Alonso *et al.*, 2011; Merino Martínez *et al.*, 2014; Orejana *et al.*, 2012; Solá *et al.*, 2009; Villaseca *et al.*, 2012). Iberian Variscan granitoids have been broadly classified in two general groups based on age of emplacement and chemical composition: 1) 'older peraluminous leucogranites', commonly associated with high grade metamorphism, and 2) 'younger peraluminous granodiorites', related with intermediate metaluminous intrusives (after Oen, 1970). Afterwards, a third group was introduced in this classification scheme by Capdevila *et al.* (1973) and Corretgé *et al.* (1977), defining the so called 'Serie

Mixta' (mixed series), with attributes intermediate between those of the two previous types, that is ranging in composition from abundant monzogranites to subordinate granodiorites, and of peraluminous character in general. Still, the chemical compositions of the rock-types that constitute these groups overlap.

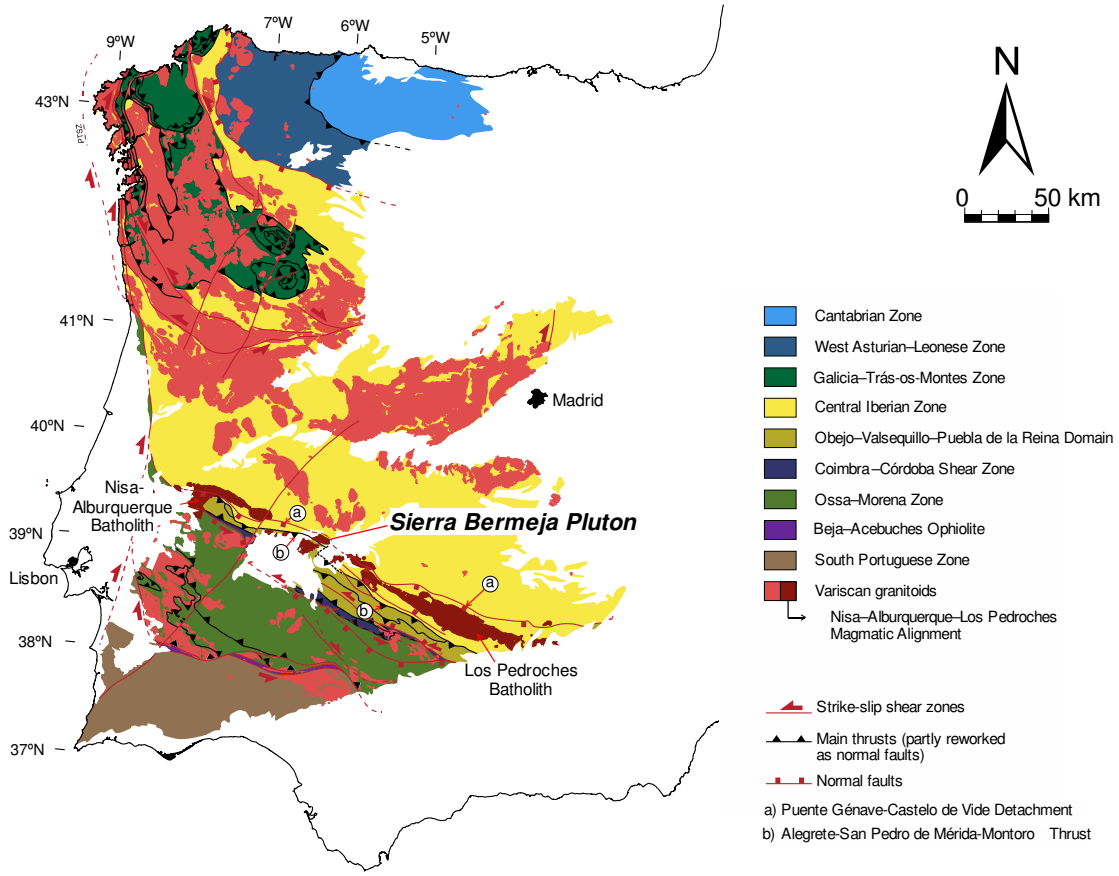


**Figure 7.** Geological sketch map of the Iberian Massif. The Nisa–Alburquerque–Los Pedroches Magmatic Alignment is emphasised. The subdivision of the Iberian Massif is after Farias *et al.* (1987), Julivert *et al.* (1972), and Lotze (1945); the extent of the Obejo-Valsequillo-Puebla de la Reina Domain is based on Bandrés *et al.* (2004) and Martín Parra *et al.* (2006); Variscan granitoids adapted from Rodríguez Fernández and Oliveira (2015); and major tectonic elements adapted from Díez Fernández and Arenas (2015).

Several authors have attempted to group Iberian granitoids based also on geochronological data (Días *et al.*, 1998; Ferreira *et al.*, 1987; Valle Aguado *et al.*, 2005). Nevertheless, the large geochemical variations and wide geochronological ranges make difficult their classification. Similarly to Capdevila *et al.* (1973) and Corretgé *et al.* (1977), Castro *et al.* (2002) proposed three suites of granitoids ('granodioritic suite', 'monzogranitic

suite with Crd', and 'peraluminous and leucogranitic suite'), avoiding the employment of emplacement ages. In this classification scheme, the distinguished suites roughly coincide with the aforementioned three groups of Variscan Iberian granitoids.

More recently, Villaseca (2011) proposed four series of S-type granites for the Central Iberian Zone of the Iberian Massif, besides another series with I-type affinity (classification scheme detailed in Roda-Robles *et al.*, 2018). The '$S_1$ suite', composed mainly by two-mica leucogranites, represents the first important Variscan magmatic event in the Central Iberian Zone. Leucogranites of this suite exhibit marked higher P contents than other granitoids and have been interpreted as melt fractions derived from either mid-to-lower crustal metasediments or, in a lesser extent, peraluminous metaigneous rocks (*e.g.* Roda-Robles *et al.*, 2018 and references therein). The '$S_2$ suite' corresponds to P-rich highly peraluminous granites, most of them cordierite-bearing monzogranites usually with $Al_2SiO_5$ polymorphs. Monzogranites of this suite were commonly emplaced at epizonal levels, after the $S_1$-type leucogranites, and would probably derived from metasedimentary sources (*e.g.* Roda-Robles *et al.*, 2018 and references therein). The P-poor moderately peraluminous granites of the '$S_3$ suite' enclose a wide range of petrographic varieties (from tonalites to two-mica leucogranites) that usually include mafic microgranular enclaves. These granitoids lack of $Al_2SiO_5$ polymorphs, and could have been derived from felsic to intermediate metaigneous sources (*e.g.* Roda-Robles *et al.*, 2018 and references therein). The '$S_4$ suite' corresponds to moderately- to low-peraluminous granites ('Early Granodiorites' of Capdevila *et al.*, 1969), comprising biotite-bearing granitoids without any indicative minerals of either peraluminous or metaluminous affinity. $S_4$-type granitoids have been interpreted as lower crustal melts derived from metagreywackes and felsic metaigneous sources that locally appear hybridized with mantle-derived melts. Finally, metaluminous to low peraluminous biotite- (± amphibole) bearing granitoids constitute the low peraluminous

'I-type granite suite', which points to a deep crustal meta-igneous source derivation (*e.g.* Roda-Robles *et al.*, 2018 and references therein). Apparently, the spatial distribution along the Central Iberian Zone of these suites do not show a particular pattern. Nevertheless, in the southern areas three main magmatic alignments, trending roughly NW–SE, may be discerned (see Figure 1 of Errandonea-Martin *et al.*, 2017). These alignments are known, from North to the South as: 1) Montes de Toledo, constituted by $S_2$- and $S_3$-type granitoids; 2) Cáceres-Valdepeñas, composed almost entirely by $S_2$-type monzogranites; and 3) Nisa–Alburquerque–Los Pedroches, with $S_2$-, I-type and other granitoids (*e.g.* Aparicio, 1977; Roda-Robles *et al.*, 2018; Errandonea-Martin *et al.*, 2017).

## 2.2. CORDIERITE-BEARING MONZOGRANITES OF THE CENTRAL IBERIAN ZONE

The cordierite-bearing monzogranites that correspond to the so called 'Serie Mixta' granitoids of Capdevila *et al.* (1973) and Corretgé *et al.* (1977), known also as the 'monzogranitic (+Crd) suite' (Castro *et al.*, 2002) or the 'P-rich highly peraluminous granite suite ($S_2$)' (Roda-Robles *et al.*, 2018) crop out in the central and southern areas of the Central Iberian Zone, intruding mainly the Neoproterozoic-Early Cambrian metasedimentary sequence of the Schist-Greywacke Complex (*e.g.* Castro *et al.*, 2002; Roda-Robles *et al.*, 2018).

These granites are generally late with respect to the main Variscan deformation stage and metamorphic peak, and usually constitute either allochthonous epizonal plutons or irregular patches showing transitional contacts with biotite granodiorites that hold mafic microgranular enclaves of tonalitic composition (Bea, 2004; Capdevila *et al.*, 1973; Castro *et al.*, 2002; Carracedo *et al.*, 2005, 2009; Corretgé, 1971; Corretgé *et al.*, 1977, 2004;

García-Moreno *et al*., 2007). Among the petrographic characteristics of these monzogranites stands out their: 1) relatively abundant large K-feldspar phenocrysts, 2) high cordierite contents, 3) prevalence of normal zonation in plagioclase with Ca-poor rims and often complex resorbed Ca-rich cores, and 4) complex assemblage of accessory minerals including: apatite, monazite, xenotime, ilmenite, zircon, andalusite/sillimanite, garnet and tourmaline (Alonso Olazabal, 2001; Alonso Olazabal *et al*., 1999; Capdevila *et al*., 1973; Carracedo, 1991; Carracedo *et al*., 2009; Castro *et al*., 2002; Corretgé *et al*., 1977, 2004; González Menéndez, 1998; Larrea, 1998). Geochemically, these monzogranites have relatively low CaO and high $P_2O_5$ contents, showing a highly peraluminous character and a marked perphosphorous trend. Additionally, in some cases they show notable coincidences in isotopic signatures (Sr, Nd, O, Hf) with the surrounding pelite and greywacke sequences of the Schist-Greywacke Complex (*e.g.* Antunes *et al*., 2008; Castro *et al*., 1999; Chicharro *et al*., 2014; García-Moreno *et al*., 2007; González Menéndez, 1998; Merino Martínez *et al*., 2014; Pesquera *et al*., 2017; Ramírez and González Menéndez, 1999).

The origin of these cordierite-bearing monzogranites of the Iberian Massif has led to a long discussion over the years after their first characterization by Capdevila *et al*. (1973) and Corretgé *et al*. (1977). Still currently the controversy sits between a hybrid (crustal + mantle) or exclusively crustal origin. The hypothesis of a hybrid origin is supported by the fact that coeval mantle-derived magmas are found in the Central Iberian Zone, by Sm–Nd isotope relationships that indicate some magmatic trends from gabbros to peraluminous granodiorites, and by different experimental studies (*e.g*. Castro *et al*., 1999; García-Moreno *et al*., 2006, 2007). According to Castro *et al*. (1999), the possible genetic link between juvenile mantle-derived materials and the studied granitoids considers two mechanisms: 1) mantle participation during the generation of the source rocks of the granitoids, and 2) incorporation of mantle-derived magmas at the time of granitoids generation. The main

outcome is that the second mechanism implies a significant role of hybridisation by assimilation and/or magma mixing processes on the origin of these monzogranites. This hypothesis has been considered in many case studies, often suggesting the contribution of the metasedimentary rocks of the Schist-Greywacke Complex (*e.g.* Alonso Olazabal, 2001; Alonso Olazabal *et al.*, 1999; Carracedo, 1991; Carracedo *et al.*, 2009; Larrea, 1998; Larrea *et al.*, 1992; Pesquera *et al.*, 2017). Furthermore, the dissolution of microgranular mafic magmatic enclaves of tonalitic composition during the magma ascent may also explain the hybridisation of mafic and felsic magmas on the genesis of these granitoids (García-Moreno *et al.*, 2006, 2007). In this case, a two-component process of assimilation is suggested, requiring the interaction, in two stages, between pure anatectic leucogranitic melts and both country rocks and tonalitic rocks (*e.g.* García-Moreno *et al.*, 2006, 2007).

On the contrary, several authors have argued in favor of a pure crustal origin to explain the genesis of these cordierite-bearing monzogranites, pointing to melting of either metasedimentary or metaigneous sources (Chicharro *et al.*, 2014; Corretgé *et al.*, 1985; Donaire *et al.*, 1999; Errandonea-Martin *et al.*, 2017; González Menéndez, 1998, 2002; Gonzalo, 1987, 1988; Merino Martínez *et al.*, 2014; Ramírez and González Menéndez, 1999; Ugidos, 1988; Ugidos and Recio, 1993). In this case, the possible hypothesis for the origin of these controversial granites may be summarized as follow: 1) derivation from metasedimentary sequences similar to those metasediments of the regional Schist–Greywacke Complex of the southern Central Iberian Zone (Chicharro *et al.*, 2014; Corretgé *et al.*, 1985; González Menéndez, 1998, 2002; Merino Martínez *et al.*, 2014; Ramírez and González Menéndez, 1999); 2) partial melting of mixed metasedimentary + metaigneous rocks from the lower crust, followed by the assimilation of cordierite-bearing country rocks (Ugidos, 1988; Ugidos and Recio, 1993); 3) provenance from transitional, mafic to intermediate source rocks from the lower crust (Donaire *et al.*, 1999); and 4) partial melting

of felsic metaigneous rocks similar to those Lower Paleozoic metavolcanics and granitic orthogneisses from Central Iberia (Errandonea-Martin *et al*., 2017). These hypotheses of an exclusively crustal origin are consistent with major- and trace-elements geochemical compositions of the studied intrusions, as well as their isotopic (Sr, Nd, O and Hf) characteristics and identified pre-Variscan zircon inheritances. Thus, as it may be observed, despite their relative abundance in the southern areas of the Central Iberian Zone, there is not yet consensus about their origin.

## 2.3. THE NISA–ALBURQUERQUE–LOS PEDROCHES MAGMATIC ALIGNMENT

The main event of magmatic activity within the southern areas of the Iberian Massif took place during late stages of the Variscan orogeny (Pennsylvanian; Carracedo *et al*., 2009; Gutiérrez-Alonso *et al*., 2011; Solá *et al*., 2009) and is almost entirely confined to the so-called Nisa–Alburquerque–Los Pedroches Magmatic Alignment (Figs. 7 and 8). This alignment is constituted by a series of granitoids that crop out along ~ 400 km following a N140ºE direction and includes two types of granitoids: 1) metaluminous, K-rich, calc-alkaline biotitic (± amphibole) granodiorites (*e.g*. Carracedo, 1991; Carracedo *et al*., 2009; Donaire, 1995; Donaire *et al*., 1999; Fernández Ruiz, 1987; Larrea, 1998), and 2) peraluminous cordierite-bearing K-rich monzogranites of the 'Serie Mixta' (*e.g*. Alonso Olazabal, 2001; Alonso Olazabal *et al*., 1999; Carracedo, 1991; Carracedo *et al*., 1990, 2009; Fernández *et al*., 1990; García-Casco *et al*., 1989; González Menéndez, 1998, 2002; Fernández Ruiz, 1987; Larrea, 1998; Larrea *et al*., 1992; Solá *et al*., 2009). Over the years, several authors have supported that cordierite-bearing monzogranites were emplaced later than the metaluminous granodiorites (*e.g*. Castro *et al*., 2002; Larrea *et al*., 2004). Nonetheless, current available radiometric data and field relationships indicate that

metaluminous granodiorites and peraluminous monzogranites were emplaced almost simultaneously in a relatively narrow time range of *ca.* 305–314 Ma (Fig. 8; Carracedo, 1991; Carracedo *et al.*, 2009; Gutiérrez-Alonso *et al.*, 2011; Solá *et al.*, 2009).

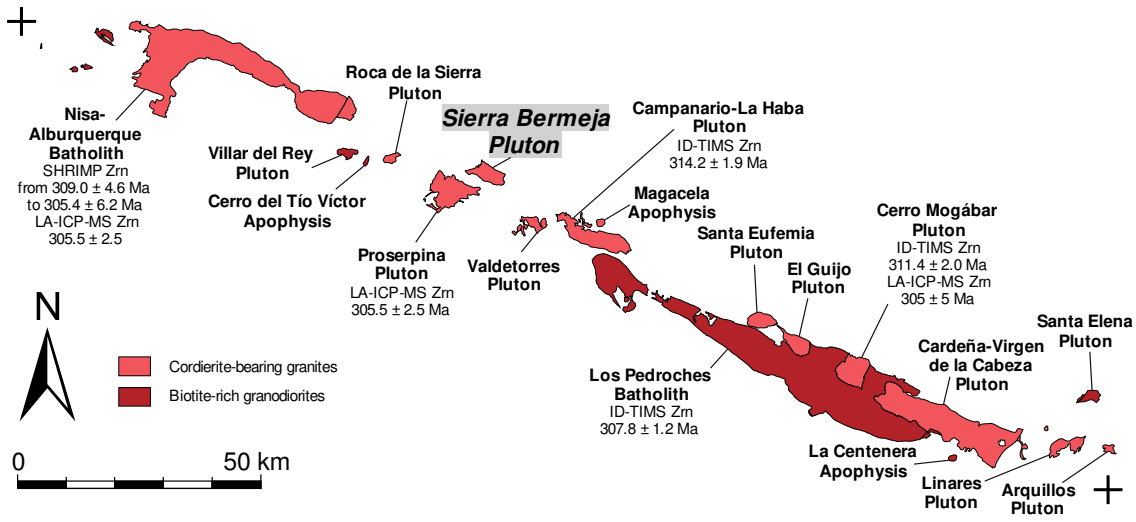


**Figure 8.** The Nisa–Alburquerque–Los Pedroches Magmatic Alignment. U-Pb Zircon geochronological data taken from Carracedo *et al.* (2009), Gutiérrez-Alonso *et al.* (2011) and Solá *et al.* (2009). Cross from the top left: X = 555 000; Y = 4 374 000 (UTM 29), and cross of the lower right: X = 459 000; Y = 4 205 000 (UTM 30).

Concerning the eastern sector of this magmatic alignment, in the Los Pedroches Batholith, structural, kinematic and magnetic susceptibility data indicate that the ascent and emplacement of this batholith was controlled by a crustal scale dextral transtensional shear zone (Carracedo *et al.*, 1994; Aranguren *et al.*, 1997). This regional transtensional shear zone is interpreted as a lateral ramp that accommodated the crustal thinning developed in the Central Iberian Zone during the collapse of the Iberian Variscan belt (Aranguren *et al.*, 1997). Similarly, the emplacement of the Campanario-La Haba Pluton would have been synkinematic with respect to a dextral strike-slip regime associated to the mentioned crustal-scale regional shear-zone (*e.g.* Alonso Olazabal *et al.*, 1999). On the contrary, a passive emplacement is suggested for the emplacement of the Nisa–Alburquerque Batholith, through a main feeding root in its eastern sector and through narrow conduits in the west (González Menéndez, 2002; González Menéndez and Bea, 2004; González Menéndez *et al.*, 2011).

Granitic magmas of this magmatic alignment were emplaced at shallow levels (< 4 kbar), generating contact metamorphic aureoles of up to 3000 m wide (Alonso Olazabal, 2001; Alonso Olazabal *et al*., 1999; Carracedo, 1991; Fernández Ruiz, 1987; González Menéndez, 1998; González Menéndez and Azor, 2003; González Menéndez *et al*., 2011). According to their whole-rock geochemical characteristics and Sr–Nd isotope systematics, the above mentioned two type of granitoids could have been derived from the same (Donaire et al., 1999) or contrasting sources (Carracedo et al., 2009 and references therein). Metaluminous granodiorites could derive from exclusively crustal sources (Donaire *et al*., 1999; Roda-Robles *et al*., 2018), although some authors have supported a hybrid (mantle + crustal) origin (Carracedo, 1991; Carracedo *et al*., 2009 and references therein; Larrea, 1998). Likewise, there is no consensus either for the 'Serie Mixta'-type granites from this alignment, since in the studied cases it has been advocated an origin by melting of pelites and greywackes (*e.g*. González Menéndez, 1998; Roda-Robles *et al*., 2018 and references therein) or mafic to intermediate metaigneous crustal sources (Donaire *et al*., 1999), and even by hybridization of mantle and crustal materials (*e.g*. Alonso Olazabal, 2001; Alonso Olazabal *et al*., 1999; Carracedo, 1991; Carracedo *et al*., 2009; Larrea, 1998).

## 2.4. MANTLE ROLE IN THE GENESIS OF THE IBERIAN VARISCAN GRANITOIDS

In the Iberian Massif, lamprophyres, vaugnerite series rocks and late-orogenic granitoids occur spatially related in many cases (Barbero *et al*., 1990; Bea *et al*., 1999; Gallastegui, 2005; Gil Ibarguchi *et al*., 1984; López-Moro *et al*., 2017; Scarrow *et al*., 2009). Nevertheless, the linkage between mantle-derived magmas and host granitoids is controversial in view of the currently most followed petrogenetic models (see previous section). In this sense, some authors argue that mantle-derived magmas (mostly vaugnerites

and appinites) were coeval or slightly older than crust-derived granitoids, providing only heat supply, albeit not enough for the generalized granitoid formation, hence, implying a totally independent genesis (Barbero *et al.*, 1990; Bea *et al.*, 1999; Gallastegui, 2005; Gil Ibarguchi *et al.*, 1984; López-Moro *et al.*, 2017; Scarrow *et al.*, 2009). Alternatively, other hypotheses suggest that mantle-derived magmas (gabbros and vaugnerites) and granitoids would be coeval and, besides the heat supply, the mafic magmas would be involved (by mixing and/or hybridization) in the genesis of S-type granitoids (*e.g.* Alonso Olazabal *et al.*, 1999; Carracedo *et al.*, 2009; Castro *et al.*, 1999; Dias *et al.*, 2002). Other mantle-derived magmas, represented by alkaline lamprophyres emplaced markedly after the granitoids in a late- to post-collisional stage (Bea *et al.*, 1999; Orejana *et al.*, 2008; Scarrow *et al.*, 2011).

Variscan rocks of vaugneritic affinity have been described particularly in central Europe areas (Buda and Dobosi, 2004; Buzzi *et al.*, 2010; Holub, 1997; Janoušek *et al.*, 1995; Kováříková *et al.*, 2007; Siebel *et al.*, 2003) and the Massif Central (Galán *et al.*, 1997; Michon, 1987; Montel, 1988; Montel and Weisbrod, 1986; Sabatier, 1980, 1991). Within the Iberian Massif, such type of rocks have also been identified in the following areas: i) West of Galicia (Gallastegui, 2005; Gil Ibarguchi, 1980, 1981; Gil Ibarguchi *et al.*, 1984), ii) North of Portugal (Dias and Leterrier, 1994; Dias *et al.*, 2002), iii) the Tormes Dome (López-Moro and López-Plaza, 2004; López-Moro *et al.*, 2017; López Plaza *et al.*, 1999), iv) the Toledo Anatectic Complex (Barbero, 1992; Barbero *et al.*, 1990; Bea, 2004; Bea *et al.*, 2006) and, v) the Ávila Batholith (Scarrow *et al.*, 2009).

Currently, vaugnerites are a focus of discussion in terms of their geodynamic significance, relative to their emplacement timing in the frame of the Variscan Orogenesis, and the role of mantle sources in their genesis (*e.g.* Couzinié *et al.*, 2014, 2015, 2016; Kubínová *et al.*, 2017 and references therein; Laurent *et al.*, 2015; Moyen *et al.*, 2017 von Raumer *et al.*, 2014). Vaugneritic magmas seem to derive from a heterogeneous

metasomatized mantle, being emplaced during late- to post-collisional extensional stages (Couzinié *et al.*, 2016; Holub, 1997; Janoušek and Holub, 2007; Scarrow *et al.*, 2009; Solgadi *et al.*, 2007; von Raumer *et al.*, 2014). As for the emplacement timing of the lamprophyres, and thus, their geodynamic significance, this is more debatable since they could indicate a late-collisional transtensional stage (*e.g.* Scarrow *et al.*, 2011), or an anorogenic passive rifting stage (*e.g.* Orejana *et al.*, 2008). Despite this unresolved matter, it seems that at least in the case of the calc-alkaline lamprophyres, which would be derived (as vaugnerites) from a metasomatised mantle source, their emplacement is related to the late-orogenic stages of the Variscan Orogeny (Turpin *et al.*, 1988). Whatever the case, the scarcity of mantle-derived rocks in the Iberian Massif (*e.g.* Bea *et al.*, 1999; Villaseca *et al.*, 1998a) compared with the huge volume of spatially related (and occasionally coeval) granitoids is an open question and calls for more detailed studies of these rocks.

# CHAPTER 3
# INTRODUCTION TO THE CASE STUDY

## 3.1. AIMS AND OBJECTIVES

The main target of this PhD project is to contribute to the progress of the scientific knowledge about the controversial cordierite-bearing monzogranites of the Iberian Massif. For this purpose, it has been selected a representative igneous massif, known in the regional literature as the Sierra Bermeja Pluton, which forms part of the Nisa–Alburquerque–Los Pedroches Magmatic Alignment (Figs. 7 and 8). Thus, the aim of the present research is to provide a new detailed geological map coupled with a petrographic and geochemical characterization (mineral and whole-rock major–trace–isotopic), to decipher the origin of these particular monzogranites as regards their sources, magma differentiation mechanisms, and emplacement age and P-T conditions. Considering the above, the specific objectives of this PhD project are those listed below:

I) Development of an accurate geological map of the Sierra Bermeja Pluton, since precise geological maps constitute the basis of petrological studies. Apart from the purely scientific interest for those studies, the geological map would be applied also in resources exploration, civil engineering, environmental geosciences and natural hazards (*e.g.* Lisle *et al.*, 2011).

II) Detailed petrographic characterization of the mapped igneous rocks from the Sierra Bermeja Pluton, both at field scale and under the microscope, as well as the establishment of their relationships and with the host rocks.

III) Mineralogical and whole-rock geochemical characterization of the studied rocks, regarding major- and trace-elements, as well as isotopes (Rb–Sr and Sm–Nd systematics).

IV) Determination of the magma sources, crystallization/emplacement ages and P-T conditions for the main distinguished granite-types.

V) Calculation of a geochemical modelling to unravel the main magmatic differentiation mechanism responsible of the observed geochemical variation within the distinguished monzogranites from the Sierra Bermeja Pluton.

VI) Development of a petrogenetic model for the Sierra Bermeja Pluton, which can be extensible to other several cordierite-bearing monzogranites of the Central Iberian Zone.

Nonetheless, the results of this PhD project would transcend the purely scientific-geological realm, since they could be applied in other areas too:

A) In the Iberian Massif, some peraluminous granitoids, similar to those of the Sierra Bermeja Pluton are petrogenetically linked to aplite-pegmatite bodies that hold strategic resources of economic interest (*e.g.* Roda-Robles *et al.*, 2016, 2018). Therefore, the petrogenetic study of this PhD may provide valuable information for future exploration surveys of Rare Earth Elements (REE), as well as precious and critical metals, highly demanded in modern technologies (*e.g.* Chakhmouradian and Zaitsev, 2012; Linnen *et al.*, 2012; Sial *et al.*, 2011).

B) Since the Sierra Bermeja Pluton is encompassed in part within a protected area of remarkable natural interest, the Cornalvo Natural Park, the obtained results in the present project would contribute in the geological knowledge of this protected region. Protected areas such as National Parks or Natural Reserves are indispensable safeguarding landscape features and rock exposures (*e.g.* Dingwall, 2000), since the preservation of geological entities involves the protection of the space where those entities are found (*e.g.* Carreras and

Druguet, 2000). Likewise, the geological knowledge of such areas is essential for the effective nature conservation and preservation of the geological heritage (*e.g.* Brilha, 2002).

C) On account of the innumerable Roman vestiges in the studied area, related to the colony of Emerita Augusta, this research may contribute to a better identification of the employed construction (granitic) materials, and would open future works about the extraction areas of such building elements. Granitoids have been highly exploited through History, especially in the Egyptian, Greek and Roman Civilizations, representing an essential construction material in dams, aqueducts and monumental buildings due to their durability (*e.g.* Barral I Altet, 1991; Sureda, 1991; Wilson Jones, 2000). Thus, future works in the Sierra Bermeja Pluton would provide historical and archaeological information of interest regarding quarry and mining techniques in Roman Era.

Finally, despite the fact that the PhD thesis usually implicitly entails the idea, if the PhD is comprehended as an academic learning and/or training process, one of the principal purposes of this research should be the acquirement of competencies, aptitudes and skills, as petrologist in this case, by the PhD student. Thus, the culmination of the learning/training process would be the achievement of the doctoral degree.

## 3.2. METHODS

Considering the stated objectives, the development of this research required different areas of work that comprise geological mapping, petrography, mineral chemistry, whole-rock geochemistry (major- and trace-elements; isotopes) and geochronology. The here presented PhD project was carried out from 2015 to 2019, applying a traditional methodology that consist on field-, laboratory and office work.

### 3.2.1. Fieldwork

Preliminary research was made by means of the interpretation of Light Detection And Ranging (LiDAR) images of 5 m resolution and ortophotographs of the National Plan of Aerial Ortophotography (PNOA, 2009, 2011, 2013). Image analysis allowed the location of the main outcrops, planning of field itineraries and delineation of the contact between granites and host rocks. This preliminary map design was at 1:25000 scale, using the Mirandilla (0752-IV), Carmonita (0752-II) and Conquista del Guadiana (0753-III) sheets of the Topographic Map of Spain (MTN).

The fieldwork in this PhD project was extensive, and although in current PhD Theses fieldwork is being left out, in this case it represents the basis of all subsequent work. The fieldwork scale was 1:5000, establishing 447 observation stations (7–8 station/km$^2$) georeferenced by a Geographical Positioning System (GPS) receiver. During 42 days of fieldwork the most representative outcrops were described in detail in terms of rock structure, texture, fabric and mineralogy. In order to determine the different rock types that constitute this pluton, a series of criteria were defined. Rocks classification in each observation station following these criteria allowed to establish the rock lithotypes with a high level of detail, resulting in a high quality geologic map of the Sierra Bermeja Pluton (Supplementary map of the Appendix).

Additionally, detailed field observations allowed to determine the emplacement timing relationships between these rock types. Meanwhile, 137 rock-samples (~2 sample/km$^2$) were collected for their petrological characterization, and concurrently an inventory of 28 Geological Point of Interest and 5 sites of interest (SI) was generated in order to contribute in the Geological Heritage of the Cornalvo Natural Park (Table 15 of the Appendix).

### 3.2.2. Laboratory work

For the petrographic characterization, classical hand specimens of each sample and ~ 300 thin sections (48 mm x 28 mm in size, and 30 μm thick) were prepared by the Technical Service of the University of the Basque Country (UPV/EHU). A number of these thin sections were stained following techniques of Friedman (1971), modified by Marsaglia and Tazaki (1992). The thin sections were exposed to a concentrated hydrofluoric acid before immersing in a supersaturated solution of sodium cobaltinitrite, and subsequently in a supersaturated solution of barium chloride.

Petrographic studies of thin sections were carried out using a polarizing microscope Leica DM LP model fitted with a CCD camera, and the proportions of rock-forming minerals were obtained by point-count modal analyses (~2000 points/sample in phaneritic rocks and ~600 points/sample in the aphanitic ones) and scanned sections image processing, both in the Mineralogy and Petrology Department of the UPV/EHU (Table 1 for a summary of monzogranite features, Table 2 for mesocratic rocks, and Table 1 of the Appendix for full data set of monzogranite modal analyses).

Within the collected 137 rock-samples, 53 were selected for the mineralogical and geochemical study, comprising 35 monzogranites, 7 dioritoids, 8 lamprophyres and 3 Mafic Microgranular Enclaves (Table 12 of the Appendix for their location). Mineralogical study was performed by means of Electron Microprobe (EMP) and Laser Ablation Inductively Coupled Plasma Mass Spectrometry (LA-ICP-MS) analyses, performing a total of ~ 700 spots by EMP and ~ 80 spots by LA-ICP-MS. EMP analyses, for major element determinations in mineral phases, were performed on thin sections at the University of Oviedo using a Cameca SX100 instrument. Operating conditions of the microprobe were 10 s counting time (peak), ~ 10 nA beam current and 15 kV accelerating voltage. Calibration was done against French Geological Survey (BRGM) standard minerals, using matrix

correction factors (PAP). Analyzed elements were Si, Ti, Al, Fe, Mn, Mg, Ca, Na, K, P, Cr, Ni, F and Cl in main rock-forming minerals, and additionally S, Zn, Cu, As, Ga, In, Ge, Zr and Hf in some accessory phases (Tables 3–6, 8–12 for representative analyses and Tables 2, 3, 5–10 of the Appendix for full data set). The Method Detection Limit (MDL) for the routine analysis of common elements was ~0.02 wt.%.

Trace-element compositions of K-feldspar, plagioclase, biotite, cordierite and apatite were determined by LA-ICP-MS at the Geochronology and Isotope Geochemistry-SGIker Facility of the University of the Basque Country (UPV/EHU). The analyses involved the ablation of minerals in ~30 µm thick petrographic sections with an UP213 Nd:YAG laser ablation system (NewWave) coupled to a Thermo Fisher Scientific iCAP Qc quadrupole ICP-MS instrument with enhanced sensitivity through a dual pumping system. Analyses were performed by applying a raster movement along ~45 µm at 1 µm/s, with nominal spot diameters of ~55 µm associated to repetition rates of 10 Hz and laser fluence at the target of ~6.5 J/cm$^2$. Tuning and mass calibration were performed using the NIST SRM 612 reference glass, also used for quality control of the results assuming major- and trace-element concentrations reported by Jochum *et al.* (2011). Iolite 3.32 (Paton *et al.*, 2011; Paul *et al.*, 2012) was used to process raw data and to calculate the errors for each element expressed as 2σ (%). Analyzed elements were Rb, Ba and Sr for feldspars, biotite and cordierite, whereas Y, Zr, Th, La, Ce, Pr, Nd, Sm, Eu, Gd, Tb, Dy, Er, Tm, Yb and Lu for apatite (Table 7 for apatite analyses, and Table 4 of the Appendix for the full data set of Kfs, Pl, Bt and Crd).

In order to determine crystallization/emplacement ages, zircon, monazite and apatite crystals were separated and concentrated in the facilities of the Science and Technology Faculty of the UPV/EHU. Rock-samples were crushed, milled and sieved before their processing in a Wilfley table, to continue with the magnetic separation using a Frantz magnetic isodynamic separator. Finally, separated minerals were concentrated employing a

magnifying binoculars glass to discard non-desired elements (*e.g.* Beranoaguirre, 2016). Backscattered Electron (BSE) images of zircon and monazite crystals were obtained also in the SGIker-Facility of the UPV/EHU.

Epoxy mounts with crystal concentrate were polished and later covered by a thin layer (20 nm) of carbon, and the measurement were performed using a Scanning Electron Microscope (SEM), model JEOL JSM-6400, equipped with a EDX Oxford Instruments Inca Energy 350 detector. Operating conditions were ~10 nA beam current and 20 kV accelerating voltage. U–Th–Pb isotope and elemental measurements on zircon, monazite and apatite grains were conducted by Laser Ablation Quadrupole Inductively Coupled Plasma Mass Spectrometry (LA-Q-IC-PMS), using the UP213 laser system and the XSeries 2 ICP-MS. Spot diameters of 30 µm associated to repetition rates of 10 Hz and laser fluence at the target of ~ 2.5 J/cm$^2$ were used. The signals of $^{202}$Hg, $^{204}$(Pb + Hg), $^{206}$Pb, $^{207}$Pb, $^{208}$Pb, $^{232}$Th, $^{235}$U and $^{238}$U masses were determined. The occurrence of common Pb in the samples was monitored by the evolution of the $^{204}$(Pb + Hg) signal intensity, and those analyses with common Pb were rejected. Data reduction was carried out with Iolite v. 3 (Paton *et al.*, 2011) and VizualAge (Petrus and Kamber, 2012), using GJ-1 zircon standard (Jackson *et al.*, 2004) for calibration, and Plešovice zircon (Sláma *et al.*, 2008) as a secondary standard. Percentage concordance was calculated as [($^{206}$Pb/$^{238}$U age) / ($^{207}$Pb/$^{206}$Pb age)] × 100 (Meinhold *et al.*, 2010; cf. Ábalos *et al.*, 2012 and Errandonea-Martin *et al.*, 2017 for additional details on the LA-ICP-MS analytical procedure).

For monazite analyses the procedure was similar but using spot diameters of 15 µm and the Bananeira standard (Gonçalves *et al.*, 2016) that was ablated every 5 unknowns. Finally, analyses in apatites were performed following techniques modified from Chew *et al.* (2014), using Madagascar apatite standard (Chew *et al.*, 2014) for the calibration. Results

of U–Th–Pb measurements on zircon and monazite are given in Tables 13, and 14, and apatite analyses are shown in Table 11 of the Appendix.

Whole-rock elemental and isotopic analyses were made at the same SGIker-Facility of the UPV/EHU. Selected rock-samples were reduced to small fragments (~0.5–1 cm long) with a jaw crusher and quartered, before mashed to a homogenised powder. Major- and trace-element concentrations (Table 15) were obtained by Inductively Coupled Plasma Mass Spectrometry (ICP-MS; Thermo Fisher XSeries 2) after sample fusion with $LiBO_2$ and subsequent dissolution in diluted $HNO_3$:HF acid mixture. The precision for all analytes is in general < 2 % (always < 4 %; cf. García de Madinabeitia *et al.*, 2008 for additional details). Analyzed elements were Si, Ti, Al, Fe, Mn, Mg, Ca, Na, K, P, Ba, Cr, Cs, Ga, Hf, Nb, Ni, Pb, Rb, Sc, Sn, Sr, Ta, Th, U, V, Y, Zn, Zr, La, Ce, Pr, Nd, Sm, Eu, Gd, Tb, Dy, Ho, Er, Tm, Yb, and Lu.

Whole-rock Sr and Sm–Nd isotopic compositions involved purification of Sr, Nd and Sm following the procedures of Pin *et al.* (1994) and Pin and Santos Zalduegui (1997). Analyses were made on a Multicollector Inductively Coupled Plasma Mass Spectrometry (Neptune, Thermo Fisher Scientific; MC-ICP-MS). Mass fractionation was corrected following Balcaen *et al.* (2005) for Sr, Hofmann (1971) for Sm, and considering exponential laws of instrumental fractionation and specific algorithms for Nd. Elemental Sm and Nd concentrations were determined by isotope dilution Thermal Ionization Mass Spectrometry (TIMS, Finnigan MAT262) after sample dissolution in closed Savillex PFA vessels using a mixed $^{149}Sm/^{150}Nd$ tracer. Sm–Nd compositions and recalculations for the selected samples are shown in Table 16.

### 3.2.3. Office work

For the creation of tracks for the fieldwork and management of georeferenced points Garmin Basecamp 4.7.0 was used, whereas for the gathering and visualization of underlying data, construction of high-resolution digital terrain models, management of field data, digitization and editing of geologic data layers, and production of the map layout ArcMap of Esri ArcGIS 10.3 was used.

For the drawing of the geologic map of the Sierra Bermeja Pluton, the cartographic standards for geologic maps (Federal Geographic Data Committee, 2006) were followed, as much as possible, and considering the shape of the mapped area, a rectangular graticulated frame was chosen. The geological legend and the legend of topographical features were placed at two of the empty corners of the rectangular frame, emphasizing the first one by reason of its relevance in this research. The geological legend was established considering the criteria specified in the 'Fieldwork' section of this chapter, differentiating three main rock-type groups. For the host rocks the legends from the geologic maps of the MAGNA series published by the Spanish Geological Survey, were considered.

In order to depict the different LiDAR morphologies given by the Cenozoic cover, the Paleozoic host rocks and the igneous rocks of the pluton, a medium transparency was used that allows to show the hillshading background model (derived from the LiDAR DTM). The color for each particular lithology and the symbolism of the linear elements were taken, as far as possible, from cartographic standards for geological maps. For this reason, the similarity between some colors of granitic rocks attests in fact to their petrological and geochemical affinity. In order to maintain map legibility, no altimetric data (*e.g.* contour lines or altimetric points) were added to the geological map. Topographic and toponymic data were however displayed to facilitate the location across the map.

Whole-rock data processing was carried out using the Geochemical Data Toolkit (GCDkit; http://www.gcdkit.org), an open-source software for handling and recalculation of geochemical data from igneous and metamorphic rocks (Janoušek *et al*., 2006, 2016). The freeware is written for R language (version for Windows) which provides a flexible and comprehensive environment for data analysis, visualisation and statistical analysis (*e.g*. Janoušek, 2006; Janoušek and Moyen, 2014, 2019; Janoušek *et al*., 2006, 2016; Vermeesch, 2018). Calculations for the major- and trace-element geochemical modelling of the main mechanism of magma differentiation were carried out for each monzogranite unit separately, using an unpublished R-language plugin for the GCDkit freeware (Tables 17, 19, 21). Finally, age calculations, Concordia plots and the relative abundance diagrams were done using the toolkit Isoplot 3.75 (Ludwig, 2012) for Microsoft Excel.

## 3.3. GEOGRAPHIC LOCATION

The studied area is encompassed within the Guadiana Basin (Figs. 9 and 10), and locates immediately north of the Sierra Bermeja Range (Fig. 11). The climate in the studied area is temperate, with dry and hot summers, often above 40 ºC, and not very cold winters (hardly ever < 0 ºC) (Agencia Estatal de Meteorología de España, AEMET and Instituto Português do Mar e da Atmosfera, IPMA, 2011; AEMET, 2012). The humidity is low (60–65 % as average) and rainfall values (450–550 mm per year as average), and specially dry and hot summers, (AEMET, 2012).

The Sierra Bermeja Pluton (X = 731774–746354; Y = 4322474–4331665; UTM zone 29N) is located 15 km northeast of the City of Mérida, at the border of Cáceres and Badajoz provinces (Spain; Fig. 10). The main accesses to the studied outcrops depart from the

villages of Aljucén, Mirandilla and Trujillanos (Figs. 10 and 11, and Supplementary map of the Appendix).


**Figure 9.** A) The Iberian Peninsula, showing the area of Figure 10 delimited with a rectangle. B) Location of the Iberian Peninsula respect to Europe and Africa.

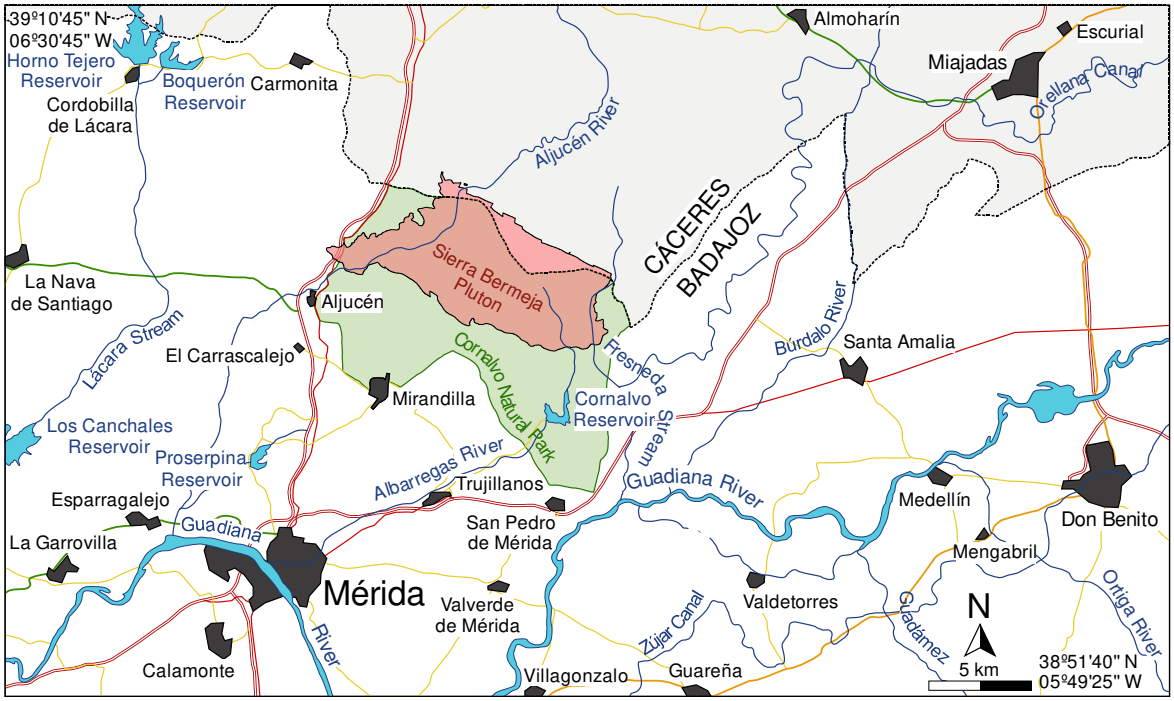


**Figure 10.** Geographical map that shows the location of the Sierra Bermeja Pluton and the Cornalvo Natural Park.

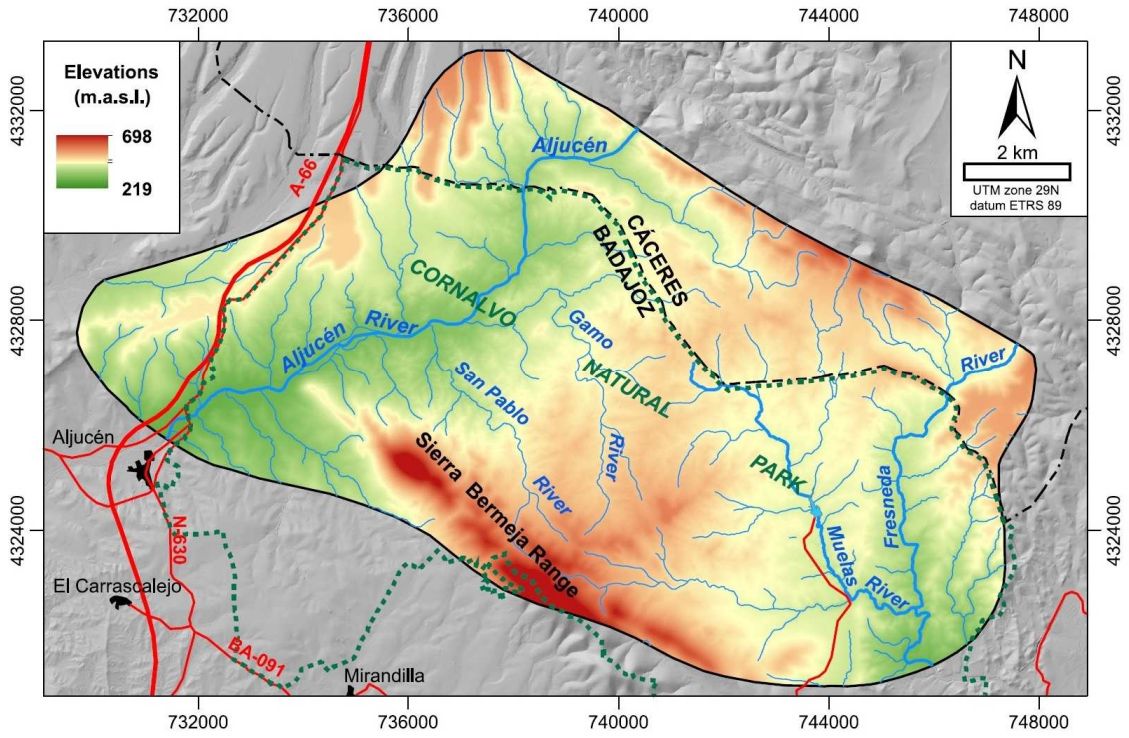


**Figure 11.** Orohydrographic map of the mapped area.

The drainage system of the mapped area is governed by the Aljucén and Albarregas Rivers (Figs. 10 and 11). This hydrographic network, defined by a roughly dendritic pattern, includes minor streams (Fresneda, Muelas, San Pablo and Gamo) and the Cornalvo and Muelas major reservoirs (Figs. 10, 11 and 12 A). The Aljucén and Fresneda Rivers produce the main depressions of the studied area, which extend trending NE–SW and N–S, and contrast markedly with the NW–SE trending Sierra Bermeja Range (Fig. 11). The landscape in the region is characterized by a sparse forest ('dehesa'; Fig. 12 B, C) composed by a variety of holm oak and cork oak groves that cover a smooth topography (250–350 m.a.s.l.). This topography appears sprinkled with formations of large rounded granitic boulders, known as 'berrocal' (Fig. 12 D, E, F). These formations show variable boulder density, with sectors where granitic blocks occupy almost completely the area (Fig. 12 C) and more clear zones where the vegetation surrounds these boulders (Fig. 12 E).

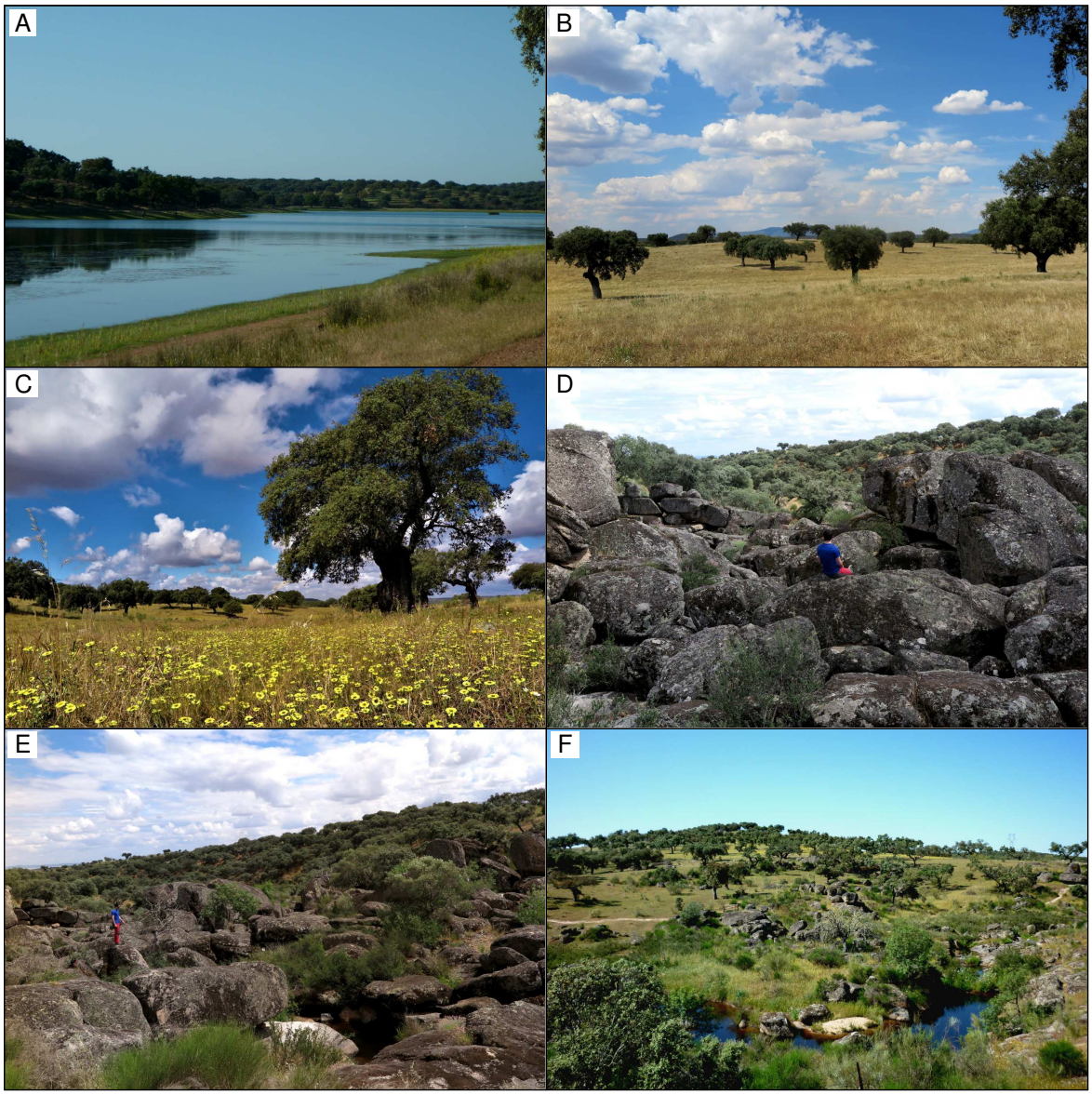


**Figure 12.** Characteristic landscape views of the Sierra Bermeja Pluton and Cornalvo Natural Park. Pictures description in the main text.

The granitic massif is almost completely included within the Cornalvo Natural Park (Decree 27/1993, of 24 February 1993; Law 7/2004, of 19 November 2004). Also, since 2000 the area is included in the European network 'Natura 2000' and is regulated as Protected Area for Birds (ZEPA; Directive 79/409/CEE, of 2 April 1989), Places of Community Interest (LIC, Directive 92/43/CEE, of 19 July 2006) and Special Conservation Area (ZEC, Decree 110/2015, of 19 May 2015). This region has been occupied since the Antiquity, standing out the uncountable Roman vestiges related to the colony of Emerita Augusta (current Mérida). In fact, the granitic rocks were used by the Romans for the

construction of roads and bridges (Camino de la Plata/Vía de la Plata), monumental buildings of Emerita Augusta (*e.g.* the amphitheatre or the theatre), and large structures for water supply such as the Cornalvo and Proserpina Dams or the Los Milagros Aqueduct (Álvarez Martínez and Nogales Basarrate, 2014; Gil Montes, 2004; Nogales Basarrate, 2007; Pizzo, 2004).Within the Sierra Bermeja Pluton, Roman vestiges are also common, represented by quartered granite boulders and small quarries (Fig. 13).


**Figure 13.** A) to E) Roman remains in the Sierra Bermeja Pluton. F) Detail of the dam of the Cornalvo Reservoir, with cordierite-bearing monzogranites similar to those of the Sierra Bermeja Pluton.

## 3.4. GEOLOGICAL SETTING

The Sierra Bermeja Pluton is one of the 15 major granitoid intrusions that conform the Nisa–Alburquerque–Los Pedroches Magmatic Alignment (Figs. 7 and 8; see section 2.3 for a detailed description of this alignment), a ~ 400 km-long magmatic alignment trending N115ºE, integrated by late-Variscan intrusions (Carracedo *et al.*, 2009; Gutiérrez-Alonso *et al.*, 2011; Solá *et al.*, 2009). It extends mainly along the southernmost Central Iberian Zone, though some of the constituent plutons trespass the limit of this Zone and intrude in the Obejo-Valsequillo-Puebla de la Reina Domain of the adjacent Ossa-Morena Zone of the Iberian Massif.

The Obejo-Valsequillo-Puebla de la Reina Domain is delimited to the south by the Blastomylonitic Corridor or Coimbra-Córdoba Shear Zone (Azor *et al.*, 1995; Martín Parra *et al.*, 2006) and to the north, depending on the authors, by the Puente Génave-Castelo de Vide Detachment (*e.g.* García-Lobón *et al.*, 2014; Martín Parra *et al.*, 2006) or the Alegrete-San Pedro de Mérida-Montoro Thrust (*e.g.* Bandrés *et al.*, 2004; c.f. Peraleda fault of Castro, 1988). Thus, following Bandrés *et al.* (2004) and considering the Alegrete-San Pedro de Mérida-Montoro Thrust as the limit, the Sierra Bermeja Pluton would be located in the southernmost part of the Central Iberian Zone occupying a mid-west to near-center position within the magmatic alignment (Fig. 14).

The southern Central Iberian Zone is characterized by the existence of a Upper Neoproterozoic–Lower Cambrian basement constituted by a thick ensemble of metasediments with interlayered volcaniclastic rocks referred to in the regional literature as the Schist-Greywacke Complex ('Complexo Xisto-Grauváquico' defined by Carrington da Costa, 1950). This ensemble was mildly affected by Cadomian tectono-metamorphic events (*e.g.* Talavera *et al.*, 2015), and was subsequently affected by Variscan events.

Unconformably/paraconformably overlying the Schist-Greywacke Complex appears a relatively thick (> 1000 m) Ordovician–Devonian siliciclastic succession, which was developed in a shallow marine platform of the passive margin of Gondwana (*e.g.* García-Alcalde *et al.*, 2002; Palacios *et al.*, 2013; Rodríguez-Alonso *et al.*, 2004). This Paleozoic succession is mainly constituted by an alternance of quartzites and slates, and includes also Cambro-Ordovician felsic meta-igneous rocks (*e.g.* García-Alcalde *et al.*, 2002; Gutiérrez-Marco *et al.*, 2002; Robardet and Gutiérrez-Marco, 2002; Rubio-Ordoñez *et al.*, 2012). These igneous rocks are markedly more scarce and show notable geochemical differences in the southern areas (closer to mantle signatures, up to +3.5 $\varepsilon Nd_i$, and affinity with I-type plutonic rocks) with respect to those of equivalent age in the northern Central Iberian Zone (highly peraluminous, S affinity, and $\varepsilon Nd_i$ from ~ -3 to -5; *e.g.* García-Arias *et al.*, 2018; Villaseca *et al.*, 2014, 2016 and references therein). The Paleozoic record of the studied area culminates with a thick Lower Carboniferous synorogenic sedimentary sequence, deposited in intracontinental shallow marine basins. These Culm facies are mainly integrated by lutites, sandstones and microconglomerates (*e.g.* Colmenero *et al.*, 2002).

On the other hand, south of the Alegrete-San Pedro de Mérida-Montoro Thrust, the basement is constituted by Late Neoproterozoic–Lower Cambrian metasedimentary and metavolcanic successions (*e.g.* Bandrés *et al.*, 2002, 2004) known in the regional literature as 'Serie Negra' (black series; Alía, 1963, Carvalhosa, 1965). In the studied area, a distinctive feature of the Obejo-Valsequillo-Puebla de la Reina Domain is the presence of Cadomian igneous intrusive rocks (570–580 Ma), diorites and leucotonalites that were emplaced into the lowermost Precambrian metavolcanic and metasedimentary sequence (Fig. 14; *e.g.* Bandrés, 2001; Bandrés *et al.*, 2002, 2004).

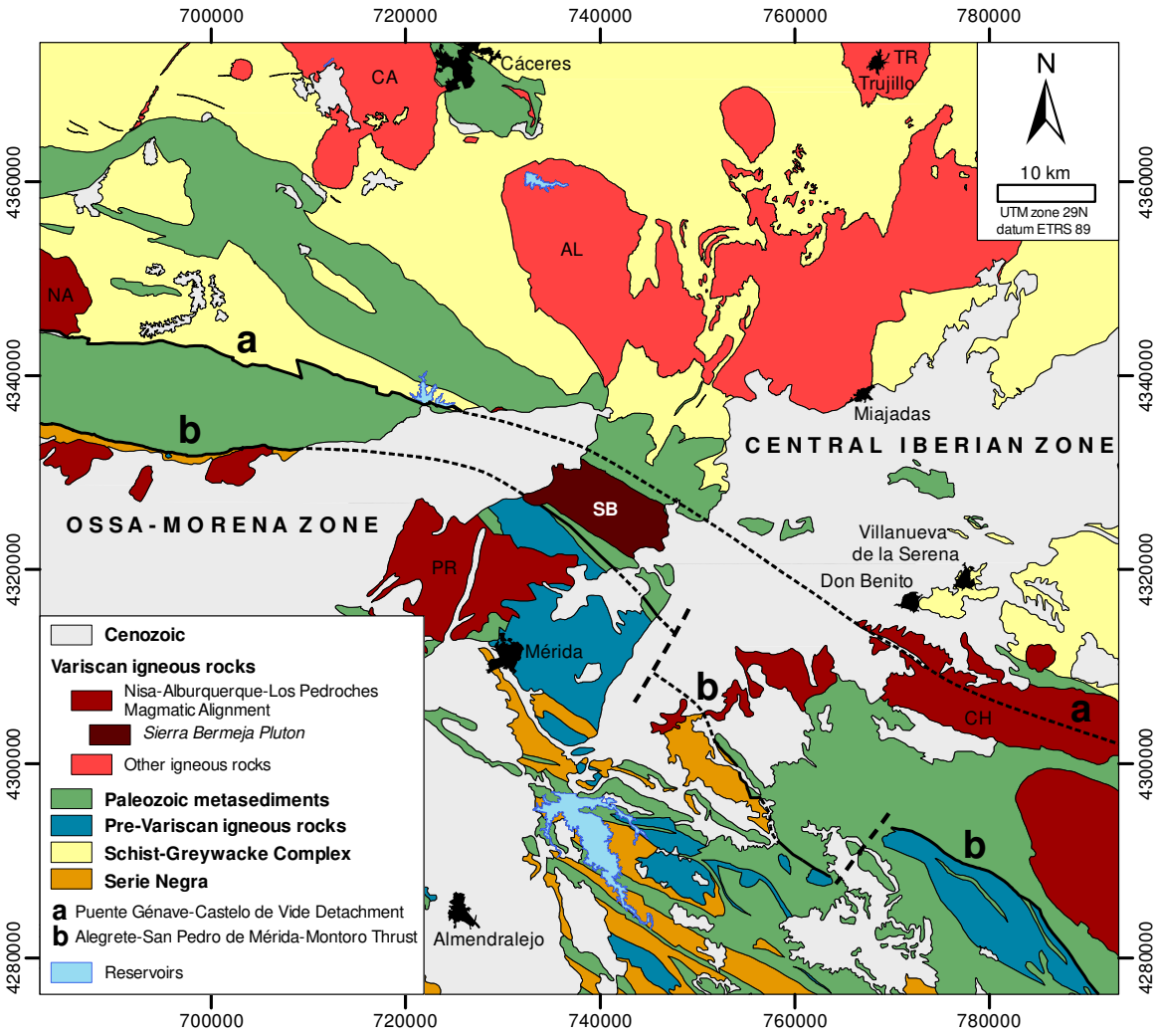


**Figure 14.** Geological map of the southern sector of the Central Iberian Zone in the central part of the Nisa–Alburquerque–Los Pedroches Magmatic Alignment (adapted from Palacios *et al.*, 2013). Main Serie Mixta-type plutons of the studied area: AL (Alcuéscar), CA (Cabeza de Araya), CH (Campanario–La Haba), NA (Nisa–Alburquerque), PR (Proserpina), SB (Sierra Bermeja), TR (Trujillo).

As mentioned above, two Orogenic Cycles are recognized in this region, the Cadomian Orogeny, better discerned south of the Alegrete-San Pedro de Mérida-Montoro Thrust, and the Variscan Orogeny, the most notorious one north of the thrust. The Cadomian Cycle corresponds to an episode of Andean-type geodynamic evolution developed in the area between the Cryogenian and Early Cambrian (Bandrés *et al.*, 2002, 2004; Sánchez-Lorda *et al.*, 2014, 2016; Orejana *et al.*, 2015), On the contrary, the Variscan Cycle is a diachronous multi-stage orogeny that resulted ultimately in the collision of Gondwana and Laurentia-Baltica-Avalonia (*e.g.* Eguíluz *et al.*, 2000; Martínez Catalán *et al.*,

2007).Variscan deformation in this sector generated wide amplitude, upright to slightly south-verging folds striking NW–SE. Associated with this folding is observable a slaty-cleavage developed under very low-grade metamorphic conditions (*e.g.* Martínez Poyatos *et al.*, 2001). Strain partitioning also promoted in some cases the development of Late-Variscan large-scale thrusts and detachments that show trends roughly parallel to the fold systems, with associated left-lateral displacements (*e.g.* Bandrés *et al.*, 2004; Díez Fernández and Arenas, 2015, García-Lobón *et al.*, 2014; Martínez Poyatos *et al.*, 2012). Among these regional scale thrusts, stands out the aforementioned north-verging Alegrete-San Pedro de Mérida-Montoro Thrust that separates the Central Iberian Zone from the Ossa-Morena Zone. This regional-scale structure is interrupted by the southern edge of the Sierra Bermeja pluton (Fig. 14).

## 3.5. BACKGROUND OF THE SIERRA BERMEJA PLUTON

Published maps that include the Sierra Bermeja Pluton were developed in the frame of regional scale geological projects. For this reason, in these maps the terminology and spatial distribution of granitic units within this pluton are imprecise. The first maps (1:50 000 scale) date back to 1946 and 1949 and were conducted by the Geological and Mining Institute of Spain (IGME) during the first MAGNA series (Marín y Bertrán de Lís, 1946; Roso de Luna and Pacheco, 1949). These maps were later updated in a second MAGNA series (Del Olmo Sanz *et al.*, 1992; López Sopena *et al.*, 1990). Previously to the second MAGNA series, Gonzalo (1987, 1988) proposed a geological scheme for the area of Mérida (1:250 000 scale) distinguishing in the Sierra Bermeja Pluton a biotite-bearing porphyritic granite in the outermost sector, and a two-mica cordierite-bearing granite in the innermost areas. This author concluded that both granite types fit properly in the 'Serie Mixta'-type granitoids, and that these granites seem to be derived exclusively from melting of mid- to lower-crustal

sialic materials. Gonzalo (1987, 1988) indicated also that the emplacement of this pluton occurred at shallow crustal levels (2–3 kbar), by a passive mechanism that leveraged the space generated by extensive faults. Afterwards, Sarrionandia *et al*. (2004) proposed another geological scheme (1:250 000 scale) of the Sierra Bermeja Pluton dividing the two mica-cordierite bearing granite defined by Gonzalo (1987, 1988) in two new granitic units. Thus, for the first time the pluton was divided in three main granite units, although the approach of the work was mostly about fracturation and quarriability of the distinguished units (*e.g*. Sarrionandia *et al*., 2004). Since 2004, the IGME is providing the Continuous Geological map of Spain (GEODE) at 1:50000 scale, but the cartographic information of the Sierra Bermeja Pluton differs considerably from that of Gonzalo (1987, 1988) and Sarrionandia *et al*. (2004). Therefore, the geological map of the pluton was still unsolved.

# CHAPTER 4
# CARTOGRAPHIC FEATURES AND FIELD CHARACTERISTICS OF THE SIERRA BERMEJA PLUTON

## 4.1. THE PLUTON AND HOST ROCKS

The Sierra Bermeja Pluton is a 59.75 km$^2$ elongated trapezoidal-shape intrusion (5.0–7.0 km width; 9.5–12.0 km length), with the long axis oriented N120ºE (Fig. 15). The pluton intrudes into a Paleozoic (Ordovician–Carboniferous) metasedimentary sequence of the Central Iberian Zone and Cadomian intrusive rocks of the Ossa-Morena Zone (Bandrés, 2001; Bandrés *et al*., 2002, 2004; Del Olmo Sanz *et al*., 1992; Gonzalo, 1989; López Sopena *et al*., 1990). The intrusive contacts of the pluton with the host rocks are sharp (Fig. 16 A), and only visible in the North and South borders of the massif, where some faults have been inferred. By contrast, in the East and West areas the contacts are hidden under a Cenozoic cover constituted by thick alluvial and colluvial deposits. As mentioned in the previous section, it is outstanding that the southern edge of the Sierra Bermeja Pluton cuts the Alegrete-San Pedro de Mérida-Montoro Thrust.

The Paleozoic metasedimentary sequence where the Sierra Bermeja Pluton is emplaced exhibits N120–140E strike, and subvertical dip to the SW (Del Olmo Sanz *et al*., 1992; Gonzalo, 1987, 1989). These metasediments constitute the Variscan synclines of Sierra de San Pedro to the North (*e.g*. Del Olmo Sanz *et al*., 1992; Martínez Poyatos *et al*., 2004) and Sierra Bermeja to the South of the pluton (*e.g*. Gonzalo, 1987, 1989). These Ordovician–Carboniferous successions exhibit a Variscan low-grade regional metamorphism, observable particularly in the metapelitic materials where metamorphic crystallization of muscovite, chlorite and occasionally chloritoid followed the slaty-cleavage schistosity (López Sopena *et al*., 1990; Martínez Poyatos *et al*., 2001).

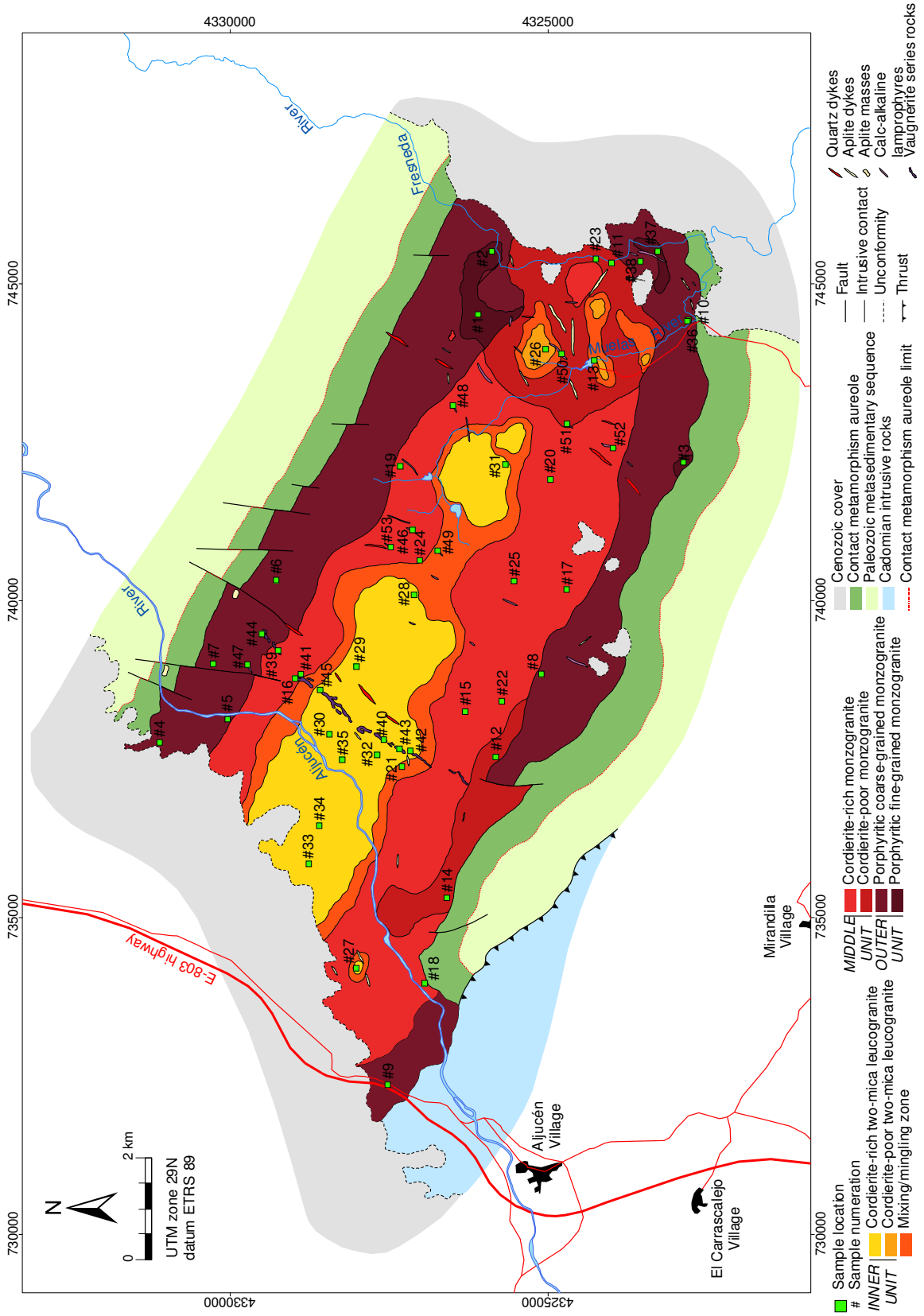


**Figure 15.** Geologic map of the Sierra Bermeja Pluton (see the Supplementary map of the Appendix for the original scale).

The base of the Paleozoic metasedimentary sequence is constituted by a sandy-pelitic succession characterized by Skolithos pipe rock ichnofossils (Palacios *et al.*, 2013). Above these materials appear metre-scale banks of Lower Ordovician quartzites (up to 300 m of total thickness) that constitute the Armorican Quartzite (Del Olmo Sanz *et al.*, 1992; Gonzalo, 1987, 1989), followed upward by dark fossiliferous shales with sandy intercalations that become more abundant towards the upper part of the Ordovician sequence (Del Olmo Sanz *et al.*, 1992). Above these materials, Silurian ampelitic slates and sapropelic phyllites that comprise a thick (up to 400 m) monotonous succession were deposited (Del Olmo Sanz *et al.*, 1992; Gonzalo, 1987, 1989). The Upper Devonian-Lower Carboniferous synorogenic sequence that culminates the Paleozoic sequence is composed by sandstones (± conglomerates and greywackes) and slates, with intercalations of marls–limestones (250–275 m of thickness) and volcanosedimentary deposits (Del Olmo Sanz *et al.*, 1992; Gonzalo, 1987, 1989; Palacios *et al.*, 2013). The intrusion of the Sierra Bermeja Pluton generated a contact metamorphism aureole, up to 400–600 m width, in this Paleozoic sequence. This aureole is constituted mainly by grano-lepidoblastic spotted slates-phyllites with porphyroblasts of andalusite ± cordierite, although close to the contact a thin belt composed by hornfels (hornblende hornfels facies) is observable in some areas (*e.g.* Del Olmo Sanz *et al.*, 1992; Gonzalo, 1987, 1988; López Sopena *et al.*, 1990).

The Sierra Bermeja Pluton intrudes also, though to a lesser extent, into the Cadomian intrusive rocks of the Mérida Massif (*e.g.* Bandrés, 2001; Bandrés *et al.*, 2002, 2004; Gonzalo, 1987; Del Olmo Sanz, 1992). In the vicinities of the pluton two types of intrusives can be discerned, dioritoids and leucotonalites/amphibole bearing granitoids (*e.g.* Bandrés, 2001; Bandrés *et al.*, 2002, 2004). Dioritoids (ultrabasic rocks–gabbros–diorites–quartz diorites) show massive or banded structure and planar or planolinear fabrics generated by magmatic processes (magmatic flow or crystal accumulation) or by later deformation phases

(milonitisation). They are constituted mainly by holocrystalline phaneritic melanocratic–ultramafic rocks that comprise amphibole, plagioclase, pyroxene, ± biotite, ± K-feldspar, ± quartz and ± olivine (*e.g.* Bandrés, 2001; Bandrés *et al.*, 2002, 2004). On the other hand, leucotonalites or amphibole bearing granitoids (monzogranites–syenogranites–granodiorites–tonalities) show massive and layered structures, the later with planolinear fabrics. They are composed by holocrystalline phaneritic mesocratic–leucocratic rocks constituted by K-feldspar, plagioclase, quartz, biotite and ± amphibole (*e.g.* Bandrés, 2001; Bandrés *et al.*, 2002, 2004). In contrast to the Paleozoic metasedimentary sequence, these Cadomian rocks lack apparently of effects caused by the intrusion of the Sierra Bermeja Pluton.

## 4.2. CORDIERITE-BEARING MONZOGRANITES

The development of an accurate geological map of the Sierra Bermeja Pluton (Supplementary map of the Appendix) has revealed the existence of diverse cordierite-bearing monzogranite lithotypes that show intrusive contacts among them. These rocks can be grouped into three main units (Fig. 15) that, according to their roughly spatial concentric arrangement have been termed as Outer Unit (OU), Middle Unit (MU) and Inner Unit (IU). The contacts between the OU and MU are sharp and curvilinear (Fig. 16 B–D), whereas those between the MU and IU are complex, resulting on a 100–400 m width belt of heterogeneous monzogranitic masses (Fig. 16 E). This pluton includes also a poorly developed dyke complex mostly represented by mafic rocks trending NE–SW. The dyke complex of the Sierra Bermeja Pluton includes also subordinate aplite and quartz dykes (Fig. 15 and Supplementary map of the Appendix).

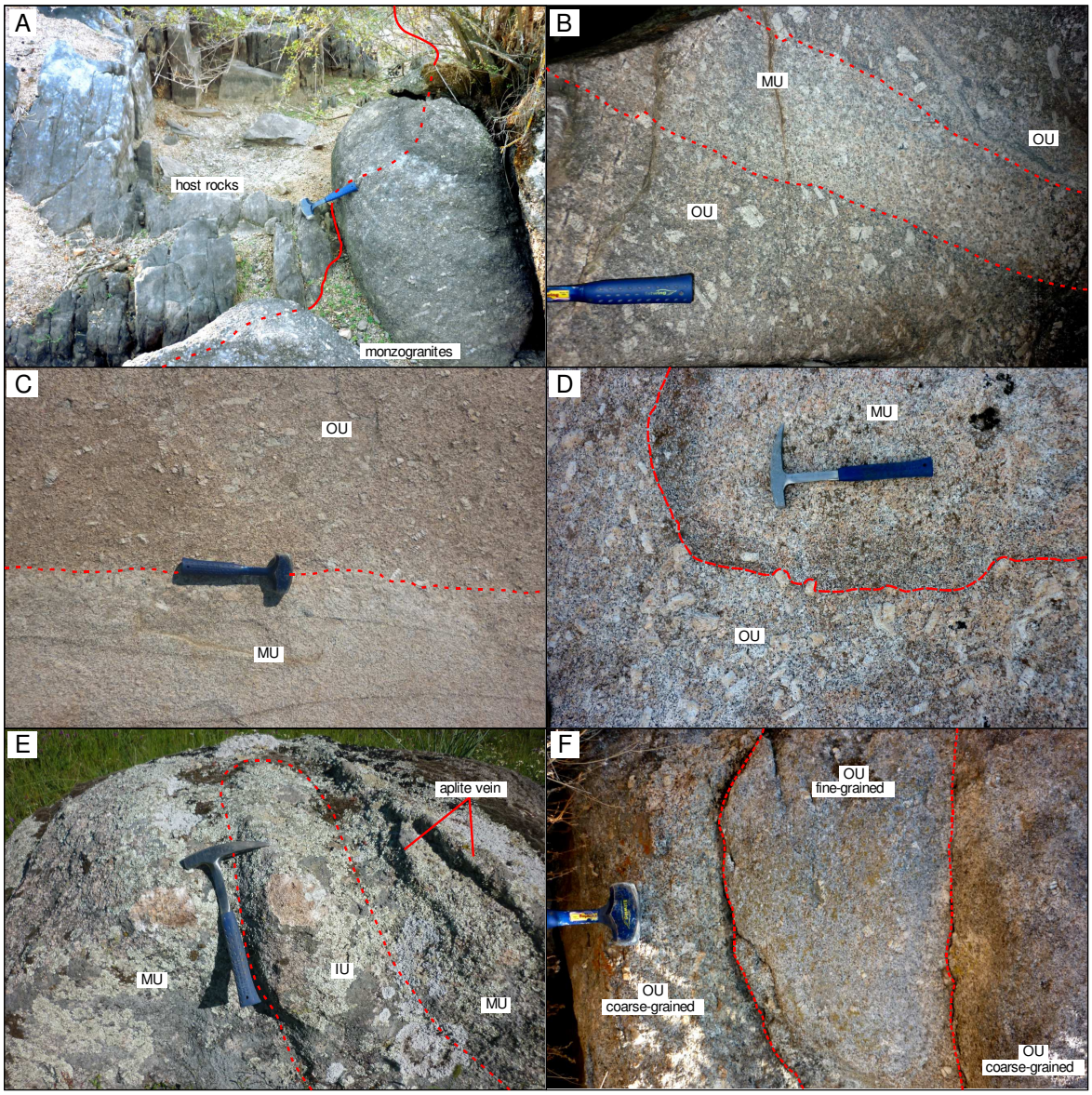


**Figure 16.** Field relationships between the different monzogranite lithotypes from the Sierra Bermeja Pluton. A) Sharp contact between monzogranites of the OU and the host rocks. B) Monzogranites of the MU intruding the OU monzogranites. C) Sharp contact between OU and MU monzogranites. D) Enclave of MU within the OU. E) Complex intrusive relationship between IU and MU monzogranites. F) Similar intrusive relationship to that of E, between the main lithotype and local variety of the OU.

The OU extends along the outermost areas of the pluton, subparallel to the northern and southern limits of the massif in three separated sectors, encompassing 20.03 $km^2$ (33.5 % of the total area of the pluton; t.a.p.; Supplementary map of the Appendix). Outward, the OU intrudes the host rocks showing sharp contacts (Fig. 16 A) that appear segmented by decametre-scale displacements (up to 250 m) along N–NE trending faults (Fig. 15). Inward this monzogranite unit appears intruded by the MU (Fig. 16 B–D). The temporal

emplacement relation between both units is deducible in several areas of the pluton, standing out the outcrop of the Rugidero Berrocal, where a dyke of the MU intrudes the OU (Fig. 16 B). The MU extends between the aforementioned OU and the IU covering a surface area of 24.49 $km^2$ (41.0 % t.a.p.; Supplementary map of the Appendix). The external limits of this unit are sharp and curvilinear, which may be regarded as a consequence of its intrusion into the host rocks and the OU monzogranites (Fig. 16 B–D). On the contrary, the relation with the IU is defined by a 100–400 m width heterogeneous belt that covers an area of 5.38 $km^2$ (9.0 % t.a.p.). This belt is constituted by rocks with intermediate characteristics between those of the MU and IU, besides the sheet-by-sheet intrusion zones between both units (Fig. 16 E). This evidences that mixing and mingling processes occurred between the MU and IU. The IU extends along the pluton axis covering a surface area of 9.38 $km^2$ (15.7 % t.a.p.). It appears dismembered in eight heterometric masses, standing out a ~ 5 km long and ~ 2 km width mass located in the westernmost zone of the pluton. All these masses are enclosed by the mixing/mingling belt that separates the IU and MU.

### 4.2.1. Field characteristics of the OU monzogranites

The OU is constituted by white monzogranites that show a massive or homophanous structure and a planar/linear fabric. This fabric is defined by fairly oriented (N100–170E, subhorizontal) K-feldspar phenocrysts that can reach up to 12 cm in length (Fig. 17). The concentration of these phenocrysts is markedly high (150–350 crystal/$m^2$; 10–35 % vol.), which confers a porphyritic texture to these rocks and constitutes the most characteristic feature of this unit (Fig. 17A–E). The phenocrysts (Fig. 17 F–H) are included in a holocrystalline phaneritic (medium- to coarse-grained) biotite-rich groundmass, constituted by euhedral plagioclase (up to 15 mm), globular quartz (up to 11 mm), K-feldspar (up to 10 mm), biotite (up to 3 mm) and cordierite (up to 6 mm). Besides the K-feldspar phenocrysts, at the outcrop scale this unit is also characterized by the relative abundance of globular quartz

and biotite, and the relative scarcity of cordierite as compared with monzogranites of the other units.

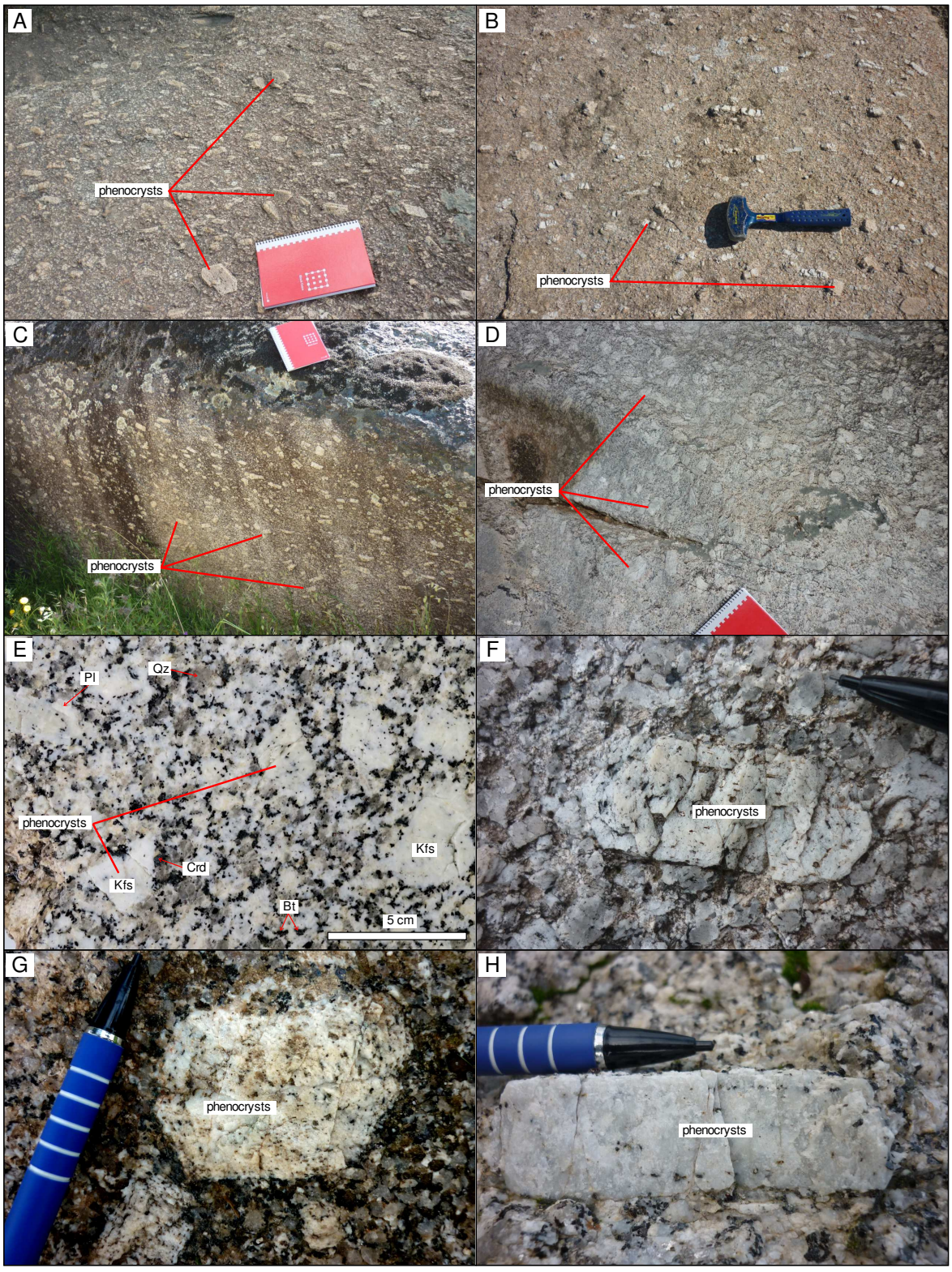


**Figure 17.** A–D) Outcrop views of the OU monzogranites. E) Detail of a cut hand specimen. F–H) Detailed picture of phenocrysts, note the oriented inclusions. The size of the notebook is (22 x 16 cm).

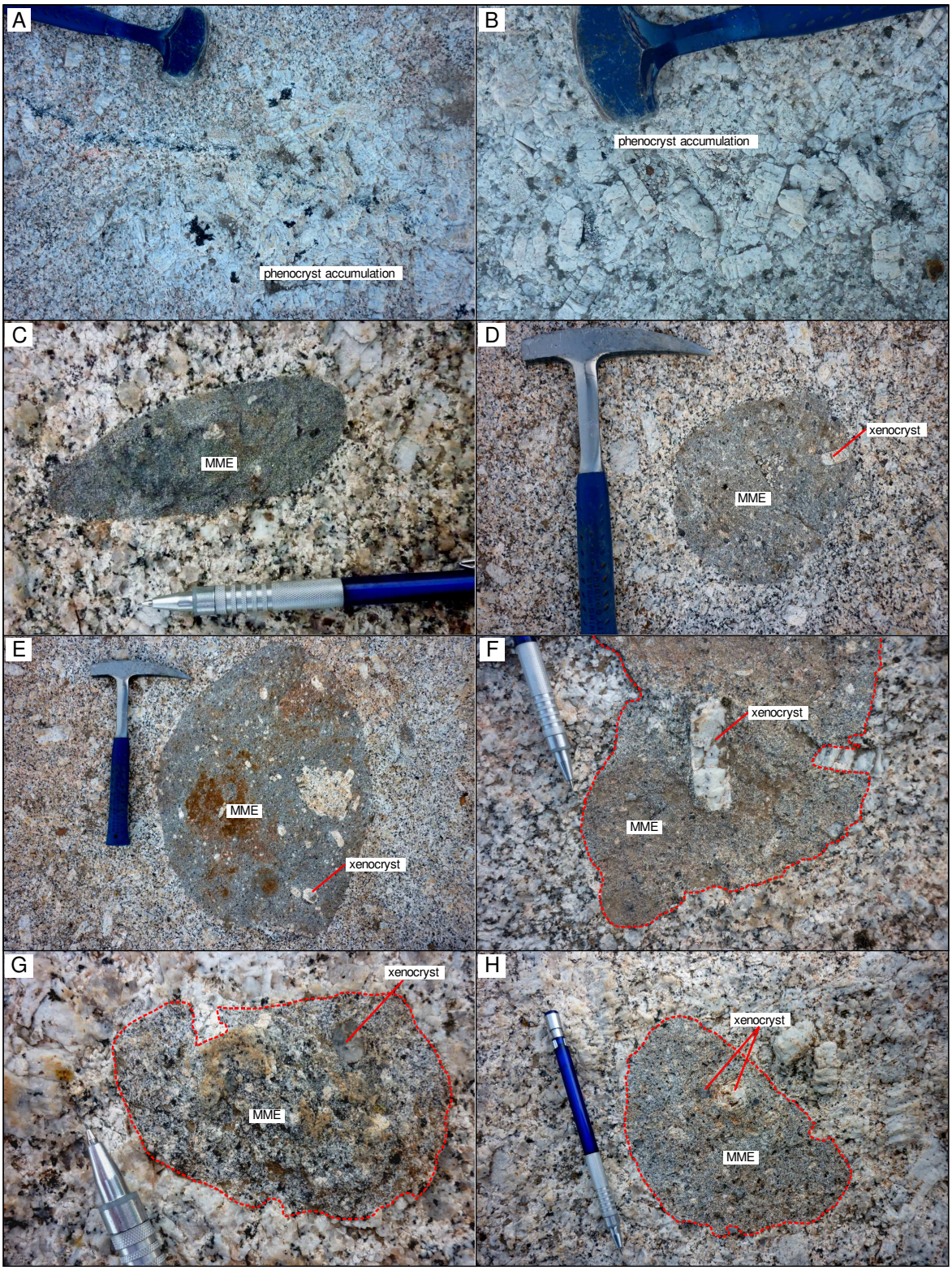


**Figure 18.** A) and B) K-feldspar phenocryst accumulations. C–H) Mafic Microgranular Enclaves (MME) showing different degrees of assimilation and some xenocrysts.

Large accumulations of phenocrysts (up to 750 crystal/m$^2$; Fig. 18 A and B), rare felsic-microgranular enclaves and pelitic xenoliths, and biotite schlieren are found sparsely

in the OU. Tonalitic mafic microgranular enclaves, oval-shaped and of centimeter to decimeter size (Fig. 18 C–H), are a conspicuous feature of this unit. They occur mainly close to the contacts with the host rocks and show variable degrees of resorption by the granitic host magma. Besides, Kfs xenocrysts captured from the host monzogranites are common (Fig. 18 D, E, F and H). Locally pegmatite, aplite and aplopegmatite segregates are observed.

Within the OU stands out a fine-grained variety characterized by a greater abundance of biotite, and lower amounts of cordierite and globular quartz (Fig. 16 F). The size of the K-feldspar phenocrysts is also smaller in this variety (up to 6 cm long) that crops out in three small irregular masses representing 4.8 % of the OU surface area (0.97 $km^2$). These masses are located in the eastern sector of the pluton in contact with the medium- to coarse-grained monzogranites of the OU, the host rocks and the MU (Fig. 15). The timing relation between this local variety and the medium- to coarse-grained monzogranites of the OU is deducible from the observed sheet-by-sheet intrusion relationships that indicate their coeval emplacement (Fig. 16 F).

### 4.2.2. Field characteristics of the MU monzogranites

The MU is constituted by apparently undeformed white monzogranites that show a massive or homophanous structure (Fig. 19 A). Only in some outcrops a planar/linear fabric related to local metre-scale shear zones is observable. These rocks exhibit a medium- to coarse-grained hypidiomorphic seriated texture (Fig. 19 B) and are constituted by globular quartz (up to 19 mm; Fig. 19 C), plagioclase (up to 15 mm), K-feldspar (up to 16 mm), euhedral cordierite (up to 18 mm; Fig. D) and biotite (up to 2 mm; Fig. 19 C–F). K-feldspar phenocrysts (up to 6 cm) are scarce (< 5 crystal/$m^2$) and are usually found close to the contacts between the OU and MU (Fig. 16 D). The monzogranites of this unit differ from those of the OU because of their drastic lower K-feldspar phenocryst amounts and markedly

higher cordierite contents (Fig. 19A). Besides that, the biotite amount is lower in the MU. Small accumulations of K-feldspar phenocrysts (20–50 crystals), as well as rare pegmatite, aplite and aplopegmatite veins/segregates are observed in this unit too.

Locally within the MU a subtype of monzogranite can be discerned. It crops out in two distinct areas of the pluton (Fig. 15) covering a surface of 5.66 km$^2$ (23.1 % of the MU). This variety is distinguished from the main type by its greater abundance of biotite and markedly lower cordierite content. The relationship between both types of the MU monzogranites is doubtful. Nevertheless, observed textural variations in this subtype, close to the contacts with the main monzogranite type, point to their coeval emplacement.

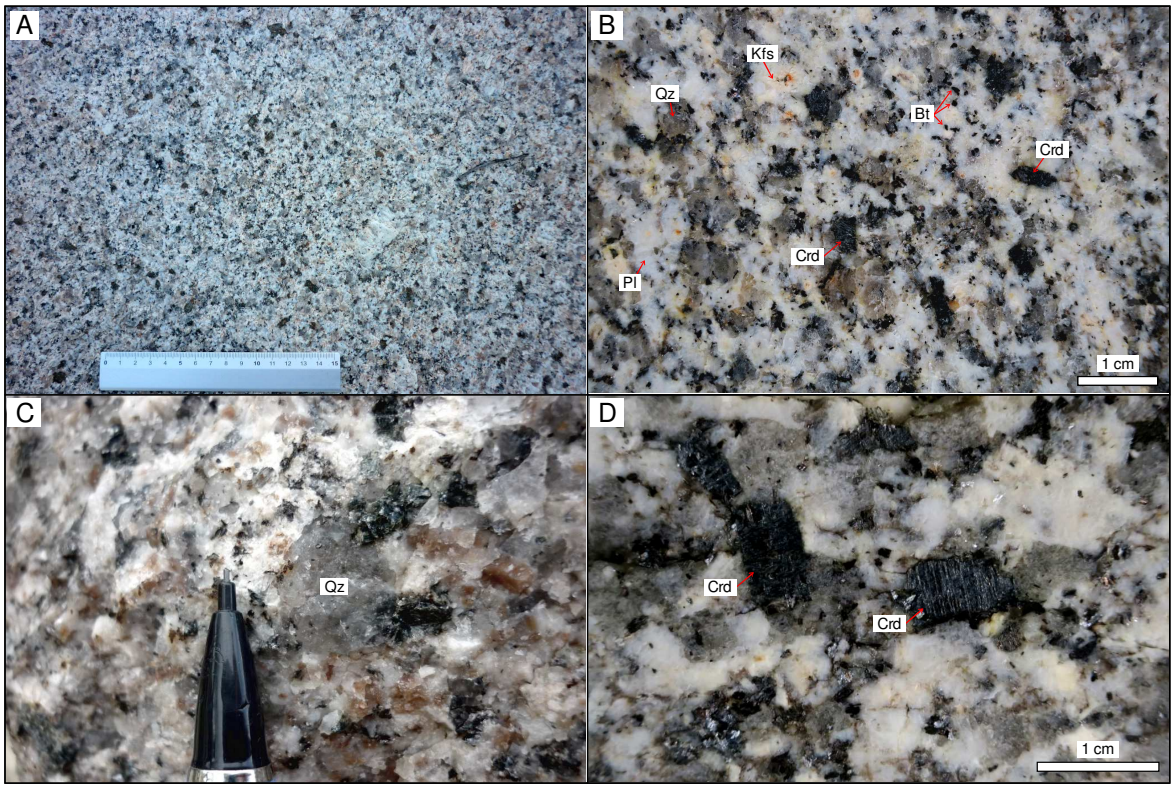


**Figure 19.** A) Characteristic outcrop view of the MU. B) Detail of a cut hand specimen of the MU. C) Detail of a globular quartz. D) Detail of cordierite prisms.

### 4.2.3. Field characteristics of the IU monzogranites

The IU is constituted by yellowish monzogranites with massive or homophanous structure and isotropic fabric (Fig. 20). In the westernmost areas of the Sierra Bermeja Pluton, an

outstanding feature of this unit is the well-developed N40–60E trending joint system (Fig. 20 A). The texture of these monzogranites is fine- to medium-grained hypidiomorphic seriated, with low contents of mafic mineral phases that allows to consider them as leucogranites (Fig. 20 B). Their main mineralogy consists of globular quartz (up to 10 mm), plagioclase (up to 9 mm), K-feldspar (up to 8 mm), muscovite (up to 4 mm; Fig. 20 C), euhedral cordierite (up to 9 mm; Fig. 20 D), and biotite (up to 2 mm). The distinctive features of these monzogranites are the fine crystal-size and the relatively high content of muscovite. As in the other monzogranite units, K-feldspar phenocryst clusters (20–50 crystals) and pegmatite, aplite and aplopegmatite veins/segregates are observable, all of decimetre-scale size.

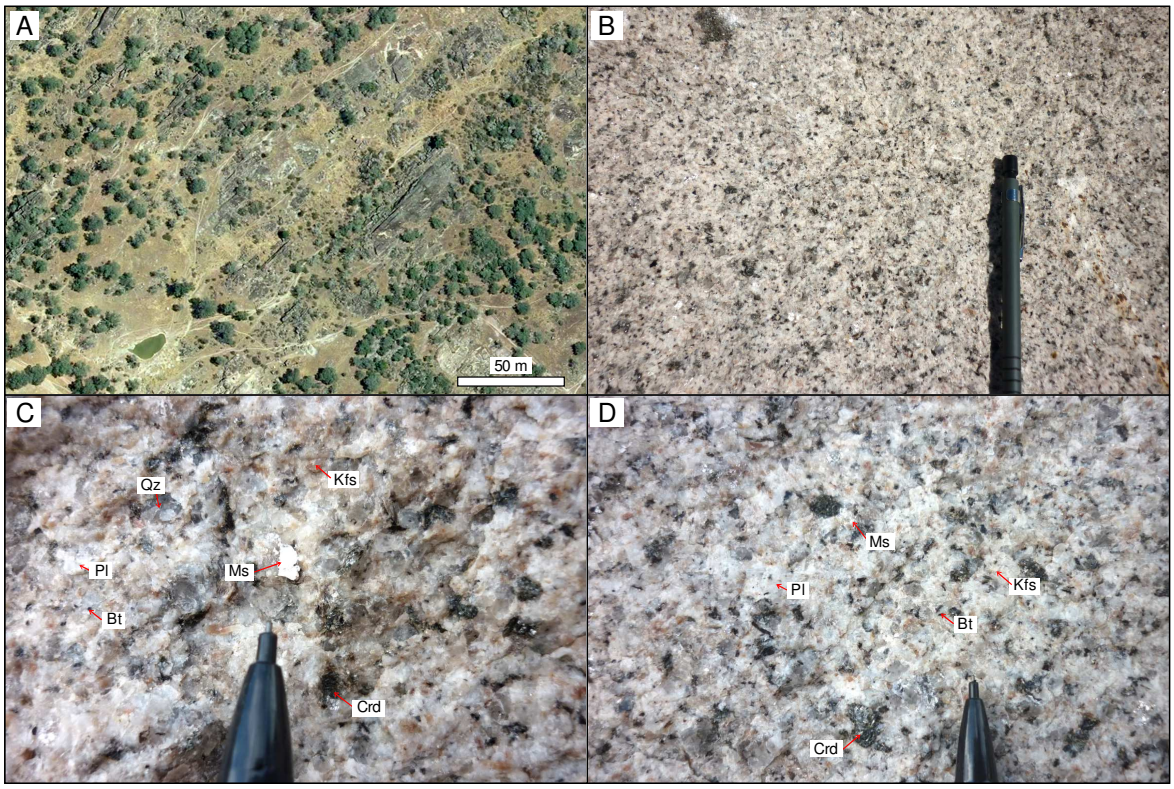


**Figure 20.** A) Well-developed joint system in the monzogranites of the IU (aerial photograph taken from PNOA). B) A Characteristic outcrop view of the IU. C) Detail of an outcrop where muscovite crystals are conspicuous. D) Detail of cordierites in the IU.

In the easternmost masses of this monzogranite unit, the cordierite content decreases markedly whereas that of biotite increases, which allows to differentiate a local

monzogranite variety in the IU (0.34 $km^2$; 3.6 % of IU). This local variety is surrounded by a mixing/mingling belt developed in the contacts with the previously cited monzogranite subtype of the MU (Fig. 15).

## 4.3. VAUGNERITE SERIES ROCKS AND LAMPROPHYRES

The three monzogranitic units of the Sierra Bermeja Pluton appear intruded by mafic rocks that define longitudinal alignments of variable length and width (Fig. 15). These mafic rocks are categorized, according to their field textural, mineralogical and modal features, in two end-member types, one phaneritic and another aphanitic. To make easier the reading of the present memory, henceforth it will be referred to as vaugnerite series rocks (phaneritic terms) and lamprophyres (aphanitic terms; see Chapter 9 for more details). Each alignment is always composed by just one of the aforementioned end members, that is, either vaugnerites *s.l.* or lamprophyres. Nevertheless, within each alignment textural and mineralogical variations are observed, denoting the heterogeneous nature of these mafic rocks. It may be noted that, at the outcrop scale, these dark-colored rocks do not show any positive relief, and usually appear even in plains or slight depressions and confined into the pluton (Figs. 15 and 21; Supplementary map of the Appendix).

Vaugnerite series rocks are restricted to a 4 km long and up to 150 m width, N30–45E trending linear belt. They cover a 0.13 $km^2$ surface area (0.2 % t.a.p.) in the middle-western sector of the pluton (Fig. 15). At the outcrop scale, this belt is defined by sinuous alignments of decimetre in size, rounded, dark-colored rock blocks. These blocks do not constitute continuous masses and show variable spacing between them (0.5–3 m) that increases progressively towards the tips of each alignment, up to finally disappear (Fig. 21 A and B). The timing relation with the host monzogranites is deducible at the cartographic

scale with vaugneritic alignments cross-cutting the contacts between the monzogranite units (Fig. 15). Yet, their sinuous trends, the absence of chilled margins, the necking of the alignments, as well as their dismembered terminations are key features to consider in their timing relationship with the host monzogranites.

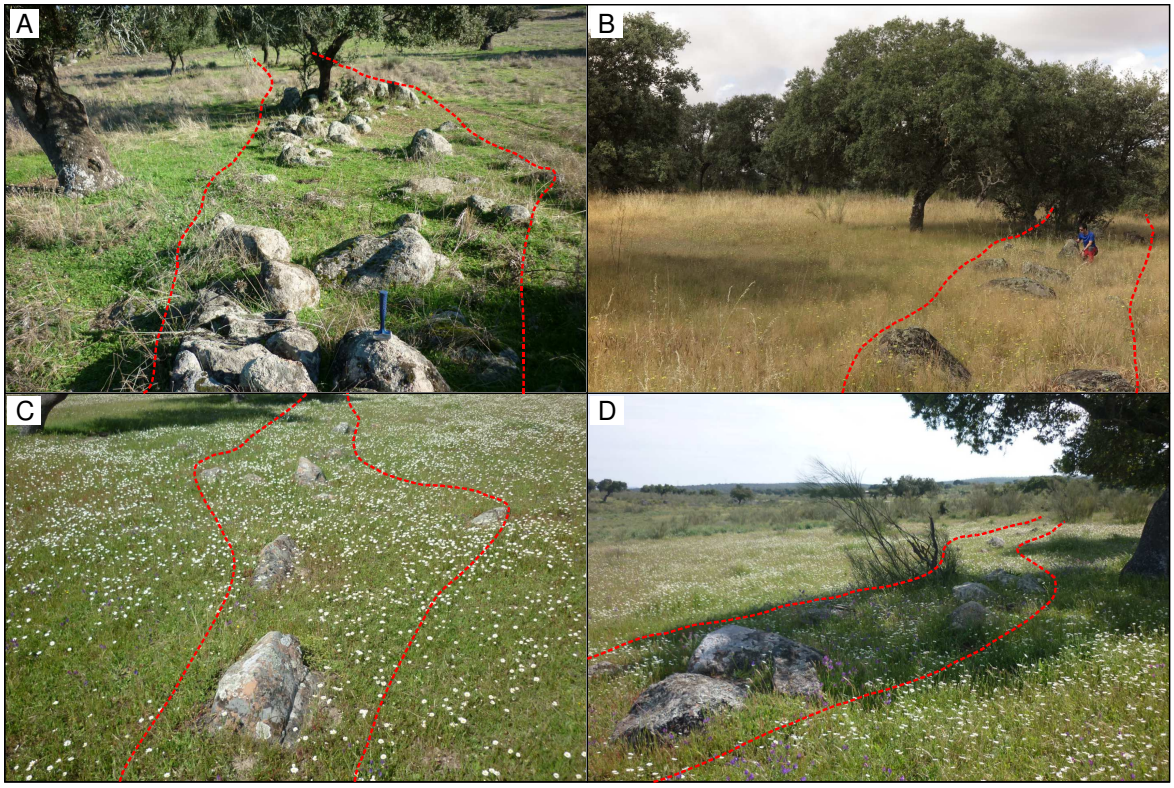


**Figure 21.** Alignments of mesocratic rocks from the Sierra Bermeja Pluton, defined by small rounded, dark-colored blocks that stand out against the more eroded host monzogranites.

Lamprophyres appear distributed throughout the pluton covering a 0.11 $km^2$ surface area (0.2 % t.a.p.). At the outcrop and map scale lamprophyres exhibit characteristics fairly similar to those of vaugnerite series rocks above described (Fig. 21 C and D). Nevertheless, they usually constitute straight and narrow (< 5 m) alignments with NE–SW trends (Fig. 15).

### 4.3.1. Field characteristics of vaugnerites and lamprophyres

Vaugnerites *s.l.* of the Sierra Bermeja Pluton show a massive or homophanous structure and present a medium-grained, hypidio–idiomorphic, inequigranular seriated texture. Their main mineralogy includes variable amounts of plagioclase, amphibole, clinopyroxene, biotite, K-

feldspar, and quartz. In detail, these mafic rocks can be subdivided in two subtypes, which, depending on the modal composition, are here termed as 'biotite-rich' (Fig. 22 A) and 'biotite-poor' (Fig. 22 B).

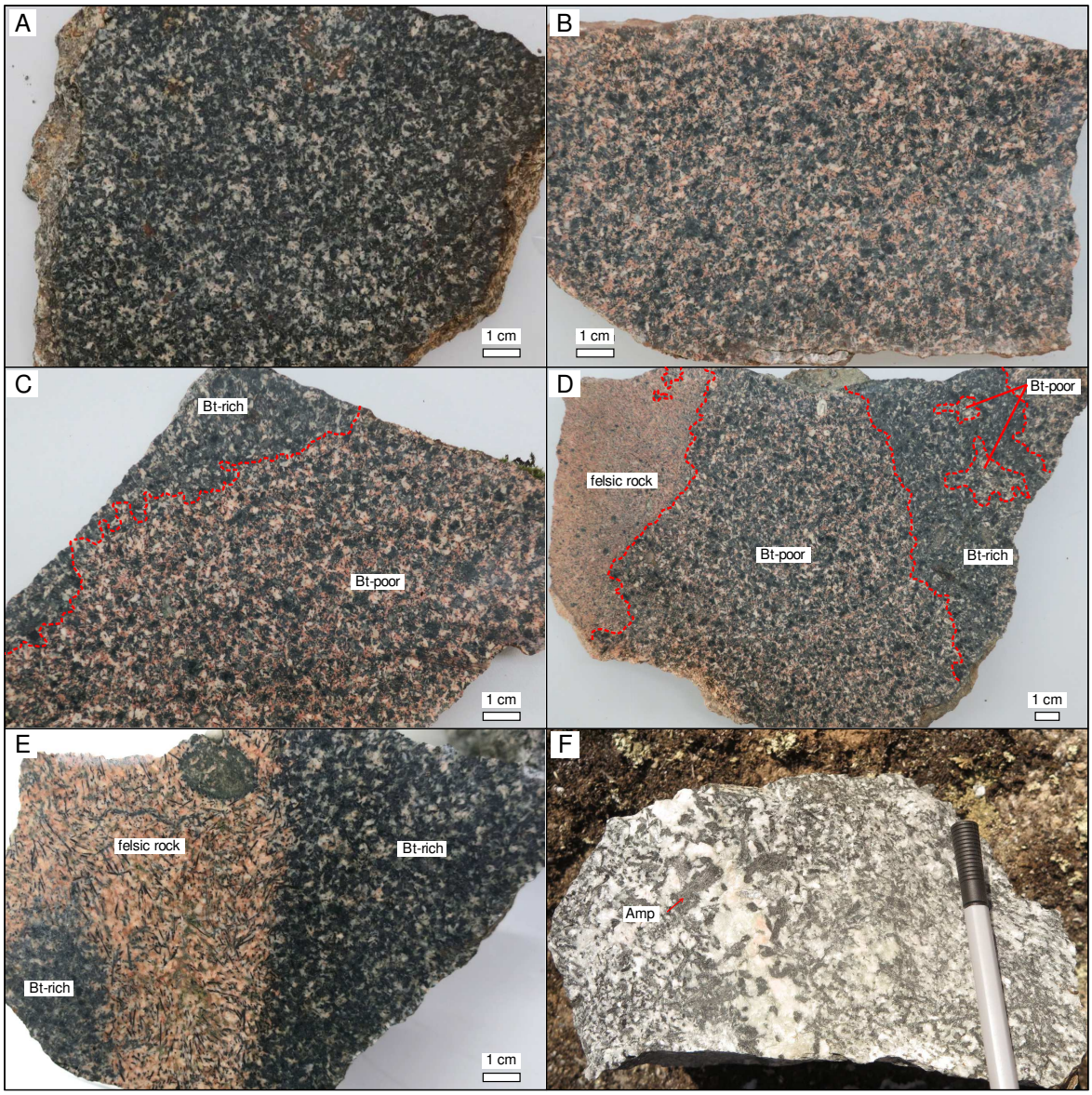


**Figure 22.** A) Biotite-rich and B) biotite-poor representative samples of vaugneritic rocks from the Sierra Bermeja Pluton. C) Hand specimen showing the contact between the Bt-rich and Bt-poor varieties. D) Contacts of the Bt-poor term with the Bt-rich variety and the related felsic rock. E) Contact between Biotite-rich vaugneritic rocks and the felsic rock. Note the textural difference of the felsic rock in D and E. F) Hand specimen showing a vein with large amphibole crystals.

In the field, the mentioned subtypes can be easily distinguished based on the color of the groundmass, since biotite-rich terms show a whitish one and that of the biotite-poor type is pinkish (Fig. 22 A–E). These subtypes show irregular contacts between them (Fig. 22 C),

and they often appear related to a more felsic pinkish rock, showing gradational-irregular contacts with it as well (Fig. 22 D and E). Rarely, in some outcrops anomalous large crystals (up to 4 cm) are observed, constituted mainly by feldspar + amphibole (Fig. 22 F). Following the IUGS recommendations (Le Maitre *et al.*, 2002) these rocks are classified as diorites, quartz diorites and quartz monzodiorites, but on account of their mineralogy and whole-rock geochemical composition are considered as a whole within the vaugnerite series rocks (see Chapter 9 for more details). Lamprophyres of the Sierra Bermeja Pluton are constituted by homophanous aphanitic mafic rocks with porphyritic texture (Fig. 23 A–D). They are characterized by the presence of clinopyroxene phenocrysts (up to 2 mm), occasionally accompanied by biotite (up to 2 mm) and amphibole (up to 2 mm), included in a microcrystalline groundmass. It is common the presence of interstitial carbonate (Fig. 23 C), and rarely host monzogranite enclaves are also found (Fig. 23 D).

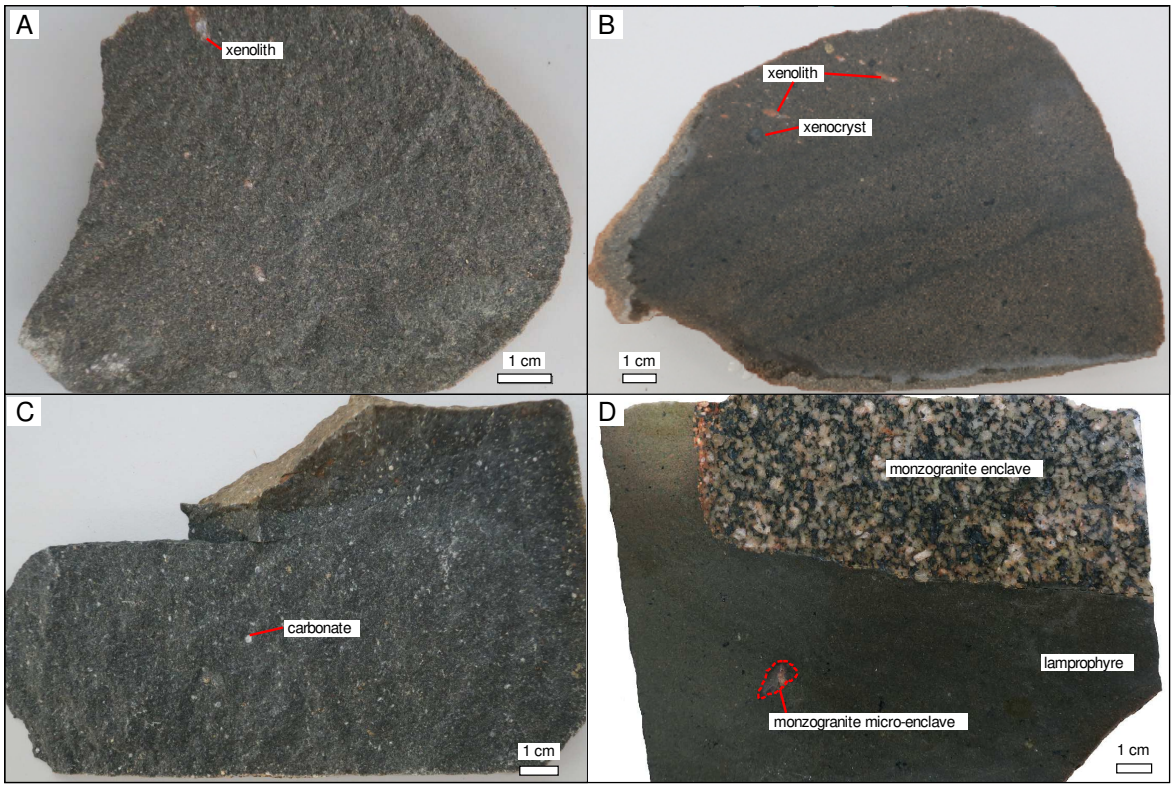


**Figure 23.** A) and B) Representative hand samples that show the texture of lamprophyres from the Sierra Bermeja Pluton. Note the banded structure in B). C) Lamprophyre sample with abundant carbonate infills. D) Scanned image of a hand sample of lamprophyre enclosing a decimetric monzogranite enclave and a microenclave.

## 4.4. APLOPEGMATITES AND QUARTZ DYKES

Mappable aplite bodies in the Sierra Bermeja Pluton occur as dykes (Fig. 24 A and B) or irregular masses, covering 0.14 km$^2$ (0.2 % t.a.p.). Aplite dykes show metre-scale widths and up to 600 m lengths, with roughly NE–SW trends. These dykes intrude into the three main monzogranitic units. The largest aplite masses crop out in the northwestern area of the pluton and intrude both the OU and the host rocks (Fig. 15). In this massif, aplites –fine-grained leucogranites– are apparently homophanous, and they show a hypidiomorphic seriated texture. Their mineralogy comprises quartz (up to 4 mm), K-feldspar (up to 5 mm), plagioclase (up to 5 mm), muscovite (up to 2 mm) and tourmaline (up to 3 mm).

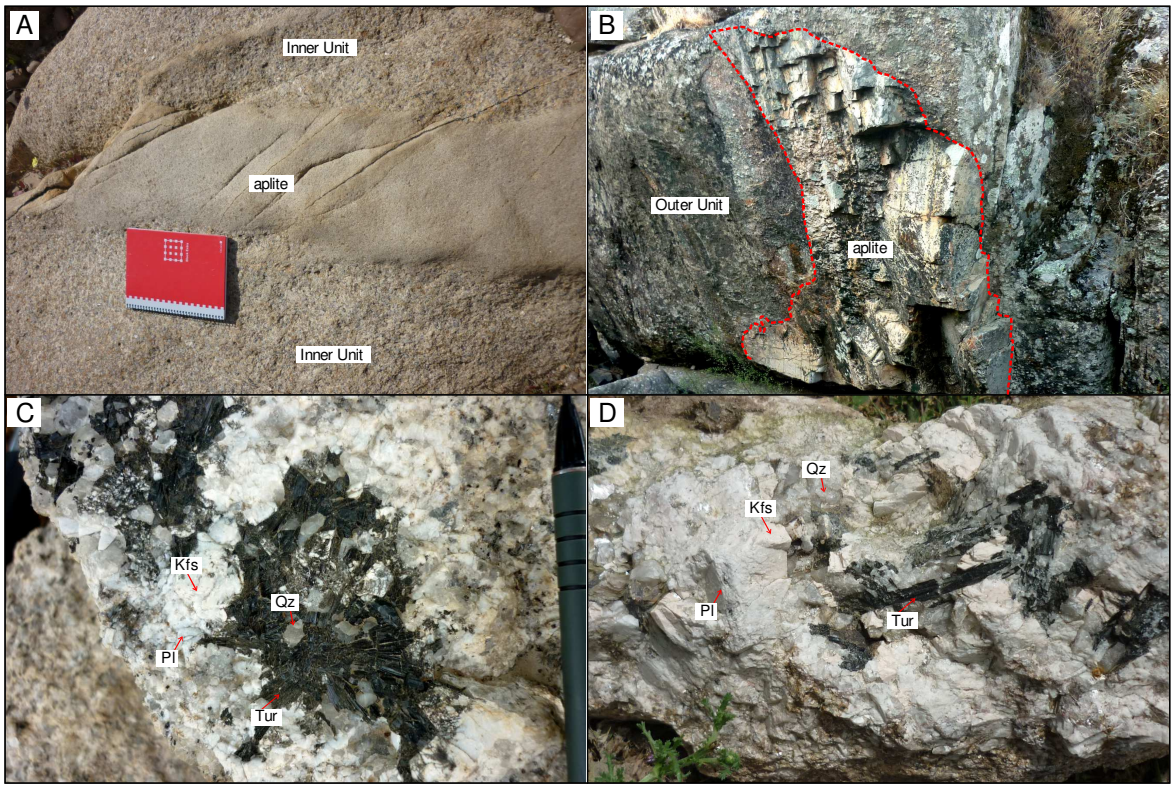


**Figure 24.** A) Synplutonic dyke of aplite with irregular contacts in the IU. B) Aplite dyke that cuts the Outer Unit, with sharp contacts. C) and D) Pegmatoid segregates, composed by Qz + Pl + Kfs + Tur.

Quartz dykes form in the landscape marked positive linear prominences up to 450 m long and 50 m width (Fig. 15). They show straight N35–45E trends and are constituted by white (locally reddish) quartz crystal aggregates. The host monzoganite close to these dykes

shows pervasive hydrothermal alteration. As mentioned previously, pegmatite and aplopegmatite veins/segregates are found in all monzogranite units (Fig. 24 C and D).

# CHAPTER 5
# PETROGRAPHY

## 5.1. CORDIERITE-BEARING MONZOGRANITES

As stated in the previous chapter, during the geological mapping of the Sierra Bermeja Pluton different rock-types have been distinguished, which have been broadly grouped into three main groups: 1) cordierite-bearing monzogranites, 2) mafic microgranular enclaves (MME), and 3) Vaugnerite series rocks and lamprophyres. Except the lamprophyres, the remaining rock-types can be plotted in the QAPF diagram (Le Maitre *et al*., 2002) for their modal classification (Fig. 25; Tables 1 and 2; Table 1 of the Appendix).

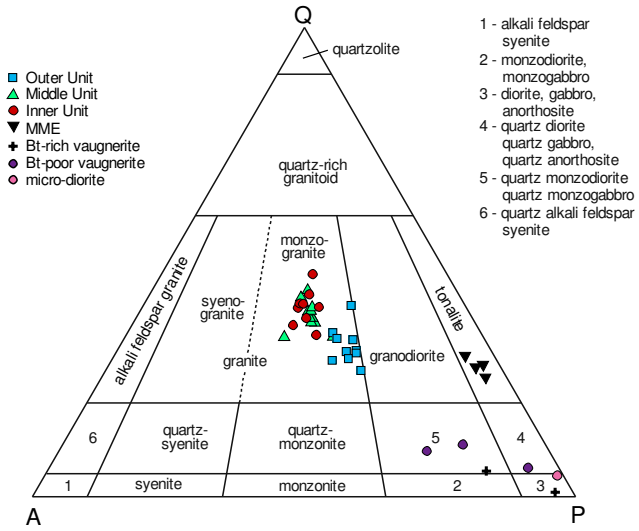


**Figure 25.** Projection of the Sierra Bermeja Pluton rocks in the QAP triangle of the QAPF classification diagram (Le Maitre *et al*., 2002).

Granites from the Sierra Bermeja Pluton plot within the monzogranite field of the QAPF diagram, showing similar proportions of plagioclase and K-feldspar (Fig. 25). Biotite and cordierite are present in the three monzogranite units, while muscovite is conspicuous in the IU. Apatite is the main accessory mineral in all units, followed by tourmaline,

monazite, zircon, ilmenite, xenotime, rutile and andalusite (the last two only observed in the IU; Table 1).

***Table 1.*** *Key petrographic features of the three monzogranitic units from the Sierra Bermeja Pluton*

| | Outer Unit (OU) | Middle Unit (MU) | Inner Unit (IU) |
|---|---|---|---|
| Enclaves | Mafic (MME) and felsic magmatic; pelitic | – | – |
| Kfs phenocrysts | 150–350/$m^2$ | Occasional | – |
| Groundmass crystal-size | Medium to coarse | Medium to coarse | Fine to medium |
| Mineral proportions (vol.%) | | | |
| Quartz | 26–38 | 31–40 | 31–41 |
| K-feldspar | 19–26 | 24–33 | 22–31 |
| Plagioclase | 33–45 | 25–35 | 24–32 |
| Cordierite | 1–5 | 4–10 | 1–7 |
| Biotite | 6–14 | 3–7 | 1–5 |
| Muscovite | 0–1 | 0–2 | 2–8 |
| Accessory minerals | Ap, Tur, Mnz, Zrn, Ilm, Xtm | Ap, Tur, Mnz, Zrn, Ilm, Xtm | Ap, Tur, Mnz, Zrn, Ilm, And, Xtm, Rt |

*In the Outer Unit K-feldspar was calculated adding an estimation of phenocryst concentration to the point count analyses.
Complete modal analyses in Supplementary Table 1 of the Appendix
Mineral abbreviations from Whitney and Evans (2010).

### 5.1.1. Outer Unit (OU)

As stated in the previous section, the most characteristic feature of this unit is its porphyritic nature, with a range of 150–350 phenocrysts of K-feldspar per $m^2$ (Table 1). These phenocrysts are enclosed in a holocrystalline phaneritic (medium- to coarse-grained; mostly in the range of 2–10 mm) biotite-rich groundmass, constituted by euhedral plagioclase, globular quartz, K-feldspar, biotite and cordierite prisms (Fig. 26). The presence of tonalitic mafic microgranular enclaves and the relatively greater biotite contents (color indexes between 10 and 15) compared to those of the other monzogranitic units are also the most conspicuous characteristics of these monzogranites (Table 1). Indeed, within the OU stands out a fine-grained variety (see Fig. 15 in Chapter 4) in which are found the highest biotite contents. In this fine-grained variety globular quartz is notably scarcer, as well as cordierite.

K-feldspar phenocrysts (up to 12 cm) are mesoscopically euhedral but at microscope scale often exhibit irregular edges due to the outgrowths that are crystallographically continuous with the K-feldspar of the groundmass. The later presents more subhedral forms (up to 10 mm). They commonly show poikilitic textures, with numerous inclusions of plagioclase, biotite, quartz, muscovite and apatite (Fig. 26 A and B), often arranged parallel to the crystallographic faces (Fig. 26 B and C). This preferential orientation of inclusions, coupled with the usual banded/zoning in the outer zones of many crystals (Fig. 26 C) points to multiple crystallization phases. This mineral phase, whether as phenocryst or crystal of the groundmass, is often Carlsbad-twinned (Fig. 26 D) and usually shows two generations of perthites, one of subsolidus exsolution that produces irregular veins, flames or films, and the other constituted by patches of replacement (*e.g.* Shelley, 1992).

Plagioclase (up to 15 mm) is euhedral (Fig. 26 E) and appears concentrically zoned (oscillatory or continuous), with often partially altered cores that show irregular shapes and/or resorption textures, and unaltered rims (Fig. 26 A–C). This alteration comprises fine-grained white phyllosilicates and, in many rims, the characteristic straight polysynthetic twinning shown in cores is lost (Fig. 26 E). Plagioclase crystals may appear also clustered into aggregates displaying a glomeroporphyritic texture formed by synneusis. Besides, myrmekitic textures are observable in contact with quartz crystals.

Quartz constitutes globular aggregates of subhedral crystals (up to 11 mm; Fig. 26 D, E) or may occur as anhedral interstitial crystals (Fig. 26 A). It shows undulatory extinction and local pressure solution at grain contacts, as well as microfractures (Fig. 26 D, E). Quartz may host small inclusions of biotite and muscovite. Minor quartz is found as euhedral crystals (up to 0.5 mm) and as inclusion in other mineral phases.

Biotite (up to 3 mm) is the main mafic mineral phase in this unit (up to 14 vol.%). It may appear as euhedral to subhedral single flakes or as polycrystalline aggregates. This mafic phase shows a strong pleochroism from reddish- to greenish-brown colors, and hosts numerous inclusions of radioactive isotope-bearing minerals such as monazite, zircon and apatite (Fig. 26 A, E, F). Biotite may be altered to chlorite or replaced by muscovite.

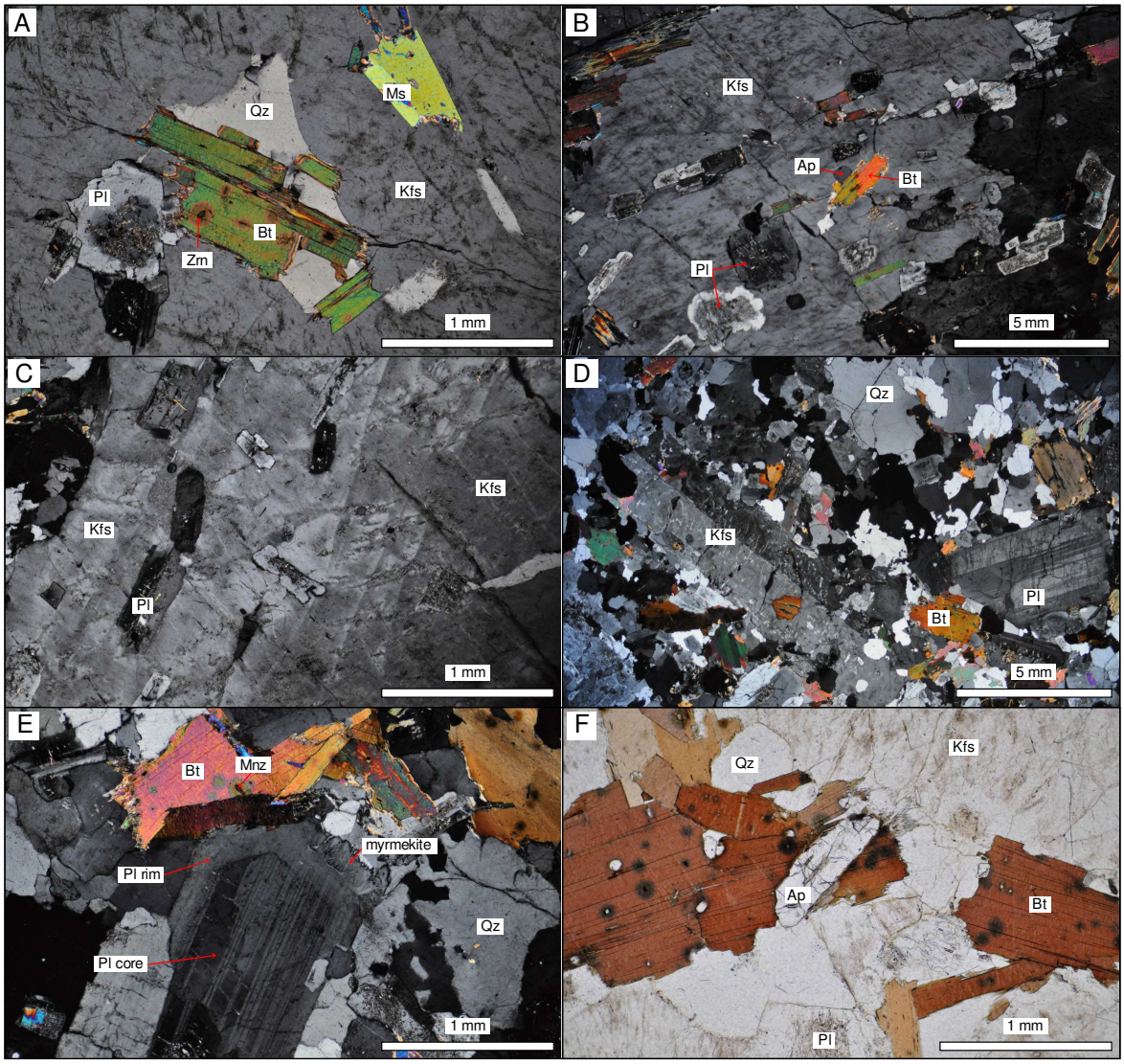


**Figure 26.** Optical photomicrographs (A–E in cross-polarized and F in plane-polarized light). A) Mineral inclusions in a poikilitic K-feldspar phenocryst. B) Detail of the marked orientation of mineral inclusions in a K-feldspar phenocryst. C) Detail of the edge of a K-feldspar phenocryst that shows oriented plagioclase crystals and banded/zoned structures. D) Representative granodioritic groundmass observed in the OU. E) Euhedral plagioclase that shows a well-developed rim with myrmekitic textures in contact with quartz. F) Prismatic apatite (center) with an inclusion. Note also that biotites hold abundant inclusions of radioactive minerals. Mineral abbreviations from Whitney and Evans (2010).

Cordierite (up to 6 mm) appears as euhedral short-prismatic single crystals. This mineral phase is variably altered, mainly through microfractures, to pinite, fine-grained pseudomorphs composed of muscovite + chlorite + biotite.

Muscovite is accessory, and postmagmatic in many cases, since arise as alteration product of K-feldspar, plagioclase, biotite and cordierite. Magmatic muscovite is displayed as single euhedral flakes (Fig. 26 A), while secondary muscovite appears as plates with irregular edges or as small subhedral crystals. Among the remaining accessory phases of this unit, apatite is the main one. Apatite usually is presented as euhedral prismatic crystals (up to 1 mm) and commonly is spatially related to biotite crystals or aggregates (Fig. 26 B, and F). This phosphate rarely shows inclusions of minor mineral phases (Fig. 26 F). Tourmaline, monazite (Fig. 26 E), zircon (Fig. 26 A), ilmenite and xenotime complete the accessory mineral assemblage of the OU.

### 5.1.2. Middle Unit (MU)

Monzogranites of the MU exhibit a medium- to coarse-grained (mostly in the range of 2–10 mm) hypidiomorphic seriated texture. The main mineralogy of these rocks include quartz, plagioclase, K-feldspar, cordierite and biotite, and the accessory mineral assemblage comprises apatite, tourmaline, monazite, zircon, ilmenite and xenotime (Fig. 27). As mentioned in the previous chapter, within the MU a subtype of monzogranite has been identified (see Fig. 15 in Chapter 4). This subtype is characterized by its greater abundance of biotite and lower content in cordierite.

K-feldspar (up to 16 mm) is euhedral–subhedral and shows similar characteristics to that from the groundmass of the OU. It often displays Carlsbad twinning and usually shows two generations of variably developed perthites, one developed under subsolidus exsolution constituting irregular veins, flames or films, and the other that form patches of replacement

(Fig. 27 A; *e.g.* Shelley, 1992). Inclusions of plagioclase, biotite, quartz, muscovite and apatite are common as well. Rarely, plagioclase-mantled K-feldspars defining rapakivi textures are observed.

Plagioclase (up to 15 mm) is euhedral and markedly zoned, showing oscillatory or continuous concentric zoning that produces well-developed rims around variably altered cores (Fig. 27 A and B). It commonly appears showing a polysynthetic-twinning and many times the outer rims or outgrowths show irregular edges in contact with other minerals from the groundmass (Fig. 27 A and B). Plagioclase crystals exhibit numerous inclusions of biotite, muscovite and quartz, often oriented parallel to the crystallographic faces (Fig. 27 B). Plagioclase may appear also clustered into aggregates that display a glomeroporphyritic texture, and myrmekitic textures are common in contact with quartz. Fine-grained white phyllosilicates constitute the alteration product of the cores, and in the case of considerably altered crystals, a well-developed patchy zoning is observed.

Quartz may appear as globular aggregates of subhedral crystals (up to 19 mm) or as anhedral interstitial crystals (Fig. 27 B–D, F). As in the OU it shows undulatory extinction, local pressure solution at grain contacts, and microfractures (Fig. 27 B–D, F). Quartz may contain small inclusions of other mineral phases such as biotite and muscovite. Fine euhedral quartz crystals (up to 1.5 mm) are also discerned in the groundmass or as inclusion in other mineral phases.

Cordierite (up to 18 mm) is the main mafic mineral phase in the monzogranites of the MU (up to 10 vol.%). It appears as euhedral short-prismatic single crystals, variably pinitized to yellowish fine-grained pseudomorphs composed by phyllosilicates, as well as larger biotite, chlorite and muscovite crystals (Fig. 27 C–E). It is easily distinguishable due to its particular alteration, which begins from the basal parting surfaces and cleavage, as well

as at the crystal edges, and progress up to replace completely some crystals. The first alteration product consist on a whitish–yellowish colored isotropic mass that evolves to yellowish–greenish micro–proto crystals that form polycrystalline aggregates. These fine-grained aggregates grow progressively to larger crystals, resulting in a replacement network of perpendicular bands (layers) coated with relatively large lamellae of white mica and light green subordinate chlorite together with brownish biotite that transects fresh cordierite (Fig. 27 D and E).

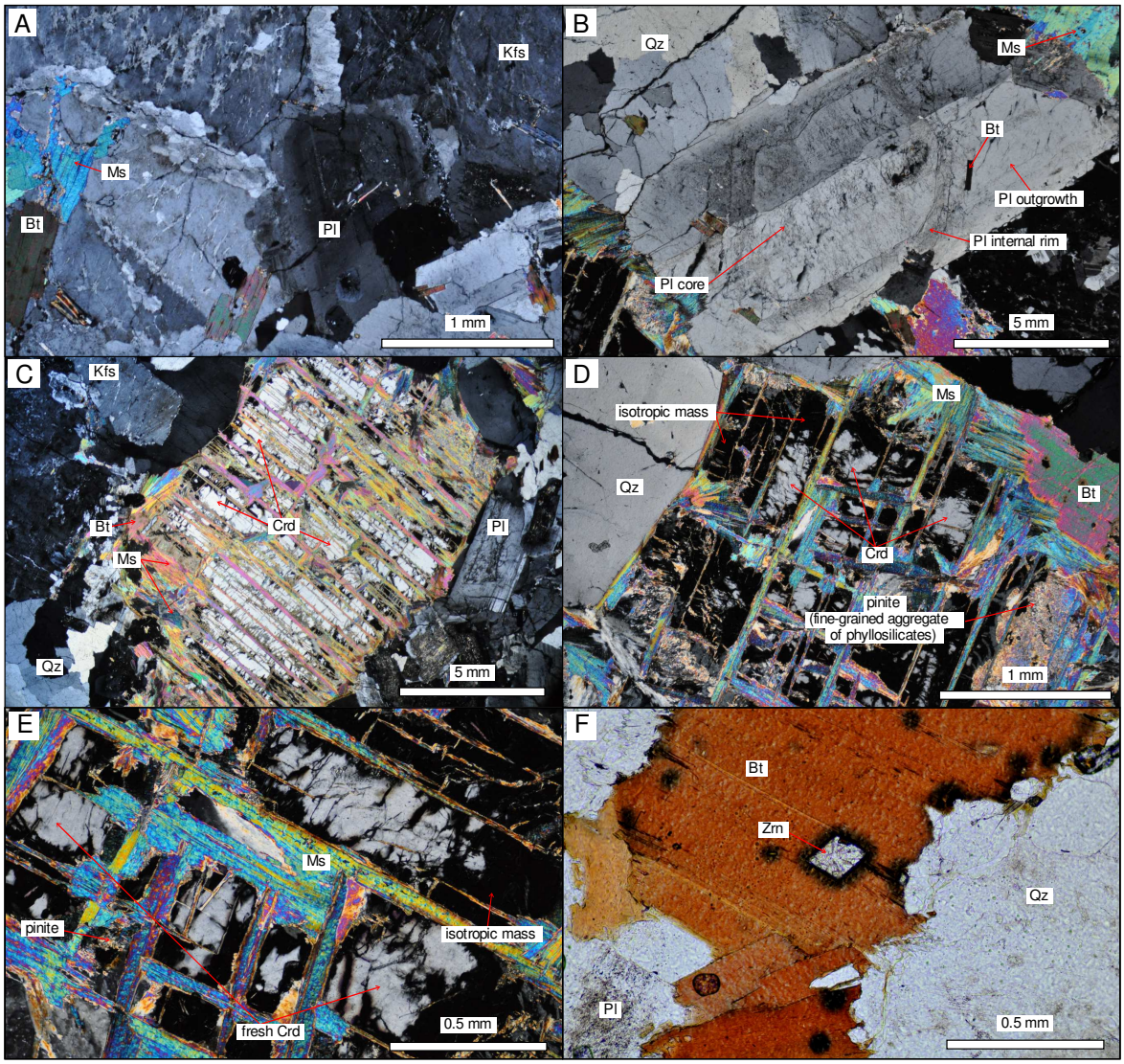


**Figure 27.** Optical photomicrographs (A–E in cross-polarized and F in plane-polarized light). A) Concentrically zoned plagioclase that shows irregular outgrowths. Note the similarity of K-feldspar with that to the OU, and the mica (biotite–muscovite) association. B) Euhedral plagioclase with different growth phases that hosts biotite inclusions. C) to E) Prismatic cordierite crystals with an advanced pinitization along their crystal edges and cleavage planes, increasing scale from C) to E). F) Detail of a zircon inclusion in a subhedral biotite crystal. Mineral abbreviations from Whitney and Evans (2010).

Biotite (up to 2 mm) appears as euhedral to subhedral single flakes or as polycrystalline micaceous aggregates that often enclose plagioclase crystals, composed by biotite or biotite + muscovite (Fig. 27 A and F). It shows a strong pleochroism from reddish- to greenish-brown colors, and bears abundant inclusions of radioactive minerals such as monazite, zircon and apatite (Fig. 27 F). Biotite may be altered to chlorite or replaced by muscovite.

Magmatic euhedral–subhedral muscovite (up to 2 mm) is slightly more abundant than in the OU monzogranites. It may appear as single euhedral flakes (Fig. 27 B) or in contact with biotite (Fig. 27 A), sometimes constituting complex polycrystalline aggregates. On the contrary, secondary muscovite constitutes the alteration product of K-feldspar, plagioclase, biotite and cordierite. This type of muscovite appears as plates with irregular edges, relatively large elongated crystals or small subhedral crystals.

The accessory mineral assemblage is constituted by apatite, tourmaline, monazite, zircon (Fig. 27 F), ilmenite and xenotime, outstanding the abundance of apatite (although in lower proportions than in the OU). This phosphate appears as euhedral prismatic crystals (up to 1 mm), often as inclusion in other mineral phases such as biotite, K-feldspar or plagioclase.

### 5.1.3. Inner Unit (IU)

The IU comprises yellowish monzogranites with fine- to medium-grained hypidiomorphic seriated texture, and low color index (generally < 6) that allows considering them as hololeucocratic. These leucogranites are constituted by K-feldspar, plagioclase, quartz, muscovite, cordierite and biotite, outstanding their finer crystal-size and higher muscovite contents respect to the other monzogranite units. The accessory mineral assemblage is constituted by apatite, tourmaline, monazite, zircon, ilmenite, andalusite, xenotime and

rutile. Similarly to the above described monzogranitic units, within the IU a subtype of monzogranite is also discernible (see Fig. 15 in Chapter 4) by its lower cordierite and higher biotite contents.

K-feldspar (up to 8 mm) is euhedral–anhedral and shows similar characteristics to that of the MU (Fig. 28 A). It often displays a murky appearance due to its alteration to phyllosilicates and Carlsbad twinning is common too. K-feldspar often shows two generations of variably developed perthites as in the other monzogranite units, one of subsolidus exsolution and the other of replacement. Inclusions of plagioclase, biotite, quartz, muscovite and apatite are common as well, and the largest crystals may exhibit undulatory extinction and microfractures filled with quartz.

Plagioclase (up to 9 mm) is euhedral and markedly zoned, with similar characteristics to that of the MU (Fig. 28 A and B). It shows an oscillatory or continuous concentric zoning that produces well-developed multiple rims enclosing variably altered cores. It bears abundant inclusions of biotite, muscovite and quartz, often oriented in parallel to the crystallographic faces, and the outer rims often show irregular edges. Plagioclase may appear also clustered into aggregates that display a glomeroporphyritic texture, and like in the other monzogranitic units, fine-grained white phyllosilicates constitute the alteration product of the cores.

Quartz is present as globular aggregates of subhedral crystals (up to 10 mm) that show slightly greater deformation than in the other two units. This feature is observable by its marked undulatory extinction and greater local pressure solutions at grain contacts. It may appear also as anhedral interstitial crystals, and as infill of microfractures (Fig. 28 B). Quartz may contain small inclusions of other mineral phases such as biotite and muscovite, and

euhedral crystals (up to 1.5 mm) are discerned in the groundmass or as inclusion in other phases.

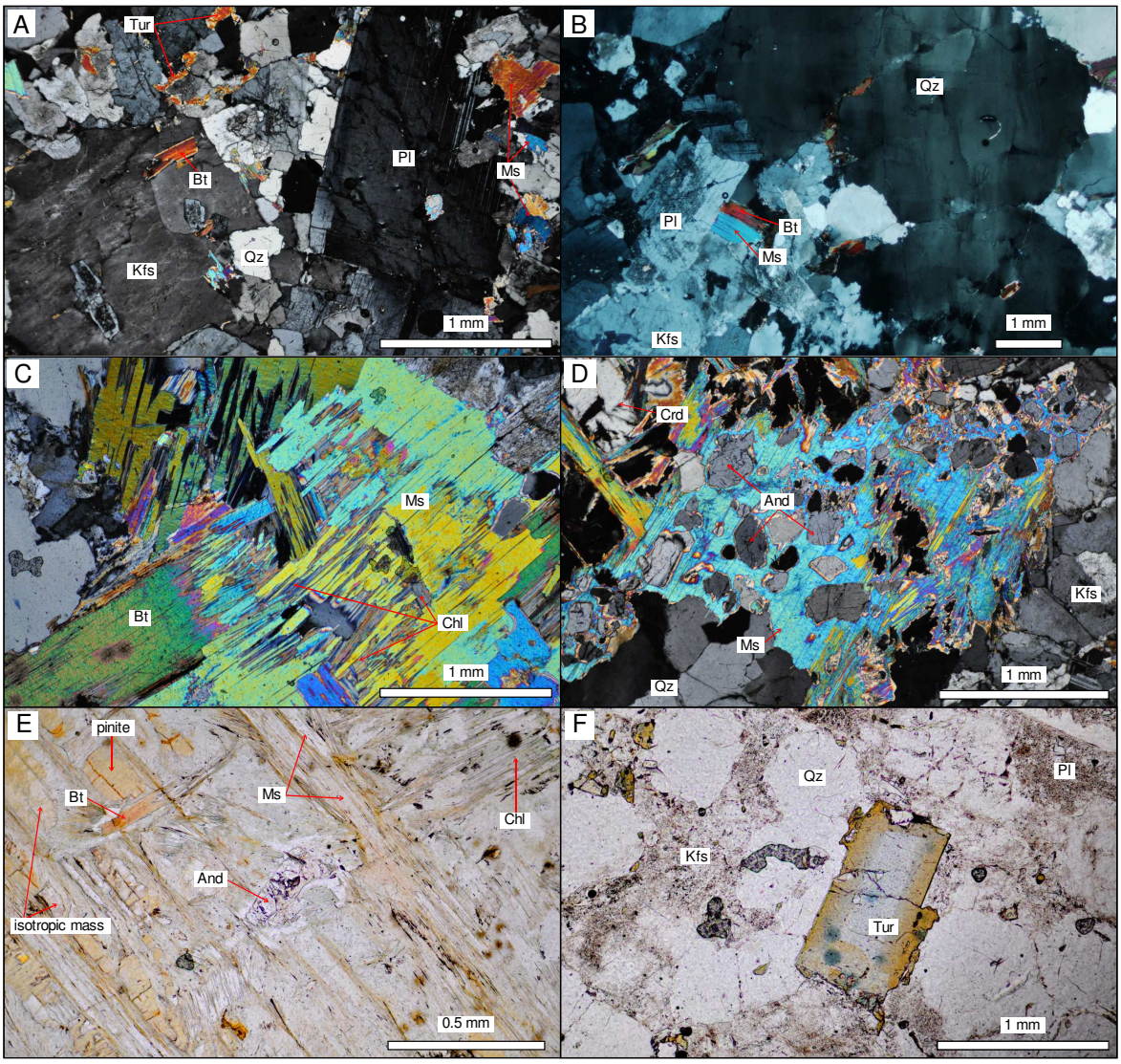


**Figure 28.** Optical photomicrographs (A–D in cross-polarized and E–F in plane-polarized light). A) Representative microphotograph of the IU monzogranites. B) Undulatory extinction in globular aggregates of subhedral quartz crystals. C) Detail of an aggregate of biotite + muscovite crystals. D) Poikilitic muscovite that encloses a number of andalusite crystals. E) Inclusion of andalusite in a completely altered cordierite prism. F) Zoned euhedral prismatic tourmaline crystal. Mineral abbreviations from Whitney and Evans (2010).

Muscovite (up to 4 mm) appears as euhedral–subhedral crystals and, compared with other monzogranitic units from the Sierra Bermeja Pluton, constitutes the most characteristic mineral phase of this unit (up to 8 vol.%). It may appear as single euhedral flakes, euhedral–subhedral plates in contact or intergrowth with biotite or as subhedral large poikilitic flakes (Fig. 28 A–E). Poikilitic muscovite encloses several mineral phases such as quartz,

plagioclase, K-feldspar, andalusite, tourmaline and apatite (Fig. 28 D). Muscovite is often pleochroic (reddish to pinkish colors) and locally the largest flakes may show undulatory extinction. On the contrary, secondary muscovite constitutes the alteration product of K-feldspar, plagioclase, biotite and cordierite, where comprises plates with irregular edges, relatively large elongated crystals (Fig. 28 E) or small subhedral crystals.

Cordierite is conspicuous in this monzogranite unit and, as in the other ones, appears as euhedral short-prismatic single crystals (up to 9 mm), variably altered to pinite, biotite, chlorite and muscovite. Its characteristic alteration that is extraordinary well-visible in these rocks begins from the basal parting surfaces and cleavage, and also from the crystal edges. The alteration, as mentioned previously, results on a network of perpendicular bands of an aggregate constituted by white micas and subordinate light green chlorite and brownish biotite (Fig. 28 E). The space between these bands is occupied by a whitish–yellowish colored isotropic product that evolves to yellowish–greenish micro–proto crystals that constitute polycrystalline aggregates. An outstanding feature of these cordierites is that occasionally they host some andalusite crystals (Fig. 28 E).

Biotite (up to 2 mm) appears as euhedral to subhedral single flakes or as polycrystalline micaceous aggregates, often coupled with muscovite. Commonly shows intercalations of muscovite plates (Fig. 28 A–C, E). It shows a strong pleochroism from reddish- to greenish-brownish colors and is rich in inclusions of radioactive minerals such as monazite, zircon and apatite. Biotite may be altered to chlorite or replaced by muscovite.

The accessory mineral assemblage is constituted by apatite, tourmaline, monazite, zircon, ilmenite, andalusite, xenotime and rutile, outstanding the abundance of apatite and tourmaline. Apatite appears as euhedral prismatic crystals (up to 1 mm), often as inclusion in other mineral phases such as biotite, K-feldspar or plagioclase. Tourmaline may appear

as euhedral single prisms (up to 2 mm) or as anhedral infill of microfractures and interstitial spaces (Fig. 28 A and F). This boron silicate exhibits a chromatic concentric zoning (Fig. 28 F) and is strongly pleochroic, with orange–yellowish tones in the core and bluish colors at rims.

## 5.2. MAFIC MICROGRANULAR ENCLAVES

Mafic microgranular enclaves (MME) of the Sierra Bermeja Pluton are tonalitic (Fig. 25) and show a porphyritic texture with phenocrysts of plagioclase, quartz and biotite enclosed in a fine-grained groundmass constituted by the same mineralogy plus accessory K-feldspar, apatite, zircon and ilmenite (Fig. 29 A). Their color index vary in a relatively wide range (18–30).

Plagioclase (up to 2 mm) is euhedral and markedly zoned, with continuous or oscillatory concentric zoning that leads to well-developed rims that enclose variably altered cores (Fig. 29 B–D). It hosts numerous inclusions of biotite, often oriented in parallel to the crystallographic faces. Frequently the outer rims or outgrowths of plagioclase crystals show irregular edges (Fig. 29 B–D). In some cases, the core is the most altered zone of the crystals (Fig. 29 C), although occasionally an intermediate rim can appear completely altered to phyllosilicates (Fig. 29 D).

Quartz appears as globular aggregates of subhedral crystals (up to 3 mm) or as an anhedral interstitial mineral phase. Quartz may contain small inclusions of other mineral phases such as biotite apatite and plagioclase. Some larger globular aggregates (up to 9 mm) have been interpreted as xenocrysts of the host monzogranites.

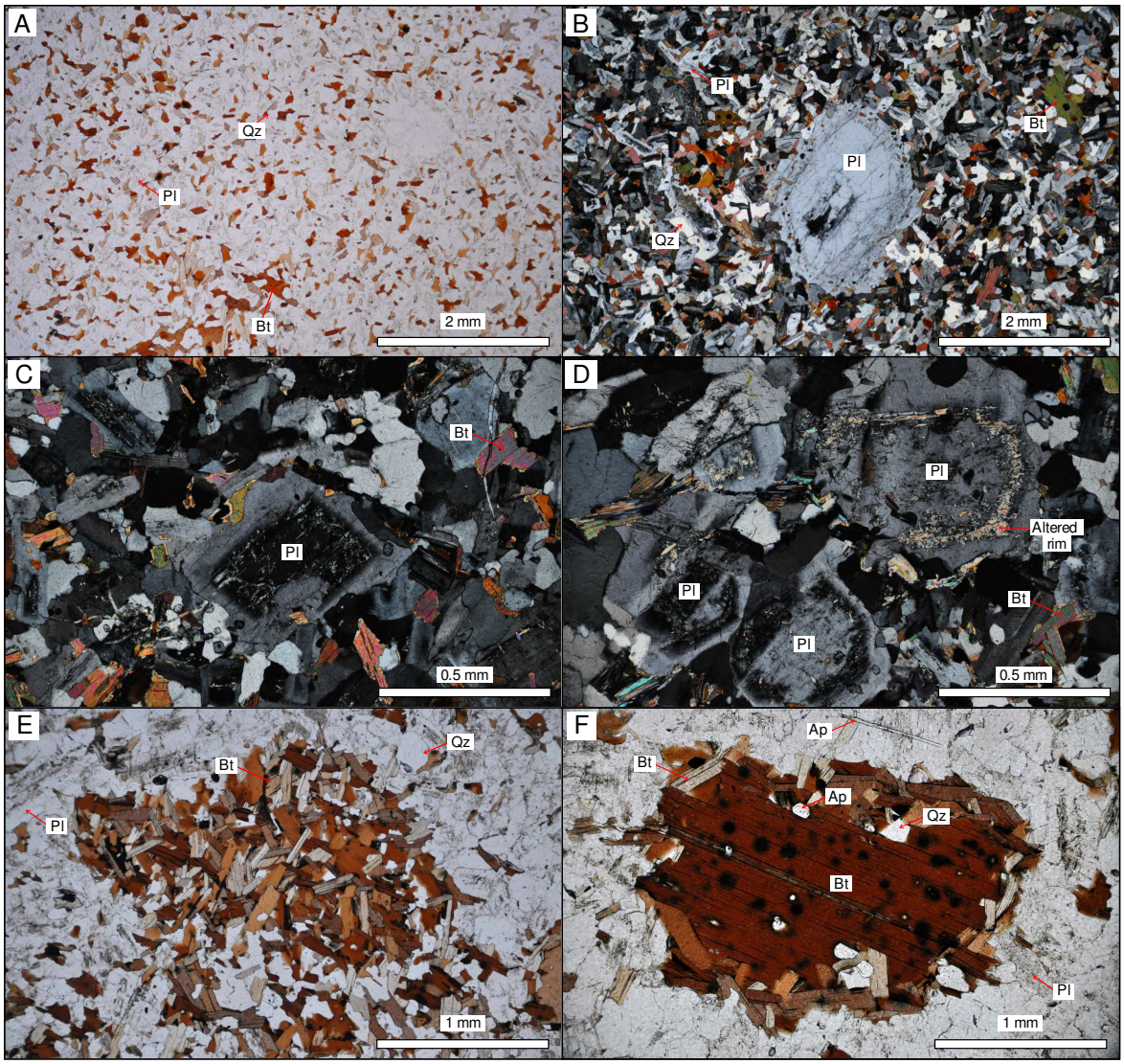


**Figure 29.** Optical photomicrographs (A, E, F in plane-polarized and B, C, D in cross-polarized light). A) Groundmass of a representative MME. B) Plagioclase phenocryst with several oriented inclusions within the outer outgrowth. C) and D) Different types of alteration in plagioclase crystals, in the core (center) and in intermediate rims, respectively. E) An aggregate of biotite + plagioclase + quartz. F) Biotite phenocryst rich in inclusions of quartz and apatite, this large crystal is enclosed by smaller biotite crystals. Mineral abbreviations from Whitney and Evans (2010).

Biotite (< 0.5 mm) mainly appears as euhedral–subhedral single flakes that constitute an essential component of the groundmass (up to 30 vol.%; Fig. 29 A–D). It may appear also as polycrystalline aggregates composed mainly by biotite but accompanied by plagioclase and quartz (Fig. 29 E). Large phenocrysts (up to 2 mm) of this mineral are also observed, coated by finer biotite crystals of the groundmass (Fig. 29 F). In general, biotite shows a strong pleochroism from reddish- to greenish-brownish colors and may contain inclusions

of radioactive minerals. Among these minerals apatite and zircon/monazite crystals have been recognized.

The accessory mineral assemblage is constituted by K-feldspar, with similar characteristics to that of the monzogranites, apatite, which appears as euhedral prismatic or acicular crystals (up to 1 mm), zircon/monazite and ilmenite.

## 5.3. VAUGNERITE SERIES ROCKS AND LAMPROPHYRES

As pointed out in the previous chapter, mafic rocks that form alignments within the Sierra Bermeja Pluton comprise phaneritic and aphanitic terms, which will be referred to as vaugnerite series rocks and lamprophyres, respectively (see Chapter 9 for more details). All studied mafic rocks are composed by variable amounts of the following minerals (Table 2): plagioclase, amphibole, clinopyroxene, biotite, K-feldspar, quartz, apatite, titanite, zircon, allanite, pyrite, ilmenite and chromite. Secondary mineralogy consists of epidote, zoisite, titanite, calcite, chlorite and sericite. Qualitatively, the mineralogy is fairly homogeneous but, as mentioned earlier, each alignment is composed by either vaugnerites or lamprophyres whose main differences in petrography are described below.

### 5.3.1. Vaugnerite series rocks

Vaugnerite series rocks from the Sierra Bermeja Pluton are phaneritic, and exhibit a mesocratic (color index: 39–47), fine- to medium-grained (0.5–3 mm), hipidio-idiomorphic, inequigranular seriated texture (Figs. 30 and 31). Mineral modal contents (Table 2) reveal the existence of two types of phaneritic rocks: biotite-rich (Fig. 30) and biotite-poor (Fig. 31). In the former, plagioclase and amphibole are the main constituents, followed by clinopyroxene and K-feldspar, whereas accessory phases are titanite, zircon, allanite, pyrite, ilmenite, chromite and biotite, standing out their relatively high quartz and apatite contents

(Table 2). The apparent absence of biotite in this biotite-poor facies (Table 2) must be taken with caution since some chlorite aggregates enclose traces of biotite microcrystals (< 0.3mm) that suggest originally biotite contents were slightly greater than those currently observed (yet < 5 vol.%). In the biotite-rich terms, plagioclase, biotite, clinopyroxene and K-feldspar are the main constituents, followed by minor contents of quartz, amphibole and apatite, besides the aforementioned accessories (Table 2). Following Le Maitre *et al.* (2002) these phaneritic rocks are classified as diorites, quartz diorites and quartz monzodiorites (Fig. 25).

***Table 2.*** *Representative modal compositions (in vol.%) of the mesocratic rocks from the Sierra Bermeja Pluton*

| Rock-type | Lamprophyre | | Vaugnerite series rocks | | | | | | | Micro-dt |
|---|---|---|---|---|---|---|---|---|---|---|
| | Mnt | Kersantite | | | Bt-rich | | Bt-poor | | | |
| Sample | JE 15 22 | JE 15 70 | JE 16 38 | JE 16 43 | JE 16 06 | JE 17 03 | JE 16 04 | JE 16 41 | JE 17 01 | JE 15 40 |
| Pl | 9.6 | 50.5 | 42.8 | 54.4 | 50.5 | 43.5 | 43.8 | 48.7 | 38.7 | 55.3 |
| Cpx | 6.7 | 8.8 | 15.6 | 12.3 | 24.0 | 19.6 | 14.0 | 9.2 | 14.9 | 4.9 |
| Bt | 18.7 | 26.2 | 21.7 | 19.2 | 21.9 | 21.7 | - | - | - | 0.5 |
| Amp | 1.1 | 13.7 | 16.1 | 12.2 | - | 2.5 | 25.2 | 32.5 | 27.7 | 31.9 |
| Kfs | 54.9 | - | 2.4 | 0.3 | 2.0 | 7.6 | 9.2 | 3.3 | 12.9 | 0.6 |
| Qz | 5.6 | - | 0.9 | 0.8 | 0.3 | 2.7 | 6.4 | 3.3 | 5.7 | 2.8 |
| Ap | 1.6 | - | 0.3 | 0.3 | 0.6 | 1.3 | 1.4 | 1.5 | 0.3 | 1.3 |
| Opq | 1.8 | 0.8 | 0.2 | 0.3 | 0.4 | 1.1 | 0.1 | 1.2 | - | 2.7 |
| Other | - | - | - | - | 0.4 | - | - | 0.5 | - | - |

Mnt (minette); Micro-dt (micro-diorite)
Mineral abbreviations from Whitney and Evans (2010).

Plagioclase (up to 3 mm) is the main rock-forming mineral of the dioritoids of the Sierra Bermeja Pluton (up to 55 vol.%; Table 2). This mineral is euhedral and relatively elongated, with a marked concentric zoning that produces well-developed thin rims around considerably altered cores (Figs. 30 and 31). It may also includesmall crystals of biotite, apatite and ilmenite. Frequently the outer rims or outgrowths of plagioclase show irregular edges, commonly unaltered, although in some cases completely replaced crystals are observed too.

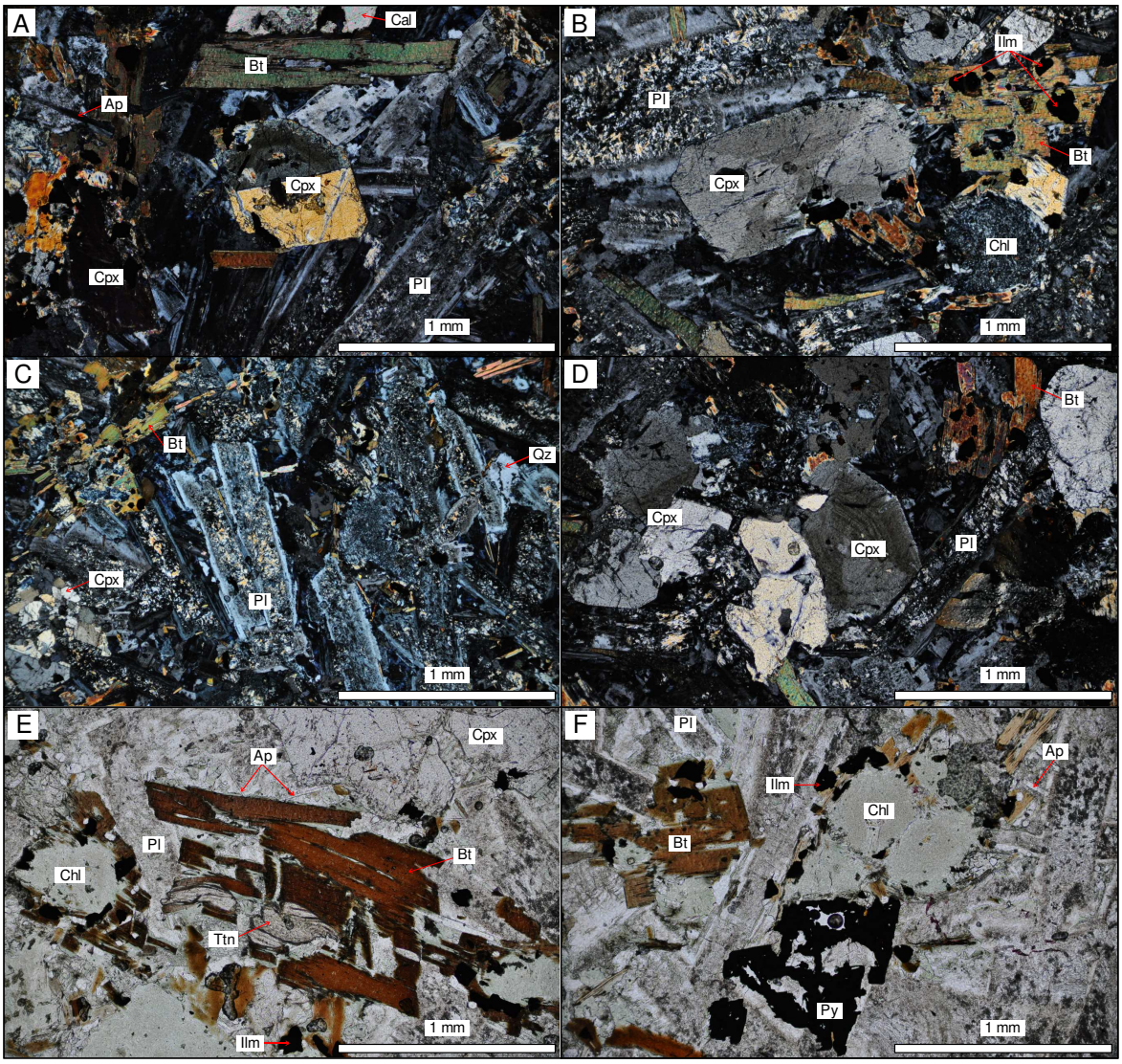


**Figure 30.** Optical photomicrographs of biotite-rich vaugnerites (A–D in cross-polarized and E–F in plane-polarized light). A) Twinned clinopyroxene that shows a concentric oscillatory zoning. B) Clinopyroxene with hour-glass sector zoning and several ilmenite inclusions in biotite. C) Fairly oriented plagioclases with notably altered cores and unaltered rims. D) Polycrystalline aggregate of clinopyroxene (center) with an outstanding well-developed concentric oscillatory zoning. E) Aggregate of relatively large biotite crystals, partially altered to titanite. F) Pyrite crystal and pseudomorph of clinopyroxene constituted by chlorite. Mineral abbreviations from Whitney and Evans (2010).

Pyroxene (up to 3 mm) is one of the most representative mineral phase of the vaugnerite series rocks from the Sierra Bermeja Pluton (up to 24 vol.% in vaugnerites) This mineral classifies as clinopyroxene, appearing mainly as euhedral prismatic colorless single crystals (Figs. 30 and 31), although it may also appear as polycrystalline aggregates. In the biotite-rich terms, it shows a concentric oscillatory zoning and a higher birefringence than

those from the biotite-poor terms (30 A, B, D and 31 C, D). Sometimes hour-glass sector zoning and simple twinning are observed as well in the biotite-rich terms (Fig. 30 D).

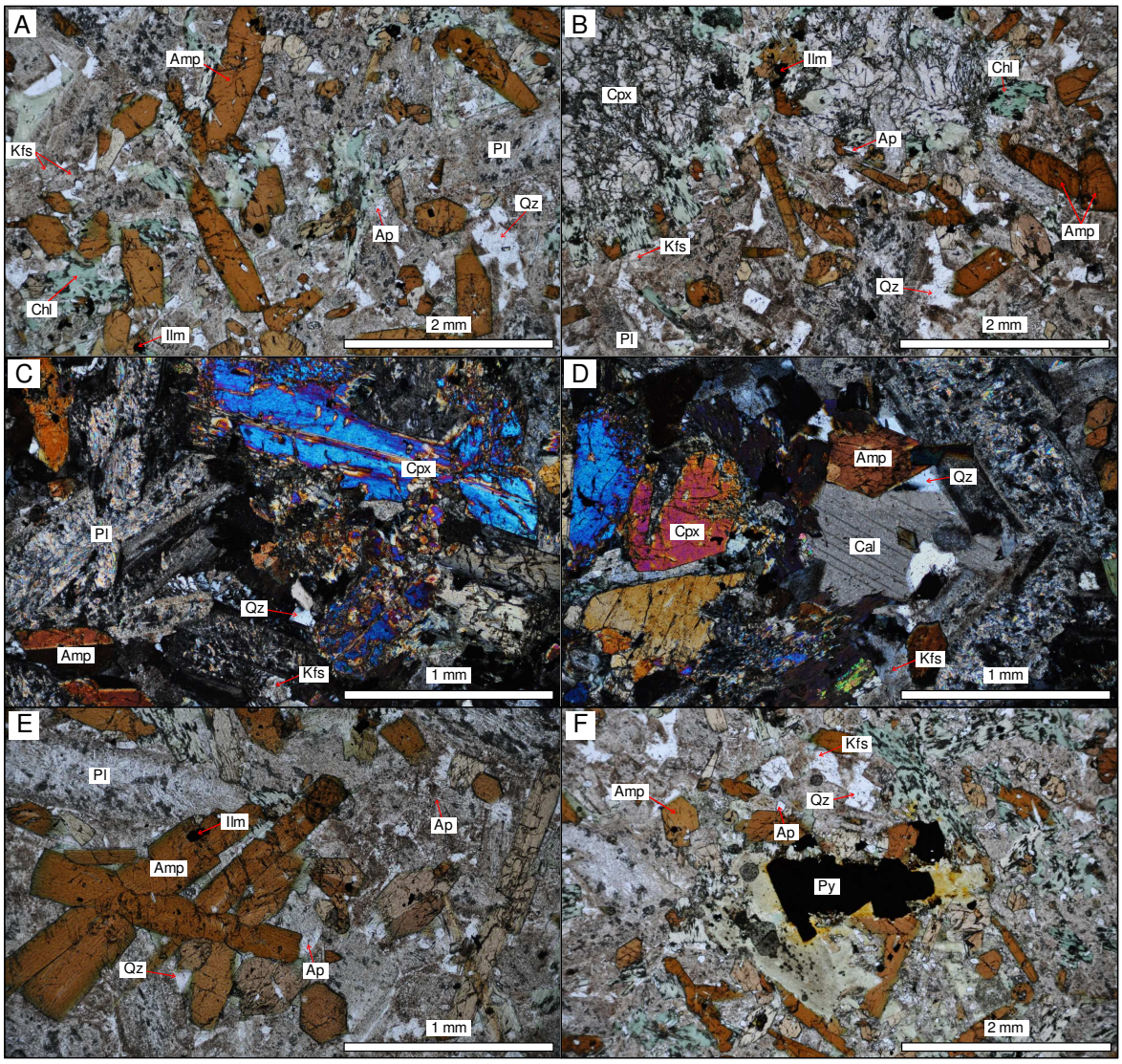


**Figure 31.** Optical photomicrographs of biotite-poor vaugnerites (A, B, E, F in plane-polarized and C–D in cross-polarized light). A) Single amphibole crystals enclosed by notably altered plagioclases. B) Fractured clinopyroxene aggregates and single amphibole crystals. C) Characteristic appearance of clinopyroxene and twinned amphiboles. D) Interstitial quartz, replacement of calcite, and alteration of a ferromagnesian phase to epidote. E) Glomeroporphyritic texture in amphibole. F) Aggregate of pyrite crystals and interstitial accessory K-feldspar. Mineral abbreviations from Whitney and Evans (2010).

Amphibole (up to 3 mm) is the second most abundant mineral phase in the biotite-poor vaugnerites (up to 33 vol.%). It appears as euhedral to subhedral prismatic–tabular elongated crystals, with notorious pleochroism from dark- to light-brown colors (Fig. 31).

Single crystals are the most abundant, although glomeroporphyritic textures are also common (Fig. 31); moreover, many amphibole crystals are twinned (Fig. 31 C).

Biotite (up to 2 mm) appears primarily as euhedral–subhedral single flakes, with a strong pleochroism from reddish- to greenish-brownish colors. Nevertheless, it may appear also as polycrystalline aggregates (Fig. 30). Biotite is commonly altered to chlorite, titanite and epidote in variable degrees, and contrarily to those biotites of the monzogranites, rarely contains inclusions of radioactive minerals (Fig. 30).

K-feldspar appears as interstitial mineral phase, with a murky appearance that allows differentiation from plagioclase. Quartz is also an interstitial phase, and apatite (up to 1.5 vol.%) may appear as euhedral prismatic crystals or as elongated acicular crystals. Finally, zircon, allanite, pyrite, ilmenite and chromite complete the accessory mineral assemblage of the vaugnerite series rocks (Table 2).

### 5.3.2. Lamprophyres

Lamprophyres from the Sierra Bermeja Pluton are mesocratic (color index 44–54) and show holocrystalline porphyritic texture (Fig. 32), although phenocrysts are relatively scarce (2–7 vol.%) and rarely exceed 2 mm in size. Phenocrysts are represented mostly by clinopyroxene, and less often, by amphibole and biotite. Plagioclase phenocrysts (up to 2 mm), sporadically arranged in glomeroporphyritic aggregates, have been identified only in one sample (thus termed as micro-dioritoid; Table 2). The groundmass is microcrystalline and constituted by these same minerals plus the same accessory mineralogy to that of the vaugnerite series rocks. According to their texture and modal contents (see Table 2), these aphanitic rocks have been classified as kersantites, except for one sample that would be classified as minette.

Plagioclase (up to 0.5 mm), is the main rock-forming mineral of these mesocratic rocks (up to 54 vol.%; Table 2). Nevertheless, in the aphanitic mesocratic rocks from the Sierra Bermeja Pluton, this mineral phase is restricted exclusively to the groundmass. It appears as euhedral relatively elongated crystals, with considerably altered cores and well-developed rims that produce a marked concentric zoning (Fig. 32 A). Inclusions of other mineral phases are uncommon and difficult to discern due to the widespread alteration. In some samples, as other mineral phases of the groundmass, plagioclase crystals show a preferential orientation.

Clinopyroxene (up to 2.5 mm) is the main mineral phase present as phenocryst, and appears mainly as euhedral prismatic colorless single crystals (Fig. 32 B–D, F). Frequently it appears clustered, constituting polycrystalline aggregates of about 4–8 crystals defining a glomeroporphyritic texture. Petrographically these clinopyroxenes are similar to those of the biotite-poor vaugnerites, characterized by their high birrefrigence, often twinned and poorly zoned. Apart from phenocrysts, clinopyroxene may be displayed as minor crystals in the groundmass too.

Biotite (up to 1 mm) is the most abundant ferromagnesian phase in the lamprophyres (Table 2) and may occur as euhedral–subhedral phenocrysts (Fig. 32 B) or as constituent of the groundmass (Fig. 32). Biotite phenocrysts may appear as fairly equidimensional single flakes, but in the groundmass the habit is notably more elongated. These biotite phenocrysts commonly show a chromatic concentric zoning (from dark-brown colors in the cores to light-brown ones in the rims; Fig. 32 B), and a strong pleochroism from reddish- to greenish-brownish colors. Biotite crystals are commonly altered to chlorite, titanite and epidote and as in vaugnerites, rarely contain inclusions of radiogenic minerals (Fig. 32).

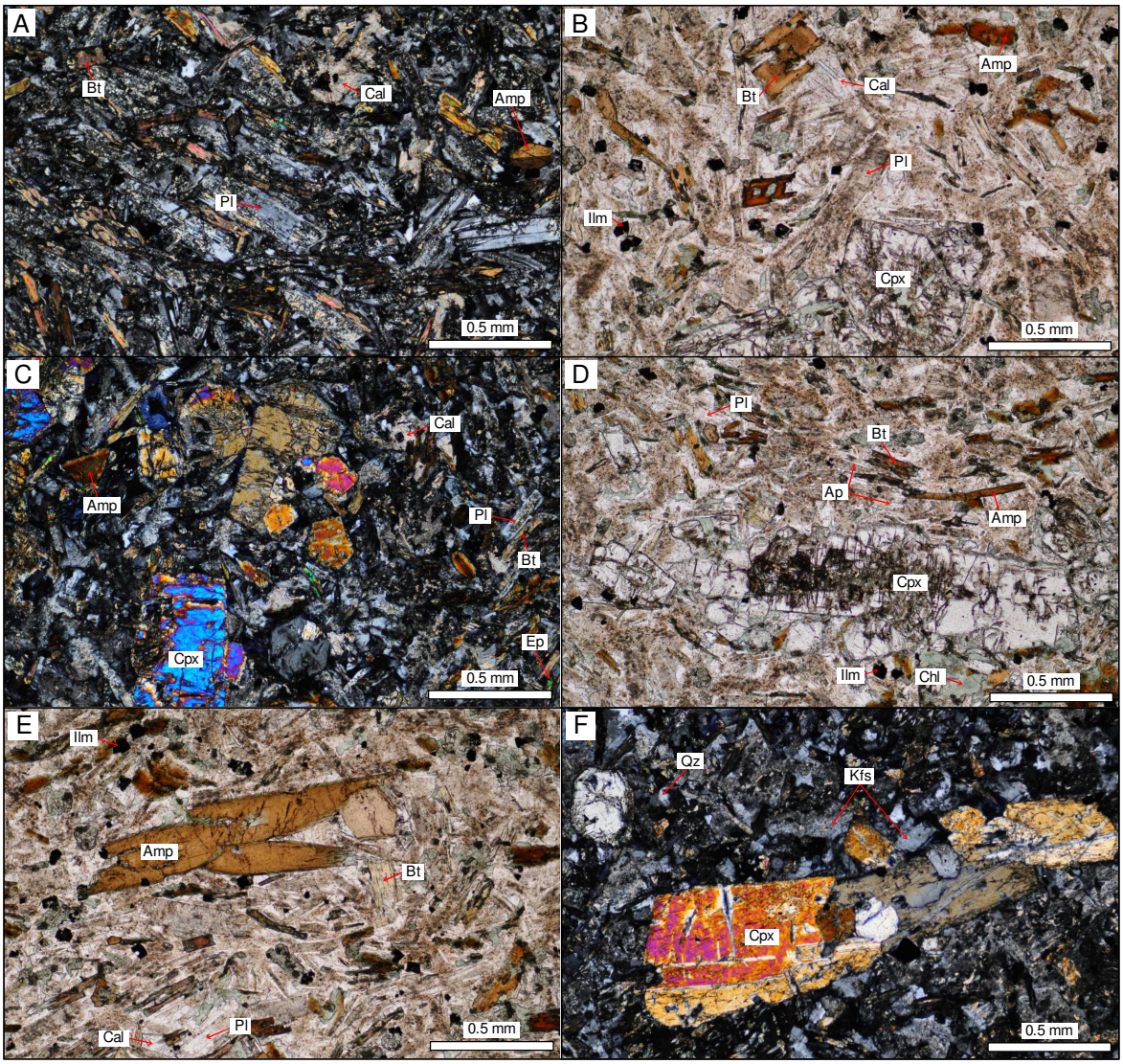


**Figure 32.** Optical photomicrographs of lamprophyres (A, C, F in cross-polarized and B, D, E in plane-polarized light). A–E: kersantites. F: minette. A) Representative plagioclase crystals that integrate the groundmass of lamprophyres. B) Concentrically zoned biotite phenocrysts and an aggregate of clinopyroxene crystals. C) Detail of clinopyroxene glomerocrystals. D) Fairly oriented crystals and a clinopyroxene aggregate. E) Aggregate of amphibole phenocrysts enclosed in a groundmass composed by biotite + plagioclase + amphibole + ilmenite. F) Clinopyroxene phenocrysts aggregate enclosed in a groundmass constituted mainly by K-feldspar. Mineral abbreviations from Whitney and Evans (2010).

Amphibole (up to 1.5 mm) is the second most abundant mineral phase in the studied lamprophyres (up to 16 vol.%). It appears as euhedral to subhedral prismatic elongated crystals that constitute phenocrysts, or as elongated–acicular crystals conforming part of the groundmass (Fig. 32 A–E). This ferromagnesian phase shows a notorious pleochroism from dark- to light-brown colors like in vaugnerites, and many phenocrysts show simple twinning

too. Although amphibole occurs mainly as single crystals, glomerocrysts of this mineral are also common (Fig. 32 E).

K-feldspar is mainly discerned in the minette (up to 55 vol.%), and rarely observed in the kersantites (Table 2). In the later it appears as an interstitial mineral phase in the groundmass, while in the minette occurs as euhedral to subhedral prismatic crystals (Fig. 32 F). K-feldspar shows a murky appearance due to its slight alteration and do not shows a zoning that leads to altered cores and well-developed rims.

Finally, the accessory mineral assemblage of the lamprophyres of the Sierra Bermeja Pluton includes minor amounts of quartz, apatite (up to 1.6 vol.%), zircon, allanite, pyrite, ilmenite and chromite.

### 5.3.3. Particular textures of the mesocratic rocks of the Sierra Bermeja Pluton

Besides the main textural features described above, a number of particular textures have been recognized in the mesocratic rocks from the Sierra Bermeja Pluton (Fig. 33). In many lamprophyres quartz ocelli have been observed, formed by relatively large quartz crystals (up to 3 mm). These quartz crystals, interpreted as xenocrysts, occur surrounded by a rim of amphibole and clinopyroxene crystals (Fig. 33 A) and often exhibit crystal embayments. Clinopyroxene clots are common in the most hybridized samples (near the contact between vaugnerites and the observed felsic rocks, see Fig. 22), and are constituted by a central, euhedral–subhedral clinopyroxene crystal that often is completely replaced by chlorite (pseudomorphs of up to 2 mm) surrounded by a polycrystalline rim of amphibole and ilmenite, principally (Fig. 33 B and C). Sparse felsic segregations, constituted primarily by K-feldspar and quartz (± plagioclase ± amphibole), are also common in those hybridized samples. These segregates may form irregular micro-veins with very irregular and diffuse

limits (Fig. 33 C), or may appear as globular textures or well-defined droplets of up to 2 mm in diameter (Fig. 33 D and E). Nevertheless, observed droplets, which are enclosed by a rim of amphibole and biotite, lack plagioclase or amphibole crystals into them, whereas the existence of euhedral to subhedral calcite is common (Fig. 33 D, E).

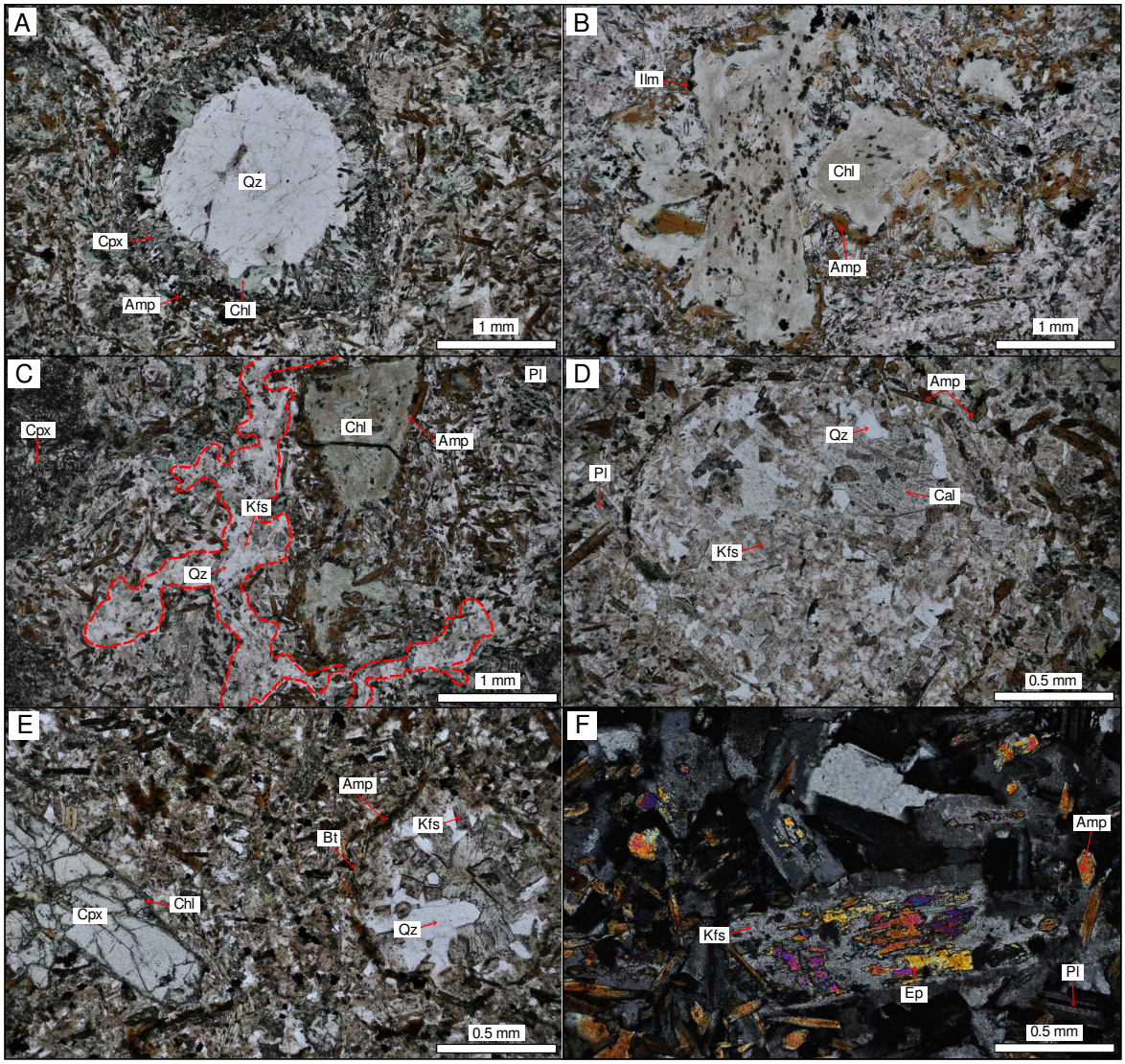


**Figure 33.** Optical photomicrographs of particular textures discerned in the studied mesocratic rocks (A–E in plane-polarized and F in cross-polarized light). A) Quartz ocelli. B) Clot of clinopyroxene pseudomorphs surrounded by amphibole and ilmenite crystals. C) Felsic segregate composed mainly by quartz and K-feldspar, note its irregular contacts. Droplet of quartz + K-feldspar enclosed by amphibole crystals. E) Clinopyroxene phenocryst that shows a fine-grained chlorite rim and a felsic droplet rimmed by amphibole and biotite crystals. F) A K-feldspar crystal showing patchy alteration to epidote. Mineral abbreviations from Whitney and Evans (2010).

In some cases, prismatic clinopyroxene crystals that do not show a notable alteration may present fine-grained chlorite rims (Fig. 33 E), and patchy alteration to epidote of

feldspar crystals is common in many samples (Fig. 33 F). The coexistence of stubby prismatic and acicular apatite and the occasional presence of host monzogranite microenclaves, characterized by their irregular and diffuse external limits, complete the observed particular textures in the mesocratic rocks from the Sierra Bermeja Pluton.

# CHAPTER 6
# MINERAL CHEMISTRY

## 6.1. INTRODUCTION

This chapter addresses the mineralogical characterization of the different rock-types from the Sierra Bermeja Pluton, such as cordierite-bearing monzogranites, mafic microgranular enclaves (MME), vaugnerite series rocks and lamprophyres. EMP and LA-ICP-MS analyses were performed in the University of Oviedo and at the Geochronology and Isotope Geochemistry-SGIker Facility of the University of the Basque Country, respectively (see the 'Methods' section in Chapter 3 for additional details). Complete data are reported in the Supplementary Table 2–10 of the Appendix, although representative analyses are shown in Tables 3–12 thorough this chapter. The chapter has been divided in two main sections, since monzogranites and MME have been handled together, as well as vaugnerite series rocks and lamprophyres.

## 6.2. CORDIERITE-BEARING MONZOGRANITES AND MME

In this section, cordierite-bearing monzogranites and MME have been considered together for their mineralogical characterization. Major- and trace-element contents in K-feldspar, plagioclase, biotite, muscovite, cordierite and apatite were determined in monzogranites of the three main units of the Sierra Bermeja Pluton (Tables 3–5, 7), and accessory minerals were also analyzed for their proper identification (Table 6). On the other hand, in MME only major elements have been analyzed.

## 6.2.1. Feldspars

Chemical characteristics of feldspars are fairly similar in the three main monzogranitic units of the pluton (Fig. 34). The compositions of non-perthitic K-feldspar, both as phenocrysts or as subhedral to interstitial crystals in the groundmass, fall in the range $Or_{81}$–$Or_{98}$. On the other hand, plagioclase shows normal zoning, from slightly altered andesine–oligoclase cores (~$An_{33}$–$An_{20}$) to fresh oligoclase–albite ($An_{20}$–$An_{01}$) rims (see Table 3). In detail, the compositional range of analyzed plagioclases is slightly narrower in the IU ($An_{18}$–$An_{04}$; Fig. 34 A). K-feldspar, which only appears as an accessory phase, has not been analyzed in the MME; their plagioclase is more calcic than those of the monzogranites, ranging from andesine to oligoclase compositions ($An_{40}$–$An_{18}$; Fig. 34 A), standing out the absence of albitic rims (Fig. 34 A).

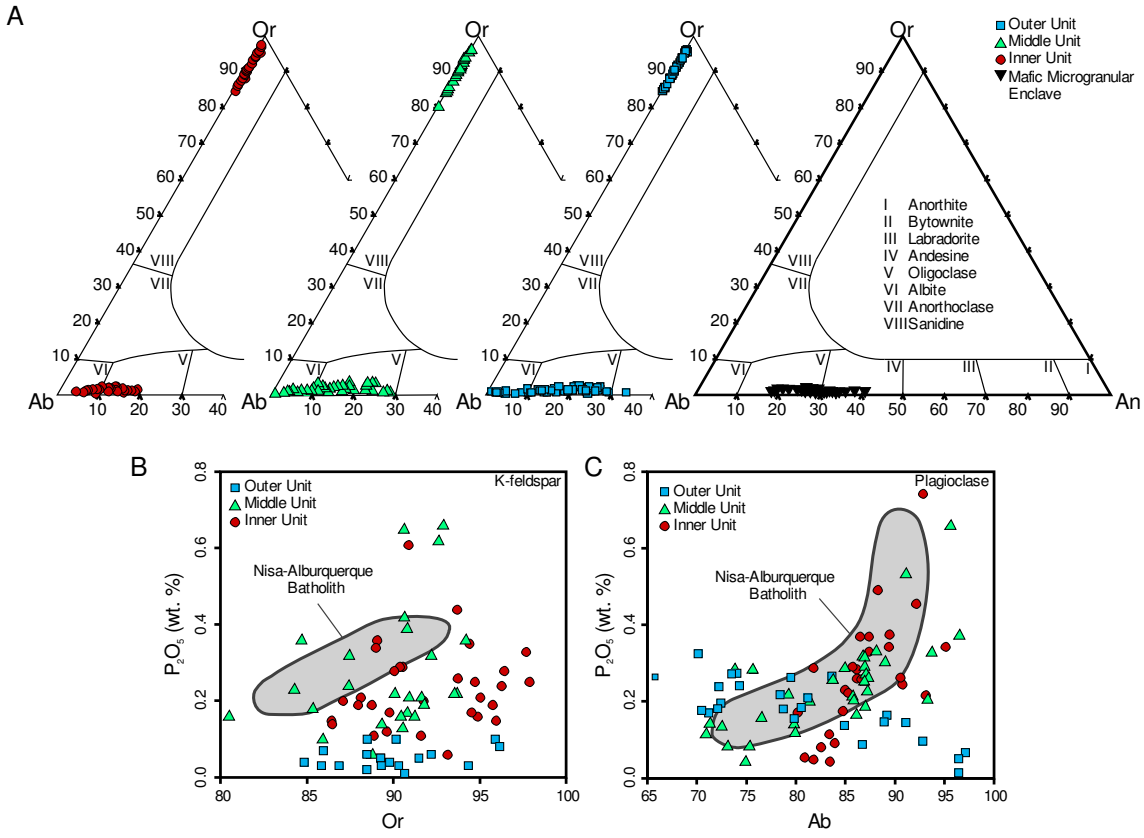


**Figure 34.** Feldspar compositions of the Sierra Bermeja Pluton. A) Or–Ab–An diagram for feldspars of monzogranites and MME (Deer *et al.*, 1963). B) Or (mol. %) *vs.* $P_2O_5$ (wt.%) diagram for K-feldspars. C) Ab (mol. %) *vs.* $P_2O_5$ (wt.%) diagram for plagioclases.

Compositional differences between feldspars of the three main units of the Sierra Bermeja Pluton are observed in relation to their $P_2O_5$ contents (Fig. 34 B and C; Table 3). K-feldspars of the OU exhibit the lowest contents in $P_2O_5$ (< 0.10 wt.%) as compared to those of the MU (up to 0.66 wt.%) and IU (up to 0.61 wt.%). A clear negative correlation between Ab and $P_2O_5$ contents is observed in plagioclases of the OU, whereas this correlation is positive, with up to ~0.70 wt.% in $P_2O_5$ in the MU and IU (Fig. 34 C).

***Table 3.*** *Representative electron microprobe analyses of feldspars from the Sierra Bermeja Pluton monzogranites*

| | K-feldspar | | | | Plagioclase | | |
|---|---|---|---|---|---|---|---|
| | OU (phenocryst) | OU (groundmass) | MU | IU | OU | MU | IU |
| | Kfs 9[a] | Kfs 8[a] | Kfs 64[a] | Kfs 86[a] | Pl 24[a] | Pl 62[a] | Pl 123[a] |
| $SiO_2$ | 64.39 | 65.10 | 64.22 | 63.85 | 61.45 | 64.08 | 65.43 |
| $TiO_2$ | < MDL | 0.03 | < MDL | < MDL | < MDL | < MDL | 0.00 |
| $Al_2O_3$ | 18.93 | 18.64 | 18.84 | 19.29 | 24.39 | 22.60 | 22.02 |
| $Cr_2O_3$ | < MDL | < MDL | 0.03 | 0.05 | < MDL | < MDL | < MDL |
| NiO | < MDL | < MDL | < MDL | < MDL | < MDL | < MDL | 0.04 |
| FeO | 0.02 | < MDL | < MDL | < MDL | < MDL | < MDL | 0.02 |
| MnO | < MDL | < MDL | < MDL | < MDL | < MDL | 0.02 | < MDL |
| MgO | 0.03 | < MDL | < MDL | < MDL | < MDL | 0.03 | < MDL |
| CaO | 0.02 | 0.02 | 0.04 | 0.03 | 5.39 | 3.60 | 1.92 |
| $Na_2O$ | 0.94 | 0.85 | 0.96 | 0.58 | 8.18 | 9.26 | 10.40 |
| $K_2O$ | 15.60 | 15.59 | 15.51 | 16.10 | 0.22 | 0.66 | 0.28 |
| $P_2O_5$ | 0.05 | 0.06 | 0.16 | 0.25 | 0.20 | 0.22 | 0.34 |
| Total | 100.00 | 100.31 | 99.78 | 100.17 | 99.84 | 100.47 | 100.49 |
| Or | 91.47 | 92.20 | 91.22 | 94.69 | 1.29 | 3.73 | 1.57 |
| Ab | 8.42 | 7.68 | 8.56 | 5.14 | 72.36 | 79.23 | 89.32 |
| An | 0.12 | 0.12 | 0.22 | 0.16 | 26.35 | 17.04 | 9.11 |

Complete data in Supplementary Tables 2 and 3 of the Appendix
[a]Code from the Supplementary Tables 2 and 3 of the Appendix
The Method Detection Limit (MDL) for the routine analysis of common elements is ~0.02 wt.%

Rb, Sr and Ba contents in feldspars are nearly identical in all monzogranites (Table 4 of the Appendix). Average contents of these trace-elements are notably higher in K-feldspar (Rb = 419 ppm; Sr = 558 ppm; Ba = 2814 ppm) than in plagioclase (Rb = 2.0 ppm; Sr = 13.1 ppm; Ba = 25.7 ppm). In this respect, the low Sr contents in plagioclase are remarkable.

## 6.2.2. Micas

All analyzed biotites correspond to Al-rich type (Table 4) and, as expected, they plot in the peraluminous field of the biotite classification diagrams of Nachit *et al.* (1985), Abdel-Rahman (1994) and Rossi and Chevremont (1987; Fig. 35 A and B). In the monzogranites there is a progressive decrease in the Mg# value [Mg/(Mg + $Fe^{2+}$)] from the OU (0.38–0.45) to the MU (0.32–0.38) and to the IU (0.27–0.35; Fig. 35 C). This reduction in the Mg# value is accompanied by a progressive decrease in the Ti content (OU and MU: 0.146–0.243 atoms per formula unit (a.p.f.u); IU: 0.001–0.195 a.p.f.u). In the same vein, the highest Mg# values are those from the MME (0.42–0.51), and consequently they plot closer to the calc-alkaline field of biotite classification diagrams (Fig. 35 A and B).

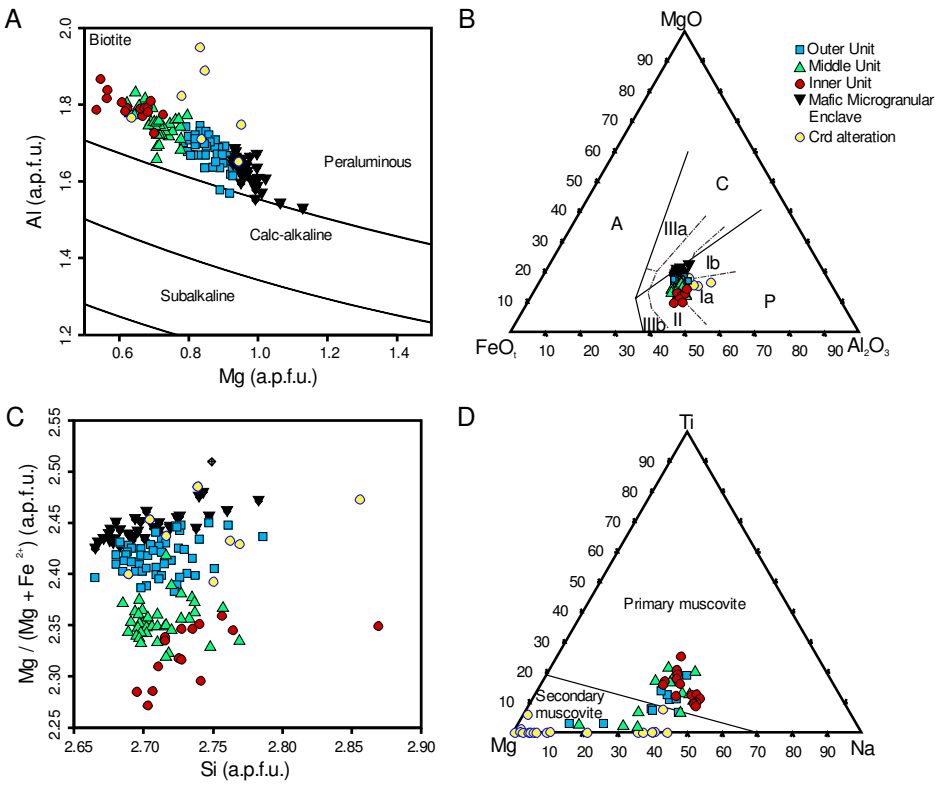


**Figure 35.** Mica compositions of the Sierra Bermeja Pluton. A) Magmatic series discrimination diagram for biotites (Nachit *et al.*, 1985). B) Magmatic series discrimination diagram based on biotite compositions; solid lines taken from Abdel-Rahman (1994) and dashed lines from Rossi and Chevremont (1987). C) Biotite-phlogopite discrimination diagram for biotites s.l. (Deer *et al.*, 1962). Fields have been omitted for a better visualization. D) Mg–Ti–Na classification diagram for muscovite (Miller *et al.*, 1981).

Conversely, there is a slight enrichment in $Al^{Tot}$(a.p.f.u.) from MME (1.53–1.69) to monzogranites, as well as from the OU (1.57–1.75) to the MU (1.66–1.83) and IU (1.73–1.95; Table 4). The lowest F contents measured in biotite come from the OU. Regarding trace elements, the analyzed biotites from the monzogranites are relatively poor in Ba (average of 424 ppm) and Sr (average of 6.01 ppm), with common Rb contents (average of 1166 ppm; Table 4 of the Appendix).

***Table 4.*** *Representative electron microprobe analyses of micas from the Sierra Bermeja Pluton MME and monzogranites*

| Mineral | Biotite | | | | Muscovite* | | |
|---|---|---|---|---|---|---|---|
| Unit | MME | OU | MU | IU | OU | MU | IU |
| | Bt 134[a] | Bt 54[a] | Bt 67[a] | Bt 101[a] | Ms 4[a] | Ms 16[a] | Ms 28[a] |
| $SiO_2$ | 35.24 | 35.60 | 34.86 | 34.92 | 45.92 | 46.34 | 45.92 |
| $TiO_2$ | 3.67 | 3.77 | 3.41 | 3.19 | 0.41 | 0.56 | 0.81 |
| $Al_2O_3$ | 17.95 | 18.41 | 19.14 | 19.76 | 34.94 | 34.67 | 35.00 |
| $Cr_2O_3$ | 0.07 | 0.08 | 0.05 | 0.04 | < MDL | < MDL | 0.02 |
| NiO | 0.02 | < MDL | < MDL | < MDL | < MDL | < MDL | < MDL |
| FeO | 19.21 | 19.18 | 20.91 | 21.33 | 1.24 | 1.37 | 1.39 |
| MnO | 0.35 | 0.32 | 0.55 | 0.33 | 0.02 | 0.04 | < MDL |
| MgO | 8.36 | 8.00 | 6.30 | 5.25 | 0.94 | 0.97 | 0.89 |
| CaO | 0.03 | < MDL | < MDL | < MDL | 0.06 | < MDL | < MDL |
| $Na_2O$ | 0.13 | 0.12 | 0.10 | 0.06 | 0.56 | 0.69 | 0.60 |
| $K_2O$ | 9.62 | 9.68 | 9.67 | 9.21 | 10.41 | 10.47 | 10.31 |
| F | 0.31 | 0.36 | 0.27 | 0.30 | 0.20 | 0.27 | 0.24 |
| Cl | 0.03 | 0.03 | 0.05 | 0.03 | < MDL | < MDL | < MDL |
| Total | 94.99 | 95.55 | 95.30 | 94.42 | 94.71 | 95.4 | 95.19 |
| Mg# | 0.44 | 0.43 | 0.35 | 0.31 | 0.17 | 0.18 | 0.16 |

Complete data in Supplementary Tables 5 and 6 of the Appendix
[a]Code from the Supplementary Tables of the Appendix
The Method Detection Limit (MDL) for the routine analysis of common elements is ~0.02 wt.%
*Primary magmatic muscovite

As mentioned in the previous chapter, muscovite can appear either as inclusions in K-feldspar phenocrysts, as an alteration product of cordierite, or as late-magmatic euhedral–subhedral crystals in the groundmass. Excluding those muscovite crystals derived from the alteration of cordierite, muscovites of the IU plot in the magmatic primary field of the Ti–Mg–Na ternary diagram of Miller *et al.* (1981), whereas those of the MU and OU both fall in the primary and in the secondary muscovite fields (Fig. 35 D). However, primary

muscovites of the three monzogranitic units of the Sierra Bermeja Pluton are compositionally very similar, being characterized by their variable contents in F (0.05–0.33 wt.%), $TiO_2$ (0.30–1.23 wt.%) and $Na_2O$ (0.44–0.80 wt.%). It is remarkable that some apparently primary muscovite crystals plot in the secondary muscovite field of the Ti–Mg–Na classification diagram (Miller *et al.*, 1981; Fig. 35 D). Muscovites that occur as alteration product of cordierite fall in the secondary muscovite field of the Ti–Mg–Na ternary diagram of Miller *et al.* (1981), although some of them have similar Mg contents to those from primary fields (Fig. 35 D).

### 6.2.3. Cordierite

Analyzed cordierites plot in the magmatic fields of the Mg/(Mg + Fe + Mn) *vs.* Σchannel cations and ($Na_2O + K_2O + CaO$) *vs.* MnO classification diagrams of Pereira and Bea (1994) and Villaseca *et al.* (2008), respectively (Fig. 36). Specifically, they would correspond to cordierites of S-type granites (Villaseca *et al.*, 2008). The Na + K values are all in the range of 0.31–0.43 (a.p.f.u.), with cordierites from the IU being the most homogeneous (0.37–0.39 a.p.f.u.). Cordierites of the IU and MU have lower MnO contents (0.23–0.62 wt.%) than those of the OU (0.56–0.81 wt.%), whereas Mg# values are slightly lower in the IU (0.47–0.56 wt.%) than in the OU and MU (0.51 to 0.60 wt.%; Table 5).

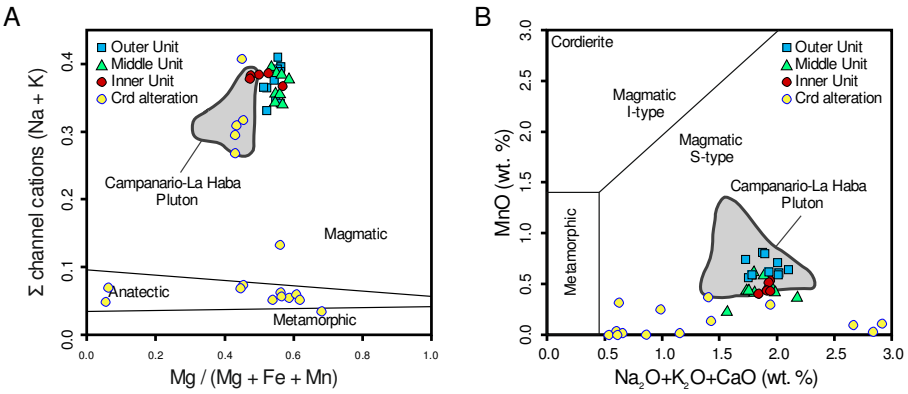


**Figure 36.** Cordierite compositions in the discriminant diagrams. A) Mg/(Mg + Fe + Mn) *vs.* Σchannel cations (Pereira and Bea, 1994) and B) $Na_2O + K_2O + CaO$ *vs.* MnO (based on Villaseca *et al.*, 2008)

***Table 5.*** *Representative electron microprobe analyses of cordierites from the Sierra Bermeja Pluton monzogranites*

| Mineral | Cordierite | | | | |
|---|---|---|---|---|---|
| Unit | OU | MU | IU | Altered Crd | |
| | Crd 7[a] | Crd 14[a] | Crd 25[a] | Crd 36[a] | Crd 40[a] |
| $SiO_2$ | 48.12 | 47.37 | 47.39 | 42.98 | 39.74 |
| $TiO_2$ | < MDL | < MDL | < MDL | < MDL | < MDL |
| $Al_2O_3$ | 31.27 | 31.89 | 31.65 | 37.04 | 32.06 |
| $Cr_2O_3$ | < MDL | < MDL | < MDL | < MDL | < MDL |
| NiO | < MDL | < MDL | < MDL | 0.17 | < MDL |
| FeO | 7.99 | 8.11 | 8.48 | 4.08 | 4.93 |
| MnO | 0.71 | 0.46 | 0.43 | < MDL | 0.25 |
| MgO | 6.28 | 6.25 | 5.54 | 0.13 | 6.19 |
| CaO | 0.07 | < MDL | 0.03 | 0.26 | 0.72 |
| $Na_2O$ | 1.91 | 1.90 | 1.90 | 0.07 | 0.06 |
| $K_2O$ | 0.03 | < MDL | 0.03 | 0.30 | 0.20 |
| F | < MDL | < MDL | < MDL | 0.09 | 0.08 |
| Cl | < MDL | < MDL | < MDL | < MDL | < MDL |
| Total | 96.37 | 96.03 | 95.46 | 85.14 | 84.25 |
| Mg# | 0.56 | 0.57 | 0.53 | 0.053 | 0.68 |

Complete data in Supplementary Table 7 of the Appendix
[a]Code from the Supplementary Tables of the Appendix
The Method Detection Limit (MDL) for the routine analysis of common elements is ~0.02 wt.%

While the differences in major-elements are relatively small, trace-element contents clearly discriminate the cordierites of the OU from those of the MU and IU (Fig. 37).

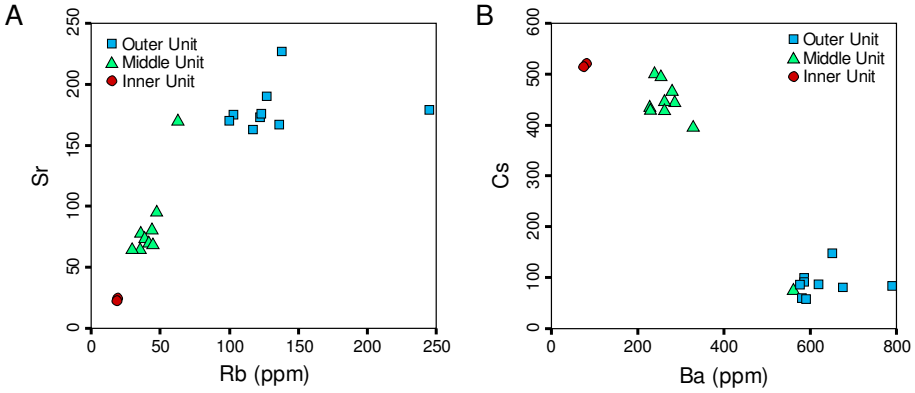


**Figure 37.** A) Rb *vs.* Sr and B) Ba *vs.* Cs binary plots for cordierites from the Sierra Bermeja Pluton.

Cordierites of the OU have average contents of Rb (135 ppm), Sr (180 ppm) and Ba (628 ppm) markedly higher than in the MU and IU (Rb: 38 ppm; Sr: 74 ppm; Ba: 257 ppm; Table 4 of the Appendix). On the contrary, Cs contents are clearly lower in cordierites from

the OU (average of 87.6 ppm) compared with those of the MU and IU cordierites (average of 430 ppm).

Most of the altered cordierites are well-discriminated in the classification diagrams of Pereira and Bea (1994) and Villaseca *et al.* (2008), showing clearly lower values of Σchannel cations and lower MnO contents (Fig. 36; Table 5). Those analyses that fall close to fresh cordierite may be enduring only slight incipient alteration.

### 6.2.4. Accessory minerals

Accessory mineralogy of monzogranites comprises apatite, tourmaline, monazite, zircon, ilmenite, andalusite, xenotime and rutile, whereas in MME is constituted by apatite, zircon and ilmenite (see Chapter 5). Compositions of accessory minerals are homogeneous in all monzogranite units, as well as in MME. Representative analyses are shown in Table 6.

***Table 6.*** *Representative electron microprobe analyses of some accessory minerals from the Sierra Bermeja Pluton MME and monzogranites*

| Min. | Ap | Ap | Ap | Ap | Tur | Ilm | Ilm | And | And | Rt |
|---|---|---|---|---|---|---|---|---|---|---|
| Unit | OU | MU | IU | MME | IU | MU | MME | IU | IU | IU |
| $SiO_2$ | 0.14 | 0.03 | < MDL | 0.15 | 36.46 | 0.03 | 0.03 | 36.65 | 36.8 | 0.14 |
| $TiO_2$ | < MDL | < MDL | < MDL | < MDL | 0.4 | 53.6 | 53.86 | 0.1 | 0.11 | 97.95 |
| $Al_2O_3$ | < MDL | < MDL | < MDL | < MDL | 35.37 | < MDL | 0.03 | 62.24 | 62.36 | 0.05 |
| $Cr_2O_3$ | < MDL | < MDL | 0.02 | < MDL | < MDL | < MDL | < MDL | < MDL | < MDL | < MDL |
| NiO | < MDL | < MDL | 0.04 | < MDL | < MDL | < MDL | < MDL | 0.02 | < MDL | < MDL |
| FeO | 0.12 | 0.3 | 0.68 | 0.34 | 10.02 | 43.32 | 42.09 | 0.4 | 0.45 | 1.79 |
| MnO | 0.65 | 1.17 | 0.99 | 0.62 | 0.09 | 3.24 | 4.64 | 0.02 | < MDL | 0.18 |
| MgO | 0.05 | 0.04 | 0.07 | 0.06 | 3.43 | 0.05 | 0.04 | 0.04 | 0.02 | < MDL |
| CaO | 54.52 | 53.88 | 53.98 | 53.95 | 0.13 | 0.01 | 0.03 | < MDL | < MDL | 0.09 |
| $Na_2O$ | < MDL | 0.08 | 0.05 | 0.07 | 1.84 | < MDL | < MDL | 0.01 | < MDL | < MDL |
| K2O | < MDL | < MDL | < MDL | 0.01 | 0.04 | < MDL | < MDL | < MDL | < MDL | < MDL |
| $P_2O_5$ | 41.69 | 42.13 | 42.4 | 41.75 | NA | NA | NA | NA | NA | NA |
| F | 2.77 | 2.84 | 2.4 | 3.12 | NA | NA | NA | NA | NA | NA |
| Cl | 0.06 | < MDL | < MDL | 0.08 | NA | NA | NA | NA | NA | NA |
| Total | 100.03 | 100.49 | 100.66 | 100.16 | 87.78 | 100.26 | 100.73 | 99.49 | 99.76 | 100.21 |

Complete data of apatites in Supplementary Table 8 of the Appendix

[a]Code from the Supplementary Tables of the Appendix

The Method Detection Limit (MDL) for the routine analysis of common elements is ~0.02 wt.%

NA not analyzed

Mineral abbreviations from Whitney and Evans (2010).

In order to develop a geochemical modelling, some trace elements have been analyzed in apatites from the different monzogranite units of the Sierra Bermeja Pluton (Table 7).

***Table 7.*** *Trace-element compositions (in ppm) of apatites from the Sierra Bermeja Pluton monzogranites*

| Sample | Ap1 | Ap2 | Ap3 | Ap4 | Ap5 | Ap6 | Ap7 | Ap8 | Ap9 | Ap10 |
|---|---|---|---|---|---|---|---|---|---|---|
| Unit | OU | OU | OU | OU | OU | OU | OU | OU | MU | MU |
| Y | 1620 | 2127 | 2280 | 2480 | 2278 | 1830 | 2106 | 1790 | 1843 | 2265 |
| Zr | 164 | 125 | 3500[a] | 2.11[a] | 84.5 | 520[a] | 1330[a] | 2380[a] | 80.2 | 15700[a] |
| Th | 14.9[a] | 8.76 | 5.00[a] | 5.89[a] | 9.12 | 5.80[a] | 11.1[a] | 20.3[a] | 4.13 | 14.9[a] |
| La | 151 | 166 | 225 | 247 | 286 | 208 | 211 | 188 | 222 | 231 |
| Ce | 547 | 628 | 887 | 1013 | 1011 | 740 | 749 | 687 | 780 | 774 |
| Pr | 87.0 | 103 | 139 | 153 | 157 | 111 | 117 | 110 | 127 | 126 |
| Nd | 461 | 575 | 712 | 770 | 799 | 574 | 597 | 565 | 674 | 685 |
| Sm | 200 | 265 | 280 | 315 | 309 | 234 | 253 | 240 | 283 | 307 |
| Eu | 4.73 | 6.85 | 9.35 | 10.7 | 5.50 | 4.86 | 5.48 | 6.52 | 4.53 | 4.45 |
| Gd | 249 | 327 | 348 | 392 | 356 | 277 | 305 | 283 | 335 | 380 |
| Tb | 46.9 | 62.9 | 66.3 | 73.7 | 64.2 | 50.3 | 56.9 | 51.1 | 59.1 | 70.9 |
| Dy | 305 | 410 | 448 | 524 | 431 | 335 | 376 | 334 | 360 | 433 |
| Er | 152 | 191 | 217 | 242 | 211 | 168 | 191 | 161 | 167 | 211 |
| Tm | 21.1 | 25.3 | 28.3 | 30.6 | 26.6 | 21.9 | 25.3 | 21.4 | 20.3 | 29.8 |
| Yb | 129 | 151 | 161 | 175 | 150 | 122 | 142 | 123 | 119 | 194 |
| Lu | 15.9 | 18.0 | 20 | 20.7 | 17.7 | 14.3 | 17.4 | 15.4 | 13.9 | 25.7 |

[a]Samples with high error (> 10 %)

***Table 7.*** *Continued*

| Sample | Ap11 | Ap12 | Ap13 | Ap14 | Ap15 | Avg.[b] | NIST 612 (n=106) | 2SE | MDL | Kd for SB[c] |
|---|---|---|---|---|---|---|---|---|---|---|
| Unit | MU | MU | MU | MU | IU | | | | | |
| Y | 2122 | 2396 | 1814 | 1760 | 1661 | 2025 | 38.0 | 0.16% | 0.29 | 141 |
| Zr | 120 | 65.5[a] | 95.0[a] | 1300 | 194 | 295 | 38.0 | 0.17% | 0.35 | 3.30 |
| Th | 3.04 | 2.78[a] | 1.73[a] | 58.0 | 4.16 | 14.5 | 37.8 | 0.23% | 0.25 | 1.47 |
| La | 197 | 217 | 147 | 340 | 159 | 213 | 35.8 | 0.16% | 0.25 | 9.46 |
| Ce | 581 | 658 | 585 | 1023 | 564 | 748 | 38.7 | 0.16% | 0.26 | 16.1 |
| Pr | 85.4 | 97.3 | 104 | 158 | 86.0 | 117 | 37.2 | 0.09% | 0.22 | 21.3 |
| Nd | 405 | 471 | 550 | 759 | 442 | 603 | 35.9 | 0.21% | 0.24 | 29.8 |
| Sm | 164 | 193 | 267 | 289 | 223 | 255 | 38.1 | 0.22% | 0.25 | 62.8 |
| Eu | 5.53 | 5.98 | 4.42 | 6.19 | 6.02 | 6.07 | 35.0 | 0.15% | 0.22 | 8.47 |
| Gd | 238 | 267 | 327 | 322 | 276 | 312 | 36.7 | 0.14% | 0.23 | 93.3 |
| Tb | 52.1 | 57.6 | 59.3 | 53.5 | 53.7 | 58.6 | 36.0 | 0.14% | 0.22 | 125 |
| Dy | 365 | 398 | 362 | 344 | 331 | 384 | 36.0 | 0.22% | 0.25 | 154 |
| Er | 203 | 218 | 151 | 157 | 139 | 185 | 38.0 | 0.15% | 0.24 | 145 |
| Tm | 28.9 | 32.2 | 18.7 | 20.3 | 18.7 | 24.6 | 38.0 | 0.11% | 0.23 | 136 |
| Yb | 180 | 199 | 104 | 116 | 112 | 145 | 39.2 | 0.20% | 0.24 | 116 |
| Lu | 21.7 | 24.1 | 11.3 | 13.9 | 12.7 | 17.5 | 36.9 | 0.14% | 0.23 | 112 |

[a]Samples with high error (> 10 %)

[b]Calculated omitting samples with high error

[c]Partition coefficients, calculated dividing the average contents in analyzed apatites by the average contents in monzogranites of the three units of the Sierra Bermeja Pluton

Total contents of Rare Earth Elements (ΣREE) vary in the range of 2369–3967 ppm, and Y contents are similarly high (1620–2480 ppm). Once discarded samples with high error, Zr and Th contents show relatively similar ranges (80.2–1300 and 3.04–58.0 ppm, respectively; Table 7).

## 6.3. VAUGNERITE SERIES ROCKS AND LAMPROPHYRES

In this section both types of mesocratic rocks of the Sierra Bermeja Pluton, vaugnerites and lamprophyres, have been considered together for their mineralogical characterization. To observe variations within the main distinguished rock-types, the minette and the micro-dioritoid have been discarded (yet included in tables) since they constitute exceptions. Major-element contents in pyroxene, amphibole, micas, feldspars and some accessories were determined in the studied mesocratic rocks (Tables 8–12).

### 6.3.1. Pyroxene

Microprobe analytical data (Table 8) of clinopyroxenes reveal that they are of the Ca–Mg–Fe type (Morimoto, 1988), with relatively narrow compositional variations: $Wo_{38–47}En_{38–51}Fs_{10–16}$. In the studied biotite-rich dioritoids the pyroxenes correspond mostly to diopside, whereas in the biotite-poor terms they are mostly augite (Fig. 38 A). Pyroxenes in the lamprophyres classify as augite (Fig. 38 A).

$TiO_2$, $FeO^t$ and CaO contents decrease in the sense Bt-rich vaugnerites → Bt-poor vaugnerites → lamprophyres, contrary to MgO that increase in that sense (*e.g.* $TiO_2$ = 1.85 → 1.43 → 0.69; MgO = 13.52 → 14.45 → 15.99). The same occurs, consequently, with Mg# values; the lowest ones are those of the biotite-rich dioritoids (average of 0.74), increasing from that of diopsides to augites in the Bt-poor terms (average = 0.76) and lamprophyres (up to 0.83). Cr contents are slightly higher in the augites of the lamprophyres

(up to 0.90 wt.% $Cr_2O_3$) than in the diopsides of dioritoids (up to 0.46 wt.%). Finally, $Al_2O_3$ and $Na_2O$ contents show a decreasing pattern from Bt-rich to Bt-poor vaugnerites, $Na_2O$ being contents particularly higher in clinopyroxenes from lamprophyres.

***Table 8.*** *Representative electron microprobe analyses of clinopyroxenes from mesocratic rocks of the Sierra Bermeja Pluton*

| Rock-type | Lamprophyre | | | Vaugnerite | | | | Micro-dt |
|---|---|---|---|---|---|---|---|---|
| | Mnt | Krs | Krs | Bt-r | Bt-r | Bt-p | Bt-p | |
| Sample | Cpx 50[a] | Cpx 72[a] | Cpx 74[a] | Cpx 18[a] | Cpx 15[a] | Cpx 32[a] | Cpx 39[a] | Cpx 69[a] |
| $SiO_2$ | 51.15 | 50.98 | 50.88 | 47.98 | 49.49 | 50.66 | 49.35 | 48.37 |
| $TiO_2$ | 1.03 | 0.57 | 0.58 | 1.99 | 1.44 | 1.15 | 1.36 | 1.91 |
| $Al_2O_3$ | 2.60 | 4.11 | 4.27 | 4.98 | 3.77 | 2.90 | 3.67 | 5.11 |
| $Cr_2O_3$ | 0.80 | 0.74 | 0.73 | 0.06 | 0.08 | 0.10 | 0.18 | 0.07 |
| NiO | 0.03 | 0.03 | 0.03 | < MDL | < MDL | 0.04 | < MDL | 0.03 |
| $FeO^t$ | 6.97 | 6.57 | 5.95 | 9.41 | 8.51 | 7.81 | 7.90 | 8.61 |
| MnO | 0.19 | 0.17 | 0.14 | 0.30 | 0.24 | 0.20 | 0.18 | 0.20 |
| MgO | 15.66 | 16.86 | 16.25 | 12.61 | 13.95 | 15.07 | 14.36 | 13.47 |
| CaO | 20.98 | 18.61 | 20.22 | 21.20 | 21.33 | 21.11 | 21.66 | 21.10 |
| $Na_2O$ | 0.22 | 0.56 | 0.49 | 0.44 | 0.38 | 0.33 | 0.41 | 0.48 |
| $K_2O$ | < MDL | < MDL | < MDL | < MDL | < MDL | < MDL | 0.02 | < MDL |
| Total | 99.63 | 99.19 | 99.54 | 98.98 | 99.19 | 99.37 | 99.10 | 99.38 |
| Wo | 43.39 | 39.32 | 42.50 | 45.76 | 44.84 | 43.68 | 45.17 | 45.16 |
| En | 45.05 | 49.57 | 47.51 | 37.87 | 40.80 | 43.39 | 41.66 | 40.11 |
| Fs | 11.56 | 11.11 | 9.99 | 16.37 | 14.36 | 12.93 | 13.16 | 14.72 |
| Mg# | 0.80 | 0.82 | 0.83 | 0.70 | 0.74 | 0.77 | 0.76 | 0.74 |

Complete data in Supplementary Table 9 of the Appendix
[a]Code from the Supplementary Tables of the Appendix
The Method Detection Limit (MDL) for the routine analysis of common elements is ~0.02 wt.%
Mnt (minette); Krs (kersantite); Bt-r (biotite-rich); Bt-p (biotite-poor); Micro-dt (micro-diorite)

## 6.3.2. Amphibole

Representative analyses of amphiboles from vaugnerites and lamprophyres of the Sierra Bermeja Pluton are shown in Table 9. These amphiboles classify as kaersutite and pargasite (Fig. 38 B), although some edenite and Mg-hornblende also exist in the phaneritic mesocratic rocks.

Considering average contents of the analyzed oxides, $TiO_2$, $FeO^t$, CaO and $Na_2O$ contents decrease in the sense Bt-rich vaugnerites → Bt-poor vaugnerites → lamprophyres (*e.g.* $TiO_2 = 5.07 \rightarrow 4.46 \rightarrow 4.03$; $FeO^t = 13.83 \rightarrow 13.16 \rightarrow 11.57$, in wt.%). On the contrary,

MgO, $K_2O$ and $Al_2O_3$ contents increase in that sense (*e.g.* MgO = 10.94 → 12.30 → 13.29), as well as average Mg# value (Mg# = 0.59 → 0.63 → 0.67). $Cr_2O_3$ contents decrease from the Bt-poor terms to lamprophyres (average contents of 0.04 wt.% and < MDL, respectively).

***Table 9.*** *Representative electron microprobe analyses of amphiboles from mesocratic rocks of the Sierra Bermeja Pluton*

| Rock-type | Lamprophyre | | Vaugnerite | | | | | Micro-dt | |
|---|---|---|---|---|---|---|---|---|---|
| | Krs | Krs | Bt-r | Bt-p | Bt-p | Bt-p | Bt-p | | |
| Sample | Amp 47[a] | Amp 44[a] | Amp 1[a] | Amp 26[a] | Amp 3[a] | Amp 30[a] | Amp 25[a] | Amp 38[a] | Amp 39[a] |
| $SiO_2$ | 40.05 | 39.83 | 40.45 | 40.55 | 40.15 | 41.32 | 40.60 | 39.23 | 39.07 |
| $TiO_2$ | 3.71 | 4.37 | 5.07 | 4.53 | 5.07 | 3.83 | 4.28 | 5.29 | 4.95 |
| $Al_2O_3$ | 12.24 | 13.54 | 11.52 | 11.46 | 11.78 | 10.76 | 11.46 | 12.26 | 11.84 |
| $Cr_2O_3$ | < MDL | < MDL | < MDL | < MDL | 0.06 | < MDL | < MDL | < MDL | < MDL |
| NiO | < MDL | < MDL | 0.02 | < MDL | < MDL | 0.08 | < MDL | 0.03 | < MDL |
| $FeO^t$ | 13.21 | 10.23 | 13.83 | 13.01 | 12.33 | 15.23 | 13.26 | 11.77 | 14.96 |
| MnO | 0.13 | 0.14 | 0.19 | 0.18 | 0.16 | 0.25 | 0.23 | 0.16 | 0.20 |
| MgO | 12.39 | 13.52 | 10.94 | 12.25 | 12.57 | 11.26 | 12.09 | 12.61 | 10.37 |
| CaO | 11.41 | 11.52 | 11.77 | 11.54 | 11.72 | 10.87 | 11.43 | 11.41 | 11.25 |
| $Na_2O$ | 2.06 | 1.97 | 2.58 | 2.38 | 2.27 | 2.36 | 2.30 | 2.33 | 2.30 |
| $K_2O$ | 1.34 | 1.64 | 1.11 | 1.27 | 1.25 | 1.10 | 1.26 | 1.06 | 1.28 |
| F | 0.15 | 0.21 | NA | NA | NA | NA | NA | 0.17 | 0.13 |
| Cl | 0.06 | 0.05 | NA | NA | NA | NA | NA | 0.02 | 0.02 |
| Total | 96.75 | 97.06 | 97.49 | 97.17 | 97.35 | 97.08 | 96.91 | 96.36 | 96.37 |
| Mg# | 0.63 | 0.70 | 0.59 | 0.63 | 0.65 | 0.57 | 0.62 | 0.66 | 0.55 |

Complete data in Supplementary Table 10 of the Appendix
[a]Code from the Supplementary Tables of the Appendix
The Method Detection Limit (MDL) for the routine analysis of common elements is ~0.02 wt.%
NA not analyzed
Krs (kersantite); Bt-r (biotite-rich); Bt-p (biotite-poor); Micro-dt (micro-diorite)

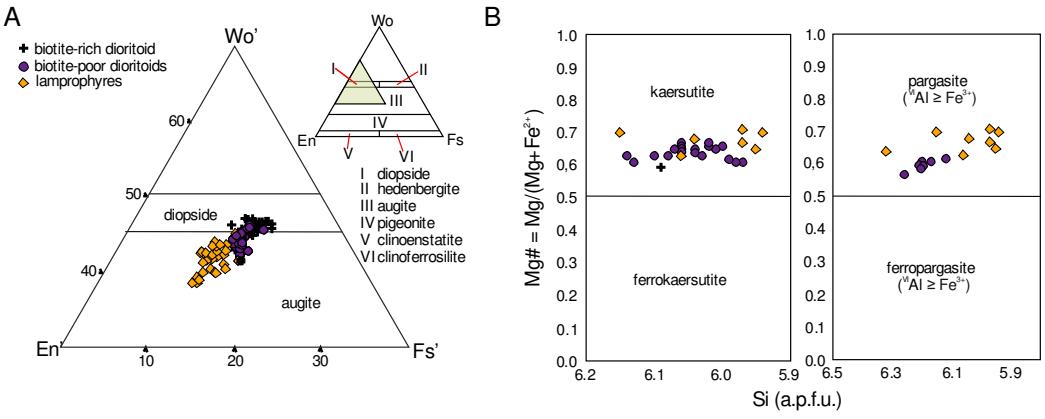


**Figure 38.** Compositions of clinopyroxenes (A) and amphiboles (B) of the Sierra Bermeja Pluton. A) Wo–En–Fs classification diagram for Ca–Mg–Fe clinopyroxenes (Morimoto, 1988). B) Si *vs.* Mg# classification diagram for calcic amphiboles (Leake *et al.*, 1997).

### 6.3.3. Micas

Biotites of the studied dioritoids are classified as biotite *s.s.* with Mg# values comprised in a relatively narrow range of 0.56–0.66. Nonetheless, in the lamprophyres several analyses plot in the phlogopite field (Fig. 39 A). Note that biotites have been analyzed only in the Bt-rich vaugneritic terms and in kersantites (representative analyses are given in Table 10). Overall, excluding some biotite cores from the lamprophyres, $TiO_2$, $FeO^t$ and $Na_2O$ contents of micas decrease from Bt-rich vaugnerites to lamprophyres (kersantites), while $K_2O$ and $Al_2O_3$ contents increase. Lamprophyres show a wide range of MgO (9.96–17.36; wt.%), outstanding that the MgO compositions of biotites from vaugnerites, which show a narrower variation (11.51–14.35; wt.%), fall within that range. Consequently, Mg# in micas of both rock-types are very similar, but overall, the compositional range is larger in the biotites from lamprophyres than those from dioritoids (Fig. 39 A).

***Table 10.*** *Representative electron microprobe analyses of biotites from mesocratic rocks of the Sierra Bermeja Pluton*

| Rock-type | Lamprophyre | | | Vaugnerite | | | Micro-dt | |
|---|---|---|---|---|---|---|---|---|
| | Krs | Krs | Krs | Bt-r | Bt-r | Bt-r | | |
| Sample | Bt 154[a] | Bt 158[a] | Bt 165[a] | Bt 169[a] | Bt 175[a] | Bt 176[a] | Bt 159[a] | Bt 164[a] |
| $SiO_2$ | 34.70 | 35.86 | 36.39 | 35.80 | 35.45 | 35.87 | 35.00 | 34.40 |
| $TiO_2$ | 5.85 | 5.56 | 4.57 | 5.78 | 5.99 | 5.16 | 6.31 | 6.79 |
| $Al_2O_3$ | 14.85 | 15.04 | 14.97 | 14.61 | 14.15 | 14.50 | 14.92 | 14.50 |
| $Cr_2O_3$ | 0.03 | 0.09 | < MDL | < MDL | 0.02 | 0.04 | 0.03 | 0.02 |
| NiO | < MDL | < MDL | 0.03 | < MDL | 0.03 | < MDL | < MDL | < MDL |
| $FeO^t$ | 19.65 | 11.68 | 13.99 | 15.57 | 17.61 | 14.76 | 14.35 | 18.26 |
| MnO | 0.16 | 0.06 | 0.12 | 0.10 | 0.13 | 0.06 | 0.08 | 0.11 |
| MgO | 9.96 | 15.35 | 14.93 | 13.50 | 11.51 | 14.35 | 12.72 | 10.20 |
| CaO | 0.18 | 0.06 | 0.04 | < MDL | < MDL | 0.02 | 0.06 | 0.10 |
| $Na_2O$ | 0.13 | 0.30 | 0.24 | 0.43 | 0.38 | 0.47 | 0.15 | 0.16 |
| $K_2O$ | 8.35 | 8.60 | 8.55 | 8.62 | 8.59 | 8.68 | 8.23 | 8.11 |
| F | 0.20 | 0.31 | 0.37 | 0.17 | 0.28 | 0.05 | 0.12 | 0.07 |
| Cl | 0.08 | 0.04 | 0.03 | 0.04 | 0.06 | 0.03 | 0.02 | 0.02 |
| Total | 94.15 | 92.94 | 94.23 | 94.62 | 94.20 | 94.01 | 91.98 | 92.76 |
| Mg# | 0.49 | 0.71 | 0.68 | 0.63 | 0.56 | 0.66 | 0.62 | 0.51 |

Complete data in Supplementary Table 5 of the Appendix
[a]Code from the Supplementary Tables of the Appendix
The Method Detection Limit (MDL) for the routine analysis of common elements is ~0.02 wt.%
Krs (kersantite); Bt-r (biotite-rich); Micro-dt (micro-diorite)

## 6.3.4. Feldspars

Alkali feldspar is always homogeneous ($Or_{98}$–$Or_{94}$) and compositions for both rock-types are close to the orthoclase vertex in the Or–Ab–An diagram (Fig. 39 B). The plagioclase cores in the dioritoids appear highly altered, as mentioned in the previous chapter, which precludes their proper geochemical characterization, while the rims exhibit marked albitic to oligoclase compositions ($An_{26}$–$An_{03}$). On the contrary, plagioclases of lamprophyres are better preserved, classifying as labradorite–andesine ($An_{63}$–$An_{43}$; Fig. 39 B; Table 11).

***Table 11.*** *Representative electron microprobe analyses of feldspars from mesocratic rocks of the Sierra Bermeja Pluton*

| Rock-type | Lamprophyre | | | Vaugnerite | | | | | Micro-dt |
|---|---|---|---|---|---|---|---|---|---|
| | Mnt | Krs | Krs | Bt-r | Bt-p | Bt-p | Bt-p | Bt-p | |
| Sample[a] | Kfs 110 | Pl 191 | Pl 188 | Pl 197 | Pl 213 | Kfs 119 | Pl 203 | Kfs 115 | Pl 174 |
| $SiO_2$ | 65.05 | 57.92 | 52.82 | 66.33 | 66.79 | 65.40 | 67.25 | 64.40 | 53.09 |
| $TiO_2$ | < MDL | < MDL | 0.05 | < MDL | 0.02 | < MDL | < MDL | 0.02 | 0.06 |
| $Al_2O_3$ | 18.40 | 26.04 | 28.78 | 21.26 | 20.70 | 17.90 | 20.45 | 18.39 | 29.37 |
| $Cr_2O_3$ | < MDL | < MDL | 0.03 | < MDL | < MDL | < MDL | 0.05 | < MDL | < MDL |
| NiO | < MDL | < MDL | < MDL | < MDL | < MDL | < MDL | < MDL | < MDL | < MDL |
| $FeO^t$ | 0.15 | 0.31 | 0.55 | 0.12 | 0.06 | 0.03 | < MDL | 0.05 | 0.47 |
| MnO | < MDL | < MDL | < MDL | 0.02 | < MDL | 0.02 | < MDL | 0.02 | < MDL |
| MgO | < MDL | 0.02 | 0.12 | < MDL | < MDL | < MDL | < MDL | < MDL | 0.08 |
| CaO | 0.03 | 8.97 | 12.89 | 2.09 | 2.04 | < MDL | 0.88 | < MDL | 12.58 |
| $Na_2O$ | 0.27 | 6.17 | 3.92 | 10.27 | 10.37 | 0.39 | 11.77 | 0.26 | 4.07 |
| $K_2O$ | 16.24 | 0.56 | 0.44 | 0.25 | 0.16 | 15.92 | 0.05 | 16.77 | 0.42 |
| Total | 100.15 | 100.00 | 99.59 | 100.35 | 100.15 | 99.67 | 100.48 | 99.91 | 100.16 |
| Or | 97.37 | 3.19 | 2.58 | 1.43 | 0.91 | 96.38 | 0.29 | 97.66 | 2.47 |
| Ab | 2.48 | 53.66 | 34.57 | 88.61 | 89.39 | 3.59 | 95.75 | 2.34 | 36.03 |
| An | 0.15 | 43.15 | 62.85 | 9.95 | 9.70 | 0.03 | 3.96 | 0.00 | 61.50 |

Complete data in Supplementary Tables 2 and 3 of the Appendix

[a]Code from the Supplementary Tables of the Appendix

The Method Detection Limit (MDL) for the routine analysis of common elements is ~0.02 wt.%

Mnt (minette); Krs (kersantite); Bt-r (biotite-rich); Bt-p (biotite-poor); Micro-dt (micro-diorite)

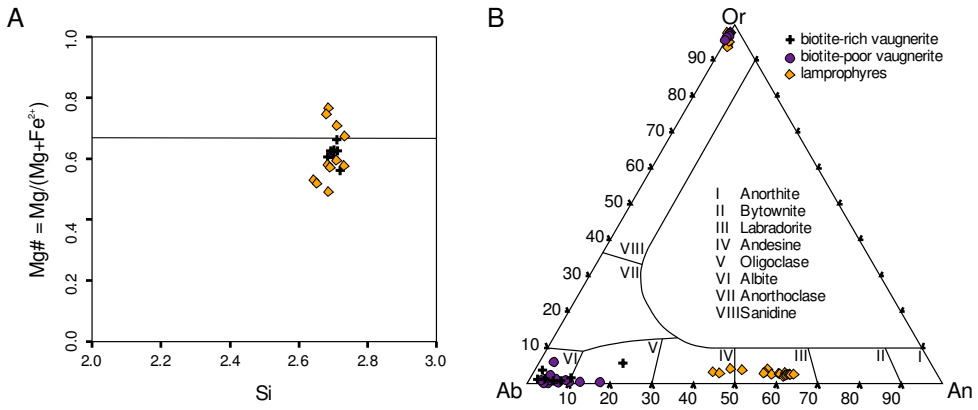


**Figure 39.** A) Biotite–phlogopite discrimination diagram for biotites *s.l.* (Deer *et al.*, 1962). B) Or–Ab–An classification diagram for feldspars (Deer *et al.*, 1963).

## 6.3.5. Accessory minerals

Accessory mineralogy of mesocratic rocks from the Sierra Bermeja Pluton comprises apatite, zircon, allanite, ilmenite, pyrite and chromite, while secondary mineralogy consists of titanite, epidote, zoisite, chlorite, calcite and sericite (see Chapter 5). Compositions of these accessory minerals are near similar between the different mesocratic rocks (Table 12).

***Table 12.*** *Representative electron microprobe analyses of some accessory and secondary mineral phases from mesocratic rocks of the Sierra Bermeja Pluton*

| Rock-type | Vaugnerite | | | | | | | Lamprophyre | |
|---|---|---|---|---|---|---|---|---|---|
| | Bt-rich | Bt-rich | Bt-poor | Bt-rich | Bt-poor | Krs | Mnt | | Krs |
| Oxide (wt.%) | Ilm | Ttn | Ep | Ap_39[a] | Zo | Chr | Ilm | Atom. (wt.%) | Py |
| $SiO_2$ | < MDL | 30.33 | 36.90 | 0.2 | 38.98 | 0.08 | 0.03 | S | 53.86 |
| $TiO_2$ | 48.47 | 33.11 | 0.16 | < MDL | 0.11 | 0.72 | 51.35 | Zn | < MDL |
| $Al_2O_3$ | < MDL | 3.20 | 22.14 | < MDL | 31.19 | 9.32 | < MDL | Fe | 46.74 |
| $Cr_2O_3$ | 0.07 | 0.34 | < MDL | < MDL | 0.02 | 54.50 | 0.18 | Cu | < MDL |
| NiO | < MDL | < MDL | < MDL | 0.02 | < MDL | 0.06 | < MDL | As | 0.11 |
| $FeO^t$ | 49.09 | 2.92 | 13.59 | 0.38 | 2.36 | 26.39 | 44.68 | Ga | < MDL |
| MnO | 2.60 | < MDL | 0.02 | 0.04 | < MDL | 0.15 | 3.52 | In | < MDL |
| MgO | 0.10 | 1.81 | 0.03 | 0.35 | 0.09 | 8.94 | 0.07 | Ge | < MDL |
| CaO | 0.14 | 26.54 | 23.24 | 54.26 | 24.98 | 0.07 | 0.20 | | NA |
| $Na_2O$ | < MDL | < MDL | < MDL | < MDL | < MDL | < MDL | < MDL | | NA |
| $K_2O$ | < MDL | 0.05 | < MDL | < MDL | < MDL | < MDL | < MDL | | NA |
| $P_2O_5$ | NA | NA | NA | 41.84 | NA | NA | NA | | NA |
| F | NA | NA | NA | 2.79 | NA | NA | NA | | NA |
| Cl | NA | NA | NA | 0.29 | NA | NA | NA | | NA |
| Total | 100.49 | 98.31 | 96.08 | 100.29 | 97.74 | 100.22 | 100.05 | Total | 100.72 |

Complete data of apatites in Supplementary Table 8 of the Appendix
[a]Code from the Supplementary Tables of the Appendix
The Method Detection Limit (MDL) for the routine analysis of common elements is ~0.02 wt.%
NA Not analysed; Mnt (minette); Krs (kersantite); Mineral abbreviations from Whitney and Evans (2010).

# CHAPTER 7
# GEOCHRONOLOGY

## 7.1. ZIRCON AND MONAZITE DATING OF MONZOGRANITES

In total 82 zircon and 24 monazite grains of the three main monzogranite units of the Sierra Bermeja Pluton have been considered for the present study. U–Th–Pb isotope and elemental measurements of zircon and monazite crystals were conducted by LA-Q-IC-PMS at the Geochronology and Isotope Geochemistry-SGIker Facility of the University of the Basque Country UPV/EHU (Tables 13 and 14; see the 'Methods' section in Chapter 3 for the employed procedures). Representative zircon and monazite Backscattered Electron (BSE) images and analyzed spots with U–Pb ages are shown in Fig. 40.

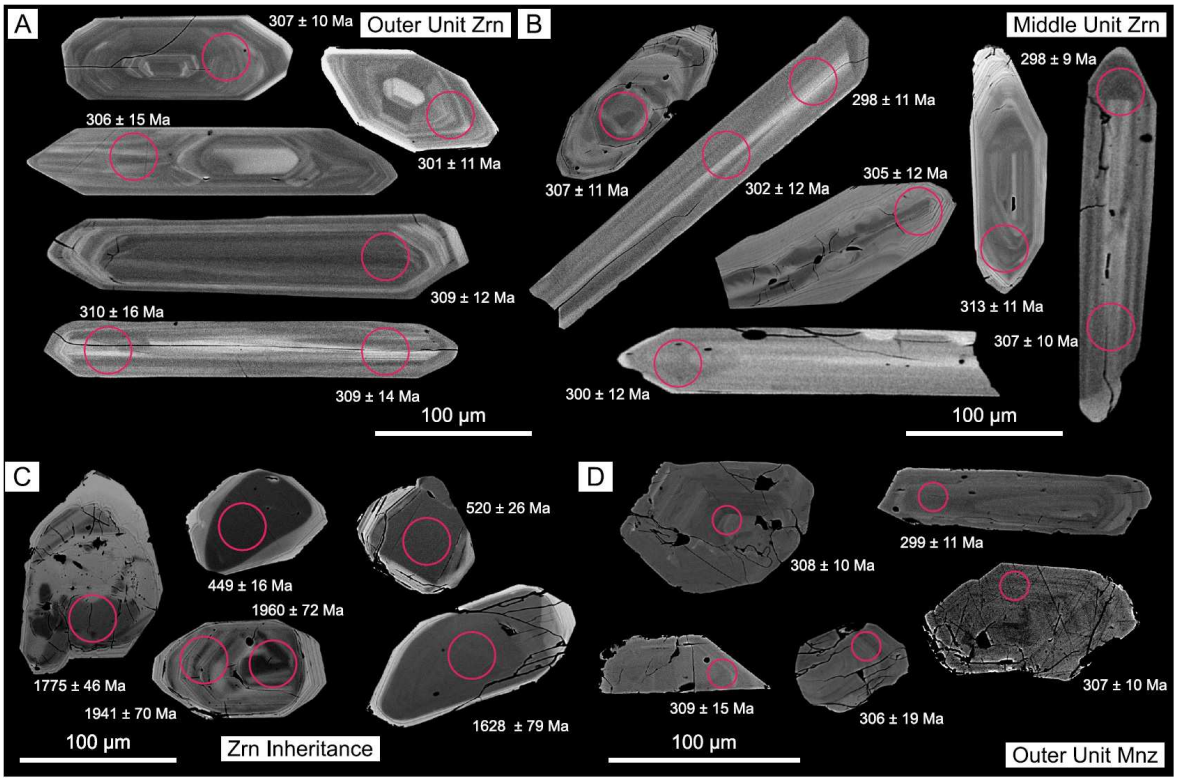


**Figure 40.** Backscattered electron (BSE) images of representative zircon and monazite grains from the Sierra Bermeja Pluton, showing the analyzed spots and $^{206}Pb/^{238}U$ ages obtained by LA-ICP-MS. A) Zircons from the OU. B) Zircons from the MU. C) Inherited zircon cores from the OU, MU and IU. d) Monazites from the OU.

### 7.1.1. Zircon U–Th–Pb systematics

Zircon grains exhibit distinct primary magmatic morphologies (Fig. 40 A–C). Most of them are represented by a well-developed {100} prism and two pyramids, {101} and {201}, although there is a less abundant group of crystals with the predominance of a {110} prism and the same {101} and {201} pyramids. Backscattered-electron images reveal the existence of a thin oscillatory magmatic zoning in most of the zircon grains with variable development from the inner to the outer zones of the crystals (Fig. 40 A–C). The images also disclose the occurrence of inherited cores in some zircon grains, particularly in the mentioned second less abundant group of crystals (Fig. 40 C).

The signal obtained in 106 U–Pb analyses was carefully checked in order to discard the presence of common Pb that cannot be properly corrected by this method or of any other analytical problem. Out of the total of analyses, and once taken into account the degree of concordance (see analytical methods), 47 analyses were retained for the age determination (Table 13). The Concordia diagram shows definite differences in the obtained results, pointing to at least two groups of ages in these samples. The first group would correspond to the youngest ages, of *ca.* ~300–310 Ma, and the second one would be represented by older ages within a broad range of 449–1960 Ma (Table 13).

According to the observed field relationships, zircon grains of the OU were handled separately from those of the apparently contemporaneous (comingled) MU and IU that were considered together. The group of 17 concordant values provides a Concordia Age of 308 ± 3 Ma for the OU (Fig. 41 A), while 15 concordant values yield an age of 304 ± 3 Ma for the MU (Fig. 41 B). Slightly lower degrees of concordance due to analytical errors in 'young' analyses of the IU zircons have impeded their consideration. Nevertheless, the two obtained Pennsylvanian emplacement ages for the MU and OU monzogranites overlap within the assigned errors.

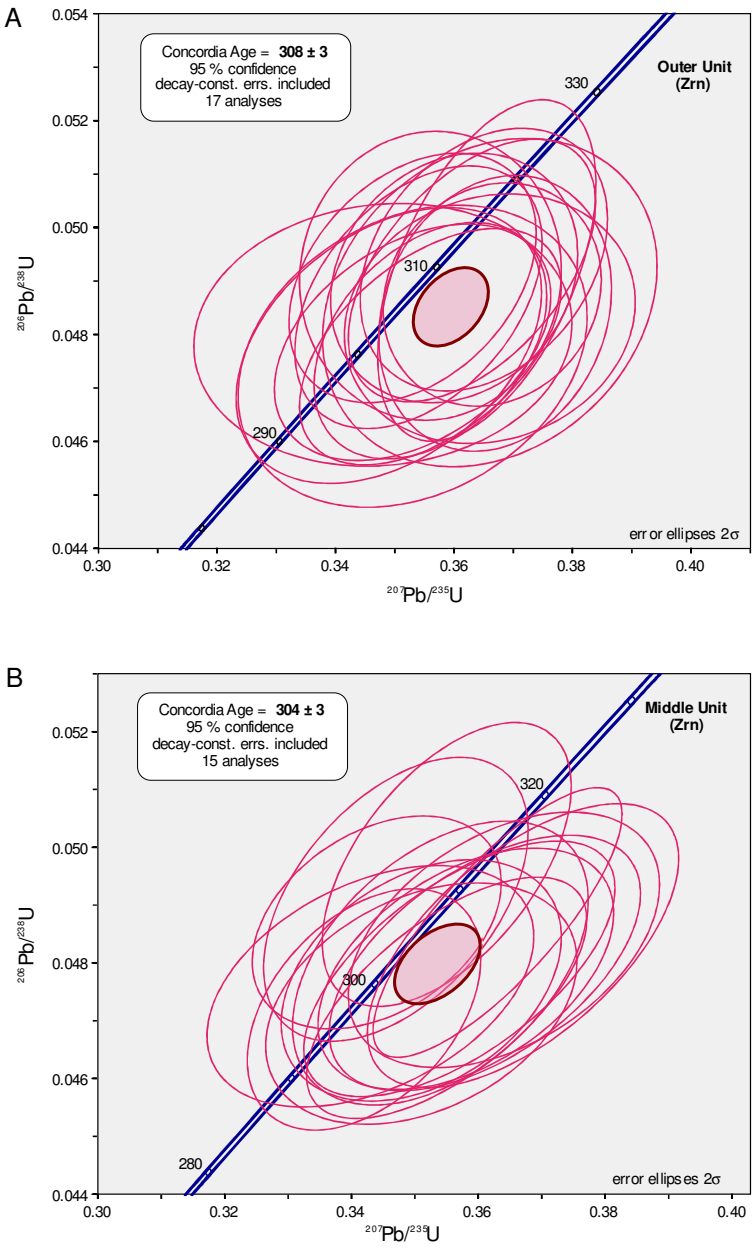


**Figure 41.** U–Pb Concordia diagrams for zircon grains of the A) OU and B) MU.

The observed inherited cores in BSE images provided 15 concordant pre-Carboniferous ages in the range of 449–1960 Ma (Table 13). In detail, most of the inherited cores are Neoproterozoic and even Paleoproterozoic (563–1960 Ma; n = 11), and are found in the OU and IU, whereas Cambrian–Ordovician ones (449–520 Ma) are less abundant (n = 4) and are found in all units (Fig. 42).

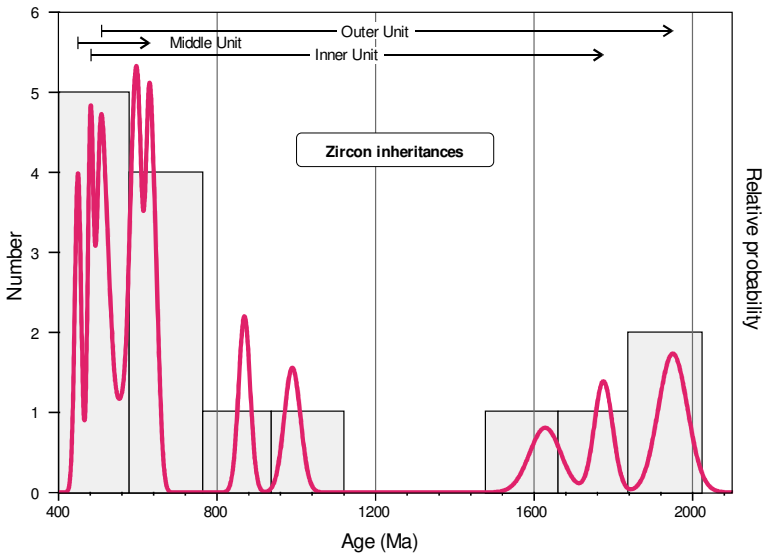


**Figure 42.** Relative probability plot and histogram of pre-Carboniferous ages for the zircon grains from the OU, MU and IU.

## 7.1.2. Monazite U–Th–Pb systematics

Twenty-four monazite crystals of the OU were selected for a complementary U–Pb age determination. Representative BSE images of monazites are shown in Figure 40 D and the Concordia diagram in Figure 43.

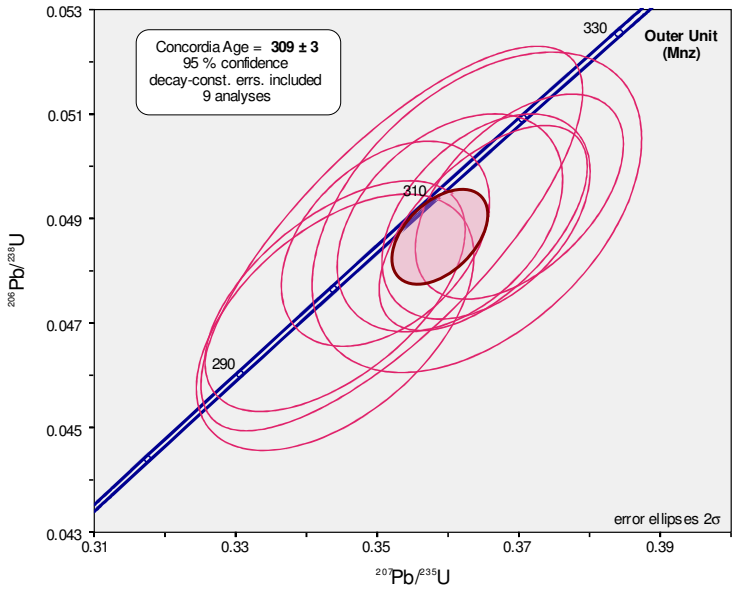


**Figure 43.** Concordia diagram for monazites of the OU.

Like zircons, euhedral crystals of monazite show different primary morphologies (Fig. 40 D): prismatic or tabular. The existence of an oscillatory magmatic zoning, with

variable development from core to rim (Fig. 40 D), is a common feature of all these crystals. Of the 37 U–Pb measurements, only 9 that provided concordant values (concordance > 97 %; Table 14) were considered for age determination yielding a Concordia Age of 309 ± 3 Ma (Fig. 43). That is, analytically the same age to that obtained from the U–Pb zircon analyses in the same unit.

## 7.2. APATITE DATING OF VAUGNERITE SERIES ROCKS

In total, 78 apatite grains of the vaugnerite series rocks from the Sierra Bermeja Pluton have been considered for an age determination of these mesocratic rocks. Out of the performed 100 analyses, 88 were taken into account (others were of too small size to be measured in optimal conditions). The plot of the 88 valid analyses (results are shown in Supplementary Table 11 of the Appendix) shows variable $^{207}Pb/^{235}U$ ratios and define a linear trend that intercepts the Concordia curve giving a lower intercept age of 305 ± 17 Ma (Fig. 44). This age, despite its high error, is analytically similar to that obtained from zircons of the MU monzogranites, and therefore is coherent with the observed field relationships.

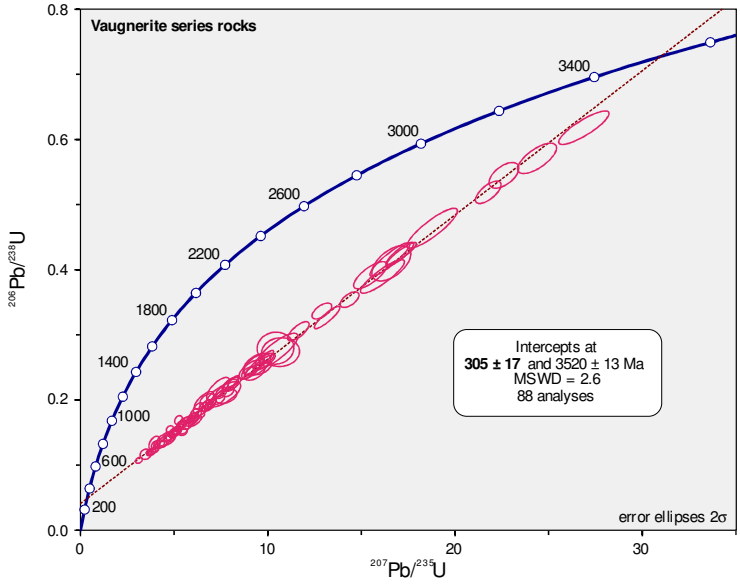


**Figure 44.** Concordia diagram for apatites of the vaugnerite series rocks from the Sierra Bermeja Pluton.

***Table 13.*** *U–Pb isotope data (LA-ICP-MS) of zircons from the Sierra Bermeja Pluton*

| Spot number | Elemental concentration (µg $g^{-1}$)[a] | | | Isotopic ratios and 2σ (abs) errors | | | |
|---|---|---|---|---|---|---|---|
| | U | Th | Pb | $^{207}Pb/^{235}U$ | 2σ | $^{206}Pb/^{238}U$ | 2σ |
| Zrn48 04B | 183 | 374 | 4.29 | 1.325 | 0.050 | 0.1444 | 0.0052 |
| Zrn48 05A | 54.4 | 39.0 | 15.3 | 0.353 | 0.024 | 0.0476 | 0.0023 |
| Zrn48 08A | 434 | 2410 | 1.97 | 6.100 | 0.240 | 0.3516 | 0.0150 |
| Zrn48 08B | 571 | 3440 | 3.24 | 6.130 | 0.260 | 0.3556 | 0.0150 |
| Zrn48 15A | 324 | 266 | 3.56 | 0.353 | 0.017 | 0.0491 | 0.0019 |
| Zrn48 17A | 181 | 145 | 2.17 | 0.348 | 0.026 | 0.0480 | 0.0020 |
| Zrn48 19A | 124 | 104 | 4.71 | 0.349 | 0.021 | 0.0478 | 0.0021 |
| Zrn48 20B | 85.6 | 78.4 | 5.37 | 0.353 | 0.019 | 0.0479 | 0.0018 |
| Zrn48 21A | 225 | 479 | 4.93 | 0.886 | 0.035 | 0.1048 | 0.0040 |
| Zrn48 22A | 72.5 | 72.1 | 4.94 | 0.366 | 0.023 | 0.0486 | 0.0025 |
| Zrn48 29A | 243 | 169 | 3.07 | 0.354 | 0.017 | 0.0487 | 0.0020 |
| Zrn48 29B | 187 | 140 | 3.44 | 0.366 | 0.020 | 0.0483 | 0.0019 |
| Zrn48 39A | 78.0 | 56.4 | 8.40 | 0.365 | 0.017 | 0.0494 | 0.0020 |
| Zrn48 40A | 353 | 259 | 2.14 | 0.363 | 0.017 | 0.0492 | 0.0020 |
| Zrn48 42A | 165 | 110 | 4.20 | 0.356 | 0.016 | 0.0479 | 0.0018 |
| Zrn48 43B | 223 | 163 | 4.12 | 0.367 | 0.016 | 0.0484 | 0.0021 |
| Zrn48 44A | 289 | 200 | 3.21 | 0.366 | 0.015 | 0.0492 | 0.0026 |
| Zrn48 44C | 219 | 157 | 4.19 | 0.356 | 0.018 | 0.0491 | 0.0022 |
| Zrn48 45A | 172 | 120 | 3.49 | 0.356 | 0.018 | 0.0478 | 0.0018 |
| Zrn48 46A | 56.0 | 52.2 | 8.38 | 0.366 | 0.015 | 0.0488 | 0.0017 |
| Zrn48 47B | 532 | 756 | 1.50 | 0.804 | 0.031 | 0.0980 | 0.0035 |
| Zrn48 49A | 422 | 617 | 1.37 | 0.783 | 0.038 | 0.0956 | 0.0037 |
| Zrn48 55A | 279 | 661 | 2.03 | 1.625 | 0.071 | 0.1661 | 0.0075 |
| Zrn48 56B | 158 | 118 | 3.76 | 0.360 | 0.017 | 0.0491 | 0.0019 |
| Zrn48 58A | 567 | 868 | 2.64 | 0.791 | 0.036 | 0.0813 | 0.0034 |
| Zrn51 24A | 273 | 457 | 5.72 | 0.780 | 0.081 | 0.0913 | 0.0095 |
| Zrn51 25A | 128 | 170 | 2.60 | 0.622 | 0.024 | 0.0774 | 0.0024 |
| Zrn51 37A | 1334 | 7960 | 1.74 | 5.446 | 0.160 | 0.3172 | 0.0095 |
| Zrn51 44A | 43.2 | 222 | 2.27 | 4.740 | 0.270 | 0.2890 | 0.0150 |
| Zrn67 01A | 63.2 | 51.3 | 6.38 | 0.343 | 0.021 | 0.0476 | 0.0017 |
| Zrn67 01B | 339 | 238 | 2.01 | 0.357 | 0.020 | 0.0479 | 0.0018 |
| Zrn67 02A | 206 | 138 | 2.61 | 0.344 | 0.016 | 0.0487 | 0.0015 |
| Zrn67 03A | 59.2 | 47.6 | 5.86 | 0.347 | 0.017 | 0.0491 | 0.0020 |
| Zrn67 16A | 339 | 476 | 1.32 | 0.698 | 0.043 | 0.0841 | 0.0044 |
| Zrn67 21A | 66.4 | 54.0 | 11.8 | 0.351 | 0.020 | 0.0473 | 0.0017 |
| Zrn67 21B | 113 | 84.7 | 4.63 | 0.363 | 0.016 | 0.0487 | 0.0019 |
| Zrn67 27A | 388 | 291 | 2.29 | 0.351 | 0.018 | 0.0477 | 0.0017 |
| Zrn67 29A | 80.0 | 63.4 | 4.51 | 0.355 | 0.016 | 0.0497 | 0.0020 |
| Zrn67 31A | 37.8 | 47.8 | 3.26 | 0.611 | 0.037 | 0.0722 | 0.0027 |
| Zrn67 33A | 90.6 | 72.6 | 8.21 | 0.364 | 0.020 | 0.0484 | 0.0018 |
| Zrn67 34B | 754 | 647 | 2.53 | 0.367 | 0.020 | 0.0483 | 0.0020 |
| Zrn67 35A | 229 | 177 | 3.05 | 0.361 | 0.020 | 0.0480 | 0.0018 |
| Zrn67 36A | 216 | 216 | 25.0 | 0.358 | 0.019 | 0.0479 | 0.0017 |
| Zrn67 36B | 94.9 | 82.3 | 5.17 | 0.355 | 0.018 | 0.0474 | 0.0017 |
| Zrn67 37A | 846 | 736 | 1.15 | 0.354 | 0.019 | 0.0480 | 0.0020 |
| Zrn67 39A | 184 | 163 | 3.54 | 0.342 | 0.015 | 0.0472 | 0.0017 |
| Zrn67 69B | 762 | 1330 | 1.53 | 0.829 | 0.029 | 0.1022 | 0.0031 |

[a]Concentration uncertainty ~20%

[b]Concordance calculated as 100× ($^{206}Pb/^{238}U$age)/ ($^{207}Pb/^{235}U$age)

Zrn48 from sample JE 15 48; Zrn 51 from sample JE 15 51; Zrn67 from sample JE 15 67

***Table 13.*** *Continued*

| Spot number | Isot. Rat. and 2σ (abs) | | Ages and 2σ (abs) errors (Ma) | | | | % conc[b] |
|---|---|---|---|---|---|---|---|
| | $^{207}Pb/^{206}Pb$ | 2σ | $^{206}Pb/^{238}U$ | 2σ error (abs) | $^{207}Pb/^{235}U$ | 2σ error (abs) | |
| Zrn48 04B | 0.0674 | 0.0011 | 869 | 29 | 856 | 22 | 102% |
| Zrn48 05A | 0.0544 | 0.0032 | 300 | 14 | 306 | 18 | 98% |
| Zrn48 08A | 0.1278 | 0.0023 | 1941 | 70 | 1990 | 34 | 98% |
| Zrn48 08B | 0.1267 | 0.0034 | 1960 | 72 | 1994 | 37 | 98% |
| Zrn48 15A | 0.0525 | 0.0016 | 309 | 12 | 307 | 12 | 101% |
| Zrn48 17A | 0.0528 | 0.0038 | 302 | 12 | 303 | 20 | 100% |
| Zrn48 19A | 0.0530 | 0.0028 | 301 | 13 | 304 | 16 | 99% |
| Zrn48 20B | 0.0536 | 0.0020 | 301 | 11 | 306 | 14 | 98% |
| Zrn48 21A | 0.0612 | 0.0013 | 642 | 23 | 644 | 19 | 100% |
| Zrn48 22A | 0.0545 | 0.0032 | 306 | 15 | 316 | 17 | 97% |
| Zrn48 29A | 0.0526 | 0.0018 | 307 | 12 | 308 | 13 | 100% |
| Zrn48 29B | 0.0548 | 0.0025 | 304 | 12 | 316 | 15 | 96% |
| Zrn48 39A | 0.0537 | 0.0019 | 311 | 13 | 315 | 13 | 99% |
| Zrn48 40A | 0.0534 | 0.0015 | 310 | 12 | 314 | 12 | 99% |
| Zrn48 42A | 0.0540 | 0.0017 | 302 | 11 | 310 | 13 | 97% |
| Zrn48 43B | 0.0542 | 0.0017 | 305 | 13 | 317 | 12 | 96% |
| Zrn48 44A | 0.0542 | 0.0023 | 310 | 16 | 316 | 11 | 98% |
| Zrn48 44C | 0.0517 | 0.0023 | 309 | 14 | 309 | 13 | 100% |
| Zrn48 45A | 0.0534 | 0.0018 | 301 | 11 | 309 | 13 | 97% |
| Zrn48 46A | 0.0538 | 0.0012 | 307 | 10 | 317 | 11 | 97% |
| Zrn48 47B | 0.0588 | 0.0012 | 603 | 20 | 599 | 18 | 101% |
| Zrn48 49A | 0.0586 | 0.0019 | 588 | 22 | 586 | 21 | 100% |
| Zrn48 55A | 0.0708 | 0.0020 | 990 | 41 | 979 | 27 | 101% |
| Zrn48 56B | 0.0540 | 0.0019 | 309 | 12 | 312 | 13 | 99% |
| Zrn48 58A | 0.0694 | 0.0018 | 504 | 20 | 591 | 21 | 85% |
| Zrn51 24A | 0.0619 | 0.0022 | 563 | 57 | 583 | 48 | 97% |
| Zrn51 25A | 0.0584 | 0.0016 | 481 | 14 | 490 | 15 | 98% |
| Zrn51 37A | 0.1244 | 0.0009 | 1775 | 46 | 1890 | 25 | 94% |
| Zrn51 44A | 0.1200 | 0.0019 | 1628 | 79 | 1765 | 53 | 92% |
| Zrn67 01A | 0.0523 | 0.0027 | 300 | 11 | 298 | 16 | 101% |
| Zrn67 01B | 0.0545 | 0.0021 | 301 | 11 | 308 | 15 | 97% |
| Zrn67 02A | 0.0518 | 0.0019 | 307 | 11 | 300 | 12 | 97% |
| Zrn67 03A | 0.0524 | 0.0023 | 309 | 11 | 305 | 15 | 98% |
| Zrn67 16A | 0.0601 | 0.0024 | 520 | 26 | 537 | 26 | 97% |
| Zrn67 21A | 0.0538 | 0.0025 | 298 | 9 | 305 | 15 | 102% |
| Zrn67 21B | 0.0539 | 0.0019 | 307 | 10 | 314 | 12 | 98% |
| Zrn67 27A | 0.0533 | 0.0024 | 300 | 12 | 305 | 14 | 98% |
| Zrn67 29A | 0.0519 | 0.0018 | 313 | 11 | 308 | 12 | 98% |
| Zrn67 31A | 0.0617 | 0.0040 | 449 | 16 | 482 | 24 | 93% |
| Zrn67 33A | 0.0547 | 0.0024 | 305 | 12 | 315 | 15 | 102% |
| Zrn67 34B | 0.0552 | 0.0023 | 304 | 11 | 317 | 15 | 97% |
| Zrn67 35A | 0.0546 | 0.0022 | 302 | 12 | 312 | 15 | 101% |
| Zrn67 36A | 0.0543 | 0.0022 | 302 | 12 | 310 | 15 | 96% |
| Zrn67 36B | 0.0543 | 0.0019 | 298 | 11 | 308 | 13 | 97% |
| Zrn67 37A | 0.0536 | 0.0024 | 302 | 12 | 307 | 14 | 98% |
| Zrn67 39A | 0.0527 | 0.0015 | 298 | 10 | 298 | 11 | 100% |
| Zrn67 69B | 0.0594 | 0.0011 | 627 | 18 | 613 | 16 | 102% |

[a]Concentration uncertainty ~20%

[b]Concordance calculated as 100× ($^{206}Pb/^{238}U$age)/ ($^{207}Pb/^{235}U$age)

Zrn48 from sample JE 15 48; Zrn 51 from sample JE 15 51; Zrn67 from sample JE 15 67

***Table 14.*** *U–Pb isotope data (LA-ICP-MS) of monazites from the Sierra Bermeja Pluton*

| Spot number | Elemental concentration (µg $g^{-1}$)[a] | | | Isotopic ratios and 2σ (abs) errors | | | | |
|---|---|---|---|---|---|---|---|---|
| | U | Th | Pb | $^{207}Pb/^{235}U$ | 2σ | $^{206}Pb/^{238}U$ | 2σ | Rho |
| Mnz01 | 8130 | 153000 | no value | 0.352 | 0.022 | 0.0486 | 0.0030 | 0.7638 |
| Mnz05 | 2166 | 84800 | no value | 0.351 | 0.012 | 0.0485 | 0.0016 | 0.4102 |
| Mnz08 | 2920 | 108100 | no value | 0.365 | 0.012 | 0.0490 | 0.0016 | 0.4379 |
| Mnz14 | 6060 | 117800 | no value | 0.370 | 0.012 | 0.0494 | 0.0016 | 0.5082 |
| Mnz16 | 6490 | 89900 | no value | 0.344 | 0.016 | 0.0470 | 0.0020 | 0.5162 |
| Mnz18 | 4120 | 111900 | no value | 0.360 | 0.013 | 0.0489 | 0.0017 | 0.3968 |
| Mnz29 | 7140 | 119000 | no value | 0.364 | 0.019 | 0.0491 | 0.0025 | 0.4556 |
| Mnz32 | 3080 | 83900 | no value | 0.344 | 0.015 | 0.0475 | 0.0018 | 0.5737 |
| Mnz36 | 6670 | 54900 | no value | 0.365 | 0.012 | 0.0488 | 0.0016 | 0.5981 |

[a]Concentration uncertainty ~20%

***Table 14.*** *Continued*

| Spot number | Isot. Rat. and 2σ (abs) | | Ages and 2σ (abs) errors (Ma) | | | | % conc[b] |
|---|---|---|---|---|---|---|---|
| | $^{207}Pb/^{206}Pb$ | 2σ | $^{206}Pb/^{238}U$ | 2σ error (abs) | $^{207}Pb/^{235}U$ | 2σ error (abs) | |
| Mnz01 | 0.0527 | 0.0024 | 306 | 19 | 305 | 17 | 100% |
| Mnz05 | 0.0528 | 0.0014 | 305 | 10 | 305 | 9 | 100% |
| Mnz08 | 0.0541 | 0.0013 | 308 | 10 | 316 | 9 | 98% |
| Mnz14 | 0.0543 | 0.0013 | 311 | 10 | 319 | 9 | 97% |
| Mnz16 | 0.0532 | 0.0019 | 296 | 13 | 300 | 12 | 99% |
| Mnz18 | 0.0535 | 0.0015 | 308 | 10 | 312 | 10 | 99% |
| Mnz29 | 0.0542 | 0.0024 | 309 | 15 | 314 | 14 | 98% |
| Mnz32 | 0.0527 | 0.0016 | 299 | 11 | 299 | 11 | 100% |
| Mnz36 | 0.0548 | 0.0011 | 307 | 10 | 314 | 9 | 98% |

[b]Concordance calculated as 100× ($^{206}Pb/^{238}U$age)/ ($^{207}Pb/^{235}U$age)

# CHAPTER 8
# WHOLE-ROCK GEOCHEMISTRY

## 8.1. CORDIERITE-BEARING MONZOGRANITES AND MME

Whole-rock elemental and isotopic analyses were made at the SGIker-Facility of the UPV/EHU. Major- and trace-element concentrations were obtained by ICP-MS, and isotopic analyses by MC-ICP-MS (see the 'Methods' section in Chapter 3 for additional details). The distinguished three monzogranite units (OU, MU and IU) and MME are handled together for a better visualization and understanding of possible geochemical variations. Similarly, vaugnerite series rocks and lamprophyres are considered together (results of whole-rock analyses are shown in Tables 15 and 16).

### 8.1.1. Major elements

A total of 35 monzogranite samples from the Sierra Bermeja Pluton were selected for major- and trace-element geochemical characterization. As mentioned, whole-rock major- and trace-element data are shown in Table 15, and the location of the studied samples is given in Figure 15 and Table 12 of the Appendix.

Studied monzogranites plot in the 'granite' field of the Total Alkali – Silica (TAS) classification diagram for plutonic rocks (Middlemost, 1994), whereas MME fall in the granodiorite field (Fig. 45 A). In the same vein, most of the samples of the MU and IU plot in the 'granite' field of the P–Q diagram of Debon and Le Fort (1983), while OU monzogranites fall mainly within the 'adamellite' field, and the MME within the 'granodiorite' and 'tonalite' fields (Fig. 45 B). Thus, the P parameter of Debon and Le Fort (1983), expressing the proportion of K-feldspar to plagioclase [K – (Na + Ca) in millications]

clearly discriminates the OU (–59.1) from the MU and IU (–22.4 in both units), and the MME (–109 to –146) from the monzogranites.

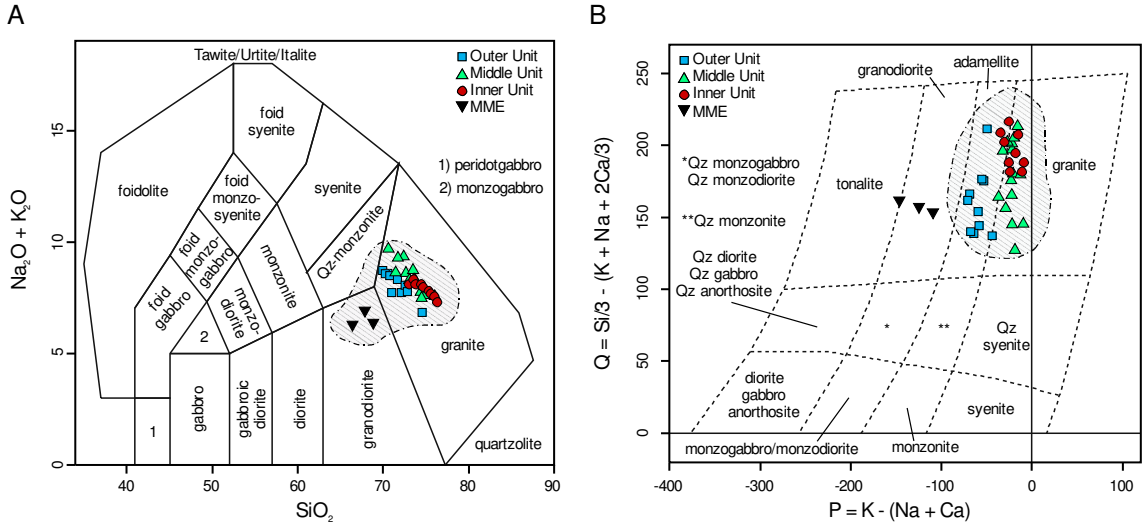


**Figure 45.** Projection of the studied monzogranite samples and MME in the A) Total Alkali Silica (TAS) classification diagram for plutonic rocks (Middlemost, 1994). B) P–Q diagram of Debon and Le Fort (1983). Data for the 'Serie Mixta' granitoids (dashed area; n = 184) from Antunes *et al.* (2008), Castro *et al.* (1999), Chicharro *et al.* (2014), Corretgé and Suárez (1994), Errandonea-Martin *et al.* (2017), García-Moreno (2004), González Menéndez (1998), Merino Martinez *et al.* (2014), Neiva *et al.* (2011), Pesquera *et al.* (2017), Ramírez and Grundvig (2000), and Ramírez and González Menéndez (1999).

Monzogranites of the Sierra Bermeja Pluton display relatively high contents of silica (67.90–74.44 wt.%), $Al_2O_3$ (12.70–15.93 wt.%), and $K_2O$ (3.58–5.72 wt.%), corresponding to high-K calc-alkaline (to shoshonitic) peraluminous rocks (Fig. 46 A and B). MME show markedly lower $K_2O$ contents than monzogranites (1.99–2.74 wt.%), but are peraluminous too (Fig. 46 A and B). Monzogranites show moderate contents of $P_2O_5$ (0.19–0.35 wt.%), as well as the MME (Fig. 46 B), and all monzogranite samples plot in the 'late-orogenic' to 'syn-collision' fields of the $R_1$–$R_2$ diagram (Batchelor and Bowden, 1985; Fig. 46 C). Nevertheless, this apparent compositional homogeneity in monzogranites contrasts with the variable peraluminous character of the analyzed samples (Fig. 46 B), which changes progressively from moderate average molar $Al_2O_3/(CaO + Na_2O + K_2O)$ (A/CNK; Shand, 1943) values in the OU (1.09), through intermediate in the MU (1.16) to high in the IU (1.25). As mentioned, MME are also peraluminous, and display a similar range of

peraluminosity to that of the monzogranites, from moderate to highly peraluminous A/CNK values (1.05–1.23; Fig. 46 B). Differences in major-element contents between the three major units are well reflected graphically in the maficity–peraluminosity (*B*–*A*) diagram (Fig. 46 D) of Debon and Le Fort (1983), modified by Villaseca *et al.* (1998a). The *B* parameter values (Fe + Mg + Ti in millications) are markedly higher in the OU (47–63), than in the MU (31–41) and in the IU (22–30). Equally, the values of *B* parameter are considerably higher in the MME (up to 113) than in the monzogranites (Fig. 46 D).

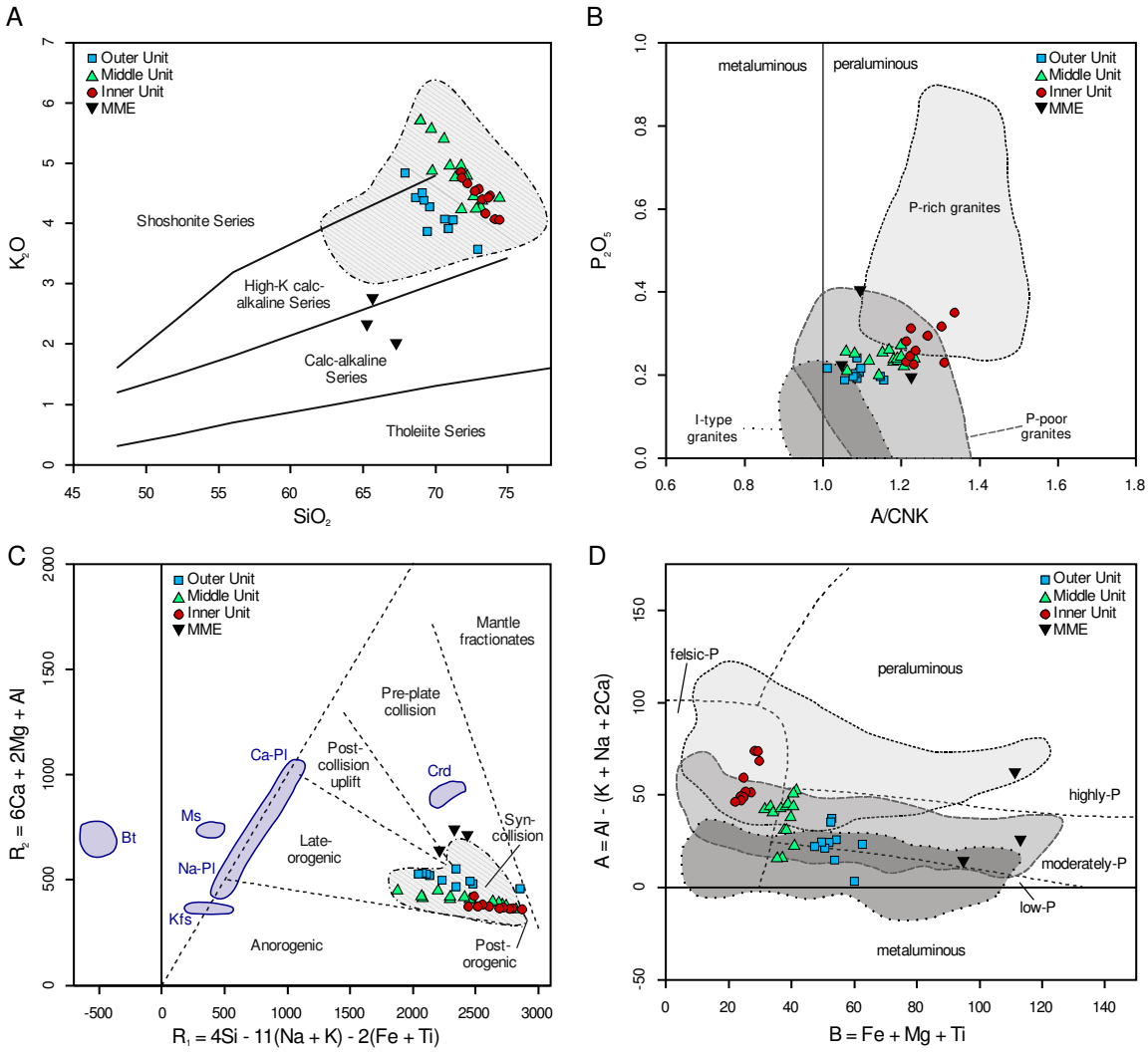


**Figure 46.** Projection of the studied monzogranite samples and MME in the A) $SiO_2$ *vs.* $K_2O$ diagram of Peccerillo and Taylor (1976). B) A/CNK *vs.* $P_2O_5$ (wt.%) diagram showing granite classification fields from Roda-Robles *et al.* (2018). C) $R_1$ *vs.* $R_2$ multicationic diagram of Batchelor and Bowden (1985); main rock-forming mineral compositions of the Sierra Bermeja Pluton are also shown. D) Maficity (*B*) *vs.* peraluminosity (*A*) diagram of Debon and Le Fort (1983) modified by Villaseca *et al.* (1998a). Dashed and dotted line-delimited fields in B and D are from Roda-Robles *et al.* (2018). Data for the 'Serie Mixta' granitoids (dashed area in A and C) from references of Fig. 45.

Compositional differences in major-elements between the main units of the Sierra Bermeja Pluton are also observable in variation diagrams (Fig. 47) featuring an overall decrease in $TiO_2$, MgO, CaO, and $FeO^t$ contents in the succession OU → MU → IU, coupled to a progressive increase in $P_2O_5$. The decrease in $Na_2O$ and, even more so in $K_2O$, with differentiation of each unit is in remarkable contrast with the patterns observed by I- and S-type granite suites of central Iberia (e.g. Villaseca et al., 1998b; Merino Martínez et al., 2014).

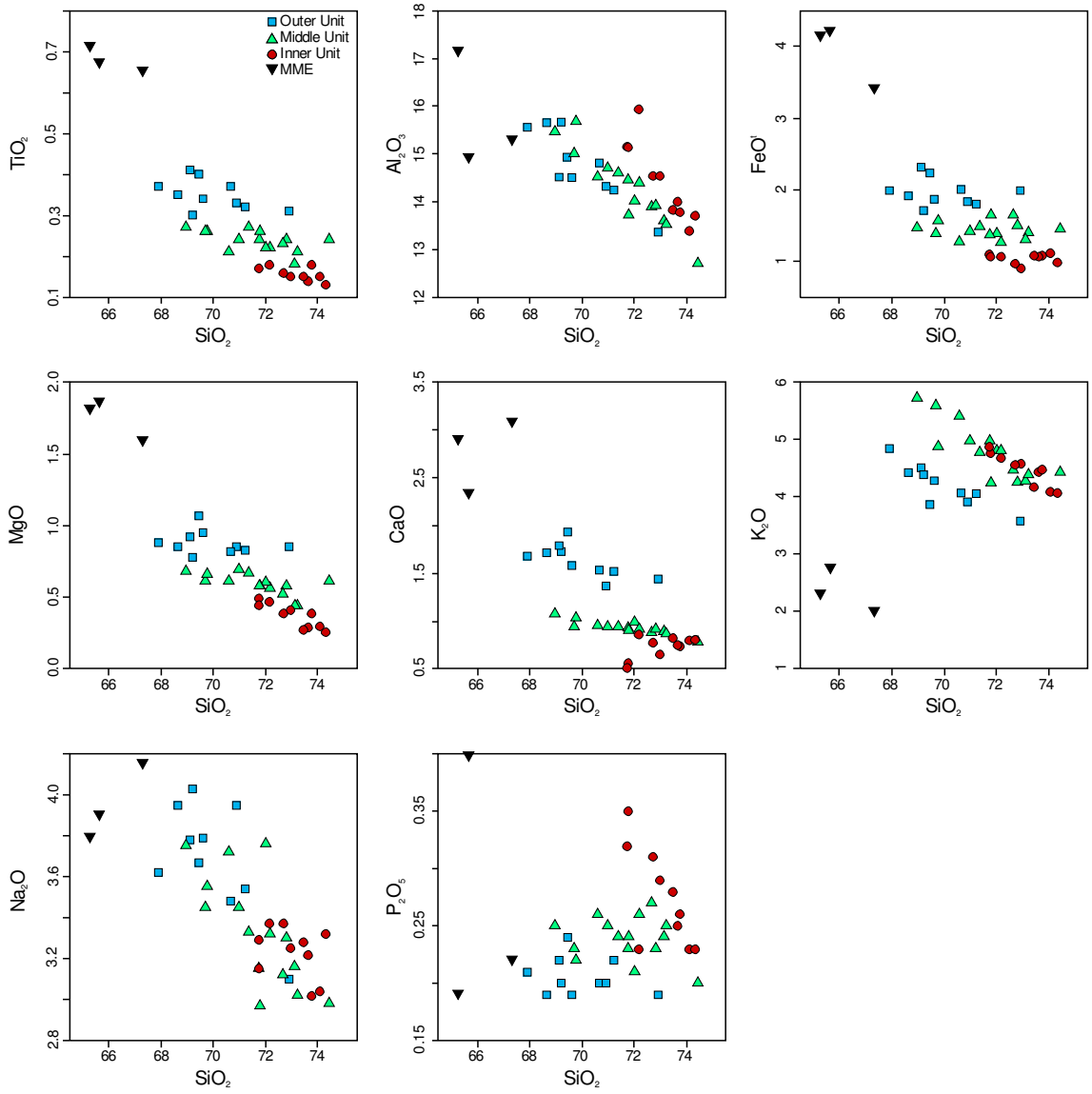


**Figure 47.** Major element variation diagrams for the studied monzogranites and MME.

Average silica contents also increase inwards (OU: 69.96 wt.%; MU: 71.69 wt.%; IU: 73.05 wt.%), whereas average Mg# values [molar MgO/(FeOt + MgO)] decrease (OU: 44.4; MU: 42.2; IU: 38.5). In the same vein, the MME show the highest $TiO_2$, MgO, CaO and $FeO^t$ contents, and the lowest $SiO_2$ and $K_2O$. The variation of $Al_2O_3$, $K_2O$ and $Na_2O$, observable in Harker diagrams, shows an outstanding overlap between the three distinguished main monzogranite units (Fig. 47).

## 8.1.2. Trace elements

The trace-element data reinforce the existence of compositional differences between the three major monzogranite units from the Sierra Bermeja Pluton (Table 15 and Figs. 48–50).

In this sense, there is an overall inward decrease in most trace elements (i.e. in the succession OU → MU → IU). Only Rb and Cs contents rise from the OU to the IU, while Ba and Pb show similar concentrations in all the three units (Fig. 48). Average Rb/Sr and Rb/Ba (Table 15) again discriminate the OU (2.15 and 0.78, respectively) on the one hand from the MU (4.15 and 1.04) and IU (3.62 and 1.06) in the other. Likewise, a general decrease (OU → MU → IU) is observed for the average contents of Zr (126 → 84 → 61 ppm), Hf (3.54 → 2.58 → 1.91 ppm), Nb (11.1 → 9.8 → 8.0 ppm), Th (12.2 → 10.0 → 7.3 ppm) and Y (22.3 → 12.3 → 9.3 ppm).

Trace-element variation diagrams (Fig. 48) show a marked decrease of Rb and U with granite differentiation in each monzogranite unit, as well as a moderate decrease in Ba, Zr and Sr contents. These patterns contrast with those observed in I- and S-type granites of central Iberia (Villaseca et al., 1998b) and match those recognized in the ‘Serie Mixta’-type granites (e.g. Villaseca et al., 1998b; Merino Martínez et al., 2014).

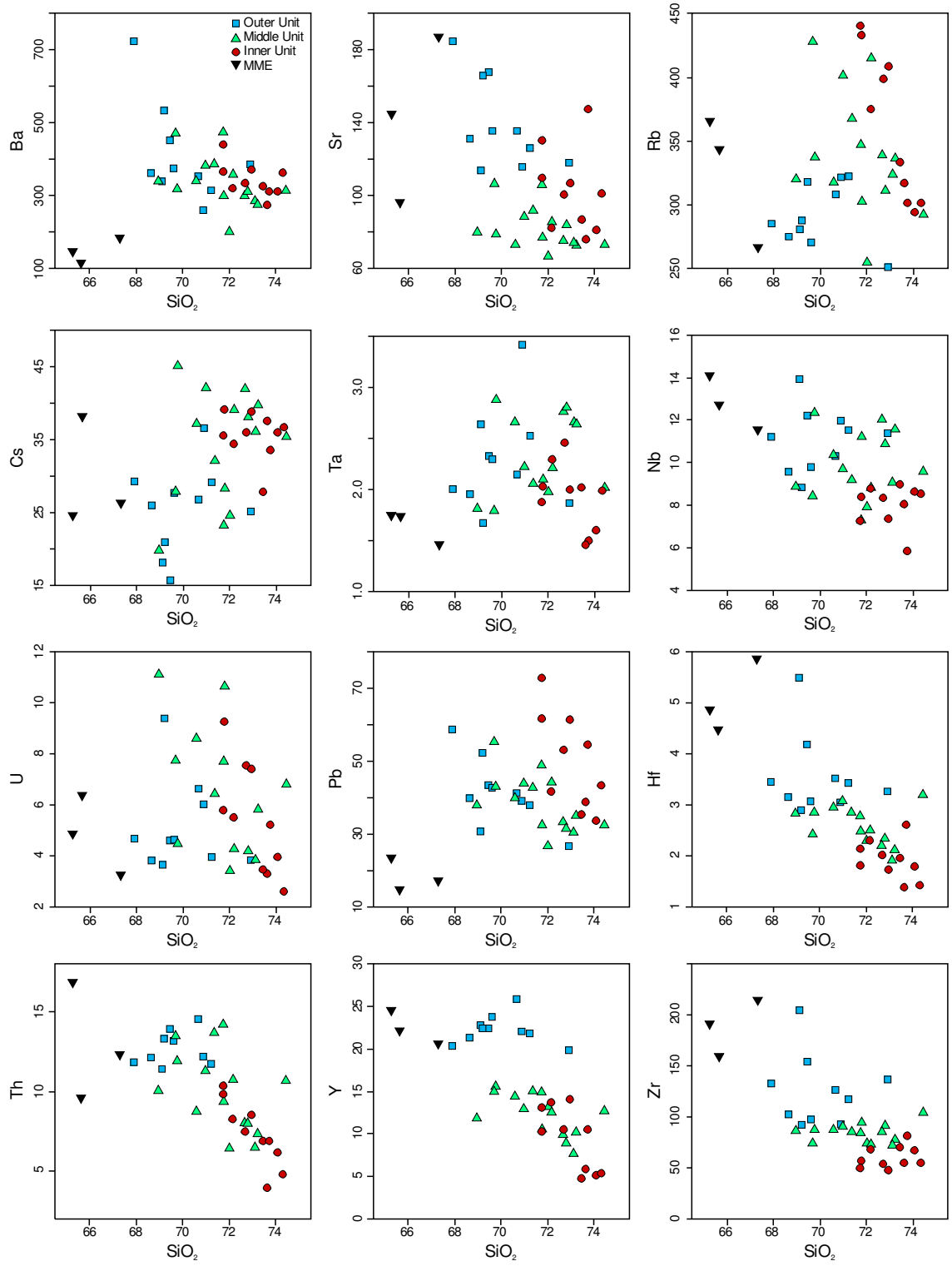


**Figure 48.** Selected trace element variation diagrams of the studied monzogranites and MME.

Multi-elemental diagrams normalized to the average bulk continental crust composition of Rudnick and Gao (2014) show fairly similar patterns for the three main units of the pluton (Fig. 49), with positive anomalies in Cs, Rb, U, Pb, Ta and P, and negative

ones in Sr and Ti. Nevertheless, a slight depletion in the Heavy Rare Earth Elements (HREE), Sr, Zr, Hf and Y is also observable in those profiles of the MU and IU with respect to the bulk continental crust and the OU (Fig. 49).

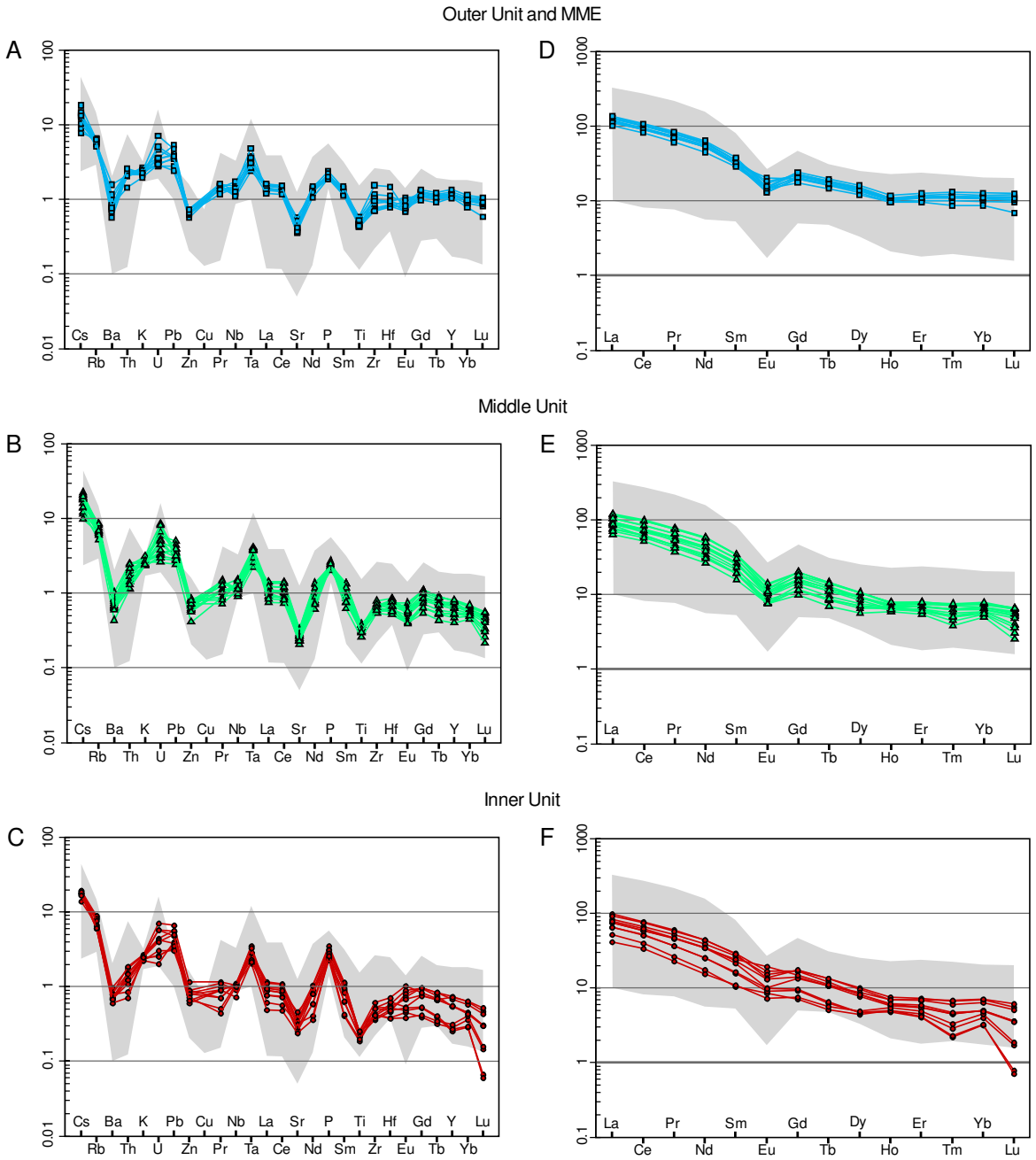


**Figure 49.** A–C) Average Bulk Continental Crust (Rudnick and Gao, 2014) normalized plots for the three monzogranite units of the Sierra Bermeja Pluton. D–F) Chondrite (Sun and McDonough, 1989) normalized REE diagrams for the three monzogranite units of the Sierra Bermeja Pluton. The gray field corresponds to the 'Serie Mixta' granitoids of the Central Iberian Zone after Antunes *et al.* (2008), Chicharro *et al.* (2014), Corretgé and Suárez (1994), Errandonea-Martin *et al.* (2017), García-Moreno (2004), González Menéndez (1998), Merino Martinez *et al.* (2014), Neiva *et al.* (2011), Pesquera *et al.* (2017), Ramírez and Grundvig (2000), and Ramírez and González Menéndez (1999).

Compared with the monzogranites, MME show the lowest Ba (111–178 ppm), Pb (14.5–23.1 ppm) and Ta (1.45–1.74 ppm) contents, as well as the highest Zr (158–214 ppm), Hf (4.44–5.83 ppm), Th (9.51–16.8 ppm) and Nb (11.5–14.0 ppm) contents (Fig. 48; Table 15). Other trace element concentrations, such as Sr, Rb and Cs, vary in the same range to that of all monzogranites, and Y and U contents are only similar to those of the OU monzogranites (Fig. 48).

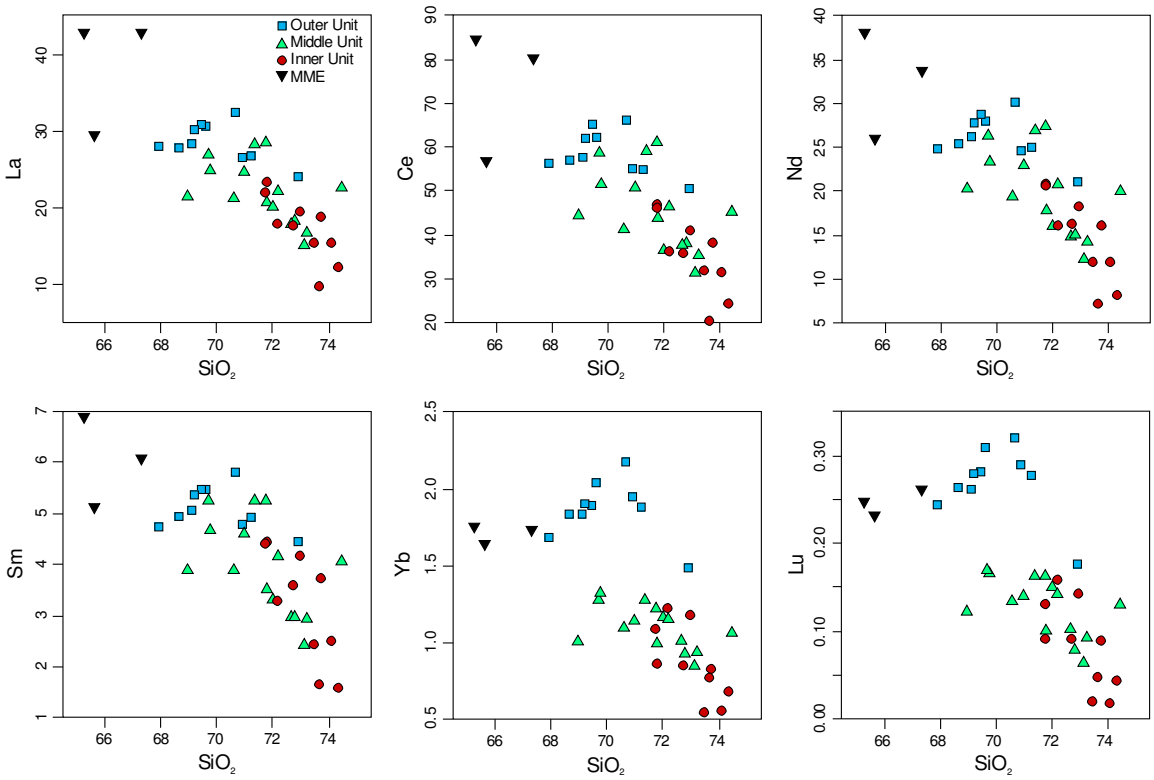


**Figure 50.** Selected REE variation diagrams of the studied monzogranites and MME from the Sierra Bermeja Pluton.

Rare Earth Element (REE) contents, and consequently average total contents (ΣREE) decrease inwards in the Sierra Bermeja Pluton (ΣREE = 140 → 106 → 83 ppm, Fig. 50). Chondrite (Sun and McDonough, 1989) normalized REE patterns are segmented, in all cases practically flat for the HREE (Fig. 49 D, E, F), and show an increasing REE degree of fractionation from the OU (average $(La/Yb)_N$ = 11.0) through the MU (14.3) to the IU (15.0). All samples display negative Eu anomalies, notably important in the OU (average Eu/Eu* =

0.59) and MU (0.52) compared with the IU (0.78). Remarkable is the presence of the lanthanide tetrad effect (Dy–Tm) in some samples of the IU (Fig. 49 F).

### 8.1.3. Whole-rock Sr–Nd isotope systematics

For whole-rock Sr–Nd isotope study nine samples that cover the full range of distinguished monzogranite types were selected, plus one MME sample. The measured Sr and Nd isotopic compositions were age-corrected to 306 Ma (average U–Pb zircon age estimated for the Sierra Bermeja Pluton, see the previous chapter) and the results are shown in Table 16.

The measured $^{87}Rb/^{86}Sr$ and $^{87}Sr/^{86}Sr$ ratios of the three types of monzogranites differ within noticeable ranges, with slightly higher ratios in the MU than in the OU and IU (Table 16). The initial $^{87}Sr/^{86}Sr_{306}$ ratios roughly increase from the OU (0.7033–0.7062) and MU (0.7037–0.7039) to the IU (0.7046–0.7107) (Fig. 51).

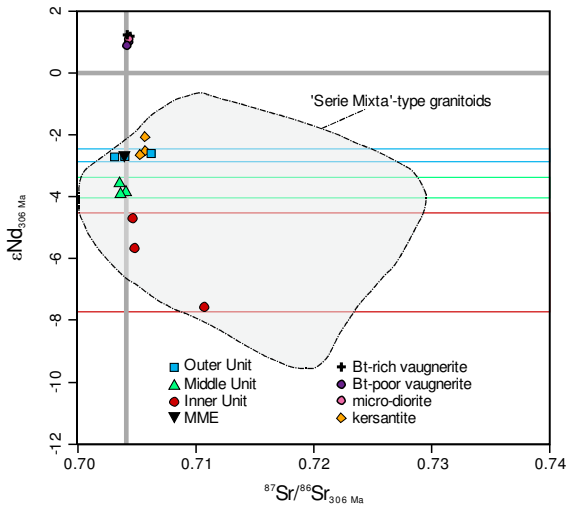


**Figure 51.** $^{87}Sr/^{86}Sr_{306}$ *vs.* $\varepsilon Nd_{306}$ binary plot for the monzogranites, MME and mesocratic rocks from the Sierra Bermeja Pluton. Data of the 'Serie Mixta'-type granitoids are from Alonso Olazabal (2001), Antunes *et al.* (2008), Castro *et al.* (1999), Chicharro *et al.* (2014), Donaire *et al.* (1999), Errandonea-Martin *et al.* (2017), González Menéndez (1998), Jiménez San Pedro (2003), Merino Martinez *et al.* (2014), Neiva *et al.* (2011), and Pesquera *et al.* (2017).

The projection of measured isotopic ratios for the OU → MU → IU in the $^{147}Sm/^{144}Nd$ *vs.* $^{143}Nd/^{144}Nd$ (isochron) diagram exhibits a roughly linear trend but with a negative correlation. Calculated initial $\varepsilon Nd_{306Ma}$ values increase progressively from the IU

(–7.5 to –4.7), through the MU (–3.9 to –3.6) to the OU (–2.7 to –2.6) (Fig. 51; Table 16). The calculated two-stage depleted-mantle Nd model ages (Liew and Hofmann, 1988) for the monzogranites vary from 1.23 to 1.62 Ga (Table 16), and the projection of the analyzed MME coincides with the host OU monzogranites, with almost identical $^{87}Sr/^{86}Sr_{306}$ and $\varepsilon Nd_{306Ma}$ values to one monzogranite sample of the OU (Fig. 51).

## 8.2. VAUGNERITE SERIES ROCKS AND LAMPROPHYRES

A total of 15 samples of mesocratic rocks from the Sierra Bermeja Pluton were selected for whole-rock major- and trace-element geochemical characterization: 2 biotite-rich vaugnerites, 4 biotite-poor vaugnerites, the micro-diorite, 7 kersantites, and the minette (Table 15).

### 8.2.1. Major elements

The vaugnerite series rocks are basic to intermediate ($SiO_2$ = 47.97–53.83 wt.%), while the micro-diorite is intermediate ($SiO_2$ = 50.92 wt.%). According to the TAS diagram (Middlemost, 1994) the biotite-rich vaugnerites and the micro-diorite would correspond to monzodiorites, as most of the biotite-poor vaugnerites (Fig. 52 A). This set of samples project into or close to the line of Irvine and Baragar (1971) that separates the alkaline–subalkaline rocks (Fig. 52 A). The biotite-rich vaugnerites plot within the 'Qz monzodiorite' and 'monzodiorite' fields of the P–Q diagram of Debon and Le Fort (1983), similarly to the Bt-poor vaugnerites that plot in the same fields plus in the 'Qz monzonite' field, like the micro-diorite (Fig. 52 B).

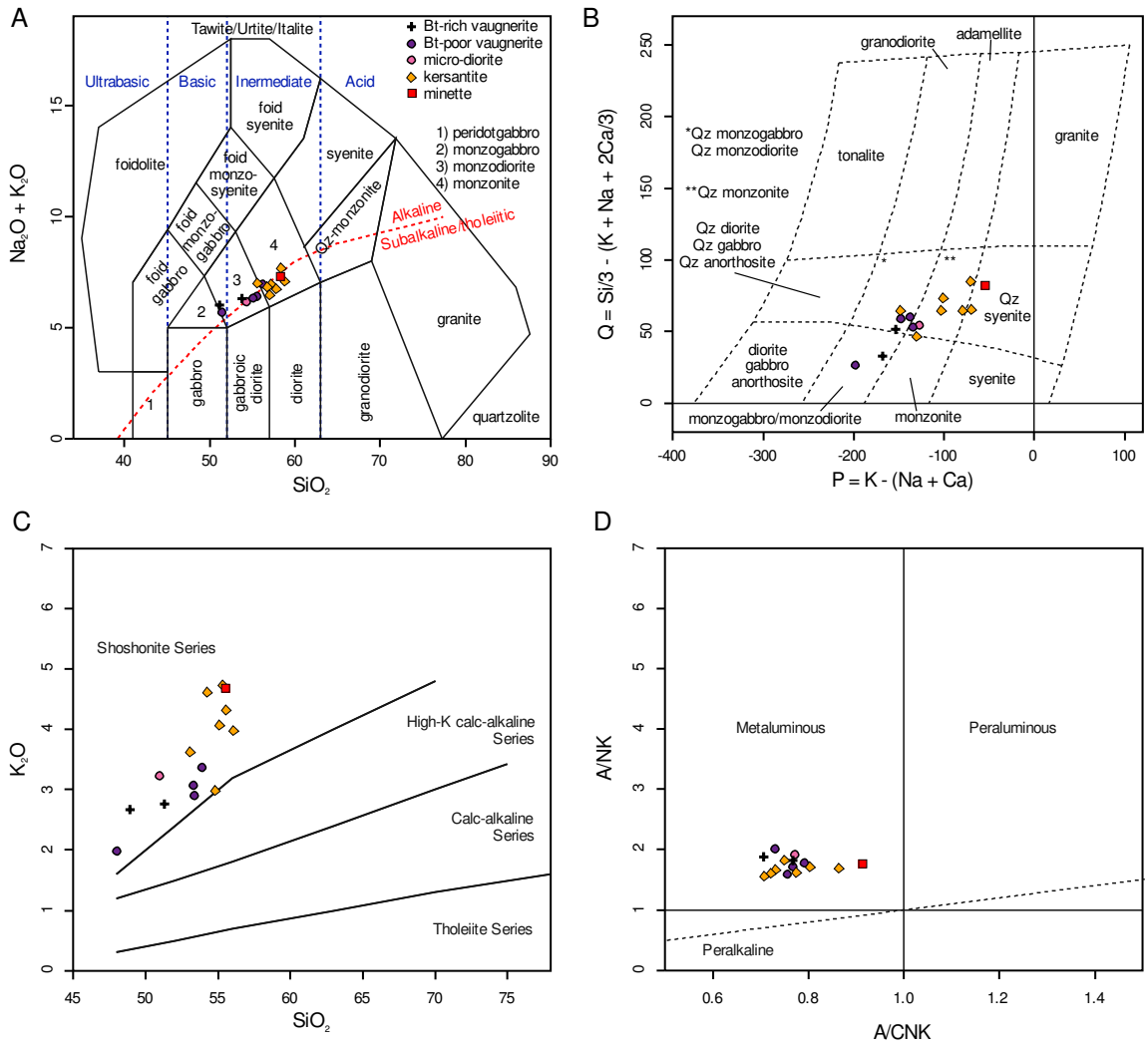


**Figure 52.** Projection of the mesocratic rocks from the Sierra Bermeja Pluton in the A) Total Alkali – Silica (TAS) classification diagram for plutonic rocks (Middlemost, 1994). B) P–Q diagram of Debon and Le Fort (1983). C) $SiO_2$ *vs.* $K_2O$ diagram of Peccerillo and Taylor (1976). D) A/CNK *vs.* A/NK diagram (Shand, 1943).

All these rocks show relatively similar contents of potassium (1.99–3.38 wt.% $K_2O$), falling in the 'shoshonite field of the $SiO_2$ *vs.* $K_2O$ diagram of Peccerillo and Taylor (1976; Fig. 52 C). They correspond with metaluminous (A/CNK = 0.71–0.79; Fig. 52 D) and calcium-rich rocks (CaO = 5.61–7.50 wt.%), with similar sodium contents (2.56–3.34 wt.% $Na_2O$; Table 15) and iron contents ($FeO^t$ = 7.40–9.10 wt.%) higher than magnesium (MgO = 5.60–7.59 wt.%). Mg# [molar MgO/(FeOt + MgO)] values are practically the same within the range of 53.96–59.80 (Table 15).

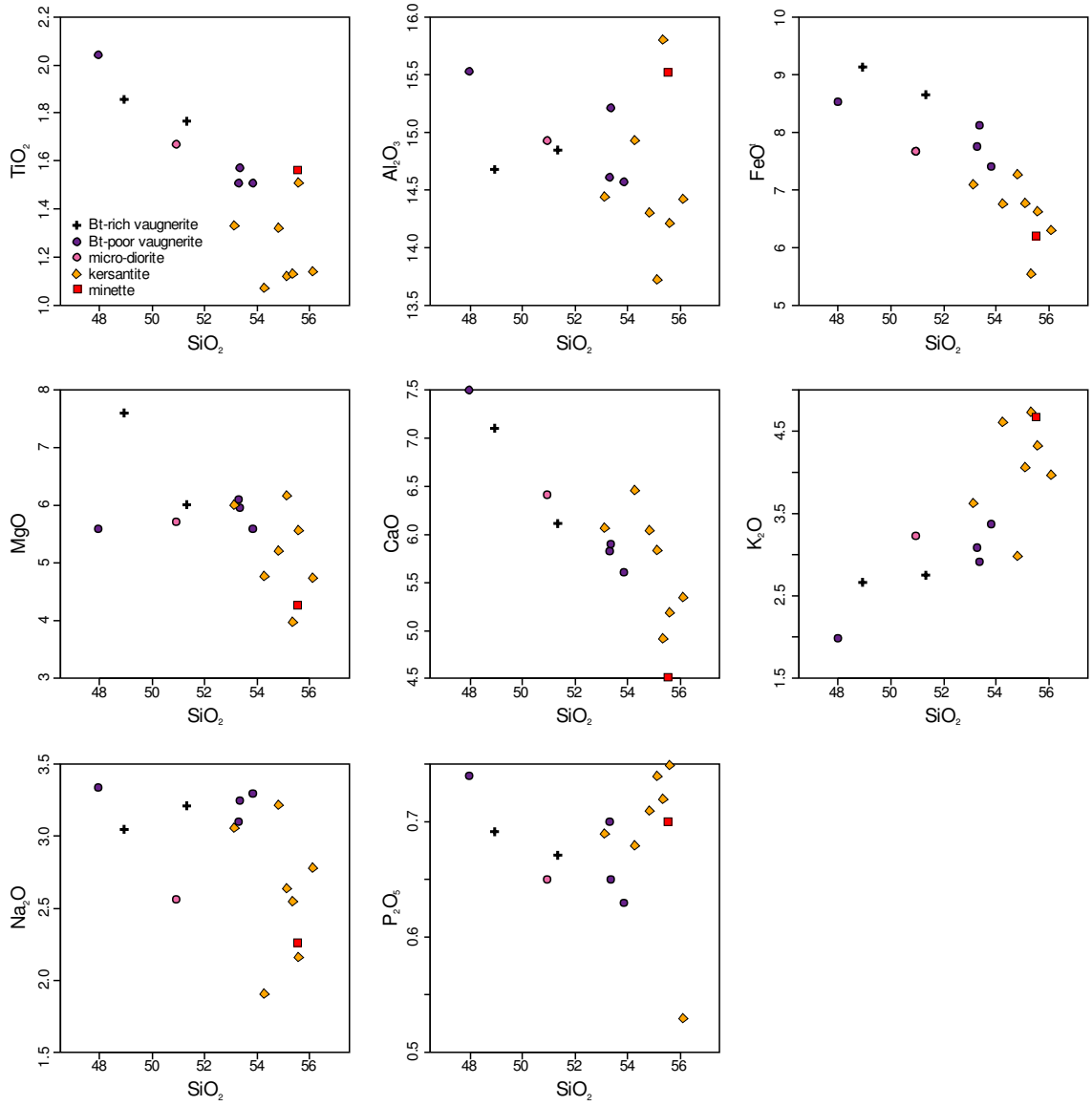


**Figure 53.** Major element variation diagrams for the studied mesocratic rocks from the Sierra Bermeja Pluton.

Considering all analyzed dioritoids (biotite-rich vaugnerites + biotite-poor vaugnerites + the micro-diorite), there is an overall decrease in $TiO_2$, $FeO^t$, CaO, and less so in $P_2O_5$, and MgO, coupled to a progressive increase in $K_2O$ observable in the variation diagrams (Fig. 53). On the contrary, $Al_2O_3$ and $Na_2O$ do not define any apparent trend.

Lamprophyres from the Sierra Bermeja Pluton are intermediate rocks ($SiO_2$ = 53.13–56.11 wt.%), with higher P parameter (Debon and Le Fort, 1983) values than those exhibited by the dioritoids (Fig. 52 A, B). These mesocratic rocks are potassium- and calcium-rich

($K_2O$ = 2.99–4.74 wt.%; CaO = 4.51–6.46 wt.%), with lower contents of sodium ($Na_2O$ = 1.91–3.22 wt.%) than of potassium, and plot within the 'shoshonite field' of the $SiO_2$ *vs*. $K_2O$ diagram of Peccerillo and Taylor (1976; Fig. 52 C). Lamprophyres of the Sierra Bermeja Pluton show metaluminous compositions, with variable A/CNK values that range from the lowest values of the above described dioritoids up to the highest values of all mesocratic rocks (A/CNK = 0.71–0.91; Fig. 52 D). The minette is the sample that shows the highest A/CNK value (Fig. 52 D).

Lamprophyres plot close to the line of Irvine and Baragar (1971) that separates alkaline and subalkaline rocks in the TAS diagram (Le Maitre *et al*., 2002), integrating in a possible transitional association as dioritoids (Fig. 52 A). They exhibit higher Mg# [molar MgO/(FeOt + MgO)] values (55.15–61.92) than those of the studied dioritoids, which is consistent with their more ferroan ($FeO^t$ = 5.54–7.27 wt.%) than magnesian (MgO = 3.99–6.18 wt.%) character. In variation diagrams, a decrease in $FeO^t$, MgO and CaO is observable, coupled to an increase of $K_2O$ and $P_2O_5$ (Fig. 53). Considering the whole set of analyzed mesocratic rocks, it is noticeable that they show decreasing trends in $TiO_2$, $FeO^t$, and less so in CaO, and an increasing trend in $K_2O$ (Fig. 53).

## 8.2.2. Trace elements

The ranges of trace element contents in the studied dioritoids are relatively narrower than in lamprophyres standing out the relatively high concentrations of Ba (963–1552 ppm), Sr (739–861 ppm), Zr (272–381 ppm) and Cr (171–230 ppm). In general, vaugnerite series rocks show lower Ba, Rb, U, and Th contents (Fig. 54) whereas Nb, Ta, and Ni contents are higher than those of the lamprophyres.

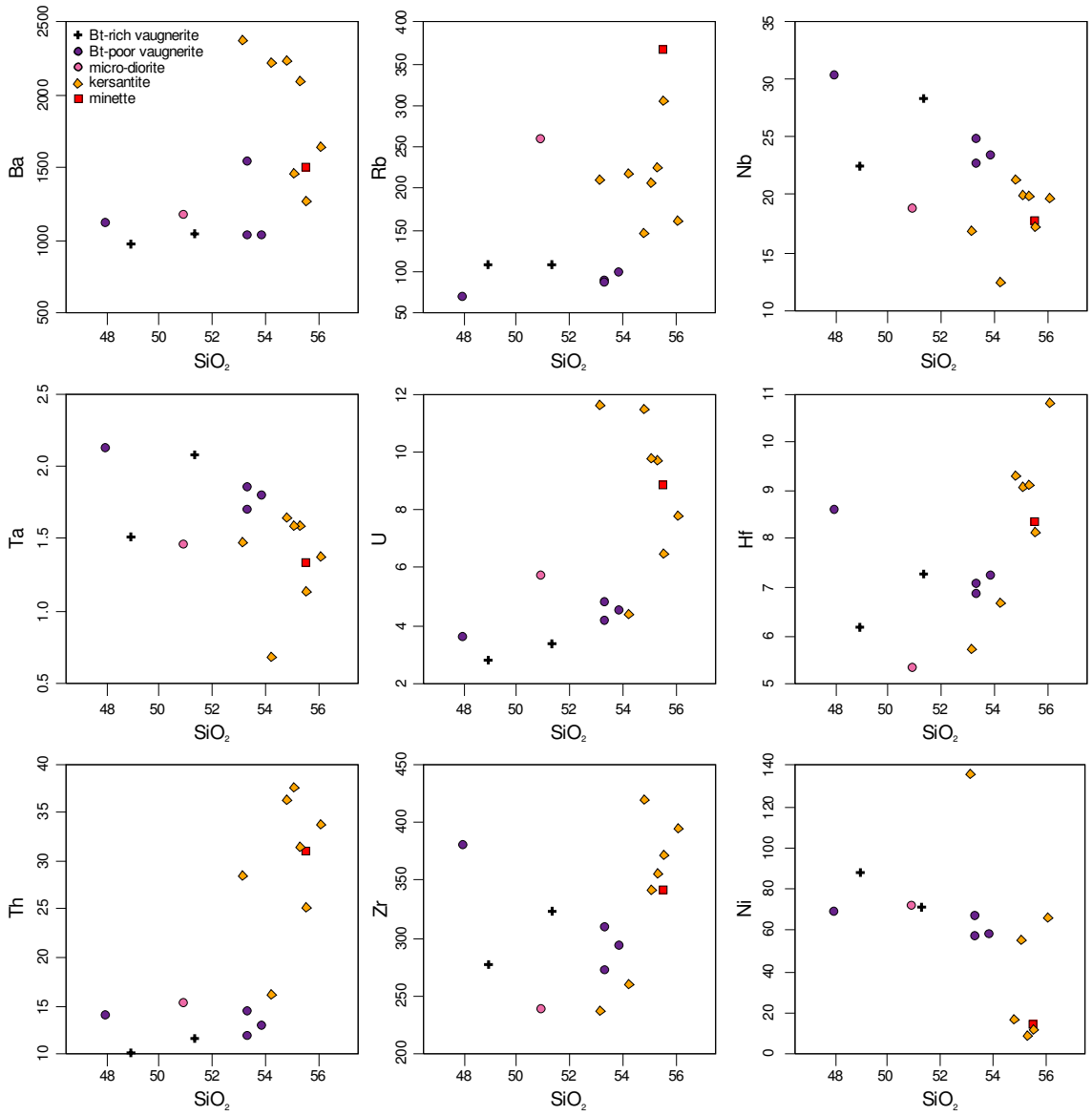


**Figure 54.** Selected trace element variation diagrams of the studied mesocratic rocks.

Overall, primitive mantle (Sun and McDonough, 1989) normalized multielemental diagrams for the dioritoids show steep trends characterized by marked enrichments in Large Ion Lithophile Elements (LILE > 100x primitive mantle) respect to High Field Strength Elements (HFSE; Fig. 55 A). Note, however, that the dioritoids are slightly depleted in LILE respect to the lamprophyres, while HFSE contents are very similar in both groups of rocks (Fig. 55 A and B). Normalized plots show a marked negative anomaly in Nb and, less pronounced, Ti. They also exhibit a marked positive anomaly in Pb and a slighter one in Nd but contrary to lamprophyres, they lack a negative anomaly in Sr (Fig. 55 A and B).

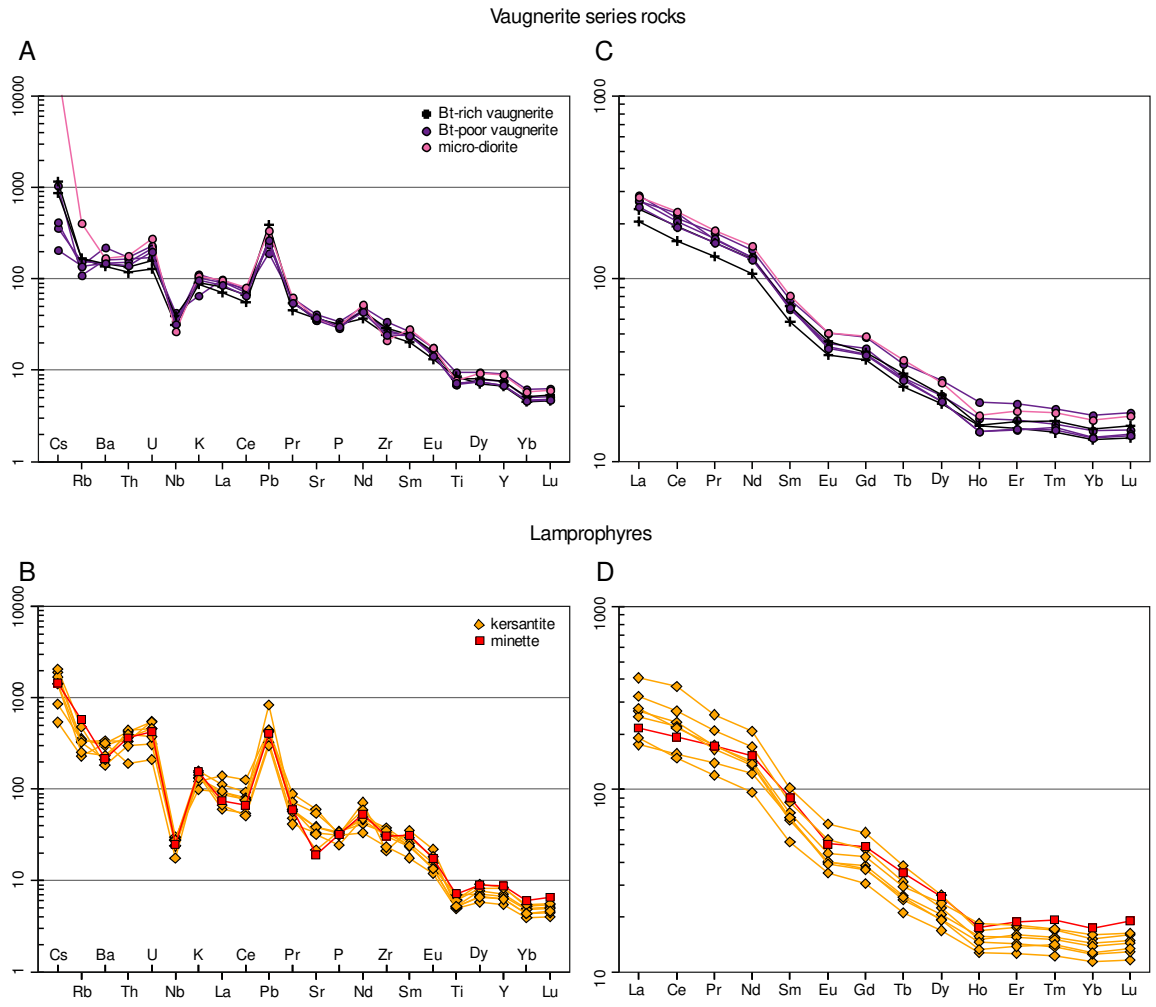


**Figure 55.** A–B) Primitive mantle (Rudnick and Gao, 2014) normalized plots for the dioritoids (A) and lamprophyres (B) of the Sierra Bermeja Pluton. C–D) Chondrite (Sun and McDonough, 1989) normalized REE diagrams for dioritoids (C) and lamprophyres (D).

REE show notable differences in Light Rare Earth Elements (LREE) and HREE, with relatively higher contents in the former elements. Total REE contents of dioritoids (ΣREE) vary in the range of 241–338 ppm (Table 15). Chondrite (Sun and McDonough, 1989) normalized patterns show strongly fractionated [$(La/Yb)_N$ = 15.7–19.8] and segmented trends with higher fractionation of LREE [$(La/Sm)_N$ = 3.39–3.91] than HREE [$(Gd/Yb)_N$ = 2.63–2.85]. Normalized patterns of vaugnerite series rocks show slight Eu negative anomalies (Eu/Eu* = 0.81–0.87) and nearly flat profiles of the HREE (Fig. 55 C). It is remarkable that the micro-diorite shows more enriched patterns in HREE (Fig. 55 C).

Trace element contents of lamprophyres are notably variable, which in cases are particularly high, as for Cr (87–336 ppm), Ni (8.7–136 ppm), Rb (147–368 ppm) and Sr (401–1260 ppm). In this sense, it is also noticeable their relatively high concentrations in Ba (1271–2385 ppm), Th (16.2–37.6 ppm) and Zr (260–420 ppm; Fig. 54). Primitive mantle (Sun and McDonough, 1989) normalized multielemental diagrams show steep trends characterized by marked enrichments in LILE (> 100x primitive mantle) respect to HFSE (Fig. 55 B). These normalized plots show a strong positive anomaly in Pb and, in a lesser extent, Nd; in addition, they are also characterized by their marked negative anomalies in Nb and, though less pronounced, Ti and Sr (Fig. 55 B).

ΣREE contents in lamprophyres are relatively high (242–380 ppm), but particularly those of the LREE (219–354 ppm) compared with the HREE (19–26 ppm). The chondrite (Sun and McDonough, 1989) normalized diagrams show highly fractionated [$(La/Yb)_N$ = 12.4–26.9] and segmented patterns, with steep slopes for LREE $(La/Sm)_N$ = 2.38–4.00) and nearly flat for the rest of the HREE (Fig. 55 D). Studied lamprophyres show slight Eu negative anomalies (Eu/Eu* = 0.76–0.88). Finally, the minette shows the most enriched patterns in HREE among the lamprophyres (Fig. 55 D).

### 8.2.3. Whole-rock Sr–Nd isotope systematics

For whole-rock Sr–Nd isotopic characterization of the mesocratic rocks from the Sierra Bermeja Pluton, eight representative samples were selected: 2 biotite-rich vaugnerites, 2 biotite-poor vaugnerites, the micro-diorite, and 3 kersantites. Moreover, vaugneritic rocks will be considered later in order to assess a possible mantle contribution in the origin of the studied monzogranites.

Vaugneritic rocks constitute a homogeneous compositional group with $^{87}Rb/^{86}Sr$ and $^{87}Sr/^{86}Sr$ ratios comprised in a narrow range (Table 16). In this sense is noticeable that their

initial $^{87}Sr/^{86}Sr_{306Ma}$ ratios (0.7041–0.7045) are similar to some of those obtained for the monzogranitic units (Table 16; Fig. 51). $^{147}Sm/^{144}Nd$ and $^{143}Nd/^{144}Nd$ ratios are also homogeneous, with positive $\varepsilon Nd_{306Ma}$ values (+0.9 to +1.2; Table 16; Fig. 51). Single-stage depleted-mantle Nd model ages (Liew and Hofmann, 1988) are in the range of 0.89–0.91 Ga (Table 16). It is noticeable that the analyzed micro-diorite shows identical isotopic characteristics to those of the analyzed vaugnerites (Table 16; Fig. 51).

The three analyzed kersantites show homogeneous $^{87}Rb/^{86}Sr$ and $^{87}Sr/^{86}Sr$ ratios, with slightly higher ones than those of the studied vaugneritic rocks (Table 16). Their initial $^{87}Sr/^{86}Sr_{306Ma}$ ratios (0.7053–0.7058) are higher than those of the vaugnerites, and similar or slightly higher also than those of the OU and MU monzogranites (Fig. 51). They present the lowest $^{147}Sm/^{144}Nd$ ratios of the whole set of analyzed rocks, and $^{143}Nd/^{144}Nd$ ratios, as well as $\varepsilon Nd_{306Ma}$ values (–2.0 to –2.6), that are similar to those of the MME and OU monzogranites (Table 16). Single-stage depleted-mantle Nd model ages (Liew and Hofmann, 1988) are in the range of 1.07–1.14 Ga (Table 16).

***Table 15.*** *Representative major- (wt.%) and trace-element (ppm) whole-rock geochemical data of monzogranites, MME and mesocratic rocks from the Sierra Bermeja Pluton*

| #Fig15 | 1 | 2 | 3 | 4 | 5 | 6 | 7 | 8 | 9 | 10 | 11 |
|---|---|---|---|---|---|---|---|---|---|---|---|
| Sample | JE 15 26 | JE 15 62 | JE 15 68 | JE 15 34 | JE 15 35 | JE 15 36 | JE 15 38 | JE 15 48 | JE 15 60 | SB 169 | JE 15 30 |
| Unit | OU | OU | OU | OU | OU | OU | OU | OU | OU | OU | MU |
| $SiO_2$ | 67.90 | 69.45 | 69.11 | 68.64 | 70.89 | 69.61 | 70.66 | 69.20 | 71.23 | 72.91 | 69.69 |
| TiO2 | 0.37 | 0.40 | 0.41 | 0.35 | 0.33 | 0.34 | 0.37 | 0.30 | 0.32 | 0.31 | 0.26 |
| $Al_2O_3$ | 15.56 | 14.93 | 14.52 | 15.65 | 14.32 | 14.50 | 14.81 | 15.66 | 14.25 | 13.37 | 15.00 |
| $Fe_2O_3^t$ | 2.21 | 2.48 | 2.57 | 2.13 | 2.04 | 2.07 | 2.23 | 1.90 | 2.00 | 2.21 | 1.54 |
| MnO | 0.04 | 0.05 | 0.05 | 0.05 | 0.04 | 0.06 | 0.04 | 0.04 | 0.05 | 0.04 | 0.04 |
| MgO | 0.88 | 1.07 | 0.92 | 0.85 | 0.85 | 0.95 | 0.82 | 0.78 | 0.83 | 0.85 | 0.61 |
| CaO | 1.68 | 1.93 | 1.79 | 1.72 | 1.37 | 1.58 | 1.53 | 1.73 | 1.52 | 1.44 | 0.94 |
| $Na_2O$ | 3.62 | 3.67 | 3.78 | 3.95 | 3.95 | 3.79 | 3.48 | 4.03 | 3.54 | 3.10 | 3.45 |
| $K_2O$ | 4.84 | 3.87 | 4.51 | 4.43 | 3.92 | 4.28 | 4.07 | 4.39 | 4.06 | 3.58 | 5.58 |
| $P_2O_5$ | 0.21 | 0.24 | 0.22 | 0.19 | 0.20 | 0.19 | 0.20 | 0.20 | 0.22 | 0.19 | 0.23 |
| LOI | 1.08 | 0.96 | 0.94 | 0.93 | 0.93 | 1.34 | 0.84 | 0.77 | 1.00 | 1.06 | 0.92 |
| Total | 98.39 | 99.06 | 98.81 | 98.87 | 98.84 | 98.71 | 99.04 | 99.01 | 99.02 | 99.04 | 98.26 |
| Mg# | 44.10 | 46.09 | 41.49 | 44.15 | 45.22 | 47.62 | 42.15 | 44.85 | 45.12 | 43.25 | 43.97 |
| A/CNK | 1.09 | 1.09 | 1.01 | 1.09 | 1.08 | 1.06 | 1.15 | 1.08 | 1.10 | 1.15 | 1.12 |
| Ba | 722 | 451 | 338 | 360 | 259 | 374 | 352 | 532 | 314 | 384 | 468 |
| Cr | 18.5 | 20.0 | 11.3 | 15.6 | 15.8 | 17.6 | 18.3 | 15.3 | 15.0 | 15.2 | 13.1 |
| Cs | 29.2 | 15.6 | 18.1 | 25.9 | 36.5 | 27.7 | 26.7 | 20.9 | 29.1 | 25.1 | 27.8 |
| Ga | 24.8 | 25.3 | 20.7 | 24.8 | 28.2 | 26.2 | 28.5 | 27.9 | 25.1 | 26.6 | 32.6 |
| Hf | 3.44 | 4.18 | 5.48 | 3.15 | 3.05 | 3.07 | 3.51 | 2.89 | 3.42 | 3.26 | 2.41 |
| Nb | 11.2 | 12.2 | 13.9 | 9.6 | 12.0 | 9.8 | 10.3 | 8.84 | 11.5 | 11.4 | 8.40 |
| Ni | 5.17 | 5.42 | < MDL | 4.19 | 3.43 | 5.82 | 4.44 | 4.03 | 3.70 | < MDL | < MDL |
| Pb | 58.8 | 43.5 | 30.8 | 39.9 | 39.3 | 42.9 | 41.4 | 52.5 | 38.2 | 26.8 | 55.3 |
| Rb | 285 | 318 | 281 | 275 | 322 | 271 | 308 | 288 | 323 | 251 | 428 |
| Sc | 6.30 | 7.10 | 6.57 | 6.88 | 7.66 | 7.51 | 6.25 | 5.27 | 6.23 | 6.39 | 4.92 |
| Sn | 18.0 | 14.5 | 8.77 | 19.5 | 24.6 | 22.3 | 25.6 | 17.6 | 21.0 | 12.0 | 21.2 |
| Sr | 185 | 168 | 114 | 131 | 116 | 136 | 136 | 166 | 126 | 118 | 106 |
| Ta | 2.01 | 2.33 | 2.64 | 1.96 | 3.42 | 2.30 | 2.15 | 1.68 | 2.53 | 1.87 | 1.79 |
| Th | 11.8 | 13.9 | 11.4 | 12.2 | 12.2 | 13.2 | 14.5 | 13.3 | 11.7 | 8.10 | 13.5 |
| U | 4.68 | 4.59 | 3.66 | 3.82 | 6.02 | 4.63 | 6.63 | 9.39 | 3.97 | 3.85 | 7.72 |
| V | 25.6 | 26.0 | 23.5 | 21.6 | 20.4 | 21.5 | 22.5 | 19.7 | 19.9 | 31.7 | 16.0 |
| Y | 20.4 | 22.5 | 22.8 | 21.3 | 22.0 | 23.8 | 25.9 | 22.5 | 21.8 | 19.9 | 14.9 |
| Zn | 48.3 | 47.1 | 41.1 | 45.4 | 52.4 | 51.8 | 52.8 | 44.9 | 47.0 | 47.5 | 56.2 |
| Zr | 133 | 154 | 205 | 103 | 92.9 | 97.5 | 127 | 92.6 | 118 | 137 | 73.6 |
| Rb/Sr | 1.54 | 1.89 | 2.47 | 2.09 | 2.78 | 1.99 | 2.27 | 1.73 | 2.55 | 2.12 | 4.02 |
| Rb/Ba | 0.395 | 0.705 | 0.832 | 0.764 | 1.24 | 0.724 | 0.875 | 0.541 | 1.03 | 0.654 | 0.914 |
| La | 28.0 | 30.9 | 28.5 | 27.8 | 26.5 | 30.6 | 32.5 | 30.1 | 26.8 | 24.1 | 27.0 |
| Ce | 56.4 | 65.3 | 57.7 | 57.1 | 55.2 | 62.3 | 66.2 | 61.9 | 55.0 | 50.6 | 58.8 |
| Pr | 6.68 | 7.71 | 7.05 | 6.73 | 6.57 | 7.46 | 8.03 | 7.42 | 6.67 | 5.83 | 7.18 |
| Nd | 24.9 | 28.8 | 26.2 | 25.5 | 24.7 | 28.1 | 30.2 | 27.8 | 25.0 | 21.1 | 26.4 |
| Sm | 4.73 | 5.46 | 5.06 | 4.94 | 4.77 | 5.46 | 5.82 | 5.37 | 4.92 | 4.44 | 5.26 |
| Eu | 1.18 | 1.00 | 0.810 | 0.866 | 0.759 | 0.886 | 0.903 | 1.07 | 0.764 | 0.849 | 0.782 |
| Gd | 4.06 | 4.71 | 4.40 | 4.22 | 4.11 | 4.67 | 4.98 | 4.55 | 4.20 | 3.62 | 4.08 |
| Tb | 0.602 | 0.687 | 0.654 | 0.620 | 0.616 | 0.693 | 0.738 | 0.671 | 0.634 | 0.549 | 0.544 |
| Dy | 3.28 | 3.76 | 3.63 | 3.51 | 3.48 | 3.84 | 4.10 | 3.66 | 3.50 | 3.07 | 2.67 |
| Ho | 0.547 | 0.616 | 0.610 | 0.578 | 0.576 | 0.620 | 0.671 | 0.599 | 0.579 | 0.544 | 0.442 |
| Er | 1.68 | 1.89 | 1.86 | 1.80 | 1.84 | 1.95 | 2.09 | 1.85 | 1.80 | 1.59 | 1.28 |
| Tm | 0.255 | 0.299 | 0.285 | 0.281 | 0.292 | 0.315 | 0.338 | 0.295 | 0.290 | 0.221 | 0.190 |
| Yb | 1.68 | 1.90 | 1.84 | 1.83 | 1.95 | 2.04 | 2.18 | 1.90 | 1.88 | 1.48 | 1.28 |
| Lu | 0.244 | 0.281 | 0.262 | 0.263 | 0.289 | 0.309 | 0.320 | 0.279 | 0.277 | 0.176 | 0.169 |
| ΣREE | 134 | 153 | 139 | 136 | 132 | 149 | 159 | 147 | 132 | 118 | 136 |
| $La_N/Yb_N$ | 12.0 | 11.7 | 11.1 | 10.9 | 9.74 | 10.8 | 10.7 | 11.4 | 10.2 | 11.7 | 15.1 |
| Eu/Eu* | 0.82 | 0.60 | 0.53 | 0.58 | 0.52 | 0.54 | 0.51 | 0.66 | 0.51 | 0.65 | 0.52 |

#Fig. 15: Sample location in Fig. 15 of Chapter 4

***Table 15.*** *Continued*

| #Fig15 | 12 | 13 | 14 | 15 | 16 | 17 | 18 | 19 | 20 | 21 | 22 |
|---|---|---|---|---|---|---|---|---|---|---|---|
| Sample | JE 15 57 | JE 16 23 | JE 16 44 | JE 15 04 | JE 15 53 | JE 15 56 | JE 15 59 | JE 15 65 | JE 15 67 | SB 160 | SB 166 |
| Unit | MU | MU | MU | MU | MU | MU | MU | MU | MU | MU | MU |
| $SiO_2$ | 71.75 | 72.01 | 74.44 | 69.77 | 72.18 | 68.96 | 71.36 | 70.98 | 70.59 | 73.23 | 71.78 |
| TiO2 | 0.24 | 0.22 | 0.24 | 0.26 | 0.22 | 0.27 | 0.27 | 0.24 | 0.21 | 0.21 | 0.26 |
| $Al_2O_3$ | 14.44 | 14.00 | 12.70 | 15.68 | 14.39 | 15.46 | 14.60 | 14.70 | 14.51 | 13.51 | 13.71 |
| $Fe_2O_3^t$ | 1.52 | 1.54 | 1.61 | 1.73 | 1.40 | 1.63 | 1.65 | 1.57 | 1.41 | 1.56 | 1.83 |
| MnO | 0.03 | 0.04 | 0.03 | 0.04 | 0.04 | 0.04 | 0.04 | 0.04 | 0.04 | 0.04 | 0.04 |
| MgO | 0.58 | 0.60 | 0.61 | 0.66 | 0.56 | 0.68 | 0.67 | 0.69 | 0.61 | 0.44 | 0.58 |
| CaO | 0.93 | 0.99 | 0.78 | 1.03 | 0.91 | 1.07 | 0.94 | 0.94 | 0.95 | 0.86 | 0.90 |
| $Na_2O$ | 3.15 | 3.76 | 2.98 | 3.55 | 3.32 | 3.75 | 3.33 | 3.45 | 3.72 | 3.02 | 2.97 |
| $K_2O$ | 4.97 | 4.80 | 4.43 | 4.88 | 4.80 | 5.72 | 4.77 | 4.97 | 5.41 | 4.38 | 4.24 |
| $P_2O_5$ | 0.23 | 0.21 | 0.20 | 0.22 | 0.26 | 0.25 | 0.24 | 0.25 | 0.26 | 0.25 | 0.24 |
| LOI | 1.24 | 0.76 | 0.87 | 0.90 | 1.00 | 0.91 | 1.20 | 1.16 | 1.20 | 1.54 | 2.58 |
| Total | 99.09 | 98.93 | 98.89 | 98.73 | 99.07 | 98.74 | 99.06 | 98.99 | 98.91 | 99.03 | 99.13 |
| Mg# | 43.05 | 43.56 | 42.88 | 43.05 | 44.21 | 45.25 | 44.58 | 46.54 | 46.15 | 35.85 | 38.57 |
| A/CNK | 1.18 | 1.06 | 1.14 | 1.21 | 1.17 | 1.08 | 1.18 | 1.15 | 1.06 | 1.20 | 1.23 |
| Ba | 472 | 199 | 311 | 316 | 356 | 338 | 384 | 379 | 340 | 273 | 298 |
| Cr | 12.8 | 6.50 | 9.6 | 12.1 | 15.5 | 8.86 | 12.3 | 10.6 | 8.15 | < MDL | < MDL |
| Cs | 23.1 | 24.5 | 35.3 | 45.0 | 39.0 | 19.7 | 32.0 | 42.1 | 37.1 | 39.7 | 28.2 |
| Ga | 29.9 | 15.8 | 22.2 | 29.6 | 28.5 | 21.7 | 27.3 | 27.2 | 23.4 | 29.1 | 30.4 |
| Hf | 2.76 | 2.29 | 3.18 | 2.83 | 2.49 | 2.82 | 2.84 | 3.07 | 2.95 | 2.11 | 2.48 |
| Nb | 7.28 | 7.89 | 9.56 | 12.3 | 8.79 | 8.86 | 9.17 | 9.69 | 10.3 | 11.6 | 11.2 |
| Ni | < MDL | 3.00 | 5.20 | 3.75 | < MDL | < MDL | < MDL | < MDL | < MDL | < MDL | < MDL |
| Pb | 49.0 | 26.8 | 32.6 | 43.1 | 44.1 | 38.0 | 42.9 | 43.9 | 39.9 | 35.2 | 32.6 |
| Rb | 347 | 255 | 292 | 337 | 415 | 320 | 368 | 401 | 317 | 337 | 302 |
| Sc | 4.16 | 4.62 | 4.42 | 5.33 | 4.35 | 4.96 | 4.48 | 4.35 | 4.54 | 4.78 | 5.20 |
| Sn | 19.9 | 11.8 | 20.6 | 27.9 | 28.3 | 14.8 | 17.7 | 24.5 | 20.0 | 25.3 | 16.2 |
| Sr | 106 | 66.7 | 73.2 | 78.7 | 85.7 | 79.8 | 91.7 | 88.6 | 73.1 | 72.7 | 77.1 |
| Ta | 1.56 | 1.98 | 2.02 | 2.88 | 2.21 | 1.81 | 2.06 | 2.22 | 2.66 | 2.64 | 2.10 |
| Th | 14.2 | 6.39 | 10.7 | 11.9 | 10.7 | 10.0 | 13.7 | 11.3 | 8.73 | 7.32 | 9.34 |
| U | 7.71 | 3.40 | 6.80 | 4.48 | 4.27 | 11.1 | 6.44 | 76.9 | 8.58 | 5.82 | 10.6 |
| V | 14.4 | 16.6 | 17.7 | 15.2 | 11.9 | 15.4 | 15.1 | 14.3 | 12.7 | 20.1 | 24.4 |
| Y | 14.9 | 13.1 | 12.7 | 15.5 | 12.5 | 11.8 | 15.0 | 13.0 | 14.4 | 10.2 | 10.5 |
| Zn | 48.2 | 29.7 | 43.0 | 57.0 | 48.9 | 40.5 | 44.7 | 50.9 | 43.7 | 57.2 | 60.7 |
| Zr | 84.3 | 73.7 | 104 | 87.0 | 73.1 | 86.3 | 85.3 | 90.5 | 87.1 | 77.6 | 94.6 |
| Rb/Sr | 3.28 | 3.82 | 3.99 | 4.28 | 4.84 | 4.01 | 4.01 | 4.53 | 4.34 | 4.63 | 3.92 |
| Rb/Ba | 0.736 | 1.28 | 0.939 | 1.07 | 1.17 | 0.946 | 0.957 | 1.06 | 0.934 | 1.23 | 1.01 |
| La | 28.4 | 20.2 | 22.5 | 24.9 | 22.2 | 21.4 | 28.2 | 24.7 | 21.3 | 16.8 | 20.7 |
| Ce | 61.1 | 36.8 | 45.3 | 51.8 | 46.4 | 44.7 | 59.0 | 50.9 | 41.4 | 35.5 | 43.9 |
| Pr | 7.39 | 4.39 | 5.48 | 6.25 | 5.59 | 5.38 | 7.10 | 6.27 | 5.21 | 4.00 | 4.99 |
| Nd | 27.5 | 16.0 | 20.1 | 23.4 | 20.8 | 20.3 | 27.0 | 23.1 | 19.4 | 14.2 | 17.9 |
| Sm | 5.24 | 3.30 | 4.06 | 4.66 | 4.15 | 3.90 | 5.24 | 4.61 | 3.89 | 2.94 | 3.53 |
| Eu | 0.817 | 0.550 | 0.550 | 0.633 | 0.613 | 0.594 | 0.708 | 0.684 | 0.645 | 0.433 | 0.445 |
| Gd | 4.09 | 2.92 | 3.25 | 3.74 | 3.31 | 3.15 | 4.12 | 3.61 | 3.24 | 2.38 | 2.71 |
| Tb | 0.539 | 0.420 | 0.450 | 0.520 | 0.450 | 0.420 | 0.546 | 0.481 | 0.451 | 0.326 | 0.358 |
| Dy | 2.65 | 2.30 | 2.30 | 2.69 | 2.30 | 2.13 | 2.74 | 2.38 | 2.34 | 1.78 | 1.91 |
| Ho | 0.428 | 0.410 | 0.400 | 0.447 | 0.389 | 0.364 | 0.441 | 0.410 | 0.397 | 0.357 | 0.384 |
| Er | 1.27 | 1.23 | 1.14 | 1.31 | 1.16 | 1.05 | 1.32 | 1.16 | 1.15 | 1.00 | 1.05 |
| Tm | 0.188 | 0.180 | 0.160 | 0.194 | 0.162 | 0.146 | 0.186 | 0.164 | 0.161 | 0.128 | 0.129 |
| Yb | 1.23 | 1.17 | 1.06 | 1.33 | 1.16 | 1.01 | 1.28 | 1.14 | 1.10 | 0.943 | 1.00 |
| Lu | 0.163 | 0.150 | 0.130 | 0.166 | 0.143 | 0.122 | 0.163 | 0.141 | 0.135 | 0.092 | 0.100 |
| ΣREE | 141 | 90 | 107 | 122 | 109 | 105 | 138 | 120 | 101 | 80.9 | 99.1 |
| $La_N/Yb_N$ | 16.6 | 12.4 | 15.3 | 13.5 | 13.8 | 15.3 | 15.8 | 15.5 | 13.8 | 12.8 | 14.9 |
| Eu/Eu* | 0.54 | 0.54 | 0.46 | 0.46 | 0.51 | 0.52 | 0.47 | 0.51 | 0.56 | 0.50 | 0.44 |

#Fig. 15: Sample location in Fig. 15 of Chapter 4

***Table 15.*** *Continued*

| #Fig15 | 23 | 24 | 25 | 26 | 27 | 28 | 29 | 30 | 31 | 32 | 33 |
|---|---|---|---|---|---|---|---|---|---|---|---|
| Sample | SB 171 | SB 176 | SB 179 | JE 16 45 | JE 15 28 | JE 15 45 | JE 15 51 | JE 15 64 | JE 15 66 | SB 162 | SB 180 |
| Unit | MU | MU | MU | IU | IU | IU | IU | IU | IU | IU | IU |
| $SiO_2$ | 72.80 | 72.66 | 73.12 | 73.74 | 72.16 | 72.95 | 71.73 | 72.70 | 71.76 | 74.08 | 74.31 |
| TiO2 | 0.24 | 0.23 | 0.18 | 0.18 | 0.18 | 0.15 | 0.17 | 0.16 | 0.17 | 0.15 | 0.13 |
| $Al_2O_3$ | 13.92 | 13.88 | 13.60 | 13.78 | 15.93 | 14.54 | 15.14 | 14.55 | 15.12 | 13.38 | 13.70 |
| $Fe_2O_3^t$ | 1.66 | 1.82 | 1.45 | 1.20 | 1.19 | 1.00 | 1.22 | 1.07 | 1.19 | 1.23 | 1.09 |
| MnO | 0.04 | 0.04 | 0.04 | 0.02 | 0.03 | 0.03 | 0.03 | 0.03 | 0.02 | 0.03 | 0.03 |
| MgO | 0.58 | 0.52 | 0.44 | 0.39 | 0.47 | 0.41 | 0.49 | 0.39 | 0.44 | 0.30 | 0.26 |
| CaO | 0.91 | 0.88 | 0.89 | 0.74 | 0.86 | 0.65 | 0.52 | 0.78 | 0.55 | 0.80 | 0.80 |
| $Na_2O$ | 3.30 | 3.12 | 3.16 | 3.02 | 3.37 | 3.25 | 3.29 | 3.37 | 3.15 | 3.04 | 3.32 |
| $K_2O$ | 4.25 | 4.46 | 4.27 | 4.47 | 4.68 | 4.58 | 4.86 | 4.55 | 4.77 | 4.08 | 4.07 |
| $P_2O_5$ | 0.23 | 0.27 | 0.24 | 0.26 | 0.23 | 0.29 | 0.32 | 0.31 | 0.35 | 0.23 | 0.23 |
| LOI | 1.09 | 1.22 | 1.71 | 1.15 | 0.91 | 1.18 | 1.27 | 1.16 | 1.56 | 1.81 | 1.11 |
| Total | 99.02 | 99.10 | 99.09 | 98.95 | 100.00 | 99.03 | 99.05 | 99.06 | 99.09 | 99.12 | 99.05 |
| Mg# | 40.91 | 36.14 | 37.55 | 39.17 | 43.90 | 44.82 | 44.31 | 41.93 | 42.28 | 32.58 | 32.09 |
| A/CNK | 1.19 | 1.20 | 1.19 | 1.24 | 1.31 | 1.27 | 1.30 | 1.22 | 1.33 | 1.23 | 1.21 |
| Ba | 310 | 297 | 283 | 310 | 318 | 369 | 364 | 334 | 439 | 310 | 363 |
| Cr | < MDL | < MDL | < MDL | 5.30 | 7.48 | 5.60 | 6.96 | 5.41 | 7.99 | < MDL | < MDL |
| Cs | 38.0 | 41.9 | 36.1 | 33.6 | 34.4 | 38.9 | 35.5 | 36.0 | 39.1 | 35.9 | 36.7 |
| Ga | 29.7 | 31.9 | 30.7 | 31.2 | 26.6 | 32.4 | 35.5 | 30.0 | 43.0 | 29.9 | 27.2 |
| Hf | 2.33 | 2.19 | 1.91 | 2.61 | 2.31 | 1.72 | 1.82 | 2.02 | 2.14 | 1.78 | 1.43 |
| Nb | 10.8 | 12.0 | 9.03 | 5.86 | 8.76 | 7.38 | 7.25 | 8.32 | 8.39 | 8.64 | 8.55 |
| Ni | < MDL | < MDL | < MDL | 2.30 | < MDL | < MDL | < MDL | < MDL | < MDL | < MDL | < MDL |
| Pb | 31.5 | 33.4 | 30.4 | 54.6 | 41.9 | 61.6 | 61.8 | 53.2 | 73.1 | 33.7 | 43.5 |
| Rb | 311 | 339 | 324 | 302 | 375 | 409 | 440 | 399 | 433 | 295 | 302 |
| Sc | 4.96 | 5.41 | 4.51 | 4.12 | 4.16 | 3.65 | 4.03 | 3.87 | 2.82 | 3.73 | 3.33 |
| Sn | 19.6 | 23.6 | 22.2 | 20.6 | 25.9 | 32.1 | 30.9 | 26.3 | 36.8 | 16.9 | 23.7 |
| Sr | 83.9 | 75.2 | 74.1 | 148 | 82.8 | 107 | 110 | 101 | 131 | 81.5 | 102 |
| Ta | 2.80 | 2.76 | 2.66 | 1.50 | 2.30 | 2.00 | 1.88 | 2.46 | 2.03 | 1.61 | 1.99 |
| Th | 7.95 | 8.01 | 6.47 | 6.88 | 8.29 | 8.56 | 10.4 | 7.49 | 9.82 | 6.19 | 4.82 |
| U | 4.18 | 4.93 | 3.84 | 5.21 | 5.52 | 7.45 | 5.79 | 7.55 | 9.28 | 3.95 | 2.62 |
| V | 24.2 | 23.7 | 18.9 | 11.2 | 11.3 | 5.93 | 7.65 | 6.58 | 7.65 | 14.6 | 12.2 |
| Y | 8.88 | 9.90 | 7.66 | 10.5 | 13.7 | 14.0 | 13.1 | 10.6 | 10.3 | 5.14 | 5.35 |
| Zn | 57.2 | 60.6 | 52.3 | 47.4 | 43.3 | 58.7 | 64.1 | 56.5 | 84.2 | 58.5 | 47.7 |
| Zr | 91.5 | 84.9 | 71.5 | 81.7 | 68.3 | 47.6 | 49.6 | 54.1 | 57.5 | 67.3 | 55.6 |
| Rb/Sr | 3.71 | 4.51 | 4.37 | 2.04 | 4.54 | 3.82 | 4.00 | 3.96 | 3.31 | 3.62 | 2.98 |
| Rb/Ba | 1.01 | 1.14 | 1.15 | 0.97 | 1.18 | 1.11 | 1.21 | 1.20 | 0.99 | 0.95 | 0.83 |
| La | 18.3 | 17.8 | 15.2 | 18.8 | 18.0 | 19.6 | 22.1 | 17.8 | 23.4 | 15.5 | 12.3 |
| Ce | 38.1 | 37.6 | 31.6 | 38.2 | 36.2 | 41.1 | 46.1 | 35.9 | 47.2 | 31.5 | 24.5 |
| Pr | 4.33 | 4.27 | 3.53 | 4.46 | 4.39 | 4.91 | 5.52 | 4.43 | 5.72 | 3.49 | 2.53 |
| Nd | 15.0 | 14.8 | 12.2 | 16.2 | 16.1 | 18.4 | 20.6 | 16.3 | 20.8 | 11.9 | 8.18 |
| Sm | 2.98 | 2.96 | 2.42 | 3.74 | 3.29 | 4.16 | 4.43 | 3.59 | 4.46 | 2.51 | 1.59 |
| Eu | 0.492 | 0.452 | 0.442 | 1.140 | 0.590 | 0.885 | 0.796 | 0.757 | 0.976 | 0.578 | 0.497 |
| Gd | 2.36 | 2.36 | 2.02 | 3.08 | 2.78 | 3.55 | 3.59 | 2.88 | 3.48 | 1.98 | 1.45 |
| Tb | 0.314 | 0.323 | 0.261 | 0.420 | 0.405 | 0.500 | 0.503 | 0.405 | 0.457 | 0.247 | 0.192 |
| Dy | 1.66 | 1.80 | 1.45 | 2.08 | 2.22 | 2.57 | 2.47 | 1.97 | 2.09 | 1.20 | 1.12 |
| Ho | 0.368 | 0.376 | 0.336 | 0.350 | 0.393 | 0.426 | 0.393 | 0.329 | 0.344 | 0.282 | 0.283 |
| Er | 0.980 | 1.05 | 0.905 | 0.970 | 1.16 | 1.20 | 1.12 | 0.904 | 0.919 | 0.689 | 0.753 |
| Tm | 0.114 | 0.132 | 0.097 | 0.120 | 0.175 | 0.169 | 0.155 | 0.116 | 0.116 | 0.058 | 0.074 |
| Yb | 0.924 | 1.01 | 0.853 | 0.830 | 1.22 | 1.19 | 1.09 | 0.856 | 0.859 | 0.555 | 0.687 |
| Lu | 0.078 | 0.102 | 0.064 | 0.090 | 0.158 | 0.142 | 0.130 | 0.091 | 0.092 | 0.018 | 0.044 |
| ΣREE | 86.1 | 85.1 | 71.4 | 90.5 | 87.0 | 98.9 | 109 | 86.3 | 111 | 70.6 | 54.1 |
| $La_N/Yb_N$ | 14.2 | 12.6 | 12.8 | 16.3 | 10.5 | 11.9 | 14.6 | 14.9 | 19.5 | 20.0 | 12.8 |
| Eu/Eu* | 0.57 | 0.52 | 0.61 | 1.03 | 0.60 | 0.70 | 0.61 | 0.72 | 0.76 | 0.79 | 1.00 |

#Fig. 15: Sample location in Fig. 15 of Chapter 4

***Table 15.*** *Continued*

| #Fig15 | 34 | 35 | 36 | 37 | 38 | 39 | 40 | 41 | 42 | 43 | 44 |
|---|---|---|---|---|---|---|---|---|---|---|---|
| Sample | SB 184 | SB 186 | JE 15 01 | JE 16 30 | JE 16 33 | JE 15 41 | JE 16 03 | JE 16 06 | JE 16 41 | JE 17 03 | JE 15 40 |
| Unit | IU | IU | MME | MME | MME | Vaugn | Vaugn | Vaugn | Vaugn | Vaugn | Micro-dt |
| $SiO_2$ | 73.45 | 73.62 | 65.26 | 67.31 | 65.64 | 47.97 | 53.29 | 48.93 | 53.83 | 51.32 | 50.92 |
| TiO2 | 0.15 | 0.14 | 0.71 | 0.65 | 0.67 | 2.04 | 1.51 | 1.85 | 1.51 | 1.76 | 1.67 |
| $Al_2O_3$ | 13.82 | 14.00 | 17.13 | 15.28 | 14.90 | 15.53 | 14.61 | 14.66 | 14.57 | 14.83 | 14.93 |
| $Fe_2O_3^t$ | 1.20 | 1.18 | 4.59 | 3.78 | 4.67 | 9.47 | 8.60 | 10.11 | 8.22 | 9.58 | 8.53 |
| MnO | 0.02 | 0.03 | 0.07 | 0.07 | 0.08 | 0.14 | 0.12 | 0.14 | 0.12 | 0.13 | 0.12 |
| MgO | 0.27 | 0.29 | 1.81 | 1.59 | 1.86 | 5.60 | 6.12 | 7.59 | 5.59 | 6.00 | 5.73 |
| CaO | 0.82 | 0.75 | 2.89 | 3.08 | 2.33 | 7.50 | 5.83 | 7.09 | 5.61 | 6.10 | 6.41 |
| $Na_2O$ | 3.28 | 3.22 | 3.79 | 4.15 | 3.90 | 3.34 | 3.10 | 3.04 | 3.30 | 3.20 | 2.56 |
| $K_2O$ | 4.18 | 4.44 | 2.30 | 1.99 | 2.74 | 1.99 | 3.09 | 2.65 | 3.38 | 2.74 | 3.24 |
| $P_2O_5$ | 0.28 | 0.25 | 0.19 | 0.22 | 0.40 | 0.74 | 0.70 | 0.69 | 0.63 | 0.67 | 0.65 |
| LOI | 1.63 | 1.12 | 1.04 | 0.88 | 1.54 | 4.95 | 2.37 | 2.65 | 2.20 | 2.71 | 4.64 |
| Total | 99.11 | 99.04 | 99.79 | 99.00 | 98.73 | 99.28 | 99.34 | 99.40 | 98.96 | 99.04 | 99.40 |
| Mg# | 30.83 | 32.75 | 43.84 | 45.45 | 44.10 | 53.96 | 58.50 | 59.80 | 57.40 | 55.37 | 57.07 |
| A/CNK | 1.21 | 1.22 | 1.23 | 1.05 | 1.09 | 0.73 | 0.77 | 0.71 | 0.76 | 0.77 | 0.77 |
| Ba | 324 | 274 | 143 | 178 | 111 | 1119 | 1552 | 963 | 1041 | 1028 | 1177 |
| Cr | < MDL | < MDL | 56.7 | 14.2 | 21.4 | 188 | 222 | 230 | 179 | 171 | 221 |
| Cs | 27.8 | 37.6 | 24.4 | 26.1 | 38.0 | 8.34 | 1.65 | 9.12 | 2.87 | 6.89 | 153 |
| Ga | 27.5 | 27.8 | 30.7 | 21.1 | 19.6 | 24.0 | 21.2 | 19.2 | 18.9 | 21.7 | 23.7 |
| Hf | 1.95 | 1.38 | 4.83 | 5.83 | 4.44 | 8.61 | 7.10 | 6.13 | 7.24 | 7.23 | 5.33 |
| Nb | 8.98 | 8.07 | 14.0 | 11.5 | 12.6 | 30.4 | 24.9 | 22.3 | 23.4 | 28.1 | 18.9 |
| Ni | < MDL | < MDL | 13.6 | 7.80 | 11.2 | 69.3 | 67.5 | 87.9 | 58.0 | 71.2 | 72.5 |
| Pb | 35.7 | 38.9 | 23.1 | 16.9 | 14.5 | 13.4 | 16.8 | 19.5 | 17.1 | 27.5 | 23.9 |
| Rb | 334 | 317 | 364 | 266 | 342 | 69.3 | 88.7 | 105 | 99.2 | 106 | 260 |
| Sc | 3.11 | 3.21 | 11.0 | 10.4 | 11.6 | 20.6 | 18.0 | 20.9 | 19.4 | 20.1 | 18.6 |
| Sn | 21.8 | 17.4 | 16.9 | 12.1 | 16.3 | 3.42 | 3.43 | 2.39 | 4.14 | 3.64 | 5.69 |
| Sr | 87.0 | 76.1 | 144 | 187 | 95.9 | 861 | 750 | 778 | 739 | 787 | 774 |
| Ta | 2.02 | 1.46 | 1.74 | 1.45 | 1.73 | 2.12 | 1.86 | 1.50 | 1.80 | 2.06 | 1.46 |
| Th | 6.93 | 3.98 | 16.8 | 12.3 | 9.51 | 14.1 | 14.5 | 10.0 | 13.0 | 11.5 | 15.3 |
| U | 3.46 | 3.32 | 4.83 | 3.21 | 6.32 | 3.60 | 4.86 | 2.73 | 4.54 | 3.31 | 5.76 |
| V | 13.3 | 13.9 | 59.8 | 48.6 | 60.3 | 148 | 134 | 157 | 128 | 131 | 128 |
| Y | 4.82 | 5.92 | 24.4 | 20.5 | 22.0 | 41.6 | 34.3 | 30.4 | 31.1 | 34.2 | 40.4 |
| Zn | 63.8 | 52.6 | 93.0 | 62.0 | 71.1 | 98.8 | 86.0 | 87.5 | 71.8 | 98.1 | 94.7 |
| Zr | 70.4 | 55.1 | 190 | 214 | 158 | 381 | 310 | 276 | 294 | 322 | 239 |
| Rb/Sr | 3.83 | 4.17 | 2.53 | 1.43 | 3.57 | 0.080 | 0.118 | 0.135 | 0.134 | 0.135 | 0.336 |
| Rb/Ba | 1.03 | 1.16 | 2.55 | 1.49 | 3.09 | 0.062 | 0.057 | 0.109 | 0.095 | 0.103 | 0.221 |
| La | 15.5 | 9.84 | 42.7 | 42.5 | 29.4 | 67.6 | 63.0 | 48.8 | 63.9 | 56.7 | 66.4 |
| Ce | 32.0 | 20.6 | 84.4 | 80.1 | 56.4 | 132 | 140 | 98.8 | 126 | 118 | 142 |
| Pr | 3.49 | 2.17 | 10.2 | 9.23 | 6.76 | 17.0 | 15.6 | 12.6 | 15.7 | 15.0 | 17.4 |
| Nd | 11.9 | 7.22 | 37.8 | 33.7 | 25.8 | 67.0 | 61.1 | 49.8 | 61.3 | 59.7 | 70.9 |
| Sm | 2.43 | 1.67 | 6.86 | 6.05 | 5.09 | 11.8 | 10.4 | 8.93 | 10.8 | 10.8 | 12.4 |
| Eu | 0.532 | 0.425 | 0.934 | 1.05 | 0.77 | 2.93 | 2.56 | 2.22 | 2.46 | 2.65 | 2.94 |
| Gd | 1.93 | 1.55 | 5.70 | 4.83 | 4.41 | 9.82 | 8.52 | 7.42 | 7.96 | 8.09 | 10.0 |
| Tb | 0.236 | 0.210 | 0.804 | 0.660 | 0.660 | 1.28 | 1.07 | 0.96 | 1.06 | 1.13 | 1.34 |
| Dy | 1.20 | 1.26 | 4.16 | 3.57 | 3.68 | 7.05 | 5.83 | 5.25 | 5.43 | 5.89 | 6.84 |
| Ho | 0.275 | 0.311 | 0.649 | 0.590 | 0.600 | 1.19 | 0.974 | 0.885 | 0.820 | 0.897 | 1.01 |
| Er | 0.672 | 0.809 | 1.92 | 1.82 | 1.81 | 3.40 | 2.78 | 2.51 | 2.47 | 2.73 | 3.13 |
| Tm | 0.056 | 0.084 | 0.282 | 0.280 | 0.270 | 0.493 | 0.407 | 0.366 | 0.390 | 0.424 | 0.469 |
| Yb | 0.548 | 0.769 | 1.74 | 1.72 | 1.63 | 3.05 | 2.49 | 2.23 | 2.31 | 2.54 | 2.87 |
| Lu | 0.020 | 0.048 | 0.246 | 0.260 | 0.230 | 0.470 | 0.378 | 0.340 | 0.360 | 0.399 | 0.451 |
| ΣREE | 70.9 | 47.0 | 198 | 186 | 137 | 325 | 315 | 241 | 301 | 285 | 338 |
| $La_N/Yb_N$ | 20.3 | 9.18 | 17.6 | 17.7 | 12.9 | 15.9 | 18.2 | 15.7 | 19.8 | 16.0 | 16.6 |
| Eu/Eu* | 0.75 | 0.81 | 0.46 | 0.59 | 0.50 | 0.83 | 0.83 | 0.84 | 0.81 | 0.86 | 0.81 |

#Fig. 15: Sample location in Fig. 15 of Chapter 4

***Table 15.*** *Continued*

| #Fig15 | 45 | 46 | 47 | 48 | 49 | 50 | 51 | 52 | 53 |
|---|---|---|---|---|---|---|---|---|---|
| Sample | JE 16 42 | JE 15 22 | JE 15 39 | JE 15 70 | JE 16 12 | JE 16 18 | JE 16 24 | JE 16 38 | JE 16 43 |
| Unit | Vaugn | Mnt | Krs | Krs | Krs | Krs | Krs | Krs | Krs |
| $SiO_2$ | 53.35 | 55.53 | 53.13 | 55.35 | 55.59 | 54.27 | 54.83 | 55.13 | 56.11 |
| TiO2 | 1.57 | 1.56 | 1.33 | 1.13 | 1.51 | 1.07 | 1.32 | 1.12 | 1.14 |
| $Al_2O_3$ | 15.21 | 15.52 | 14.44 | 15.80 | 14.21 | 14.93 | 14.30 | 13.72 | 14.42 |
| $Fe_2O_3^t$ | 9.02 | 6.88 | 7.89 | 6.16 | 7.37 | 7.51 | 8.08 | 7.53 | 7.00 |
| MnO | 0.13 | 0.13 | 0.12 | 0.09 | 0.11 | 0.11 | 0.13 | 0.12 | 0.10 |
| MgO | 5.97 | 4.27 | 6.02 | 3.99 | 5.58 | 4.78 | 5.22 | 6.18 | 4.75 |
| CaO | 5.90 | 4.51 | 6.07 | 4.92 | 5.19 | 6.46 | 6.05 | 5.84 | 5.35 |
| $Na_2O$ | 3.25 | 2.26 | 3.06 | 2.55 | 2.16 | 1.91 | 3.22 | 2.64 | 2.78 |
| $K_2O$ | 2.92 | 4.68 | 3.63 | 4.74 | 4.33 | 4.62 | 2.99 | 4.07 | 3.98 |
| $P_2O_5$ | 0.65 | 0.70 | 0.69 | 0.72 | 0.75 | 0.68 | 0.71 | 0.74 | 0.53 |
| LOI | 2.54 | 3.18 | 2.84 | 3.76 | 2.56 | 3.31 | 2.48 | 2.27 | 3.66 |
| Total | 100.51 | 99.20 | 99.22 | 99.22 | 99.36 | 99.65 | 99.33 | 99.36 | 99.82 |
| Mg# | 56.73 | 55.15 | 60.21 | 56.23 | 60.00 | 55.77 | 56.14 | 61.92 | 57.34 |
| A/CNK | 0.79 | 0.91 | 0.72 | 0.87 | 0.80 | 0.75 | 0.73 | 0.71 | 0.77 |
| Ba | 1039 | 1504 | 2385 | 2095 | 1271 | 2220 | 2236 | 1466 | 1644 |
| Cr | 184 | 324 | 336 | 87.0 | 330 | 39.5 | 171 | 224 | 171 |
| Cs | 3.30 | 11.5 | 14.9 | 13.4 | 16.3 | 6.75 | 4.25 | 11.2 | 11.2 |
| Ga | 18.3 | 25.7 | 26.2 | 23.8 | 21.1 | 19.2 | 22.3 | 19.8 | 18.4 |
| Hf | 6.86 | 8.35 | 5.71 | 9.13 | 8.15 | 6.68 | 9.31 | 9.06 | 10.8 |
| Nb | 22.7 | 17.8 | 16.9 | 19.9 | 17.2 | 12.5 | 21.3 | 20.0 | 19.7 |
| Ni | 57.7 | 14.3 | 136 | 8.68 | 12.0 | < MDL | 17.1 | 55.7 | 66.6 |
| Pb | 18.9 | 28.9 | 31.4 | 31.0 | 22.9 | 21.1 | 59.7 | 30.3 | 31.4 |
| Rb | 87.7 | 368 | 210 | 226 | 306 | 219 | 147 | 207 | 162 |
| Sc | 20.0 | 20.5 | 16.4 | 17.7 | 22.2 | 22.7 | 22.2 | 20.4 | 17.4 |
| Sn | 3.31 | 5.65 | 9.16 | 3.06 | 10.5 | 2.86 | 5.28 | 6.70 | 3.66 |
| Sr | 800 | 401 | 1260 | 1149 | 455 | 699 | 818 | 810 | 680 |
| Ta | 1.70 | 1.34 | 1.48 | 1.59 | 1.14 | 0.679 | 1.65 | 1.59 | 1.38 |
| Th | 12.0 | 31.0 | 28.4 | 31.4 | 25.2 | 16.2 | 36.4 | 37.6 | 33.7 |
| U | 4.19 | 8.85 | 11.6 | 9.72 | 6.49 | 4.41 | 11.5 | 9.75 | 7.81 |
| V | 132 | 142 | 135 | 142 | 155 | 187 | 174 | 162 | 127 |
| Y | 31.2 | 39.7 | 38.3 | 32.6 | 30.6 | 24.8 | 37.7 | 28.5 | 28.4 |
| Zn | 75.2 | 93.3 | 86.8 | 68.8 | 89.0 | 67.5 | 82.6 | 68.3 | 61.5 |
| Zr | 272 | 341 | 237 | 355 | 372 | 260 | 420 | 341 | 394 |
| Rb/Sr | 0.110 | 0.918 | 0.167 | 0.197 | 0.673 | 0.313 | 0.180 | 0.255 | 0.238 |
| Rb/Ba | 0.084 | 0.245 | 0.088 | 0.108 | 0.241 | 0.099 | 0.066 | 0.141 | 0.099 |
| La | 58.6 | 51.3 | 96.7 | 76.6 | 41.7 | 45.6 | 63.5 | 59.4 | 65.7 |
| Ce | 117 | 119 | 224 | 164 | 96.0 | 91.1 | 143 | 136 | 133 |
| Pr | 15.0 | 16.5 | 24.4 | 20.0 | 13.2 | 11.4 | 16.4 | 15.7 | 16.6 |
| Nd | 59.3 | 71.7 | 97.1 | 80.3 | 56.9 | 44.9 | 66.8 | 63.0 | 64.5 |
| Sm | 10.6 | 13.9 | 15.6 | 13.1 | 10.7 | 7.88 | 11.4 | 10.4 | 10.7 |
| Eu | 2.41 | 2.93 | 3.73 | 3.08 | 2.32 | 2.02 | 2.60 | 2.33 | 2.27 |
| Gd | 7.87 | 10.0 | 11.9 | 9.65 | 7.85 | 6.29 | 8.76 | 7.54 | 7.44 |
| Tb | 1.04 | 1.31 | 1.43 | 1.17 | 0.973 | 0.790 | 1.10 | 0.927 | 0.960 |
| Dy | 5.42 | 6.57 | 6.71 | 5.68 | 5.26 | 4.29 | 6.03 | 4.91 | 4.88 |
| Ho | 0.820 | 0.995 | 0.953 | 0.852 | 0.882 | 0.719 | 1.04 | 0.821 | 0.750 |
| Er | 2.48 | 3.12 | 2.91 | 2.65 | 2.57 | 2.09 | 2.99 | 2.35 | 2.28 |
| Tm | 0.380 | 0.492 | 0.431 | 0.396 | 0.381 | 0.311 | 0.439 | 0.350 | 0.360 |
| Yb | 2.29 | 2.96 | 2.58 | 2.44 | 2.36 | 1.94 | 2.71 | 2.13 | 2.16 |
| Lu | 0.350 | 0.484 | 0.405 | 0.376 | 0.365 | 0.295 | 0.413 | 0.327 | 0.340 |
| ΣREE | 284 | 301 | 488 | 380 | 242 | 220 | 327 | 306 | 311 |
| $La_N/Yb_N$ | 18.4 | 12.4 | 26.9 | 22.5 | 12.7 | 16.9 | 16.8 | 20.0 | 21.8 |
| Eu/Eu* | 0.81 | 0.76 | 0.84 | 0.84 | 0.77 | 0.88 | 0.80 | 0.80 | 0.78 |

#Fig. 15: Sample location in Fig. 15 of Chapter 4

***Table 16.*** *Whole-rock Sr–Nd isotopic compositions of the monzogranites, MME and mesocratic rocks from the Sierra Bermeja Pluton (measured and age-corrected to 306 Ma)*

| Sample | Unit | #[a] | Rb (ppm) | Sr (ppm) | $^{87}Rb/^{86}Sr$ | $^{87}Sr/^{86}Sr$ | 2σ Error (abs) | $^{87}Sr/^{86}Sr_{306}$ |
|---|---|---|---|---|---|---|---|---|
| JE 15 62 | Mzgr (OU) | 2 | 318 | 168 | 5.494 | 0.727900 | 0.000008 | 0.7040 |
| JE 15 48 | Mzgr (OU) | 8 | 288 | 166 | 5.028 | 0.728140 | 0.000008 | 0.7062 |
| JE 15 60 | Mzgr (OU) | 9 | 323 | 126 | 7.413 | 0.735544 | 0.000007 | 0.7033 |
| JE 15 30 | Mzgr (MU) | 11 | 428 | 106 | 11.682 | 0.754696 | 0.000007 | 0.7038 |
| JE 15 04 | Mzgr (MU) | 15 | 337 | 79 | 12.455 | 0.758127 | 0.000007 | 0.7039 |
| JE 15 67 | Mzgr (MU) | 20 | 317 | 73 | 12.626 | 0.758665 | 0.000008 | 0.7037 |
| JE 16 45 | Mzgr (IU) | 26 | 302 | 148 | 5.917 | 0.736483 | 0.000008 | 0.7107 |
| JE 15 51 | Mzgr (IU) | 29 | 440 | 110 | 11.621 | 0.755252 | 0.000008 | 0.7046 |
| SB 180 | Mzgr (IU) | 33 | 302 | 102 | 8.641 | 0.742239 | 0.000010 | 0.7046 |
| JE 16 30 | MME | 37 | 266 | 187 | 4.129 | 0.721888 | 0.000008 | 0.7039 |
| JE 16 06 | Bt-rich Vaugn | 41 | 105 | 778 | 0.392 | 0.706182 | 0.000007 | 0.7045 |
| JE 17 03 | Bt-rich Vaugn | 43 | 106 | 787 | 0.390 | 0.705912 | 0.000008 | 0.7042 |
| JE 16 03 | Bt-poor Vaugn | 40 | 89 | 750 | 0.342 | 0.705822 | 0.000007 | 0.7043 |
| JE 16 41 | Bt-poor Vaugn | 42 | 99 | 739 | 0.388 | 0.705831 | 0.000008 | 0.7041 |
| JE 15 70 | Kersantite | 48 | 226 | 1149 | 0.569 | 0.708244 | 0.000007 | 0.7058 |
| JE 16 38 | Kersantite | 52 | 207 | 810 | 0.739 | 0.708569 | 0.000009 | 0.7053 |
| JE 16 43 | Kersantite | 53 | 162 | 680 | 0.690 | 0.708760 | 0.000007 | 0.7058 |
| JE 15 41 | Micro-dt | 39 | 69 | 861 | 0.233 | 0.705340 | 0.000006 | 0.7043 |

Mzgr (monzogranite); MME (mafic microgranular enclave); Vaugn (vaugnerite series rock); Micro-dt (micro-diorite

#[a]Sample location in Fig. 15 of Chapter 4

***Table 16.*** *Continued*

| Sample | Sm (ppm) | Nd (ppm) | $^{147}Sm/^{144}Nd$ | $^{143}Nd/^{144}Nd$ | 2σ Error (abs) | $^{143}Nd/^{144}Nd_{306}$ | $\varepsilon Nd_{306}$ | TDM (Ga) | TDM.2stg (Ga) |
|---|---|---|---|---|---|---|---|---|---|
| JE 15 62 | 4.78 | 24.7 | 0.1171 | 0.512341 | 0.000006 | 0.512106 | -2.7 | 1.21 | 1.24 |
| JE 15 48 | 3.65 | 18.2 | 0.1212 | 0.512354 | 0.000007 | 0.512112 | -2.6 | 1.24 | 1.23 |
| JE 15 60 | 3.81 | 19.5 | 0.1177 | 0.512342 | 0.000008 | 0.512106 | -2.7 | 1.22 | 1.24 |
| JE 15 30 | 3.80 | 18.8 | 0.1219 | 0.512306 | 0.000009 | 0.512062 | -3.6 | 1.33 | 1.31 |
| JE 15 04 | 3.64 | 17.6 | 0.1251 | 0.512297 | 0.000008 | 0.512047 | -3.9 | 1.38 | 1.33 |
| JE 15 67 | 3.47 | 16.7 | 0.1257 | 0.512296 | 0.000007 | 0.512044 | -3.9 | 1.40 | 1.33 |
| JE 16 45 | 3.24 | 14.2 | 0.1375 | 0.512134 | 0.000008 | 0.511859 | -7.5 | 1.90 | 1.62 |
| JE 15 51 | 2.92 | 13.8 | 0.1282 | 0.512260 | 0.000012 | 0.512003 | -4.7 | 1.49 | 1.40 |
| SB 180 | 2.12 | 10.2 | 0.1251 | 0.512206 | 0.000005 | 0.511955 | -5.6 | 1.53 | 1.47 |
| JE 16 30 | 5.20 | 27.7 | 0.1132 | 0.512332 | 0.000006 | 0.512105 | -2.7 | 1.18 | 1.24 |
| JE 16 06 | 8.33 | 43.9 | 0.1149 | 0.512536 | 0.000008 | 0.512305 | 1.2 | 0.90 | 0.93 |
| JE 17 03 | 9.37 | 50.1 | 0.1131 | 0.512534 | 0.000009 | 0.512307 | 1.2 | 0.89 | 0.93 |
| JE 16 03 | 8.89 | 47.7 | 0.1128 | 0.512523 | 0.000009 | 0.512297 | 1.0 | 0.90 | 0.94 |
| JE 16 41 | 9.20 | 49.8 | 0.1117 | 0.512514 | 0.000008 | 0.512291 | 0.9 | 0.91 | 0.96 |
| JE 15 70 | 10.3 | 59.1 | 0.1051 | 0.512327 | 0.000008 | 0.512117 | -2.5 | 1.10 | 1.22 |
| JE 16 38 | 10.0 | 55.9 | 0.1086 | 0.512326 | 0.000008 | 0.512109 | -2.6 | 1.14 | 1.23 |
| JE 16 43 | 10.6 | 60.5 | 0.1055 | 0.512351 | 0.000010 | 0.51214 | -2.0 | 1.07 | 1.19 |
| JE 15 41 | 8.98 | 47.6 | 0.1140 | 0.512531 | 0.000008 | 0.512302 | 1.1 | 0.90 | 0.94 |

# CHAPTER 9
# PETROGENESIS OF THE SIERRA BERMEJA MONZOGRANITES

## 9.1. CONSIDERATIONS ON THE MESOCRATIC ROCKS FROM THE SIERRA BERMEJA PLUTON

In order to decipher the petrogenesis of the monzogranites from the Sierra Bermeja Pluton, the existence of the basic-intermediate dyke intrusions in this massif cannot not be ignored. Field relationships of these dykes, such as their sinuous trends within the monzogranite masses, the absence of chilled margins, the necking of such alignments, as well as their dismembered terminations are key features that point, at first glance, to their coeval emplacement timing respect to the host monzogranites (see Chapter 4). Moreover, vaugnerite series rocks are medium-grained, which suggests that they emplacement into the monzogranites developed under a relatively low temperature contrast, thus, probably before the complete consolidation of the monzogranites. The obtained U–Pb apatite age of 305 ± 17 Ma definitely supports that hypothesis and therefore, vaugnerite series rocks from the Sierra Bermeja Pluton would correspond to syn-plutonic mafic dykes (*e.g.* Pitcher, 1997). Additionally, particular textures observed in these mesocratic rocks, including quartz ocelli, clinopyroxene clots, droplets or segregates of felsic liquids, feldspar crystals showing patchy alteration to epidote, or coexistence of stubby prismatic and acicular apatite (see Chapter 5; *e.g.* Fig. 33), point to the fact that the studied mesocratic rocks may have suffered some hybridization process. Thus, and since it has been referred to the studied dioritoids as vaugnerites throughout the PhD dissertation, some notions about these rocks and lamprophyres are required before to undertake the petrogenetic study of the monzogranites from the Sierra Bermeja Pluton.

Mg-rich ultrapotassic igneous rocks are generally related to volcanic and hypabyssal settings and, among them, lamprophyres are some of the most representative, which usually form subvolcanic dykes, sills, plugs or stocks (Rock, 1991). Calc-alkaline lamprophyres (minettes, kersantites, spessartites and vogesites) constitute a group of rocks enriched in volatiles, LILE, alkaline earth and some transition metals (Rock, 1991). Plutonic equivalents of these calc-alkaline types are found across the Variscan Orogeny being referred to with local names such as 'durbachites' (Sauer, 1893), 'vaugnerites' (Fournet, 1837) and 'redwitzites' (Willmann, 1920). Nevertheless, in orogenic areas elsewhere these rocks are known as 'appinites', 'high Sr-Ba granitoids' and 'sanukitoids' (*e.g.* von Raumer *et al.*, 2014, and references therein; Moyen *et al.*, 2017, and references therein). Traditionally, durbachites, vaugnerites and redwitzites are encompassed in the 'vaugnerite series' and although they share several characteristics, they also display a number of differences as pointed out by Rock (1991) and Sabatier (1991), for instance. Fournet (1837), Michon (1987) and Sabatier (1991) coined the term 'vaugnerite' for a kind of mica-rich diorite composed by biotite, amphibole and plagioclase, with quartz, K-feldspar and abundant accessory apatite. Vaugnerites are basic to intermediate ($SiO_2$ = 45–60 wt.%). metaluminous rocks with high-K to shoshonitic affinity, characterized by their relatively high $FeO^t$ + MgO values (10–24 wt.%) and marked enrichments in both compatible (Mg, Fe, Ni, Cr) and incompatible (K, Rb, Ba, Sr) elements, standing out in particular the high contents in Ba (1000–3000 ppm). Sr (500–1000 ppm) and Cr (100–600 ppm).

Biotite-rich dioritoids from the Sierra Bermeja Pluton show singular characteristics that fit with those of the vaugnerites *s.l.* described elsewhere in the Variscan Orogen (*e.g.* Holub, 1997; Sabatier, 1991; von Raumer *et al.*, 2014, and references therein). The studied dioritoids exhibit relatively high biotite contents and accessory alkali feldspar and apatite (see Chapter 5). They correspond to basic metaluminous rocks, enriched in LILE (K, Rb,

Ba, Sr) and also in $FeO^t$, MgO and Cr. According to these characteristics, they can classify as vaugnerites. On the other hand, the biotite-poor dioritoids from the Sierra Bermeja Pluton, because of their low biotite contents, would be in contrast with the 'kind of micaceous diorites' of Sabatier (1991). Nevertheless, the elevated modal amounts of kaersutite and the existence of accessory K-feldspar and apatite suggest their vaugneritic nature. This affinity would be also supported by their whole-rock geochemical characteristics, which are very similar to those of the biotite-rich terms (see Chapter 8; Figs. 51–55). Consequently, these intermediate rocks may correspond as well to vaugnerites. Finally, despite the fine-grained texture of the micro-diorite, the existence of plagioclase phenocrystals make them different from the lamprophyres from the Sierra Bermeja Pluton. In addition, mineral-chemistry data and whole-rock geochemical characteristics are close to those of the dioritoids (see Chapter 8; Figs. 51–55), thus, this rock could also be classified as a vaugnerite.

Since 'vaugnerite' is a somewhat generic term, Rock (1991) and Sabatier (1991) proposed a *mg* [$100MgO / (MgO + FeO^t)$] *vs. k* [$100K_2O / (K_2O + Na_2O)$] comparative diagram for appinites and 'vaugnerite series' rocks (Fig. 56). The dioritoids (Bt-rich and Bt-poor vaugnerites) and micro-diorite of the Sierra Bermeja Pluton plot in the redwitzites and vaugnerite *s.s.* fields, respectively, of this diagram (Fig. 56). Several analyses of similar rocks from the Iberian Massif are included for a comparison, and it may be noted that, despite the consideration of this kind of Mg- and K-rich rocks as vaugnerites, most of them plot actually in the redwitzite field (Fig. 56). Only in a few cases, like the granodioritic association of the Tormes Dome (*e.g.* López-Moro *et al.*, 2017; López Plaza *et al.*, 1999), the North of Portugal granites (*e.g.* Dias and Leterrier, 1994; Dias *et al.*, 2002), and in the granites and granodiorites of western Galicia (*e.g.* Gallastegui, 2005) are found some rocks that could be classified as vaugnerites *s.s.* out of the full range of mesocratic rocks in question (Fig. 56). The *mg* values of vaugnerite series rocks of the Sierra Bermeja Pluton are

comprised between those of the high-Mg and low-Mg vaugnerites of western areas of Galicia and, in terms of *k* values, are also close to some samples of the Tormes Dome. Thus, according to the *mg vs. k* comparative diagram (Rock, 1991; Sabatier, 1991), the studied rocks of the Sierra Bermeja Pluton are to be classified correctly as redwitzites of the vaugnerite series, just like would be most equivalent rocks found in the Iberian Massif, showing *mg* and *k* ratios close to those of the redwitzites of western areas of Galicia (Gallastegui, 2005) and the vaugnerites *s.s.* of the Tormes Dome (López Plaza *et al.*, 1999). On the other hand, the studied calc-alkaline lamprophyres from the Sierra Bermeja Pluton plot mainly within the 'vaugnerite' field of the *mg vs. k* diagram (Fig. 56), arguing in favor to the equivalence (vaugnerite = plutonic and calc-alkaline lamprophyre = subvolcanic) pointed out by Rock (1991).

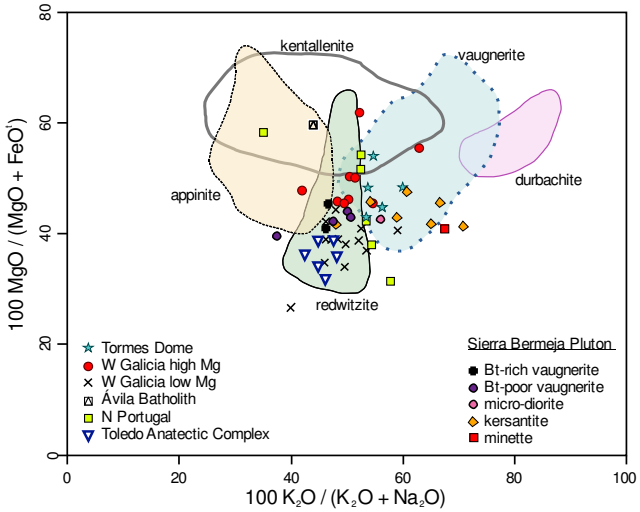


**Figure 56.** Projection of the vaugnerite series rocks of the Sierra Bermeja Pluton in the *mg* (100MgO / [MgO+FeO$^t$]) *vs. k* (100$K_2O$ / [$K_2O$+$Na_2O$]) comparative diagram (Rock, 1991; Sabatier, 1991). Data of other Iberian vaugneritic rocks from Barbero (1992), Barbero *et al.* (1990), Dias *et al.* (2002), Gallastegui (2005), Gil Ibarguchi (1981), López Plaza *et al.* (1999), and Scarrow *et al.* (2009).

Though the absence of a detailed petrological study of the vaugnerite series rocks and calc-alkaline lamprophyres from the Sierra Bermeja Pluton (out of the scope of this PhD project) precludes a precise assignment, their geochemical and isotopic characteristics close to those of vaugnerite series and equivalents point to a probable provenance from a

heterogeneous metasomatized mantle source, as it is generally accepted for similar rocks elsewhere (*e.g.* Couzinié *et al.*, 2016; Holub, 1997; Janoušek and Holub, 2007; Rock, 1991; Scarrow *et al.*, 2009; Solgadi *et al.*, 2007; Turpin *et al.*, 1988; von Raumer *et al.*, 2014).

Vaugneritic rocks in the Iberian Massif appear most often in spatial relation with Variscan syn- to late/post-collisional peraluminous granitoids, including anatectic sub-autochthonous granites in thermal dome areas to elongated granodiorite massifs. Within central sectors of the Central Iberian Zone, vaugnerites of La Calzadilla Pluton in the Tormes Dome were emplaced at *ca.* 318 Ma (López-Moro *et al.*, 2017). Though coeval mantle and crustal melting in this area might have taken place at that time, heating effects on crustal rocks by mantle-derived melts seem negligible (López-Moro *et al.*, 2017). To the South, in the Ávila Batholith, the emplacement of mafic and ultramafic rocks has been dated at *ca.* 312 Ma (Montero *et al.*, 2004), being regarded as coeval with the granitoids generation. Nevertheless, this age is markedly later than the maximum of crustal melting there, discarding again the involvement of mantle-derived melts in the crustal heating (Scarrow *et al.*, 2009). Furthermore, alkaline lamprophyres intruding into this batholith clearly post-date the emplacement of the host granitoids (Scarrow *et al.*, 2006, 2011; Orejana *et al.*, 2008). Finally, more to the South, in the Toledo Anatectic Complex, vaugnerites dated at *ca.* 308 Ma (Bea *et al.*, 2006) provide relative young emplacement ages respect to the host migmatites.

Studied dioritoids and lamprophyres from the Sierra Bermeja Pluton crop out separately each other and define N20–40E-trending longitudinal mappable discrete bodies, parallel to one of the main cooling joint systems identified in this massif (see Chapter 4; Sarrionandia *et al.*, 2004). As previously stated, these rocks cross-cut the contacts between the different monzogranitic units of this pluton (Fig. 15). At first glance, field and cartographic relationships suggest that the emplacement of the intermediate melts would be

markedly later respect to that of peraluminous monzogranitic magmas, constituting two unrelated magmatic events. Nevertheless, vaugnerite series rocks and lamprophyres are exclusively confined within the limits of this monzogranitic massif, pointing undoubtedly to a constricted timing between the respective magmatic pulses. Furthermore, the obtained U–Pb age for vaugnerites (305 ± 17 Ma; apatite) is in the range of that obtained for the host monzogranites (309 ± 3 to 304 ± 3 Ma; zircon; see Chapter 7). This fact, together with the previously stated field and cartographic characteristics, demonstrate that the emplacement of the vaugnerite series rocks and monzogranites from the Sierra Bermeja Pluton was near coeval, similarly to other areas of the Iberian Massif (*e.g.* López-Moro *et al.*, 2017; Montero *et al.*, 2004). Obtained U–Pb apatite age of 305 ± 17 Ma in the Sierra Bermeja Pluton vaugnerites is slightly younger to the zircon age-range of *ca.* 319–308 Ma for vaugnerites *s.l.* elsewhere within the Iberian Massif (Montero *et al.*, 2004; Bea *et al.*, 2006; Rodríguez *et al.*, 2007; López-Moro *et al.*, 2017), but it may equally argue for an almost contemporary mantle and crustal melting in southern areas of the Iberian Massif.

Finally, textural and structural differences between dioritoids and lamprophyres from the Sierra Bermeja Pluton attest to the existence of at least two independent mantle-derived magma pulses in the studied area. Lamprophyres show marked rectilinear trends and aphanitic textures at the field scale, which suggest brittle fracturing of monzogranites and higher temperature contrast during their emplacement. Moreover, the monzogranite enclaves found within these lamprophyres (Fig. 23) show thermal (hydrothermal) effects on biotite and feldspars. These characteristics evidence that monzogranites were highly consolidated and cool during the emplacement of lamprophyres. Thus, despite the absence of a precise radiometric dating of these mesocratic rocks, their emplacement somewhat would post-date the emplacement of monzogranites and vaugnerites from the Sierra Bermeja Pluton.

## 9.2. GRANITE SOURCE MATERIALS

Petrogenetic studies of granitic plutons require the understanding of diverse processes that operate on different temporal and spatial scales during melt generation, magma segregation, transport and final emplacement (Brown, 1994, 2013; Petford *et al.*, 2000). Through these stages, source materials, mechanism of melting, magma differentiation processes, with emplacement timing and P–T conditions are key points to decipher (*e.g.* Anderson, 1996; Clemens and Stevens, 2012; Petford *et al.*, 2000; Wilson, 1993). In this and following sections we will address these points in regard to the origin of the cordierite-bearing peraluminous monzogranites from the Sierra Bermeja Pluton. The conclusions gathered constitute the base of a proposed petrogenetic model that could be extensible to other intrusions integrated in the Iberian 'Serie Mixta'-type granitoids, primarily those of the Nisa–Alburquerque–Los Pedroches Magmatic Alignment (Fig. 8).

### 9.2.1. Testing the role of mantle-derived (vaugneritic) magmas

As previously indicated, a broad range of potential sources have been proposed for the controversial 'Serie Mixta'-type peraluminous granitoids of the Central Iberian Zone (Iberian Massif). The models can be assigned to two main groups (see Chapter 2): 1) exclusively crustal (*e.g.* Bea *et al.*, 1999, 2003; Chicharro *et al.*, 2014; Corretgé *et al.*, 1985; Donaire *et al.*, 1999; Errandonea-Martin *et al.*, 2017; González Menéndez, 1998, 2002; Gonzalo, 1987, 1988; Merino Martínez *et al.*, 2014; Ramírez and González Menéndez, 1999; Roda-Robles *et al.*, 2018; Ugidos, 1988; Ugidos and Recio, 1993; Villaseca *et al.*, 2008) or, 2) hybrid, involving different degrees of mantle input (*e.g.* Alonso Olazabal, 2001; Alonso Olazabal *et al.*, 1999; Carracedo, 1991; Carracedo *et al.*, 2009; Castro *et al.*, 1999; García-Moreno *et al.*, 2006, 2007; Larrea, 1998; Larrea *et al.*, 1992; Pesquera *et al.*, 2017). Considering the existence of vaugneritic syn-plutonic dykes emplaced into the Sierra

Bermeja Pluton, the studied peraluminous monzogranites offer an excellent opportunity to test these hypotheses. The contamination of mantle-derived magmas by crust-derived materials or their mixing with crustally derived, felsic melts are typically reflected in Rb–Sr and Sm–Nd isotopic compositions (*e.g.* De Paolo and Wasserburg, 1979; McCulloch and Chappell, 1982). To model this scenario, we have considered the sample JE 17 03 as the mantle end-member according to its low $^{87}Sr/^{86}Sr_i$ ratio and the highest $\varepsilon Nd_i$ value (Table 16). On the other hand, the monzogranite JE 16 45 could correspond to the crustal end-member, considering its highest $^{87}Sr/^{86}Sr_i$ ratio and lowest $\varepsilon Nd_i$ value (Table 16). The mixing model trend obtained (after De Paolo and Wasserburg, 1979) in the $^{87}Sr/^{86}Sr_{306}$ *vs.* $\varepsilon Nd_{306}$ diagram (Fig. 57) reveals that nearly the complete dataset of monzogranites projects markedly away from this theoretical mixing trend.

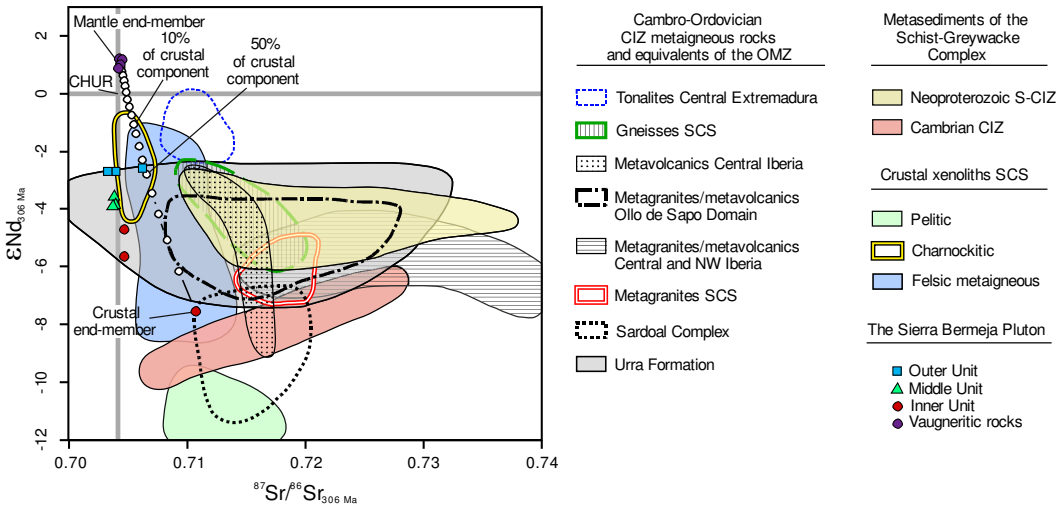


**Figure 57.** $^{87}Sr/^{86}Sr_{306}$ *vs.* $\varepsilon Nd_{306}$ binary plot for the monzogranites and vaugneritic rocks of the Sierra Bermeja Pluton. The theoretical mixing hyperbola between vaugneritic rocks and a possible crustal end-member is also drawn (see text for the explanation). Data for the Neoproterozoic and Cambrian metasediments of the Central Iberian Zone are from Beetsma (1995), Castro *et al.* (1999), Ugidos *et al.* (1997, 2003, 2008) and Villaseca *et al.* (2014). Pelitic xenoliths of the SCS from Villaseca *et al.* (1999). Data for the Cambro–Ordovician metaigneous rocks of the Central Iberian Zone (CIZ) and their equivalents of the Ossa-Morena Zone (OMZ) are from: Castro *et al.* (1999): tonalites from Central Extremadura and gneisses from the SCS; Henriques *et al.* (2015): Sardoal Complex; Montero *et al.* (2007): metagranites/metavolcanics from the Ollo de Sapo Domain; Rodríguez-Alonso *et al.* (2004): metavolcanics from Central Iberia; Solá *et al.* (2008): Urra Formation; Talavera *et al.* (2013): metagranites/metavolcanics from Central and NW Iberia; Villaseca *et al.* (1999): felsic metaigneous xenoliths from the SCS; Villaseca *et al.* (2007): charnockites from the SCS; Villaseca *et al.* (2016): metagranites from the SCS.

Furthermore, a theoretical mixing would imply up to 50 % of mantle component in the mixture (Fig. 57), but vaugneritic rocks in the Sierra Bermeja Pluton encompass only 0.2 % of the total area of the pluton (see chapter 4). In this sense, the absence of intermediate terms (*e.g.* quartz diorites–tonalites) in this pluton also suggests that hybridization of vaugneritic magmas did not play a considerable role in the genesis of the studied monzogranites.

Additionally, some authors have considered MME as a key piece of evidence to decipher genesis of these particular monzogranites (e.g. Castro et al., 1999; Donaire et al., 1999; García-Moreno et al., 2006, 2007; Pesquera et al., 2017). These enclaves, regarded as magma blobs of tonalitic to granodioritic compositions in the host monzogranites, would represent hybrid rocks from the lower crust, resulting from mixing between felsic and mafic magmas (e.g. Castro et al., 1999; García-Moreno et al., 2006; Pesquera et al., 2017). Despite the fact that the nature of the mafic component in the mixing is not clear, the MME would evidence, following these hypotheses, an involvement of the mantle-derived material in the origin of the monzogranites. Since MME only appear in one of the three monzogranitic units from the Sierra Bermeja Pluton and coeval mantle-derived vaugneritic magmas occur everywhere, the MME have been discarded to model mixing processes in the Sierra Bermeja Pluton.

### 9.2.2. Plausible crustal sources

Taking into account the available experimental data, different crustal sources can be expected in the generation of granitic melts (*e.g.* Jung *et al.*, 2009; Montel and Vielzeuf, 1997; Patiño Douce, 1999; Patiño Douce and Beard, 1995; Patiño Douce and Johnston, 1991; Sylvester, 1998; Vielzeuf and Holloway, 1988; Vielzeuf and Montel, 1994). For the discrimination of metapelitic, metapsammitic and metabasic sources, Patiño Douce (1999)

proposed the $Al_2O_3 + FeO^t + MgO + TiO_2$ *vs.* $Al_2O_3/(FeO^t + MgO + TiO_2)$ binary diagram. In this diagram, the monzogranites of the Sierra Bermeja Pluton plot within the metapsammitic field that encloses greywacke- and orthogneiss-derived melts (Fig. 58 A), although most of the IU samples overlap with the $Al_2O_3$ / $(FeO^t + MgO + TiO_2)$ values of pelite-derived melts (Fig. 58A).

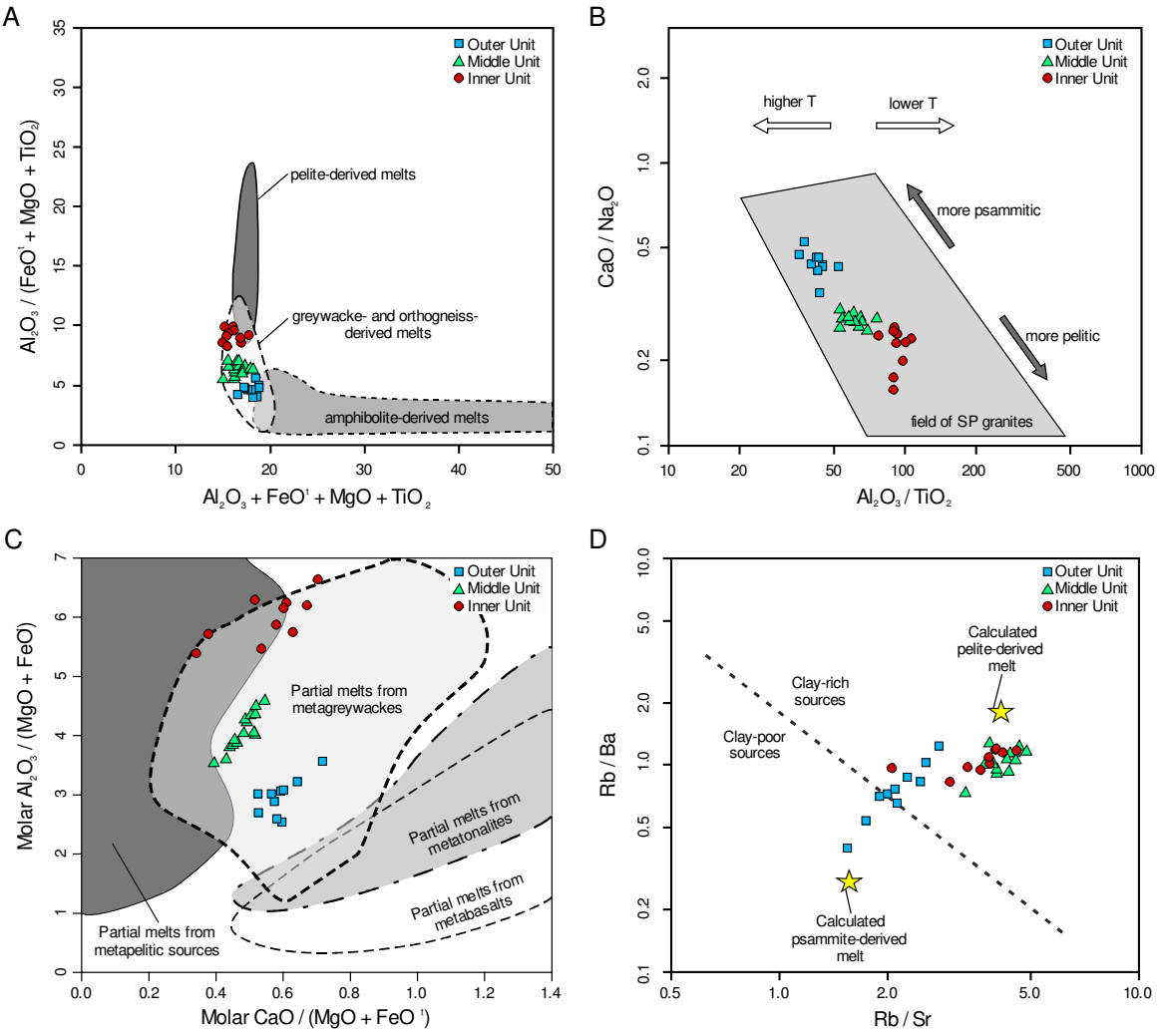


**Figure 58.** Source discrimination diagrams for the monzogranite units of Sierra Bermeja. a) $Al_2O_3 + FeO^t + MgO + TiO_2$ *vs.* $Al_2O_3/(FeO^t + MgO + TiO_2)$ (wt.%) diagram showing fields of experimental melts derived from partial melting of amphibolites, greywackes and orthogneisses, and pelites (Patiño Douce, 1999; Jung *et al.*, 2009). b) $Al_2O_3/TiO_2$ *vs.* $CaO/Na_2O$ plot based on Sylvester (1998), reflecting the variation in composition of the source and temperature. c) Molar $CaO/(MgO + FeO^t)$ *vs.* $Al_2O_3/(MgO + FeO^t)$ diagram based on Gerdes *et al.* (2002) including fields of experimental melts derived from partial melting of metabasalts, metatonalites, metagreywackes and metapelites. d) Rb/Sr *vs.* Rb/Ba diagram, for the discrimination of clay-poor and clay-rich sources (Sylvester, 1998).

The possibility of different crustal sources in the generation of the Sierra Bermeja Pluton monzogranites seems to be also reflected by the $CaO/Na_2O$ ratios (Sylvester, 1998). In this respect, the average $CaO/Na_2O$ ratios of the OU (0.44), MU (0.28) and IU (0.23) differ from each other and point to a mostly psammitic source for the OU monzogranites and a pelitic one for the IU monzogranites, with intermediate character for the MU (Fig. 58 B). The projection in the molar $CaO/(MgO + FeO^t)$ *vs.* $Al_2O_3/(MgO + FeO^t)$ diagram (Fig. 58 C; based on Gerdes *et al.*, 2002) also implies a psammitic/orthogneiss source for the OU, a mainly pelitic one for the IU and an intermediate one for the MU monzogranites (Fig. 58 C). Trace-element compositions would be consistent with such sources (*e.g.* Harris and Inger, 1992; Sylvester, 1998), since OU monzogranites show relatively low Rb/Sr and Rb/Ba ratios compared to the MU and IU monzogranites (Fig. 58 D).

Moreover, a variable contribution of the aforementioned crustal sources in the generation of each monzogranitic unit seems probable. As previously mentioned, monzogranites of the Sierra Bermeja Pluton display roughly similar low $^{87}Sr/^{86}Sr_i$ values (~0.7033–0.7062), whereas the $\varepsilon Nd_i$ values are distinct for each of the three monzogranite units (Fig. 57; Table 16). The Nd isotope systematics thus supports different parental magmas (sources) for individual monzogranite units making up the Sierra Bermeja Pluton. As regards the existence of mixing processes between the monzogranitic magmas, it appears that they can be discarded in view of the observed differences in $\varepsilon Nd_i$ values between the three units (Fig. 57; Table 16). Likewise, significant mixing between contrasting granitic melts may be discarded, either, given the existence of marked compositional gaps between the three units in a number of variation diagrams (see Figs. 45–48, 50, and 58).

For a proper identification of the most likely crustal sources involved in the formation of the monzogranite magmas, we must consider the regional geological record at the time of the emplacement and available whole-rock isotope data from the literature. As stated

previously, the Sierra Bermeja Pluton intrudes mostly Lower to Middle Paleozoic metasediments of the Central Iberian Zone and, to a lesser extent, Cadomian dioritoids (Mérida Massif) of the adjacent Ossa-Morena Zone. Considering the relative allochthonous character of the studied monzogranites, it appears plausible that the source materials could correspond to the lowermost sections of the known geological record in the area, which are represented by: 1) Neoproterozoic–Lower Cambrian metasediments of the Schist–Greywacke Complex, and/or 2) Cambro–Ordovician metasedimentary and metaigneous rocks.

The $^{87}Sr/^{86}Sr_i$ *vs.* $\varepsilon Nd_i$ plot shows data for the studied monzogranites and the fields of hypothetical crustal sources recalculated at 306 Ma (Fig. 57). As may be seen, monzogranites of the OU, MU and IU plot within the Cambro–Ordovician metaigneous rocks field of the Urra Formation. At the same time, they fall within, or really close to, the charnockitic and felsic metaigneous xenoliths fields from the Spanish Central System (Villaseca et al., 1999, 2007) that are considered to have their origins at lower crustal levels. Studied monzogranites exhibit also $\varepsilon Nd_i$ resembling the metasediments of the Schist–Greywacke Complex, but with lower Sr isotopic ratios. At lower crustal levels, where much Rb could have been lost due to high-grade metamorphism, the Sr isotopic ratios of these metasediments should be closer to the Bulk Silicate Earth. In contrast, analogous rocks in the upper crust should keep relatively high time-integrated Rb/Sr ratios (e.g. Villaseca et al., 1999 and references therein). In this sense, it would be common that the lower crustal metasedimentary source materials had lower Sr isotopic compositions than their equivalents that crop out at the current exposure level. Thus, accordingly to major- and trace-element data that denote implication of metasedimentary sources in the genesis of the studied monzogranites, the support of the mentioned Neoproterozoic–Lower Cambrian succession seems suitable. Moreover, the analyzed monzogranites define, in the sense OU → MU →

IU, a broadly linear array to the field of the Lower Cambrian metasediments of the Schist–Greywacke Complex (Fig. 57). Hence, such potential sources, Neoproterozoic–Lower Cambrian metasediments and Cambro–Ordovician metaigneous rocks, are in accordance with the observed major-, trace-element and isotopic characteristics of monzogranites.

Moreover, the inherited cores identified in a number of zircon grains of the monzogranites would support this Neoproterozoic to Cambro–Ordovician source hypothesis. Note that Cambro–Ordovician inherited cores were found in all units and the Neoproterozoic and Paleoproterozoic cores, common in materials ascribed to the Schist–Greywacke Complex (Talavera *et al.*, 2012), in the OU and IU (Table 13, Fig. 42). In summary, both metaigneous and metasedimentary source materials were likely involved in the origin of each monzogranite pulse. The metasedimentary source component would increase inward the pluton, from a mainly metaigneous source for the OU monzogranites, to an almost exclusively metasedimentary derivation for those from the IU.

Regarding MME, experimental studies show that isotopic equilibration is induced by diffusion processes, being easier and faster to achieve than chemical equilibration, and that is markedly faster in the Sr isotopic system than in the Nd due to the lower diffusion coefficients and lower sensitivity to temperature for the later (Lesher, 1990, 1994). These differences in the isotopic equilibration have been observed between MME and their host granitoids (*e.g.* Barbarin, 2005; Holden *et al.*, 1991; Pin *et al.*, 1990). In this case, during magma ascent and emplacement, and prior to the complete cooling of the pluton, diffusion processes are active, producing the isotopic equilibration at the emplacement level (*e.g.* Barbarin, 2005). This homogenization process would explain the similar $^{87}Sr/^{86}Sr_i$ of the OU monzogranites and the analyzed MME (Fig. 51).

## 9.3. THERMOBAROMETRY

Experimental studies demonstrate that the nature of source materials is a critical factor controlling the amount of melt fraction generated (Patiño Douce and Johnston, 1991). Relatively large amounts of melt (45–50 vol.%) can be produced under moderate pressures (7–10 kbar) in pelitic systems by dehydration-melting of biotite with ~4 wt.% $H_2O$ (*e.g.* Clemens and Vielzeuf, 1987; Patiño Douce and Harris, 1998; Vielzeuf and Holloway, 1988). Leucogranitic melts can be generated under lower pressures (6–8 kbar) and temperatures (750–800 ºC) by dehydration-melting of metapelites (Patiño Douce, 1999; Patiño Douce and Harris, 1998).

In psammitic systems, a production of lower melt fractions is expected under similar temperature (800–900 ºC) and pressure (7–10 kbar) conditions (Montel and Vielzeuf, 1997). Experimental studies indicate that relatively high melt fractions could be also produced, reaching up to 30–60 vol.% at 800–900 ºC, from Ca-poor Al-metagreywackes (Vielzeuf and Montel, 1994), or up to 44 vol.% at 950 ºC from biotite gneisses (Patiño Douce and Beard, 1995).

According to the geochemical and isotope data, two different crustal sources could be envisaged for the Sierra Bermeja Pluton monzogranites: 1) the Neoproterozoic–Lower Cambrian metasediments of the Schist–Greywacke Complex, and 2) the Cambro–Ordovician metaigneous and metasedimentary rocks. By considering only the least evolved monzogranite sample of each unit, the melting temperatures obtained from the whole-rock $Al_2O_3/TiO_2$ ratios (after Jung and Pfänder, 2007; based on Sylvester, 1998) would be close to those obtained from experimental data (Clemens and Vielzeuf, 1987; Montel and Vielzeuf, 1997; Patiño Douce and Beard, 1995; Patiño Douce and Harris, 1998; Vielzeuf and Montel, 1994; Vielzeuf and Holloway, 1988). Thus, temperature estimations for the least

evolved monzogranite samples of the OU and MU suggest that melting of Cambro–Ordovician metaigneous and Neoproterozoic metasedimentary rocks occurred at ~830–870 ºC, whereas the least evolved sample of the IU points to melting of the Schist–Greywacke Complex metasediments at ~855 ºC (Fig. 59 A).

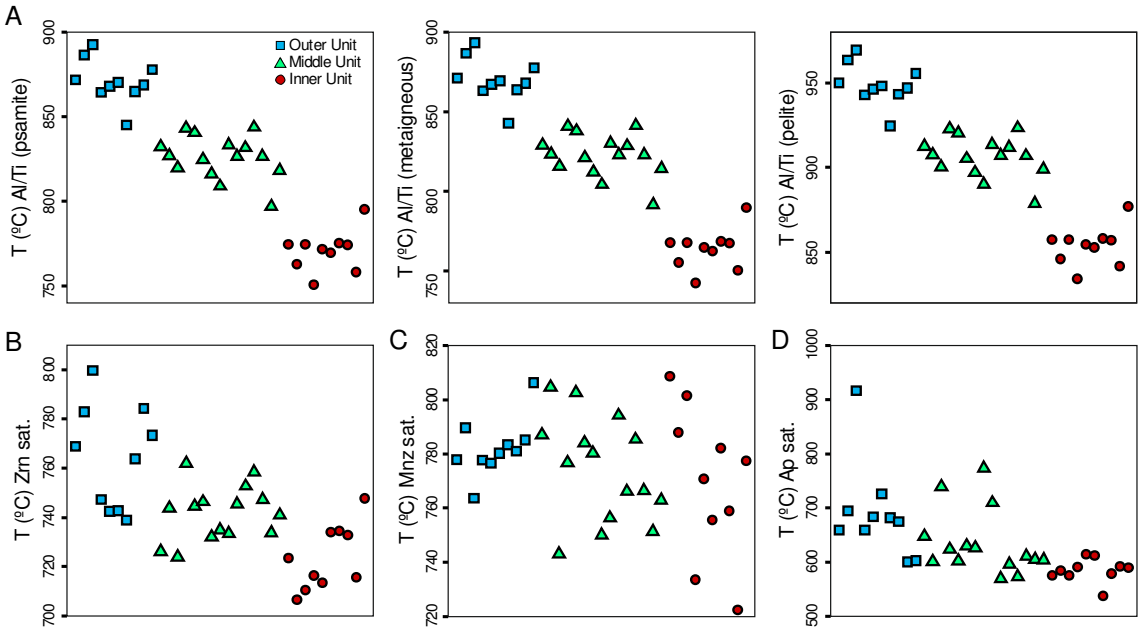


**Figure 59.** A) Estimated temperatures for the three distinguished monzogranite units from the Sierra Bermeja Pluton, obtained from whole-rock $Al_2O_3/TiO_2$ ratios (after Jung and Pfänder, 2007; based on Sylvester, 1998). B) Zircon saturation temperatures (after Watson and Harrison, 1983); C) Monazite saturation temperatures (based on Montel, 1993); and D) Apatite saturation temperatures (Pichavant *et al.*, 1992), for the OU, MU and IU monzogranites. Full dataset in Table 13 of the Appendix.

It is remarkable that, despite the contrasting nature of inferred crustal sources for the Sierra Bermeja monzogranites, estimated melting temperatures of those sources are well comparable (~830–870 ºC). Moreover, these temperatures are in accordance with thermobarometric estimations of ~800 ºC at the middle crust and ~900–1000 ºC at the lower crust proposed for the Central System Batholith, 30 km to the north of the studied pluton (*e.g.* Merino Martínez *et al.*, 2014, and references therein). According to those estimates, the sources of the Sierra Bermeja Pluton monzogranites could be located in the middle to lower crust of the study area.

The heat supply for the formation of this type of peraluminous magmas still remains controversial. As mentioned above, some authors advocate an input of mantle magmas (Annen and Sparks, 2002; Castro, 2014; Patiño Douce, 1999), whereas others appeal to an exclusively crustal origin through thickening and radiogenic heating (*e.g.* Bea, 2012; England and Thompson, 1984; Merino Martínez *et al.*, 2014). In the case of the Sierra Bermeja Pluton, the existence of syn-plutonic dykes of vaugnerite series rocks proves that mantle-derived magmas were available at the time of the pluton emplacement. Nevertheless, hybridization of crustal and mantle-derived magmas played a minor, if any, role in the generation of the studied monzogranites (see the previous 9.2.1. section of this chapter). This implies that the mantle-derived magmas could have been only a supplementary heat source. On the other hand, *in situ* radiogenic heating of crustal materials, could have induced the generation of large granitic magmatism after 30–40 Ma of thermal incubation (Bea, 2012). Considering that the inferred sources for the Sierra Bermeja Pluton monzogranites are rich in heat-producing elements (K, Th and U) (*e.g.* Villaseca *et al.*, 2016, and references therein), the most plausible scenario would be a combination of both the radiogenic heating and the heat transfer from mantle-derived magmas.

Shallow emplacement conditions of the Sierra Bermeja Pluton are in accord with the observed coexistence of andalusite, tourmaline and magmatic muscovite in monzogranites of the IU, similarly to the nearby Nisa–Alburquerque Batholith (Fig. 8; ~2–3 kbar; González Menéndez *et al.*, 2011). Similar conditions (< 3 kbar and 550–650 ºC) were also estimated for the emplacement of the Campanario–La Haba Pluton (Fig. 8) of the same magmatic alignment based on the mineral assemblage of the host metasedimentary rocks (Alonso Olazabal *et al.*, 1999). Since the same mineral assemblage is observed in the host rocks of the Sierra Bermeja Pluton, the inferred shallow emplacement conditions (< 3 kbar) seem feasible.

To unravel whether the emplaced parental magmas would correspond to liquids unmodified by any post-segregation process, solubility equations of accessory minerals could be of use as they are an important tool to estimate crystallization temperatures (*e.g.* Bea *et al.*, 1992; Boehnke *et al.*, 2013; Harrison and Watson, 1984; Montel, 1993; Pichavant *et al.*, 1992; Rapp and Watson, 1986; Watson and Harrison, 1983). In peraluminous magmas, zircon, monazite and apatite are the key accessory minerals since they hold significant amounts of trace elements such as Th, U and REE (Bea, 1996a, b; Pérez-Soba *et al.*, 2014, 2017). In the studied monzogranites, the zircon saturation temperatures (Watson and Harrison, 1983) are 739–800 ºC (OU), 724–762 ºC (MU) and 706–748 ºC (IU), which could be slightly overestimated due to the (limited) presence of inherited zircon cores. Nonetheless, the calculated temperatures are close to those obtained from monazite solubility equations (based on Montel, 1993) for the same units: 764–806 ºC (OU); 743–805 ºC (MU); 722–809 ºC (IU; Fig. 59 B).

Apatite solubility is enhanced in peraluminous magmas and the saturation temperatures depend strongly on the formulation. Following Bea *et al.* (1992), the saturation temperatures are 773–972 ºC, whereas according to Pichavant *et al.* (1992), this range is unrealistically wide: 537–917 ºC. In any case, the observed deviations in the apatite saturation temperature attest to variations in whole-rock $P_2O_5$, CaO and A/CNK (peraluminosity index) within each monzogranite unit (Bea *et al.*, 1992; Pichavant *et al.*, 1992). It also reflects the sensitivity of the method to even small errors in $P_2O_5$ determinations (Janoušek, 2006). Excluding apatite saturation temperatures, those calculated from zircon and monazite are close to melting temperatures estimated from whole-rock $Al_2O_3/TiO_2$ ratios, which suggests that both accessories crystallized close to the liquidus temperatures. This fact supports that post-segregation processes were not very significant prior to the emplacement of the monzogranite magmas, and that the less evolved (parental)

monzogranite samples would not depart very much from the compositions of the melted sources.

## 9.4. DIFFERENTIATION PROCESSES MODELLING

In order to explain the observed geochemical variations within each monzogranite unit of the Sierra Bermeja Pluton, whole-rock major- and trace-element modelling has been undertaken. To discern between partial-melting and fractional crystallization processes, firstly log(incompatible element) *vs*. log(compatible element) diagrams were used, as they result in almost horizontal and subvertical trends, respectively (*e.g.* Janoušek *et al.*, 2016). Yet, in granitoid rocks it can be rather difficult to find a suitable incompatible element given that constituent accessory minerals often hold many trace elements that behave as incompatible in other types of magmas (Bea, 1996a, b; Harris and Inger, 1992; Janoušek *et al.*, 2014; Pérez-Soba et al., 2014; Sawka, 1988). In the OU of the Sierra Bermeja Pluton it can be observed that Y and Th behave as incompatible up to the monazite/xenotime saturation point (Fig. 60 A–B). The undersaturated samples of this unit in the log(Y) *vs*. log(Ba) and log(Th) *vs*. log(Ba) diagrams define near vertical trends, underlining fractional crystallization as the main differentiation process in the OU (Fig. 60 C). For the rest of the pluton, we have identified only a single incompatible element, gallium, which shows a reasonable linear correlation with $SiO_2$ in the binary plot. A steep trend in the log(Ga) *vs*. log(Ba) diagram proves also the importance of fractional crystallization (Fig. 60 D, E). The fractional crystallization mechanism is also supported by the fact that biotite and K-feldspar phenocryst accumulations have been observed in a number of outcrops.

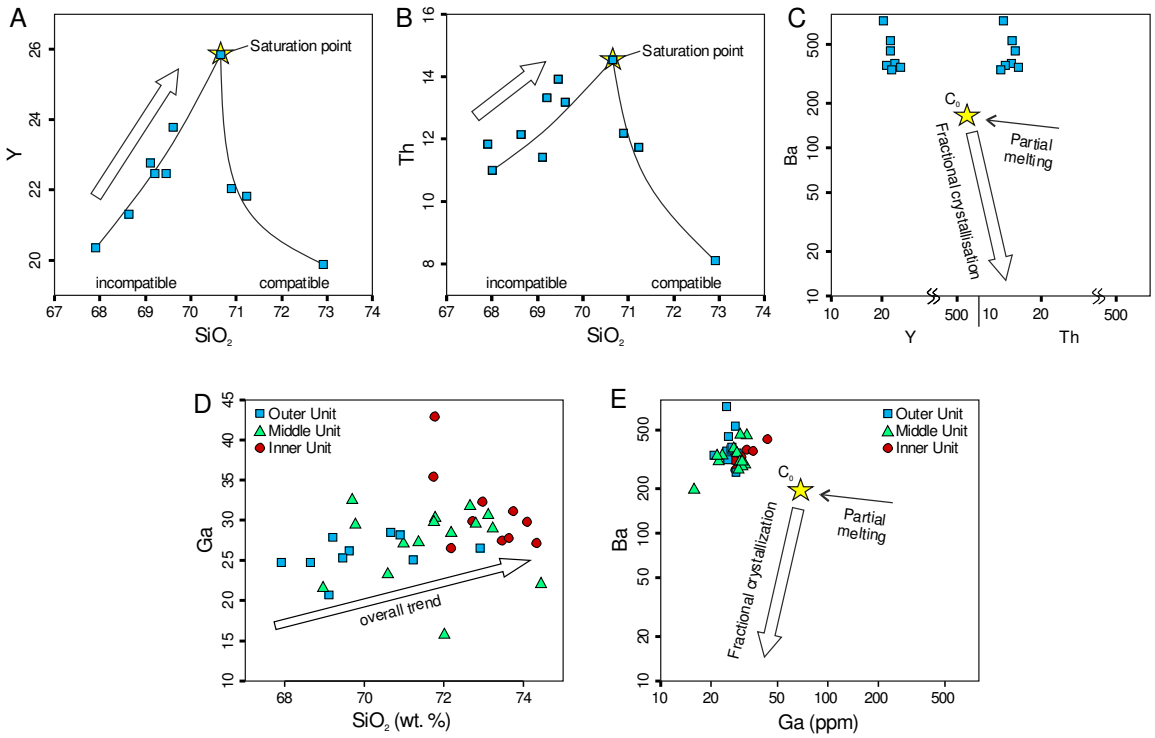


**Figure 60.** A) $SiO_2$ *vs.* Y and B) $SiO_2$ *vs.* Th variation diagrams, where it is observable the evolution of Y and Th from incompatible to compatible behaviour in the OU. C) Log(incompatible = Y, Th) *vs.* log(compatible = Ba) plots for monzogranites from the Sierra Bermeja Pluton. D) $SiO_2$ *vs.* Ga binary diagram for the Sierra Bermeja Pluton monzogranites, where it is observable the evolution of Ga as incompatible element. E) Log(incompatible = Ga) *vs.* log(compatible = Ba) plot for the same monzogranite set.

Once the most plausible mechanism of magma differentiation has been identified, we carried out major- and trace-element modelling to constrain the degree of fractionation and the crystallizing mineral assemblage. For major-element modelling, mass-balance equations (following Janoušek *et al.*, 2016) and constrained least-square method (Albarède, 1995) were used. For selected key trace-elements, Rayleigh-type fractional crystallization ($C_L = C_0 F^{(D-1)}$) was modelled (distribution coefficients are given in Table 14 of the Appendix). Calculations were carried out for each monzogranite unit separately using an unpublished R-language plugin for the *GCDkit* software (Janoušek *et al.*, 2006). Taking into account the accessory mineral assemblage in the studied monzogranites (see Chapter 5) monazite, xenotime and apatite were considered for the REE, Y, Th and U modelling, discarding zircon as fractionating phase because Zr contents do not vary significantly within each unit.

Moreover, the lanthanide tetrad effect observed in some IU monzogranites, that can be caused by monazite and xenotime fractionation (Duc-Tin and Keppler, 2015), would support the consideration of monazite and xenotime as fractionating phases. Monazite would incorporate most of the LREE, Th and U in these magmas, xenotime the HREE + Y + U and apatite would allocate relatively high amounts of Y, Th, MREE and HREE (*e.g.* Bea, 1996a, b; Pérez-Soba *et al.*, 2014, 2017).

### 9.4.1. OU monzogranites geochemical modelling

For the geochemical modelling of the OU, composition of the sample JE 15 26 was considered as approximating that of the parental magma ($C_0$) and sample JE 15 60 as the evolved (daughter) magma ($C_L$). The model yielded an acceptable sum of squares of the residuals ($\Sigma R^2 = 0.27$), assuming a 21% fractional crystallization of K-feldspar + plagioclase (andesine) > biotite (Fig. 61; Table 17).

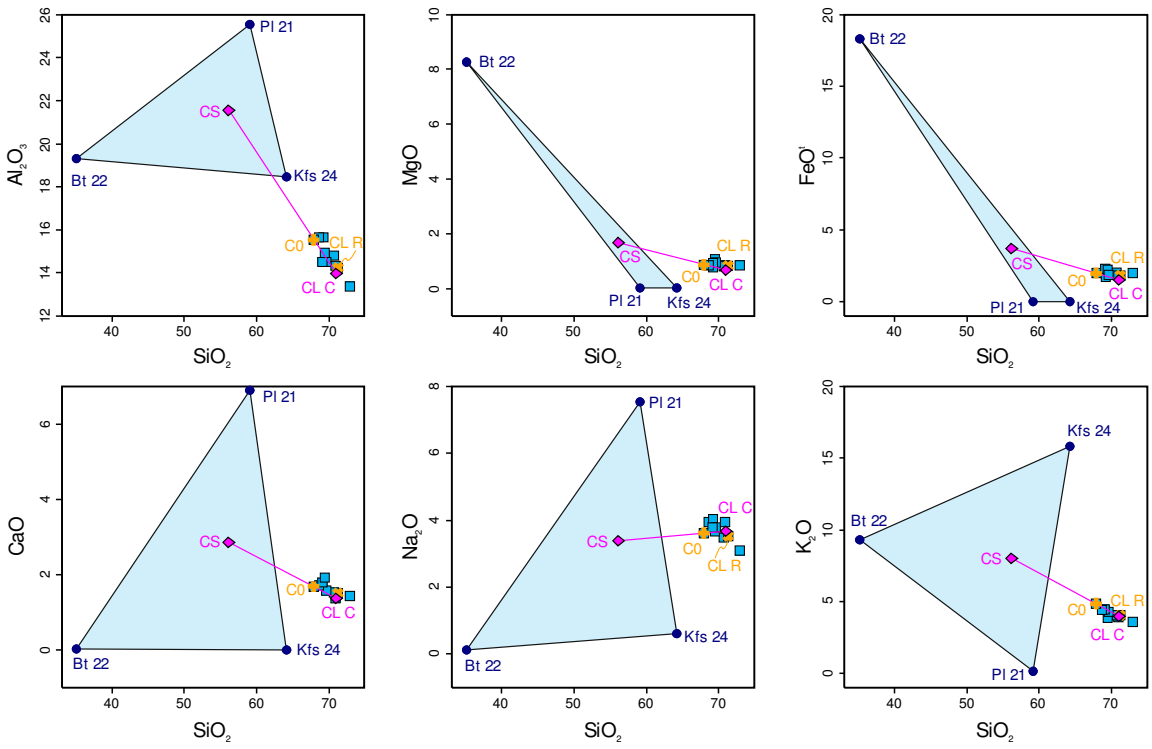


**Figure 61.** Geometric representation of the major-element geochemical modelling of the OU monzogranites.

This result would be consistent with the trends observed in the log(Ba) *vs*. log(Sr) and log(Ba) *vs*. log(Rb) diagrams, that is, controlled in fact by the main rock-forming minerals (Fig. 62 A). In the same vein, feldspar extraction would also explain the increase of negative Eu anomaly for the most evolved terms of the OU. As mentioned above, since REE, Th and Y behave as incompatible in the least evolved samples of the OU, only saturated samples were considered to model the variation of selected trace-elements in this unit. In this case, sample JE 15 38 that plots at the saturation point in Fig. 60 A–B was considered as the $C_0$ ('$C_0$ sat' of Table 18). According to this modelling, minor amounts of apatite, monazite and xenotime would also need to be added to the fractionating mineral assemblage in order to reproduce the REE, Y, Th and U analytical data (Fig. 62 B; Table 18).

***Table 17.*** *Results of the fractional crystallization modelling of the OU monzogranites*

Degree of fractional crystallization 21.0 %
$\Sigma R^2 = 0.27$

| OU | $C_0$ JE 15 26 | Kfs 24[a] (38.4 %) | Pl 21[a] (41.3 %) | Bt 22[a] (20.3 %) | $C_{L\,R}$ JE 15 60 | $C_{L\,C}$ | Difference | $C_S$ |
|---|---|---|---|---|---|---|---|---|
| $SiO_2$ | 67.9 | 64.17 | 59.09 | 35.16 | 71.23 | 71.02 | 0.21 | 56.19 |
| $Al_2O_3$ | 15.56 | 18.44 | 25.54 | 19.29 | 14.25 | 13.97 | 0.28 | 21.55 |
| $FeO^t$ | 1.99 | 0.00 | 0.01 | 18.31 | 1.8 | 1.53 | 0.27 | 3.71 |
| MgO | 0.88 | 0.01 | 0.00 | 8.28 | 0.83 | 0.67 | 0.16 | 1.68 |
| CaO | 1.68 | 0.00 | 6.9 | 0.03 | 1.52 | 1.37 | 0.15 | 2.86 |
| $Na_2O$ | 3.62 | 0.62 | 7.54 | 0.12 | 3.54 | 3.68 | -0.14 | 3.38 |
| $K_2O$ | 4.84 | 15.8 | 0.15 | 9.28 | 4.06 | 4.00 | 0.06 | 8.01 |

$\Sigma R^2$: sum of squared residuals
$C_0$: Parent; $C_{L\,R}$: Real daughter; $C_{L\,C}$: Calculated daughter; $C_S$: Cumulate
[a]Code from the Supplementary Tables of the Appendix
The calculations were carried out using an unpublished R-language plugin for the GCDkit software (Janoušek *et al.*, 2006)

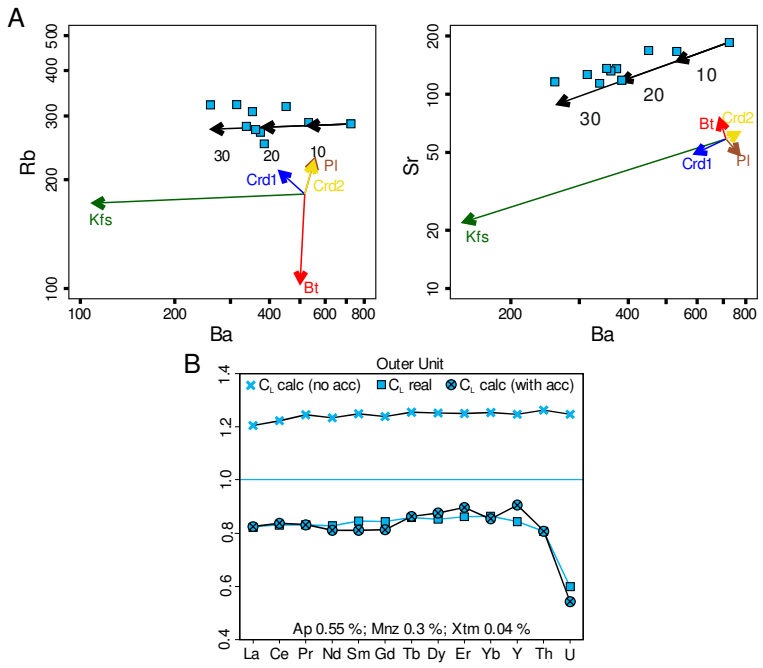


**Figure 62.** A) Results of the Rb–Ba–Sr modelling of the OU monzogranites from the Sierra Bermeja Pluton. The partition coefficients calculated dividing the average contents in analyzed main rock-forming minerals (Table 4 of the Appendix) by the average contents considering all monzogranite samples of the three units (Table 15). B) Results of the trace-element modelling of the OU monzogranites. Daughters ($C_L$) have been normalized to the saturated sample (see text for explanation). Bulk distribution coefficient in Table 18 and distribution coefficients (Kds) in Table 14 of the Appendix.

***Table 18.*** *Data and results of the fractional crystallization modelling of selected trace element and REE of the OU monzogranites*

| | D No acc. | D Yes acc. | $C_0$ real JE 15 26 | $C_{0\,sat}$ JE 15 38 | $C_{L\,R}$ JE 15 60 | $C_{L\,C}$ No acc. | $C_{L\,C}$ Yes acc. |
|---|---|---|---|---|---|---|---|
| La | 0.209 | 1.81 | 28.0 | 32.5 | 26.8 | 39.1 | 26.8 |
| Ce | 0.146 | 1.75 | 56.4 | 66.2 | 55.0 | 81.0 | 55.5 |
| Pr | 0.069 | 1.78 | 6.68 | 8.03 | 6.67 | 10.0 | 6.70 |
| Nd | 0.108 | 1.89 | 24.9 | 30.2 | 25.0 | 37.2 | 24.5 |
| Sm | 0.057 | 1.89 | 4.73 | 5.82 | 4.92 | 7.27 | 4.72 |
| Gd | 0.092 | 1.88 | 4.06 | 4.98 | 4.20 | 6.16 | 4.05 |
| Tb | 0.037 | 1.62 | 0.602 | 0.738 | 0.634 | 0.926 | 0.637 |
| Dy | 0.047 | 1.56 | 3.28 | 4.10 | 3.50 | 5.14 | 3.59 |
| Er | 0.053 | 1.46 | 1.68 | 2.09 | 1.80 | 2.61 | 1.88 |
| Yb | 0.040 | 1.67 | 1.68 | 2.18 | 1.88 | 2.73 | 1.86 |
| Y | 0.063 | 1.42 | 20.4 | 25.9 | 21.8 | 32.2 | 23.4 |
| Th | 0.010 | 1.89 | 11.8 | 14.5 | 11.7 | 18.4 | 11.8 |
| U | 0.064 | 3.59 | 4.68 | 6.63 | 3.97 | 8.27 | 3.60 |

D: Bulk distribution coefficient; $C_0$: Parent; $C_{L\,R}$: Real daughter; $C_{L\,C}$: Calculated daughter; acc.: Accessory minerals

Distribution coefficients (Kds) for D in Table 14 of the Appendix

## 9.4.2. MU monzogranites geochemical modelling

For the geochemical modelling of the MU were considered the samples JE 15 30 ($C_0$) and SB 160 ($C_L$). Again, the model obtained shows a good fit, with a sum of squared residuals ($\Sigma R^2$) of 0.23, assuming 26% fractional crystallization of K-feldspar + plagioclase (oligoclase) > biotite (Fig. 63; Table 19).

This model also reproduces the observed trend in the log(Ba) *vs*. log(Sr) diagram (Fig. 64 A). However, in contrast to the OU, the model would predict somewhat higher amounts of Rb in the evolved magma. To reproduce the REE, Y, Th and U analytical data, different minor amounts of apatite, monazite and xenotime should be also included in the fractionating mineral assemblage (Fig. 64 B; Table 20).

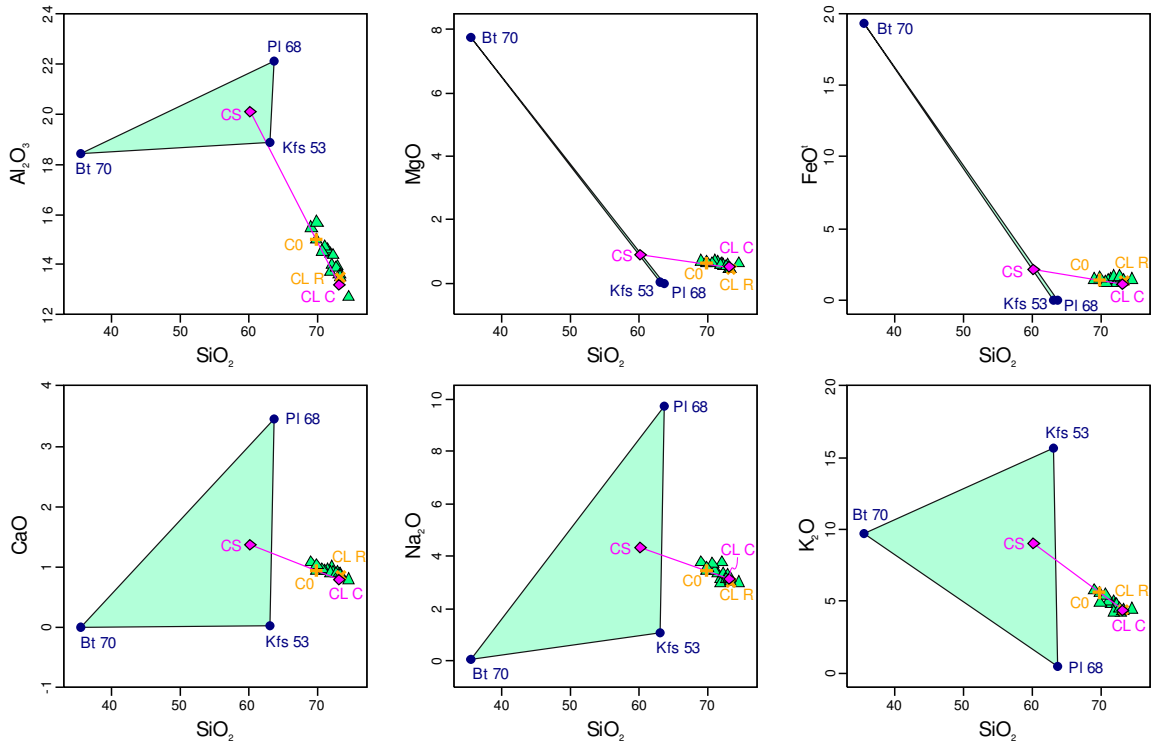


**Figure 63.** Geometric representation of the major-element geochemical modelling of the MU monzogranites.

***Table 19.*** *Results of the fractional crystallization modelling of the MU monzogranites*

Degree of fractional crystallization 26.1 %
$\Sigma R^2 = 0.23$

| MU | $C_0$ JE 15 30 | Kfs 53[a] (49.6 %) | Pl 68[a] (39.2 %) | Bt 70[a] (11.2 %) | $C_{L\,R}$ SB 160 | $C_{L\,C}$ | Difference | $C_S$ |
|---|---|---|---|---|---|---|---|---|
| $SiO_2$ | 69.69 | 62.97 | 63.64 | 35.46 | 73.23 | 73.06 | 0.17 | 60.16 |
| $Al_2O_3$ | 15.00 | 18.88 | 22.12 | 18.40 | 13.51 | 13.20 | 0.31 | 20.10 |
| $FeO^t$ | 1.39 | 0.01 | 0.01 | 19.32 | 1.40 | 1.12 | 0.28 | 2.16 |
| MgO | 0.61 | 0.05 | 0.00 | 7.73 | 0.44 | 0.51 | -0.07 | 0.89 |
| CaO | 0.94 | 0.01 | 3.46 | 0.00 | 0.86 | 0.79 | 0.07 | 1.36 |
| $Na_2O$ | 3.45 | 1.06 | 9.74 | 0.05 | 3.02 | 3.13 | -0.11 | 4.35 |
| $K_2O$ | 5.58 | 15.66 | 0.49 | 9.73 | 4.38 | 4.35 | 0.03 | 9.05 |

$\Sigma R^2$: sum of squared residuals
$C_0$: Parent; $C_{L\,R}$: Real daughter; $C_{L\,C}$: Calculated daughter; $C_S$: Cumulate
[a]Code from the Supplementary Tables of the Appendix
The calculations were carried out using an unpublished R-language plugin for the GCDkit software (Janoušek *et al.*, 2006)

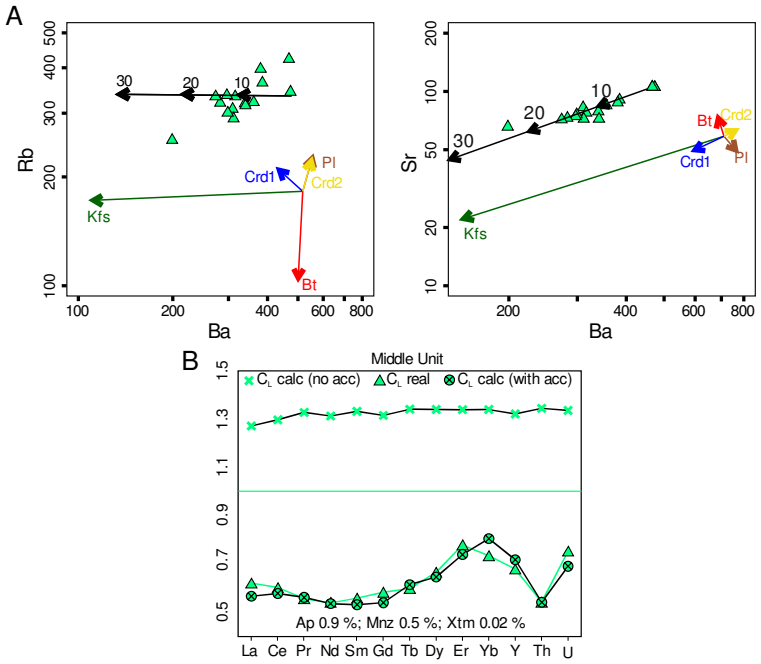


**Figure 64.** A) Results of the Rb–Ba–Sr modelling of the MU monzogranites from the Sierra Bermeja Pluton. The partition coefficients calculated dividing the average contents in analyzed main rock-forming minerals (Table 4 of the Appendix) by the average contents considering all monzogranite samples of the three units (Table 15). B) Results of the trace-element modelling of the MU monzogranites. Daughters (CL) have been normalized to the parent (C0) selected for major-element modelling. Bulk distribution coefficient in Table 20 and distribution coefficients (Kds) in Table 14 of the Appendix.

***Table 20.*** *Data and results of the fractional crystallization modelling of selected trace element and REE of the MU monzogranites*

| | D No acc. | D Yes acc. | $C_0$ JE 15 30 | $C_{L\,R}$ SB 160 | $C_{L\,C}$ No acc. | $C_{L\,C}$ Yes acc. |
|---|---|---|---|---|---|---|
| La | 0.204 | 2.87 | 27.0 | 16.8 | 34.4 | 15.3 |
| Ce | 0.139 | 2.81 | 58.8 | 35.5 | 76.3 | 34.0 |
| Pr | 0.061 | 2.90 | 7.18 | 4.00 | 9.54 | 4.04 |
| Nd | 0.100 | 3.06 | 26.4 | 14.2 | 34.6 | 14.2 |
| Sm | 0.051 | 3.08 | 5.26 | 2.94 | 7.01 | 2.80 |
| Gd | 0.092 | 3.03 | 4.08 | 2.38 | 5.36 | 2.20 |
| Tb | 0.029 | 2.61 | 0.544 | 0.326 | 0.730 | 0.335 |
| Dy | 0.032 | 2.44 | 2.67 | 1.78 | 3.58 | 1.73 |
| Er | 0.034 | 2.00 | 1.28 | 0.995 | 1.71 | 0.944 |
| Yb | 0.032 | 1.71 | 1.28 | 0.943 | 1.72 | 1.03 |
| Y | 0.077 | 2.09 | 14.9 | 10.2 | 19.7 | 10.7 |
| Th | 0.020 | 3.02 | 13.5 | 7.32 | 18.1 | 7.31 |
| U | 0.042 | 2.22 | 7.72 | 5.82 | 10.3 | 5.34 |

D: Bulk distribution coefficient; $C_0$: Parent; $C_{L\,R}$: Real daughter; $C_{L\,C}$: Calculated daughter; acc.: Accessory minerals
Distribution coefficients (Kds) for D in Table 14 of the Appendix

## 9.4.3. IU monzogranites geochemical modelling

Finally, in the case of the IU, the geochemical modelling results in two plausible models (IU-A model: $\Sigma R2 = 0.47$ and IU-B model $\Sigma R2 = 0.17$) that would explain the observed variations in major-elements.

In both models, the sample JE 15 66 was considered as $C_0$ and the sample SB 162 as $C_L$. One of these models (IU-A) considers biotite as the mafic fractionating mineral (Fig. 65), whereas in the other model (IU-B) it is replaced by cordierite (Table 21). In both cases it is required a 18–20% fractional crystallization, where the mineral assemblage would be constituted by K-feldspar + plagioclase (oligoclase) + a mafic phase (biotite or cordierite, respectively). The first model (IU-A) implies lower proportions of the fractionated mafic phase (7 % of biotite) and shows a higher $\Sigma R^2$ (0.47).

In fact, the extremely low contents of Rb in analyzed cordierites from the Sierra Bermeja Pluton (Table 4 of the Appendix) denotes that cordierite takes insignificant amounts

of Rb, systematically compromising the results for the modelling of the observed behaviour of Rb.

Likewise, the tendency defined by the studied monzogranites in the $R_1$ *vs*. $R_2$ diagram (Fig. 46 C) points to biotite as the principal mafic fractionating mineral instead of cordierite. Consequently, the IU-A model would be the most suitable. Moreover, this model reproduces well the variation of Ba and Rb in log(Ba) *vs*. log (Sr) diagram (Fig. 66 A). In this model, minor amounts of apatite, monazite and xenotime were also included to adjust for the REE, Y, Th and U data (Fig. 66 B; Table 22).

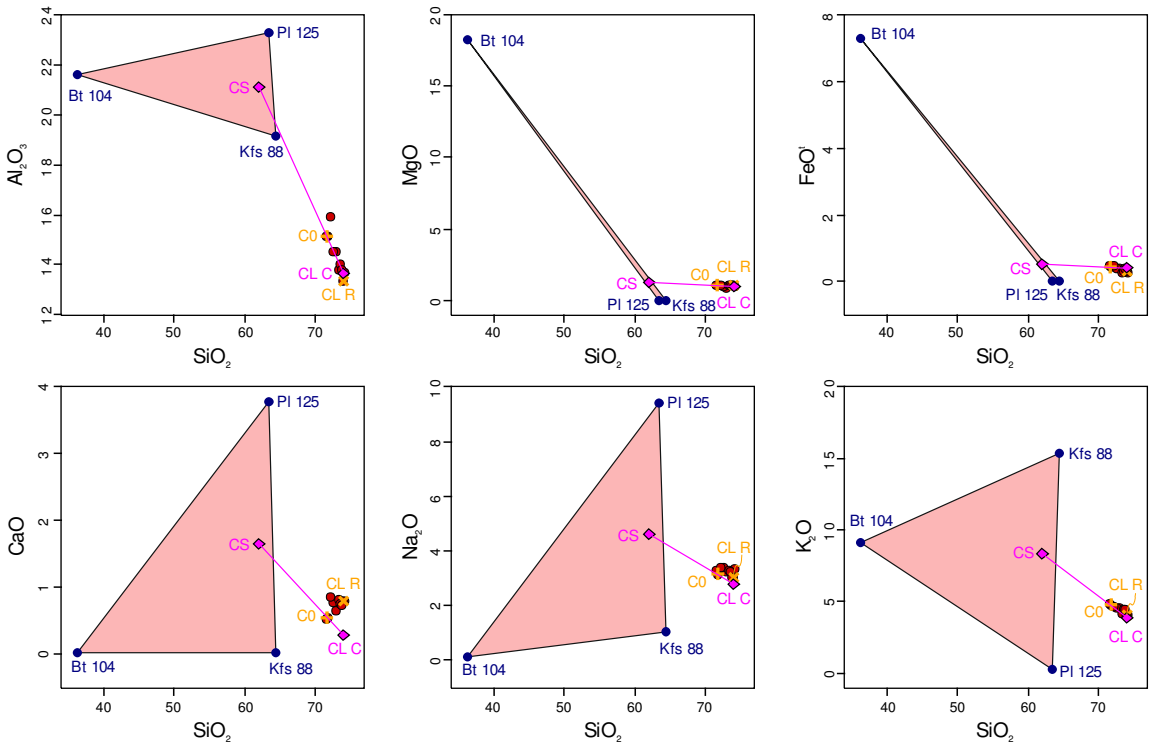


**Figure 65.** Geometric representation of the major-element geochemical modelling of the IU monzogranites.

***Table 21.*** *Results of the fractional crystallization modelling of the IU monzogranites*

| Degree of fractional crystallization 19.6 %<br>$\Sigma R^2 = 0.47$ | | | | | | | | |
|---|---|---|---|---|---|---|---|---|
| IU-A | $C_0$<br>JE 15 66 | Kfs 88[a]<br>(49.6 %) | Pl 125[a]<br>(43.4 %) | Bt 104[a]<br>(7.0 %) | $C_{L\,R}$<br>SB 162 | $C_{L\,C}$ | Difference | $C_S$ |
| $SiO_2$ | 71.76 | 64.44 | 63.46 | 36.13 | 74.08 | 74.13 | -0.05 | 62.03 |
| $Al_2O_3$ | 15.12 | 19.14 | 23.25 | 21.59 | 13.38 | 13.67 | -0.29 | 21.09 |
| $FeO^t$ | 1.07 | 0.00 | 0.00 | 18.19 | 1.11 | 1.02 | 0.09 | 1.27 |
| MgO | 0.44 | 0.01 | 0.02 | 7.27 | 0.30 | 0.42 | -0.12 | 0.52 |
| CaO | 0.55 | 0.03 | 3.77 | 0.03 | 0.80 | 0.28 | 0.52 | 1.65 |
| $Na_2O$ | 3.15 | 1.05 | 9.41 | 0.14 | 3.04 | 2.79 | 0.25 | 4.61 |
| $K_2O$ | 4.77 | 15.40 | 0.23 | 9.12 | 4.08 | 3.89 | 0.19 | 8.38 |
| Degree of fractional crystallization 17.8 %<br>$\Sigma R^2 = 0.17$ | | | | | | | | |
| IU-B | C0<br>JE 15 66 | Kfs 88[a]<br>(52.7 %) | Pl 125[a]<br>(27.9 %) | Crd 24[a]<br>(19.5 %) | $C_{L\,R}$<br>SB 162 | $C_{L\,C}$ | Difference | $C_S$ |
| $SiO_2$ | 71.76 | 64.44 | 63.46 | 47.61 | 74.08 | 74.12 | -0.04 | 60.89 |
| $Al_2O_3$ | 15.12 | 19.14 | 23.25 | 31.49 | 13.38 | 13.48 | -0.10 | 22.69 |
| $FeO^t$ | 1.07 | 0.00 | 0.00 | 7.99 | 1.11 | 0.96 | 0.15 | 1.56 |
| MgO | 0.44 | 0.01 | 0.02 | 6.15 | 0.30 | 0.27 | 0.03 | 1.21 |
| CaO | 0.55 | 0.03 | 3.77 | 0.01 | 0.80 | 0.44 | 0.36 | 1.07 |
| $Na_2O$ | 3.15 | 1.05 | 9.41 | 1.81 | 3.04 | 3.07 | -0.03 | 3.53 |
| $K_2O$ | 4.77 | 15.40 | 0.23 | 0.01 | 4.08 | 4.03 | 0.05 | 8.18 |

$\Sigma R^2$: sum of squared residuals

$C_0$: Parent; $C_{L\,R}$: Real daughter; $C_{L\,C}$: Calculated daughter; $C_S$: Cumulate

[a]Code from the Supplementary Tables of the Appendix

The calculations were carried out using an unpublished R-language plugin for the GCDkit software (Janoušek *et al.*, 2006)

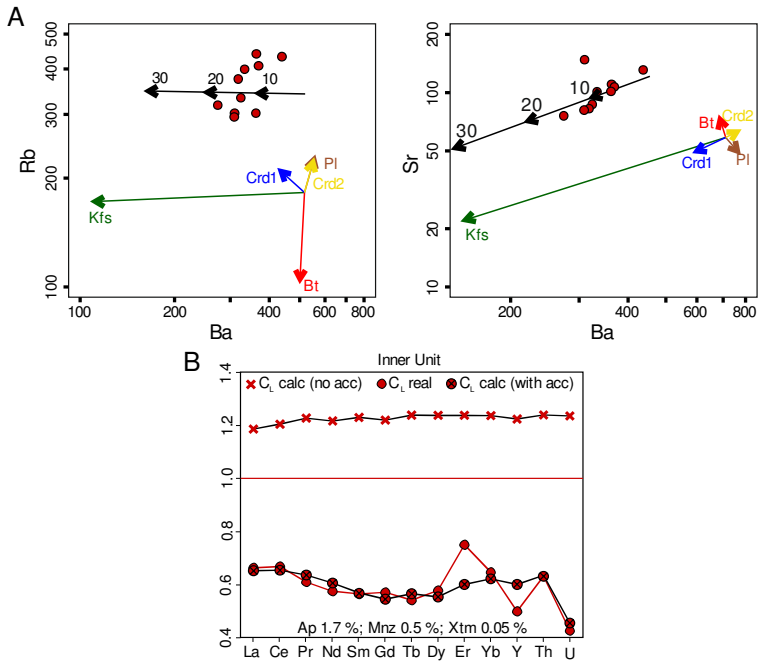


**Figure 66.** A) Results of the Rb–Ba–Sr modelling of the IU monzogranites from the Sierra Bermeja Pluton (considering model IU-A of Table 21). The partition coefficients calculated dividing the average contents in analyzed main rock-forming minerals (Table 4 of the Appendix) by the average contents considering all monzogranite samples of the three units (Table 15). B) Results of the trace-element modelling of the IU monzogranites (considering model IU-A of Table 21). Daughters ($C_L$)

have been normalized to the parent ($C_0$) selected for major-element modelling. Bulk distribution coefficient in Table 22 and distribution coefficients (Kds) in Table 14 of the Appendix.

***Table 22.*** *Data and results of the fractional crystallization modelling of selected trace element and REE of the IU monzogranites*

| | D No acc. | D Yes acc. | $C_0$ JE 15 66 | $C_{L\,R}$ SB 162 | $C_{L\,C}$ No acc. | $C_{L\,C}$ Yes acc. |
|---|---|---|---|---|---|---|
| La | 0.218 | 2.96 | 23.4 | 15.5 | 27.8 | 15.3 |
| Ce | 0.149 | 2.95 | 47.2 | 31.5 | 56.8 | 30.9 |
| Pr | 0.063 | 3.08 | 5.72 | 3.49 | 7.02 | 3.64 |
| Nd | 0.105 | 3.30 | 20.8 | 11.9 | 25.3 | 12.6 |
| Sm | 0.053 | 3.59 | 4.46 | 2.51 | 5.48 | 2.53 |
| Gd | 0.091 | 3.79 | 3.48 | 1.98 | 4.24 | 1.89 |
| Tb | 0.022 | 3.62 | 0.457 | 0.247 | 0.566 | 0.258 |
| Dy | 0.026 | 3.72 | 2.09 | 1.20 | 2.58 | 1.15 |
| Er | 0.025 | 3.34 | 0.919 | 0.689 | 1.14 | 0.551 |
| Yb | 0.028 | 3.19 | 0.859 | 0.555 | 1.06 | 0.533 |
| Y | 0.077 | 3.34 | 10.3 | 5.14 | 12.6 | 6.18 |
| Th | 0.020 | 3.09 | 9.82 | 6.19 | 12.2 | 6.22 |
| U | 0.031 | 4.62 | 9.28 | 3.95 | 11.5 | 4.21 |

D: Bulk distribution coefficient; $C_0$: Parent; $C_{L\,R}$: Real daughter; $C_{L\,C}$: Calculated daughter; acc.: Accessory minerals
Distribution coefficients (Kds) for D in Table 14 of the Appendix

## 9.5. GEOTECTONIC CONSIDERATIONS

The newly obtained zircon and monazite U–Pb emplacement ages for the monzogranite units are the same within error, *ca.* 306 Ma (Pennsylvanian), which coincides with the extension and collapse of the Iberian sector of the Variscan Belt (320–300 Ma; Martínez Catalán *et al.*, 2009). This age falls also within the main Variscan magmatic event recorded in the Iberian Massif that generated huge magma volumes of granitic (s.l.) composition, developed mainly in the age range of 330–290 Ma (*e.g.* Bea *et al.*, 1999, 2003; Carracedo *et al.*, 2009; Dias *et al.*, 1998; Gutiérrez-Alonso *et al.*, 2011; Merino Martínez *et al.*, 2014; Orejana *et al.*, 2012; Solá *et al.*, 2009; Villaseca *et al.*, 2012).

At *ca.* 310–305 Ma, melting of the lower crust and asthenospheric mantle, resulting from thinning of the lithosphere and asthenospheric upwelling, led to the generation of mafic

rocks, infracrustal I-type granitoids and peraluminous Bt–Crd granodiorites and monzogranites (Carracedo *et al*., 2009; Gutiérrez-Alonso *et al*., 2011). In this period, the development of an orocline may have controlled the localization of the Variscan Iberian granitoids (Gutiérrez-Alonso *et al*., 2011). The melting for the production of granitoids occurred mainly due to long-term *in situ* radiogenic heat production in a thickened crust (*e.g*. Bea *et al*., 1999, 2003; Merino Martínez *et al*., 2014; Villaseca *et al*., 2012), supplemented by an input of mantle-derived magmas during crustal extension and decompression (*e.g*. Carracedo *et al*., 2009; Castro *et al*., 1999; Dias *et al*., 1998). In this sense, although little mantle contribution is suggested, some mantle–crust interaction is widely accepted in many areas of the Central Iberian Zone (*e.g*. Carracedo *et al*., 2009; Castro *et al*., 1999; Dias *et al*., 1998). Additionally, lithospheric shear zones seem to have played a crucial role during this period of voluminous magmatism, since they may favored the ascent of the magmas (Alonso Olazabal *et al*., 1999; Carracedo *et al*., 2009; Gutiérrez-Alonso *et al*., 2011).

The suggested melting of lower crustal materials for the origin of the studied monzogranites and the apparent absence of a genetic linkage with the coeval vaugnerite series rocks reinforce an exclusively crustal origin. Although mantle heat supply was not critical for the melting of such materials, the near coeval emplacement of mantle-derived magmas (vaugnerites) denotes that some kind of heat supply bu mantle-derived magmas may existed during granite generation. On the other hand, considering the spatial relation of the studied pluton with the Alegrete–San Pedro de Mérida–Montoro Thrust, which puts into contact the Cadomian dioritoids of the Ossa-Morena Zone (the Mérida Massif) and the metasedimentary Schist and Greywacke sequence of the Central Iberian Zone (Fig. 15 in Chapter 4) it seems probable that magma ascent took place by the leveraging of this large-scale brittle crustal structure.

## 9.6. PETROGENETIC MODEL FOR THE SIERRA BERMEJA PLUTON

As stated in the second section of this chapter, key points to decipher in petrogenetic studies of granitic plutons are such as source materials, mechanism of melting and magma differentiation processes, together with emplacement timing and P–T conditions (*e.g.* Anderson, 1996; Clemens and Stevens, 2012; Petford *et al.*, 2000; Wilson, 1993). In this sense, the main outcomes from previous sections allow to propose a petrogenetic model for the monzogranites from the Sierra Bermeja Pluton, which is summarized below and illustrated in Fig. 67.

The geological setting that governed since the early stages of the development of the Sierra Bermeja Pluton was framed in the boundary between the Ossa-Morena and Central Iberian Zones of the Iberian Massif, which was demarcated by the lithospheric-scale Alegrete–San Pedro de Mérida–Montoro Thrust (Fig. 67 A). Melting of monzogranites sources occurred at middle to lower crustal levels, after a thermal maturation by radiogenic heating of a thickened crust. For the OU monzogranites, melting process took place at ~870ºC, and subsequent crystallization started in the range of 760–780ºC. Cambro-Ordovician felsic metaigneous rocks plus subordinate metasediments similar to those of the Schist Greywacke Complex are the most plausible sources for the generation of the OU magmas, which probably ascended through the Alegrete–San Pedro de Mérida–Montoro Thrust and emplaced at *ca.* 308 Ma and ~3 kbar (Fig. 67 B).

MU magmas were derived from similar sources to those of the OU monzogranites, with higher input of the Neoproterozoic–Lower Cambrian metasediments. Melting of such hybrid sources happened at slightly lower temperatures (~830 ºC) and depths, and concomitant crystallization started at 740–770 ºC. MU magmas probably followed the same

ascent and emplacement mechanism to those of the OU, emplacing at 304 ± 3 Ma (Zrn) and < 3 kbar (Fig. 67 C).

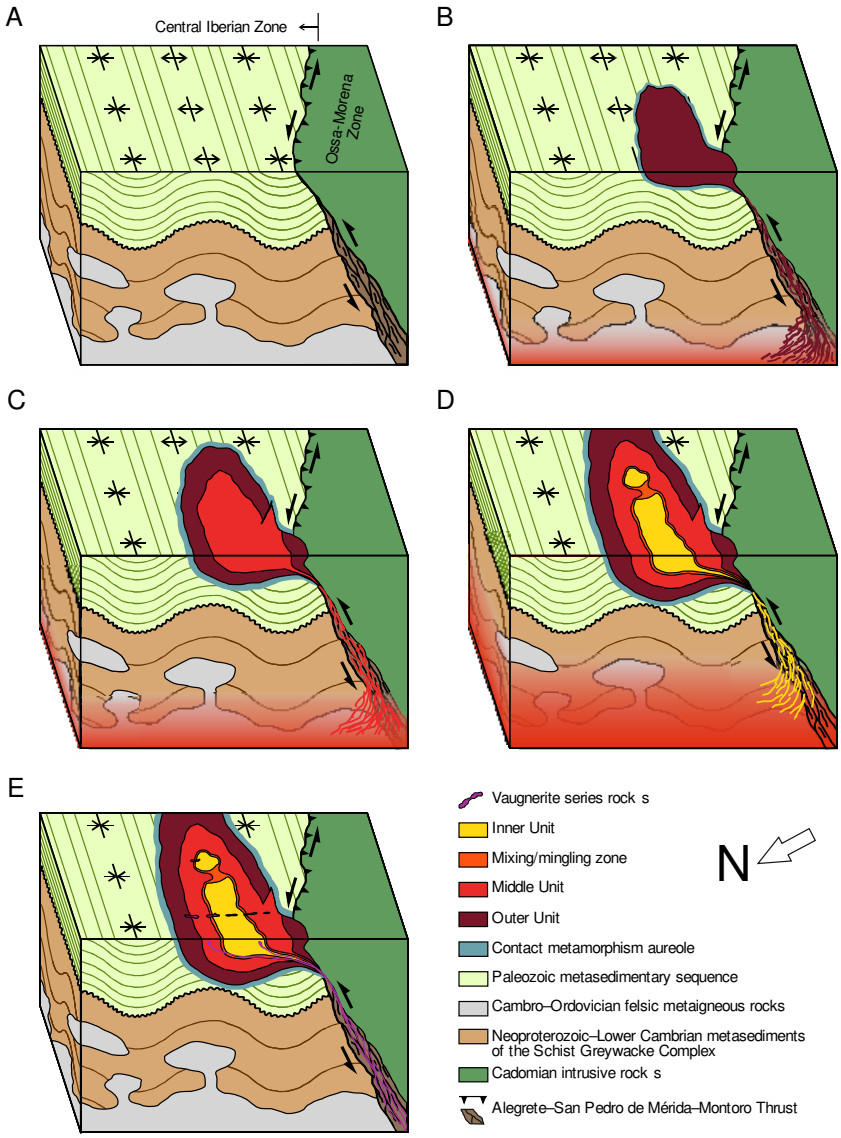


**Figure 67.** Schematic 3D block diagrams that illustrate the proposed petrogenetic model for the genesis of the Sierra Bermeja Pluton. See text for a description.

Neoproterozoic–Lower Cambrian metasediments, similar to those of the Schist–Greywacke Complex, controlled almost completely the source of the IU (with minor amounts of Cambro-Ordovician felsic metaigneous rocks), which melted at ~810 ºC and consequently at slightly shallower depths. IU magmas started crystallizing at 720–770 ºC, and probably ascended as other monzogranite magmas by the leveraging of the Alegrete–

San Pedro de Mérida–Montoro Thrust. The ascent and emplacement (at < 3 kbar) of these magmas took place subsequently, but almost concurrently, to those of the MU, generating the observed mixing/mingling belt between these two monzogranite units (Fig. 67 D). The three distinguished monzogranite units evolved independently, by 21–26% fractionational crystallization of a mineral assemblage constituted by Kfs + Pl > Bt >> Ap + Mnz + Xtm. Finally, before the almost complete consolidation of studied monzogranites, emplaced the studied vaugnerite series rocks (Fig. 67 E), follower by later calc-alkaline lamprophyres.

## 9.7. OPEN QUESTIONS

Although the here presented petrogenetic model reproduces well the field, textural, mineralogical, and geochemical characteristics/variations observed in the monzogranites from the Sierra Bermeja Pluton, some questions still remain open. These questions could be grouped into three main subjects: 1) the extension of the proposed model to other 'Serie Mixta'-type granitoids, 2) the petrogenesis of the vaugnerite series rocks and calc-alkaline lamprophyres emplaced in the monzogranites from the here studied pluton, and finally, 3) magma ascent and emplacement mechanisms.

### 9.7.1. Extrapolation of the proposed model

Overall, the assignment of the Sierra Bermeja Pluton as 'Serie Mixta'-type it does not require an important discussion. Nevertheless, the detailed characterization of the monzogranites from the studied massif has allowed to distinguish three main monzogranite-types with different petrographic and geochemical characteristics. Consequently, it is essential to highlight the main features of these monzogranite units in order to analyze the suitability of their individual inclusion into the 'Serie Mixta'-type granitoids.

As summarized in the introduction section, the so-called 'Serie Mixta' granitoids show relatively abundant large K-feldspar phenocrysts and include high cordierite contents. Plagioclase displays Ca-poor rims and Ca-rich cores, and the accessory mineral assemblage includes apatite, monazite, xenotime, ilmenite, zircon, andalusite/sillimanite, garnet and tourmaline (*e.g.* Alonso Olazabal, 2001; Alonso Olazabal *et al.*, 1999; Bea, 2004; Capdevila *et al.*, 1973; Carracedo, 1991; Carracedo *et al.*, 2005, 2009; Castro *et al.*, 2002; Corretgé *et al.*, 1977, 2004; García-Moreno *et al.*, 2007; González Menéndez, 1998; Larrea, 1998). Geochemically, these monzogranites have relatively low CaO and high $P_2O_5$ contents, showing a highly peraluminous character and a marked perphosphorous trend. In some cases these granitoids show notable coincidences in isotopic signatures (Sr, Nd, O, Hf) with the surrounding metasedimentary Schist-Greywacke Complex (*e.g.* Roda-Robles *et al.*, 2018 and references therein).

In the Sierra Bermeja Pluton, OU monzogranites show high K-feldspar phenocryst contents (up to ~350 crystals/$m^2$), but cordierite is not particularly abundant (up to 5 vol.%). Plagioclase cores show andesine–oligoclase compositions (up to $An_{\sim 30}$), and accessory minerals coincide with those of the 'Serie Mixta'-type granitoids. CaO contents are moderate to relatively low (average of 1.63 wt.%), as well as $P_2O_5$ contents (0.19–0.24 wt.%) and peraluminosity indexes (A/CNK = 1.01–1.15). On the other hand, the MU and IU monzogranites do not show K-feldspar phenocrysts, but cordierite contents are particularly high (up to 10 vol.%). Plagioclase cores display oligoclase compositions(up to $An_{\sim 20}$), with the same accessory mineral assemblage to that of the OU. Whole-rock compositions show that CaO contents are low in both units, with average contents of 0.93 wt.% in the MU and 0.73 wt.% in the IU. MU monzogranites have moderate $P_2O_5$ contents (0.20–0.27 wt.%) and peraluminosity indexes (1.06–1.23), whereas those parameters in the IU monzogranites are high ($P_2O_5$ = 0.23–0.35 wt.%; A/CNK = 1.21–1.33). Thus, none of the monzogranite units

meets all requirements of the 'Serie Mixta' granitoids *s.s.*, which leads to a possible consideration of the 'Serie Mixta' granitoids as a heterogeneous group of granites.

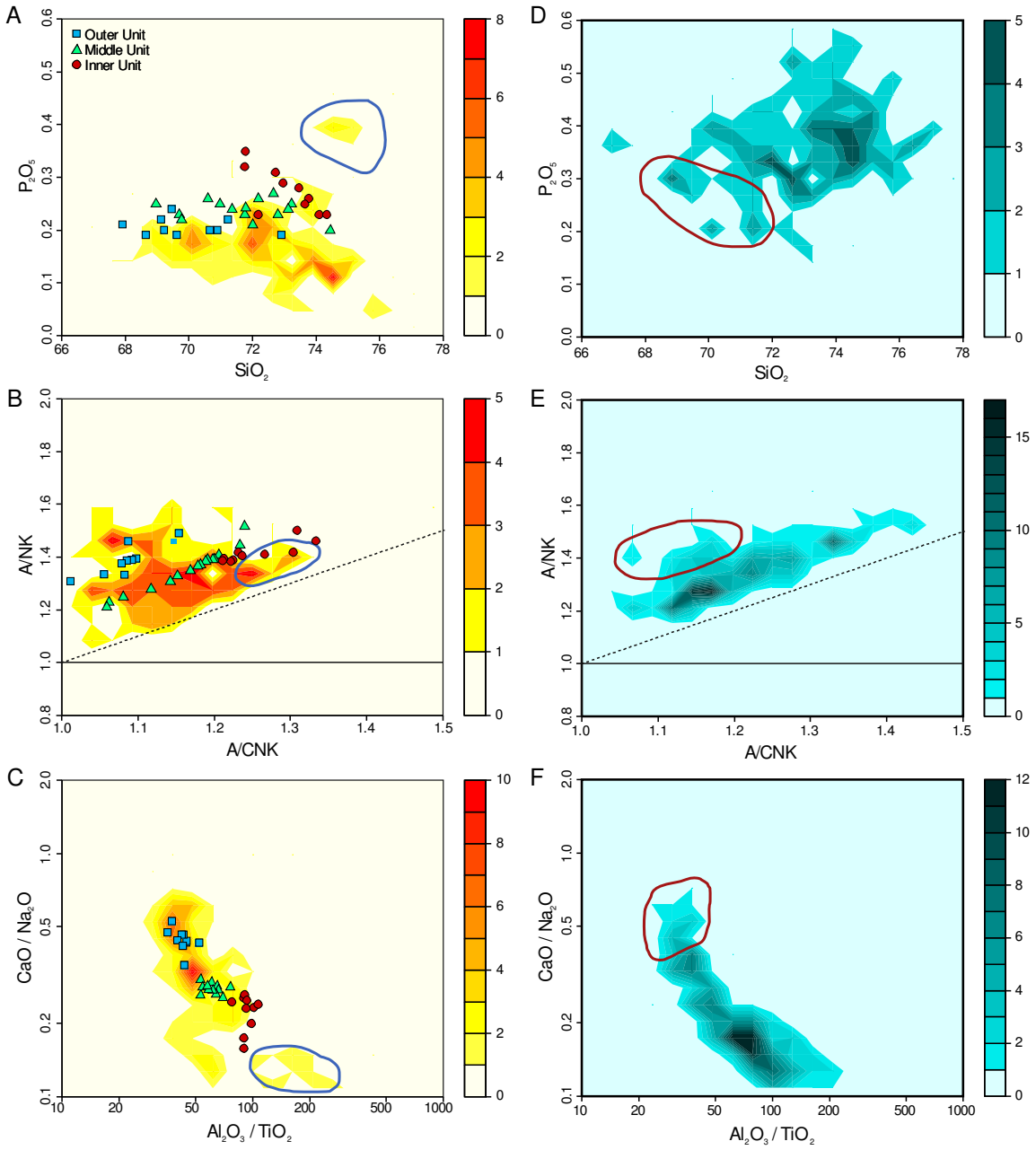


**Figure 68.** A), B) and C) Whole-rock composition density diagrams for the granitoids from the central and eastern areas of the Nisa–Alburquerque–Los Pedroches Magmatic Alignment (n = 130, data of the Sierra Bermeja Pluton not included). D), E) and F) Whole-rock composition density diagrams for the granitoids from the Nisa–Alburquerque Batholith and the rest of the granitoids traditionally considered as of the 'Serie Mixta'-type (n = 176). Fields delimited in blue and red lines correspond to some leucogranites and most of the granodioritic terms, respectively (see tect). Data from Alonso Olazabal (2001), Antunes *et al.* (2008), Carracedo (1991), Chicharro *et al.* (2014), Corretgé and Suárez (1994), Corretgé *et al.* (1985), Errandonea-Martin *et al.* (2017), Fernández *et al.* (1990), García-Casco *et al.* (1989), García-Moreno (2004), García-Moreno and Corretgé (2000), González Menéndez (1998, 2002), Larrea (1998), Matia Villarino *et al.* (1990), Merino Martinez *et al.* (2014), Neiva *et al.* (2011), Pesquera *et al.* (2017), Ramírez and Grundvig (2000) and Ramírez and González Menéndez (1999).

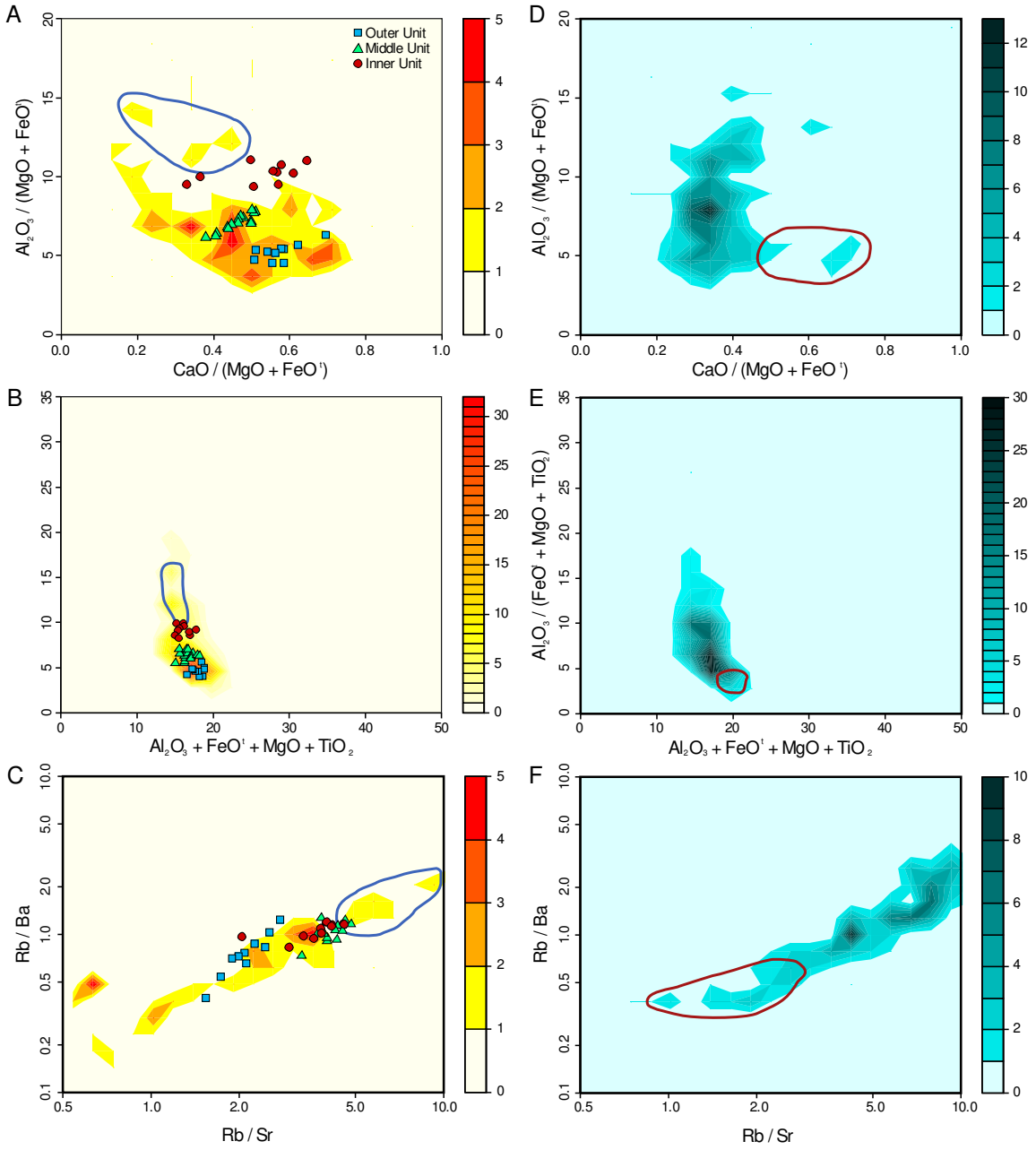


**Figure 69.** A), B) and C) Whole-rock composition density diagrams for the granitoids from the central and eastern areas of the Nisa–Alburquerque–Los Pedroches Magmatic Alignment (n = 130, data of the Sierra Bermeja Pluton not included). D), E) and F) Whole-rock composition density diagrams for the granitoids from the Nisa–Alburquerque Batholith and the rest of the granitoids traditionally considered as of the 'Serie Mixta'-type (n = 176). Fields delimited in blue and red lines correspond to some leucogranites and most of the granodioritic terms, respectively (see tect). Data from Alonso Olazabal (2001), Antunes *et al.* (2008), Carracedo (1991), Chicharro *et al.* (2014), Corretgé and Suárez (1994), Corretgé *et al.* (1985), Errandonea-Martin *et al.* (2017), Fernández *et al.* (1990), García-Casco *et al.* (1989), García-Moreno (2004), García-Moreno and Corretgé (2000), González Menéndez (1998, 2002), Larrea (1998), Matia Villarino *et al.* (1990), Merino Martinez *et al.* (2014), Neiva *et al.* (2011), Pesquera *et al.* (2017), Ramírez and Grundvig (2000) and Ramírez and González Menéndez (1999).

In this sense, a preliminary study of several 'Serie Mixta'-type granitoids (> 300 analyses) show differences between 1) those intrusions from the central and eastern areas of

the Nisa–Alburquerque–Los Pedroches Magmatic Alignment, and 2) the Nisa–Alburquerque Batholith and the rest of the granitoids of the Central Iberian Zone traditionally considered as 'Serie Mixta'-type. These differences are observable in major- and trace-elements, as well as in Sr–Nd isotopes (Figs. 68 to 70). At first glance, it seems that the first group shows lower $P_2O_5$ and $SiO_2$ contents (Fig. 68 A and D), and higher $CaO/Na_2O$ ratios and A/NK values, with slightly lower ones of A/CNK (Fig. 68 B, C, E and F). $CaO/(MgO + FeO^t)$ parameter is also higher in this group (Fig. 69 A and D), whereas Rb/Sr, Rb/Ba, and $Al_2O_3 / (FeO^t + MgO + TiO_2)$ ratios are, in general, lower (Fig. 69 B, C, E and F).

As it can be observed, leucogranites from the central and eastern areas of the Nisa–Alburquerque–Los Pedroches Magmatic Alignment (fields outlined in blue in Fig. 68 A, B, C and 68 A, B, C) show closer compositions to those granitoids of the second group, as well as to those of the IU monzogranites from the Sierra Bermeja Pluton. On the other hand, the MU and OU monzogranites plot within the most represented compositions of the central and eastern areas of the cited alignment, with slightly higher $P_2O_5$ contents (Figs. 68 and 69). In the same vein, the most granodioritic terms of the second group of granitoids (fields outlined in red in Fig. 68 D, E, F and 68 D, E, F) plot close to the granitoids from the central and eastern areas of the Nisa–Alburquerque–Los Pedroches Magmatic Alignment (Figs. 68 and 69).

Sr–Nd isotope systematics show slight differences between these two groups of granitoids too, since those intrusions from the central and eastern areas of the Nisa–Alburquerque–Los Pedroches Magmatic Alignment exhibit lower $^{87}Sr/^{86}Sr$ initials (recalculated to 300 Ma) respect to the remaining 'Serie Mixta'-type granitoids (Fig. 70). Nevertheless, in this respect, the scarce published Sr–Nd isotope data of the first group of granitoids (only 18 samples) prevents any robust conclusion.

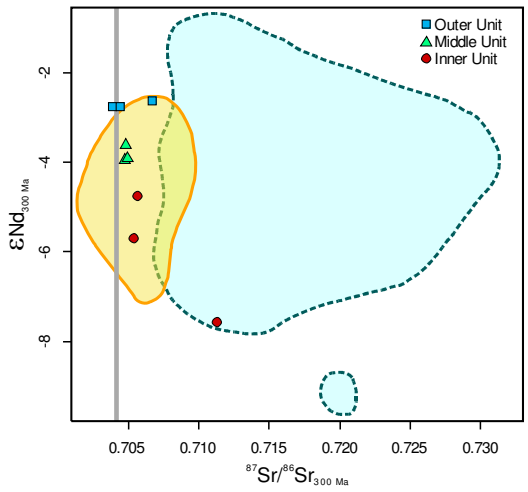


**Figure 70.** $^{87}Sr/^{86}Sr_{300}$ *vs.* $\varepsilon Nd_{300}$ binary plot for the granitoids from the central and eastern areas of the Nisa–Alburquerque–Los Pedroches Magmatic Alignment (solid line delimited field; n = 18, data of the Sierra Bermeja Pluton not included) and granitoids from the Nisa–Alburquerque Batholith and the rest of the granitoids traditionally considered as of the 'Serie Mixta'-type (dashed line delimited field; n = 68). Data from Alonso Olazabal (2001), Antunes *et al.* (2008), Castro *et al.* (1999), Chicharro *et al.* (2014), Donaire *et al.* (1999), Errandonea-Martin *et al.* (2017), González Menéndez (1998), Jiménez San Pedro (2003), Merino Martínez *et al.* (2014), Neiva *et al.* (2011), Pesquera *et al.* (2017).

Although the present study provides a petrogenetic model that could be extensible to other granitoids integrated in the Iberian 'Serie Mixta', considering the above outlined geochemical characteristics, the extrapolation would require more detailed studies. Currently, it seems that the most suitable intrusives are those of the central and eastern areas of the Nisa–Alburquerque–Los Pedroches Magmatic Alignment.

## 9.7.2. Petrogenesis of the studied mesocratic rocks

The detailed characterization of the mesocratic rocks from the Sierra Bermeja Pluton has allowed their classification as of vaugnerite series rocks and calc-alkaline lamprophyres. Thus, based on petrogenetic studies of such rock types (*e.g.* Couzinié *et al.*, 2016; Holub, 1997; Janoušek and Holub, 2007; Rock, 1991; Scarrow *et al.*, 2009; Solgadi *et al.*, 2007; Turpin *et al.*, 1988; von Raumer *et al.*, 2014) it has been possible to point to a a probable provenance from a heterogeneous metasomatized mantle source, as it is generally accepted for similar rocks elsewhere. Nevertheless, some subjects regarding these rocks keep unresolved.

It seems that calc-alkaline lamprophyres from the Sierra Bermeja Pluton were emplaced markedly later respect to the studied vaugnerite series rocks, but the radiometric age of these aphanitic terms remains undetermined. If finally these lamprophyres and vaugnerites *s.l.* were near coeval, a new petrogenetic discussion may arise about the possible petrogenetic linkage between these two rock-types. Additionally, considering field and petrographic characteristics of the studied mesocratic rocks is obvious that they have suffered some hybridization process with a felsic component (Fig. 22), but the nature of the later and the scale of the process remain open. Thus, several petrogenetic questions about the mesocratic rocks from the Sierra Bermeja Pluton continue pending.

### 9.7.3. Emplacement mechanism of the Sierra Bermeja Pluton

In this study shallow emplacement conditions (~3 kbar) are suggested for the Sierra Bermeja Pluton, which is in accordance with other intrusions of the Nisa–Alburquerque–Los Pedroches Magmatic Alignment (Alonso Olazabal, 2001; Alonso Olazabal *et al.*, 1999; González Menéndez, 1998, 2002; González Menéndez *et al.*, 2011;). Nevertheless, detailed studies of magma ascent and emplacement mechanisms persist undetermined in the Sierra Bermeja Pluton.

In the cited magmatic alignment different emplacement mechanisms are suggested. Ascent and emplacement of magmas controlled by a crustal scale dextral transtensional shear zone has been proposed in the Los Pedroches Batholith (Carracedo *et al.*, 1994; Aranguren *et al.*, 1997), similarly to the nearby Campanario-La Haba Pluton (Alonso Olazabal, 2001; Alonso Olazabal *et al.*, 1999). Contrarily, a passive emplacement is suggested for the emplacement of the Nisa–Alburquerque Batholith (González Menéndez, 2002; González Menéndez and Bea, 2004; González Menéndez *et al.*, 2011).

Regarding the Sierra Bermeja Pluton, the only published structural study is that of Sarrionandia *et al*. (2004), but it deals mainly with the fracturing of the monzogranites. Nevertheless, its spatial proximity to the Alegrete–San Pedro de Mérida–Montoro Thrust and to the Campanario-La Haba Pluton, the elongated morphology of the pluton, and the local shear zones observed in some outcrops of the MU monzogranites argues in favor of a similar mechanism controlled by the mentioned thrust. Nonetheless, as mentioned, a detailed study of magma ascent and emplacement mechanisms remains unsolved in the Sierra Bermeja Pluton.

# CHAPTER 10
# CONCLUSIONS

## MAIN CONCLUSIONS

1) The Sierra Bermeja Pluton is a nested intrusion, representative of the 'Serie Mixta'-type granioids, located within the regional scale Nisa–Alburquerque–Los Pedroches Magmatic Alignment (southern Iberian Massif). The massif is comprised by several cordierite-bearing peraluminous monzogranite lithotypes, plus NE–SW trending mesocratic rocks, aplites and quartz dykes.

2) Monzogranites of the Sierra Bermeja Pluton can be grouped into three main units, whose emplacement proceeded in the sequence of Outer Unit (OU) → Middle Unit (MU) → Inner Unit (IU), that is, inwards. On the other hand, the mesocratic rocks are classified as dioritoid members of the vaugnerite series rocks and calc-alkaline lamprophyres.

3) The studied monzogranites were most likely produced by partial melting of distinct crustal sources. The source of OU was presumably dominated by Cambro–Ordovician felsic metaigneous rocks, whereas metasediments similar to those of the Neoproterozoic–Lower Cambrian Schist–Greywacke Complex became more important for the MU and controlled almost completely the source of the IU.

4) Melting of the abovementioned sources occurred at ~830–870 ºC and middle to lower crustal levels. Crystallization temperatures, slightly decreasing inward, vary in the range of 710–810 ºC, and all monzogranites were emplaced at relatively shallow crustal levels (< 3 kbar). Taken together, thermobarometric data suggest that melting and melt

extraction could have progressed upward through the geological record by the leveraging of the Alegrete–San Pedro de Mérida–Montoro Thrust.

5) Geochemical modelling indicates that the evolution of each unit was controlled by 21–26% fractionation of a mineral assemblage constituted by Kfs + Pl > Bt >> Ap + Mnz + Xtm.

6) The newly obtained LA-ICP-MS U–Pb ages on zircon and monazite yield, within the error, the same Pennsylvanian (Variscan) ages of 306 Ma (OU: 308 ± 3 Ma Zrn, 309 ± 3 Ma Mnz; MU: 304 ± 3 Ma Zrn) for the emplacement of the Sierra Bermeja Pluton monzogranites, which coincides with the age of the main granite generation event of the Central Iberian Zone. In the same vein, the newly obtained LA-ICP-MS U–Pb ages on apatite gives an age of 305 ± 17 Ma for the emplacement of the studied vaugneritic dioritoids.

7) At least two different mantle-derived magma pulses, a first one of vaugneritic type, and a later one of calc-alkaline lamprophyres, were emplaced in the Sierra Bermeja Pluton. Vaugneritic syn-plutonic dykes would depict coeval mantle- and crustal-melting processes during late-Variscan stages, while calc-alkaline lamprophyres may mark the ending of the cited stage.

8) The current study provides a petrogenetic model that deals with the 'Serie Mixta'-type granitoids of the Iberian Massif, constituting a pertinent basis for future experimental and petrogenetic works on the origin of these particular granitoids. Yet, a detailed comparison would be required to extend the model to other plutons, although those from the central and eastern areas of the Nisa–Alburquerque–Los Pedroches Magmatic Alignment seem suitable.

# CHAPTER 11
# REFERENCES

Ábalos, B., Gil Ibarguchi, J.I., Sánchez Lorda, M.E., Paquette, J.L., 2012. Detrital zircon U–Pb study of early Cambrian conglomerates from the Sierra de la Demanda (N Spain): implications for West-African/Amazonian Proterozoic correlations of Iberia. Tectonics 31 (3), 22. https://doi.org/10.1029/2011TC003041

Abdel-Rahman, A.-F.M., 1994. Nature of biotites from alkaline, calc-alkaline, and peraluminous magmas. Journal of Petrology 35 (2), 525–541. https://doi.org/10.1093/petrology/35.2.525

Agencia Estatal de Meteorología de España, AEMET (2012). Guía resumida del clima en España (1981-2010). Retrieved from http://www.aemet.es/es/conocermas/recursos_en_linea/publicaciones_y_estudios/publicaciones/detalles/guia_resumida_2010

Agencia Estatal de Meteorología de España, AEMET, Instituto de Meteorologia de Portugal, IPMA (2011). *Iberian Climate Atlas*. Madrid: Closas-Orcoyen.

Albarède, F., 1995. Introduction to Geochemical Modeling. Cambridge University Press, Cambridge.

Alía-Medina, M., 1963. Rasgos estructurales de la baja Extremadura. Boletín de la Real Sociedad Española de Historia Natural (Geología) 20, 247 – 262.

Alonso Olazabal, A., 2001. El plutón de Campanario–La Haba: caracterización petrológica y fábrica magnética. PhD Thesis, University of the Basque Country (323 pp.).

Alonso Olazabal, A., Carracedo, M., Aranguren, A., 1999. Petrology, magnetic fabric and emplacement in a strike-slip regime of a zoned peraluminous granite: the Campanario–La Haba Pluton, Spain. In: Castro, A., Fernandez, C., Vigneresse, J.L. (Eds.), Understanding Granites: Integrating New and Classical Techniques. Geological Society, London, Special Publications 168, 177–190. https://doi.org/10.1144/GSL.SP.1999.168.01.12

Álvarez Martínez, J. M., Nogales Basarrarte, T., 2014. Presas de Augusta Emerita y de sus alrededores. In F. Baratte, C. J. Robin, and E. Rocca, (Eds.), Regards croisés d'Orient et d'Occident. Les barrages dans l'Antiquité tardivet. Actes du colloque organisé dans le cadre du programme ANR EauMaghreb, 163–177.

Anderson, J.L., 1996. Status of thermobarometry in granitic batholiths. Transactions of the Royal Society of Edinburgh: Earth Sciences 87 (1–2), 125-138. https://doi.org/10.1017/S0263593300006544

Annen, C., Sparks, R.S.J., 2002. Effects of repetitive emplacement of basaltic intrusions on thermal evolution and melt generation in the crust. Earth and Planetary Science Letters 203 (3–4), 937–955. https://doi.org/10.1016/S0012-821X(02)00929-9

Annen, C., Blundy, J.D., Sparks, R.S.J., 2006. The Genesis of Intermediate and Silicic Magmas in Deep Crustal Hot Zones. Journal of Petrology 47 (3), 505–539. https://doi.org/10.1093/petrology/egi084

Antunes, I.M.H.R., Neiva, A.M.R., Silva, M.M.V.G., 2010. Isotopic geochronology of granitic rocks from the Central Iberian Zone: comparison of methodologies. Estudios Geológicos 66 (1), 45–50. https://doi.org/10.3989/egeol.40143.097

Aparicio, A., Barrera, J.L., Casquet, C., Peinado, M., Tinao, J.M., 1977. Caracterización Geoquímica del plutonismo post-metamórfico del SO del Macizo Hespérico. Studia Geologica XII, 9–39.

Aranguren, A., Larrea, J.F., Carracedo, M., Cuevas, J., Tubía, J.M., 1997. The Los Pedroches Batholith (Southern Spain): Polyphase Interplay between Shear Zones in Transtension and Setting of Granites. In: Bouchez J.L., Hutton D.H.W., Stephens W.E. (Eds.), Granite: From Segregation of Melt to Emplacement Fabrics. Petrology and Structural Geology, Springer, Dordrecht, pp. 215–229. https://doi.org/10.1007/978-94-017-1717-5_14

Artemieva, I.M., Thybo, H., Jakobsen, K., Sørensen, N.K., Nielsen, L.S.K., 2017. Heat production in granitic rocks: Global analysis based on a new data compilation GRANITE2017. Earth-Science Reviews 172, 1–26. https://doi.org/10.1016/j.earscirev.2017.07.003

Azor, A., Lodeiro, F.G., Simancas, J.F., Bea, F., 1995. Geochronological constraints on the evolution of a suture: the Ossa-Morena/Central Iberian contact (Variscan Belt, south-west Iberian Peninsula). International Journal of Earth Sciences (Geologische Rundschau) 84 (2), 375–383. https://doi.org/10.1007/BF00260447

Bachmann, O., Dungan, M.A., Bussy, F., 2005. Insights into shallow magmatic processes in large silicic magma bodies: the trace element record in the Fish Canyon magma body, Colorado. Contributions to Mineralogy and Petrology 149 (3), 338–349. https://doi.org/10.1007/s00410-005-0653-z

Balcaen, L., De Schrijver, I., Moens, L., Vanhaecke, F., 2005. Determination of the $^{87}Sr/^{86}Sr$ isotope ratio in USGS silicate reference materials by multi-collector ICP-mass spectrometry. International Journal of Mass Spectrometry 242 (2–3), 251–255. https://doi.org/10.1016/j.ijms.2004.10.025

Bandrés, A., 2001. Evolución geodinámica poliorogénica de los dominios septentrionales de la zona de Ossa–Morena. PhD Thesis, University of the Basque Country (377 pp.).

Bandrés, A., Eguíluz, L., Gil Ibarguchi, J. I., Palacios, T., 2002. Geodynamic evolution of a Cadomian arc region: the northern Ossa-Morena zone, Iberian massif. Tectonophysics 352 (1–2), 105–120. https://doi.org/10.1016/S0040-1951(02)00191-9

Bandrés, A., Eguíluz, L., Pin, C., Paquette, J. L., Ordoñez, B., Le Fèvre, B., Ortega, L. A., Gil Ibarguchi, J. I., 2004. The northern Ossa-Morena Cadomian batholith (Iberian Massif): magmatic arc origin and early evolution. International Journal of Earth Sciences 93 (5), 860–885. https://doi.org/10.1007/s00531-004-0423-6

Barbarin, B., 1990. Granitoids: main petrogenetic classifications in relation to origin and tectonic setting. Geological Journal 25 (3–4), 227–238. https://doi.org/10.1002/gj.3350250306

Barbarin, B., 1996. Genesis of the two main types of peraluminous granitoids. Geology 24 (4), 295–298. https://doi.org/10.1130/0091-7613(1996)024<0295:GOTTMT>2.3.CO;2

Barbarin, B., 1999. A review of the relationships between granitoid types, their origins and their geodynamic environments. Lithos 46 (3), 605–626. https://doi.org/10.1016/S0024-4937(98)00085-1

Barbarin, B., 2005. Mafic magmatic enclaves and mafic rocks associated with some granitoids of the central Sierra Nevada batholith, California: nature, origin, and relations with the hosts. Lithos 80 (1–4) 155–177. https://doi.org/10.1016/j.lithos.2004.05.010

Barbero, L., 1992. Tres tipos de rocas gabroideas en el complejo de Toledo. Cadernos do Laboratorio Xeolóxico de Laxe 17, 173–186.

Barbero, L., Villaseca, C., Andonaegui, P., 1990. On the origin of the gabbro-tonalite-monzogranite association from Toledo area (Hercynian Iberian Belt). Schweizerische Mineralogische und Petrografische Mitterlung 70 (2), 207–219. http://doi.org/10.5169/seals-53614

Barral I Altet, X., 1991. La Antigüedad Clásica: Grecia, Roma y El Mundo Mediterraneo. In: J. Milicua (Ed.), Historia Universal del Arte, Vol. 2, Planeta, Vitoria.

Batchelor, R.A., Bowden, P., 1985. Petrogenetic interpretation of granitic rock series using multicationic parameters. Chemical Geology 48 (1–4), 43–55. https://doi.org/10.1016/0009-2541(85)90034-8

Bea, F., 1996a. Controls on the trace element composition of crustal melts. Transaction of the Royal Society of Edinburg: Earth Sciences 87 (1–2), 33–41. https://doi.org/10.1017/S0263593300006453

Bea, F., 1996b. Residence of REE, Y, Th and U in granites and crustal protoliths; implications for the chemistry of crustal melts. Journal of Petrology 37 (3), 521–552. https://doi.org/10.1093/petrology/37.3.521

Bea, F., 2004. La naturaleza del magmatismo de la Zona Centro Ibérica: consideraciones generales y ensayo de correlación. In: Vera, J.A., (Ed.), Geología de España. Sociedad Geológica de España-Instituto Geológico y Minero de España (SGE-IGME), Madrid, pp. 128–133.

Bea, F., 2012. The sources of energy for crustal melting and the geochemistry of heat-producing elements. Lithos 153, 278–291. https://doi.org/10.1016/j.lithos.2012.01.017

Bea, F., Fershtater, G., Corretgé, L.G., 1992. The geochemistry of phosphorus in granite rocks and the effect of aluminium. Lithos 29 (1–2), 43–56. http://dx.doi.org/10.1016/0024-4937(92)90033-U

Bea, F., Pereira, M.D., Corretgé, L.G., Fershtater, G.B., 1994a. Differentiation of strongly peraluminous, perphoshorous granites. The Pedrobernardo pluton, central Spain. Geochimica et Cosmochimica Acta 58, 2609–2628. http://dx.doi.org/10.1016/0016-7037(94)90132-5

Bea, F., Pereira, M.D., Stroh, A., 1994b. Mineral/leucosome trace-element partitioning in a peraluminous migmatite (a laser ablation-ICP-MS study). Chemical Geology 117 (1–4), 291–312. https://doi.org/10.1016/0009-2541(94)90133-3

Bea, F., Montero, P., Molina, J.F., 1999. Mafic precursors, peraluminous granitoids, and late lamprophyres in the Avila Batholith: a model for the generation of Variscan batholiths in Iberia. The Journal of Geology 107 (4), 399–419. http://dx.doi.org/10.1086/314356

Bea, F., Montero, P., Zinger, T., 2003. The nature, origin, and thermal influence of the granite source layer of Central Iberia. The Journal of Geology 111 (5), 579–595. http://dx.doi.org/10.1086/376767

Bea, F., Montero, P., González-Lodeiro, F., Talavera, C., Molina, J.F., Scarrow, J.H., Whitehouse, M.J., Zinger, T.F., 2006. Zircon thermometry and U-Pb ion-microprobe dating of the gabbros and associated migmatites of the Variscan Toledo Anatectic Complex, Central Iberia. Journal of the Geological Society, London 163, 847–855. https://doi.org/10.1144/0016-76492005-143

Beard, J.S., Ragland, P.C., Crawford, M.L., 2005. Reactive bulk assimilation: A model for crust-mantle mixing in silicic magmas. Geology 33 (8), 681–684. https://doi.org/10.1130/G21470.1

Beranoaguirre, A., 2016. Development of new analytical procedures of isotope geochemistry by mass spectrometry. Application to the study of high-pressure metamorphic rocks from the Iberian Massif. PhD Thesis, University of the Basque Country (248 pp.).

Blundy, J.D., Annen, C.J., 2016. Crustal Magmatic Systems from the Perspective of Heat Transfer. Elements 12 (2), 115–120. https://doi.org/10.2113/gselements.12.2.115

Bonin, B., 2004. Do coeval mafic and felsic magmas in post-collisional to within-plate regimes necessarily imply two contrasting, mantle and crustal, sources? A review. Lithos 78 (1–2), 1–24. https://doi.org/10.1016/j.lithos.2004.04.042

Bonin, B., 2007. A-type granites and related rocks: Evolution of a concept, problems and prospects. Lithos 97 (1–2), 1–29. https://doi.org/10.1016/j.lithos.2006.12.007

Bonin, B., Azzouni-Sekkal, A., Bussy, F., Ferrag, S., 1998. Alkali-calcic and alkaline post-orogenic (PO) granite magmatism: petrologic constraints and geodynamic settings. Lithos 45 (1–4), 45–70. https://doi.org/10.1016/S0024-4937(98)00025-5

Bonin, B., Bébien, J., Masson, P., 2002. Granite: A Planetary Point of View. Gondwana Research 5 (2), 261–273. https://doi.org/10.1016/S1342-937X(05)70722-X

Bons, P.D., Arnold, J., Elburg, M.A., Kalda, J., Soesoo, A., van Milligen, B.P., 2004. Melt extraction and accumulation from partially molten rocks. Lithos 78 (1–2), 25–42. https://doi.org/10.1016/j.lithos.2004.04.041

Bowen, N.L., 1928. The Evolution of the Igneous Rocks. Princeton University Press, Princeton.

Brilha, J., 2002. Geoconservation and protected areas. Environmental Conservation 29 (3), 273–276. https://doi.org/10.1017/S0376892902000188

Beetsma, J.J., 1995. The late Proterozoic/Paleozoic and Hercynian crustal evolution of the Iberian Massif, N Portugal, as traced by geochemistry and Sr–Nd–Pb isotope systematics of pre-Hercynian terrigenous sediments and Hercynian granitoids. PhD Thesis, Vrije Universiteit of Amsterdam (223 pp.).

Belcher, R.W., Kisters, A.F.M., 2006. Progressive adjustments of ascent and emplacement controls during incremental construction of the 3.1 Ga Heerenveen batholith, South Africa. Journal of Structural Geology 28 (8), 1406–1421. https://doi.org/10.1016/j.jsg.2006.05.001

Boehnke, P., Watson, E.B., Trail, D., Harrison, T.M., Schmitt, A.K., 2013. Zircon saturation re-revisited. Chemical Geology 351, 324–334. https://doi.org/10.1016/j.chemgeo.2013.05.028

Brown, G.C., 1977. Mantle origin of Cordilleran granites. Nature 265, 21–24. https://doi.org/10.1038/265021a0

Brown, M., 1994. The generation, segregation, ascent and emplacement of granite magma: the migmatite-to-crustally-derived granite connection in thickened orogens. Earth-Science Reviews 36 (1–2), 83-130. https://doi.org/10.1016/0012-8252(94)90009-4

Brown, M., 2013. Granite: From genesis to emplacement. Geological Society of America Bulletin 125 (7–8), 1079–1113. https://doi.org/10.1130/B30877.1

Buda, G., Dobosi, G., 2004. Lamprophyre-derived high-K mafic enclaves in Variscan granitoids from the Mecsek Mts. (South Hungary). Neues Jahrbuch für Mineralogie-Abhandlungen: Journal of Mineralogy and Geochemistry 180 (2), 115–147. https://doi.org/10.1127/0077-7757/2004/0180-0115

Buzzi, L., Gaggero, L., Grozdanov, L.,Yanev, S., Slejko, F., 2010. High-Mg potassic rocks in the Balkan segment of the Variscan belt (Bulgaria): implications for the genesis of orogenic lamproite magmas. Geological Magazine 147 (3), 434–450. https://doi.org/10.1017/S0016756809990550

Campbell, E.M., 1997. Granite landforms. Journal of the Royal Society of Western Australia 80, 101–112.

Capdevila, R., 1969. Le métamorphisme régional progressif et les granites dans le segment hercynien de Galice Nord orientale (NW de l'Espagne). PhD Thesis, University of Montpellier (430 pp.).

Capdevila, R., Corretgé, L.G., Floor, P., 1973. Les granitoídes varisques de la Meseta ibérique. Bulletin de la Société Géologique de France 15/7 (3–4), 209–228.

Carracedo, M., 1991. Contribución al estudio del batolito de los Pedroches: cartografía, petrología y geoquímica del batolito de Los Pedroches en las Hojas de El Viso, Pozoblanco y Fuencaliente (provincia de Córdoba). PhD Thesis, University of the Basque Country (443 pp.).

Carracedo, M., Eguíluz, L., Gil Ibarguchi, J.I., Tijero, F., 1990. Cartografía, petrología y geoquímica del plutón del Cerro Mogábar, batolito de Los Pedroches (Córdoba, España). Cadernos do Laboratorio Xeolóxico de Laxe 15, 105–118.

Carracedo, M., Larrea, F.J., Aranguren, A., Cuevas, J., Tubía, J.M., 1994. La falla de Conquista: una zona de cizalla dúctil transtensiva asociada al emplazamiento del batolito de Los Pedroches. Resúmenes de la XVI Reunión de Xeoloxía e Minería do NO Peninsular, Laboratorio Xeolóxico de Laxe, A Coruña, 51–55.

Carracedo, M., Gil Ibarguchi, J.I., García de Madinabeitia, S., Berrocal, T., 2005. Geocronología de los granitoides Hercínicos de la Serie Mixta: Edad U-Th-$Pb_{total}$ de monacitas del plutón de Cabeza de Araya (Zona Centro Ibérica) y de las manifestaciones filonianas asociadas. Revista de la Sociedad Geológica de España 18 (1–2), 75–86.

Carracedo, M., Paquette, J.L., Alonso Olazabal, A., Santos Zalduegui, J.F., García de Madinabeitia, S., Tiepolo, M., Gil Ibarguchi, J.I., 2009. U–Pb dating of granodiorite and granite units of the Los Pedroches Batholith. Implications for geodynamic models of the southern Central Iberian Zone (Iberian Massif). International Journal of Earth Sciences 98, 1609–1624. http://dx.doi.org/10.1007/s00531-008-0317-0

Carreras, J., Druguet, E., 2000. Geological Heritage, an essential part of the integral management of world heritage in protected sites. In: Barettino, D., Wimbledon, W.A.P., Gallego, E. (Eds.), Geological Heritage: its conservation and management. III International Symposium ProGEO on the Conservation of the Geological Heritage. Instituto Tecnológico Geominero de España, Madrid, pp. 95–110.

Carrington da Costa, J., 1950. Noticia sobre uma carta geologica do Buçaco, de Nery Delgado. Lisboa, Publicación Especial de la Comision de Servicio Geológico de Portugal 1–27.

Carvalhosa, B.A., 1965. Contribuçao para o conhecimiento geologico da regiao entre Portel y Ficalho (Alentejo). Memórias do Serviçio Geologico de Portugal 11, 130pp.

Castro, A., 1987. On granitoid emplacement and related structures. A review. Geologische Rundschau 76 (1), 101–124. https://doi.org/10.1007/BF01820576

Castro, A., 1988. Los granitoides deformados de la banda del Guadámez (La Serena, Badajoz). In: Bea, F., Carnicero, A., Gonzalo, J.C., López Plaza, M., Rodríguez Alonso, M.D. (Eds.), Geología de los granitoides y rocas asociadas del Macizo Hespérico: Libro homenaje a L.C. García Figuerola. Rueda, Madrid, pp. 413–426.

Castro, A., 2014. The off-crust origin of granite batholiths. Geoscience Frontiers 5 (1), 63–75. http://dx.doi.org/10.1016/j.gsf.2013.06.006

Castro, A., Patiño Douce, A.E., Corretgé, L.G., de la Rosa, J.D., El-Biad, M., El-Hmidi, H., 1999. Origin of peraluminous granites and granodiorites, Iberian Massif, Spain: an experimental test of granite petrogenesis. Contributions to Mineralogy and Petrology 135 (2–3), 255–276. https://doi.org/10.1007/s004100050511

Castro, A., Corretgé, L.G., De la Rosa, J., Enrique, P., Martínez, F.J., Pascual, E., Lago, M., Arranz, E., Galé, C., Fernández, C., Donaire, T., López, S., 2002. Paleozoic Magmatism. In: Gibbons, W., Moreno, T. (Eds.), The Geology of Spain. Geological Society, London, pp. 117–153.

Chakhmouradian, A. R., Zaitsev, A. N., 2012. Rare Earth Mineralization in Igneous Rocks: Sources and Processes. Elements 8 (5), 347–353. https://doi.org/10.2113/gselements.8.5.347

Champion, D.C., Bultitude, R.J., 2013. The geochemical and Sr–Nd isotopic characteristics of Paleozoic fractionated S-types granites of north Queensland: Implications for S-Type granite petrogénesis. Lithos 162–163, 37–56. https://doi.org/10.1016/j.lithos.2012.11.022

Chapman, J.B., Gehrels, G.E., Ducea, M.N., Giesler, N., Pullen, A., 2016. A new method for estimating parent rock trace element concentrations from zircon. Chemical Geology 439, 59–70. https://doi.org/10.1016/j.chemgeo.2016.06.014

Chappel, B.W., 1999. Aluminium saturation in I- and S-type granites and the characterization of fractionated haplogranites. Lithos 46 (3), 535–551. https://doi.org/10.1016/S0024-4937(98)00086-3

Chappel, B.W., Stephens, W.E., 1988. Origin of infracrustal (I-type) granite magmas. Transactions of the Royal Society of Edinburgh: Earth Sciences 79, 71–86. https://doi.org/10.1017/S0263593300014139

Chappell, B.W., White, A.J.R., 1974. Two contrasting granite types. Pacific Geology 8, 173–174.

Chappell, B.W., White, A.J.R., 1992. I- and S-type granites in the Lachlan Fold Belt. Transactions of the Royal Society of Edinburgh: Earth Sciences 83, 1–26. https://doi.org/10.1017/S0263593300007720

Chew, D.M., Petrus, J.A., Kamber, B.S., 2014. U–Pb LA–ICPMS dating using accessory mineral standards with variable common Pb. Chemical Geology 363, 185–199. https://doi.org/10.1016/j.chemgeo.2013.11.006

Chicharro, E., Villaseca, C., Valverde-Vaquero, P., Belousova, E., López-García, J.A., 2014. Zircon U–Pb and Hf isotopic constraints on the genesis of a post-kinematic S-type Variscan tin granite: the Logrosán cupola (Central Iberian Zone). Journal of Iberian Geology 40 (3), 451–470. http://dx.doi.org/10.5209/rev_JIGE.2014.v40.n3.43928

Claiborne, L.L., Miller, C.F., Gualda, G.A.R., Carley, T.L., Covey, A.K., Wooden, J.L., Fleming, M.A., 2018. Zircon as Magma Monitor. In: Moser, D.E., Corfu, F., Darling, J.R., Reddy, S.M., Tait, K. (Eds.), Microstructural Geochronology. American Geophysical Union and John Wiley and Sons, Inc., Washington, D.C., pp. 1–33. https://doi.org/10.1002/9781119227250.ch1

Clemens, J.D., 2003. S-type granitic magmas - petrogenetic issues, models and evidence. Earth-Science Reviews 61 (1–2), 1–18. https://doi.org/10.1016/S0012-8252(02)00107-1

Clemens, J.D. 2006. Melting of the continental crust: fluid regimes, melting reactions and source-rock fertility. In: Brown, M., Rushmer, T. (Eds.), Evolution and differentiation of the continental crust. Cambridge University Press, Cambridge, pp 297–331.

Clemens, J.D., 2012. Granitic magmatism, from source to emplacement: a personal view. Applied Earth Science 121 (3), 107–136. https://doi.org/10.1179/1743275813Y.0000000023

Clemens, J.D., Stevens, G., 2012. What controls chemical variation in granitic magmas? Lithos 134–135, 317–329. https://doi.org/10.1016/j.lithos.2012.01.001

Clemens, J.D., Vielzeuf, D., 1987. Constraints on melting and magma production in the crust. Earth and Planetary Science Letters 86 (2–4), 287–306. https://doi.org/10.1016/0012-821X(87)90227-5

Clemens, J.D., Helps, P.A., Stevens, G., 2010. Chemical structure in granitic magmas – a signal from the source? Transactions of the Royal Society of Edinburgh: Earth Sciences 100, 159–172., https://doi.org/10.1017/s1755691009016053

Clemens, J.D., Stevens, G., Farina, F., 2011. The enigmatic sources of I-type granites: The peritectic connexion. Lithos 126 (3–4), 174–181. https://doi.org/10.1016/j.lithos.2011.07.004

Coleman, D.S., Mills, R.D., Zimmerer, M.J., 2016. The Pace of Plutonism. Elements 12, 97–102. https://doi.org/10.2113/gselements.12.2.97

Colmenero, J.R., Fernández, L.P., Moreno, C., Bahamonde, J.R., Barba, P., Heredia, N., González, F., 2002. Carboniferous. In: Gibbons, W., Moreno, T. (Eds.), The Geology of Spain. Geological Society, London, pp. 93–115.

Corretgé, L.G., 1971. Estudio petrológico del Batolito de Cabeza de Araya (Cáceres). PhD Thesis, University of Salamanca (453 pp.).

Corretgé, L.G., Suárez, O., 1994. A garnet–cordierite granite porphyry containing rapakivi feldspars in the Cabeza de Araya Batholith (Extremadura, Spanish Hercynian Belt). Mineralogy and Petrology 50 (1–3), 97–111. https://doi.org/10.1007/BF01160142

Corretgé, L. G., Ugidos, J. M., Martínez, F. J., 1977. Les series granitiques varisques du secteur Centre–Occidental Espagnol. La chaine varisque d'Europe moyenne et occidentale. Colloque International du Centre National de la Recherche Scientffique 243, 453–461.

Corretgé, L.G., Bea, F., Suárez, O., 1985. Las características geoquímicas del batolito de Cabeza de Araya (Cáceres, España): Implicaciones petrogenéticas. Trabajos de Geología 15, 219–238. https://doi.org/10.17811/tdg.15.1985.219-239

Corretgé, L.G., Castro, A., García-Moreno, O., 2004. Granitoides de la "serie mixta". In: Vera, J.A. (Ed.), Geología de España. Sociedad Geológica de España e Instituto Geológico y Minero de España, Madrid, pp. 115–116.

Couzinié, S., Moyen, J.-F., Villaros, A., Paquette, J.-L., Scarrow, J.H., Marignac, C., 2014. Temporal relationships between Mg-K mafic magmatism and catastrophic melting of the Variscan crust in the southern part of Velay Complex (Massif Central, France). Journal of Geosciences 59, 69–86. https://doi.org/10.3190/jgeosci.155

Couzinié, S., Laurent, O., Moyen, J.-F., Zeh, A., Vézinet, A., Villaros, A., 2015. Mg-K magmatic suites as a tool to scan the composition of the Variscan orogenic mantle, case studies from the French Massif Central. Geologié de la France, The Variscan belt: correlations and plate dynamics-Special meeting of the French and Spanish Geological Societies 1, 43.

Couzinié, S., Laurent, O., Moyen, J.-F., Zeh, A., Bouilhol, P., Villaros, A., 2016. Post-collisional magmatism: Crustal growth not identified by zircon Hf–O isotopes. Earth and Planetary Science Letters 456, 182–195. https://doi.org/10.1016/j.epsl.2016.09.033

Cruden, A.R., 1998. On the emplacement of tabular granites. Journal of the Geological Society, London 155, 853–862. https://doi.org/10.1144/gsjgs.155.5.0853

De la Roche, H., Leterrier, J., Grandclaude, P., Marchal, M., 1980. A classification of volcanic and plutonic rocks using $R_1R_2$-diagram and major-element analyses – Its relationships with current nomenclature. Chemical Geology 29 (1–4), 183–210. https://doi.org/10.1016/0009-2541(80)90020-0

De Paolo, D.J., Wasserburg, G.J., 1979. Petrogenetic mixing models and Nd–Sr isotopic patterns. Geochimica et Cosmochimica Acta 43 (4), 615–627. https://doi.org/10.1016/0016-7037(79)90169-8

Debon, F., Le Fort, P., 1983. A chemical–mineralogical classification of common plutonic rocks and associations. Transactions of the Royal Society of Edinburgh: Earth Sciences 73, 135–149. https://doi.org/10.1017/S0263593300010117

Deer, W.A., Howie, R.A., Zussman, J., 1962. Rock-Forming Minerals. Vol. 3: Sheet Silicates. Longman, London, 270 pp.

Deer, W.A., Howie, R.A., Zussman, J., 1963. Rock-Forming Minerals. Vol. 4: Framework Silicates. Longman, London, 435 pp.

Del Olmo Sanz, A., Matia Villarino, G., Olivé Davó, A., Huerta Carmona, J., 1992. Hoja geológica número 752 (Mirandilla). Mapa Geológico de España a Escala 1:50.000 (2ª serie). Instituto Geológico y Minero de España (IGME), Madrid. http://info.igme.es/cartografiadigital/geologica/Magna50Hoja.aspx?Id=752

Devès, M.H., Tait, S.R., King, G.C.P., Grandin, R., 2014. Strain heating in process zones; implications for metamorphism and partial melting in the lithosphere. Earth and Planetary Science Letters 394, 216–228. https://doi.org/10.1016/j.epsl.2014.03.002

Dias, G., Leterrier, J., 1994. The genesis of felsic-mafic plutonic associations: a Sr and Nd isotopic study of the Hercynian Braga Granitoid Massif (Northern Portugal). Lithos 32 (3–4), 207–223. https://doi.org/10.1016/0024-4937(94)90040-X

Dias, G., Leterrier, J., Mendes, A., Simões, P.P., Bertrand, J., 1998. U–Pb zircon and monazite geochronology of post-collisional Hercynian granitoids from the Central Iberian Zone (Northern Portugal). Lithos 45 (1–4), 349–369. https://doi.org/10.1016/S0024-4937(98)00039-5

Dias, G., Simões, P.P., Ferreira, N., Leterrier, J., 2002. Mantle and crustal sources in the genesis of Late-Hercynian granitoids (NW Portugal): geochemical and Sr–Nd isotopic constraints. Gondwana Research 5 (2), 287–305. https://doi.org/10.1016/S1342-937X(05)70724-3

Didier, J., Barbarin, B., 1991. Enclaves and Granite Petrology. Elsevier, Amsterdam. 625 pp.

Didier, J., Duthou, J.L., Lameyre, J., 1982. Mantle and crustal granites: genetic classification of orogenic granites and the nature of their enclaves. Journal of Volcanology and Geothermal Research 14 (1–2), 125–132. https://doi.org/10.1016/0377-0273(82)90045-2

Díez Fernández, R., Arenas, R., 2015. The Late Devonian Variscan suture of the Iberian Massif: a correlation of high-pressure belts in NW and SW Iberia. Tectonophysics 654, 96–100. https://doi.org/10.1016/j.tecto.2015.05.001

Dingwall, P. R., 2000. Legislation and International Agreements: the integration of the Geological Heritage in nature conservation policies. In: Barettino, D., Wimbledon, W.A.P., Gallego, E. (Eds.), Geological Heritage: its conservation and management. III International Symposium ProGEO on the Conservation of the Geological Heritage, Madrid, pp. 15–28.

Donaire, T., 1995. Petrología y geoquímica de rocas granitoides y enclaves asociados del batolito de los Pedroches (Macizo Ibérico). PhD Thesis, University of Huelva (232 pp.).

Donaire, T., Pascual, E., Pin, C., Duthou, J.-L., 1999. Two-stage granitoid-forming event from an isotopically homogeneous crustal source: the Los Pedroches Batholith,

Iberian Massif, Spain. Geological Society of America Bulletin 111 (12), 1897–1906. https://doi.org/10.1130/0016-7606(1999)111< 1897:TSGFEF> 2.3.CO;2

Duc-Tin, Q., Keppler, H., 2015. Monazite and xenotime solubility in granitic melts and the origin of the lanthanide tetrad effect. Contributions to Mineralogy and Petrology 169: 8. https://doi.org/10.1007/s00410-014-1100-9

Eguíluz, L., Gil Ibarguchi, J.I., Ábalos, B., Apraiz, A., 2000. Superposed Hercynian and Cadomian orogenic cycles in the Ossa-Morena zone and related areas of the Iberian Massif. Geological Society of America Bulletin 112 (9), 1398–1413. https://doi.org/10.1130/0016-7606(2000)112< 1398:SHACOC> 2.0.CO;2

England, P.C., Thompson, A.B., 1984. Pressure–temperature–time paths of regional metamorphisms I. Heat transfer during the evolution of regions of thickened continental crust. Journal of Petrology 25 (4), 894–928. https://doi.org/10.1093/petrology/25.4.894

Errandonea-Martin, J., Carracedo-Sánchez, M., Sarrionandia, F., Santos Zalduegui, J.F., García de Madinabeitia, S., Gil-Ibarguchi, J.I., 2017. The late-Variscan peraluminous Valdepeñas Pluton (southern Central Iberian Zone). Geologica Acta 15 (4), 361–378. https://doi.org/10.1344/GeologicaActa2017.15.4.7

Farias, P., Gallastegui, G., González Lodeiro, F., Marquínez, J., Martín-Parra, L.M., Martínez Catalán, J.R., Pablo Maciá, J.G., Rodríguez-Fernández, L.R., 1987. Aportaciones al conocimiento de la litoestratigrafía y estructura de Galicia Central. Memórias da Museu e Laboratorio Mineralógico e Geológico da Faculdade de Ciencias da Universidade do Porto 1, 411–431.

Federal Geographic Data Committee (prepared for the Federal Geographic Data Committee by the U.S. Geological Survey) 2006. FGDC Digital Cartographic Standard for Geologic Map Symbolization: Reston, Va., Federal Geographic Data Committee Document Number FGDC-STD-013-2006, 290 pp.

Fernández, F.J., Cueto, L.A., Larrea, F.J., Quesada, C., 1990. El plutón de El Guijo: petrología, geoquímica, edad y relación con otras rocas del Batolito de Los Pedroches. Cuadernos Laboratorio Xeolóxico de Laxe 15, 89–103.

Fernández Ruiz, F.J., 1987. Caracterización petrológica y geoquímica de la Granodiorita de Los Pedroches y el plutón de El Guijo (Batolito de Los Pedroches, Córdoba, España). Tesis de Licenciatura, University of Oviedo (118 pp.).

Ferré, E.C., Galland, O., Montanari, D., Kalakay, T.J., 2012. Granite magma migration and emplacement along thrusts. International Journal of Earth Sciences 101 (7), 1673–1688. https://doi.org/10.1007/s00531-012-0747-6

Ferreira, E., Iglesias, M., Noronha, F., Pereira, E., Ribeiro, A., Ribeiro, M.L., 1987. Granitoides da zona Centro-Ibérica e seu enquadramento geodinâmico. In: Bea, F., Carnicero, A., Gonzalo, J.C., López-Plaza, M., Rodríguez Alonso, M.D. (Eds.),

Geología de los granitoides y rocas asociadas del macizo Ibérico. Rueda, Madrid, pp. 37–53.

Fournet, J., 1837. Geologie lyonnaise. Lyon, De Barret, 744pp.

Friedman, G.M., 1971. Staining. In: Carver, R.E. (Ed.), Procedures in Sedimentary Petrology. Wiley-Interscience, New York, 511–530.

Frost, B.R., Barnes, C.G., Collins, W.J., Arculus, R.J., Ellis, D.J., Frost, C.D., 2001. A geochemical classification for granitic rocks. Journal of Petrology 42 (11), 2033–2048. https://doi.org/10.1093/petrology/42.11.2033

Galán, G., Corretgé, L.G., Laurent, O., 1997. Low-potassium vaugnerites from Guéret (Massif Central, France). Mafic magma evolution influenced by contemporaneous granitoids. Mineralogy and Petrology 59 (3–4), 165–187. https://doi.org/10.1007/BF01161858

Gallastegui, G., 2005. Petrología del Macizo Granodiorítico de Bayo-Vigo (Provincia de Pontevedra, España). PhD Thesis, University of Oviedo (414 pp.).

Gao, P., Zheng, Y.-F., Zhao, Z.-F., 2016. Distinction between S-type and peraluminous I-type granites: Zircon versus whole-rock geochemistry. Lithos 258–259, 77–91. https://doi.org/10.1016/j.lithos.2016.04.019

Garate-Olave, I., Müller, A., Roda-Robles, E., Gil-Crespo, P.P., Pesquera, A., 2017. Extreme fractionation in a granite–pegmatite system documented by quartz chemistry: The case study of Tres Arroyos (Central Iberian Zone, Spain). Lithos 286–287, 162–174. https://doi.org/10.1016/j.lithos.2017.06.009

García de Madinabeitia, S., Sánchez Lorda, M.E., Gil Ibarguchi, J.I., 2008. Simultaneous determination of major to ultratrace elements in geological samples by fusion-dissolution and inductively coupled plasma mass spectrometry techniques. Analytica Chimica Acta 625 (2), 117–130. http://dx.doi.org/10.1016/j.aca.2008.07.024

García-Alcalde, J.L., Carls, P., Pardo Alonso, M.V., Sanz López, J., Soto, F., Truyols-Massoni, M., Valenzuela- Ríos, J.I., 2002. Devonian. In: Gibbons, W., Moreno, T. (Eds.), The Geology of Spain. Geological Society, London, pp. 67–91.

García-Arias, M., Díez-Montes, A., Villaseca, C., Blanco-Quintero, I.F., 2018. The Cambro–Ordovician Ollo de Sapo magmatism in the Iberian Massif and its Variscan evolution: a review. Earth-Science Reviews 176, 345–372. https://doi.org/10.1016/j.earscirev.2017.11.004

García-Casco, A., Pascual, E., Fenol, H. A., 1989. Petrogénesis del plutón monzogranítico peralumínico de Santa Eufemia (batolito de Los Pedroches, Córdoba). Estudios Geológicos 45, 3–20.

García-Lobón, J.L., Rey-Moral, C., Ayala, C., Martín-Parra, L.M., Matas, J., Reguera, M.I., 2014. Regional structure of the southern segment of Central Iberian Zone (Spanish Variscan Belt) interpreted from potential field images and 2.5 D modelling of

Alcudia gravity transect. Tectonophysics 614, 185–202. https://doi.org/10.1016/j.tecto.2013.12.005

García-Moreno, O., 2004. Estudio experimental de las relaciones texturales y de fases en granitos peralumínicos de la "Serie Mixta" del Macizo Ibérico: El caso de Cabeza de Araya (Cáceres). PhD Thesis, University of Granada (248 pp.).

García-Moreno, O., Corretgé, L.G., 2000. Enclaves en granitos peralumínicos alóctonos: El caso del Batolito de Cabeza de Araya (Cáceres, España). Geogaceta 27, 67–70.

García-Moreno, O., Castro, A., Corretgé, L.G., El-Hmidi, H., 2006. Dissolution of tonalitic enclaves in ascending hydrous granitic magmas: An experimental study. Lithos 89 (3–4), 245–258. https://doi.org/10.1016/j.lithos.2005.12.008

García-Moreno, O., Corretgé, L.G., Castro, A., 2007. Processes of assimilation in the genesis of cordierite leucomonzogranites from the Iberian Massif: a short review. The Canadian Mineralogist 45 (1), 71–85. https://doi.org/10.2113/gscanmin.45.1.71

Gerdes, A., Wörner, G., Finger, F., 2000. Hybrids, magma mixing and enriched mantle melts in post-collisional Variscan granitoids: the Rastenberg Pluton, Austria. Geological Society, London 179, 415–431. https://doi.org/10.1144/GSL.SP.2000.179.01.25

Gerdes, A., Montero, P., Bea, F., Fershater, G., Borodina, N., Osipova, T., Shardakova, G., 2002. Peraluminous granites frequently with mantle-like isotope compositions: the continental-type Murzinka and Dzhabyk batholiths of the eastern Urals. International Journal of Earth Sciences 91 (1), 3–19. https://doi.org/10.1007/s005310100195

Gil Ibarguchi, J.I., 1980. Las vaugneritas de la región de Finisterre (Galicia, NW. España). Probables productos de magmas anatécticos residuales. Cadernos do Laboratorio Xeolóxico de Laxe 1, 21–32.

Gil Ibarguchi, J.I., 1981. A comparative study of vaugnerites and metabasic rocks from the Finisterre region (NW Spain). Neues Jahrbuch für Mineralogie–Abhandlungen 143 (1), 91–101.

Gil Ibarguchi, J.I., Bowden, P., Whitley, J.E., 1984. Rare Earth Element Distribution in Some Hercynian Granitoids from the Finisterre Region, NW Spain. The Journal of Geology 92 (4), 397–416. https://doi.org/10.1086/628875

Gil Montes, J., 2004. Via delapidata. Identificación de una carretera romana por la procedencia de los materiales. In: Colegio de Ingenieros Técnicos de Obras Públicas (Ed.), Elementos de ingeniería romana. Congreso europeo "Las obras públicas romanas". Tarragona.

Glazner, A.F., Bartley, J.M., Coleman, D.S., 2019. A More Informative Way to Name Plutonic Rocks. Geological Society of America Today 29 (2), 4–10. https://doi.org/10.1130/GSATG384A.1

Gonçalves, G.O., Lana, C., Scholz, R., Buick, I., Gerdes, A., Kamo, S.L., Corfu, F., Marinho, M.M., Chaves, A.O., Valeriano, C., Nalini Jr., H.A., 2016. An assessment of

monazite from the Itambé pegmatite district for use as U–Pb isotope reference material for microanalysis and implications for the origin of the "Moacyr" monazite. Chemical Geology 424, 30–50. https://doi.org/10.1016/j.chemgeo.2015.12.019

González Menéndez, L., 1998. Petrología y geoquímica del batolito granítico de Nisa-Alburquerque (Alto Alentejo, Portugal; Extremadura, España). PhD Thesis, University of Granada (223 pp.).

González Menéndez, L., 2002. Petrología del batolito granítico de Nisa-Alburquerque. Revista de la Sociedad Geológica de España 15 (3–4), 233–246.

González Menéndez, L., Azor, A., 2003. Condiciones PT de emplazamiento del Batolito de Nisa-Alburquerque. Geogaceta 34, 103–106.

González Menéndez, L., Bea, F., 2004. El batolito de Nisa-Alburquerque. In: Vera, J.A., (Ed.), Geología de España. Sociedad Geológica de España-Instituto Geológico y Minero de España (SGE-IGME), Madrid, pp. 120–1122.

González Menéndez, L., Azor, A., Rubio Ordóñez, A., Sánchez-Almazo, I., 2011. The metamorphic aureole of the Nisa–Alburquerque Batholith (SW Iberia): implications for deep structure and emplacement mode. International Journal of Earth Sciences 100 (7), 1533–1550. https://doi.org/10.1007/s00531-010-0568-4

Gonzalo, J.C., 1987. Petrología y estructura del basamento hercínico del área de Mérida (Extremadura Central). PhD Thesis, University of Salamanca (327 pp.).

Gonzalo, J.C., 1988. El plutonismo hercínico en el área de Mérida (Extremadura Central. España). In: Bea, F., Carnicero, A., Gonzalo, J.C., López Plaza, M., Rodríguez Alonso, M.D. (Eds.), Geología de los granitoides y rocas asociadas del Macizo Hespérico. Libro Homenaje a L.C. García de Figuerola. Rueda, Madrid, pp. 345–355.

Gonzalo, J.C., 1989. Litoestratigrafía y tectónica del basamento en el área de Mérida (Extremadura Central). Boletín Geológico y Minero 100 (1), 48–72.

Gutiérrez-Alonso, G., Fernández-Suárez, J., Jeffries, T.E., Johnston, S.T., Pastor-Galán, D., Murphy, J.B., Franco, M.P., Gonzalo, J.C., 2011. Diachronous post-orogenic magmatism within a developing orocline in Iberia, European Variscides. Tectonics 30 (5), 17. http://dx.doi.org/10.1029/2010TC002845

Gutiérrez-Marco, J.C., Robardet, M., Rábano, I., Sarmiento, G.N., San José Lancha, M.A., Herranz Araújo, P., Pieren Pidal, P., 2002. Ordovician. In: Gibbons, W., Moreno, T. (Eds.), The Geology of Spain. Geological Society, London, pp. 31–49.

Harris, N.B.W., Inger, S., 1992. Trace element modelling of pelite-derived granites. Contributions to Mineralogy and Petrology 110 (1), 46–56. https://doi.org/10.1007/BF00310881

Harrison, T.M., Watson, E.B., 1984. The behavior of apatite during crustal anatexis: equilibrium and kinetic considerations. Geochimica et Cosmochimica Acta 48 (7), 1467–1477. https://doi.org/10.1016/0016-7037(84)90403-4

Hawkesworth, C.J., Dhuime, B., Pietranik, A.B., Cawood, P.A., Kemp, A.I.S., Storey, C.D., 2010. The generation and evolution of the continental crust. Journal of the Geological Society, London 167 (2), 229–248. https://doi.org/10.1144/0016-76492009-072

Healy, B., Collins, W.J., Richards, S.W., 2004. A hybrid origin for Lachlan S-type granites: the Murrumbidgee Batholith example. Lithos 78 (1–2), 197–216. https://doi.org/10.1016/j.lithos.2004.04.047

Henriques, S.B.A., Neiva, A.M.R., Ribeiro, M.L., Dunning, G.R., Tajčmanová, L., 2015. Evolution of a Neoproterozoic suture in the Iberian Massif, Central Portugal: new U–Pb ages of igneous and metamorphic events at the contact between the Ossa Morena Zone and Central Iberian Zone. Lithos 220–223, 43–59. https://doi.org/10.1016/j.lithos.2015.02.001

Hofmann, A., 1971. Fractionation corrections for mixed-isotope spikes of Sr, K, and Pb. Earth and Planetary Science Letters 10 (4), 397–402. https://doi.org/10.1016/0012-821X(71)90087-2

Holden, P., Halliday, A.N., Stephens, W.E., Henney, P.J., 1991. Chemical and isotopic evidence for major mass transfer between mafic enclaves and felsic magma. Chemical Geology 92 (1–3), 135–152. https://doi.org/10.1016/0009-2541(91)90053-T

Holtz, F., Johannes, W., Tamic, N., Behrens, H., 2001. Maximum and minimum water contents of granitic melts generated in the crust: a reevaluation and implications. Lithos 56 (1), 1–14. https://doi.org/10.1016/S0024-4937(00)00056-6

Holub, F.V., 1997. Ultrapotassic plutonic rocks of the durbachite series in the Bohemian Massif: Petrology, geochemistry and petrogenetic interpretation. Sborník Geologických Věd, Ložisková Geologie-Mineralogie 31, 5–26.

Hutton, D.H.W., 1988. Granite emplacement mechanisms and tectonic controls: inferences from deformation studies. Transactions of the Royal Society of Edinburgh: Earth Sciences 79 (2–3), 245–255. https://doi.org/10.1017/S0263593300014255

Irvine, T.N., Baragar, W.R.A., 1971. A guide to the chemical classification of the common volcanic rocks. Canadian Journal of Earth Sciences 8 (5), 523–548. https://doi.org/10.1139/e71-055

Jackson, S.E., Pearson, N.J., Griffin, W.L., Belousova, E.A., 2004. The application of laser ablation-inductively coupled plasma-mass spectrometry to in situ U–Pb zircon geochronology. Chemical Geology 211 (1–2), 47–69. https://doi.org/10.1016/j.chemgeo.2004.06.017

Janoušek, V., 2006. *Saturnin*, R language script for application of accessory-mineral saturation models in igneous geochemistry. Geologica Carpathica, 57 (2), 131–142.

Janoušek, V., Holub, F.V., 2007. The causal link between HP-HT metamorphism and ultrapotassic magmatism in collisional orogens: case study from the Moldanubian Zone of the Bohemian Massif. Proceedings of the Geologists' Association 118 (1), 75–86. https://doi.org/10.1016/S0016-7878(07)80049-6

Janoušek, V., Moyen, J.-F., 2014. Mass Balance Modelling of Magmatic Processes in GCDkit. In: Kumar, S., Singh, R.N., (Eds.), Modelling of magmatic and allied processes. The Society of Earth Scientists Series 83, Springer, Berlin, pp. 225–238. https://doi.org/10.1007/978-3-319-06471-0_11

Janoušek, V., Moyen, J.-F., 2019. Whole-rock geochemical modelling of granite genesis: the current state of play. In: Janoušek, V., Bonin, B., Collins, W.J., Farina, F., Bowden, P. (Eds.), Post-Archean Granitic Rocks: Petrogenetic Processes and Tectonic Environments. Geological Society, London, Special Publications, 491 https://doi.org/10.6084/m9.figshare.c.4386692

Janoušek, V., Rogers, G., Bowes, D.R., 1995. Sr–Nd isotopic constraints on the petrogénesis of the Central Bohemian Pluton, Czech Republic. Geologische Rundschau 84 (3), 520–534. https://doi.org/10.1007/BF00284518

Janoušek, V., Finger, F., Roberts, M., Frýda, J., Pin, C., Dolejš, D., 2004. Deciphering the petrogenesis of deeply buried granites: whole-rock geochemical constraints on the origin of largely undepleted felsic granulites from the Moldanubian Zone of the Bohemian Massif. Transactions of the Royal Society of Edinburgh: Earth Sciences 95 (1–2), 141–159. https://doi.org/10.1017/S0263593300000985

Janoušek, V., Farrow, C.M., Erban, V., 2006. Interpretation of whole-rock geochemical data in igneous geochemistry: introducing Geochemical Data Toolkit (GCDkit). Journal of Petrology 47 (6), 1255–1259. https://doi.org/10.1093/petrology/egl013

Janoušek, V., Navrátil, T., Trubač, J., Strnad, L., Laufek, F., Minařík, L., 2014. Distribution of elements among minerals of a single (muscovite-) biotite granite sample – an optimal approach and general implications. Geologica Carpathica 65 (4), 257–271. https://doi.org/10.2478/geoca-2014-0017

Janoušek, V., Moyen, J.-F., Martin, H., Erban, V., Farrow, C., 2016. Geochemical Modelling of Igneous Processes – Principles And Recipes in R Language. Springer-Verlag, Berlin. https://doi.org/10.1007/978-3-662-46792-3

Jiménez San Pedro, R., 2003. El complejo filoniano tardihercínico asociado al batolito de Los Pedroches (Zona Centro-Ibérica, España). PhD Thesis, University of the Basque Country (398 pp.).

Jochum, K.P., Weis, U., Stoll, B., Kuzmin, D., Yang, Q., Raczek, I., Jabob, D.E., Stracke, A., Birbaum, K., Frick, D.A., Günther, D., Enzweiler, J., 2011. Determination of reference values for NIST SRM 610–617 glasses following ISO guidelines. Geostandards and Geoanalytical Research 35 (4), 397–429. https://doi.org/10.1111/j.1751-908X.2011.00120.x

Julivert, M., Marcos, A., Truyols, J., 1972. L'évolution paléogéographique du NW de l'Espagne pendant l'Ordovicien–Silurien. Bulletin de la Société Géologique et minéralogique de Bretagne 4, 1–7.

Jung, S., Pfänder, J.A., 2007. Source composition and melting temperatures of orogenic granitoids: constraints from $CaO/Na_2O$, $Al_2O_3/TiO_2$ and accessory mineral saturation thermometry. European Journal of Mineralogy 19 (6), 859–870. https://doi.org/10.1127/0935-1221/2007/0019-1774

Jung, S., Masberg, P., Mihm, D., Hoernes, S., 2009. Partial melting of diverse crustal sources — constraints from Sr–Nd–O isotope compositions of quartz diorite–granodiorite–leucogranite associations (Kaoko Belt, Namibia). Lithos 111 (3–4), 236–251. https://doi.org/10.1016/j.lithos.2008.10.010

Kováříková , P., Siebel, W., Jelínek, E., Štemprok, M., Kachlík, V., Holub, F.V., Blecha, V., 2007. Petrology, geochemistry and zircon age for redwitzite at Abertamy, NW Bohemian Massif (Czech Republic): tracing the mantle component in Late Variscan intrusions. Chemie der Erde-Geochemistry 67 (2), 151–174. https://doi.org/10.1016/j.chemer.2007.04.002

Kubínová, Š., Faryad, S.W., Verner, K., SchmitzM., Holub, F.V., 2017. Ultrapotassic dykes in the Moldanubian Zone and their significance for understanding of the post-collisional mantle dynamics during Variscan orogeny in the Bohemian Massif. Lithos (272–273), 205–221. https://doi.org/10.1016/j.lithos.2016.12.007

Larrea, F.J., 1998. Caracterización petrológica y geoquímica del sector oriental del Batolito de Los Pedroches. PhD Thesis, University of the Basque Country (537 pp.).

Larrea, F.J., Carracedo, M., Cueto, L.A., Quesada, C., Gil Ibarguchi, J.I., Fernández, F.J., Ortega, L.A., 1992. Petrología y geoquímica del plutón de Cardeña-Virgen de La Cabeza (batolito de Los Pedroches). Cadernos do Laboratorio Xeolóxico de Laxe 17, 209–222.

Larrea, F.J., Carracedo, M., Alonso Olazabal, A., Donaire, T., Pascual, E., 2004. El batolito de Los Pedroches. In: Vera, J.A., (Ed.), Geología de España. Sociedad Geológica de España-Instituto Geológico y Minero de España (SGE-IGME), Madrid, pp. 122–124.

Laurent, O., Couzinié, S., Vanderhaeghe, O., Zeh, A., Moyen, J.-F., Villaros, A., Gardien V., 2015. U-Pb dating of Variscan igneous rocks from the eastern French Massif Central: southward migration of coeval crust- and mantle-melting witnesses late-orogenic slab retreat. Geologié de la France, The Variscan belt: correlations and plate dynamics-Special meeting of the French & Spanish Geological Societies 1, 82.

Le Maitre, R.W., Streckeisen, A., Zanettin, B., Le Bas, M.J., Bonin, B., Bateman, P., Bellieni, G., Dudek, A., Efremova, S., Keller, J., Lameyre, J., Sabine, P.A., Schmid, R., Sorensen, H., Woolley, A.R., 2002. Igneous rocks: a classification and glossary of terms. Cambridge University Press, Cambridge, 236pp. https://doi.org/10.2113/gscanmin.40.6.1737

Leake, B.E., Woolley, A.R., Arps, C.E.S., Birch, W.D., Gilbert, M.C., Grice, J.D., Hawthorne, F.C., Kato, A., Kisch, H.J., Krivovichev, V.G., Linthout, K., Laird, J., Mandarino, J.A., Maresch, W.V., Nickel, E.H., Rock, N.M.S., Schumacher, J.C., Smith, D.C., Stephenson, N.C.N., Ungaretti, L., Whittaker, E.J.W., Guo, Y., 1997. Nomenclature of amphiboles: Report of the subcommittee on amphiboles of the International Mineralogical Association, Commission on New Minerals and Mineral Names. The Canadian Mineralogist 35, 219–246.

Lefort, J.P., 1989. Basement correlation across the north Atlantic. Springer-Verlag, Berlin, 148pp.

Lesher, C.E., 1990. Decoupling of chemical and isotopic exchange during magma mixing. Nature 344, 235-237. https://doi.org/10.1038/344235a0

Lesher, C.E., 1994. Kinetics of Sr and Nd exchange in silicate liquids: Theory, experiments, and applications to uphill diffusion, isotopic equilibration, and irreversible mixing of magmas. Journal of Geophysical Research 99 (B5), 9585–9604. https://doi.org/10.1029/94JB00469

Liew, T.C., Hofmann, A.W., 1988. Precambrian crustal components, plutonic associations, plate environment of the Hercynian Fold Belt of Central Europe: indications from a Nd and Sr isotopic study. Contributions to Mineralogy and Petrology 98 (2), 129–138. https://doi.org/10.1007/BF00402106

Linnen, R.L., Lichtervelde, M.V., Černý, P., 2012. Granitic Pegmatites as Sources of Strategic Metals. Elements 8 (4), 275–280. https://doi.org/10.2113/gselements.8.4.275

Lisle, R.J., Brabham, P., Barnes J., 2011. Basic Geological Mapping (5th ed.). Wiley-Blackwell, Chichester, 217pp.

Loiselle, M.C., Wones, D.R., 1979. Characteristics and origin of anorogenic granites. Geological Society of America Abstracts with Programs 11 (7), 468.

López-Moro, F.-J., López-Plaza, M., 2004. Monzonitic series from the Variscan Tormes Dome (Central Iberian Zone): petrogenetic evolution from monzogabbro to granite magmas. Lithos 72 (1–2), 19–44. https://doi.org/10.1016/j.lithos.2003.08.002

López-Moro, F.-J., Romer, R.L., López-Plaza, M., González Sánchez, M., 2017. Zircon and allanite U-Pb ID-TIMS ages of vaugnerites from the Calzadilla pluton, Salamanca (Spain): dating mantle-derived magmatism and post-magmatic subsolidus overprint. Geologica Acta 15 (4), 395–408. http://dx.doi.org/10.1344/GeologicaActa2017.15.4.9

López Plaza, M., López Moro, F.J., Gonzalo Corral, J.C., Carnicero, A., 1999. Asociaciones de rocas plutónicas básicas e intermedias de afinidad calcoalcalina y shoshonítica y granitoides relacionados en el Domo Hercínico del Tormes (Salamanca y Zamora). Boletín de la Sociedad Española de Mineralogía 22, 211–234.

López Sopena, F., Matia Villarino, G., del Olmo, A., Ortega Ruiz, I., 1990. Hoja geológica número 753 (Miajadas). Mapa Geológico de España a Escala 1:50.000 (2ª serie). Instituto Geológico y Minero de España (IGME), Madrid. http://info.igme.es/cartografiadigital/geologica/Magna50Hoja.aspx?id=753

Lotze, F., 1945. Zur Gliederung der Varisziden der Iberischen Meseta. Geotektonische Forschungen 6, 78–92.

Ludwig, K.R., 2012. Isoplot/Ex Version 3.75. A geochronological toolkit for Microsoft Excel, User's Manual. Berkeley Geochronology Center Special Publications 5, Berkeley.

Marín y Bertrán de Lís, A., 1946. Hoja geológica número 753 (Miajadas). Mapa Geológico de España a Escala 1:50.000 (1ª serie). Instituto Geológico y Minero de España (IGME), Madrid. http://info.igme.es/cartografiadigital/geologica/Geo50Hoja.aspx?Id=753&language=es

Marsaglia, K.M., Tazaki, K., 1992. Diagenetic trends in Leg 126 sandstones. In: Taylor, B., Fujioka, K., et al. (Eds.), Proceedings of the Ocean Drilling Program, Scientific Results, College Station, TX (Ocean Drilling Program) 126, 125–138. https://doi.org/10.2973/odp.proc.sr.126.123.1992

Martín Parra, L.M., Lodeiro, F.G., Martínez Poyatos, D., Matas, J., 2006. The Puente Génave-Castelo de Vide shear zone (southern Central Iberian Zone, Iberian Massif): geometry, kinematics and regional implications. Bulletin de la Société Géologique de France 177 (4), 191–202. https://doi.org/10.2113/gssgfbull.177.4.191

Martínez Catalán, J.R., 2012. The Central Iberian arc, an orocline centered in the Iberian Massif and some implications for the Variscan belt. International Journal of Earth Sciences 101 (5), 1299–1314. https://doi.org/10.1007/s00531-011-0715-6

Martínez Catalán, J.R., Arenas, R., Díaz García, F., González Cuadra, P., Gómez-Barreiro, J., Abati, J., Castiñeiras, P., Fernández-Suárez, J., Sánchez Martínez, S., Andonaegui, P., González Clavijo, E., Díez Montes, A., Rubio Pascual, F.J., Valle Aguado, B., 2007. Space and time in the tectonic evolution of the northwestern Iberian Massif: Implications for the Variscan belt. In: Hatcher, Jr., R.D., Carlson, M.P., McBride, J.H., Martínez Catalán, J.R. (Eds.), 4-D Framework of Continental Crust. Geological Society of America Memoir 200, pp. 403–423. https://doi.org/10.1130/2007.1200(21)

Martínez Catalán, J.R., Arenas, R., Abati, J., Sánchez Martínez, S., Díaz García, F., Fernández Suárez, J., González Cuadra, P., Castiñeiras, P., Gómez Barreiro, J., Díez Montes, A., González Clavijo, E., Rubio Pascual, F.J., Andonaegui, P., Jeffries, T.E., Alcock, J.E., Díez Fernández, R., López Carmona, A., 2009. A rootless suture and the loss of the roots of a mountain chain: the Variscan belt of NW Iberia. Comptes Rendus Geoscience 341, 114–126. https://doi.org/10.1016/j.crte.2008.11.004

Martínez Catalán, J.R., Rubio Pascual, F.J., Díez Montes, A., Díez Fernández, R., Gómez Barreiro, J., Dias da Silva, Í., González Clavijo, E., Ayarza, P., Alcock, J.E., 2014. The late Variscan HT/LP metamorphic event in NW and Central Iberia: relationships to crustal thickening, extension, orocline development and crustal evolution. In: Schulmann, K., Martínez Catalán, J.R., Lardeaux, J.M., Janoušek, V., Oggiano, G. (Eds.), The Variscan Orogeny: Extent, Timescale and the Formation of the European Crust. Geological Society, London, Special Publications 405, 225–247. https://doi.org/10.1144/SP405.1

Martínez Poyatos, D., Nieto, F., Azor, A., Simancas, J.F., 2001. Relationships between very low-grade metamorphism and tectonic deformation: examples from the southern Central Iberian Zone (Iberian Massif, Variscan Belt). Journal of the Geological Society, London 158, 953–968. https://doi.org/10.1144/0016-764900-206

Martínez Poyatos, D., Díez Balda, M.A., Macaya, J., González Lodeiro, F., Martínez Catalán, J.R., Vegas, R., 2004. El acortamiento varisco inicial. In: Vera, J.A. (Ed.), Geología de España. Sociedad Geológica de España e Instituto Geológico y Minero de España, Madrid, pp. 84–87.

Martínez Poyatos, D., Carbonell, R., Palomeras, I., Simancas, J.F., Ayarza, P., Martí, D., Azor, A., Jabaloy, A., González Cuadra, P., Tejero, R., Martín Parra, L.M., Matas, J., González Lodeiro, F., Pérez-Estaún, A., García Lobón, J.L., Mansilla, L., 2012. Imaging the crustal structure of the Central Iberian Zone (Variscan Belt): The ALCUDIA deep seismic reflection transect. Tectonics 31 (3), 21. https://doi.org/10.1029/2011TC002995

Matia Villarino, G., Hernández Samaniego, A., Ramírez Merino, J.F., 1990. Hoja geológica número 778 (Don Benito). Mapa Geológico de España a Escala 1:50.000 (2ª serie). Instituto Geológico y Minero de España (IGME), Madrid. http://info.igme.es/cartografiadigital/geologica/Magna50Hoja.aspx?Id=778&language=es

Matte, P., 2001. The Variscan collage and orogeny (480–290 Ma) and the tectonic definition of the Armorica microplate: a review. Terra Nova 13, 122–128. https://doi.org/10.1046/j.1365-3121.2001.00327.x

McCulloch, M.T., Chappell, B.W., 1982. Nd isotopic characteristics of S- and I-type granites. Earth and Planetary Science Letters 58 (1), 51–64. https://doi.org/10.1016/0012-821X(82)90102-9

Meinhold, G., Kostopoulos, D., Frei, D., Himmerkus, F., Reischmann, T., 2010. U–Pb LA-SF-ICP-MS zircon geochronology of the Serbo-Macedonian Massif, Greece: palaeotectonic constraints for Gondwana-derived terranes in the Eastern Mediterranean. International Journal of Earth Sciences 99 (4), 813–832. https://doi.org/10.1007/s00531-009-0425-5

Merino Martínez, E., Villaseca, C., Orejana, D., Pérez-Soba, C., Belousova, E., Andersen, T., 2014. Tracing magma sources of three different S-type peraluminous granitoid

series by in situ U–Pb geochronology and Hf isotope zircon composition: the Variscan Montes de Toledo Batholith (central Spain). Lithos 200–201, 273–298. http://dx.doi.org/10.1016/j.lithos.2014.04.013

Michon, G., 1987. Les vaugnérites de l'Est du Massif central français: apport de l'analyse statistique multivariée à l'étude géochimique des éléments majeurs. Bulletin de la Société Géologique de France 8, 591–600.

Middlemost, E.A.K., 1994. Naming materials in the magma/igneous rock system. Earth-Science Reviews 37 (3–4), 215–224. https://doi.org/10.1016/0012-8252(94)90029-9

Miller, C.F., 1985. Are strongly peraluminous magmas derived from pelitic sedimentary sources? The Journal of Geology 93 (6), 673–689. http://dx.doi.org/10.1086/628995

Miller, C.F., Stoddard, E.F., Bradfish, L.J., Dollase, W.A., 1981. Composition of plutonic muscovite: genetic implications. The Canadian Mineralogist 19 (1), 25–34.

Miyashiro, A., 1970. Volcanic rock series in island arcs and active continental margins. American Journal of Science 274, 321–355. http://dx.doi.org/10.2475/ajs.274.4.321

Montel, J.-M., 1988. First discovery of an orthopyroxene bearing vaugnerite: petrography, geochemistry, and implications on the genesis of vaugnerites. Comptes Rendus de l'Académie des Sciences de Paris, 306, 985–990.

Montel, J.-M., 1993. A model for monazite/melt equilibrium and application to the generation of granitic magmas. Chemical Geology 110 (1–3), 127–146. http://dx.doi.org/10.1016/0009-2541(93)90250-M

Montel, J.-M., Vielzeuf, D., 1997. Partial melting of metagreywackes, Part II. Composition of minerals and melts. Contributions to Mineralogy and Petrology 128 (2), 176–196. https://doi.org/10.1007/s004100050302

Montel, J.-M., Weisbrod, A., 1986. Charactéristiques and évolution of 'vaugnéritic magmas' an analytical and experimental approach, on the exemple of Cévennes Médianes (French Massif Central). Bulletin de Minéralogie 109, 557–587.

Montero, P., Bea, F., Zinger, T.F., 2004. Edad $^{207}Pb/^{206}Pb$ en cristal único de circón de las rocas máficas y ultramáficas del sector de Gredos, Batolito de Ávila (Iberia Central). Revista de la Sociedad Geologica de España 17, 157–165.

Montero, P., Bea, F., González-Lodeiro, F., Talavera, C., Whitehouse, M.J., 2007. Zircon ages of the metavolcanic rocks and metagranites of the Ollo de Sapo Domain in central Spain: implications for the Neoproterozoic to Early Palaeozoic evolution of Iberia. Geological Magazine 144 (6), 963–976. https://doi.org/10.1017/S0016756807003858

Morimoto, N., 1988. Nomenclature of Pyroxenes. Mineralogy and Petrology 39 (1), 55–76. https://doi.org/10.1007/BF01226262

Moyen, J.-F., Laurent, O., Chelle-Michou, C., Couzinié, S., Vanderhaeghe, O., Zeh, A., Villaros, A., Gardien, V., 2017. Collision vs. subduction-related magmatism: two contrasting ways of granite formation and implications for crustal growth. Lithos 277, 154–177. https://doi.org/10.1016/j.lithos.2016.09.018

Nabelek, P.I., Whittington, A.G., Hofmeister, A.M., 2010. Strain heating as a mechanism for partial melting and ultrahigh temperature metamorphism in convergent orogens: Implications of temperature-dependent thermal diffusivity and rheology. Journal of Geophysical Research 115 (B12), 417 https://doi.org/10.1029/2010JB007727

Nachit, H., Razafimahefa, N., Stussi, J.-M., Carron, P.J., 1985. Composition chimique des biotites et typologie magmatique des granitoïdes. Comptes Rendus de l'Académie des Sciences 301 (11), 813–818.

Neiva, A.M.R., Silva, P.B., Corfu, F., Ramos, J.M.F., 2011. Sequential melting and fractional crystallization: granites from Guarda–Sabugal area, central Portugal. Chemie der Erde – Geochemistry 71 (3), 227–245. https://doi.org/10.1016/j.chemer.2011.06.002

Nogales Basarrarte, T., 2007. Teatro romano de Augusta Emerita. Evolución y programas decorativos. Mainake 29, 103–138.

Oen, I.S., 1970. Granite intrusion, folding and metamorphism in central northern Portugal. Boletín Geológico y Minero 81, 271–298.

Orejana, D., Villaseca, C., Billström, K., Paterson, B.A., 2008. Petrogenesis of Permian alkaline lamprophyres and diabases from the Spanish Central System and their geodynamic context within western Europe. Contributions to Mineralogy and Petrology 156 (4), 477–500. https://doi.org/10.1007/s00410-008-0297-x

Orejana, D., Villaseca, C., Valverde-Vaquero, P., Belousova, E., Armstrong, A., 2012. U–Pb geochronology and zircon composition of late Variscan S- and I-type granitoids from the Spanish Central System Batholith. International Journal of Earth Sciences 101 (7), 1789–1815. https://doi.org/10.1007/s00531-012-0750-y

Orejana, D., Merino Martínez, E., Villaseca, C., Andersen, T., 2015. Ediacaran–Cambrian paleogeography and geodynamic setting of the Central Iberian Zone: Constraints from coupled U–Pb–Hf isotopes of detrital zircons. Precambrian Research 261, 234–251. https://doi.org/10.1016/j.precamres.2015.02.009

Padilla, A.J., Gualda, G.A.R., 2016. Crystal-melt elemental partitioning in silicic magmatic systems: An example from the Peach Spring Tuff high-silica rhyolite, Southwest USA. Chemical Geology 440, 326–344. https://doi.org/10.1016/j.chemgeo.2016.07.004

Palacios, T., Eguíluz, L., Apalategui, O., Jensen, S., Martínez-Torres, L.M., Carracedo, M., Gil Ibarguchi, J.I., Sarrionandia, F., Martí, M., 2013. Mapa Geológico de Extremadura 1/350.000 y su memoria. Bilbao, Servicio Editorial de la UPV-EHU, 68x98cm, 222pp.

Paterson, S.R., Vernon, R.H., 1995. Bursting the bubble of ballooning plutons: A return to nested diapirs emplaced by multiple processes. Geological Society of America Bulletin 107 (11), 1356–1380. https://doi.org/10.1130/0016-7606(1995)107<1356:BTBOBP>2.3.CO;2

Patiño Douce, A.E., 1996. Effects of pressure and H2O content on the compositions of primary crustal melts. Transactions of the Royal Society of Edinburgh: Earth Sciences 87 (1–2), 11–21. https://doi.org/10.1017/S026359330000643X

Patiño Douce, A.E., 1999. What do experiments tell us about the relative contributions of crust and mantle to the origin of granitic magmas? In: Castro, A., Fernandez, C., Vigneresse, J.L. (Eds.), Understanding Granites: Integrating New and Classical Techniques. Geological Society, London, Special Publications,168, pp. 55–75. http://dx.doi.org/10.1144/GSL.SP.1999.168.01.05

Patiño Douce, A.E., Beard, J.S., 1995. Dehydration-melting of biotite gneiss and quartz amphibolite from 3 to 15 kbar. Journal of Petrology 36 (3), 707–738. https://doi.org/10.1093/petrology/36.3.707

Patiño Douce, A.E., Harris, N., 1998. Experimental constraints on Himalayan anatexis. Journal of Petrology 39 (4), 689–710. https://doi.org/10.1093/petroj/39.4.689

Patiño Douce, A.E., Johnston, A. D., 1991. Phase equilibria and melt productivity in the pelitic system: implications for the origin of peraluminous granitoids and aluminous granulites. Contributions to Mineralogy and Petrology 107 (2), 202–218. https://doi.org/10.1007/BF00310707

Paton, C., Hellstrom, J., Paul, B., Woodhead, J., Hergt, J., 2011. Iolite: Freeware for the visualisation and processing of mass spectrometric data. Journal of Analytical Atomic Spectrometry 26 (12), 2508–2518. https://doi.org/10.1039/C1JA10172B

Paul, B., Paton, C., Norris, A., Woodhead, J., Hellstrom, J., Hergt, J., Greig, A., 2012. CellSpace: A module for creating spatially registered laser ablation images within the Iolite freeware environment. Journal of Analytical Atomic Spectrometry 27 (4), 700–706. https://doi.org/10.1039/C2JA10383D

Peacock, M.A., 1931. Classification of igneous rock series. Journal of Geology 39 (1), 54–67. https://doi.org/10.1086/623788

Pearce, J.A., Harris, N.B.W., Tindle, A.G., 1984. Trace element discrimination diagrams for the tectonic interpretation of granitic rocks. Journal of Petrology 25 (4), 956–983. https://doi.org/10.1093/petrology/25.4.956

Peccerillo, A., Taylor, S.R., 1976. Geochemistry of Eocene calc-alkaline volcanic rocks from the Kastamonu area, Northern Turkey. Contributions to Mineralogy and Petrology 58 (1), 63–81. https://doi.org/10.1007/BF00384745

Pereira, M.D., Bea, F., 1994. Cordierite-producing reactions in the Pena Negra Complex, Avila Batholith, central Spain; the key role of cordierite in low-pressure anatexis. The Canadian Mineralogist 32 (4), 763–780.

Pérez-Soba, C., Villaseca, C., Orejana, D., and Jeffries, T., 2014. Uranium-rich accessory minerals in the peraluminous and perphosphorous granites of the Belvís de Monroy pluton (Iberian Variscan Belt). Contributions to Mineralogy and Petrology 167, 1–25. https://doi.org/10.1007/s00410-014-1008-4

Pérez-Soba, C., Villaseca, C., Fernández, A., 2017. Magmatic graphite inclusions in Mn-Fe-rich fluorapatite of perphosphorus granites (the Belvís pluton, Variscan Iberian Belt). American Mineralogist 102 (4), 728–742. https://doi.org/10.2138/am-2017-5895

Pesquera, A., Gil-Crespo, P.P., Torres-Ruiz, J., Roda-Robles, E., 2017. Insights into petrogenesis of the Jálama Pluton (Central Iberian Zone, western Spain). International Geology Review 60 (2), 157–187. https://doi.org/10.1080/00206814.2017.1316687

Petford, N., Koenders, M.A., 1998. Self-organisation and fracture connectivity in rapidly heated continental crust. Journal of Structural Geology 20 (9–10), 1425–1434. https://doi.org/10.1016/S0191-8141(98)00081-9

Petford, N., Cruden, A.R., McCaffrey, K.J.W., Vigneresse, J.-L., 2000. Granite magma formation, transport and emplacement in the Earth's crust. Nature 408, 669–673. https://doi.org/10.1038/35047000

Petrus, J.A., Kamber, B.S., 2012. VizualAge: A Novel Approach to Laser Ablation ICP-MS U-Pb Geochronology Data Reduction. Geostandards and Geoanalytical Research 36, 247–270. http://dx.doi.org/10.1111/j.1751-908X.2012.00158.x

Pichavant, M., Montel, J-M., Richard, L.R., 1992. Apatite solubility in peraluminous liquids: experimental data and an extension of the Harrison–Watson model. Geochimica et Cosmochimica Acta 56 (10), 3855–3861. http://dx.doi.org/10.1016/0016-7037(92)90178-L

Pin, C., Santos Zalduegui, J.F., 1997. Sequential separation of light rare-earth elements, thorium and uranium by miniaturized extraction chromatography: Application to isotopic analyses of silicate rocks. Analytica Chimica Acta 339 (1–2), 79–89. https://doi.org/10.1016/S0003-2670(96)00499-0

Pin, C., Binon, M., Belin, J.M., Barbarin, B., Clemens, J.D., 1990. Origin of Microgranular Enclaves in Granitoids' Equivocal Sr-Nd Evidence From Hercynian Rocks in the Massif Central (France). Journal of Geophysical Research 951 (B11), 17821–17827. https://doi.org/10.1029/JB095iB11p17821

Pin, C., Briot, D., Bassin, C., Poitrasson, F., 1994. Concomitant separation of strontium and samarium-neodymium for isotopic analysis in silicate samples, based on specific extraction chromatography. Analytica Chimica Acta 298 (2), 209–217. https://doi.org/10.1016/0003-2670(94)00274-6

Pitcher, W.S., 1979. The nature, ascent and emplacement of granitic magmas. Journal of the Geological Society, London 136, 627–662. https://doi.org/10.1144/gsjgs.136.6.0627

Pitcher, W.S., 1987. Granites and yet more granites forty years on. Geologische Rundschau 76 (1), 51–79. https://doi.org/10.1007/BF01820573

Pitcher, W.S., 1997. The nature and origin of granite (2nd ed). Chapman & Hall, London, 387 pp. https://doi.org/10.1093/petroj/39.6.1249-a

Pizzo, A., 2001. La casa del Anfiteatro de Augusta Emerita. Mérida, excavaciones arqueológicas 7, 335–350.

Ramírez, J.A., González Menéndez, L., 1999. A geochemical study of two peraluminous granites from south-central Iberia: the Nisa–Albuquerque and Jálama batholiths. Mineralogical Magazine 63 (1), 85–104. https://doi.org/10.1180/002646199548330

Ramírez, J.A., Grundvig, S., 2000. Causes of geochemical diversity in peraluminous granitic plutons: the Jálama Pluton, Central-Iberian Zone (Spain and Portugal). Lithos 50 (1–3), 171–190. https://doi.org/10.1016/S0024-4937(99)00047-X

Rapp, R.P., Watson, E.B., 1986. Monazite solubility and dissolution kinetics: implications for the thorium and light rare earth chemistry of felsic magmas. Contributions to Mineralogy and Petrology 94 (3), 304–316. http://dx.doi.org/10.1007/BF00371439

Read, H.H., 1957. The Granite Controversy. Thomas Murby & Co., London, 430 pp.

Rock, N.M.S., 1991. Lamprophyres. Boston, MA, Springer US, 285pp. https://doi.org/10.1007/978-1-4757-0929-2

Robardet, M., Gutiérrez-Marco, J.C., 2002. Silurian. In: Gibbons, W., Moreno, T. (Eds.), The Geology of Spain. Geological Society, London, pp. 51–65.

Roda-Robles, E., Pesquera, A., Gil-Crespo, P.P., Vieira, R., Lima, A., Garate-Olave, I., Martins, T., Torres.Ruiz, J., 2016. Geology and mineralogy of Li mineralization in the Central Iberian zone (Spain and Portugal). Mineralogical Magazine 80 (1), 103–126. https://doi.org/10.1180/minmag.2016.080.049

Roda-Robles, E., Villaseca, C., Pesquera, A., Gil-Crespo, P.P., Vieira, R., Lima, A., Garate-Olave, I., 2018. Petrogenetic relationships between Variscan granitoids and Li–(F–P)-rich aplite–pegmatites in the Central Iberian Zone: geological and geochemical constraints and implications for other regions from the European Variscides. Ore Geology Reviews 95, 408–430. https://doi.org/10.1016/j.oregeorev.2018.02.027

Rodríguez, C., Castro, A., 2017. Silicic magma differentiation in ascent conduits. Experimental constraints. Lithos 272–273, 261–277. https://doi.org/10.1016/j.lithos.2016.12.017

Rodríguez, J., Gil Ibarguchi, J.I., Paquette, J.L., 2007. Sincronía del magmatismo Varisco en el Macizo Ibérico: nuevas edades U-Pb en granitoides de la región de Finisterre

(La Coruña, España). XV Semana – VI Congreso Ibérico de Geoquímica, Vila Real, Portugal, DVD-ROM (ISBN: 978-972-669-805-0), 146–149

Rodríguez Fernández, L.R., Oliveira, J.T., 2015. Mapa geológico de España y Portugal a escala 1:1.000.000. Instituto Geológico y Minero de España, Laboratório Nacional de Energia e Geologia de Portugal. http://info.igme.es/cartografiadigital/geologica/Geologicos1MMapa.aspx?Id=Geologico1000_(2015)

Rodríguez-Alonso, M.D., Peinado, M., López-Plaza, M., Franco, P., Carnicero, A., Gonzalo, J.C., 2004. Neoproterozoic–Cambrian synsedimentary magmatism in the Central Iberian Zone (Spain): geology, petrology and geodynamic significance. International Journal of Earth Sciences 93 (5), 897–920. https://doi.org/10.1007/s00531-004-0425-4

Roso de Luna, I., Pacheco, F.H., 1949. Hoja geológica número 752 (Mirandilla). Mapa Geológico de España a Escala 1:50.000 (1ª serie). Madrid: Instituto Geológico y Minero de España (IGME). http://info.igme.es/cartografiadigital/geologica/Geo50Hoja.aspx?Id=752&language=es

Rossi, P., Chevremont, P., 1987. Classification des associations magmatiques granitoides. Géochronique 21, 14–18.

Rubio-Ordóñez, A., Valverde-Vaquero, P., Corretgé, L.G., Cuesta-Fernández, A., Gallastegui, G., Fernández-González, M., Gerdes, A., 2012. An Early Ordovician tonalitic–granodioritic belt along the Schistose–Greywacke Domain of the Central Iberian Zone (Iberian Massif, Variscan Belt). Geological Magazine 149 (5), 927–939. https://doi.org/10.1017/S0016756811001129

Rudnick, R.L., Gao, S., 2003. Composition of the continental crust. In: Holland, H.D., Turekian, K.K. (Eds.). Treatise on Geochemistry. Oxford, Elsevier-Pergamon, 1–64.

Rudnick, R.L., Gao, S., 2014. Composition of the Continental Crust. In: Holland, H.D., Turekian, K.K. (Eds.), Treatise on Geochemistry, second Edition, Volume 4: The Crust. Elsevier Science, Oxford, pp. 1–51. https://doi.org/10.1016/B978-0-08-095975-7.00301-6

Sabatier, H., 1980. Vaugérites et granites: une association particulière de roches grenues acides et basiques. Bulletin de Minéralogie, 103, 507–522.

Sabatier, H., 1991. Vaugnerites: special lamprophyre-derived mafic enclaves in some Hercynian granites from Western and Central Europe. In: Didier, J., Barbarin, B. (Eds.). Enclaves and Granite Petrology. Developments in Petrology, Amsterdam, Elsevier, 63–81.

Sánchez Lorda, M.E., Sarrionandia, F., Ábalos, B., Carrracedo, M., Eguíluz, L., Gil Ibarguchi, J.I., 2014. Geochemistry and paleotectonic setting of Ediacaran

metabasites from the Ossa-Morena Zone (SW Iberia). International Journal of Earth Sciences 103 (5) 1263–1286. https://doi.org/10.1007/s00531-013-0937-x

Sánchez Lorda, M.E., Ábalos, B., García de Madinabeitia, S., Eguíluz, L., Gil Ibarguchi, J.I., Paquette, J.-L., 2016. Radiometric discrimination of pre-Variscan amphibolites in the Ediacaran Serie Negra (Ossa-Morena Zone, SW Iberia). Tectonophysics 681, 31–45. https://doi.org/10.1016/j.tecto.2015.09.020

Sarrionandia, F., Carracedo, M., Eguíluz, L., Apalategui, O., 2004. Potencial ornamental del plutón de Sierra Bermeja (Badajoz): evaluación de su canterabilidad. Geogaceta 35, 103–106.

Sauer, A., 1893. Der Granitit von Durbach im nordlichen Schwarzwald un seine Grenzfacies von Glimmersyenit (Durbachit). Mitteilung der Badischen Geologischen Landesanstalt 2, 233–276.

Sawka, W.N., 1988. REE and trace element variations in accessory minerals and hornblende from the strongly zoned McMurry Meadows Pluton, California. Transactions of the Royal Society of Edinburgh: Earth Sciences 79 (2–3), 157–168. https://doi.org/10.1017/S0263593300014188

Sawyer, E.W., Cesare, B., Brown, M., 2011. When the Continental Crust Melts. Elements 7 (4), 229–234. https://doi.org/10.2113/gselements.7.4.229

Scaillet, B., Holtz, F., Pichavant, M., 2016. Experimental Constraints on the Formation of Silicic Magmas. Elements 12 (2), 109–114. https://doi.org/10.2113/gselements.12.2.109

Scarrow, J.H., Bea, F., Montero, P., Molina, J.F., Vaughan, A.P.M., 2006. A precise late Permian $^{40}Ar/^{39}Ar$ age for Central Iberian camptonitic lamprohyres. Geologica Acta 4, 451–459. http://dx.doi.org/10.1344/105.000000346

Scarrow, J.H., Molina, J.F., Bea, F., Montero, P., 2009. Within-plate calc-alkaline rocks: Insights from alkaline mafic magma–peraluminous crustal melt hybrid appinites of the Central Iberian Variscan continental collision. Lithos 110 (1–4), 50–64. https://doi.org/10.1016/j.lithos.2008.12.007

Scarrow, J.H., Molina, J.F., Bea, F., Montero, P., Vaughan, A.P.M., 2011. Lamprophyre dikes as tectonic markers of late orogenic transtension timing and kinematics: A case study from the Central Iberian Zone. Tectonics 30 (4), TC4007. https://doi.org/10.1029/2010TC002755

Schulmann, K., Martínez Catalán, J.R., Lardeaux, J.M., Janoušek, V., Oggiano, G., 2014. The Variscan orogeny: extent, timescale and the formation of the European crust. In: Schulmann, K., Martínez Catalán, J.R., Lardeaux, J.M., Janoušek, V., Oggiano, G. (Eds.), The Variscan Orogeny: Extent, Timescale and the Formation of the European Crust. Geological Society, London, Special Publications 405, 1–6. https://doi.org/10.1144/SP405.15

Shand, S.J., 1943. Eruptive rocks. Their Genesis, Composition, Classification, and Their Relation to Ore-Deposits with a Chapter on Meteorite. John Wiley and Sons, New York.

Sial, A.N., Bettencourt, J.S., De Campos, C.P., Ferreira, V.P., 2011. Granite-related ore deposits: an introduction. Geological Society of London, Special Publications 350, 1–5. https://doi.org/10.1144/SP350.1

Siebel, W., Chen, F., Satir, M., 2003. Late-Variscan magmatism revisited: New implications from Pb-evaporation zircon ages on the emplacement of redwitzites and granites in NE Bavaria. International Journal of Earth Sciences 92 (1), 36–53. https://doi.org/10.1007/s00531-002-0305-8

Sláma, J., Kosler, J., Condon, D.J., Crowley, J.L., Gerdes, A., Hanchar, J.M., Horstwood, M.S.A., Morris, G.A., Nasdala, L., Norberg, N., Schaltegger, U., Schoene, B., Tubrett, M.N., Whitehouse, M.J., 2008. Plešovice zircon - a new natural reference material for U–Pb and Hf isotopic microanalysis. Chemical Geology 249 (1–2), 1–35. https://doi.org/10.1016/j.chemgeo.2007.11.005

Solá, A.R., Pereira, M.F., Williams, I.S., Ribeiro, L.M., Neiva, A.M.R., Montero, P., Bea, F., Zinger, T., 2008. New insights from U–Pb zircon dating of Early Ordovician magmatism on the northern Gondwana margin: the Urra Formation (SW Iberian Massif, Portugal). Tectonophysics 461 (1–4), 114–129. https://doi.org/10.1016/j.tecto.2008.01.011

Solá, A.R., Williams, I.S., Neiva, A.M.R., Ribeiro, L.M., 2009. U–Th–Pb SHRIMP ages and oxygen isotope composition of zircon from two contrasting late Variscan granitoids, Nisa–Albuquerque Batholith, SW Iberian Massif: petrologic and regional implications. Lithos 111 (3–4), 156–167. https://doi.org/10.1016/j.lithos.2009.03.045

Solgadi, F., Moyen, J.-F., Vanderhaeghe, O., Sawyer, E.W., Reisberg, L., 2007. The role of crustal anatexis and mantle-derived magmas in the genesis of synorogenic Hercynian granites of the Livradois Area, French Massif Central. The Canadian Mineralogist 45, 581–606. http://dx.doi.org/10.2113/gscanmin.45.3.581

Spencer, C.J., Roberts, N.M.W., Santosh, M., 2017. Growth, destruction, and preservation of Earth's continental crust. Earth-Science Reviews 172, 87-106. https://doi.org/10.1016/j.earscirev.2017.07.013

Stepanov, A.S., Hermann, J., Rubatto, D., Rapp, R.P., 2012. Experimental study of monazite/melt partitioning with implications for the REE, Th and U geochemistry of crustal rocks. Chemical Geology 300–301, 200–220. https://doi.org/10.1016/j.chemgeo.2012.01.007

Streckeisen, A., 1976. To Each Plutonic Rock Its Proper Name. Earth Science Reviews 12 (1), 1-33. http://dx.doi.org/10.1016/0012-8252(76)90052-0

Sun, S.S., McDonough, W.F., 1989. Chemical and isotopic systematics of oceanic basalts; implications for mantle composition and processes. In: Saunders, A.D., Norry, M.J. (Eds.), Magmatism in the Ocean Basins. Geological Society of London Special Publications 42, 313–345. https://doi.org/10.1144/GSL.SP.1989.042.01.19

Sureda, J., 1991. Las Primeras Civilizaciones: Prehistoria. Egipto. Próximo Oriente. In: Milicua, J., (Ed.), Historia Universal del Arte (Vol. 1). Planeta, Vitoria.

Sylvester, P.J., 1998. Post-collisional strongly peraluminous granites. Lithos 45 (1–4), 29–44. https://doi.org/10.1016/S0024-4937(98)00024-3

Talavera, C., Montero, P., Martínez Poyatos, D., Williams, I.S., 2012. Ediacaran to Lower Ordovician age for rocks ascribed to the Schist–Graywacke Complex (Iberian Massif, Spain): evidence from detrital zircon SHRIMP U–Pb geochronology. Gondwana Research 22 (3–4), 928–942. https://doi.org/10.1016/j.gr.2012.03.008

Talavera, C., Montero, P., Bea, F., González Lodeiro, F., Whitehouse, M., 2013. U–Pb Zircon geochronology of the Cambro–Ordovician metagranites and metavolcanic rocks of central and NW Iberia. International Journal of Earth Sciences 102 (1), 1–23. https://doi.org/10.1007/s00531-012-0788-x

Talavera, C., Martínez Poyatos, D., González Lodeiro, F., 2015. SHRIMP U–Pb geochronological constraints on the timing of the intra-Alcudian (Cadomian) angular unconformity in the Central Iberian Zone (Iberian Massif, Spain). International Journal of Earth Sciences 104 (7), 1739–1757. https://doi.org/10.1007/s00531-015-1171-5

Turpin, L., Velde, D., Pinte, G., 1988. Geochemical comparison between minettes and kersantites from the Western European Hercynian orogen: trace element and Pb-Sr-Nd isotope constraints on their origin. Earth and Planetary Science Letters 87, 73–86.

Tuttle, O.F., Bowen, N.L., 1958. Origin of Granite in the Light of Experimental Studies in the System $NaAlSi_3O_8$–$KAlSi_3O_8$–$SiO_2$–$H_2O$. Geological Society of America Memoirs 74, 1–146. https://doi.org/10.1130/MEM74

Twidale, C.R., Romaní, J.R.V., 2005. Landforms and geology of granite terrains. CRC Press, 348 pp.

Ugidos, J.M., 1988. New aspects and considerations on the assimilation of cordierite-bearing rocks. Revista de la Sociedad Geológica de España 1 (1–2), 129–133.

Ugidos, J.M., Recio, C., 1993. Origin of cordierite-bearing granites by assimilation in the Central Iberian Massif (CIM), Spain. Chemical Geology 103 (1–4), 27–43. https://doi.org/10.1016/0009-2541(93)90289-U

Ugidos, J.M., Valladares, M.I., Recio, C., Rogers, G., Fallick, A.E., Stephens, W.E., 1997. Provenance of Upper Precambrian–Lower Cambrian shales in the Central Iberian

Zone, Spain: evidence from a chemical and isotopic study. Chemical Geology 136 (1-2), 55–70. https://doi.org/10.1016/S0009-2541(96)00138-6

Ugidos, J.M., Valladares, M.I., Barba, P., Ellam, R.M., 2003. The Upper Neoproterozoic–Lower Cambrian of the Central Iberian Zone, Spain: chemical and isotopic (Sm–Nd) evidence that the sedimentary succession records an inverted stratigraphy of its source. Geochimica et Cosmochimica Acta 67 (14), 2615–2629. https://doi.org/10.1016/S0016-7037(03)00027-9

Ugidos, J.M., Stephens, W.E., Carnicero, A., Ellam, R.M., 2008. A reactive assimilation model for regional-scale cordierite-bearing granitoids: geochemical evidence from the Late Variscan granites of the Central Iberian Zone, Spain. Transactions of the Royal Society of Edinburgh: Earth Sciences 99 (3–4), 225–250. https://doi.org/10.1017/S1755691009008159

Valle Aguado, B., Azevedo, M.R., Schaltegger, U., Martínez Catalán, J.R., Nolan, J., 2005. U–Pb zircon and monazite geochronology of Variscan magmatism related to syn-convergence extension in Central Northern Portugal. Lithos 82 (1–2), 169–184. https://doi.org/10.1016/j.lithos.2004.12.012

Vermeesch, P., 2018. IsoplotR: A free and open toolbox for geochronology. Geoscience Frontiers 9 (5), 1479–1493. https://doi.org/10.1016/j.gsf.2018.04.001

Vielzeuf, D., Holloway, J.R., 1988. Experimental determination of the fluid-absent melting relations in the pelitic system. Consequences for crustal differentiation. Contributions to Mineralogy and Petrology 98 (3), 257–276. https://doi.org/10.1007/BF00375178

Vielzeuf, D., Montel, J.M., 1994. Partial melting of Al-metagreywackes. Part 1: Fluid absent experiments and phase relationships. Contributions to Mineralogy and Petrology 117 (4), 375–393. https://doi.org/10.1007/BF00307272

Villaseca, C., 2011. On the origin of granite types in the Central Iberian Zone: contribution from integrated U–Pb and Hf isotope studies of zircon. VIII Congresso Ibérico de Geoquímica, 271–276.

Villaseca, C., Barbero, L., Herreros, V., 1998a. A re-examination of the typology of peraluminous granite types in intracontinental orogenic belts. Transactions of the Royal Society of Edinburgh: Earth Sciences 89 (2), 113–119. https://doi.org/10.1017/S0263593300007045

Villaseca, C., Barbero, L., Rogers, G., 1998b. Crustal origin of Hercynian peraluminous granitic batholiths of central Spain: petrological, geochemical and isotopic (Sr, Nd) constraints. Lithos 43 (2), 55–79. https://doi.org/10.1016/S0024-4937(98)00002-4

Villaseca, C., Downes, H., Pin, C., Barbero, L., 1999. Nature and composition of the lower continental crust in Central Spain and the granulite-granite linkage: inferences from granulitic xenoliths. Journal of Petrology 40 (10), 1465–1496. https://doi.org/10.1093/petroj/40.10.1465

Villaseca, C., Pérez-Soba, C., Merino, E., Orejana, D., López-García, J.A., Billstrom, K., 2008. Contrasting crustal sources for peraluminous granites of the segmented Montes de Toledo Batholith (Iberian Variscan Belt). Journal of Geosciences 53 (3–4), 263–280. http://dx.doi.org/10.3190/jgeosci.035

Villaseca, C., Orejana, D., Paterson, B.A., Billstrom, K., Pérez-Soba, C., 2007. Metaluminous pyroxene-bearing granulite xenoliths from the lower continental crust in central Spain: their role in the genesis of Hercynian I-type granites. European Journal of Mineralogy 19 (4), 463–477. https://doi.org/10.1127/0935-1221/2007/0019-1746

Villaseca, C., Orejana, D., Belousova, E., 2012. Recycled metaigneous crustal sources for S- and I-type Variscan granitoids from the Spanish Central System Batholith: constraints from Hf isotope zircon composition. Lithos 153, 84–93. https://doi.org/10.1016/j.lithos.2012.03.024

Villaseca, C., Merino, E., Oyarzun, R., Orejana, D., Pérez-Soba, C., Chicharro, E., 2014. Contrasting chemical and isotopic signatures from Neoproterozoic metasediments in the Central-Iberian Zone of pre-Variscan Europe (Spain): implications for terrane analysis and Early Ordovician magmatic belts. Precambrian Research 245, 131–145. https://doi.org/10.1016/j.precamres.2014.02.006

Villaseca, C., Merino Martínez, E., Orejana, D., Andersen, T., Belousova, E., 2016. Zircon Hf signatures from granitic orthogneisses of the Spanish Central System: Significance and sources of the Cambro–Ordovician magmatism in the Iberian Variscan Belt. Gondwana Research 34, 60–83. https://doi.org/10.1016/j.gr.2016.03.004

von Raumer, J.F., Finger, F., Veselá, P., Stampfli, G.M., 2014. Durbachites–Vaugnerites–a geodynamic marker in the central European Variscan orogen. Terra Nova 26 (2), 85–95. https://doi.org/10.1111/ter.12071

Watson, E.B., Harrison, T.M., 1983. Zircon saturation revisited: temperature and composition effects in a variety of crustal magma types. Earth and Planetary Science Letters 64 (2), 295–304. http://dx.doi.org/10.1016/0012-821X(83)90211-X

Whalen, J.B., 1985. Geochemistry of an island-arc plutonic suite: the Uasilau–Yau Yau Intrusive Complex, New Britain, P.N.G. Journal of Petrology 26 (3), 603–632. https://doi.org/10.1093/petrology/26.3.603

Whitney, D.L., Evans, B.W., 2010. Abbreviations for names of rock-forming minerals. American Mineralogist 95 (1), 185–187. https://doi.org/10.2138/am.2010.3371

Willmann, K., 1920. Die Redwitzite, eine neue Gruppe von granitischen Lamprophyren. Zeitschrift der Deutschen Geologischen Gesellschaft, 71, 1–33.

Wilson Jones, M., 2000. Principles of Roman architecture. Yale University Press, Singapore. 284pp.

Wilson, M., 1993. Magmatic differentiation. Journal of the Geological Society, London 150, 611–624. https://doi.org/10.1144/gsjgs.150.4.0611

Winter, J.D., 2014. Principles of Igneous and Metamorphic Petrology (2nd ed.). Prentice Hall, New York, 738pp.

Zen, E., 1988. Phase Relations of Peraluminous Granitic Rocks and Their Petrogenetic Implications. Annual Review of Earth and Planetary Sciences 16, 21–51. https://doi.org/10.1146/annurev.ea.16.050188.000321

# CHAPTER 12
# APPENDIX

***Supplementary Table 1.*** *Modal compositions (vol. %) of the monzogranites from the Sierra Bermeja Pluton*

| Unit | Sample | Qz | Kfs* | Pl | Crd | Bt | Ms | Ap | Tur | Mnz | Zrn | Xtm | Ilm | Rt | And |
|---|---|---|---|---|---|---|---|---|---|---|---|---|---|---|---|
| Outer Unit (OU) | JE_15_26 | 25.5 | 26.6 | 35.6 | 0.9 | 12.3 | - | 2 | - | < 1 | < 1 | - | - | - | - |
| | JE_15_62 | 26.3 | 20.9 | 37.1 | 1.3 | 14.3 | < 1 | 2.1 | - | < 1 | - | < 1 | < 1 | - | - |
| | JE_15_68 | 25.6 | 24.7 | 44.5 | 1.9 | 7.9 | - | 1.8 | < 1 | < 1 | < 1 | - | < 1 | - | - |
| | JE_15_34 | 26.3 | 24.2 | 38.7 | 4.0 | 7.0 | - | 0.8 | - | < 1 | < 1 | - | - | - | - |
| | JE_15_35 | 29.3 | 21.2 | 36.9 | 1.7 | 7.9 | < 1 | 1.5 | - | - | < 1 | < 1 | - | - | - |
| | JE_15_36 | 26.9 | 23.3 | 36.7 | 2.5 | 8.4 | < 1 | 1.6 | - | < 1 | < 1 | - | < 1 | - | - |
| | JE_15_48 | 26.7 | 21.9 | 38.5 | 3.9 | 9.8 | - | 1.4 | < 1 | < 1 | < 1 | - | - | - | - |
| | JE_15_60 | 31.2 | 25.0 | 36.1 | 1.0 | 5.6 | < 1 | 0.9 | - | < 1 | - | - | < 1 | - | - |
| | SB_169 | 37.5 | 19.2 | 35.1 | 4.9 | 8.0 | < 1 | 1.7 | < 1 | - | < 1 | < 1 | - | - | - |
| | JE_15_38 | 30.9 | 24.1 | 33.4 | 2.5 | 7.4 | < 1 | 1.2 | < 1 | < 1 | < 1 | < 1 | < 1 | - | - |
| Middle Unit (MU) | JE_15_30 | 31.2 | 33.3 | 26.6 | 4.1 | 3.6 | - | 1.2 | < 1 | < 1 | - | - | < 1 | - | - |
| | JE_15_57 | 33.7 | 26.8 | 27.8 | 3.5 | 7.1 | < 1 | 1.1 | - | - | < 1 | < 1 | - | - | - |
| | JE_16_23 | 33.4 | 26.3 | 29.1 | 3.6 | 6.7 | - | 0.9 | < 1 | < 1 | - | - | - | - | - |
| | JE_16_44 | 38.5 | 26.5 | 25.4 | 3.7 | 4.6 | 1.6 | 1.3 | - | < 1 | - | - | < 1 | - | - |
| | JE_15_59 | 32.4 | 26.2 | 28.3 | 8.4 | 4.1 | < 1 | 0.6 | < 1 | - | < 1 | < 1 | - | - | - |
| | JE_15_65 | 34.2 | 25.7 | 28.2 | 7.2 | 3.2 | < 1 | 1.5 | < 1 | < 1 | < 1 | - | - | - | - |
| | JE_15_53 | 34.1 | 26.6 | 28.4 | 6.5 | 3.3 | < 1 | 1.1 | - | < 1 | - | < 1 | < 1 | - | - |
| | JE_15_67 | 32.5 | 25.6 | 29.1 | 8.4 | 3.2 | < 1 | 1.2 | - | < 1 | < 1 | - | - | - | - |
| | JE_15_56 | 32.1 | 25.1 | 35.4 | 6.3 | 3.1 | < 1 | 0.5 | < 1 | - | < 1 | - | < 1 | - | - |
| | JE_15_04 | 33.2 | 26.1 | 28.7 | 6.5 | 4.7 | < 1 | 0.8 | - | < 1 | < 1 | - | - | - | - |
| | SB_171 | 35.2 | 24.4 | 26.9 | 7.6 | 4.6 | < 1 | 1.3 | - | < 1 | - | - | < 1 | - | - |
| | SB_166 | 34.1 | 25.4 | 26.6 | 10.3 | 3.7 | < 1 | 0.8 | < 1 | < 1 | < 1 | < 1 | < 1 | - | - |
| | SB_176 | 37.1 | 26.7 | 29 | 6.9 | 3.3 | < 1 | 1.0 | - | - | < 1 | - | - | - | - |
| | SB_179 | 35.1 | 25.5 | 27.6 | 9.3 | 3.5 | 1.7 | 0.7 | < 1 | < 1 | - | < 1 | - | - | - |
| | SB_160 | 39.6 | 24.5 | 25.5 | 6.6 | 3.1 | 1.5 | 1.1 | < 1 | < 1 | < 1 | < 1 | < 1 | - | - |
| Inner Unit (IU) | JE_15_66 | 34.0 | 24.4 | 23.7 | 6.6 | 3.1 | 6.7 | 1.5 | - | - | < 1 | - | - | < 1 | < 1 |
| | JE_15_45 | 35.3 | 26.7 | 28.3 | 2.2 | 3.1 | 4.8 | 1.2 | - | < 1 | < 1 | - | - | - | - |
| | JE_15_51 | 33.1 | 30.6 | 26.7 | 3.1 | 2.8 | 3.6 | 1.3 | - | - | < 1 | - | < 1 | < 1 | - |
| | SB_180 | 39 | 24.1 | 25.6 | 2.7 | 3.4 | 5.1 | 1.1 | < 1 | < 1 | - | < 1 | - | - | < 1 |
| | JE_15_64 | 33.5 | 26.9 | 27.8 | 3.8 | 4.6 | 2.2 | 1.2 | < 1 | < 1 | < 1 | - | - | < 1 | - |
| | SB_184 | 37 | 24.7 | 29.5 | 0.9 | 2.3 | 4.7 | 0.9 | - | - | - | - | < 1 | - | - |
| | JE_15_28 | 31.4 | 27.7 | 31.6 | 4.5 | 1.8 | 1.8 | 1.1 | < 1 | < 1 | < 1 | < 1 | - | < 1 | - |
| | SB_162 | 41.4 | 21.6 | 24 | 4.8 | 0.6 | 7.8 | 1.2 | < 1 | < 1 | - | - | - | - | - |
| | SB_186 | 36.6 | 26.6 | 25.3 | 4.7 | 0.8 | 6.3 | 0.8 | - | - | < 1 | - | < 1 | - | - |
| | JE_16_45 | 37.6 | 28.9 | 26.5 | 2.3 | 0.9 | 5.4 | 0.6 | < 1 | < 1 | < 1 | - | - | < 1 | < 1 |

*In the Outer Unit Kfs was calculated adding an estimation of phenocryst concentration to the point count analyses

Mineral abbreviations from Whitney and Evans (2010)

***Supplementary Table 2.*** *Electron microprobe analyses of K-feldspar from the Sierra Bermeja Pluton*

| Sample | Kfs 1 | Kfs 2 | Kfs 3 | Kfs 4 | Kfs 5 | Kfs 6 | Kfs 7 | Kfs 8 | Kfs 9 | Kfs 10 |
|---|---|---|---|---|---|---|---|---|---|---|
| Unit | OU | OU | OU | OU | OU | OU | OU | OU | OU | OU |
| Type | * | * | * | * | * | ** | ** | ** | * | * |
| $SiO_2$ | 64.57 | 64.25 | 64.29 | 64.37 | 63.95 | 65.33 | 64.86 | 65.10 | 64.39 | 64.28 |
| $TiO_2$ | < MDL | 0.02 | 0.01 | 0.06 | 0.02 | 0.02 | < MDL | 0.03 | < MDL | 0.01 |
| $Al_2O_3$ | 18.58 | 18.34 | 18.15 | 18.58 | 18.26 | 18.80 | 18.70 | 18.64 | 18.93 | 18.55 |
| $Cr_2O_3$ | < MDL | < MDL | < MDL | 0.04 | 0.05 | < MDL | < MDL | 0.01 | < MDL | < MDL |
| NiO | < MDL | 0.15 | < MDL | 0.07 | < MDL | < MDL | < MDL | < MDL | < MDL | < MDL |
| FeO | < MDL | 0.02 | 0.03 | 0.02 | 0.02 | 0.02 | < MDL | < MDL | 0.02 | < MDL |
| MnO | < MDL | < MDL | 0.12 | 0.05 | 0.10 | 0.02 | 0.01 | 0.01 | < MDL | < MDL |
| MgO | < MDL | 0.01 | < MDL | 0.01 | 0.01 | 0.01 | < MDL | < MDL | 0.03 | 0.01 |
| CaO | 0.04 | 0.13 | 0.03 | 0.04 | 0.06 | 0.01 | 0.03 | 0.02 | 0.02 | 0.01 |
| $Na_2O$ | 0.76 | 0.39 | 0.38 | 0.63 | 0.45 | 1.28 | 1.20 | 0.85 | 0.94 | 1.29 |
| $K_2O$ | 15.60 | 16.20 | 16.37 | 16.25 | 16.33 | 15.08 | 15.31 | 15.59 | 15.60 | 15.08 |
| $P_2O_5$ | NA | NA | NA | NA | NA | 0.10 | 0.05 | 0.06 | 0.05 | 0.02 |
| Total | 99.55 | 99.51 | 99.37 | 100.10 | 99.25 | 100.67 | 100.15 | 100.31 | 100.00 | 99.23 |
| Or | 92.95 | 95.87 | 96.45 | 94.27 | 95.69 | 88.49 | 89.25 | 92.20 | 91.47 | 88.48 |
| Ab | 6.87 | 3.48 | 3.40 | 5.54 | 3.99 | 11.46 | 10.59 | 7.68 | 8.42 | 11.49 |
| An | 0.18 | 0.65 | 0.14 | 0.19 | 0.32 | 0.04 | 0.16 | 0.12 | 0.12 | 0.03 |

* (phenocryst)
** (groundmass)
NA not analyzed
The Method Detection Limit (MDL) for the routine analysis of common elements is ~0.02 wt.%

***Supplementary Table 2.*** *Continued*

| Sample | Kfs 11 | Kfs 12 | Kfs 13 | Kfs 14 | Kfs 15 | Kfs 16 | Kfs 17 | Kfs 18 | Kfs 19 | Kfs 20 |
|---|---|---|---|---|---|---|---|---|---|---|
| Unit | OU | OU | OU | OU | OU | OU | OU | OU | OU | OU |
| Type | ** | ** | * | ** | * | * | * | * | * | * |
| $SiO_2$ | 64.56 | 64.25 | 65.08 | 64.72 | 65.89 | 64.12 | 65.20 | 64.43 | 64.48 | 64.68 |
| $TiO_2$ | < MDL | 0.01 | 0.01 | 0.02 | 0.04 | < MDL | 0.01 | 0.02 | 0.01 | < MDL |
| $Al_2O_3$ | 18.63 | 18.66 | 18.82 | 18.99 | 18.52 | 18.86 | 18.89 | 18.61 | 18.61 | 18.85 |
| $Cr_2O_3$ | 0.02 | < MDL | 0.01 | < MDL | 0.01 | < MDL | 0.01 | < MDL | < MDL | 0.05 |
| NiO | < MDL | 0.04 | 0.05 | < MDL | < MDL | 0.01 | < MDL | 0.08 | 0.02 | 0.02 |
| FeO | 0.04 | < MDL | < MDL | < MDL | < MDL | 0.02 | 0.01 | < MDL | 0.06 | 0.01 |
| MnO | < MDL | 0.07 | < MDL | < MDL | < MDL | < MDL | < MDL | < MDL | < MDL | < MDL |
| MgO | 0.02 | < MDL | 0.01 | < MDL | 0.02 | < MDL | 0.01 | < MDL | < MDL | < MDL |
| CaO | 0.03 | 0.04 | 0.01 | 0.02 | < MDL | 0.01 | < MDL | < MDL | 0.02 | 0.03 |
| $Na_2O$ | 1.58 | 1.25 | 1.56 | 1.70 | 1.08 | 1.03 | 1.60 | 0.43 | 0.44 | 1.54 |
| $K_2O$ | 14.67 | 14.79 | 14.54 | 14.55 | 15.25 | 15.20 | 14.29 | 16.28 | 16.14 | 14.43 |
| $P_2O_5$ | 0.03 | 0.06 | 0.07 | 0.04 | 0.03 | 0.01 | < MDL | < MDL | 0.10 | < MDL |
| Total | 99.57 | 99.17 | 100.16 | 100.02 | 100.85 | 99.26 | 100.02 | 99.85 | 99.89 | 99.60 |
| Or | 85.84 | 88.48 | 85.93 | 84.84 | 90.31 | 90.65 | 85.45 | 96.15 | 95.91 | 85.92 |
| Ab | 14.03 | 11.33 | 14.03 | 15.07 | 9.69 | 9.32 | 14.55 | 3.85 | 4.00 | 13.91 |
| An | 0.13 | 0.18 | 0.04 | 0.09 | 0.00 | 0.03 | 0.00 | 0.00 | 0.09 | 0.17 |

***Supplementary Table 2.*** *Continued*

| Sample | Kfs 21 | Kfs 22 | Kfs 23 | Kfs 24 | Kfs 25 | Kfs 26 | Kfs 27 | Kfs 28 | Kfs 29 | Kfs 30 |
|---|---|---|---|---|---|---|---|---|---|---|
| Unit | OU | OU | OU | OU | OU | OU | OU | OU | OU | OU |
| Type | * | * | * | * | * | * | * | * | * | * |
| $SiO_2$ | 64.99 | 63.88 | 63.43 | 64.17 | 64.26 | 65.27 | 65.71 | 64.79 | 64.64 | 65.37 |
| $TiO_2$ | < MDL | 0.02 | < MDL | < MDL | < MDL | 0.03 | 0.02 | 0.03 | 0.01 | 0.01 |
| $Al_2O_3$ | 18.89 | 18.52 | 18.59 | 18.44 | 18.55 | 18.78 | 18.73 | 18.88 | 18.55 | 18.15 |
| $Cr_2O_3$ | 0.01 | 0.04 | 0.02 | < MDL | 0.03 | < MDL | < MDL | < MDL | 0.01 | 0.01 |
| NiO | < MDL | < MDL | < MDL | 0.02 | 0.02 | < MDL | 0.02 | 0.01 | < MDL | < MDL |
| FeO | < MDL | < MDL | 0.03 | < MDL | < MDL | < MDL | < MDL | 0.02 | 0.02 | 0.06 |
| MnO | 0.03 | 0.01 | 0.03 | 0.02 | < MDL | 0.01 | < MDL | < MDL | < MDL | < MDL |
| MgO | < MDL | 0.02 | 0.01 | 0.01 | 0.03 | < MDL | 0.02 | 0.03 | 0.01 | < MDL |
| CaO | 0.01 | < MDL | 0.03 | < MDL | 0.02 | 0.02 | 0.01 | 0.05 | 0.03 | 0.01 |
| $Na_2O$ | 1.08 | 0.43 | 1.44 | 0.62 | 0.49 | 1.12 | 1.28 | 1.15 | 0.47 | 0.91 |
| $K_2O$ | 15.11 | 16.29 | 14.61 | 15.80 | 16.05 | 15.17 | 14.85 | 15.00 | 16.15 | 15.19 |
| $P_2O_5$ | 0.10 | 0.08 | 0.03 | 0.03 | < MDL | 0.04 | < MDL | 0.03 | NA | NA |
| Total | 100.23 | 99.28 | 98.21 | 99.12 | 99.45 | 100.44 | 100.65 | 100.00 | 99.90 | 99.70 |
| Or | 90.15 | 96.16 | 86.86 | 94.34 | 95.46 | 89.79 | 88.35 | 89.31 | 95.59 | 91.59 |
| Ab | 9.77 | 3.84 | 12.97 | 5.66 | 4.42 | 10.11 | 11.59 | 10.44 | 4.26 | 8.37 |
| An | 0.07 | 0.00 | 0.17 | 0.00 | 0.12 | 0.10 | 0.06 | 0.26 | 0.15 | 0.04 |

* (phenocryst)
** (groundmass)
NA not analyzed
The Method Detection Limit (MDL) for the routine analysis of common elements is ~0.02 wt.%

***Supplementary Table 2.*** *Continued*

| Sample | Kfs 31 | Kfs 32 | Kfs 33 | Kfs 34 | Kfs 35 | Kfs 36 | Kfs 37 | Kfs 38 | Kfs 39 | Kfs 40 |
|---|---|---|---|---|---|---|---|---|---|---|
| Unit | OU | OU | OU | OU | OU | OU | OU | OU | OU | OU |
| Type | * | ** | ** | | ** | ** | ** | ** | ** | ** |
| $SiO_2$ | 65.64 | 65.45 | 65.95 | 65.40 | 65.95 | 65.02 | 65.23 | 65.34 | 65.31 | 65.58 |
| $TiO_2$ | < MDL | < MDL | 0.02 | 0.02 | 0.01 | < MDL | < MDL | < MDL | 0.02 | < MDL |
| $Al_2O_3$ | 18.16 | 17.96 | 18.14 | 18.06 | 18.11 | 18.28 | 18.00 | 18.01 | 17.96 | 18.20 |
| $Cr_2O_3$ | 0.02 | 0.04 | 0.00 | < MDL | 0.03 | < MDL | 0.02 | < MDL | < MDL | < MDL |
| NiO | < MDL | 0.05 | < MDL | < MDL | 0.02 | 0.02 | < MDL | 0.03 | < MDL | 0.01 |
| FeO | < MDL | < MDL | < MDL | 0.03 | 0.01 | < MDL | < MDL | < MDL | 0.01 | < MDL |
| MnO | < MDL | < MDL | < MDL | 0.01 | < MDL | 0.02 | < MDL | < MDL | 0.01 | < MDL |
| MgO | < MDL | 0.01 | < MDL | < MDL | < MDL | 0.01 | 0.01 | < MDL | < MDL | < MDL |
| CaO | 0.03 | 0.03 | 0.01 | < MDL | 0.01 | 0.02 | < MDL | < MDL | 0.04 | < MDL |
| $Na_2O$ | 0.90 | 0.60 | 1.07 | 1.05 | 0.72 | 0.50 | 0.42 | 0.65 | 0.62 | 1.00 |
| $K_2O$ | 15.25 | 15.64 | 15.28 | 15.18 | 15.67 | 16.00 | 15.81 | 15.61 | 15.60 | 15.13 |
| $P_2O_5$ | NA | NA | NA | NA | NA | NA | NA | NA | NA | NA |
| Total | 100.00 | 99.78 | 100.47 | 99.76 | 100.55 | 99.85 | 99.49 | 99.64 | 99.56 | 99.93 |
| Or | 91.62 | 94.35 | 90.35 | 90.49 | 93.43 | 95.35 | 96.09 | 94.05 | 94.13 | 90.84 |
| Ab | 8.24 | 5.51 | 9.59 | 9.51 | 6.51 | 4.56 | 3.91 | 5.95 | 5.68 | 9.13 |
| An | 0.14 | 0.13 | 0.06 | 0.00 | 0.05 | 0.09 | 0.00 | 0.00 | 0.19 | 0.02 |

***Supplementary Table 2.*** *Continued*

| Sample | Kfs 41 | Kfs 42 | Kfs 43 | Kfs 44 | Kfs 45 | Kfs 46 | Kfs 47 | Kfs 48 | Kfs 49 | Kfs 50 |
|---|---|---|---|---|---|---|---|---|---|---|
| Unit | MU | MU | MU | MU | MU | MU | MU | MU | MU | MU |
| Type | * | * | * | * | * | * | * | * | * | * |
| $SiO_2$ | 64.33 | 63.98 | 63.80 | 64.13 | 64.81 | 65.61 | 63.91 | 64.51 | 64.36 | 63.95 |
| $TiO_2$ | < MDL | < MDL | < MDL | < MDL | 0.02 | < MDL | 0.01 | 0.03 | 0.01 | < MDL |
| $Al_2O_3$ | 18.34 | 18.35 | 18.73 | 18.32 | 18.54 | 18.69 | 18.72 | 18.27 | 19.12 | 18.99 |
| $Cr_2O_3$ | 0.01 | 0.01 | 0.02 | < MDL | 0.02 | 0.01 | < MDL | < MDL | < MDL | < MDL |
| NiO | < MDL | 0.02 | 0.03 | 0.06 | < MDL | 0.02 | < MDL | < MDL | < MDL | 0.04 |
| FeO | 0.13 | 0.03 | < MDL | 0.03 | 0.02 | 0.05 | 0.05 | 0.04 | 0.04 | 0.01 |
| MnO | 0.03 | < MDL | 0.01 | 0.01 | 0.02 | 0.02 | 0.02 | < MDL | < MDL | 0.01 |
| MgO | < MDL | < MDL | < MDL | < MDL | < MDL | 0.01 | 0.02 | < MDL | < MDL | < MDL |
| CaO | 0.01 | 0.01 | 0.08 | 0.04 | 0.02 | 0.01 | < MDL | 0.02 | 0.01 | 0.02 |
| $Na_2O$ | 0.49 | 0.42 | 0.40 | 1.13 | 1.58 | 1.25 | 0.64 | 0.71 | 0.86 | 0.82 |
| $K_2O$ | 16.06 | 16.43 | 16.39 | 15.71 | 14.78 | 15.00 | 15.77 | 15.77 | 15.62 | 15.88 |
| $P_2O_5$ | NA | NA | NA | NA | 0.10 | 0.06 | 0.36 | 0.22 | 0.32 | 0.62 |
| Total | 99.39 | 99.23 | 99.45 | 99.43 | 99.91 | 100.72 | 99.48 | 99.59 | 100.34 | 100.34 |
| Or | 95.56 | 96.22 | 96.10 | 89.97 | 85.90 | 88.76 | 94.19 | 93.50 | 92.19 | 92.61 |
| Ab | 4.40 | 3.74 | 3.52 | 9.84 | 14.00 | 11.20 | 5.81 | 6.41 | 7.76 | 7.28 |
| An | 0.04 | 0.03 | 0.38 | 0.19 | 0.10 | 0.04 | 0.00 | 0.09 | 0.05 | 0.12 |

* (phenocryst)
** (groundmass)
NA not analyzed
The Method Detection Limit (MDL) for the routine analysis of common elements is ~0.02 wt.%

***Supplementary Table 2.*** *Continued*

| Sample | Kfs 51 | Kfs 52 | Kfs 53 | Kfs 54 | Kfs 55 | Kfs 56 | Kfs 57 | Kfs 58 | Kfs 59 | Kfs 60 |
|---|---|---|---|---|---|---|---|---|---|---|
| Unit | MU | MU | MU | MU | MU | MU | MU | MU | MU | MU |
| Type | * | * | * | * | * | * | * | * | * | * |
| $SiO_2$ | 64.58 | 63.87 | 62.97 | 64.00 | 64.17 | 63.47 | 64.02 | 63.71 | 64.18 | 63.34 |
| $TiO_2$ | 0.01 | < MDL | 0.02 | < MDL | < MDL | 0.01 | < MDL | < MDL | 0.02 | 0.01 |
| $Al_2O_3$ | 18.69 | 18.64 | 18.88 | 18.52 | 18.68 | 18.85 | 18.92 | 18.71 | 19.05 | 18.76 |
| $Cr_2O_3$ | 0.05 | < MDL | 0.01 | < MDL | 0.02 | < MDL | < MDL | < MDL | < MDL | 0.03 |
| NiO | < MDL | < MDL | < MDL | 0.02 | < MDL | 0.03 | 0.01 | 0.03 | 0.06 | < MDL |
| FeO | < MDL | < MDL | 0.01 | < MDL | 0.01 | 0.04 | 0.02 | < MDL | < MDL | 0.01 |
| MnO | < MDL | < MDL | < MDL | < MDL | < MDL | < MDL | < MDL | 0.01 | < MDL | 0.03 |
| MgO | < MDL | 0.06 | 0.05 | < MDL | 0.03 | 0.03 | < MDL | < MDL | < MDL | 0.06 |
| CaO | 0.01 | 0.06 | 0.01 | < MDL | 0.04 | < MDL | 0.01 | 0.02 | < MDL | 0.01 |
| $Na_2O$ | 0.79 | 1.42 | 1.06 | 1.13 | 1.01 | 1.04 | 1.05 | 0.94 | 0.72 | 1.82 |
| $K_2O$ | 15.75 | 15.36 | 15.66 | 15.58 | 15.63 | 15.54 | 15.44 | 15.79 | 16.09 | 14.86 |
| $P_2O_5$ | 0.66 | 0.32 | 0.42 | 0.22 | 0.21 | 0.17 | 0.65 | 0.21 | 0.22 | 0.23 |
| Total | 100.54 | 99.74 | 99.09 | 99.46 | 99.79 | 99.17 | 100.13 | 99.41 | 100.34 | 99.15 |
| Or | 92.89 | 87.44 | 90.62 | 90.07 | 90.90 | 90.77 | 90.61 | 91.61 | 93.66 | 84.26 |
| Ab | 7.08 | 12.27 | 9.33 | 9.93 | 8.90 | 9.23 | 9.32 | 8.27 | 6.34 | 15.70 |
| An | 0.03 | 0.30 | 0.05 | 0.00 | 0.20 | 0.00 | 0.07 | 0.12 | 0.00 | 0.04 |

***Supplementary Table 2.*** *Continued*

| Sample | Kfs 61 | Kfs 62 | Kfs 63 | Kfs 64 | Kfs 65 | Kfs 66 | Kfs 67 | Kfs 68 | Kfs 69 | Kfs 70 |
|---|---|---|---|---|---|---|---|---|---|---|
| Unit | MU | MU | MU | MU | MU | MU | MU | MU | MU | MU |
| Type | * | * | * | * | * | * | * | * | * | * |
| $SiO_2$ | 63.91 | 64.41 | 63.80 | 64.22 | 64.40 | 64.56 | 64.53 | 64.49 | 64.75 | 64.28 |
| $TiO_2$ | 0.01 | < MDL | 0.01 | < MDL | 0.03 | 0.04 | < MDL | 0.01 | 0.02 | < MDL |
| $Al_2O_3$ | 18.62 | 18.83 | 18.93 | 18.84 | 19.04 | 18.96 | 18.55 | 19.30 | 19.09 | 19.04 |
| $Cr_2O_3$ | < MDL | 0.04 | 0.01 | 0.03 | < MDL | 0.04 | < MDL | 0.01 | 0.01 | < MDL |
| NiO | < MDL | < MDL | < MDL | < MDL | 0.04 | < MDL | 0.05 | 0.01 | 0.06 | 0.01 |
| FeO | 0.02 | < MDL | 0.01 | 0.01 | < MDL | 0.01 | 0.01 | < MDL | 0.02 | 0.02 |
| MnO | 0.03 | 0.04 | 0.02 | < MDL | 0.02 | < MDL | 0.01 | < MDL | < MDL | < MDL |
| MgO | 0.02 | 0.03 | < MDL | < MDL | < MDL | < MDL | 0.02 | < MDL | 0.01 | 0.17 |
| CaO | < MDL | 0.01 | 0.03 | 0.04 | 0.04 | 0.03 | < MDL | 0.03 | 0.03 | < MDL |
| $Na_2O$ | 1.21 | 1.07 | 1.42 | 0.96 | 0.90 | 1.65 | 1.08 | 2.19 | 1.69 | 1.04 |
| $K_2O$ | 15.37 | 15.66 | 15.21 | 15.51 | 15.62 | 14.75 | 15.50 | 13.82 | 14.32 | 15.61 |
| $P_2O_5$ | 0.14 | 0.13 | 0.24 | 0.16 | 0.19 | 0.18 | 0.16 | 0.16 | 0.36 | 0.39 |
| Total | 99.32 | 100.22 | 99.68 | 99.78 | 100.28 | 100.23 | 99.90 | 100.03 | 100.34 | 100.56 |
| Or | 89.33 | 90.52 | 87.40 | 91.22 | 91.81 | 85.34 | 90.42 | 80.49 | 84.67 | 90.77 |
| Ab | 10.65 | 9.41 | 12.44 | 8.56 | 8.02 | 14.51 | 9.58 | 19.36 | 15.20 | 9.23 |
| An | 0.02 | 0.07 | 0.15 | 0.22 | 0.17 | 0.16 | 0.01 | 0.15 | 0.13 | 0.00 |

* (phenocryst)
** (groundmass)
NA not analyzed
The Method Detection Limit (MDL) for the routine analysis of common elements is ~0.02 wt.%

***Supplementary Table 2.*** *Continued*

| Sample | Kfs 71 | Kfs 72 | Kfs 73 | Kfs 74 | Kfs 75 | Kfs 76 | Kfs 77 | Kfs 78 | Kfs 79 | Kfs 80 |
|---|---|---|---|---|---|---|---|---|---|---|
| Unit | IU | IU | IU | IU | IU | IU | IU | IU | IU | IU |
| Type | * | * | * | * | * | * | * | * | * | * |
| $SiO_2$ | 64.88 | 64.82 | 64.29 | 64.37 | 64.35 | 63.65 | 63.55 | 63.76 | 63.73 | 63.36 |
| $TiO_2$ | 0.02 | < MDL | 0.03 | < MDL | < MDL | < MDL | < MDL | < MDL | < MDL | 0.01 |
| $Al_2O_3$ | 18.90 | 18.58 | 18.62 | 18.28 | 19.21 | 19.09 | 19.05 | 19.26 | 19.01 | 19.27 |
| $Cr_2O_3$ | < MDL | < MDL | < MDL | 0.03 | 0.04 | < MDL | < MDL | 0.01 | < MDL | < MDL |
| NiO | < MDL | 0.05 | 0.05 | < MDL | 0.07 | 0.03 | < MDL | < MDL | < MDL | < MDL |
| FeO | < MDL | < MDL | 0.05 | < MDL | 0.01 | < MDL | < MDL | < MDL | < MDL | 0.01 |
| MnO | < MDL | < MDL | 0.01 | 0.03 | < MDL | < MDL | < MDL | 0.04 | 0.02 | 0.02 |
| MgO | < MDL | < MDL | < MDL | < MDL | 0.02 | < MDL | < MDL | 0.02 | < MDL | < MDL |
| CaO | 0.04 | < MDL | 0.06 | 0.02 | < MDL | 0.02 | 0.04 | < MDL | 0.02 | 0.05 |
| $Na_2O$ | 1.50 | 0.93 | 1.67 | 0.46 | 1.12 | 1.45 | 1.12 | 1.02 | 1.07 | 0.39 |
| $K_2O$ | 14.68 | 15.45 | 14.50 | 16.39 | 15.41 | 14.90 | 15.20 | 15.34 | 15.41 | 16.44 |
| $P_2O_5$ | 0.15 | 0.11 | NA | NA | 0.28 | 0.20 | 0.17 | 0.61 | 0.29 | 0.24 |
| Total | 100.16 | 99.96 | 99.27 | 99.58 | 100.51 | 99.33 | 99.13 | 100.06 | 99.55 | 99.78 |
| Or | 86.40 | 91.59 | 84.86 | 95.85 | 90.04 | 87.07 | 89.74 | 90.86 | 90.35 | 96.23 |
| Ab | 13.42 | 8.39 | 14.85 | 4.06 | 9.96 | 12.84 | 10.07 | 9.14 | 9.57 | 3.51 |
| An | 0.18 | 0.02 | 0.30 | 0.09 | 0.00 | 0.09 | 0.19 | 0.00 | 0.08 | 0.26 |

***Supplementary Table 2.*** *Continued*

| Sample | Kfs 81 | Kfs 82 | Kfs 83 | Kfs 84 | Kfs 85 | Kfs 86 | Kfs 87 | Kfs 88 | Kfs 89 | Kfs 90 |
|---|---|---|---|---|---|---|---|---|---|---|
| Unit | IU | IU | IU | IU | IU | IU | IU | IU | IU | IU |
| Type | * | * | * | * | * | * | * | * | * | * |
| $SiO_2$ | 64.22 | 64.03 | 64.43 | 64.34 | 63.90 | 63.85 | 64.28 | 64.44 | 64.18 | 63.93 |
| $TiO_2$ | 0.00 | 0.02 | 0.01 | 0.01 | 0.01 | < MDL | 0.01 | < MDL | 0.02 | 0.02 |
| $Al_2O_3$ | 18.93 | 19.52 | 19.38 | 19.59 | 19.01 | 19.29 | 19.24 | 19.14 | 19.22 | 19.05 |
| $Cr_2O_3$ | 0.02 | 0.01 | 0.01 | < MDL | < MDL | 0.05 | 0.03 | 0.02 | < MDL | 0.03 |
| NiO | 0.02 | 0.05 | 0.02 | 0.01 | < MDL | < MDL | < MDL | < MDL | 0.04 | 0.02 |
| FeO | < MDL | 0.04 | < MDL | < MDL | < MDL | 0.01 | 0.03 | < MDL | < MDL | 0.01 |
| MnO | 0.02 | < MDL | 0.03 | 0.03 | 0.01 | < MDL | < MDL | 0.01 | < MDL | 0.01 |
| MgO | 0.04 | < MDL | < MDL | < MDL | 0.01 | < MDL | 0.01 | 0.01 | < MDL | 0.02 |
| CaO | 0.02 | 0.03 | 0.01 | 0.03 | 0.03 | 0.03 | < MDL | 0.03 | 0.02 | 0.06 |
| $Na_2O$ | 1.22 | 1.24 | 1.22 | 0.54 | 0.24 | 0.58 | 0.70 | 1.05 | 1.33 | 0.36 |
| $K_2O$ | 15.09 | 15.07 | 15.22 | 15.76 | 16.46 | 16.10 | 15.89 | 15.40 | 14.85 | 16.15 |
| $P_2O_5$ | 0.34 | 0.19 | 0.36 | 0.16 | 0.33 | 0.25 | 0.26 | 0.29 | 0.19 | 0.28 |
| Total | 99.93 | 100.20 | 100.70 | 100.48 | 100.01 | 100.17 | 100.46 | 100.38 | 99.85 | 99.94 |
| Or | 88.95 | 88.72 | 89.05 | 94.85 | 97.67 | 94.69 | 93.72 | 90.49 | 87.92 | 96.41 |
| Ab | 10.94 | 11.13 | 10.89 | 4.97 | 2.19 | 5.14 | 6.28 | 9.38 | 12.00 | 3.30 |
| An | 0.11 | 0.15 | 0.06 | 0.18 | 0.14 | 0.16 | 0.00 | 0.13 | 0.08 | 0.28 |

* (phenocryst)
** (groundmass)
NA not analyzed
The Method Detection Limit (MDL) for the routine analysis of common elements is ~0.02 wt.%

***Supplementary Table 2.*** *Continued*

| Sample | Kfs 91 | Kfs 92 | Kfs 93 | Kfs 94 | Kfs 95 | Kfs 96 | Kfs 97 | Kfs 98 | Kfs 99 | Kfs 100 |
|---|---|---|---|---|---|---|---|---|---|---|
| Unit | IU | IU | IU | IU | IU | IU | IU | IU | IU | IU |
| Type | * | * | * | * | * | * | * | * | * | * |
| $SiO_2$ | 63.89 | 63.84 | 63.39 | 64.20 | 63.94 | 64.10 | 63.96 | 64.92 | 64.21 | 63.91 |
| $TiO_2$ | 0.01 | < MDL | 0.01 | < MDL | < MDL | 0.02 | 0.01 | 0.01 | 0.01 | < MDL |
| $Al_2O_3$ | 19.13 | 19.28 | 19.33 | 19.99 | 19.04 | 19.21 | 19.03 | 19.07 | 18.40 | 18.85 |
| $Cr_2O_3$ | < MDL | < MDL | < MDL | < MDL | < MDL | 0.06 | < MDL | 0.02 | < MDL | < MDL |
| NiO | < MDL | < MDL | < MDL | < MDL | 0.05 | 0.01 | < MDL | < MDL | < MDL | < MDL |
| FeO | < MDL | < MDL | < MDL | 0.05 | < MDL | < MDL | 0.02 | 0.03 | < MDL | < MDL |
| MnO | < MDL | < MDL | 0.04 | < MDL | < MDL | < MDL | 0.01 | < MDL | < MDL | < MDL |
| MgO | < MDL | 0.02 | 0.08 | 0.04 | < MDL | < MDL | 0.03 | < MDL | 0.03 | 0.09 |
| CaO | 0.03 | 0.02 | 0.03 | 0.10 | 0.07 | 0.04 | 0.19 | < MDL | 0.03 | 0.10 |
| $Na_2O$ | 1.31 | 1.48 | 0.70 | 1.17 | 0.59 | 0.53 | 0.37 | 0.24 | 0.92 | 0.56 |
| $K_2O$ | 14.88 | 14.51 | 15.93 | 14.78 | 16.13 | 16.02 | 16.06 | 16.26 | 15.86 | 16.22 |
| $P_2O_5$ | 0.21 | 0.14 | 0.44 | 0.11 | 0.35 | 0.21 | 0.19 | 0.25 | 0.20 | 0.17 |
| Total | 99.46 | 99.29 | 99.94 | 100.44 | 100.18 | 100.20 | 99.86 | 100.80 | 99.66 | 99.90 |
| Or | 88.10 | 86.45 | 93.65 | 88.84 | 94.38 | 95.02 | 95.71 | 97.84 | 91.74 | 94.50 |
| Ab | 11.75 | 13.45 | 6.21 | 10.67 | 5.26 | 4.77 | 3.34 | 2.16 | 8.12 | 4.99 |
| An | 0.15 | 0.10 | 0.14 | 0.50 | 0.36 | 0.21 | 0.95 | 0.00 | 0.14 | 0.51 |

***Supplementary Table 2.*** *Continued*

| Sample | Kfs 101 | Kfs 102 | Kfs 103 | Kfs 104 | Kfs 105 | Kfs 106 | Kfs 107 | Kfs 108 | Kfs 109 | Kfs 110 |
|---|---|---|---|---|---|---|---|---|---|---|
| Unit | IU | IU | IU | Lamp | Lamp | Lamp | Lamp | Lamp | Lamp | Lamp |
| Type | * | * | * | Mnt | Mnt | Mnt | Mnt | Mnt | Mnt | Mnt |
| $SiO_2$ | 64.05 | 63.92 | 64.07 | 64.58 | 64.54 | 64.78 | 65.31 | 64.49 | 64.24 | 65.05 |
| $TiO_2$ | < MDL | < MDL | 0.02 | 0.01 | 0.00 | 0.02 | 0.01 | 0.00 | 0.00 | 0.01 |
| $Al_2O_3$ | 19.11 | 19.16 | 19.05 | 18.58 | 18.54 | 18.11 | 18.55 | 18.53 | 18.48 | 18.40 |
| $Cr_2O_3$ | 0.04 | < MDL | < MDL | 0.02 | 0.00 | 0.02 | 0.00 | 0.00 | 0.02 | 0.00 |
| NiO | < MDL | < MDL | < MDL | 0.01 | 0.00 | 0.00 | 0.04 | 0.00 | 0.02 | 0.00 |
| FeO | < MDL | 0.03 | 0.03 | 0.06 | 0.08 | 0.08 | 0.05 | 0.08 | 0.04 | 0.15 |
| MnO | < MDL | 0.01 | < MDL | 0.00 | 0.01 | 0.00 | 0.01 | 0.00 | 0.00 | 0.00 |
| MgO | 0.03 | < MDL | 0.04 | 0.00 | 0.00 | 0.00 | 0.01 | 0.00 | 0.01 | 0.00 |
| CaO | 0.02 | 0.01 | 0.02 | 0.03 | 0.14 | 0.00 | 0.06 | 0.04 | 0.01 | 0.03 |
| $Na_2O$ | 0.44 | 0.76 | 1.15 | 0.27 | 0.40 | 0.36 | 0.32 | 0.26 | 0.30 | 0.27 |
| $K_2O$ | 16.34 | 15.84 | 15.16 | 16.32 | 15.48 | 16.19 | 15.84 | 16.22 | 16.32 | 16.24 |
| $P_2O_5$ | 0.15 | 0.06 | 0.12 | NA | NA | NA | NA | NA | NA | NA |
| Total | 100.19 | 99.80 | 99.65 | 99.87 | 99.20 | 99.56 | 100.21 | 99.62 | 99.44 | 100.15 |
| Or | 95.94 | 93.12 | 89.58 | 97.43 | 95.51 | 96.73 | 96.71 | 97.48 | 97.18 | 97.37 |
| Ab | 3.95 | 6.81 | 10.32 | 2.44 | 3.77 | 3.25 | 2.97 | 2.34 | 2.75 | 2.48 |
| An | 0.11 | 0.07 | 0.10 | 0.13 | 0.72 | 0.02 | 0.32 | 0.19 | 0.07 | 0.15 |

* (phenocryst)
** (groundmass)
NA not analyzed
The Method Detection Limit (MDL) for the routine analysis of common elements is ~0.02 wt.%

***Supplementary Table 2.*** *Continued*

| Sample | Kfs 111 | Kfs 112 | Kfs 113 | Kfs 114 | Kfs 115 | Kfs 116 | Kfs 117 | Kfs 118 | Kfs 119 | Kfs 120 |
|---|---|---|---|---|---|---|---|---|---|---|
| Unit | Lamp | Lamp | Lamp | Vaugn | Vaugn | Vaugn | Vaugn | Vaugn | Vaugn | Vaugn |
| Type | Mnt | Mnt | Mnt | Bt-poor | Bt-poor | Bt-poor | Bt-poor | Bt-poor | Bt-poor | Bt-poor |
| $SiO_2$ | 64.45 | 65.25 | 64.51 | 64.29 | 64.40 | 64.44 | 64.13 | 65.02 | 65.40 | 64.43 |
| $TiO_2$ | 0.02 | 0.01 | 0.00 | 0.01 | 0.02 | 0.03 | 0.00 | 0.02 | 0.01 | 0.01 |
| $Al_2O_3$ | 18.72 | 18.44 | 18.49 | 18.17 | 18.39 | 18.25 | 18.37 | 18.04 | 17.90 | 18.17 |
| $Cr_2O_3$ | 0.00 | 0.00 | 0.00 | 0.00 | 0.00 | 0.01 | 0.00 | 0.00 | 0.00 | 0.01 |
| NiO | 0.00 | 0.00 | 0.00 | 0.00 | 0.00 | 0.00 | 0.00 | 0.00 | 0.00 | 0.05 |
| FeO | 0.06 | 0.01 | 0.06 | 0.06 | 0.05 | 0.03 | 0.07 | 0.02 | 0.03 | 0.06 |
| MnO | 0.00 | 0.00 | 0.00 | 0.00 | 0.02 | 0.00 | 0.00 | 0.00 | 0.02 | 0.00 |
| MgO | 0.01 | 0.00 | 0.00 | 0.01 | 0.00 | 0.00 | 0.00 | 0.00 | 0.00 | 0.01 |
| CaO | 0.26 | 0.03 | 0.17 | 0.04 | 0.00 | 0.05 | 0.03 | 0.09 | 0.01 | 0.02 |
| $Na_2O$ | 0.49 | 0.36 | 0.38 | 0.25 | 0.26 | 0.31 | 0.31 | 0.32 | 0.39 | 0.49 |
| $K_2O$ | 15.71 | 16.16 | 15.75 | 16.37 | 16.77 | 16.32 | 16.30 | 16.07 | 15.92 | 16.08 |
| $P_2O_5$ | NA | NA | NA | NA | NA | NA | NA | NA | NA | NA |
| Total | 99.73 | 100.25 | 99.36 | 99.21 | 99.91 | 99.45 | 99.21 | 99.57 | 99.67 | 99.33 |
| Or | 94.21 | 96.63 | 95.60 | 97.47 | 97.66 | 96.91 | 97.11 | 96.62 | 96.38 | 95.43 |
| Ab | 4.47 | 3.23 | 3.54 | 2.31 | 2.34 | 2.84 | 2.76 | 2.95 | 3.59 | 4.45 |
| An | 1.33 | 0.14 | 0.87 | 0.22 | 0.00 | 0.25 | 0.13 | 0.43 | 0.03 | 0.12 |

***Supplementary Table 3.*** *Electron microprobe analyses of plagioclase from the Sierra Bermeja Pluton*

| Sample | Pl 1 | Pl 2 | Pl 3 | Pl 4 | Pl 5 | Pl 6 | Pl 7 | Pl 8 | Pl 9 | Pl 10 |
|---|---|---|---|---|---|---|---|---|---|---|
| Unit | OU | OU | OU | OU | OU | OU | OU | OU | OU | OU |
| $SiO_2$ | 61.69 | 62.63 | 65.96 | 62.28 | 66.35 | 62.12 | 65.07 | 64.74 | 63.21 | 62.63 |
| $TiO_2$ | 0.04 | 0.01 | < MDL | 0.04 | 0.01 | 0.02 | 0.02 | < MDL | 0.02 | 0.01 |
| $Al_2O_3$ | 24.25 | 23.35 | 20.88 | 23.49 | 20.87 | 23.47 | 21.86 | 21.96 | 23.70 | 23.87 |
| $Cr_2O_3$ | < MDL | < MDL | 0.01 | 0.04 | 0.01 | 0.03 | 0.08 | 0.02 | < MDL | 0.02 |
| NiO | 0.10 | 0.03 | 0.17 | < MDL | 0.10 | < MDL | < MDL | < MDL | 0.03 | 0.03 |
| FeO | 0.03 | < MDL | 0.06 | < MDL | 0.03 | 0.05 | 0.02 | 0.08 | 0.05 | 0.08 |
| MnO | 0.01 | < MDL | < MDL | < MDL | < MDL | < MDL | 0.05 | < MDL | < MDL | < MDL |
| MgO | < MDL | < MDL | 0.00 | 0.02 | < MDL | 0.01 | < MDL | 0.00 | < MDL | 0.01 |
| CaO | 5.65 | 4.89 | 2.10 | 5.24 | 2.02 | 4.87 | 2.88 | 2.99 | 5.06 | 5.00 |
| $Na_2O$ | 8.34 | 8.59 | 10.56 | 8.70 | 10.36 | 8.57 | 10.13 | 9.90 | 8.70 | 8.61 |
| $K_2O$ | 0.30 | 0.37 | 0.14 | 0.21 | 0.14 | 0.35 | 0.13 | 0.15 | 0.25 | 0.11 |
| $P_2O_5$ | NA | NA | NA | NA | NA | NA | NA | NA | NA | NA |
| Total | 100.41 | 99.85 | 99.88 | 100.02 | 99.87 | 99.49 | 100.24 | 99.84 | 101.00 | 100.36 |
| Or | 1.70 | 2.11 | 0.79 | 1.17 | 0.77 | 2.01 | 0.70 | 0.86 | 1.38 | 0.63 |
| Ab | 71.52 | 74.47 | 89.38 | 74.17 | 89.58 | 74.56 | 85.81 | 84.94 | 74.63 | 75.24 |
| An | 26.77 | 23.42 | 9.83 | 24.67 | 9.65 | 23.43 | 13.49 | 14.20 | 23.99 | 24.13 |

NA not analyzed

The Method Detection Limit (MDL) for the routine analysis of common elements is ~0.02 wt.%

***Supplementary Table 3.*** *Continued*

| Sample | Pl 11 | Pl 12 | Pl 13 | Pl 14 | Pl 15 | Pl 16 | Pl 17 | Pl 18 | Pl 19 | Pl 20 |
|---|---|---|---|---|---|---|---|---|---|---|
| Unit | OU | OU | OU | OU | OU | OU | OU | OU | OU | OU |
| $SiO_2$ | 62.67 | 68.85 | 63.58 | 63.56 | 64.58 | 62.05 | 63.45 | 67.25 | 64.47 | 66.29 |
| $TiO_2$ | 0.00 | 0.02 | 0.03 | < MDL | < MDL | 0.05 | < MDL | < MDL | 0.03 | 0.01 |
| $Al_2O_3$ | 23.72 | 19.52 | 22.60 | 22.43 | 21.89 | 23.50 | 22.49 | 19.69 | 22.42 | 21.34 |
| $Cr_2O_3$ | 0.05 | < MDL | 0.06 | < MDL | < MDL | < MDL | 0.02 | 0.08 | 0.01 | 0.01 |
| NiO | 0.06 | < MDL | < MDL | < MDL | < MDL | < MDL | 0.01 | 0.03 | < MDL | < MDL |
| FeO | 0.04 | 0.05 | 0.01 | 0.01 | 0.03 | < MDL | < MDL | < MDL | 0.02 | < MDL |
| MnO | 0.03 | < MDL | 0.02 | < MDL | 0.03 | 0.09 | < MDL | < MDL | < MDL | < MDL |
| MgO | < MDL | < MDL | < MDL | < MDL | 0.01 | < MDL | < MDL | < MDL | 0.00 | < MDL |
| CaO | 4.89 | 0.86 | 4.33 | 4.19 | 3.22 | 5.38 | 4.37 | 0.90 | 3.43 | 1.68 |
| $Na_2O$ | 8.63 | 10.47 | 8.97 | 8.97 | 9.47 | 8.48 | 8.73 | 10.96 | 9.59 | 10.31 |
| $K_2O$ | 0.34 | 0.10 | 0.47 | 0.42 | 0.33 | 0.23 | 0.50 | 0.21 | 0.16 | 0.12 |
| $P_2O_5$ | NA | NA | NA | NA | NA | NA | NA | NA | NA | 0.14 |
| Total | 100.43 | 99.88 | 100.07 | 99.58 | 99.57 | 99.77 | 99.57 | 99.12 | 100.14 | 99.91 |
| Or | 1.95 | 0.62 | 2.63 | 2.38 | 1.89 | 1.28 | 2.89 | 1.20 | 0.93 | 0.71 |
| Ab | 74.68 | 95.05 | 76.87 | 77.60 | 82.59 | 73.10 | 76.09 | 94.53 | 82.72 | 91.10 |
| An | 23.36 | 4.33 | 20.51 | 20.02 | 15.53 | 25.62 | 21.03 | 4.26 | 16.35 | 8.19 |

NA not analyzed

The Method Detection Limit (MDL) for the routine analysis of common elements is ~0.02 wt.%

***Supplementary Table 3.*** *Continued*

| Sample | Pl 21 | Pl 22 | Pl 23 | Pl 24 | Pl 25 | Pl 26 | Pl 27 | Pl 28 | Pl 29 | Pl 30 |
|---|---|---|---|---|---|---|---|---|---|---|
| Unit | OU | OU | OU | OU | OU | OU | OU | OU | OU | OU |
| $SiO_2$ | 59.09 | 66.31 | 61.45 | 67.62 | 64.20 | 65.39 | 68.05 | 65.05 | 63.26 | 67.99 |
| $TiO_2$ | < MDL | < MDL | < MDL | 0.00 | < MDL | 0.03 | < MDL | < MDL | < MDL | < MDL |
| $Al_2O_3$ | 25.54 | 21.70 | 24.39 | 19.95 | 21.92 | 21.71 | 20.08 | 21.63 | 23.35 | 20.07 |
| $Cr_2O_3$ | < MDL | < MDL | < MDL | 0.03 | 0.05 | < MDL | < MDL | < MDL | < MDL | 0.01 |
| NiO | 0.04 | < MDL | < MDL | 0.04 | 0.01 | 0.05 | 0.04 | 0.03 | < MDL | 0.01 |
| FeO | 0.01 | < MDL | < MDL | 0.02 | < MDL | 0.03 | < MDL | 0.00 | < MDL | < MDL |
| MnO | 0.01 | 0.01 | < MDL | < MDL | < MDL | < MDL | 0.02 | 0.02 | 0.00 | < MDL |
| MgO | < MDL | 0.02 | 0.01 | 0.01 | 0.01 | 0.01 | < MDL | 0.01 | 0.01 | < MDL |
| CaO | 6.90 | 1.88 | 5.39 | 0.59 | 2.98 | 2.47 | 0.60 | 2.10 | 4.25 | 0.43 |
| $Na_2O$ | 7.54 | 10.24 | 8.18 | 11.14 | 9.71 | 10.04 | 11.44 | 10.11 | 9.19 | 11.47 |
| $K_2O$ | 0.15 | 0.31 | 0.22 | 0.14 | 0.13 | 0.28 | 0.15 | 0.15 | 0.22 | 0.16 |
| $P_2O_5$ | 0.26 | 0.16 | 0.20 | 0.01 | 0.14 | 0.09 | 0.05 | 0.15 | 0.18 | 0.07 |
| Total | 99.55 | 100.64 | 99.84 | 99.56 | 99.14 | 100.08 | 100.43 | 99.25 | 100.47 | 100.20 |
| Or | 0.87 | 1.79 | 1.29 | 0.79 | 0.75 | 1.57 | 0.82 | 0.87 | 1.25 | 0.90 |
| Ab | 65.82 | 89.15 | 72.36 | 96.37 | 84.87 | 86.66 | 96.37 | 88.91 | 78.65 | 97.11 |
| An | 33.31 | 9.06 | 26.35 | 2.84 | 14.38 | 11.77 | 2.81 | 10.22 | 20.10 | 1.99 |

The Method Detection Limit (MDL) for the routine analysis of common elements is ~0.02 wt.%

***Supplementary Table 3.*** *Continued*

| Sample | Pl 31 | Pl 32 | Pl 33 | Pl 34 | Pl 35 | Pl 36 | Pl 37 | Pl 38 | Pl 39 | Pl 40 |
|---|---|---|---|---|---|---|---|---|---|---|
| Unit | OU | OU | OU | OU | OU | OU | OU | OU | OU | OU |
| $SiO_2$ | 63.85 | 61.75 | 61.79 | 61.23 | 62.02 | 64.22 | 63.12 | 62.11 | 61.39 | 63.34 |
| $TiO_2$ | 0.00 | < MDL | < MDL | 0.00 | 0.00 | < MDL | 0.02 | 0.00 | < MDL | 0.01 |
| $Al_2O_3$ | 23.07 | 23.99 | 24.20 | 24.34 | 24.26 | 22.69 | 23.07 | 23.95 | 24.48 | 23.54 |
| $Cr_2O_3$ | < MDL | < MDL | 0.03 | 0.03 | < MDL | 0.01 | 0.02 | 0.02 | 0.01 | < MDL |
| NiO | < MDL | 0.05 | 0.02 | < MDL | < MDL | 0.02 | 0.06 | 0.01 | 0.06 | 0.04 |
| FeO | 0.01 | 0.04 | 0.00 | < MDL | 0.03 | < MDL | 0.04 | 0.02 | 0.00 | 0.01 |
| MnO | < MDL | < MDL | < MDL | 0.03 | < MDL | < MDL | 0.01 | 0.00 | 0.01 | < MDL |
| MgO | < MDL | 0.00 | < MDL | < MDL | < MDL | < MDL | 0.01 | 0.01 | < MDL | 0.01 |
| CaO | 3.80 | 5.01 | 5.34 | 5.45 | 5.08 | 3.38 | 3.99 | 4.86 | 5.93 | 4.10 |
| $Na_2O$ | 9.12 | 8.61 | 8.31 | 8.18 | 8.40 | 9.32 | 9.29 | 8.41 | 7.89 | 8.84 |
| $K_2O$ | 0.17 | 0.31 | 0.40 | 0.45 | 0.34 | 0.43 | 0.22 | 0.42 | 0.14 | 0.26 |
| $P_2O_5$ | 0.18 | 0.24 | 0.18 | 0.17 | 0.27 | 0.21 | 0.16 | 0.27 | 0.33 | 0.22 |
| Total | 100.21 | 100.00 | 100.27 | 99.87 | 100.39 | 100.28 | 99.99 | 100.08 | 100.24 | 100.38 |
| Or | 1.00 | 1.79 | 2.29 | 2.55 | 1.93 | 2.49 | 1.22 | 2.41 | 0.83 | 1.52 |
| Ab | 80.49 | 74.31 | 72.08 | 71.20 | 73.51 | 81.22 | 79.84 | 73.97 | 70.07 | 78.39 |
| An | 18.51 | 23.90 | 25.62 | 26.24 | 24.56 | 16.30 | 18.95 | 23.62 | 29.10 | 20.10 |

The Method Detection Limit (MDL) for the routine analysis of common elements is ~0.02 wt.%

***Supplementary Table 3.*** *Continued*

| Sample | Pl 41 | Pl 42 | Pl 43 | Pl 44 | Pl 45 | Pl 46 | Pl 47 | Pl 48 | Pl 49 | Pl 50 |
|---|---|---|---|---|---|---|---|---|---|---|
| Unit | OU | OU | OU | OU | OU | OU | OU | OU | OU | OU |
| $SiO_2$ | 61.49 | 66.52 | 61.04 | 63.60 | 64.21 | 68.87 | 68.32 | 62.44 | 63.01 | 61.15 |
| $TiO_2$ | 0.01 | < MDL | < MDL | 0.02 | 0.01 | < MDL | < MDL | < MDL | 0.03 | 0.02 |
| $Al_2O_3$ | 24.15 | 20.83 | 24.96 | 22.97 | 22.44 | 19.43 | 19.68 | 23.32 | 23.60 | 24.31 |
| $Cr_2O_3$ | 0.00 | 0.05 | < MDL | 0.03 | < MDL | 0.00 | 0.01 | 0.03 | < MDL | 0.03 |
| NiO | 0.01 | < MDL | < MDL | 0.04 | 0.03 | < MDL | 0.02 | < MDL | < MDL | < MDL |
| FeO | 0.02 | 0.01 | 0.02 | < MDL | 0.05 | 0.08 | 0.00 | 0.02 | 0.04 | 0.01 |
| MnO | 0.02 | 0.01 | < MDL | 0.02 | < MDL | < MDL | < MDL | < MDL | 0.00 | 0.01 |
| MgO | 0.03 | < MDL | < MDL | 0.01 | < MDL | 0.01 | 0.01 | 0.01 | 0.01 | < MDL |
| CaO | 5.50 | 1.37 | 5.88 | 3.95 | 3.19 | 0.17 | 0.40 | 4.86 | 4.99 | 5.54 |
| $Na_2O$ | 8.55 | 10.58 | 8.05 | 9.15 | 9.78 | 11.76 | 11.76 | 9.09 | 8.84 | 8.68 |
| $K_2O$ | 0.38 | 0.10 | 0.18 | 0.26 | 0.24 | 0.18 | 0.19 | 0.27 | 0.21 | 0.22 |
| $P_2O_5$ | 0.24 | 0.10 | 0.18 | 0.26 | 0.27 | NA | NA | NA | NA | NA |
| Total | 100.39 | 99.57 | 100.30 | 100.31 | 100.21 | 100.49 | 100.39 | 100.04 | 100.74 | 99.96 |
| Or | 2.10 | 0.59 | 1.02 | 1.50 | 1.33 | 0.99 | 1.06 | 1.48 | 1.19 | 1.22 |
| Ab | 72.23 | 92.79 | 70.52 | 79.52 | 83.59 | 98.24 | 97.14 | 76.06 | 75.31 | 73.03 |
| An | 25.67 | 6.62 | 28.46 | 18.98 | 15.07 | 0.77 | 1.80 | 22.46 | 23.50 | 25.75 |

NA not analyzed

The Method Detection Limit (MDL) for the routine analysis of common elements is ~0.02 wt.%

***Supplementary Table 3.*** *Continued*

| Sample | Pl 51 | Pl 52 | Pl 53 | Pl 54 | Pl 55 | Pl 56 | Pl 57 | Pl 58 | Pl 59 | Pl 60 |
|---|---|---|---|---|---|---|---|---|---|---|
| Unit | OU | OU | OU | OU | OU | OU | OU | OU | MU | MU |
| $SiO_2$ | 68.39 | 68.29 | 65.14 | 65.66 | 64.91 | 68.04 | 62.38 | 66.19 | 64.16 | 65.28 |
| $TiO_2$ | 0.03 | < MDL | < MDL | 0.01 | < MDL | < MDL | < MDL | < MDL | < MDL | < MDL |
| $Al_2O_3$ | 19.74 | 19.39 | 21.63 | 21.15 | 21.56 | 19.56 | 23.36 | 21.41 | 22.23 | 21.63 |
| $Cr_2O_3$ | 0.02 | 0.04 | < MDL | 0.01 | 0.04 | < MDL | 0.03 | 0.01 | < MDL | < MDL |
| NiO | < MDL | < MDL | 0.01 | 0.05 | 0.03 | 0.01 | < MDL | 0.03 | 0.01 | < MDL |
| FeO | 0.01 | 0.03 | < MDL | < MDL | < MDL | < MDL | 0.04 | 0.01 | 0.01 | 0.02 |
| MnO | < MDL | 0.00 | < MDL | 0.00 | 0.01 | < MDL | 0.01 | < MDL | < MDL | 0.03 |
| MgO | 0.01 | < MDL | < MDL | 0.00 | < MDL | 0.01 | 0.01 | 0.01 | 0.00 | < MDL |
| CaO | 0.49 | 0.50 | 2.87 | 2.31 | 2.65 | 0.48 | 5.01 | 2.71 | 2.83 | 2.03 |
| $Na_2O$ | 11.57 | 11.54 | 10.18 | 10.59 | 10.25 | 11.64 | 8.93 | 10.17 | 10.21 | 10.19 |
| $K_2O$ | 0.13 | 0.20 | 0.31 | 0.14 | 0.26 | 0.15 | 0.23 | 0.25 | 0.21 | 0.64 |
| $P_2O_5$ | NA | NA | NA | NA | NA | NA | NA | NA | 0.21 | 0.29 |
| Total | 100.39 | 99.98 | 100.15 | 99.92 | 99.71 | 99.89 | 99.98 | 100.80 | 99.89 | 100.11 |
| Or | 0.74 | 1.07 | 1.73 | 0.75 | 1.46 | 0.83 | 1.27 | 1.41 | 1.18 | 3.61 |
| Ab | 97.01 | 96.63 | 85.01 | 88.58 | 86.23 | 96.96 | 75.37 | 85.95 | 85.68 | 86.85 |
| An | 2.26 | 2.30 | 13.26 | 10.67 | 12.31 | 2.22 | 23.37 | 12.64 | 13.13 | 9.54 |

NA not analyzed

The Method Detection Limit (MDL) for the routine analysis of common elements is ~0.02 wt.%

***Supplementary Table 3.*** *Continued*

| Sample | Pl 61 | Pl 62 | Pl 63 | Pl 64 | Pl 65 | Pl 66 | Pl 67 | Pl 68 | Pl 69 | Pl 70 |
|---|---|---|---|---|---|---|---|---|---|---|
| Unit | MU | MU | MU | MU | MU | MU | MU | MU | MU | MU |
| $SiO_2$ | 65.29 | 64.08 | 62.17 | 64.54 | 62.68 | 63.12 | 65.70 | 63.64 | 65.52 | 67.98 |
| $TiO_2$ | 0.02 | < MDL | < MDL | 0.01 | 0.02 | 0.01 | 0.03 | 0.01 | < MDL | < MDL |
| $Al_2O_3$ | 22.09 | 22.60 | 23.32 | 22.43 | 23.52 | 22.66 | 21.75 | 22.12 | 21.37 | 19.82 |
| $Cr_2O_3$ | 0.02 | < MDL | 0.08 | < MDL | 0.01 | < MDL | 0.01 | 0.04 | 0.01 | < MDL |
| NiO | 0.05 | < MDL | 0.03 | 0.01 | 0.02 | < MDL | 0.07 | 0.02 | < MDL | 0.03 |
| FeO | 0.02 | < MDL | 0.05 | 0.03 | < MDL | 0.01 | 0.02 | 0.01 | < MDL | 0.02 |
| MnO | 0.02 | 0.02 | 0.02 | 0.02 | 0.03 | 0.02 | < MDL | < MDL | 0.00 | 0.02 |
| MgO | < MDL | 0.03 | 0.03 | < MDL | < MDL | 0.00 | 0.00 | < MDL | < MDL | 0.00 |
| CaO | 2.53 | 3.60 | 4.70 | 2.91 | 4.45 | 3.68 | 1.97 | 3.46 | 2.03 | 0.85 |
| $Na_2O$ | 9.88 | 9.26 | 8.48 | 9.61 | 8.59 | 9.66 | 10.49 | 9.74 | 10.85 | 11.54 |
| $K_2O$ | 0.35 | 0.66 | 0.62 | 0.40 | 0.45 | 0.27 | 0.31 | 0.49 | 0.24 | 0.09 |
| $P_2O_5$ | 0.20 | 0.22 | 0.29 | 0.26 | 0.28 | 0.20 | 0.30 | NA | NA | NA |
| Total | 100.48 | 100.47 | 99.79 | 100.22 | 100.06 | 99.63 | 100.67 | 99.52 | 100.02 | 100.35 |
| Or | 2.03 | 3.73 | 3.57 | 2.26 | 2.63 | 1.50 | 1.74 | 2.68 | 1.30 | 0.49 |
| Ab | 85.85 | 79.23 | 73.82 | 83.73 | 75.70 | 81.35 | 89.01 | 81.34 | 89.45 | 95.62 |
| An | 12.13 | 17.04 | 22.62 | 14.00 | 21.67 | 17.15 | 9.25 | 15.99 | 9.25 | 3.90 |

NA not analyzed

The Method Detection Limit (MDL) for the routine analysis of common elements is ~0.02 wt.%

***Supplementary Table 3.*** *Continued*

| Sample | Pl 71 | Pl 72 | Pl 73 | Pl 74 | Pl 75 | Pl 76 | Pl 77 | Pl 78 | Pl 79 | Pl 80 |
|---|---|---|---|---|---|---|---|---|---|---|
| Unit | MU | MU | MU | MU | MU | MU | MU | MU | MU | MU |
| $SiO_2$ | 68.63 | 67.52 | 64.85 | 63.19 | 66.75 | 63.54 | 68.94 | 64.91 | 64.86 | 61.15 |
| $TiO_2$ | < MDL | 0.03 | < MDL | 0.00 | 0.01 | < MDL | < MDL | 0.02 | < MDL | < MDL |
| $Al_2O_3$ | 19.70 | 20.16 | 22.27 | 22.76 | 20.82 | 22.67 | 19.62 | 21.88 | 21.90 | 24.68 |
| $Cr_2O_3$ | 0.02 | 0.03 | 0.03 | < MDL | < MDL | 0.05 | 0.03 | < MDL | 0.05 | 0.07 |
| NiO | < MDL | < MDL | 0.04 | < MDL | < MDL | 0.01 | < MDL | 0.01 | < MDL | < MDL |
| FeO | 0.02 | 0.02 | 0.03 | 0.01 | 0.07 | < MDL | 0.00 | 0.00 | 0.03 | 0.02 |
| MnO | 0.01 | 0.01 | 0.00 | < MDL | 0.01 | < MDL | 0.03 | 0.02 | 0.02 | 0.03 |
| MgO | < MDL | 0.00 | < MDL | < MDL | 0.00 | 0.06 | 0.00 | 0.01 | < MDL | 0.00 |
| CaO | 0.18 | 0.90 | 3.22 | 4.14 | 1.41 | 3.47 | 0.15 | 3.02 | 3.03 | 5.90 |
| $Na_2O$ | 11.99 | 11.36 | 9.85 | 9.41 | 10.76 | 9.49 | 11.90 | 9.99 | 10.03 | 8.13 |
| $K_2O$ | 0.08 | 0.08 | 0.45 | 0.26 | 0.25 | 0.18 | 0.13 | 0.37 | 0.37 | 0.13 |
| $P_2O_5$ | NA | NA | NA | NA | NA | NA | NA | NA | NA | 0.12 |
| Total | 100.61 | 100.12 | 100.74 | 99.77 | 100.09 | 99.47 | 100.80 | 100.22 | 100.28 | 100.22 |
| Or | 0.42 | 0.46 | 2.49 | 1.43 | 1.38 | 1.02 | 0.71 | 2.03 | 2.02 | 0.74 |
| Ab | 98.76 | 95.37 | 82.59 | 79.29 | 91.94 | 82.35 | 98.60 | 83.97 | 83.98 | 70.87 |
| An | 0.82 | 4.16 | 14.91 | 19.28 | 6.67 | 16.63 | 0.69 | 14.01 | 14.00 | 28.39 |

NA not analyzed

The Method Detection Limit (MDL) for the routine analysis of common elements is ~0.02 wt.%

***Supplementary Table 3.*** *Continued*

| Sample | Pl 81 | Pl 82 | Pl 83 | Pl 84 | Pl 85 | Pl 86 | Pl 87 | Pl 88 | Pl 89 | Pl 90 |
|---|---|---|---|---|---|---|---|---|---|---|
| Unit | MU | MU | MU | MU | MU | MU | MU | MU | MU | MU |
| $SiO_2$ | 61.32 | 62.53 | 66.01 | 65.69 | 65.15 | 63.95 | 62.30 | 64.68 | 63.32 | 63.39 |
| $TiO_2$ | < MDL | 0.01 | 0.02 | < MDL | 0.01 | 0.02 | 0.02 | < MDL | 0.01 | 0.00 |
| $Al_2O_3$ | 24.07 | 23.42 | 21.41 | 21.76 | 22.27 | 23.14 | 23.18 | 21.95 | 23.39 | 23.25 |
| $Cr_2O_3$ | 0.00 | 0.03 | < MDL | 0.00 | < MDL | < MDL | < MDL | 0.00 | 0.01 | < MDL |
| NiO | < MDL | 0.03 | < MDL | < MDL | < MDL | < MDL | < MDL | < MDL | 0.02 | < MDL |
| FeO | 0.01 | 0.02 | 0.04 | 0.02 | < MDL | 0.01 | 0.04 | < MDL | 0.03 | 0.01 |
| MnO | < MDL | 0.04 | 0.03 | < MDL | < MDL | 0.00 | 0.00 | < MDL | < MDL | < MDL |
| MgO | < MDL | < MDL | 0.04 | < MDL | < MDL | < MDL | < MDL | 0.01 | 0.02 | 0.00 |
| CaO | 5.85 | 4.76 | 1.78 | 2.15 | 2.47 | 3.77 | 4.97 | 2.79 | 4.62 | 3.88 |
| $Na_2O$ | 8.42 | 9.17 | 10.66 | 10.54 | 10.38 | 9.44 | 8.55 | 9.89 | 8.84 | 9.51 |
| $K_2O$ | 0.23 | 0.29 | 0.08 | 0.36 | 0.25 | 0.48 | 0.62 | 0.33 | 0.53 | 0.38 |
| $P_2O_5$ | 0.14 | 0.16 | 0.53 | 0.33 | 0.23 | 0.14 | 0.08 | 0.29 | 0.08 | 0.12 |
| Total | 100.04 | 100.44 | 100.60 | 100.86 | 100.76 | 100.96 | 99.77 | 99.94 | 100.85 | 100.53 |
| Or | 1.27 | 1.57 | 0.46 | 1.95 | 1.38 | 2.67 | 3.47 | 1.84 | 2.95 | 2.11 |
| Ab | 71.33 | 76.50 | 91.13 | 88.10 | 87.17 | 79.75 | 73.06 | 84.90 | 75.30 | 79.89 |
| An | 27.40 | 21.93 | 8.41 | 9.94 | 11.46 | 17.58 | 23.47 | 13.25 | 21.75 | 18.00 |

The Method Detection Limit (MDL) for the routine analysis of common elements is ~0.02 wt.%

***Supplementary Table 3.*** *Continued*

| Sample | Pl 91 | Pl 92 | Pl 93 | Pl 94 | Pl 95 | Pl 96 | Pl 97 | Pl 98 | Pl 99 | Pl 100 |
|---|---|---|---|---|---|---|---|---|---|---|
| Unit | MU | MU | MU | MU | MU | MU | MU | MU | MU | MU |
| $SiO_2$ | 61.27 | 65.56 | 67.01 | 65.18 | 65.31 | 65.33 | 65.06 | 62.16 | 66.33 | 65.99 |
| $TiO_2$ | 0.03 | 0.01 | < MDL | 0.02 | 0.01 | < MDL | 0.00 | < MDL | 0.00 | 0.02 |
| $Al_2O_3$ | 24.14 | 22.17 | 20.71 | 21.83 | 21.49 | 21.52 | 22.00 | 24.14 | 20.49 | 20.84 |
| $Cr_2O_3$ | 0.02 | 0.01 | 0.00 | < MDL | 0.01 | 0.02 | < MDL | < MDL | < MDL | < MDL |
| NiO | 0.01 | 0.04 | < MDL | 0.07 | 0.03 | 0.04 | < MDL | < MDL | 0.08 | < MDL |
| FeO | 0.02 | 0.03 | 0.06 | < MDL | 0.02 | 0.02 | 0.04 | 0.02 | < MDL | 0.00 |
| MnO | < MDL | 0.02 | 0.00 | < MDL | < MDL | 0.00 | < MDL | 0.02 | 0.00 | < MDL |
| MgO | 0.03 | 0.02 | < MDL | 0.00 | < MDL | 0.01 | 0.02 | 0.01 | 0.03 | < MDL |
| CaO | 5.63 | 2.37 | 1.27 | 2.43 | 2.07 | 2.20 | 2.43 | 5.09 | 0.61 | 0.97 |
| $Na_2O$ | 8.47 | 10.07 | 11.12 | 10.15 | 10.32 | 10.21 | 10.22 | 8.82 | 11.39 | 10.88 |
| $K_2O$ | 0.15 | 0.31 | 0.15 | 0.46 | 0.60 | 0.47 | 0.22 | 0.23 | 0.11 | 0.29 |
| $P_2O_5$ | 0.13 | 0.32 | 0.21 | 0.17 | 0.19 | 0.27 | 0.26 | 0.04 | 0.37 | 0.33 |
| Total | 99.90 | 100.93 | 100.54 | 100.30 | 100.05 | 100.09 | 100.25 | 100.54 | 99.42 | 99.32 |
| Or | 0.84 | 1.77 | 0.83 | 2.56 | 3.31 | 2.61 | 1.22 | 1.26 | 0.62 | 1.65 |
| Ab | 72.54 | 86.91 | 93.28 | 86.08 | 87.03 | 87.05 | 87.30 | 74.87 | 96.50 | 93.72 |
| An | 26.61 | 11.32 | 5.89 | 11.37 | 9.67 | 10.34 | 11.48 | 23.87 | 2.88 | 4.63 |

The Method Detection Limit (MDL) for the routine analysis of common elements is ~0.02 wt.%

***Supplementary Table 3.*** *Continued*

| Sample | Pl 101 | Pl 102 | Pl 103 | Pl 104 | Pl 105 | Pl 106 | Pl 107 | Pl 108 | Pl 109 | Pl 110 |
|---|---|---|---|---|---|---|---|---|---|---|
| Unit | MU | MU | MU | IU | IU | IU | IU | IU | IU | IU |
| $SiO_2$ | 65.88 | 64.66 | 64.59 | 65.69 | 64.25 | 66.16 | 66.55 | 64.28 | 65.51 | 64.81 |
| $TiO_2$ | 0.02 | 0.00 | 0.02 | < MDL | 0.04 | < MDL | < MDL | 0.01 | 0.03 | 0.00 |
| $Al_2O_3$ | 20.65 | 21.99 | 21.68 | 21.38 | 22.37 | 21.21 | 20.80 | 22.22 | 21.52 | 22.14 |
| $Cr_2O_3$ | 0.00 | 0.02 | 0.03 | 0.05 | 0.01 | 0.02 | < MDL | 0.04 | 0.01 | < MDL |
| NiO | 0.00 | 0.02 | 0.03 | 0.02 | 0.03 | 0.01 | < MDL | 0.02 | < MDL | < MDL |
| FeO | 0.01 | 0.02 | 0.04 | 0.00 | < MDL | < MDL | < MDL | 0.00 | 0.01 | 0.01 |
| MnO | < MDL | 0.00 | 0.03 | 0.01 | 0.02 | 0.04 | < MDL | 0.04 | < MDL | < MDL |
| MgO | 0.00 | < MDL | < MDL | < MDL | 0.01 | < MDL | 0.02 | < MDL | < MDL | < MDL |
| CaO | 0.74 | 2.40 | 2.31 | 1.38 | 2.86 | 1.56 | 1.21 | 1.91 | 1.30 | 2.39 |
| $Na_2O$ | 11.16 | 10.43 | 9.93 | 10.84 | 10.24 | 10.32 | 10.77 | 10.08 | 11.02 | 9.97 |
| $K_2O$ | 0.16 | 0.41 | 0.33 | 0.26 | 0.30 | 0.29 | 0.19 | 0.44 | 0.20 | 0.34 |
| $P_2O_5$ | 0.66 | 0.32 | 0.25 | 0.46 | 0.22 | 0.25 | 0.22 | 0.49 | 0.74 | 0.26 |
| Total | 99.29 | 100.28 | 99.25 | 100.09 | 100.34 | 99.86 | 99.77 | 99.52 | 100.35 | 99.93 |
| Or | 0.92 | 2.25 | 1.91 | 1.43 | 1.63 | 1.66 | 1.06 | 2.53 | 1.13 | 1.97 |
| Ab | 95.57 | 86.74 | 86.91 | 92.11 | 85.23 | 90.75 | 93.14 | 88.22 | 92.80 | 86.55 |
| An | 3.51 | 11.01 | 11.18 | 6.46 | 13.14 | 7.60 | 5.80 | 9.25 | 6.06 | 11.49 |

The Method Detection Limit (MDL) for the routine analysis of common elements is ~0.02 wt.%

***Supplementary Table 3.*** *Continued*

| Sample | Pl 111 | Pl 112 | Pl 113 | Pl 114 | Pl 115 | Pl 116 | Pl 117 | Pl 118 | Pl 119 | Pl 120 |
|---|---|---|---|---|---|---|---|---|---|---|
| Unit | IU | IU | IU | IU | IU | IU | IU | IU | IU | IU |
| $SiO_2$ | 64.33 | 66.69 | 64.15 | 64.88 | 63.40 | 63.49 | 64.57 | 65.10 | 64.91 | 62.83 |
| $TiO_2$ | < MDL | < MDL | < MDL | < MDL | 0.00 | 0.01 | < MDL | < MDL | < MDL | < MDL |
| $Al_2O_3$ | 22.90 | 21.11 | 22.30 | 22.43 | 23.08 | 22.92 | 22.77 | 22.31 | 22.08 | 22.47 |
| $Cr_2O_3$ | < MDL | < MDL | 0.01 | < MDL | < MDL | < MDL | 0.01 | 0.00 | < MDL | 0.04 |
| NiO | < MDL | < MDL | 0.03 | 0.01 | < MDL | 0.03 | 0.02 | < MDL | 0.01 | 0.03 |
| FeO | 0.02 | < MDL | < MDL | < MDL | 0.00 | 0.02 | < MDL | < MDL | < MDL | 0.01 |
| MnO | 0.03 | 0.02 | < MDL | < MDL | 0.01 | 0.02 | 0.01 | < MDL | 0.01 | 0.03 |
| MgO | < MDL | 0.04 | 0.01 | 0.01 | < MDL | 0.01 | < MDL | < MDL | 0.04 | < MDL |
| CaO | 2.44 | 0.79 | 2.53 | 1.83 | 3.43 | 3.47 | 2.62 | 2.69 | 2.37 | 3.37 |
| $Na_2O$ | 9.92 | 11.21 | 10.09 | 10.35 | 9.19 | 9.39 | 9.78 | 9.90 | 10.17 | 10.22 |
| $K_2O$ | 0.38 | 0.21 | 0.31 | 0.33 | 0.25 | 0.28 | 0.46 | 0.46 | 0.26 | 0.16 |
| $P_2O_5$ | 0.28 | 0.34 | 0.26 | 0.38 | 0.29 | 0.05 | 0.23 | 0.18 | 0.37 | 0.09 |
| Total | 100.31 | 100.41 | 99.69 | 100.21 | 99.66 | 99.68 | 100.46 | 100.63 | 100.23 | 99.26 |
| Or | 2.16 | 1.17 | 1.77 | 1.86 | 1.45 | 1.59 | 2.60 | 2.59 | 1.47 | 0.85 |
| Ab | 86.13 | 95.12 | 86.29 | 89.41 | 81.70 | 81.71 | 84.86 | 84.71 | 87.29 | 83.87 |
| An | 11.71 | 3.71 | 11.94 | 8.73 | 16.85 | 16.70 | 12.54 | 12.70 | 11.24 | 15.28 |

The Method Detection Limit (MDL) for the routine analysis of common elements is ~0.02 wt.%

***Supplementary Table 3.*** *Continued*

| Sample | Pl 121 | Pl 122 | Pl 123 | Pl 124 | Pl 125 | Pl 126 | Pl 127 | Pl 128 | Pl 129 | Pl 130 |
|---|---|---|---|---|---|---|---|---|---|---|
| Unit | IU | IU | IU | IU | IU | IU | IU | IU | IU | IU |
| $SiO_2$ | 64.71 | 64.23 | 65.43 | 63.74 | 63.46 | 63.91 | 62.74 | 64.42 | 64.31 | 62.97 |
| $TiO_2$ | < MDL | < MDL | 0.00 | 0.02 | 0.01 | 0.00 | < MDL | < MDL | 0.01 | < MDL |
| $Al_2O_3$ | 23.22 | 22.28 | 22.02 | 22.86 | 23.25 | 22.41 | 23.29 | 22.49 | 22.33 | 23.30 |
| $Cr_2O_3$ | 0.01 | < MDL | 0.01 | < MDL | < MDL | 0.00 | 0.07 | < MDL | 0.00 | 0.03 |
| NiO | 0.02 | 0.01 | 0.04 | 0.04 | < MDL | < MDL | 0.03 | 0.01 | 0.00 | < MDL |
| FeO | 0.01 | 0.01 | 0.02 | 0.01 | < MDL | 0.03 | < MDL | < MDL | 0.04 | 0.03 |
| MnO | 0.01 | < MDL | 0.01 | < MDL | 0.01 | 0.01 | 0.01 | 0.01 | < MDL | < MDL |
| MgO | < MDL | 0.08 | 0.01 | 0.01 | 0.02 | 0.06 | 0.01 | < MDL | < MDL | 0.00 |
| CaO | 3.11 | 1.87 | 1.92 | 3.05 | 3.77 | 2.74 | 3.79 | 2.43 | 2.47 | 3.36 |
| $Na_2O$ | 9.47 | 10.55 | 10.40 | 9.61 | 9.41 | 10.12 | 9.35 | 9.98 | 10.30 | 9.63 |
| $K_2O$ | 0.27 | 0.11 | 0.28 | 0.34 | 0.23 | 0.26 | 0.34 | 0.35 | 0.20 | 0.28 |
| $P_2O_5$ | 0.12 | 0.26 | 0.34 | 0.04 | 0.05 | 0.29 | 0.17 | 0.37 | 0.33 | 0.08 |
| Total | 100.94 | 99.38 | 100.49 | 99.72 | 100.22 | 99.84 | 99.79 | 100.05 | 100.00 | 99.69 |
| Or | 1.56 | 0.62 | 1.57 | 1.96 | 1.32 | 1.42 | 1.92 | 1.99 | 1.11 | 1.55 |
| Ab | 83.31 | 90.53 | 89.32 | 83.42 | 80.78 | 85.73 | 80.14 | 86.41 | 87.30 | 82.52 |
| An | 15.14 | 8.86 | 9.11 | 14.62 | 17.90 | 12.84 | 17.94 | 11.60 | 11.59 | 15.92 |

The Method Detection Limit (MDL) for the routine analysis of common elements is ~0.02 wt.%

***Supplementary Table 3.*** *Continued*

| Sample | Pl 131 | Pl 132 | Pl 133 | Pl 134 | Pl 135 | Pl 136 | Pl 137 | Pl 138 | Pl 139 | Pl 140 |
|---|---|---|---|---|---|---|---|---|---|---|
| Unit | MME | MME | MME | MME | MME | MME | MME | MME | MME | MME |
| $SiO_2$ | 59.63 | 59.53 | 61.96 | 61.12 | 60.68 | 61.72 | 59.10 | 58.88 | 61.42 | 60.73 |
| $TiO_2$ | 0.01 | 0.01 | < MDL | 0.01 | 0.01 | < MDL | < MDL | 0.01 | 0.01 | 0.02 |
| $Al_2O_3$ | 24.97 | 25.25 | 23.41 | 24.22 | 24.88 | 24.20 | 25.35 | 25.35 | 23.78 | 24.68 |
| $Cr_2O_3$ | 0.02 | < MDL | < MDL | 0.03 | < MDL | < MDL | < MDL | 0.03 | 0.01 | 0.03 |
| NiO | < MDL | 0.04 | 0.01 | 0.01 | 0.01 | 0.01 | < MDL | < MDL | 0.01 | < MDL |
| FeO | 0.04 | 0.09 | 0.03 | < MDL | 0.01 | 0.03 | 0.07 | 0.05 | 0.10 | 0.02 |
| MnO | < MDL | 0.01 | < MDL | < MDL | < MDL | < MDL | 0.03 | < MDL | < MDL | 0.03 |
| MgO | < MDL | 0.01 | 0.01 | < MDL | < MDL | < MDL | < MDL | 0.01 | 0.01 | 0.01 |
| CaO | 6.43 | 6.76 | 4.64 | 5.48 | 6.03 | 5.23 | 7.08 | 7.17 | 5.32 | 5.77 |
| $Na_2O$ | 8.13 | 7.88 | 9.09 | 8.40 | 8.20 | 8.64 | 7.75 | 7.67 | 8.29 | 8.38 |
| $K_2O$ | 0.16 | 0.15 | 0.25 | 0.30 | 0.19 | 0.26 | 0.12 | 0.11 | 0.19 | 0.25 |
| Total | 99.39 | 99.72 | 99.41 | 99.57 | 100.01 | 100.10 | 99.50 | 99.29 | 99.15 | 99.92 |
| Or | 0.89 | 0.84 | 1.39 | 1.70 | 1.07 | 1.46 | 0.67 | 0.62 | 1.10 | 1.40 |
| Ab | 68.97 | 67.27 | 76.91 | 72.25 | 70.34 | 73.84 | 66.01 | 65.53 | 73.01 | 71.42 |
| An | 30.14 | 31.89 | 21.70 | 26.05 | 28.58 | 24.70 | 33.32 | 33.85 | 25.89 | 27.18 |

The Method Detection Limit (MDL) for the routine analysis of common elements is ~0.02 wt.%

***Supplementary Table 3.*** *Continued*

| Sample | Pl 141 | Pl 142 | Pl 143 | Pl 144 | Pl 145 | Pl 146 | Pl 147 | Pl 148 | Pl 149 | Pl 150 |
|---|---|---|---|---|---|---|---|---|---|---|
| Unit | MME | MME | MME | MME | MME | MME | MME | MME | MME | MME |
| $SiO_2$ | 60.54 | 62.11 | 61.82 | 61.30 | 62.30 | 61.19 | 60.85 | 62.82 | 62.08 | 61.24 |
| $TiO_2$ | 0.01 | 0.03 | < MDL | < MDL | 0.03 | 0.03 | < MDL | 0.02 | < MDL | < MDL |
| $Al_2O_3$ | 24.70 | 24.50 | 24.17 | 24.37 | 24.08 | 24.63 | 24.39 | 22.90 | 24.32 | 24.01 |
| $Cr_2O_3$ | 0.01 | 0.04 | 0.01 | < MDL | < MDL | < MDL | 0.02 | < MDL | 0.01 | < MDL |
| NiO | 0.03 | < MDL | < MDL | < MDL | < MDL | 0.01 | < MDL | < MDL | 0.02 | 0.05 |
| FeO | 0.02 | 0.04 | 0.03 | 0.01 | < MDL | 0.02 | 0.05 | 0.01 | 0.03 | < MDL |
| MnO | 0.01 | < MDL | < MDL | 0.02 | 0.01 | 0.01 | 0.02 | 0.01 | < MDL | < MDL |
| MgO | < MDL | 0.01 | < MDL | 0.01 | < MDL | 0.01 | < MDL | < MDL | < MDL | < MDL |
| CaO | 6.09 | 5.32 | 5.23 | 5.44 | 5.07 | 5.83 | 5.27 | 4.02 | 5.20 | 5.31 |
| $Na_2O$ | 8.21 | 8.48 | 8.59 | 8.56 | 8.81 | 8.41 | 8.68 | 9.33 | 8.85 | 8.72 |
| $K_2O$ | 0.28 | 0.33 | 0.34 | 0.28 | 0.28 | 0.19 | 0.19 | 0.25 | 0.21 | 0.26 |
| Total | 99.92 | 100.86 | 100.19 | 100.01 | 100.58 | 100.31 | 99.48 | 99.35 | 100.72 | 99.60 |
| Or | 1.57 | 1.87 | 1.91 | 1.57 | 1.56 | 1.06 | 1.07 | 1.40 | 1.16 | 1.45 |
| Ab | 69.82 | 72.87 | 73.39 | 72.85 | 74.69 | 71.53 | 74.08 | 79.63 | 74.61 | 73.74 |
| An | 28.62 | 25.26 | 24.69 | 25.58 | 23.75 | 27.40 | 24.85 | 18.96 | 24.23 | 24.81 |

The Method Detection Limit (MDL) for the routine analysis of common elements is ~0.02 wt.%

***Supplementary Table 3.*** *Continued*

| Sample | Pl 151 | Pl 152 | Pl 153 | Pl 154 | Pl 155 | Pl 156 | Pl 157 | Pl 158 | Pl 159 | Pl 160 |
|---|---|---|---|---|---|---|---|---|---|---|
| Unit | MME | MME | MME | MME | MME | MME | MME | MME | MME | MME |
| $SiO_2$ | 59.40 | 59.13 | 58.75 | 60.53 | 60.26 | 61.24 | 61.16 | 63.62 | 61.58 | 57.49 |
| $TiO_2$ | 0.02 | 0.03 | 0.02 | 0.03 | 0.02 | 0.02 | < MDL | < MDL | 0.01 | 0.01 |
| $Al_2O_3$ | 25.45 | 26.11 | 25.57 | 24.71 | 24.46 | 24.31 | 23.99 | 22.64 | 24.27 | 26.16 |
| $Cr_2O_3$ | < MDL | 0.01 | 0.01 | < MDL | < MDL | 0.03 | 0.05 | 0.01 | 0.04 | 0.01 |
| NiO | < MDL | 0.02 | < MDL | < MDL | < MDL | < MDL | < MDL | 0.01 | < MDL | 0.03 |
| FeO | 0.04 | 0.09 | 0.04 | 0.02 | 0.12 | 0.03 | 0.01 | 0.05 | 0.02 | 0.07 |
| MnO | 0.01 | < MDL | < MDL | 0.03 | < MDL | 0.02 | < MDL | < MDL | 0.01 | < MDL |
| MgO | < MDL | < MDL | < MDL | < MDL | 0.01 | 0.01 | < MDL | 0.01 | < MDL | < MDL |
| CaO | 6.76 | 7.26 | 7.71 | 6.34 | 6.63 | 6.14 | 6.01 | 4.01 | 5.72 | 8.56 |
| $Na_2O$ | 7.94 | 7.69 | 7.57 | 8.23 | 8.07 | 8.21 | 8.44 | 9.63 | 8.57 | 6.89 |
| $K_2O$ | 0.18 | 0.12 | 0.13 | 0.18 | 0.16 | 0.18 | 0.19 | 0.22 | 0.23 | 0.13 |
| Total | 99.81 | 100.44 | 99.80 | 100.06 | 99.73 | 100.20 | 99.86 | 100.19 | 100.45 | 99.37 |
| Or | 1.00 | 0.67 | 0.72 | 1.00 | 0.89 | 1.01 | 1.05 | 1.21 | 1.27 | 0.73 |
| Ab | 67.32 | 65.28 | 63.53 | 69.44 | 68.16 | 70.04 | 71.01 | 80.31 | 72.12 | 58.86 |
| An | 31.67 | 34.05 | 35.75 | 29.56 | 30.95 | 28.95 | 27.94 | 18.48 | 26.60 | 40.41 |

The Method Detection Limit (MDL) for the routine analysis of common elements is ~0.02 wt.%

***Supplementary Table 3.*** *Continued*

| Sample | Pl 161 | Pl 162 | Pl 163 | Pl 164 | Pl 165 | Pl 166 | Pl 167 | Pl 168 | Pl 169 |
|---|---|---|---|---|---|---|---|---|---|
| Unit | MME | MME | MME | MME | MME | MME | MME | MME | MME |
| $SiO_2$ | 63.99 | 61.68 | 59.25 | 61.21 | 61.72 | 61.40 | 58.40 | 63.54 | 61.44 |
| $TiO_2$ | < MDL | 0.01 | < MDL | < MDL | < MDL | 0.01 | < MDL | 0.01 | < MDL |
| $Al_2O_3$ | 22.32 | 23.68 | 25.36 | 24.41 | 24.09 | 23.84 | 25.68 | 22.75 | 24.00 |
| $Cr_2O_3$ | < MDL | 0.05 | < MDL | < MDL | < MDL | < MDL | < MDL | 0.05 | < MDL |
| NiO | < MDL | 0.05 | 0.02 | < MDL | 0.04 | 0.01 | 0.02 | < MDL | 0.03 |
| FeO | < MDL | 0.07 | 0.01 | 0.01 | 0.03 | < MDL | < MDL | 0.04 | 0.02 |
| MnO | 0.02 | 0.01 | < MDL | 0.02 | 0.01 | 0.03 | 0.02 | 0.04 | < MDL |
| MgO | < MDL | < MDL | 0.01 | 0.01 | < MDL | < MDL | < MDL | < MDL | < MDL |
| CaO | 3.84 | 5.27 | 6.99 | 5.77 | 5.54 | 5.69 | 8.01 | 4.34 | 5.73 |
| $Na_2O$ | 9.67 | 8.63 | 7.79 | 8.44 | 8.64 | 8.47 | 7.19 | 9.27 | 8.28 |
| $K_2O$ | 0.18 | 0.23 | 0.13 | 0.31 | 0.28 | 0.29 | 0.15 | 0.29 | 0.23 |
| Total | 100.02 | 99.67 | 99.56 | 100.19 | 100.35 | 99.73 | 99.47 | 100.31 | 99.73 |
| Or | 0.99 | 1.29 | 0.73 | 1.72 | 1.55 | 1.62 | 0.84 | 1.61 | 1.30 |
| Ab | 81.19 | 73.80 | 66.36 | 71.33 | 72.69 | 71.75 | 61.37 | 78.17 | 71.39 |
| An | 17.82 | 24.90 | 32.91 | 26.95 | 25.76 | 26.64 | 37.78 | 20.22 | 27.30 |

The Method Detection Limit (MDL) for the routine analysis of common elements is ~0.02 wt.%

***Supplementary Table 3.*** *Continued*

| Sample | Pl 170 | Pl 171 | Pl 172 | Pl 173 | Pl 174 | Pl 175 | Pl 176 | Pl 177 | Pl 178 | Pl 179 |
|---|---|---|---|---|---|---|---|---|---|---|
| Unit | Lamp | Lamp | Lamp | Lamp | Lamp | Lamp | Lamp | Lamp | Lamp | Lamp |
| Type | Mnt | Mnt | Micr-dt | Micr-dt | Micr-dt | Micr-dt | Micr-dt | Micr-dt | Micr-dt | Micr-dt |
| $SiO_2$ | 66.14 | 67.43 | 51.29 | 52.11 | 53.09 | 54.21 | 53.21 | 52.69 | 52.24 | 54.97 |
| $TiO_2$ | < MDL | < MDL | 0.09 | 0.11 | 0.06 | 0.10 | 0.09 | 0.11 | 0.10 | 0.04 |
| $Al_2O_3$ | 21.33 | 21.33 | 29.78 | 29.11 | 29.37 | 28.31 | 29.13 | 29.43 | 29.59 | 28.20 |
| $Cr_2O_3$ | < MDL | < MDL | 0.01 | 0.02 | < MDL | 0.04 | 0.01 | < MDL | < MDL | < MDL |
| NiO | 0.02 | < MDL | 0.01 | 0.02 | < MDL | 0.03 | < MDL | < MDL | < MDL | 0.02 |
| FeO | 0.07 | 0.07 | 0.59 | 0.58 | 0.47 | 0.57 | 0.55 | 0.53 | 0.58 | 0.38 |
| MnO | < MDL | < MDL | < MDL | < MDL | < MDL | 0.01 | < MDL | < MDL | < MDL | < MDL |
| MgO | 0.02 | 0.07 | 0.09 | 0.10 | 0.08 | 0.09 | 0.11 | 0.10 | 0.10 | 0.18 |
| CaO | 1.36 | 0.81 | 12.81 | 12.28 | 12.58 | 11.36 | 12.46 | 12.59 | 12.69 | 9.47 |
| $Na_2O$ | 10.68 | 10.70 | 4.08 | 4.26 | 4.07 | 4.71 | 4.30 | 4.23 | 4.16 | 5.47 |
| $K_2O$ | 0.44 | 0.55 | 0.40 | 0.47 | 0.42 | 0.50 | 0.44 | 0.42 | 0.43 | 0.71 |
| Total | 100.05 | 100.96 | 99.15 | 99.07 | 100.16 | 99.92 | 100.30 | 100.10 | 99.89 | 99.43 |
| Or | 2.45 | 3.16 | 2.33 | 2.75 | 2.47 | 2.89 | 2.55 | 2.40 | 2.47 | 4.16 |
| Ab | 91.12 | 92.94 | 35.70 | 37.50 | 36.03 | 41.62 | 37.47 | 36.91 | 36.30 | 48.96 |
| An | 6.43 | 3.90 | 61.97 | 59.75 | 61.50 | 55.49 | 59.99 | 60.68 | 61.23 | 46.88 |

The Method Detection Limit (MDL) for the routine analysis of common elements is ~0.02 wt.%

***Supplementary Table 3.*** *Continued*

| Sample | Pl 180 | Pl 181 | Pl 182 | Pl 183 | Pl 184 | Pl 185 | Pl 186 | Pl 187 | Pl 188 | Pl 189 |
|---|---|---|---|---|---|---|---|---|---|---|
| Unit | Lamp | Lamp | Lamp | Lamp | Lamp | Lamp | Lamp | Lamp | Lamp | Lamp |
| Type | Micr-dt | Krs | Krs | Krs | Krs | Krs | Krs | Krs | Krs | Krs |
| $SiO_2$ | 55.91 | 53.32 | 54.46 | 52.32 | 53.96 | 52.95 | 55.91 | 54.03 | 52.82 | 53.57 |
| $TiO_2$ | 0.02 | 0.03 | 0.03 | 0.02 | 0.09 | 0.06 | 0.03 | 0.03 | 0.05 | 0.04 |
| $Al_2O_3$ | 27.38 | 29.02 | 28.19 | 29.29 | 28.71 | 29.44 | 27.52 | 28.00 | 28.78 | 28.36 |
| $Cr_2O_3$ | 0.07 | < MDL | 0.03 | 0.01 | 0.02 | 0.01 | < MDL | < MDL | 0.03 | 0.04 |
| NiO | < MDL | 0.01 | < MDL | < MDL | 0.02 | 0.02 | < MDL | 0.01 | < MDL | < MDL |
| FeO | 0.26 | 0.56 | 0.55 | 0.57 | 0.59 | 0.61 | 0.56 | 0.55 | 0.55 | 0.55 |
| MnO | 0.02 | 0.04 | 0.03 | < MDL | 0.02 | < MDL | 0.02 | 0.02 | < MDL | < MDL |
| MgO | 0.01 | 0.20 | 0.07 | 0.10 | 0.12 | 0.08 | 0.06 | 0.07 | 0.12 | 0.08 |
| CaO | 9.34 | 12.00 | 11.47 | 12.66 | 11.46 | 12.61 | 10.21 | 11.91 | 12.89 | 12.34 |
| $Na_2O$ | 6.00 | 4.27 | 4.70 | 4.22 | 4.56 | 4.02 | 5.24 | 4.56 | 3.92 | 4.16 |
| $K_2O$ | 0.50 | 0.47 | 0.52 | 0.50 | 0.61 | 0.45 | 0.64 | 0.43 | 0.44 | 0.46 |
| Total | 99.51 | 99.92 | 100.05 | 99.70 | 100.15 | 100.24 | 100.20 | 99.61 | 99.59 | 99.59 |
| Or | 2.87 | 2.76 | 3.02 | 2.85 | 3.53 | 2.63 | 3.74 | 2.48 | 2.58 | 2.69 |
| Ab | 52.19 | 38.08 | 41.27 | 36.55 | 40.37 | 35.64 | 46.36 | 39.89 | 34.57 | 36.88 |
| An | 44.94 | 59.16 | 55.70 | 60.60 | 56.10 | 61.73 | 49.90 | 57.63 | 62.85 | 60.43 |

The Method Detection Limit (MDL) for the routine analysis of common elements is ~0.02 wt.%

***Supplementary Table 3.*** *Continued*

| Sample | Pl 190 | Pl 191 | Pl 192 | Pl 193 | Pl 194 | Pl 195 | Pl 196 | Pl 197 | Pl 198 | Pl 199 |
|---|---|---|---|---|---|---|---|---|---|---|
| Unit | Lamp | Lamp | Lamp | Vaugn | Vaugn | Vaugn | Vaugn | Vaugn | Vaugn | Vaugn |
| Type | Krs | Krs | Krs | Bt-rich | Bt-rich | Bt-rich | Bt-rich | Bt-rich | Bt-rich | Bt-rich |
| $SiO_2$ | 52.74 | 57.92 | 53.37 | 68.22 | 68.59 | 68.38 | 68.47 | 66.33 | 67.55 | 66.87 |
| $TiO_2$ | 0.04 | < MDL | 0.03 | < MDL | < MDL | < MDL | < MDL | 0.01 | 0.01 | < MDL |
| $Al_2O_3$ | 28.51 | 26.04 | 28.35 | 19.97 | 19.80 | 19.88 | 19.98 | 21.26 | 20.03 | 20.46 |
| $Cr_2O_3$ | < MDL | < MDL | < MDL | < MDL | < MDL | < MDL | < MDL | < MDL | 0.04 | 0.01 |
| NiO | 0.01 | < MDL | < MDL | 0.06 | < MDL | 0.03 | < MDL | < MDL | < MDL | < MDL |
| FeO | 0.66 | 0.31 | 0.49 | 0.06 | 0.03 | 0.09 | 0.03 | 0.12 | 0.08 | 0.09 |
| MnO | < MDL | 0.01 | < MDL | < MDL | 0.01 | 0.03 | 0.03 | 0.02 | < MDL | < MDL |
| MgO | 0.10 | 0.02 | 0.12 | < MDL | < MDL | < MDL | 0.02 | < MDL | < MDL | < MDL |
| CaO | 12.83 | 8.97 | 12.30 | 0.78 | 0.41 | 0.83 | 0.78 | 2.09 | 1.26 | 1.67 |
| $Na_2O$ | 3.90 | 6.17 | 4.28 | 11.41 | 11.57 | 11.35 | 11.23 | 10.27 | 10.80 | 10.59 |
| $K_2O$ | 0.40 | 0.56 | 0.47 | 0.12 | 0.17 | 0.17 | 0.18 | 0.25 | 0.10 | 0.14 |
| Total | 99.19 | 100.00 | 99.43 | 100.61 | 100.59 | 100.75 | 100.71 | 100.35 | 99.88 | 99.83 |
| Or | 2.36 | 3.19 | 2.71 | 0.65 | 0.96 | 0.93 | 1.01 | 1.43 | 0.58 | 0.77 |
| Ab | 34.64 | 53.66 | 37.61 | 95.74 | 97.14 | 95.23 | 95.33 | 88.61 | 93.41 | 91.29 |
| An | 63.00 | 43.15 | 59.68 | 3.61 | 1.90 | 3.84 | 3.66 | 9.95 | 6.01 | 7.94 |

The Method Detection Limit (MDL) for the routine analysis of common elements is ~0.02 wt.%

***Supplementary Table 3.*** *Continued*

| Sample | Pl 200 | Pl 201 | Pl 202 | Pl 203 | Pl 204 | Pl 205 | Pl 206 | Pl 207 | Pl 208 | Pl 209 |
|---|---|---|---|---|---|---|---|---|---|---|
| Unit | Vaugn | Vaugn | Vaugn | Vaugn | Vaugn | Vaugn | Vaugn | Vaugn | Vaugn | Vaugn |
| Type | Bt-rich | Bt-rich | Bt-rich | Bt-poor | Bt-poor | Bt-poor | Bt-poor | Bt-poor | Bt-poor | Bt-poor |
| $SiO_2$ | 68.75 | 62.95 | 68.29 | 67.25 | 67.33 | 67.35 | 67.72 | 66.18 | 63.56 | 66.90 |
| $TiO_2$ | < MDL | 0.06 | 0.01 | < MDL | 0.01 | < MDL | < MDL | < MDL | 0.02 | < MDL |
| $Al_2O_3$ | 19.80 | 22.81 | 18.97 | 20.45 | 20.30 | 20.13 | 19.40 | 21.00 | 22.22 | 21.22 |
| $Cr_2O_3$ | 0.04 | 0.03 | < MDL | 0.05 | 0.02 | 0.03 | < MDL | 0.03 | 0.04 | 0.01 |
| NiO | < MDL | < MDL | 0.02 | < MDL | 0.01 | < MDL | 0.01 | < MDL | 0.03 | < MDL |
| FeO | 0.05 | 0.26 | 0.13 | < MDL | 0.02 | 0.34 | 0.06 | 0.07 | 0.04 | 0.07 |
| MnO | 0.02 | < MDL | < MDL | 0.01 | < MDL | < MDL | 0.01 | 0.05 | 0.01 | 0.02 |
| MgO | < MDL | < MDL | < MDL | 0.01 | < MDL | 0.10 | < MDL | 0.04 | 0.01 | 0.05 |
| CaO | 0.64 | 4.42 | 0.46 | 0.88 | 1.08 | 0.97 | 0.74 | 1.64 | 3.76 | 1.68 |
| $Na_2O$ | 11.45 | 8.81 | 10.72 | 11.77 | 11.43 | 11.09 | 10.43 | 10.98 | 9.84 | 9.59 |
| $K_2O$ | 0.19 | 0.97 | 0.59 | 0.05 | 0.05 | 0.26 | 1.08 | 0.07 | 0.10 | 0.17 |
| Total | 100.94 | 100.31 | 99.19 | 100.48 | 100.25 | 100.27 | 99.44 | 100.06 | 99.63 | 99.73 |
| Or | 1.05 | 5.35 | 3.43 | 0.29 | 0.29 | 1.48 | 6.16 | 0.39 | 0.57 | 1.07 |
| Ab | 95.97 | 74.08 | 94.35 | 95.75 | 94.77 | 94.00 | 90.31 | 92.03 | 82.11 | 90.21 |
| An | 2.98 | 20.57 | 2.22 | 3.96 | 4.95 | 4.52 | 3.52 | 7.58 | 17.33 | 8.72 |

The Method Detection Limit (MDL) for the routine analysis of common elements is ~0.02 wt.%

***Supplementary Table 3.*** *Continued*

| Sample | Pl 210 | Pl 211 | Pl 212 | Pl 213 | Pl 214 | Pl 215 | Pl 216 | Pl 217 | Pl 218 |
|---|---|---|---|---|---|---|---|---|---|
| Unit | Vaugn | Vaugn | Vaugn | Vaugn | Vaugn | Vaugn | Vaugn | Vaugn | Vaugn |
| Type | Bt-poor | Bt-poor | Bt-poor | Bt-poor | Bt-poor | Bt-poor | Bt-poor | Bt-poor | Bt-poor |
| $SiO_2$ | 67.42 | 66.21 | 66.27 | 66.79 | 67.37 | 65.15 | 65.88 | 66.83 | 67.25 |
| $TiO_2$ | < MDL | < MDL | 0.01 | 0.02 | < MDL | < MDL | < MDL | 0.01 | 0.01 |
| $Al_2O_3$ | 20.53 | 20.14 | 20.79 | 20.70 | 20.23 | 20.98 | 21.23 | 20.66 | 20.40 |
| $Cr_2O_3$ | < MDL | < MDL | < MDL | 0.01 | < MDL | 0.02 | < MDL | 0.01 | < MDL |
| NiO | < MDL | 0.03 | < MDL | < MDL | < MDL | < MDL | 0.04 | < MDL | < MDL |
| FeO | < MDL | 0.68 | 0.17 | 0.06 | 0.03 | 0.32 | 0.02 | 0.09 | 0.03 |
| MnO | 0.03 | 0.01 | < MDL | < MDL | < MDL | 0.02 | < MDL | < MDL | < MDL |
| MgO | < MDL | 0.27 | 0.05 | < MDL | < MDL | 0.04 | < MDL | 0.03 | < MDL |
| CaO | 1.35 | 0.93 | 2.09 | 2.04 | 1.43 | 2.58 | 2.18 | 1.55 | 1.41 |
| $Na_2O$ | 11.15 | 10.67 | 10.79 | 10.37 | 11.02 | 9.86 | 10.59 | 11.05 | 11.17 |
| $K_2O$ | 0.25 | 0.43 | 0.10 | 0.16 | 0.15 | 0.10 | 0.09 | 0.11 | 0.10 |
| Total | 100.73 | 99.37 | 100.27 | 100.15 | 100.22 | 99.07 | 100.04 | 100.34 | 100.38 |
| Or | 1.38 | 2.49 | 0.56 | 0.91 | 0.80 | 0.60 | 0.53 | 0.62 | 0.53 |
| Ab | 92.43 | 93.02 | 89.84 | 89.39 | 92.57 | 86.86 | 89.31 | 92.24 | 93.01 |
| An | 6.19 | 4.49 | 9.60 | 9.70 | 6.63 | 12.54 | 10.17 | 7.15 | 6.47 |

The Method Detection Limit (MDL) for the routine analysis of common elements is ~0.02 wt.%

***Supplementary Table 4.*** *LA-ICP-MS analyses of trace-elements of main rock-forming minerals from the Sierra Bermeja Pluton monzogranites*

| Sample[b] | Kfs 1 | Kfs 2 | Kfs 3 | Kfs 4 | Kfs 5 | Kfs 6 | Kfs 7 | Kfs 8 | Kfs 9 | Kfs 10 |
|---|---|---|---|---|---|---|---|---|---|---|
| Unit | IU | OU | OU | OU | OU | MU | MU | OU | OU | OU |
| Rb (ppm) | 421 | 378 | 337 | 354 | 340 | 400 | 332 | 428 | 491 | 569 |
| 2SE (%) | 3 | 11 | 5 | 9 | 11 | 11 | 5 | 7 | 6 | 5 |
| MDL | 0.57 | 1.9 | 13 | 15 | 1.4 | 12 | 18 | 0.48 | 0.25 | 0.2 |
| Sr (ppm) | 239 | 747 | 664 | 699 | 387 | 945 | 1612 | 195 | 191 | 223 |
| 2SE (%) | 4 | 10 | 10 | 8 | 6 | 9 | 4 | 4 | 3 | 3 |
| MDL | 3.1 | 0.059 | 13 | 14 | - | 44 | 70 | 0.0074 | 0.0066 | 0.0064 |
| Ba (ppm) | 973 | 4030 | 3900 | 2650 | 1830 | 3020 | 3430 | 2190 | 1095 | 4000 |
| 2SE (%) | 3 | 10 | 6 | 7 | 5 | 8 | 4 | 5 | 4 | 4 |
| MDL | 6.1 | - | 260 | 290 | - | 78 | 120 | 0.041 | 0.058 | - |

[b]The sample code do not corresponds with codes from microprobe result tables
MDL (Method Detection Limit)

***Supplementary Table 4.*** *Continued*

| Sample[b] | Kfs 11 | Pl 1 | Pl 2 | Pl 3 | Pl 4 | Pl 5 | Pl 6 | Pl 7 | Pl 8 | Pl 9 | Pl 10 |
|---|---|---|---|---|---|---|---|---|---|---|---|
| Unit | OU | IU | OU | OU | OU | IU | IU | MU | MU | OU | OU |
| Rb (ppm) | 559 | 47.1 | 34.9 | 55.5 | 30.5 | 20.22 | 17.12 | 16.3 | 18.6 | 11.1 | 5.98 |
| 2SE (%) | 7 | 12 | 11 | 16 | 15 | 4 | 6 | 7 | 8 | 17 | 7 |
| MDL | 0.23 | 0.79 | 0.47 | 0.41 | 0.37 | 0.34 | 0.25 | 0.74 | 0.35 | 0.2 | 0.21 |
| Sr (ppm) | 241 | 195 | 467 | 287 | 268 | 176 | 119 | 90.00 | 62.2 | 106 | 99.5 |
| 2SE (%) | 4 | 8 | 2 | 5 | 3 | 3 | 7 | 5 | 5 | 4 | 3 |
| MDL | 0.018 | 4.2 | 6.2 | 0.015 | - | 3.5 | 0.0053 | 4.5 | 0.012 | 0.12 | - |
| Ba (ppm) | 3840 | 526 | 509 | 411 | 308 | 230 | 207.9 | 146 | 139 | 96.7 | 87.8 |
| 2SE (%) | 5 | 11 | 8 | 10 | 8 | 5 | 3 | 9 | 9 | 7 | 7 |
| MDL | 0.061 | 8.4 | 7.3 | - | 0.038 | 4.4 | 0.02 | 5.2 | - | - | 0.021 |

[b]The sample code do not corresponds with codes from microprobe result tables
MDL (Method Detection Limit)

***Supplementary Table 4.*** *Continued*

| Sample[b] | Pl 11 | Bt 1 | Bt 2 | Bt 3 | Bt 4 | Bt 5 | Bt 6 | Bt 7 | Bt 8 | Bt 9 | Bt 10 |
|---|---|---|---|---|---|---|---|---|---|---|---|
| Unit | MU | OU | OU | OU | OU | OU | IU | OU | OU | MU | IU |
| Rb (ppm) | 6.7 | 1450 | 1036 | 752 | 1424 | 891 | 911 | 996 | 914 | 1115 | 971 |
| 2SE (%) | 9 | 6 | 6 | 3 | 4 | 5 | 1 | 3 | 2 | 4 | 1 |
| MDL | 0.28 | 410 | 0.068 | 0.086 | 0.076 | 0.079 | 0.16 | 0.15 | 0.087 | 0.24 | 14 |
| Sr (ppm) | 83.6 | 26.5 | 1.13 | 1.41 | 0.83 | 1.04 | 34.3 | 0.722 | 1.16 | 1.38 | 35.7 |
| 2SE (%) | 3 | 15 | 8 | 26 | 13 | 5 | 10 | 13 | 11 | 49 | 10 |
| MDL | 1.1 | 5.8 | 0.0018 | 0.0045 | 0.0032 | 0.0035 | 0.0051 | 0.67 | 0.086 | 0.76 | 0.55 |
| Ba (ppm) | 75.5 | 1011 | 902 | 726 | 648 | 625 | 617 | 503 | 480 | 454 | 425 |
| 2SE (%) | 7 | 6 | 3 | 4 | 4 | 3 | 2 | 5 | 4 | 5 | 6 |
| MDL | 2.6 | 280 | - | 0.045 | - | 0.019 | 0.02 | 1.2 | 0.61 | 2.2 | 8.4 |

[b]The sample code do not corresponds with codes from microprobe result tables
MDL (Method Detection Limit)

***Supplementary Table 4.*** *Continued*

| Sample[b] | Bt 11 | Bt 12 | Bt 13 | Bt 14 | Bt 15 | Bt 16 | Bt 17 | Bt 18 | Bt 19 |
|---|---|---|---|---|---|---|---|---|---|
| Unit | MU | OU | OU | OU | IU | IU | IU | IU | IU |
| Rb (ppm) | 1058 | 1062 | 911 | 770 | 964 | 1669 | 1807 | 1707 | 1747 |
| 2SE (%) | 5 | 6 | 4 | 3 | 3 | 3 | 5 | 5 | 4 |
| MDL | 12 | 5.1 | 37 | 11 | 4.1 | 0.09 | 0.069 | 0.22 | 10 |
| Sr (ppm) | 1.00 | 0.73 | 0.8 | 0.99 | 1.98 | 1.33 | 1.25 | 0.612 | 1.37 |
| 2SE (%) | 8 | 32 | 30 | 19 | 47 | 32 | 50 | 7 | 19 |
| MDL | 0.38 | 0.055 | 0.73 | 0.72 | 1.9 | 0.0061 | 0.0044 | 0.25 | 0.27 |
| Ba (ppm) | 391 | 348 | 342 | 235 | 94.5 | 89.1 | 81.7 | 42.3 | 41.2 |
| 2SE (%) | 6 | 4 | 6 | 3 | 5 | 2 | 5 | 4 | 4 |
| MDL | 14 | 4.1 | 26 | 12 | 36 | 0.01 | 0.062 | 1.2 | 1.3 |

[b]The sample code do not corresponds with codes from microprobe result tables
MDL (Method Detection Limit)

***Supplementary Table 4.*** *Continued*

| Sample[b] | Crd 1 | Crd 2 | Crd 3 | Crd 4 | Crd 5 | Crd 6 | Crd 7 | Crd 8 |
|---|---|---|---|---|---|---|---|---|
| Unit | MU | MU | MU | MU | MU | MU | MU | MU |
| Rb ppm | 29.5 | 35.3 | 62.7 | 47.3 | 40.7 | 39.6 | 44.0 | 41.6 |
| Rb 2SE | 3% | 3% | 4% | 4% | 3% | 2% | 3% | 3% |
| Rb MDL | 0.300 | 0.650 | 0.720 | 0.560 | 0.450 | 0.340 | 0.340 | 0.460 |
| Sr ppm | 64.8 | 64.8 | 170 | 95.5 | 72.4 | 73.0 | 80.8 | 70.0 |
| Sr 2SE | 6% | 4% | 4% | 7% | 4% | 4% | 5% | 3% |
| Sr MDL | 0.016 | 0.930 | 1.60 | 1.30 | 0.800 | 0.500 | 0.500 | 0.500 |
| Ba ppm | 229 | 228 | 561 | 329 | 262 | 262 | 286 | 254 |
| Ba 2SE | 6% | 4% | 4% | 6% | 4% | 4% | 5% | 4% |
| Ba MDL | 0.030 | 3.70 | 4.60 | 3.60 | 2.90 | 2.70 | 2.80 | 2.20 |
| Cs ppm | 428 | 436 | 75 | 396 | 447 | 429 | 445 | 496 |
| Cs 2SE | 4% | 2% | 6% | 5% | 3% | 2% | 2% | 4% |
| Cs MDL | 0.150 | 4.60 | 0.690 | 0.540 | 3.80 | 3.70 | 3.70 | 3.00 |

[b]The sample code do not corresponds with codes from microprobe result tables
MDL (Method Detection Limit)

***Supplementary Table 4.*** *Continued*

| Sample | Crd 9 | Crd 10 | Crd 11 | Crd 12 | Crd 13 | Crd 14 | Crd 15 | Crd 16 |
|---|---|---|---|---|---|---|---|---|
| Unit | MU | MU | IU | IU | OU | OU | OU | OU |
| Rb ppm | 44.6 | 35.7 | 18.8 | 18.0 | 122 | 138 | 136 | 245 |
| Rb 2SE | 6% | 6% | 6% | 6% | 2% | 2% | 2% | 9% |
| Rb MDL | 0.480 | 0.430 | 3.40 | 0.360 | 0.540 | 0.420 | 0.390 | 0.470 |
| Sr ppm | 68.8 | 78.0 | 24.4 | 22.6 | 173 | 227 | 167 | 179 |
| Sr 2SE | 4% | 5% | 12% | 12% | 4% | 4% | 4% | 3% |
| Sr MDL | 0.960 | 0.770 | 2.30 | 0.530 | 0.027 | 0.020 | 0.015 | 0.015 |
| Ba ppm | 239 | 280 | 81 | 74 | 576 | 789 | 586 | 651 |
| Ba 2SE | 4% | 6% | 12% | 12% | 4% | 4% | 4% | 3% |
| Ba MDL | 2.80 | 1.90 | 3.10 | 1.70 | - | 0.170 | - | 0.059 |
| Cs ppm | 502 | 467 | 522 | 516 | 85.3 | 82.8 | 98.6 | 147 |
| Cs 2SE | 2% | 2% | 2% | 2% | 3% | 2% | 2% | 5% |
| Cs MDL | 4.40 | 4.10 | 19.0 | 11.0 | 0.290 | 0.220 | 0.140 | 0.099 |

[b]The sample code do not corresponds with codes from microprobe result tables
MDL (Method Detection Limit)

***Supplementary Table 4.*** *Continued*

| Sample[b] | Crd 17 | Crd 18 | Crd 19 | Crd 20 | Crd 21 | Crd average | NIST 612 (n=65) Mean value |
|---|---|---|---|---|---|---|---|
| Unit | OU | OU | OU | OU | OU | | |
| Rb ppm | 103 | 100 | 123 | 117 | 127 | 38.1 (135)** | 31.4 |
| Rb 2SE | 3% | 2% | 2% | 2% | 2% | | 0.45% |
| Rb MDL | 0.290 | 0.320 | 0.220 | 0.180 | 0.360 | | 0.63 |
| Sr ppm | 175 | 170 | 176 | 163 | 190 | 73.8 (180)** | 78.4 |
| Sr 2SE | 4% | 3% | 3% | 4% | 3% | | 0.39% |
| Sr MDL | - | 0.020 | - | - | - | | 0.84 |
| Ba ppm | 590 | 581 | 619 | 586 | 675 | 257 (628)** | 39.7 |
| Ba 2SE | 5% | 3% | 4% | 4% | 4% | | 0.45% |
| Ba MDL | - | - | 0.054 | 0.098 | 0.077 | | 0.71 |
| Cs ppm | 57.3 | 59.4 | 86.4 | 91.1 | 80.2 | 430 (87.6)** | 42.1 |
| Cs 2SE | 2% | 2% | 2% | 2% | 2% | | 0.54% |
| Cs MDL | 0.240 | 0.210 | 0.130 | 0.180 | 0.210 | | 0.54 |

[b]The sample code do not corresponds with codes from microprobe result tables

** MU+IU out of brackets, OU between brackets

2SE (2 sigma error)

MDL (Method Detection Limit)

***Supplementary Table 5.*** *Electron microprobe analyses of biotite from the Sierra Bermeja Pluton*

| Sample | Bt 1 | Bt 2 | Bt 3 | Bt 4 | Bt 5 | Bt 6 | Bt 7 | Bt 8 | Bt 9 | Bt 10 |
|---|---|---|---|---|---|---|---|---|---|---|
| Unit | OU | OU | OU | OU | OU | OU | OU | OU | OU | OU |
| $SiO_2$ | 35.55 | 35.62 | 34.78 | 35.30 | 35.56 | 35.53 | 35.34 | 35.36 | 35.57 | 36.18 |
| $TiO_2$ | 3.86 | 3.47 | 3.59 | 3.48 | 4.02 | 4.03 | 4.03 | 3.46 | 3.73 | 3.78 |
| $Al_2O_3$ | 19.09 | 18.89 | 18.45 | 18.74 | 18.46 | 18.57 | 19.01 | 18.65 | 19.02 | 19.45 |
| $Cr_2O_3$ | 0.05 | 0.08 | < MDL | 0.08 | 0.08 | < MDL | < MDL | 0.16 | 0.22 | 0.11 |
| NiO | 0.07 | 0.11 | < MDL | 0.01 | 0.06 | 0.16 | 0.07 | 0.02 | 0.03 | < MDL |
| FeO | 20.39 | 20.40 | 19.74 | 19.29 | 19.02 | 19.53 | 18.12 | 18.63 | 19.07 | 17.95 |
| MnO | 0.41 | 0.39 | 0.31 | 0.37 | 0.39 | 0.33 | 0.52 | 0.41 | 0.41 | 0.37 |
| MgO | 7.09 | 6.88 | 7.04 | 7.07 | 7.03 | 6.96 | 7.16 | 7.33 | 7.00 | 6.99 |
| CaO | < MDL | 0.01 | 0.01 | < MDL | 0.01 | < MDL | 0.03 | 0.02 | 0.01 | 0.04 |
| $Na_2O$ | 0.11 | 0.13 | 0.06 | 0.07 | 0.11 | 0.09 | 0.11 | 0.07 | 0.09 | 0.04 |
| $K_2O$ | 9.31 | 9.16 | 9.34 | 9.25 | 9.53 | 9.85 | 9.66 | 9.56 | 9.41 | 9.45 |
| F | NA | NA | NA | NA | NA | NA | NA | NA | NA | NA |
| Cl | NA | NA | NA | NA | NA | NA | NA | NA | NA | NA |
| Total | 95.92 | 95.13 | 93.31 | 93.65 | 94.28 | 95.04 | 94.05 | 93.65 | 94.55 | 94.35 |

The Method Detection Limit (MDL) for the routine analysis of common elements is ~0.02 wt.%
NA not analyzed

***Supplementary Table 5.*** *Continued*

| Sample | Bt 11 | Bt 12 | Bt 13 | Bt 14 | Bt 15 | Bt 16 | Bt 17 | Bt 18 | Bt 19 | Bt 20 |
|---|---|---|---|---|---|---|---|---|---|---|
| Unit | OU | OU | OU | OU | OU | OU | OU | OU | OU | OU |
| $SiO_2$ | 35.64 | 35.74 | 35.53 | 35.72 | 35.89 | 35.18 | 35.56 | 35.21 | 35.16 | 35.64 |
| $TiO_2$ | 3.83 | 4.23 | 4.23 | 3.89 | 3.48 | 4.11 | 4.10 | 3.98 | 3.43 | 3.99 |
| $Al_2O_3$ | 18.64 | 18.30 | 17.49 | 19.08 | 19.37 | 18.13 | 18.66 | 18.97 | 18.34 | 18.62 |
| $Cr_2O_3$ | < MDL | < MDL | < MDL | 0.05 | 0.02 | < MDL | 0.02 | < MDL | 0.05 | 0.18 |
| NiO | 0.15 | < MDL | 0.05 | 0.09 | < MDL | < MDL | 0.09 | 0.07 | < MDL | < MDL |
| FeO | 19.99 | 20.54 | 20.38 | 20.34 | 19.56 | 20.16 | 20.07 | 20.70 | 21.36 | 19.96 |
| MnO | 0.36 | 0.45 | 0.37 | 0.36 | 0.28 | 0.40 | 0.33 | 0.43 | 0.43 | 0.38 |
| MgO | 7.84 | 7.49 | 7.81 | 7.83 | 7.52 | 7.61 | 7.50 | 7.55 | 7.71 | 7.29 |
| CaO | 0.02 | 0.01 | < MDL | 0.01 | < MDL | 0.03 | 0.03 | 0.03 | 0.02 | 0.01 |
| $Na_2O$ | 0.13 | 0.12 | 0.08 | 0.17 | 0.12 | 0.15 | 0.11 | 0.10 | 0.09 | 0.12 |
| $K_2O$ | 9.18 | 9.23 | 9.35 | 9.75 | 9.54 | 9.35 | 9.50 | 9.67 | 9.22 | 9.30 |
| F | NA | NA | NA | NA | NA | NA | NA | NA | NA | NA |
| Cl | NA | NA | NA | NA | NA | NA | NA | NA | NA | NA |
| Total | 95.77 | 96.11 | 95.29 | 97.28 | 95.78 | 95.12 | 95.96 | 96.70 | 95.80 | 95.49 |

The Method Detection Limit (MDL) for the routine analysis of common elements is ~0.02 wt.%
NA not analyzed

***Supplementary Table 5.*** *Continued*

| Sample | Bt 21 | Bt 22 | Bt 23 | Bt 24 | Bt 25 | Bt 26 | Bt 27 | Bt 28 | Bt 29 | Bt 30 |
|---|---|---|---|---|---|---|---|---|---|---|
| Unit | OU | OU | OU | OU | OU | OU | OU | OU | OU | OU |
| $SiO_2$ | 35.11 | 34.59 | 35.31 | 34.89 | 35.45 | 35.16 | 35.44 | 35.15 | 35.24 | 35.33 |
| $TiO_2$ | 3.76 | 3.31 | 3.71 | 3.43 | 3.62 | 3.45 | 3.75 | 3.65 | 3.58 | 3.80 |
| $Al_2O_3$ | 18.38 | 18.47 | 19.16 | 18.41 | 19.21 | 19.33 | 18.46 | 18.76 | 18.32 | 18.33 |
| $Cr_2O_3$ | 0.13 | 0.03 | 0.07 | 0.02 | < MDL | 0.02 | 0.05 | 0.03 | 0.04 | 0.01 |
| NiO | 0.09 | 0.04 | < MDL | 0.04 | < MDL | < MDL | 0.02 | < MDL | 0.03 | 0.04 |
| FeO | 20.48 | 19.66 | 19.39 | 20.37 | 19.24 | 19.58 | 19.20 | 19.47 | 19.05 | 19.55 |
| MnO | 0.44 | 0.39 | 0.40 | 0.41 | 0.42 | 0.36 | 0.35 | 0.27 | 0.29 | 0.32 |
| MgO | 7.09 | 7.25 | 7.56 | 7.95 | 7.30 | 7.29 | 7.90 | 7.93 | 8.23 | 7.83 |
| CaO | < MDL | 0.07 | < MDL | 0.01 | 0.01 | < MDL | 0.01 | 0.01 | < MDL | 0.04 |
| $Na_2O$ | 0.07 | 0.11 | 0.15 | 0.07 | 0.17 | 0.11 | 0.12 | 0.11 | 0.11 | 0.11 |
| $K_2O$ | 9.37 | 9.32 | 9.59 | 9.47 | 9.40 | 9.55 | 9.64 | 9.55 | 9.49 | 9.39 |
| F | NA | 0.32 | 0.42 | 0.41 | 0.29 | 0.41 | 0.30 | 0.22 | 0.33 | 0.33 |
| Cl | NA | 0.07 | 0.03 | 0.03 | 0.05 | 0.02 | 0.06 | 0.02 | 0.09 | 0.12 |
| Total | 94.91 | 93.62 | 95.78 | 95.53 | 95.16 | 95.29 | 95.30 | 95.17 | 94.80 | 95.21 |

The Method Detection Limit (MDL) for the routine analysis of common elements is ~0.02 wt.%
NA not analyzed

***Supplementary Table 5.*** *Continued*

| Sample | Bt 31 | Bt 32 | Bt 33 | Bt 34 | Bt 35 | Bt 36 | Bt 37 | Bt 38 | Bt 39 | Bt 40 |
|---|---|---|---|---|---|---|---|---|---|---|
| Unit | OU | OU | OU | OU | OU | OU | OU | OU | OU | OU |
| $SiO_2$ | 35.15 | 35.15 | 34.98 | 34.88 | 35.52 | 34.38 | 35.12 | 35.08 | 34.97 | 35.57 |
| $TiO_2$ | 3.62 | 3.86 | 3.40 | 3.97 | 4.04 | 3.77 | 3.81 | 3.77 | 3.82 | 3.67 |
| $Al_2O_3$ | 18.67 | 18.43 | 18.39 | 18.24 | 18.10 | 18.11 | 18.78 | 18.52 | 18.63 | 18.86 |
| $Cr_2O_3$ | < MDL | < MDL | 0.03 | 0.01 | 0.02 | 0.03 | 0.02 | 0.03 | 0.08 | 0.01 |
| NiO | 0.02 | < MDL | 0.04 | < MDL | < MDL | 0.04 | 0.04 | < MDL | < MDL | < MDL |
| FeO | 19.56 | 19.19 | 19.99 | 19.31 | 19.14 | 19.29 | 19.52 | 20.15 | 19.31 | 19.18 |
| MnO | 0.42 | 0.33 | 0.31 | 0.29 | 0.41 | 0.29 | 0.29 | 0.42 | 0.44 | 0.42 |
| MgO | 7.72 | 7.83 | 8.06 | 7.78 | 7.79 | 7.89 | 7.72 | 7.73 | 7.74 | 7.73 |
| CaO | < MDL | 0.03 | 0.01 | < MDL | < MDL | 0.01 | < MDL | < MDL | 0.01 | 0.03 |
| $Na_2O$ | 0.11 | 0.18 | 0.13 | 0.12 | 0.14 | 0.13 | 0.21 | 0.13 | 0.13 | 0.12 |
| $K_2O$ | 9.50 | 9.08 | 9.36 | 9.26 | 9.41 | 9.17 | 9.52 | 9.38 | 9.44 | 9.43 |
| F | 0.22 | 0.24 | 0.27 | 0.22 | 0.26 | 0.29 | 0.17 | 0.25 | 0.22 | 0.28 |
| Cl | 0.04 | 0.06 | 0.05 | 0.05 | 0.05 | 0.05 | 0.04 | 0.03 | 0.04 | 0.03 |
| Total | 95.03 | 94.37 | 95.01 | 94.13 | 94.89 | 93.44 | 95.23 | 95.50 | 94.83 | 95.35 |

The Method Detection Limit (MDL) for the routine analysis of common elements is ~0.02 wt.%
NA not analyzed

***Supplementary Table 5.*** *Continued*

| Sample | Bt 41 | Bt 42 | Bt 43 | Bt 44 | Bt 45 | Bt 46 | Bt 47 | Bt 48 | Bt 49 | Bt 50 |
|---|---|---|---|---|---|---|---|---|---|---|
| Unit | OU | OU | OU | OU | OU | OU | OU | OU | OU | OU |
| $SiO_2$ | 35.30 | 35.20 | 35.47 | 35.39 | 35.84 | 36.00 | 35.48 | 36.53 | 35.68 | 35.46 |
| $TiO_2$ | 3.42 | 3.70 | 3.89 | 3.70 | 3.76 | 3.56 | 3.94 | 3.48 | 3.54 | 3.71 |
| $Al_2O_3$ | 18.12 | 18.05 | 18.98 | 18.30 | 17.78 | 18.29 | 17.31 | 18.95 | 17.89 | 18.16 |
| $Cr_2O_3$ | 0.03 | 0.03 | < MDL | 0.03 | 0.06 | 0.04 | < MDL | 0.02 | 0.04 | 0.06 |
| NiO | 0.02 | 0.04 | 0.02 | < MDL | 0.01 | 0.05 | 0.02 | 0.01 | < MDL | 0.04 |
| FeO | 18.65 | 18.43 | 19.00 | 18.58 | 18.27 | 18.39 | 20.07 | 18.00 | 19.28 | 19.40 |
| MnO | 0.29 | 0.32 | 0.31 | 0.31 | 0.28 | 0.26 | 0.32 | 0.33 | 0.39 | 0.36 |
| MgO | 8.23 | 8.11 | 7.70 | 8.03 | 8.08 | 8.27 | 8.00 | 7.59 | 8.04 | 8.11 |
| CaO | 0.01 | 0.01 | < MDL | 0.01 | 0.01 | < MDL | 0.01 | 0.07 | 0.01 | 0.01 |
| $Na_2O$ | 0.11 | 0.15 | 0.14 | 0.17 | 0.15 | 0.15 | 0.09 | 0.11 | 0.09 | 0.13 |
| $K_2O$ | 9.54 | 9.51 | 9.23 | 9.24 | 9.38 | 9.56 | 9.62 | 8.44 | 9.53 | 9.51 |
| F | 0.40 | 0.42 | 0.37 | 0.39 | 0.50 | 0.47 | 0.38 | 0.33 | 0.34 | 0.34 |
| Cl | 0.02 | 0.05 | 0.03 | 0.05 | 0.08 | 0.04 | 0.09 | 0.08 | 0.05 | 0.03 |
| Total | 94.15 | 94.02 | 95.14 | 94.21 | 94.20 | 95.10 | 95.35 | 93.94 | 94.88 | 95.32 |

The Method Detection Limit (MDL) for the routine analysis of common elements is ~0.02 wt.%
NA not analyzed

***Supplementary Table 5.*** *Continued*

| Sample | Bt 51 | Bt 52 | Bt 53 | Bt 54 | Bt 55 | Bt 56 | Bt 57 | Bt 58 | Bt 59 | Bt 60 |
|---|---|---|---|---|---|---|---|---|---|---|
| Unit | OU | OU | MU | MU | MU | MU | MU | MU | MU | MU |
| $SiO_2$ | 35.31 | 35.60 | 35.58 | 35.24 | 35.40 | 35.76 | 35.29 | 35.11 | 35.25 | 34.81 |
| $TiO_2$ | 3.68 | 3.77 | 4.02 | 2.67 | 3.77 | 3.34 | 4.21 | 3.35 | 3.77 | 3.88 |
| $Al_2O_3$ | 18.20 | 18.41 | 18.41 | 18.71 | 19.44 | 19.40 | 18.80 | 19.13 | 19.01 | 18.51 |
| $Cr_2O_3$ | 0.03 | 0.08 | 0.14 | 0.03 | 0.08 | 0.15 | 0.08 | 0.10 | 0.05 | 0.02 |
| NiO | 0.03 | < MDL | 0.16 | 0.08 | 0.05 | 0.04 | < MDL | 0.08 | 0.03 | < MDL |
| FeO | 19.53 | 19.18 | 21.29 | 20.51 | 21.28 | 20.32 | 21.09 | 21.04 | 20.75 | 21.49 |
| MnO | 0.43 | 0.32 | 0.47 | 0.41 | 0.48 | 0.45 | 0.34 | 0.29 | 0.28 | 0.31 |
| MgO | 7.88 | 8.00 | 6.21 | 6.71 | 6.01 | 6.23 | 6.26 | 6.17 | 6.11 | 6.12 |
| CaO | < MDL | < MDL | 0.01 | 0.01 | < MDL | 0.01 | 0.01 | 0.02 | 0.04 | 0.03 |
| $Na_2O$ | 0.10 | 0.12 | 0.08 | 0.06 | 0.10 | 0.07 | 0.12 | 0.05 | 0.12 | 0.07 |
| $K_2O$ | 9.51 | 9.68 | 9.63 | 9.66 | 9.46 | 9.40 | 9.42 | 9.28 | 9.28 | 9.39 |
| F | 0.33 | 0.36 | NA | NA | NA | NA | NA | NA | 0.48 | 0.47 |
| Cl | 0.03 | 0.03 | NA | NA | NA | NA | NA | NA | 0.05 | 0.05 |
| Total | 95.05 | 95.55 | 95.99 | 94.09 | 96.06 | 95.17 | 95.60 | 94.61 | 95.22 | 95.15 |

The Method Detection Limit (MDL) for the routine analysis of common elements is ~0.02 wt.%
NA not analyzed

***Supplementary Table 5.*** *Continued*

| Sample | Bt 61 | Bt 62 | Bt 63 | Bt 64 | Bt 65 | Bt 66 | Bt 67 | Bt 68 | Bt 69 | Bt 70 |
|---|---|---|---|---|---|---|---|---|---|---|
| Unit | MU | MU | MU | MU | MU | MU | MU | MU | MU | MU |
| $SiO_2$ | 34.92 | 35.27 | 34.98 | 34.86 | 34.84 | 35.08 | 35.46 | 34.78 | 35.15 | 35.04 |
| $TiO_2$ | 3.17 | 2.51 | 3.45 | 3.41 | 3.82 | 3.72 | 3.95 | 2.93 | 3.24 | 3.09 |
| $Al_2O_3$ | 19.26 | 19.51 | 19.33 | 19.14 | 18.86 | 19.17 | 18.40 | 18.40 | 19.28 | 19.09 |
| $Cr_2O_3$ | 0.09 | 0.06 | 0.01 | 0.05 | 0.03 | 0.04 | 0.01 | 0.03 | 0.09 | 0.04 |
| NiO | 0.02 | < MDL | 0.05 | < MDL | 0.04 | < MDL | < MDL | < MDL | 0.02 | < MDL |
| FeO | 21.01 | 20.11 | 21.42 | 20.91 | 20.53 | 20.53 | 19.32 | 21.87 | 20.68 | 21.31 |
| MnO | 0.41 | 0.34 | 0.35 | 0.55 | 0.28 | 0.46 | 0.23 | 0.37 | 0.21 | 0.37 |
| MgO | 6.22 | 6.91 | 6.13 | 6.30 | 6.44 | 6.11 | 7.73 | 6.71 | 6.77 | 6.57 |
| CaO | < MDL | 0.05 | 0.01 | < MDL | < MDL | 0.03 | < MDL | 0.01 | 0.01 | 0.01 |
| $Na_2O$ | 0.10 | 0.07 | 0.11 | 0.10 | 0.15 | 0.05 | 0.05 | 0.06 | 0.09 | 0.10 |
| $K_2O$ | 9.40 | 9.25 | 9.40 | 9.67 | 9.54 | 9.43 | 9.73 | 9.54 | 9.52 | 9.47 |
| F | 0.37 | 0.42 | 0.34 | 0.27 | 0.43 | 0.31 | 0.45 | 0.40 | 0.51 | 0.43 |
| Cl | 0.02 | 0.02 | 0.04 | 0.05 | 0.06 | 0.06 | 0.11 | 0.02 | 0.01 | 0.03 |
| Total | 94.99 | 94.52 | 95.61 | 95.30 | 95.01 | 95.01 | 95.44 | 95.11 | 95.57 | 95.53 |

The Method Detection Limit (MDL) for the routine analysis of common elements is ~0.02 wt.%
NA not analyzed

***Supplementary Table 5.*** *Continued*

| Sample | Bt 71 | Bt 72 | Bt 73 | Bt 74 | Bt 75 | Bt 76 | Bt 77 | Bt 78 | Bt 79 | Bt 80 |
|---|---|---|---|---|---|---|---|---|---|---|
| Unit | MU | MU | MU | MU | MU | MU | MU | MU | MU | MU |
| $SiO_2$ | 35.71 | 34.94 | 34.25 | 35.29 | 35.04 | 35.18 | 34.86 | 36.15 | 35.66 | 35.34 |
| $TiO_2$ | 2.92 | 3.56 | 2.68 | 3.81 | 3.45 | 3.96 | 3.52 | 3.38 | 3.68 | 3.62 |
| $Al_2O_3$ | 19.40 | 19.25 | 19.09 | 18.91 | 19.00 | 19.31 | 19.25 | 19.64 | 19.88 | 19.51 |
| $Cr_2O_3$ | 0.05 | 0.03 | 0.04 | < MDL | 0.09 | 0.02 | 0.02 | 0.03 | < MDL | 0.10 |
| NiO | 0.06 | < MDL | < MDL | < MDL | < MDL | < MDL | 0.02 | 0.01 | < MDL | < MDL |
| FeO | 20.07 | 20.58 | 21.03 | 20.26 | 20.46 | 20.54 | 20.19 | 20.16 | 19.59 | 21.18 |
| MnO | 0.51 | 0.47 | 0.42 | 0.50 | 0.48 | 0.39 | 0.40 | 0.32 | 0.33 | 0.30 |
| MgO | 6.51 | 6.05 | 6.59 | 6.16 | 6.35 | 6.20 | 6.18 | 5.62 | 5.41 | 5.55 |
| CaO | 0.03 | 0.01 | 0.12 | 0.08 | < MDL | 0.03 | 0.02 | 0.01 | 0.02 | < MDL |
| $Na_2O$ | 0.11 | 0.14 | 0.05 | 0.10 | 0.08 | 0.14 | 0.15 | 0.06 | 0.07 | 0.08 |
| $K_2O$ | 9.52 | 9.40 | 8.77 | 8.91 | 9.45 | 9.41 | 9.45 | 9.07 | 9.22 | 9.06 |
| F | 0.60 | 0.39 | 0.29 | 0.49 | 0.41 | 0.55 | 0.46 | NA | NA | NA |
| Cl | 0.02 | 0.02 | 0.02 | 0.01 | 0.02 | 0.03 | < MDL | NA | NA | NA |
| Total | 95.52 | 94.85 | 93.34 | 94.49 | 94.80 | 95.77 | 94.51 | 94.46 | 93.85 | 94.73 |

The Method Detection Limit (MDL) for the routine analysis of common elements is ~0.02 wt.%
NA not analyzed

***Supplementary Table 5.*** *Continued*

| Sample | Bt 81 | Bt 82 | Bt 83 | Bt 84 | Bt 85 | Bt 86 | Bt 87 | Bt 88 | Bt 89 | Bt 90 |
|---|---|---|---|---|---|---|---|---|---|---|
| Unit | MU | MU | MU | MU | MU | MU | MU | MU | MU | MU |
| $SiO_2$ | 34.80 | 34.90 | 35.20 | 35.45 | 35.53 | 35.04 | 34.79 | 34.30 | 34.67 | 34.75 |
| $TiO_2$ | 3.22 | 3.27 | 3.38 | 3.77 | 3.56 | 2.97 | 3.05 | 2.95 | 3.36 | 3.30 |
| $Al_2O_3$ | 19.33 | 19.97 | 20.21 | 18.92 | 19.10 | 19.20 | 19.60 | 19.35 | 19.13 | 19.66 |
| $Cr_2O_3$ | 0.09 | 0.04 | 0.16 | 0.03 | 0.03 | < MDL | 0.01 | 0.02 | 0.03 | 0.08 |
| NiO | < MDL | 0.02 | 0.01 | < MDL | < MDL | < MDL | < MDL | < MDL | 0.01 | < MDL |
| FeO | 21.38 | 20.55 | 20.09 | 19.92 | 19.20 | 19.73 | 20.98 | 20.62 | 20.92 | 20.81 |
| MnO | 0.31 | 0.29 | 0.24 | 0.33 | 0.33 | 0.39 | 0.32 | 0.38 | 0.19 | 0.35 |
| MgO | 5.42 | 5.85 | 5.63 | 6.27 | 6.18 | 6.55 | 5.92 | 5.94 | 5.94 | 5.67 |
| CaO | < MDL | < MDL | < MDL | < MDL | < MDL | 0.05 | < MDL | < MDL | < MDL | 0.04 |
| $Na_2O$ | 0.02 | 0.11 | 0.06 | 0.07 | 0.05 | 0.13 | 0.10 | 0.10 | 0.10 | 0.12 |
| $K_2O$ | 8.84 | 9.37 | 9.38 | 9.26 | 9.21 | 8.98 | 9.37 | 9.12 | 9.47 | 9.18 |
| F | NA | NA | NA | NA | NA | 0.41 | 0.44 | 0.56 | 0.55 | 0.50 |
| Cl | NA | NA | NA | NA | NA | 0.01 | 0.02 | 0.02 | 0.03 | 0.04 |
| Total | 93.41 | 94.36 | 94.35 | 94.02 | 93.19 | 93.47 | 94.61 | 93.34 | 94.39 | 94.49 |

The Method Detection Limit (MDL) for the routine analysis of common elements is ~0.02 wt.%
NA not analyzed

***Supplementary Table 5.*** *Continued*

| Sample | Bt 91 | Bt 92 | Bt 93 | Bt 94 | Bt 95 | Bt 96 | Bt 97 | Bt 98 | Bt 99 | Bt 100 |
|---|---|---|---|---|---|---|---|---|---|---|
| Unit | MU | MU | IU | IU | IU | IU | IU | IU | IU | IU |
| $SiO_2$ | 35.10 | 34.96 | 35.28 | 37.70 | 35.99 | 35.39 | 35.23 | 34.92 | 35.10 | 35.00 |
| $TiO_2$ | 3.22 | 3.26 | 3.14 | 0.86 | 2.84 | 3.20 | 3.30 | 3.19 | 2.92 | 3.14 |
| $Al_2O_3$ | 18.87 | 19.23 | 20.20 | 19.75 | 20.48 | 20.73 | 19.76 | 19.76 | 19.57 | 19.43 |
| $Cr_2O_3$ | 0.05 | 0.04 | 0.08 | 0.03 | 0.10 | 0.10 | 0.13 | 0.04 | 0.04 | 0.01 |
| NiO | 0.02 | 0.01 | 0.03 | < MDL | 0.02 | 0.12 | 0.13 | < MDL | < MDL | < MDL |
| FeO | 21.23 | 20.85 | 22.66 | 20.72 | 21.68 | 21.57 | 22.93 | 21.33 | 21.28 | 21.01 |
| MnO | 0.33 | 0.39 | 0.38 | 0.40 | 0.35 | 0.32 | 0.43 | 0.33 | 0.29 | 0.37 |
| MgO | 6.20 | 6.20 | 4.94 | 5.86 | 4.98 | 4.80 | 4.67 | 5.25 | 5.38 | 5.31 |
| CaO | 0.01 | 0.02 | 0.01 | 0.04 | < MDL | < MDL | 0.01 | < MDL | 0.01 | < MDL |
| $Na_2O$ | 0.08 | 0.23 | 0.08 | 0.03 | 0.09 | 0.07 | 0.05 | 0.06 | 0.10 | 0.09 |
| $K_2O$ | 9.42 | 9.16 | 9.26 | 9.23 | 8.90 | 9.09 | 9.27 | 9.21 | 9.37 | 9.33 |
| F | 0.47 | 0.36 | NA | NA | NA | NA | NA | 0.30 | 0.27 | 0.47 |
| Cl | 0.02 | 0.01 | NA | NA | NA | NA | NA | 0.03 | 0.02 | 0.02 |
| Total | 95.02 | 94.72 | 96.06 | 94.62 | 95.41 | 95.37 | 95.90 | 94.42 | 94.36 | 94.18 |

The Method Detection Limit (MDL) for the routine analysis of common elements is ~0.02 wt.%
NA not analyzed

***Supplementary Table 5.*** *Continued*

| Sample | Bt 101 | Bt 102 | Bt 103 | Bt 104 | Bt 105 | Bt 106 | Bt 107 | Bt 108 | Bt 109 | Bt 110 |
|---|---|---|---|---|---|---|---|---|---|---|
| Unit | IU | IU | IU | IU | IU | IU | IU | MME | MME | MME |
| $SiO_2$ | 35.46 | 35.72 | 35.53 | 35.53 | 35.01 | 35.01 | 35.29 | 35.09 | 34.77 | 35.30 |
| $TiO_2$ | 1.77 | 2.56 | 2.70 | 3.38 | 2.74 | 3.17 | 3.05 | 3.41 | 3.32 | 3.40 |
| $Al_2O_3$ | 19.37 | 19.65 | 19.92 | 19.68 | 19.62 | 19.62 | 18.91 | 17.71 | 17.98 | 17.65 |
| $Cr_2O_3$ | < MDL | 0.01 | < MDL | 0.07 | 0.05 | 0.10 | 0.04 | 0.04 | 0.03 | 0.05 |
| NiO | < MDL | 0.03 | < MDL | 0.02 | < MDL | < MDL | 0.04 | 0.05 | 0.00 | 0.05 |
| FeO | 21.06 | 20.28 | 20.14 | 20.27 | 21.03 | 20.61 | 21.07 | 19.90 | 19.95 | 19.32 |
| MnO | 0.31 | 0.33 | 0.28 | 0.15 | 0.24 | 0.29 | 0.29 | 0.37 | 0.33 | 0.27 |
| MgO | 6.25 | 5.82 | 6.00 | 5.96 | 5.86 | 5.71 | 6.06 | 8.67 | 8.66 | 8.56 |
| CaO | < MDL | 0.03 | < MDL | 0.02 | < MDL | < MDL | < MDL | 0.01 | 0.00 | 0.01 |
| $Na_2O$ | 0.05 | 0.03 | 0.06 | 0.09 | 0.07 | 0.08 | 0.03 | 0.14 | 0.14 | 0.13 |
| $K_2O$ | 9.34 | 9.16 | 9.45 | 9.49 | 9.57 | 9.42 | 9.42 | 9.26 | 9.21 | 9.13 |
| F | 0.37 | 0.44 | 0.34 | 0.35 | 0.33 | 0.26 | 0.32 | 0.38 | 0.31 | 0.35 |
| Cl | 0.01 | < MDL | 0.02 | 0.03 | 0.01 | 0.02 | 0.02 | 0.07 | 0.06 | 0.04 |
| Total | 93.98 | 94.05 | 94.44 | 95.05 | 94.53 | 94.29 | 94.57 | 95.10 | 94.77 | 94.26 |

The Method Detection Limit (MDL) for the routine analysis of common elements is ~0.02 wt.%

***Supplementary Table 5.*** *Continued*

| Sample | Bt 111 | Bt 112 | Bt 113 | Bt 114 | Bt 115 | Bt 116 | Bt 117 | Bt 118 | Bt 119 | Bt 120 |
|---|---|---|---|---|---|---|---|---|---|---|
| Unit | MME | MME | MME | MME | MME | MME | MME | MME | MME | MME |
| $SiO_2$ | 35.20 | 35.05 | 34.89 | 35.18 | 34.93 | 35.51 | 35.24 | 34.94 | 35.68 | 35.06 |
| $TiO_2$ | 3.34 | 3.43 | 3.10 | 3.25 | 3.11 | 3.39 | 3.30 | 3.70 | 3.46 | 3.24 |
| $Al_2O_3$ | 17.79 | 17.75 | 18.40 | 17.91 | 18.31 | 16.92 | 17.38 | 17.98 | 17.75 | 17.41 |
| $Cr_2O_3$ | 0.07 | 0.06 | 0.02 | 0.06 | 0.02 | 0.01 | 0.02 | 0.04 | 0.01 | 0.04 |
| NiO | < MDL | 0.02 | 0.04 | 0.03 | 0.05 | 0.02 | 0.07 | < MDL | 0.03 | < MDL |
| FeO | 19.87 | 19.82 | 20.17 | 19.52 | 18.81 | 18.91 | 19.38 | 19.94 | 18.38 | 19.30 |
| MnO | 0.33 | 0.32 | 0.34 | 0.38 | 0.44 | 0.41 | 0.37 | 0.27 | 0.27 | 0.38 |
| MgO | 8.35 | 8.72 | 8.53 | 8.43 | 8.63 | 9.23 | 8.64 | 8.44 | 8.91 | 8.49 |
| CaO | < MDL | 0.02 | 0.03 | 0.02 | 0.02 | 0.02 | 0.02 | < MDL | < MDL | 0.03 |
| $Na_2O$ | 0.15 | 0.16 | 0.14 | 0.19 | 0.06 | 0.08 | 0.08 | 0.21 | 0.16 | 0.17 |
| $K_2O$ | 9.37 | 9.29 | 9.31 | 9.20 | 9.19 | 9.22 | 9.44 | 9.20 | 9.23 | 9.17 |
| F | 0.28 | 0.35 | 0.34 | 0.37 | 0.28 | 0.37 | 0.34 | 0.41 | 0.42 | 0.40 |
| Cl | 0.04 | 0.06 | 0.08 | 0.09 | 0.05 | 0.08 | 0.10 | 0.08 | 0.06 | 0.09 |
| Total | 94.79 | 95.04 | 95.38 | 94.62 | 93.90 | 94.16 | 94.38 | 95.21 | 94.35 | 93.77 |

The Method Detection Limit (MDL) for the routine analysis of common elements is ~0.02 wt.%

***Supplementary Table 5.*** *Continued*

| Sample | Bt 121 | Bt 122 | Bt 123 | Bt 124 | Bt 125 | Bt 126 | Bt 127 | Bt 128 | Bt 129 | Bt 130 |
|---|---|---|---|---|---|---|---|---|---|---|
| Unit | MME | MME | MME | MME | MME | MME | MME | MME | MME | MME |
| $SiO_2$ | 35.49 | 34.87 | 35.59 | 34.78 | 35.48 | 34.70 | 35.29 | 35.24 | 35.00 | 35.15 |
| $TiO_2$ | 3.42 | 3.47 | 3.60 | 3.38 | 3.33 | 3.38 | 3.40 | 3.67 | 3.92 | 4.07 |
| $Al_2O_3$ | 16.73 | 17.81 | 18.13 | 17.88 | 18.13 | 18.55 | 18.21 | 17.95 | 18.00 | 18.44 |
| $Cr_2O_3$ | 0.01 | 0.05 | 0.03 | 0.01 | < MDL | 0.04 | 0.06 | 0.07 | < MDL | < MDL |
| NiO | 0.03 | 0.01 | < MDL | < MDL | 0.03 | < MDL | < MDL | 0.02 | < MDL | < MDL |
| FeO | 17.82 | 19.80 | 19.27 | 19.94 | 19.25 | 19.71 | 19.81 | 19.21 | 2< MDL | 19.65 |
| MnO | 0.31 | 0.34 | 0.36 | 0.35 | 0.35 | 0.31 | 0.29 | 0.35 | 0.35 | 0.30 |
| MgO | 9.77 | 8.31 | 8.37 | 8.18 | 8.42 | 8.12 | 8.26 | 8.36 | 8.35 | 8.27 |
| CaO | 0.04 | < MDL | 0.02 | 0.01 | 0.02 | 0.03 | 0.04 | 0.03 | < MDL | < MDL |
| $Na_2O$ | 0.14 | 0.18 | 0.18 | 0.11 | 0.12 | 0.13 | 0.08 | 0.13 | 0.14 | 0.10 |
| $K_2O$ | 9.33 | 9.30 | 9.28 | 9.78 | 9.66 | 9.40 | 9.85 | 9.62 | 9.61 | 9.67 |
| F | 0.43 | 0.29 | 0.36 | 0.43 | 0.33 | 0.25 | 0.46 | 0.31 | 0.29 | 0.34 |
| Cl | 0.08 | 0.08 | 0.09 | 0.03 | 0.06 | 0.05 | 0.04 | 0.03 | 0.04 | 0.05 |
| Total | 93.60 | 94.51 | 95.29 | 94.89 | 95.19 | 94.67 | 95.78 | 94.99 | 95.72 | 96.04 |

The Method Detection Limit (MDL) for the routine analysis of common elements is ~0.02 wt.%

***Supplementary Table 5.*** *Continued*

| Sample | Bt 131 | Bt 132 | Bt 133 | Bt 134 | Bt 135 | Bt 136 | Bt 137 | Bt 138 | Bt 139 | Bt 140 |
|---|---|---|---|---|---|---|---|---|---|---|
| Unit | MME | MME | MME | MME | MME | MME | MME | MME | MME | MME |
| $SiO_2$ | 35.62 | 34.89 | 35.46 | 34.82 | 34.68 | 36.36 | 36.20 | 34.75 | 34.89 | 35.13 |
| $TiO_2$ | 3.71 | 4.05 | 3.41 | 3.51 | 3.52 | 3.09 | 3.43 | 3.43 | 3.62 | 3.55 |
| $Al_2O_3$ | 17.59 | 17.91 | 18.17 | 18.20 | 18.51 | 17.40 | 17.55 | 18.30 | 18.13 | 18.09 |
| $Cr_2O_3$ | < MDL | 0.06 | < MDL | < MDL | 0.01 | 0.02 | 0.06 | 0.06 | 0.08 | 0.06 |
| NiO | < MDL | < MDL | < MDL | < MDL | < MDL | < MDL | < MDL | < MDL | < MDL | < MDL |
| FeO | 19.13 | 19.88 | 18.99 | 20.07 | 19.87 | 18.60 | 18.85 | 2< MDL | 20.01 | 19.91 |
| MnO | 0.27 | 0.26 | 0.25 | 0.40 | 0.32 | 0.29 | 0.29 | 0.31 | 0.35 | 0.30 |
| MgO | 8.29 | 8.45 | 8.35 | 8.23 | 8.16 | 8.85 | 8.72 | 8.31 | 8.09 | 8.40 |
| CaO | 0.01 | < MDL | 0.02 | 0.03 | 0.03 | 0.01 | 0.01 | 0.03 | < MDL | 0.01 |
| $Na_2O$ | 0.13 | 0.09 | 0.08 | 0.13 | 0.14 | 0.12 | 0.12 | 0.12 | 0.11 | 0.15 |
| $K_2O$ | 9.78 | 9.52 | 9.67 | 9.52 | 9.63 | 9.52 | 9.67 | 9.78 | 9.70 | 9.62 |
| F | 0.38 | 0.40 | 0.35 | 0.36 | 0.33 | 0.40 | 0.44 | 0.34 | 0.28 | 0.39 |
| Cl | 0.04 | 0.03 | 0.04 | 0.05 | 0.03 | 0.05 | 0.05 | 0.03 | 0.05 | 0.04 |
| Total | 94.94 | 95.55 | 94.80 | 95.32 | 95.24 | 94.70 | 95.39 | 95.45 | 95.31 | 95.65 |

The Method Detection Limit (MDL) for the routine analysis of common elements is ~0.02 wt.%

***Supplementary Table 5.*** *Continued*

| Sample | Bt 141 | Bt 142 | Bt 143 | Bt 144 | Bt 145 | Bt 146 | Bt 147 | Bt 148 | Bt 149 | Bt 150 | Bt 151 |
|---|---|---|---|---|---|---|---|---|---|---|---|
| Unit | MME | MME | MME | Crd Alt | Crd Alt | Crd Alt | Crd Alt | Crd Alt | Crd Alt | Crd Alt | Crd Alt |
| $SiO_2$ | 34.52 | 35.02 | 35.76 | 34.93 | 35.16 | 35.34 | 36.13 | 35.86 | 35.48 | 35.88 | 34.91 |
| $TiO_2$ | 3.55 | 3.75 | 3.64 | 3.48 | 2.73 | 2.98 | 0.01 | 0.19 | 1.57 | 1.10 | 2.73 |
| $Al_2O_3$ | 18.17 | 17.87 | 17.13 | 18.85 | 19.29 | 18.24 | 21.59 | 23.28 | 19.94 | 20.82 | 19.12 |
| $Cr_2O_3$ | 0.05 | 0.06 | 0.08 | 0.05 | <MDL | 0.05 | <MDL | <MDL | <MDL | <MDL | 0.03 |
| NiO | 0.02 | <MDL | 0.03 | 0.01 | 0.04 | 0.01 | 0.03 | 0.04 | 0.01 | 0.02 | <MDL |
| FeO | 20.31 | 19.76 | 19.25 | 20.01 | 18.31 | 19.59 | 18.19 | 16.23 | 19.46 | 18.47 | 21.12 |
| MnO | 0.32 | 0.29 | 0.28 | 0.50 | 0.61 | 0.60 | 0.76 | 0.60 | 0.79 | 0.35 | 0.54 |
| MgO | 8.07 | 8.30 | 8.66 | 7.29 | 8.28 | 8.22 | 7.27 | 7.97 | 6.73 | 7.38 | 5.43 |
| CaO | 0.02 | 0.01 | <MDL | 0.02 | 0.03 | 0.02 | 0.03 | 0.14 | <MDL | 0.06 | <MDL |
| $Na_2O$ | 0.12 | 0.13 | 0.11 | 0.14 | 0.12 | 0.07 | 0.14 | 0.07 | 0.11 | 0.12 | 0.09 |
| $K_2O$ | 9.62 | 9.69 | 9.59 | 9.42 | 9.28 | 9.54 | 9.12 | 6.47 | 9.18 | 8.20 | 9.23 |
| F | 0.42 | 0.36 | 0.35 | 0.31 | 0.37 | 0.35 | 0.51 | 0.57 | 0.31 | 0.41 | 0.35 |
| Cl | 0.01 | 0.04 | 0.05 | 0.02 | 0.05 | 0.02 | 0.01 | 0.03 | 0.01 | <MDL | 0.03 |
| Total | 95.19 | 95.28 | 94.93 | 95.03 | 94.27 | 95.04 | 93.78 | 91.45 | 93.59 | 92.79 | 93.58 |

The Method Detection Limit (MDL) for the routine analysis of common elements is ~0.02 wt.%

***Supplementary Table 5.*** *Continued*

| Sample | Bt 152 | Bt 153 | Bt 154 | Bt 155 | Bt 156 | Bt 157 | Bt 158 | Bt 160 | Bt 165 | Bt 166 |
|---|---|---|---|---|---|---|---|---|---|---|
| Unit | Lamp | Lamp | Lamp | Lamp | Lamp | Lamp | Lamp | Lamp | Lamp | Lamp |
| Type | Krs | Krs | Krs | Krs | Krs | Krs | Krs | Krs | Krs | Krs |
| $SiO_2$ | 34.09 | 34.04 | 34.70 | 35.74 | 36.15 | 36.22 | 35.86 | 35.68 | 36.39 | 35.94 |
| $TiO_2$ | 6.54 | 6.06 | 5.85 | 5.64 | 5.70 | 5.54 | 5.56 | 5.60 | 4.57 | 3.94 |
| $Al_2O_3$ | 15.11 | 15.18 | 14.85 | 14.54 | 15.39 | 15.64 | 15.04 | 14.64 | 14.97 | 18.80 |
| $Cr_2O_3$ | < MDL | < MDL | 0.03 | 0.02 | 0.22 | 0.05 | 0.09 | 0.01 | < MDL | 0.03 |
| NiO | < MDL | < MDL | 0.01 | < MDL | < MDL | 0.07 | < MDL | 0.02 | 0.03 | < MDL |
| FeO | 17.90 | 18.19 | 19.65 | 16.55 | 9.31 | 10.20 | 11.68 | 16.59 | 13.99 | 14.83 |
| MnO | 0.17 | 0.14 | 0.16 | 0.15 | 0.03 | 0.08 | 0.06 | 0.11 | 0.12 | 0.15 |
| MgO | 10.43 | 10.93 | 9.96 | 12.05 | 17.36 | 17.02 | 15.35 | 12.73 | 14.93 | 11.60 |
| CaO | 0.01 | 0.04 | 0.18 | 0.01 | 0.05 | 0.05 | 0.06 | 0.01 | 0.04 | < MDL |
| $Na_2O$ | 0.21 | 0.16 | 0.13 | 0.15 | 0.28 | 0.30 | 0.30 | 0.26 | 0.24 | 0.28 |
| $K_2O$ | 8.61 | 8.40 | 8.35 | 9.27 | 8.81 | 9.01 | 8.60 | 8.54 | 8.55 | 9.48 |
| F | 0.16 | 0.27 | 0.20 | 0.34 | 0.40 | 0.30 | 0.31 | 0.32 | 0.37 | 0.20 |
| Cl | 0.07 | 0.10 | 0.08 | 0.15 | 0.04 | 0.04 | 0.04 | 0.10 | 0.03 | < MDL |
| Total | 93.29 | 93.49 | 94.15 | 94.63 | 93.75 | 94.50 | 92.94 | 94.61 | 94.23 | 95.24 |

The Method Detection Limit (MDL) for the routine analysis of common elements is ~0.02 wt.%

***Supplementary Table 5.*** *Continued*

| Sample | Bt 167 | Bt 159 | Bt 161 | Bt 162 | Bt 163 | Bt 164 | Bt 168 | Bt 169 | Bt 170 | Bt 171 |
|---|---|---|---|---|---|---|---|---|---|---|
| Unit | Lamp | Lamp | Lamp | Lamp | Lamp | Lamp | Vaugn | Vaugn | Vaugn | Vaugn |
| Type | Krs | Micr-dt | Micr-dt | Micr-dt | Micr-dt | Micr-dt | Bt-rich | Bt-rich | Bt-rich | Bt-rich |
| $SiO_2$ | 35.87 | 35.00 | 35.41 | 35.16 | 35.14 | 34.40 | 35.37 | 35.80 | 35.96 | 35.59 |
| $TiO_2$ | 4.09 | 6.31 | 6.99 | 4.28 | 6.55 | 6.79 | 5.74 | 5.78 | 5.34 | 5.77 |
| $Al_2O_3$ | 18.41 | 14.92 | 14.69 | 14.52 | 14.77 | 14.50 | 14.62 | 14.61 | 14.26 | 14.39 |
| $Cr_2O_3$ | < MDL | 0.03 | < MDL | < MDL | < MDL | 0.02 | 0.01 | < MDL | 0.06 | < MDL |
| NiO | 0.01 | < MDL | 0.01 | 0.02 | 0.01 | < MDL | < MDL | < MDL | 0.05 | 0.03 |
| FeO | 15.19 | 14.35 | 13.26 | 17.38 | 15.85 | 18.26 | 16.94 | 15.57 | 16.34 | 15.94 |
| MnO | 0.11 | 0.08 | 0.04 | 0.10 | 0.08 | 0.11 | 0.16 | 0.10 | 0.08 | 0.10 |
| MgO | 11.60 | 12.72 | 13.24 | 12.19 | 12.01 | 10.20 | 12.54 | 13.50 | 13.60 | 13.42 |
| CaO | 0.03 | 0.06 | 0.02 | 0.06 | 0.06 | 0.10 | 0.03 | 0.01 | 0.04 | 0.03 |
| $Na_2O$ | 0.22 | 0.15 | 0.19 | 0.08 | 0.21 | 0.16 | 0.38 | 0.43 | 0.42 | 0.58 |
| $K_2O$ | 9.29 | 8.23 | 8.52 | 8.83 | 8.15 | 8.11 | 8.51 | 8.62 | 8.57 | 8.68 |
| F | 0.18 | 0.12 | 0.13 | 0.14 | 0.07 | 0.07 | 0.18 | 0.17 | 0.18 | 0.21 |
| Cl | < MDL | 0.02 | 0.03 | 0.06 | 0.04 | 0.02 | 0.03 | 0.04 | 0.04 | 0.04 |
| Total | 95.01 | 91.98 | 92.53 | 92.82 | 92.94 | 92.76 | 94.50 | 94.62 | 94.95 | 94.79 |

The Method Detection Limit (MDL) for the routine analysis of common elements is ~0.02 wt.%

***Supplementary Table 5.*** *Continued*

| Sample | Bt 172 | Bt 173 | Bt 174 | Bt 175 | Bt 176 | Bt 177 |
|---|---|---|---|---|---|---|
| Unit | Vaugn | Vaugn | Vaugn | Vaugn | Vaugn | Vaugn |
| Type | Bt-rich | Bt-rich | Bt-rich | Bt-rich | Bt-rich | Bt-rich |
| $SiO_2$ | 35.39 | 35.67 | 35.77 | 35.45 | 35.87 | 35.50 |
| $TiO_2$ | 6.53 | 6.14 | 6.19 | 5.99 | 5.16 | 6.19 |
| $Al_2O_3$ | 14.56 | 14.36 | 14.27 | 14.15 | 14.50 | 14.36 |
| $Cr_2O_3$ | < MDL | < MDL | 0.04 | 0.02 | 0.04 | < MDL |
| NiO | 0.01 | 0.02 | 0.03 | 0.03 | < MDL | < MDL |
| FeO | 15.97 | 16.18 | 16.95 | 17.61 | 14.76 | 16.16 |
| MnO | 0.10 | 0.08 | 0.14 | 0.13 | 0.06 | 0.17 |
| MgO | 12.78 | 12.77 | 12.48 | 11.51 | 14.35 | 12.66 |
| CaO | 0.03 | < MDL | 0.03 | 0.01 | 0.02 | 0.03 |
| $Na_2O$ | 0.43 | 0.47 | 0.47 | 0.38 | 0.47 | 0.43 |
| $K_2O$ | 8.39 | 8.65 | 8.46 | 8.59 | 8.68 | 8.55 |
| F | 0.13 | 0.29 | 0.18 | 0.28 | 0.05 | 0.14 |
| Cl | 0.01 | 0.05 | 0.04 | 0.06 | 0.03 | 0.03 |
| Total | 94.33 | 94.71 | 95.07 | 94.20 | 94.01 | 94.21 |

The Method Detection Limit (MDL) for the routine analysis of common elements is ~0.02 wt.%

***Supplementary Table 6.*** *Electron microprobe analyses of muscovite from the Sierra Bermeja Pluton*

| Sample | Ms 1 | Ms 2 | Ms 3 | Ms 4 | Ms 5 | Ms 6 | Ms 7 | Ms 8 | Ms 9 | Ms 10 |
|---|---|---|---|---|---|---|---|---|---|---|
| Type | mag | mag | mag | mag | mag | alt | alt | alt | alt | alt |
| Unit | OU | OU | OU | OU | OU | OU | OU | OU | OU | OU |
| $SiO_2$ | 46.55 | 46.57 | 46.39 | 45.92 | 46.83 | 46.52 | 52.27 | 46.68 | 46.63 | 47.43 |
| $TiO_2$ | 0.45 | 0.66 | 0.39 | 0.41 | 0.50 | 0.09 | 0.11 | 0.22 | 0.25 | 0.27 |
| $Al_2O_3$ | 36.31 | 35.33 | 36.59 | 34.94 | 36.06 | 34.76 | 29.30 | 35.35 | 36.22 | 35.50 |
| $Cr_2O_3$ | < MDL | 0.02 | < MDL | < MDL | < MDL | < MDL | 0.14 | 0.07 | < MDL | < MDL |
| NiO | < MDL | < MDL | 0.06 | < MDL | < MDL | 0.01 | 0.01 | < MDL | 0.03 | 0.06 |
| FeO | 1.16 | 1.04 | 1.24 | 1.24 | 1.38 | 1.60 | 1.68 | 1.33 | 1.30 | 1.41 |
| MnO | < MDL | 0.10 | 0.01 | 0.02 | 0.05 | 0.02 | 0.11 | 0.06 | < MDL | 0.02 |
| MgO | 0.85 | 0.72 | 0.84 | 0.94 | 1.00 | 0.97 | 1.44 | 0.85 | 0.98 | 0.98 |
| CaO | 0.01 | 0.01 | < MDL | 0.06 | 0.01 | 0.02 | < MDL | 0.01 | < MDL | 0.01 |
| $Na_2O$ | 0.46 | 0.54 | 0.56 | 0.56 | 0.59 | 0.24 | 0.20 | 0.58 | 0.48 | 0.47 |
| $K_2O$ | 10.66 | 10.42 | 10.61 | 10.41 | 10.34 | 10.80 | 11.05 | 10.40 | 10.65 | 10.66 |
| F | 0.05 | NA | 0.18 | 0.20 | 0.16 | NA | NA | NA | 0.17 | NA |
| Cl | < MDL | NA | < MDL | 0.01 | < MDL | NA | NA | NA | < MDL | NA |
| Total | 96.51 | 95.39 | 96.86 | 94.71 | 96.91 | 95.01 | 96.31 | 95.55 | 96.71 | 96.81 |

mag: magmatic
alt: alteration product
The Method Detection Limit (MDL) for the routine analysis of common elements is ~0.02 wt.%
NA not analyzed

***Supplementary Table 6.*** *Continued*

| Sample | Ms 11 | Ms 12 | Ms 13 | Ms 14 | Ms 15 | Ms 16 | Ms 17 | Ms 18 | Ms 19 | Ms 20 |
|---|---|---|---|---|---|---|---|---|---|---|
| Type | mag | mag | mag | mag | mag | mag | mag | mag | alt | alt |
| Unit | MU | MU | MU | MU | MU | MU | MU | MU | MU | MU |
| $SiO_2$ | 46.55 | 46.12 | 45.92 | 46.37 | 46.65 | 46.34 | 46.34 | 46.59 | 46.06 | 46.37 |
| $TiO_2$ | 0.60 | 0.83 | 0.78 | 0.74 | 0.49 | 0.56 | 0.93 | 0.46 | 0.07 | 0.09 |
| $Al_2O_3$ | 35.14 | 35.96 | 35.66 | 35.76 | 34.76 | 34.67 | 34.56 | 36.05 | 35.35 | 34.41 |
| $Cr_2O_3$ | < MDL | < MDL | < MDL | < MDL | 0.02 | < MDL | < MDL | < MDL | 0.02 | 0.07 |
| NiO | 0.01 | 0.05 | < MDL | 0.01 | 0.04 | < MDL | 0.09 | < MDL | 0.01 | < MDL |
| FeO | 1.11 | 1.24 | 1.42 | 1.41 | 1.31 | 1.37 | 1.25 | 1.38 | 1.37 | 1.86 |
| MnO | < MDL | 0.01 | < MDL | 0.02 | 0.03 | 0.04 | 0.02 | 0.03 | 0.01 | 0.04 |
| MgO | 0.89 | 0.86 | 0.88 | 1.02 | 0.84 | 0.97 | 0.87 | 0.92 | 1.06 | 1.26 |
| CaO | 0.02 | 0.01 | < MDL | < MDL | < MDL | 0.01 | 0.02 | 0.04 | < MDL | 0.01 |
| $Na_2O$ | 0.44 | 0.50 | 0.56 | 0.62 | 0.66 | 0.69 | 0.75 | 0.77 | 0.44 | 0.43 |
| $K_2O$ | 10.84 | 10.48 | 10.55 | 10.58 | 10.59 | 10.47 | 10.06 | 9.87 | 10.92 | 10.28 |
| F | NA | 0.09 | 0.17 | 0.17 | 0.33 | 0.27 | 0.29 | 0.15 | 0.23 | NA |
| Cl | NA | 0.01 | 0.01 | < MDL | 0.02 | < MDL | 0.01 | < MDL | < MDL | NA |
| Total | 95.59 | 96.18 | 95.95 | 96.70 | 95.74 | 95.40 | 95.19 | 96.26 | 95.53 | 94.81 |

mag: magmatic
alt: alteration product
The Method Detection Limit (MDL) for the routine analysis of common elements is ~0.02 wt.%
NA not analyzed

***Supplementary Table 6.*** *Continued*

| Sample | Ms 21 | Ms 22 | Ms 23 | Ms 24 | Ms 25 | Ms 26 | Ms 27 | Ms 28 | Ms 29 | Ms 30 |
|---|---|---|---|---|---|---|---|---|---|---|
| Type | alt | alt | alt | mag | mag | mag | mag | mag | mag | mag |
| Unit | MU | MU | MU | IU | IU | IU | IU | IU | IU | IU |
| $SiO_2$ | 47.64 | 46.75 | 45.66 | 46.84 | 45.69 | 46.73 | 46.06 | 45.92 | 46.54 | 46.30 |
| $TiO_2$ | 0.10 | 0.24 | 0.26 | 0.68 | 0.65 | 0.60 | 0.30 | 0.81 | 1.23 | 0.54 |
| $Al_2O_3$ | 34.20 | 34.60 | 35.61 | 34.59 | 34.56 | 34.71 | 34.94 | 35.00 | 35.07 | 35.07 |
| $Cr_2O_3$ | < MDL | 0.05 | < MDL | < MDL | 0.04 | 0.04 | 0.01 | 0.02 | < MDL | < MDL |
| NiO | < MDL | 0.08 | < MDL | 0.01 | < MDL | 0.02 | 0.03 | < MDL | < MDL | 0.02 |
| FeO | 2.08 | 1.43 | 1.26 | 1.29 | 1.55 | 1.47 | 1.12 | 1.39 | 1.37 | 1.78 |
| MnO | 0.05 | < MDL | < MDL | < MDL | 0.08 | < MDL | 0.04 | 0.01 | < MDL | < MDL |
| MgO | 1.60 | 1.12 | 0.98 | 0.97 | 1.01 | 0.81 | 0.66 | 0.89 | 0.96 | 1.04 |
| CaO | < MDL | < MDL | 0.02 | 0.02 | < MDL | 0.01 | 0.02 | < MDL | < MDL | < MDL |
| $Na_2O$ | 0.27 | 0.45 | 0.68 | 0.53 | 0.55 | 0.56 | 0.56 | 0.60 | 0.67 | 0.69 |
| $K_2O$ | 11.05 | 10.45 | 9.97 | 10.38 | 10.08 | 9.95 | 10.65 | 10.31 | 10.40 | 10.22 |
| F | 0.27 | NA | 0.15 | 0.07 | NA | 0.19 | 0.18 | 0.24 | 0.24 | NA |
| Cl | < MDL | NA | < MDL | < MDL | NA | 0.01 | < MDL | < MDL | < MDL | NA |
| Total | 97.26 | 95.17 | 94.60 | 95.37 | 94.21 | 95.10 | 94.55 | 95.19 | 96.50 | 95.66 |

mag: magmatic
alt: alteration product
The Method Detection Limit (MDL) for the routine analysis of common elements is ~0.02 wt.%
NA not analyzed

***Supplementary Table 6.*** *Continued*

| Sample | Ms 31 | Ms 32 | Ms 33 | Ms 34 | Ms 35 | Ms 36 | Ms 37 | Ms 38 | Ms 39 | Ms 40 |
|---|---|---|---|---|---|---|---|---|---|---|
| Type | mag | mag | mag | mag | mag | mag | mag | Crd Alt | Crd Alt | Crd Alt |
| Unit | IU | IU | IU | IU | IU | IU | IU | MU | MU | MU |
| $SiO_2$ | 46.72 | 46.97 | 46.65 | 46.02 | 46.25 | 45.78 | 46.55 | 38.48 | 42.10 | 41.60 |
| $TiO_2$ | 0.83 | 0.54 | 1.09 | 0.48 | 0.37 | 0.58 | 0.43 | 0.00 | 0.02 | 0.01 |
| $Al_2O_3$ | 33.58 | 35.70 | 33.92 | 35.04 | 35.32 | 34.64 | 35.00 | 22.79 | 29.63 | 28.84 |
| $Cr_2O_3$ | 0.04 | 0.04 | 0.01 | < MDL | 0.01 | < MDL | 0.03 | 0.02 | 0.00 | 0.04 |
| NiO | < MDL | < MDL | < MDL | < MDL | 0.04 | < MDL | < MDL | 0.00 | 0.08 | 0.02 |
| FeO | 1.49 | 1.25 | 1.51 | 1.49 | 1.64 | 1.78 | 1.73 | 14.70 | 7.80 | 9.55 |
| MnO | 0.01 | 0.01 | 0.01 | 0.02 | < MDL | 0.02 | 0.08 | 0.52 | 0.28 | 0.37 |
| MgO | 1.03 | 0.84 | 1.13 | 0.84 | 0.91 | 0.99 | 0.97 | 8.68 | 4.25 | 5.21 |
| CaO | 0.04 | 0.01 | 0.01 | 0.02 | < MDL | 0.02 | < MDL | 0.02 | 0.00 | 0.01 |
| $Na_2O$ | 0.68 | 0.71 | 0.73 | 0.76 | 0.77 | 0.79 | 0.80 | 0.14 | 0.34 | 0.27 |
| $K_2O$ | 10.18 | 10.54 | 10.20 | 10.32 | 9.86 | 10.00 | 9.82 | 9.33 | 9.86 | 10.01 |
| F | 0.14 | NA | 0.22 | 0.05 | NA | NA | NA | 0.52 | 0.28 | 0.37 |
| Cl | < MDL | NA | < MDL | < MDL | NA | NA | NA | 0.00 | 0.01 | 0.00 |
| Total | 94.74 | 96.61 | 95.48 | 95.03 | 95.16 | 94.58 | 95.41 | 95.21 | 94.64 | 96.30 |

mag: magmatic
alt: alteration product
The Method Detection Limit (MDL) for the routine analysis of common elements is ~0.02 wt.%
NA not analyzed

***Supplementary Table 6.*** *Continued*

| Sample | Ms 41 | Ms 42 | Ms 43 | Ms 44 | Ms 45 | Ms 46 | Ms 47 | Ms 48 | Ms 49 | Ms 50 |
|---|---|---|---|---|---|---|---|---|---|---|
| Type | Crd Alt | Crd Alt | Crd Alt | Crd Alt | Crd Alt | Crd Alt | Crd Alt | Crd Alt | Crd Alt | Crd Alt |
| Unit | MU | MU | MU | MU | MU | MU | MU | MU | MU | OU |
| $SiO_2$ | 44.02 | 43.42 | 35.50 | 35.69 | 44.33 | 46.02 | 40.11 | 36.35 | 44.81 | 37.18 |
| $TiO_2$ | 0.00 | 0.03 | 0.00 | 0.02 | 0.00 | 0.00 | 0.00 | 0.01 | 0.00 | 0.02 |
| $Al_2O_3$ | 30.38 | 30.95 | 22.03 | 21.18 | 31.22 | 35.49 | 27.21 | 21.25 | 33.21 | 20.66 |
| $Cr_2O_3$ | 0.01 | 0.00 | 0.01 | 0.00 | 0.04 | 0.02 | 0.00 | 0.03 | 0.00 | 0.01 |
| NiO | 0.00 | 0.01 | 0.00 | 0.01 | 0.04 | 0.01 | 0.01 | 0.00 | 0.00 | 0.05 |
| FeO | 5.92 | 6.24 | 16.57 | 16.58 | 8.56 | 1.58 | 11.49 | 16.14 | 3.31 | 14.94 |
| MnO | 0.14 | 0.20 | 0.62 | 0.51 | 0.20 | 0.04 | 0.41 | 0.26 | 0.10 | 0.49 |
| MgO | 3.58 | 4.08 | 9.87 | 10.16 | 4.36 | 1.17 | 6.25 | 10.43 | 2.42 | 10.71 |
| CaO | 0.03 | 0.00 | 0.01 | 0.00 | 0.01 | 0.00 | 0.01 | 0.01 | 0.00 | 0.04 |
| $Na_2O$ | 0.19 | 0.35 | 0.11 | 0.11 | 0.14 | 0.59 | 0.28 | 0.12 | 0.49 | 0.13 |
| $K_2O$ | 10.24 | 10.38 | 9.44 | 9.65 | 10.49 | 10.45 | 9.90 | 9.38 | 10.43 | 9.38 |
| F | 0.20 | 0.37 | 0.42 | 0.39 | 0.37 | 0.21 | 0.40 | 0.40 | 0.16 | 0.48 |
| Cl | 0.00 | 0.00 | 0.01 | 0.02 | 0.01 | 0.01 | 0.01 | 0.02 | 0.01 | 0.02 |
| Total | 94.70 | 96.04 | 94.60 | 94.31 | 99.79 | 95.58 | 96.08 | 94.41 | 94.94 | 94.10 |

mag: magmatic
alt: alteration product
The Method Detection Limit (MDL) for the routine analysis of common elements is ~0.02 wt.%

***Supplementary Table 6.*** *Continued*

| Sample | Ms 51 | Ms 52 | Ms 53 | Ms 54 | Ms 55 | Ms 56 | Ms 57 | Ms 58 | Ms 59 | Ms 60 |
|---|---|---|---|---|---|---|---|---|---|---|
| Type | Crd Alt | Crd Alt | Crd Alt | Crd Alt | Crd Alt | Crd Alt | Crd Alt | Crd Alt | Crd Alt | Crd Alt |
| Unit | OU | IU | IU | IU | IU | IU | IU | IU | IU | IU |
| $SiO_2$ | 42.97 | 46.37 | 40.78 | 43.56 | 45.87 | 36.23 | 35.39 | 35.62 | 46.98 | 36.67 |
| $TiO_2$ | 0.00 | 0.00 | 0.00 | 0.00 | 0.00 | 0.15 | 0.26 | 0.00 | 0.01 | 0.01 |
| $Al_2O_3$ | 29.68 | 34.75 | 26.75 | 29.27 | 30.90 | 20.92 | 21.05 | 21.50 | 36.12 | 20.79 |
| $Cr_2O_3$ | 0.01 | 0.02 | 0.00 | 0.00 | 0.00 | 0.00 | 0.00 | 0.00 | 0.00 | 0.00 |
| NiO | 0.00 | 0.01 | 0.00 | 0.00 | 0.00 | 0.02 | 0.01 | 0.05 | 0.00 | 0.00 |
| FeO | 7.67 | 1.88 | 11.19 | 7.97 | 4.12 | 18.11 | 18.68 | 17.35 | 1.37 | 16.89 |
| MnO | 0.23 | 0.04 | 0.57 | 0.31 | 0.09 | 0.31 | 0.27 | 0.34 | 0.00 | 0.45 |
| MgO | 5.14 | 1.24 | 4.92 | 3.75 | 3.27 | 7.96 | 7.86 | 9.15 | 1.26 | 9.39 |
| CaO | 0.01 | 0.00 | 0.02 | 0.00 | 0.03 | 0.00 | 0.01 | 0.00 | 0.00 | 0.01 |
| $Na_2O$ | 0.27 | 0.56 | 0.23 | 0.14 | 0.11 | 0.11 | 0.07 | 0.13 | 0.66 | 0.14 |
| $K_2O$ | 10.50 | 10.24 | 9.58 | 10.19 | 10.23 | 9.13 | 8.89 | 9.06 | 10.36 | 8.93 |
| F | 0.38 | 0.13 | 0.40 | 0.32 | 0.41 | 0.46 | 0.46 | 0.50 | 0.24 | 0.46 |
| Cl | 0.01 | 0.01 | 0.01 | 0.01 | 0.00 | 0.03 | 0.02 | 0.02 | 0.02 | 0.00 |
| Total | 96.85 | 95.24 | 94.46 | 95.51 | 95.03 | 93.44 | 92.97 | 93.73 | 97.02 | 93.74 |

mag: magmatic
alt: alteration product
The Method Detection Limit (MDL) for the routine analysis of common elements is ~0.02 wt.%

***Supplementary Table 6.*** *Continued*

| Sample | Ms 61 | Ms 62 | Ms 63 | Ms 64 | Ms 65 | Ms 66 | Ms 67 | Ms 69 |
|---|---|---|---|---|---|---|---|---|
| Type | Crd Alt | Crd Alt | Crd Alt | Crd Alt | Crd Alt | Crd Alt | Crd Alt | Crd Alt |
| Unit | IU | IU | IU | IU | IU | IU | IU | IU |
| $SiO_2$ | 35.29 | 46.62 | 36.01 | 26.01 | 28.27 | 46.89 | 46.52 | 33.62 |
| $TiO_2$ | 0.00 | 0.01 | 0.04 | 0.04 | 0.00 | 0.32 | 0.00 | 0.82 |
| $Al_2O_3$ | 22.06 | 35.80 | 21.78 | 22.31 | 22.05 | 35.41 | 34.95 | 20.90 |
| $Cr_2O_3$ | 0.00 | 0.00 | 0.02 | 0.00 | 0.03 | 0.01 | 0.00 | 0.00 |
| NiO | 0.04 | 0.02 | 0.00 | 0.00 | 0.00 | 0.00 | 0.00 | 0.00 |
| FeO | 17.37 | 1.35 | 16.04 | 27.91 | 27.57 | 1.63 | 1.99 | 22.02 |
| MnO | 0.32 | 0.01 | 0.32 | 0.78 | 0.73 | 0.05 | 0.05 | 0.49 |
| MgO | 8.39 | 1.17 | 8.88 | 7.73 | 7.49 | 1.07 | 1.30 | 6.39 |
| CaO | 0.01 | 0.01 | 0.00 | 0.09 | 0.06 | 0.00 | 0.00 | 0.03 |
| $Na_2O$ | 0.14 | 0.70 | 0.11 | 0.00 | 0.01 | 0.60 | 0.55 | 0.05 |
| $K_2O$ | 9.36 | 10.30 | 9.38 | 0.10 | 1.66 | 10.50 | 10.49 | 6.86 |
| F | 0.35 | 0.22 | 0.49 | 0.08 | 0.14 | 0.36 | 0.26 | 0.26 |
| Cl | 0.01 | 0.01 | 0.01 | 0.01 | 0.00 | 0.01 | 0.00 | 0.01 |
| Total | 93.34 | 96.22 | 93.08 | 85.05 | 88.01 | 96.84 | 96.11 | 91.45 |

mag: magmatic
alt: alteration product
The Method Detection Limit (MDL) for the routine analysis of common elements is ~0.02 wt.%

***Supplementary Table 7.*** *Electron microprobe analyses of cordierite from the Sierra Bermeja Pluton*

| Sample | Crd 1 | Crd 2 | Crd 3 | Crd 4 | Crd 5 | Crd 6 | Crd 7 | Crd 8 | Crd 9 |
|---|---|---|---|---|---|---|---|---|---|
| Unit | OU | OU | OU | OU | OU | OU | OU | OU | OU |
| $SiO_2$ | 47.86 | 47.57 | 47.97 | 48.12 | 47.48 | 48.50 | 48.12 | 47.52 | 47.31 |
| $TiO_2$ | < MDL | < MDL | < MDL | 0.03 | 0.02 | 0.01 | < MDL | < MDL | < MDL |
| $Al_2O_3$ | 31.48 | 31.61 | 31.78 | 31.58 | 31.04 | 31.54 | 31.27 | 32.12 | 32.30 |
| $Cr_2O_3$ | 0.01 | < MDL | < MDL | 0.02 | 0.06 | 0.02 | < MDL | < MDL | 0.02 |
| NiO | 0.02 | 0.02 | 0.01 | 0.05 | 0.05 | < MDL | < MDL | < MDL | < MDL |
| FeO | 8.49 | 8.67 | 8.13 | 8.21 | 8.29 | 8.42 | 7.99 | 8.23 | 8.11 |
| MnO | 0.62 | 0.59 | 0.64 | 0.59 | 0.61 | 0.56 | 0.71 | 0.74 | 0.80 |
| MgO | 6.07 | 6.31 | 6.11 | 6.35 | 6.19 | 6.44 | 6.28 | 5.52 | 5.47 |
| CaO | 0.06 | 0.05 | 0.07 | 0.04 | 0.07 | 0.05 | 0.07 | 0.08 | 0.08 |
| $Na_2O$ | 1.85 | 1.70 | 2.02 | 1.94 | 1.94 | 1.69 | 1.91 | 1.62 | 1.79 |
| $K_2O$ | 0.02 | 0.03 | 0.02 | 0.04 | 0.01 | 0.01 | 0.03 | 0.02 | 0.01 |
| F | 0.13 | 0.07 | 0.15 | < MDL | < MDL | 0.09 | < MDL | < MDL | < MDL |
| Cl | 0.01 | 0.01 | < MDL | < MDL | 0.01 | 0.01 | < MDL | < MDL | 0.01 |
| Total | 96.61 | 96.62 | 96.90 | 96.97 | 95.76 | 97.34 | 96.37 | 95.85 | 95.90 |

The Method Detection Limit (MDL) for the routine analysis of common elements is ~0.02 wt.%

***Supplementary Table 7.*** *Continued*

| Sample | Crd 10 | Crd 11 | Crd 12 | Crd 13 | Crd 14 | Crd 15 | Crd 16 | Crd 17 | Crd 18 |
|---|---|---|---|---|---|---|---|---|---|
| Unit | OU | MU | MU | MU | MU | MU | MU | MU | MU |
| $SiO_2$ | 47.22 | 47.67 | 47.60 | 47.87 | 47.37 | 47.38 | 46.95 | 47.08 | 47.09 |
| $TiO_2$ | < MDL | < MDL | < MDL | 0.02 | < MDL | 0.01 | < MDL | < MDL | < MDL |
| $Al_2O_3$ | 31.73 | 31.90 | 32.15 | 31.99 | 31.89 | 31.86 | 32.04 | 31.87 | 31.86 |
| $Cr_2O_3$ | < MDL | < MDL | < MDL | < MDL | 0.01 | < MDL | < MDL | 0.01 | < MDL |
| NiO | 0.02 | < MDL | 0.05 | 0.04 | 0.01 | < MDL | < MDL | 0.01 | 0.01 |
| FeO | 8.32 | 7.91 | 7.50 | 7.87 | 8.11 | 8.03 | 8.39 | 8.33 | 8.35 |
| MnO | 0.81 | 0.62 | 0.59 | 0.23 | 0.46 | 0.44 | 0.44 | 0.42 | 0.42 |
| MgO | 5.39 | 6.10 | 6.42 | 6.81 | 6.25 | 6.24 | 5.87 | 5.93 | 5.67 |
| CaO | 0.05 | 0.03 | 0.01 | 0.02 | < MDL | 0.05 | 0.03 | 0.03 | 0.02 |
| $Na_2O$ | 1.80 | 1.75 | 1.86 | 1.54 | 1.90 | 1.69 | 1.69 | 1.77 | 1.96 |
| $K_2O$ | 0.02 | 0.01 | 0.01 | 0.01 | < MDL | < MDL | 0.01 | < MDL | < MDL |
| F | 0.20 | < MDL | 0.05 | < MDL | 0.01 | 0.04 | 0.01 | < MDL | < MDL |
| Cl | < MDL | 0.01 | 0.01 | < MDL | 0.01 | < MDL | 0.01 | < MDL | < MDL |
| Total | 95.57 | 96.00 | 96.24 | 96.38 | 96.03 | 95.74 | 95.45 | 95.45 | 95.38 |

The Method Detection Limit (MDL) for the routine analysis of common elements is ~0.02 wt.%

***Supplementary Table 7.*** *Continued*

| Sample | Crd 19 | Crd 20 | Crd 21 | Crd 22 | Crd 23 | Crd 24 | Crd 25 | Crd 26 | Crd 27 |
|---|---|---|---|---|---|---|---|---|---|
| Unit | MU | MU | IU | IU | IU | IU | IU | Crd Alt | Crd Alt |
| $SiO_2$ | 47.04 | 47.26 | 47.28 | 47.01 | 46.87 | 47.61 | 47.39 | 40.02 | 42.77 |
| $TiO_2$ | < MDL | 0.01 | 0.01 | < MDL | < MDL | < MDL | < MDL | < MDL | < MDL |
| $Al_2O_3$ | 31.81 | 31.51 | 31.46 | 31.55 | 30.90 | 31.49 | 31.65 | 22.46 | 34.89 |
| $Cr_2O_3$ | 0.02 | 0.01 | 0.04 | < MDL | < MDL | 0.03 | < MDL | < MDL | < MDL |
| NiO | 0.02 | 0.06 | < MDL | < MDL | 0.02 | < MDL | 0.01 | 0.09 | 0.03 |
| FeO | 8.23 | 8.09 | 9.41 | 8.77 | 9.23 | 7.99 | 8.48 | 14.49 | 5.18 |
| MnO | 0.47 | 0.37 | 0.52 | 0.54 | 0.44 | 0.40 | 0.43 | 0.30 | 0.03 |
| MgO | 5.87 | 5.89 | 5.02 | 5.20 | 4.85 | 6.15 | 5.54 | 10.48 | 2.19 |
| CaO | 0.04 | 0.04 | 0.02 | 0.03 | 0.03 | 0.01 | 0.03 | 0.90 | 0.39 |
| $Na_2O$ | 1.90 | 2.12 | 1.89 | 1.90 | 1.88 | 1.81 | 1.90 | 0.14 | 0.05 |
| $K_2O$ | 0.02 | 0.02 | 0.02 | < MDL | < MDL | 0.01 | 0.03 | 0.90 | 2.39 |
| F | < MDL | 0.03 | 0.02 | < MDL | 0.03 | 0.05 | 0.01 | 0.07 | 0.05 |
| Cl | < MDL | < MDL | < MDL | < MDL | < MDL | < MDL | < MDL | < MDL | 0.02 |
| Total | 95.40 | 95.41 | 95.67 | 95.00 | 94.26 | 95.56 | 95.46 | 89.86 | 87.99 |

The Method Detection Limit (MDL) for the routine analysis of common elements is ~0.02 wt.%

***Supplementary Table 7.*** *Continued*

| Sample | Crd 28 | Crd 29 | Crd 30 | Crd 31 | Crd 32 | Crd 33 | Crd 34 | Crd 35 | Crd 36 |
|---|---|---|---|---|---|---|---|---|---|
| Unit | Crd Alt | Crd Alt | Crd Alt | Crd Alt | Crd Alt | Crd Alt | Crd Alt | Crd Alt | Crd Alt |
| $SiO_2$ | 42.98 | 43.64 | 42.55 | 42.80 | 39.05 | 41.04 | 40.42 | 41.76 | 42.98 |
| $TiO_2$ | < MDL | < MDL | < MDL | < MDL | < MDL | < MDL | < MDL | < MDL | 0.01 |
| $Al_2O_3$ | 34.08 | 33.05 | 33.86 | 33.63 | 32.08 | 40.64 | 40.52 | 37.36 | 37.04 |
| $Cr_2O_3$ | < MDL | 0.04 | 0.01 | < MDL | 0.01 | < MDL | 0.02 | < MDL | < MDL |
| NiO | < MDL | < MDL | < MDL | < MDL | < MDL | 0.11 | 0.15 | 0.14 | 0.17 |
| FeO | 5.20 | 4.56 | 5.23 | 4.64 | 7.67 | 2.15 | 2.11 | 4.93 | 4.08 |
| MnO | 0.11 | 0.06 | 0.10 | 0.08 | 0.37 | 0.00 | 0.00 | 0.00 | 0.00 |
| MgO | 2.28 | 2.10 | 2.25 | 2.18 | 5.76 | 1.40 | 1.83 | 0.18 | 0.13 |
| CaO | 0.33 | 0.43 | 0.43 | 0.43 | 0.90 | 0.14 | 0.16 | 0.31 | 0.26 |
| $Na_2O$ | 0.02 | 0.07 | 0.03 | 0.05 | 0.05 | 0.09 | 0.09 | 0.07 | 0.07 |
| $K_2O$ | 2.56 | 3.30 | 2.20 | 2.58 | 0.45 | 0.30 | 0.36 | 0.48 | 0.30 |
| F | 0.12 | 0.14 | 0.10 | 0.07 | 0.04 | 0.06 | 0.08 | 0.06 | 0.09 |
| Cl | 0.01 | < MDL | < MDL | < MDL | 0.01 | 0.03 | 0.01 | 0.01 | 0.01 |
| Total | 87.69 | 87.39 | 86.77 | 86.46 | 86.38 | 85.97 | 85.76 | 85.29 | 85.14 |

The Method Detection Limit (MDL) for the routine analysis of common elements is ~0.02 wt.%

***Supplementary Table 7.*** *Continued*

| Sample | Crd 37 | Crd 38 | Crd 39 | Crd 40 | Crd 41 | Crd 42 |
|---|---|---|---|---|---|---|
| Unit | Crd Alt | Crd Alt | Crd Alt | Crd Alt | Crd Alt | Crd Alt |
| $SiO_2$ | 40.98 | 39.12 | 38.88 | 39.74 | 37.16 | 36.94 |
| $TiO_2$ | < MDL | 0.01 | < MDL | < MDL | 0.01 | < MDL |
| $Al_2O_3$ | 39.85 | 40.37 | 38.24 | 32.06 | 34.50 | 28.92 |
| $Cr_2O_3$ | < MDL | 0.03 | < MDL | 0.01 | 0.03 | < MDL |
| NiO | 0.18 | 0.08 | 0.07 | 0.00 | 0.16 | 0.02 |
| FeO | 1.85 | 2.36 | 3.46 | 4.93 | 4.90 | 6.36 |
| MnO | 0.02 | 0.32 | 0.04 | 0.25 | 0.02 | 0.14 |
| MgO | 1.48 | 1.94 | 3.17 | 6.19 | 2.20 | 3.01 |
| CaO | 0.25 | 0.20 | 0.23 | 0.72 | 0.64 | 0.84 |
| $Na_2O$ | 0.11 | 0.11 | 0.11 | 0.06 | 0.13 | 0.07 |
| $K_2O$ | 0.29 | 0.31 | 0.26 | 0.20 | 0.38 | 0.51 |
| F | 0.05 | 0.07 | 0.07 | 0.08 | 0.05 | 0.01 |
| Cl | 0.01 | < MDL | 0.01 | 0.01 | 0.01 | 0.01 |
| Total | 85.08 | 84.91 | 84.54 | 84.25 | 80.18 | 76.85 |

The Method Detection Limit (MDL) for the routine analysis of common elements is ~0.02 wt.%

***Supplementary Table 8.*** *Electron microprobe analyses of apatite from the Sierra Bermeja Pluton*

| Sample | Ap 1 | Ap 2 | Ap 3 | Ap 4 | Ap 5 | Ap 6 | Ap 7 | Ap 8 | Ap 9 |
|---|---|---|---|---|---|---|---|---|---|
| Unit | OU | OU | OU | OU | OU | OU | OU | MU | MU |
| $SiO_2$ | 0.05 | 0.06 | 0.03 | 0.07 | 0.14 | 0.07 | 0.03 | 0.02 | 0.01 |
| $TiO_2$ | 0.01 | 0.01 | 0.02 | 0.01 | 0.01 | < MDL | < MDL | 0.01 | 0.01 |
| $Al_2O_3$ | < MDL | 0.01 | < MDL | < MDL | < MDL | < MDL | < MDL | 0.01 | < MDL |
| $Cr_2O_3$ | < MDL | 0.03 | 0.03 | < MDL | < MDL | < MDL | 0.02 | 0.02 | < MDL |
| NiO | < MDL | < MDL | < MDL | < MDL | < MDL | < MDL | 0.03 | < MDL | < MDL |
| FeO | 0.41 | 0.71 | 0.43 | 0.58 | 0.12 | 0.63 | 0.55 | 1.07 | 0.29 |
| MnO | 1.12 | 0.78 | 0.77 | 1.01 | 0.65 | 0.84 | 0.91 | 1.23 | 1.23 |
| MgO | 0.09 | 0.09 | 0.07 | 0.10 | 0.05 | 0.10 | 0.10 | 0.13 | 0.05 |
| CaO | 53.89 | 53.68 | 54.28 | 53.84 | 54.52 | 53.69 | 54.01 | 53.04 | 54.58 |
| $Na_2O$ | 0.05 | 0.07 | 0.05 | 0.05 | 0.01 | 0.05 | 0.01 | 0.09 | 0.03 |
| $K_2O$ | 0.01 | 0.01 | 0.01 | 0.02 | < MDL | < MDL | 0.04 | < MDL | < MDL |
| $P_2O_5$ | 41.71 | 42.28 | 41.33 | 41.45 | 41.69 | 41.49 | 41.67 | 41.96 | 42.38 |
| F | 3.10 | 2.22 | 3.08 | 2.21 | 2.77 | 2.99 | 3.39 | 3.15 | 2.23 |
| Cl | 0.03 | 0.16 | 0.02 | 0.04 | 0.06 | 0.11 | 0.06 | 0.04 | 0.01 |
| Total | 100.46 | 100.12 | 100.11 | 99.37 | 100.03 | 99.98 | 100.82 | 100.78 | 100.81 |

The Method Detection Limit (MDL) for the routine analysis of common elements is ~0.02 wt.%

***Supplementary Table 8.*** *Continued*

| Sample | Ap 10 | Ap 11 | Ap 12 | Ap 13 | Ap 14 | Ap 15 | Ap 16 | Ap 17 | Ap 18 |
|---|---|---|---|---|---|---|---|---|---|
| Unit | MU | MU | MU | MU | MU | MU | IU | IU | IU |
| $SiO_2$ | 0.03 | 0.07 | 0.03 | 0.01 | 0.05 | 0.11 | 0.05 | 0.03 | 0.03 |
| $TiO_2$ | 0.01 | 0.02 | < MDL | 0.06 | 0.01 | < MDL | 0.02 | 0.02 | < MDL |
| $Al_2O_3$ | < MDL | < MDL | < MDL | 0.02 | 0.01 | < MDL | < MDL | < MDL | < MDL |
| $Cr_2O_3$ | < MDL | < MDL | < MDL | < MDL | < MDL | 0.02 | < MDL | 0.01 | < MDL |
| NiO | < MDL | 0.03 | 0.06 | < MDL | < MDL | < MDL | < MDL | 0.09 | 0.02 |
| FeO | 0.30 | 0.80 | 0.12 | 0.38 | 1.01 | 0.30 | 0.63 | 0.63 | 0.12 |
| MnO | 1.17 | 0.89 | 0.53 | 1.34 | 1.00 | 1.20 | 1.13 | 1.17 | 0.79 |
| MgO | 0.04 | 0.12 | 0.05 | 0.07 | 0.14 | 0.05 | 0.07 | 0.10 | 0.05 |
| CaO | 53.88 | 53.84 | 54.59 | 54.53 | 53.00 | 52.28 | 53.22 | 53.54 | 55.17 |
| $Na_2O$ | 0.08 | 0.07 | < MDL | < MDL | 0.05 | 0.04 | 0.04 | 0.07 | 0.02 |
| $K_2O$ | 0.01 | 0.01 | < MDL | < MDL | < MDL | < MDL | < MDL | < MDL | < MDL |
| $P_2O_5$ | 42.13 | 41.49 | 43.18 | 43.31 | 42.50 | 41.81 | 41.97 | 41.85 | 42.24 |
| F | 2.84 | 3.22 | 2.89 | 3.11 | 3.08 | 2.78 | 3.13 | 2.96 | 2.28 |
| Cl | 0.01 | 0.03 | 0.02 | 0.01 | 0.02 | 0.01 | 0.03 | 0.02 | < MDL |
| Total | 100.49 | 100.58 | 101.48 | 102.84 | 100.88 | 98.60 | 100.29 | 100.48 | 100.71 |

The Method Detection Limit (MDL) for the routine analysis of common elements is ~0.02 wt.%

***Supplementary Table 8.*** *Continued*

| Sample | Ap 19 | Ap 20 | Ap 21 | Ap 22 | Ap 23 | Ap 24 | Ap 25 | Ap 26 | Ap 27 |
|---|---|---|---|---|---|---|---|---|---|
| Unit | IU | IU | MME | MME | MME | MME | MME | MME | MME |
| $SiO_2$ | 0.01 | 0.03 | 0.09 | 0.04 | 0.07 | 0.07 | 0.04 | 0.06 | 0.03 |
| $TiO_2$ | 0.01 | < MDL | 0.02 | 0.01 | 0.01 | 0.01 | 0.01 | < MDL | 0.01 |
| $Al_2O_3$ | < MDL | < MDL | < MDL | < MDL | 0.01 | 0.02 | 0.01 | 0.01 | < MDL |
| $Cr_2O_3$ | 0.02 | 0.03 | < MDL | 0.01 | < MDL | 0.01 | < MDL | 0.02 | 0.01 |
| NiO | 0.04 | < MDL | < MDL | < MDL | < MDL | 0.05 | 0.05 | 0.01 | < MDL |
| FeO | 0.68 | 0.49 | 0.30 | 0.24 | 0.32 | 0.31 | 0.18 | 0.46 | 0.37 |
| MnO | 0.99 | 1.11 | 0.62 | 0.51 | 0.46 | 0.42 | 0.42 | 0.64 | 0.73 |
| MgO | 0.07 | 0.05 | 0.06 | 0.08 | 0.06 | 0.06 | 0.04 | 0.07 | 0.08 |
| CaO | 53.98 | 54.03 | 54.31 | 54.42 | 53.53 | 55.00 | 54.68 | 54.16 | 54.14 |
| $Na_2O$ | 0.05 | 0.04 | 0.04 | 0.04 | 0.05 | 0.01 | 0.02 | 0.07 | 0.07 |
| $K_2O$ | 0.01 | < MDL | 0.01 | 0.01 | 0.02 | 0.02 | < MDL | 0.01 | 0.01 |
| $P_2O_5$ | 42.40 | 41.97 | 41.91 | 41.77 | 42.20 | 42.21 | 42.01 | 42.14 | 41.89 |
| F | 2.40 | 2.94 | 2.56 | 3.15 | 2.98 | 2.17 | 1.99 | 2.81 | 2.19 |
| Cl | 0.01 | < MDL | 0.07 | 0.02 | 0.05 | 0.02 | 0.02 | 0.11 | 0.11 |
| Total | 100.66 | 100.70 | 99.97 | 100.30 | 99.76 | 100.36 | 99.44 | 100.57 | 99.63 |

The Method Detection Limit (MDL) for the routine analysis of common elements is ~0.02 wt.%

| Sample | Ap 28 | Ap 29 | Ap 30 | Ap 31 | Ap 32 | Ap 33 |
|---|---|---|---|---|---|---|
| Unit | MME | MME | MME | MME | MME | MME |
| $SiO_2$ | 0.15 | 0.05 | < MDL | < MDL | 0.02 | < MDL |
| $TiO_2$ | < MDL | 0.01 | 0.01 | 0.03 | < MDL | < MDL |
| $Al_2O_3$ | < MDL | < MDL | < MDL | < MDL | 0.02 | < MDL |
| $Cr_2O_3$ | 0.01 | 0.02 | < MDL | < MDL | < MDL | < MDL |
| NiO | < MDL | < MDL | 0.02 | < MDL | 0.04 | < MDL |
| FeO | 0.34 | 0.24 | 0.27 | 0.25 | 0.18 | 0.34 |
| MnO | 0.62 | 0.59 | 0.75 | 0.49 | 0.54 | 0.60 |
| MgO | 0.06 | 0.07 | 0.06 | 0.08 | 0.03 | 0.08 |
| CaO | 53.95 | 54.55 | 54.64 | 54.85 | 54.63 | 54.14 |
| $Na_2O$ | 0.07 | 0.03 | 0.03 | 0.04 | 0.03 | 0.03 |
| $K_2O$ | 0.01 | < MDL | < MDL | 0.01 | < MDL | < MDL |
| $P_2O_5$ | 41.75 | 42.22 | 42.00 | 41.74 | 41.77 | 41.57 |
| F | 3.12 | 2.58 | 2.89 | 2.79 | 2.84 | 2.82 |
| Cl | 0.08 | 0.06 | 0.03 | 0.02 | 0.03 | 0.03 |
| Total | 100.16 | 100.42 | 100.71 | 100.30 | 100.12 | 99.61 |

The Method Detection Limit (MDL) for the routine analysis of common elements is ~0.02 wt.%

***Supplementary Table 8.*** *Continued*

| Sample | Ap 34 | Ap 35 | Ap 36 | Ap 37 | Ap 38 | Ap 39 | Ap 40 |
|---|---|---|---|---|---|---|---|
| Unit | Vaugn | Vaugn | Vaugn | Vaugn | Vaugn | Vaugn | Vaugn |
| Type | Bt-rich | Bt-rich | Bt-rich | Bt-rich | Bt-rich | Bt-rich | Bt-poor |
| $SiO_2$ | 0.15 | 0.27 | 0.28 | 0.21 | 0.27 | 0.20 | 0.18 |
| $TiO_2$ | 0.02 | < MDL | 0.02 | < MDL | < MDL | < MDL | 0.04 |
| $Al_2O_3$ | < MDL | < MDL | 0.02 | < MDL | 0.01 | < MDL | 0.01 |
| $Cr_2O_3$ | < MDL | < MDL | < MDL | 0.05 | < MDL | 0.01 | < MDL |
| NiO | < MDL | < MDL | 0.03 | < MDL | 0.01 | 0.02 | 0.04 |
| FeO | 0.51 | 0.42 | 0.54 | 0.36 | 0.39 | 0.38 | 0.32 |
| MnO | 0.01 | 0.10 | 0.07 | 0.02 | 0.07 | 0.04 | 0.07 |
| MgO | 0.36 | 0.12 | 0.35 | 0.33 | 0.34 | 0.35 | 0.37 |
| CaO | 54.63 | 55.32 | 55.15 | 54.85 | 54.23 | 54.26 | 55.71 |
| $Na_2O$ | < MDL | < MDL | < MDL | < MDL | < MDL | < MDL | < MDL |
| $K_2O$ | 0.03 | < MDL | 0.02 | 0.01 | 0.02 | < MDL | 0.01 |
| $P_2O_5$ | 42.01 | 41.48 | 41.62 | 41.52 | 41.91 | 41.84 | 40.94 |
| F | 2.27 | 2.34 | 2.39 | 3.02 | 2.90 | 2.79 | 2.23 |
| Cl | 0.22 | 0.33 | 0.18 | 0.29 | 0.28 | 0.29 | 0.24 |
| Total | 100.22 | 100.37 | 100.65 | 100.67 | 100.42 | 100.19 | 100.17 |

The Method Detection Limit (MDL) for the routine analysis of common elements is ~0.02 wt.%

***Supplementary Table 8.*** *Continued*

| Sample | Ap 41 | Ap 42 | Ap 43 | Ap 44 | Ap 45 | Ap 46 |
|---|---|---|---|---|---|---|
| Unit | Vaugn | Vaugn | Vaugn | Vaugn | Vaugn | Vaugn |
| Type | Bt-poor | Bt-poor | Bt-poor | Bt-poor | Bt-poor | Bt-poor |
| $SiO_2$ | 0.16 | 0.21 | 0.08 | 0.12 | 0.18 | 0.29 |
| $TiO_2$ | 0.01 | 0.01 | 0.01 | 0.01 | < MDL | 0.01 |
| $Al_2O_3$ | < MDL | 0.01 | 0.02 | 0.04 | 0.02 | 0.01 |
| $Cr_2O_3$ | < MDL | < MDL | 0.03 | < MDL | 0.01 | 0.05 |
| NiO | 0.01 | 0.01 | < MDL | 0.06 | 0.01 | < MDL |
| FeO | 0.48 | 0.51 | 0.33 | 0.15 | 0.25 | 0.26 |
| MnO | 0.08 | 0.09 | 0.09 | 0.22 | 0.17 | 0.13 |
| MgO | 0.36 | 0.25 | 0.33 | 0.06 | 0.14 | 0.26 |
| CaO | 54.19 | 54.04 | 53.98 | 55.45 | 55.31 | 54.60 |
| $Na_2O$ | < MDL | < MDL | 0.01 | < MDL | 0.03 | 0.18 |
| $K_2O$ | 0.02 | < MDL | < MDL | < MDL | < MDL | < MDL |
| $P_2O_5$ | 42.75 | 42.57 | 41.31 | 41.75 | 41.51 | 41.77 |
| F | 2.26 | 2.11 | 2.30 | 2.71 | 2.55 | 2.32 |
| Cl | 0.65 | 0.36 | 0.58 | 0.27 | 0.32 | 0.40 |
| Total | 100.97 | 100.15 | 99.05 | 100.84 | 100.51 | 100.27 |

The Method Detection Limit (MDL) for the routine analysis of common elements is ~0.02 wt.%

***Supplementary Table 9.*** *Electron microprobe analyses of pyroxene from the Sierra Bermeja Pluton*

| Sample | Cpx 1 | Cpx 2 | Cpx 3 | Cpx 4 | Cpx 5 | Cpx 6 | Cpx 7 | Cpx 8 | Cpx 9 | Cpx 10 |
|---|---|---|---|---|---|---|---|---|---|---|
| Unit | Vaugn | Vaugn | Vaugn | Vaugn | Vaugn | Vaugn | Vaugn | Vaugn | Vaugn | Vaugn |
| Type | Bt-rich | Bt-rich | Bt-rich | Bt-rich | Bt-rich | Bt-rich | Bt-rich | Bt-rich | Bt-rich | Bt-rich |
| $SiO_2$ | 49.89 | 48.56 | 47.90 | 48.29 | 49.96 | 48.16 | 47.70 | 47.91 | 48.96 | 47.23 |
| $TiO_2$ | 1.23 | 1.87 | 1.98 | 1.88 | 1.47 | 2.03 | 2.13 | 2.13 | 1.59 | 2.29 |
| $Al_2O_3$ | 3.57 | 4.76 | 5.21 | 5.03 | 3.88 | 5.27 | 5.38 | 5.67 | 4.30 | 5.69 |
| FeO | 7.10 | 7.67 | 8.18 | 8.01 | 7.89 | 8.40 | 8.67 | 8.14 | 8.51 | 8.46 |
| $Cr_2O_3$ | 0.45 | 0.34 | 0.28 | 0.27 | 0.21 | 0.16 | 0.15 | 0.14 | 0.14 | 0.13 |
| NiO | 0.08 | < MDL | < MDL | 0.05 | < MDL | < MDL | 0.02 | 0.02 | < MDL | < MDL |
| MnO | 0.15 | 0.11 | 0.17 | 0.12 | 0.13 | 0.19 | 0.18 | 0.11 | 0.24 | 0.18 |
| MgO | 14.72 | 13.69 | 13.46 | 13.61 | 14.18 | 13.57 | 13.24 | 13.35 | 13.43 | 13.16 |
| CaO | 22.22 | 22.13 | 21.76 | 21.72 | 21.60 | 21.57 | 21.28 | 21.85 | 21.86 | 21.68 |
| $Na_2O$ | 0.34 | 0.40 | 0.44 | 0.40 | 0.37 | 0.41 | 0.43 | 0.39 | 0.41 | 0.47 |
| $K_2O$ | < MDL | 0.02 | 0.01 | < MDL | < MDL | 0.01 | 0.01 | < MDL | 0.02 | < MDL |
| Total | 99.75 | 99.53 | 99.39 | 99.39 | 99.71 | 99.78 | 99.19 | 99.71 | 99.45 | 99.30 |
| Mg# | 0.79 | 0.76 | 0.75 | 0.75 | 0.76 | 0.74 | 0.73 | 0.75 | 0.74 | 0.73 |
| Wo | 45.94 | 46.85 | 46.29 | 46.21 | 45.38 | 45.74 | 45.65 | 46.63 | 46.13 | 46.39 |
| En | 42.35 | 40.31 | 39.84 | 40.28 | 41.45 | 40.04 | 39.52 | 39.63 | 39.44 | 39.18 |
| Fs | 11.72 | 12.84 | 13.87 | 13.51 | 13.17 | 14.22 | 14.83 | 13.74 | 14.42 | 14.43 |

The Method Detection Limit (MDL) for the routine analysis of common elements is ~0.02 wt.%

***Supplementary Table 9.*** *Continued*

| Sample | Cpx 11 | Cpx 12 | Cpx 13 | Cpx 14 | Cpx 15 | Cpx 16 | Cpx 17 | Cpx 18 | Cpx 19 | Cpx 20 |
|---|---|---|---|---|---|---|---|---|---|---|
| Unit | Vaugn | Vaugn | Vaugn | Vaugn | Vaugn | Vaugn | Vaugn | Vaugn | Vaugn | Vaugn |
| Type | Bt-rich | Bt-rich | Bt-rich | Bt-rich | Bt-rich | Bt-rich | Bt-rich | Bt-rich | Bt-rich | Bt-rich |
| $SiO_2$ | 49.85 | 47.17 | 50.63 | 48.68 | 49.49 | 47.42 | 48.64 | 47.98 | 46.57 | 49.14 |
| $TiO_2$ | 1.22 | 2.38 | 1.22 | 1.82 | 1.44 | 2.23 | 1.57 | 1.99 | 2.80 | 1.34 |
| $Al_2O_3$ | 3.09 | 5.62 | 3.05 | 4.52 | 3.77 | 5.47 | 4.27 | 4.98 | 6.48 | 3.94 |
| FeO | 8.90 | 8.82 | 8.35 | 8.23 | 8.51 | 8.62 | 9.15 | 9.41 | 9.32 | 9.06 |
| $Cr_2O_3$ | 0.11 | 0.11 | 0.11 | 0.10 | 0.08 | 0.07 | 0.06 | 0.06 | 0.04 | 0.02 |
| NiO | < MDL | 0.04 | < MDL | 0.05 | < MDL | 0.02 | < MDL | < MDL | 0.01 | < MDL |
| MnO | 0.20 | 0.19 | 0.23 | 0.16 | 0.24 | 0.17 | 0.22 | 0.30 | 0.16 | 0.31 |
| MgO | 15.07 | 12.91 | 15.06 | 13.68 | 13.95 | 13.11 | 13.20 | 12.61 | 12.45 | 13.04 |
| CaO | 19.83 | 21.48 | 20.86 | 21.98 | 21.33 | 21.56 | 21.64 | 21.20 | 21.23 | 21.80 |
| $Na_2O$ | 0.35 | 0.44 | 0.36 | 0.41 | 0.38 | 0.42 | 0.44 | 0.44 | 0.46 | 0.45 |
| $K_2O$ | 0.01 | 0.01 | 0.02 | 0.01 | < MDL | 0.01 | 0.01 | < MDL | < MDL | < MDL |
| Total | 98.63 | 99.19 | 99.89 | 99.64 | 99.19 | 99.10 | 99.21 | 98.98 | 99.51 | 99.11 |
| Mg# | 0.75 | 0.72 | 0.76 | 0.75 | 0.74 | 0.73 | 0.72 | 0.70 | 0.70 | 0.72 |
| Wo | 41.39 | 46.21 | 43.00 | 46.21 | 44.84 | 46.21 | 45.73 | 45.76 | 46.20 | 46.13 |
| En | 43.77 | 38.64 | 43.19 | 40.01 | 40.80 | 39.09 | 38.81 | 37.87 | 37.69 | 38.39 |
| Fs | 14.84 | 15.15 | 13.81 | 13.77 | 14.36 | 14.70 | 15.46 | 16.37 | 16.11 | 15.48 |

The Method Detection Limit (MDL) for the routine analysis of common elements is ~0.02 wt.%

***Supplementary Table 9.*** *Continued*

| Sample | Cpx 21 | Cpx 22 | Cpx 23 | Cpx 24 | Cpx 25 | Cpx 26 | Cpx 27 | Cpx 28 | Cpx 29 | Cpx 30 |
|---|---|---|---|---|---|---|---|---|---|---|
| Unit | Vaugn | Vaugn | Vaugn | Vaugn | Vaugn | Vaugn | Vaugn | Vaugn | Vaugn | Vaugn |
| Type | Bt-rich | Bt-rich | Bt-poor | Bt-poor | Bt-poor | Bt-poor | Bt-poor | Bt-poor | Bt-poor | Bt-poor |
| $SiO_2$ | 46.78 | 49.36 | 47.84 | 48.61 | 49.63 | 48.99 | 48.55 | 49.59 | 50.20 | 50.47 |
| $TiO_2$ | 2.68 | 1.39 | 1.94 | 1.82 | 1.49 | 1.57 | 1.60 | 1.47 | 1.26 | 1.20 |
| $Al_2O_3$ | 6.42 | 3.96 | 5.22 | 4.54 | 3.79 | 4.33 | 4.08 | 3.82 | 3.33 | 2.91 |
| FeO | 9.18 | 9.18 | 7.95 | 8.07 | 7.97 | 7.97 | 8.19 | 7.93 | 8.14 | 8.06 |
| $Cr_2O_3$ | < MDL | < MDL | 0.46 | 0.24 | 0.21 | 0.20 | 0.18 | 0.17 | 0.15 | 0.13 |
| NiO | 0.03 | < MDL | 0.01 | < MDL | < MDL | 0.04 | 0.05 | 0.02 | 0.01 | 0.08 |
| MnO | 0.19 | 0.21 | 0.18 | 0.14 | 0.16 | 0.20 | 0.16 | 0.18 | 0.16 | 0.20 |
| MgO | 12.64 | 13.20 | 13.56 | 13.86 | 14.40 | 14.23 | 14.05 | 14.50 | 14.66 | 15.14 |
| CaO | 21.52 | 21.43 | 21.70 | 21.72 | 21.19 | 21.22 | 21.09 | 21.48 | 21.19 | 21.18 |
| $Na_2O$ | 0.46 | 0.42 | 0.38 | 0.40 | 0.37 | 0.39 | 0.40 | 0.36 | 0.38 | 0.33 |
| $K_2O$ | < MDL | < MDL | < MDL | < MDL | < MDL | < MDL | < MDL | 0.01 | < MDL | < MDL |
| Total | 99.90 | 99.14 | 99.23 | 99.42 | 99.20 | 99.14 | 98.34 | 99.53 | 99.49 | 99.70 |
| Mg# | 0.71 | 0.72 | 0.75 | 0.75 | 0.76 | 0.76 | 0.75 | 0.77 | 0.76 | 0.77 |
| Wo | 46.35 | 45.48 | 46.25 | 45.80 | 44.55 | 44.77 | 44.71 | 44.75 | 44.09 | 43.49 |
| En | 37.89 | 38.98 | 40.22 | 40.68 | 42.12 | 41.76 | 41.46 | 42.04 | 42.43 | 43.26 |
| Fs | 15.76 | 15.55 | 13.54 | 13.52 | 13.33 | 13.46 | 13.83 | 13.21 | 13.48 | 13.24 |

The Method Detection Limit (MDL) for the routine analysis of common elements is ~0.02 wt.%

***Supplementary Table 9.*** *Continued*

| Sample | Cpx 31 | Cpx 32 | Cpx 33 | Cpx 34 | Cpx 35 | Cpx 36 | Cpx 37 | Cpx 38 | Cpx 39 | Cpx 40 |
|---|---|---|---|---|---|---|---|---|---|---|
| Unit | Vaugn | Vaugn | Vaugn | Vaugn | Vaugn | Vaugn | Vaugn | Vaugn | Vaugn | Vaugn |
| Type | Bt-poor | Bt-poor | Bt-poor | Bt-poor | Bt-poor | Bt-poor | Bt-poor | Bt-poor | Bt-poor | Bt-poor |
| $SiO_2$ | 49.95 | 50.66 | 50.30 | 47.81 | 50.04 | 49.11 | 48.45 | 49.91 | 49.35 | 50.30 |
| $TiO_2$ | 1.30 | 1.15 | 1.21 | 1.93 | 1.27 | 1.45 | 1.84 | 1.41 | 1.36 | 1.19 |
| $Al_2O_3$ | 3.35 | 2.90 | 2.96 | 5.44 | 2.97 | 3.93 | 5.15 | 3.27 | 3.67 | 3.28 |
| FeO | 8.72 | 7.81 | 8.63 | 9.08 | 8.47 | 8.14 | 8.02 | 8.00 | 7.90 | 7.52 |
| $Cr_2O_3$ | 0.12 | 0.10 | 0.10 | 0.07 | 0.07 | 0.25 | 0.23 | 0.19 | 0.18 | 0.18 |
| NiO | < MDL | 0.04 | 0.03 | < MDL | < MDL | 0.05 | < MDL | 0.01 | < MDL | 0.02 |
| MnO | 0.17 | 0.20 | 0.27 | 0.19 | 0.22 | 0.20 | 0.17 | 0.17 | 0.18 | 0.22 |
| MgO | 14.97 | 15.07 | 15.04 | 13.12 | 14.84 | 14.45 | 13.60 | 14.38 | 14.36 | 14.89 |
| CaO | 20.24 | 21.11 | 20.48 | 21.33 | 20.82 | 21.42 | 21.51 | 21.63 | 21.66 | 21.36 |
| $Na_2O$ | 0.34 | 0.33 | 0.36 | 0.47 | 0.36 | 0.41 | 0.42 | 0.43 | 0.41 | 0.37 |
| $K_2O$ | < MDL | < MDL | < MDL | < MDL | 0.01 | 0.01 | < MDL | 0.01 | 0.02 | 0.01 |
| Total | 99.16 | 99.37 | 99.38 | 99.45 | 99.05 | 99.41 | 99.40 | 99.41 | 99.10 | 99.34 |
| Mg# | 0.75 | 0.77 | 0.76 | 0.72 | 0.76 | 0.76 | 0.75 | 0.76 | 0.76 | 0.78 |
| Wo | 42.16 | 43.68 | 42.35 | 45.55 | 43.15 | 44.60 | 45.94 | 45.05 | 45.17 | 44.39 |
| En | 43.39 | 43.39 | 43.28 | 38.99 | 42.80 | 41.85 | 40.40 | 41.66 | 41.66 | 43.04 |
| Fs | 14.45 | 12.93 | 14.37 | 15.46 | 14.05 | 13.55 | 13.66 | 13.29 | 13.16 | 12.57 |

The Method Detection Limit (MDL) for the routine analysis of common elements is ~0.02 wt.%

***Supplementary Table 9.*** *Continued*

| Sample | Cpx 41 | Cpx 42 | Cpx 43 | Cpx 44 | Cpx 45 | Cpx 46 | Cpx 47 | Cpx 48 | Cpx 49 | Cpx 50 |
|---|---|---|---|---|---|---|---|---|---|---|
| Unit | Vaugn | Vaugn | Vaugn | Vaugn | Vaugn | Vaugn | Vaugn | Vaugn | Vaugn | Lamp |
| Type | Bt-poor | Bt-poor | Bt-poor | Bt-poor | Bt-poor | Bt-poor | Bt-poor | Bt-poor | Bt-poor | Mnt |
| $SiO_2$ | 49.36 | 50.08 | 49.51 | 50.25 | 49.85 | 49.92 | 50.05 | 50.31 | 50.45 | 51.15 |
| $TiO_2$ | 1.45 | 1.24 | 1.48 | 1.28 | 1.27 | 1.39 | 1.27 | 1.46 | 1.39 | 1.03 |
| $Al_2O_3$ | 3.88 | 3.16 | 3.68 | 3.21 | 3.37 | 3.37 | 3.20 | 3.77 | 3.18 | 2.60 |
| FeO | 7.83 | 8.27 | 7.92 | 7.73 | 8.34 | 8.51 | 8.46 | 7.83 | 8.99 | 6.97 |
| $Cr_2O_3$ | 0.16 | 0.13 | 0.12 | 0.09 | 0.09 | 0.08 | 0.07 | 0.05 | 0.05 | 0.80 |
| NiO | < MDL | < MDL | 0.06 | 0.05 | < MDL | 0.01 | 0.01 | < MDL | < MDL | 0.03 |
| MnO | 0.16 | 0.15 | 0.22 | 0.18 | 0.20 | 0.12 | 0.16 | 0.17 | 0.22 | 0.19 |
| MgO | 14.40 | 14.78 | 14.47 | 14.68 | 14.54 | 14.67 | 14.67 | 14.25 | 14.48 | 15.66 |
| CaO | 21.60 | 21.09 | 21.32 | 21.61 | 21.14 | 21.04 | 21.21 | 21.49 | 20.51 | 20.98 |
| $Na_2O$ | 0.37 | 0.37 | 0.40 | 0.41 | 0.40 | 0.36 | 0.37 | 0.36 | 0.34 | 0.22 |
| $K_2O$ | 0.02 | < MDL | < MDL | 0.02 | 0.01 | < MDL | 0.01 | 0.01 | 0.01 | < MDL |
| Total | 99.23 | 99.27 | 99.17 | 99.52 | 99.21 | 99.48 | 99.48 | 99.68 | 99.61 | 99.63 |
| Mg# | 0.77 | 0.76 | 0.77 | 0.77 | 0.76 | 0.75 | 0.76 | 0.76 | 0.74 | 0.80 |
| Wo | 45.11 | 43.73 | 44.59 | 44.82 | 44.01 | 43.66 | 43.88 | 45.19 | 42.87 | 43.39 |
| En | 41.85 | 42.63 | 42.11 | 42.37 | 42.10 | 42.36 | 42.21 | 41.69 | 42.10 | 45.05 |
| Fs | 13.03 | 13.63 | 13.30 | 12.81 | 13.88 | 13.98 | 13.92 | 13.13 | 15.03 | 11.56 |

The Method Detection Limit (MDL) for the routine analysis of common elements is ~0.02 wt.%

***Supplementary Table 9.*** *Continued*

| Sample | Cpx 51 | Cpx 52 | Cpx 53 | Cpx 54 | Cpx 55 | Cpx 56 | Cpx 57 | Cpx 58 | Cpx 59 | Cpx 60 |
|---|---|---|---|---|---|---|---|---|---|---|
| Unit | Lamp | Lamp | Lamp | Lamp | Lamp | Lamp | Lamp | Lamp | Lamp | Lamp |
| Type | Mnt | Mnt | Mnt | Mnt | Mnt | Mnt | Mnt | Mnt | Mnt | Mnt |
| $SiO_2$ | 52.58 | 51.04 | 51.90 | 51.97 | 51.70 | 50.23 | 52.18 | 51.80 | 51.57 | 50.19 |
| $TiO_2$ | 0.91 | 1.12 | 1.11 | 1.06 | 1.18 | 1.36 | 0.97 | 0.90 | 1.29 | 1.50 |
| $Al_2O_3$ | 2.30 | 2.75 | 2.70 | 2.57 | 2.98 | 3.44 | 2.34 | 2.42 | 3.09 | 3.31 |
| FeO | 6.53 | 6.94 | 7.09 | 6.92 | 7.07 | 7.48 | 6.44 | 6.81 | 7.31 | 7.54 |
| $Cr_2O_3$ | 0.78 | 0.72 | 0.71 | 0.70 | 0.69 | 0.67 | 0.62 | 0.61 | 0.50 | 0.49 |
| NiO | < MDL | < MDL | < MDL | < MDL | 0.03 | < MDL | < MDL | 0.04 | < MDL | 0.05 |
| MnO | 0.17 | 0.19 | 0.18 | 0.17 | 0.16 | 0.20 | 0.19 | 0.17 | 0.23 | 0.23 |
| MgO | 15.74 | 15.62 | 15.40 | 15.32 | 15.18 | 15.13 | 15.49 | 15.72 | 15.08 | 14.50 |
| CaO | 20.94 | 20.69 | 20.64 | 20.76 | 20.80 | 20.26 | 21.03 | 21.06 | 20.75 | 21.46 |
| $Na_2O$ | 0.22 | 0.20 | 0.21 | 0.21 | 0.22 | 0.24 | 0.22 | 0.21 | 0.18 | 0.22 |
| $K_2O$ | < MDL | 0.01 | 0.02 | < MDL | 0.01 | < MDL | < MDL | 0.01 | < MDL | 0.01 |
| Total | 100.16 | 99.27 | 99.95 | 99.68 | 100.02 | 99.02 | 99.48 | 99.76 | 100.01 | 99.49 |
| Mg# | 0.81 | 0.80 | 0.79 | 0.80 | 0.79 | 0.78 | 0.81 | 0.80 | 0.79 | 0.77 |
| Wo | 43.57 | 43.12 | 43.23 | 43.59 | 43.73 | 42.82 | 44.03 | 43.53 | 43.59 | 44.99 |
| En | 45.56 | 45.29 | 44.88 | 44.78 | 44.40 | 44.50 | 45.13 | 45.21 | 44.06 | 42.30 |
| Fs | 10.87 | 11.59 | 11.89 | 11.63 | 11.88 | 12.67 | 10.83 | 11.26 | 12.35 | 12.71 |

The Method Detection Limit (MDL) for the routine analysis of common elements is ~0.02 wt.%

***Supplementary Table 9.*** *Continued*

| Sample | Cpx 61 | Cpx 62 | Cpx 63 | Cpx 64 | Cpx 65 | Cpx 66 | Cpx 67 | Cpx 68 | Cpx 69 | Cpx 70 |
|---|---|---|---|---|---|---|---|---|---|---|
| Unit | Lamp | Lamp | Lamp | Lamp | Lamp | Lamp | Lamp | Lamp | Lamp | Lamp |
| Type | Mnt | Mnt | Mnt | Mnt | Mnt | Mnt | Micr-dt | Micr-dt | Micr-dt | Krs |
| $SiO_2$ | 53.38 | 51.95 | 52.37 | 51.10 | 51.46 | 52.45 | 49.61 | 47.03 | 48.37 | 50.88 |
| $TiO_2$ | 0.67 | 0.85 | 0.96 | 1.50 | 1.31 | 0.80 | 1.22 | 1.82 | 1.91 | 0.65 |
| $Al_2O_3$ | 1.36 | 1.78 | 2.16 | 3.44 | 3.20 | 1.57 | 3.52 | 4.83 | 5.11 | 4.61 |
| FeO | 7.40 | 7.90 | 7.62 | 7.63 | 7.70 | 8.37 | 7.78 | 7.65 | 8.61 | 6.24 |
| $Cr_2O_3$ | 0.44 | 0.40 | 0.37 | 0.30 | 0.19 | 0.17 | 0.25 | 0.13 | 0.07 | 0.90 |
| NiO | < MDL | < MDL | 0.02 | 0.05 | < MDL | < MDL | < MDL | 0.03 | 0.03 | 0.01 |
| MnO | 0.18 | 0.19 | 0.26 | 0.20 | 0.23 | 0.30 | 0.21 | 0.15 | 0.20 | 0.18 |
| MgO | 16.64 | 16.46 | 15.71 | 14.56 | 14.53 | 16.09 | 14.84 | 13.36 | 13.47 | 16.15 |
| CaO | 19.70 | 19.36 | 20.55 | 20.87 | 21.24 | 19.78 | 20.87 | 20.47 | 21.10 | 19.51 |
| $Na_2O$ | 0.15 | 0.15 | 0.16 | 0.24 | 0.20 | 0.16 | 0.39 | 0.38 | 0.48 | 0.57 |
| $K_2O$ | < MDL | < MDL | < MDL | < MDL | < MDL | < MDL | 0.01 | 0.01 | 0.01 | < MDL |
| Total | 99.94 | 99.03 | 100.17 | 99.90 | 100.07 | 99.69 | 98.72 | 95.86 | 99.38 | 99.72 |
| Mg# | 0.80 | 0.79 | 0.79 | 0.77 | 0.77 | 0.77 | 0.77 | 0.76 | 0.74 | 0.82 |
| Wo | 40.40 | 39.85 | 42.32 | 44.18 | 44.58 | 40.42 | 43.69 | 45.34 | 45.16 | 41.51 |
| En | 47.46 | 47.15 | 45.01 | 42.87 | 42.43 | 45.74 | 43.24 | 41.17 | 40.11 | 47.83 |
| Fs | 12.14 | 13.00 | 12.67 | 12.95 | 12.99 | 13.83 | 13.07 | 13.49 | 14.72 | 10.67 |

The Method Detection Limit (MDL) for the routine analysis of common elements is ~0.02 wt.%

***Supplementary Table 9.*** *Continued*

| Sample | Cpx 71 | Cpx 72 | Cpx 73 | Cpx 74 | Cpx 75 | Cpx 76 | Cpx 77 | Cpx 78 | Cpx 79 | Cpx 80 |
|---|---|---|---|---|---|---|---|---|---|---|
| Unit | Lamp | Lamp | Lamp | Lamp | Lamp | Lamp | Lamp | Lamp | Lamp | Lamp |
| Type | Krs | Krs | Krs | Krs | Krs | Krs | Krs | Krs | Krs | Krs |
| $SiO_2$ | 51.03 | 50.98 | 51.08 | 50.88 | 51.29 | 50.55 | 49.89 | 51.31 | 50.98 | 50.17 |
| $TiO_2$ | 0.58 | 0.57 | 0.71 | 0.58 | 0.69 | 0.67 | 0.80 | 0.67 | 0.72 | 0.72 |
| $Al_2O_3$ | 4.16 | 4.11 | 4.81 | 4.27 | 4.90 | 4.62 | 5.42 | 4.71 | 4.47 | 5.28 |
| FeO | 5.97 | 6.57 | 6.26 | 5.95 | 6.74 | 6.46 | 6.85 | 6.52 | 6.15 | 6.69 |
| $Cr_2O_3$ | 0.81 | 0.74 | 0.74 | 0.73 | 0.72 | 0.65 | 0.64 | 0.64 | 0.63 | 0.62 |
| NiO | < MDL | 0.03 | < MDL | 0.03 | 0.04 | < MDL | < MDL | < MDL | < MDL | < MDL |
| MnO | 0.13 | 0.17 | 0.20 | 0.14 | 0.16 | 0.18 | 0.15 | 0.15 | 0.13 | 0.14 |
| MgO | 16.10 | 16.86 | 15.95 | 16.25 | 16.53 | 15.84 | 15.24 | 15.87 | 15.92 | 15.61 |
| CaO | 20.20 | 18.61 | 19.13 | 20.22 | 18.05 | 19.97 | 19.95 | 19.32 | 19.89 | 19.83 |
| $Na_2O$ | 0.52 | 0.56 | 0.55 | 0.49 | 0.57 | 0.53 | 0.59 | 0.55 | 0.46 | 0.57 |
| $K_2O$ | < MDL | < MDL | 0.01 | 0.01 | 0.02 | < MDL | < MDL | 0.01 | < MDL | 0.01 |
| Total | 99.50 | 99.19 | 99.44 | 99.54 | 99.72 | 99.49 | 99.51 | 99.75 | 99.37 | 99.63 |
| Mg# | 0.83 | 0.82 | 0.82 | 0.83 | 0.81 | 0.81 | 0.80 | 0.81 | 0.82 | 0.81 |
| Wo | 42.65 | 39.32 | 41.27 | 42.50 | 38.87 | 42.32 | 42.80 | 41.46 | 42.37 | 42.30 |
| En | 47.30 | 49.57 | 47.86 | 47.51 | 49.52 | 46.69 | 45.49 | 47.37 | 47.19 | 46.32 |
| Fs | 10.05 | 11.11 | 10.87 | 9.99 | 11.61 | 10.99 | 11.72 | 11.17 | 10.44 | 11.37 |

The Method Detection Limit (MDL) for the routine analysis of common elements is ~0.02 wt.%

***Supplementary Table 9.*** *Continued*

| Sample | Cpx 81 | Cpx 82 | Cpx 83 | Cpx 84 | Cpx 85 | Cpx 86 | Cpx 87 | Cpx 88 | Cpx 89 |
|---|---|---|---|---|---|---|---|---|---|
| Unit | Lamp | Lamp | Lamp | Lamp | Lamp | Lamp | Lamp | Lamp | Lamp |
| Type | Krs | Krs | Krs | Krs | Krs | Krs | Krs | Krs | Krs |
| $SiO_2$ | 50.46 | 49.91 | 49.00 | 51.56 | 52.22 | 50.05 | 49.33 | 50.77 | 52.89 |
| $TiO_2$ | 0.72 | 0.79 | 1.03 | 0.51 | 0.44 | 0.74 | 1.09 | 0.70 | 0.42 |
| $Al_2O_3$ | 4.98 | 5.37 | 6.60 | 3.91 | 2.90 | 5.49 | 7.11 | 4.85 | 2.84 |
| FeO | 6.62 | 6.85 | 7.56 | 6.83 | 6.65 | 7.04 | 8.22 | 7.55 | 6.93 |
| $Cr_2O_3$ | 0.61 | 0.61 | 0.54 | 0.50 | 0.47 | 0.44 | 0.40 | 0.31 | 0.24 |
| NiO | < MDL | < MDL | < MDL | < MDL | < MDL | < MDL | < MDL | 0.01 | < MDL |
| MnO | 0.20 | 0.15 | 0.22 | 0.19 | 0.14 | 0.17 | 0.19 | 0.18 | 0.19 |
| MgO | 15.99 | 15.47 | 14.99 | 16.74 | 17.51 | 15.42 | 14.06 | 16.00 | 17.31 |
| CaO | 19.84 | 19.41 | 18.76 | 19.15 | 18.55 | 19.54 | 18.57 | 18.77 | 18.58 |
| $Na_2O$ | 0.56 | 0.58 | 0.67 | 0.51 | 0.43 | 0.62 | 0.67 | 0.58 | 0.39 |
| $K_2O$ | < MDL | < MDL | < MDL | < MDL | < MDL | < MDL | < MDL | < MDL | < MDL |
| Total | 99.99 | 99.13 | 99.37 | 99.90 | 99.30 | 99.52 | 99.65 | 99.72 | 99.80 |
| Mg# | 0.81 | 0.80 | 0.78 | 0.81 | 0.82 | 0.80 | 0.75 | 0.79 | 0.82 |
| Wo | 41.84 | 41.83 | 41.06 | 39.97 | 38.47 | 41.91 | 41.54 | 39.87 | 38.52 |
| En | 46.92 | 46.40 | 45.65 | 48.59 | 50.53 | 46.01 | 43.77 | 47.30 | 49.95 |
| Fs | 11.24 | 11.77 | 13.29 | 11.44 | 11.00 | 12.08 | 14.69 | 12.83 | 11.53 |

The Method Detection Limit (MDL) for the routine analysis of common elements is ~0.02 wt.%

***Supplementary Table 10.*** *Electron microprobe analyses of amphibole from the Sierra Bermeja Pluton*

| Sample | Amp 1 | Amp 2 | Amp 3 | Amp 4 | Amp 5 | Amp 6 | Amp 7 | Amp 8 | Amp 9 | Amp 10 |
|---|---|---|---|---|---|---|---|---|---|---|
| Unit | Vaugn | Vaugn | Vaugn | Vaugn | Vaugn | Vaugn | Vaugn | Vaugn | Vaugn | Vaugn |
| Type | Bt-rich | Bt-poor | Bt-poor | Bt-poor | Bt-poor | Bt-poor | Bt-poor | Bt-poor | Bt-poor | Bt-poor |
| $SiO_2$ | 40.45 | 40.35 | 40.15 | 40.20 | 40.73 | 40.43 | 40.24 | 40.72 | 40.94 | 40.08 |
| $TiO_2$ | 5.07 | 5.06 | 5.07 | 5.19 | 5.07 | 4.96 | 5.32 | 4.44 | 4.82 | 5.25 |
| $Al_2O_3$ | 11.52 | 11.70 | 11.78 | 11.95 | 11.51 | 11.84 | 11.87 | 11.44 | 11.08 | 11.90 |
| $Cr_2O_3$ | < MDL | 0.03 | 0.06 | 0.07 | 0.09 | 0.02 | 0.05 | 0.05 | 0.05 | 0.12 |
| NiO | 0.02 | 0.01 | < MDL | 0.02 | < MDL | < MDL | < MDL | < MDL | 0.04 | 0.02 |
| FeO | 13.83 | 12.43 | 12.33 | 11.76 | 11.50 | 12.44 | 11.65 | 13.59 | 12.89 | 11.25 |
| MnO | 0.19 | 0.20 | 0.16 | 0.14 | 0.17 | 0.21 | 0.12 | 0.20 | 0.20 | 0.13 |
| MgO | 10.94 | 12.62 | 12.57 | 12.81 | 13.20 | 12.51 | 12.88 | 11.92 | 12.32 | 12.82 |
| CaO | 11.77 | 11.75 | 11.72 | 11.79 | 11.72 | 11.63 | 11.79 | 11.29 | 11.65 | 11.68 |
| $Na_2O$ | 2.58 | 2.31 | 2.27 | 2.28 | 2.31 | 2.32 | 2.33 | 2.32 | 2.07 | 2.13 |
| $K_2O$ | 1.11 | 1.18 | 1.25 | 1.27 | 1.27 | 1.22 | 1.21 | 1.25 | 1.12 | 1.21 |
| F | NA | NA | NA | NA | NA | NA | NA | NA | NA | NA |
| Cl | NA | NA | NA | NA | NA | NA | NA | NA | NA | NA |
| Total | 97.49 | 97.63 | 97.35 | 97.48 | 97.57 | 97.58 | 97.46 | 97.22 | 97.19 | 96.59 |

NA not analyzed

The Method Detection Limit (MDL) for the routine analysis of common elements is ~0.02 wt.%

***Supplementary Table 10.*** *Continued*

| Sample | Amp 11 | Amp 12 | Amp 13 | Amp 14 | Amp 15 | Amp 16 | Amp 17 | Amp 18 | Amp 19 | Amp 20 |
|---|---|---|---|---|---|---|---|---|---|---|
| Unit | Vaugn | Vaugn | Vaugn | Vaugn | Vaugn | Vaugn | Vaugn | Vaugn | Vaugn | Vaugn |
| Type | Bt-poor | Bt-poor | Bt-poor | Bt-poor | Bt-poor | Bt-poor | Bt-poor | Bt-poor | Bt-poor | Bt-poor |
| $SiO_2$ | 40.16 | 40.35 | 40.42 | 40.35 | 40.37 | 40.25 | 40.99 | 40.56 | 40.46 | 40.40 |
| $TiO_2$ | 4.91 | 5.21 | 5.10 | 4.96 | 4.90 | 5.25 | 3.99 | 5.19 | 4.79 | 5.07 |
| $Al_2O_3$ | 11.55 | 11.91 | 11.54 | 11.59 | 11.57 | 11.91 | 11.25 | 11.75 | 11.56 | 11.68 |
| $Cr_2O_3$ | 0.02 | 0.08 | 0.01 | 0.08 | 0.08 | 0.10 | < MDL | 0.09 | 0.07 | 0.09 |
| NiO | 0.01 | < MDL | 0.04 | 0.02 | < MDL | < MDL | 0.01 | < MDL | 0.02 | 0.02 |
| FeO | 12.14 | 11.95 | 12.16 | 12.46 | 12.17 | 11.87 | 14.19 | 12.03 | 12.72 | 11.67 |
| MnO | 0.16 | 0.15 | 0.18 | 0.13 | 0.14 | 0.12 | 0.20 | 0.16 | 0.18 | 0.13 |
| MgO | 12.45 | 12.74 | 12.65 | 12.38 | 12.55 | 12.81 | 11.62 | 12.71 | 12.38 | 12.62 |
| CaO | 11.58 | 11.59 | 11.54 | 11.64 | 11.56 | 11.67 | 11.13 | 11.71 | 11.42 | 11.62 |
| $Na_2O$ | 2.32 | 2.29 | 2.30 | 2.23 | 2.29 | 2.27 | 2.30 | 2.31 | 2.31 | 2.21 |
| $K_2O$ | 1.16 | 1.25 | 1.21 | 1.16 | 1.23 | 1.23 | 1.16 | 1.20 | 1.21 | 1.18 |
| F | NA | NA | NA | NA | NA | NA | NA | NA | NA | NA |
| Cl | NA | NA | NA | NA | NA | NA | NA | NA | NA | NA |
| Total | 96.45 | 97.52 | 97.14 | 96.98 | 96.85 | 97.47 | 96.85 | 97.71 | 97.13 | 96.68 |

NA not analyzed

The Method Detection Limit (MDL) for the routine analysis of common elements is ~0.02 wt.%

***Supplementary Table 10.*** *Continued*

| Sample | Amp 21 | Amp 22 | Amp 23 | Amp 24 | Amp 25 | Amp 26 | Amp 27 | Amp 28 | Amp 29 | Amp 30 |
|---|---|---|---|---|---|---|---|---|---|---|
| Unit | Vaugn | Vaugn | Vaugn | Vaugn | Vaugn | Vaugn | Vaugn | Vaugn | Vaugn | Vaugn |
| Type | Bt-poor | Bt-poor | Bt-poor | Bt-poor | Bt-poor | Bt-poor | Bt-poor | Bt-poor | Bt-poor | Bt-poor |
| $SiO_2$ | 49.27 | 41.11 | 39.72 | 39.63 | 40.60 | 40.55 | 39.92 | 41.28 | 41.11 | 41.32 |
| $TiO_2$ | 0.68 | 4.08 | 5.00 | 4.98 | 4.28 | 4.53 | 5.14 | 4.19 | 4.08 | 3.83 |
| $Al_2O_3$ | 3.54 | 11.12 | 12.12 | 12.28 | 11.46 | 11.46 | 12.15 | 11.09 | 11.01 | 10.76 |
| $Cr_2O_3$ | < MDL | 0.02 | 0.01 | 0.03 | 0.01 | 0.01 | 0.05 | < MDL | 0.04 | 0.01 |
| NiO | 0.04 | < MDL | < MDL | < MDL | < MDL | < MDL | < MDL | 0.03 | < MDL | 0.08 |
| FeO | 17.94 | 14.02 | 13.46 | 13.41 | 13.26 | 13.01 | 12.89 | 13.88 | 13.99 | 15.23 |
| MnO | 0.47 | 0.27 | 0.17 | 0.15 | 0.23 | 0.18 | 0.18 | 0.21 | 0.15 | 0.25 |
| MgO | 12.10 | 11.82 | 11.88 | 11.78 | 12.09 | 12.25 | 12.00 | 11.97 | 11.71 | 11.26 |
| CaO | 11.55 | 11.16 | 11.35 | 11.50 | 11.43 | 11.54 | 11.39 | 11.21 | 11.25 | 10.87 |
| $Na_2O$ | 1.01 | 2.34 | 2.38 | 2.33 | 2.30 | 2.38 | 2.32 | 2.42 | 2.30 | 2.36 |
| $K_2O$ | 0.28 | 1.19 | 1.18 | 1.23 | 1.26 | 1.27 | 1.21 | 1.16 | 1.26 | 1.10 |
| F | NA | NA | NA | NA | NA | NA | NA | NA | NA | NA |
| Cl | NA | NA | NA | NA | NA | NA | NA | NA | NA | NA |
| Total | 96.90 | 97.13 | 97.27 | 97.33 | 96.91 | 97.17 | 97.25 | 97.45 | 96.90 | 97.08 |

NA not analyzed

The Method Detection Limit (MDL) for the routine analysis of common elements is ~0.02 wt.%

***Supplementary Table 10.*** *Continued*

| Sample | Amp 31 | Amp 32 | Amp 33 | Amp 34 | Amp 35 | Amp 36 | Amp 37 | Amp 38 | Amp 39 | Amp 40 |
|---|---|---|---|---|---|---|---|---|---|---|
| Unit | Vaugn | Vaugn | Vaugn | Vaugn | Lamp | Lamp | Lamp | Lamp | Lamp | Lamp |
| Type | Bt-poor | Bt-poor | Bt-poor | Bt-poor | Micr-dt | Micr-dt | Micr-dt | Micr-dt | Micr-dt | Micr-dt |
| $SiO_2$ | 40.11 | 40.84 | 45.16 | 45.11 | 39.49 | 39.16 | 39.43 | 39.23 | 39.07 | 40.66 |
| $TiO_2$ | 4.69 | 4.10 | 1.02 | 2.16 | 5.04 | 5.41 | 4.62 | 5.29 | 4.95 | 3.41 |
| $Al_2O_3$ | 11.80 | 11.17 | 8.08 | 6.86 | 12.23 | 12.08 | 12.23 | 12.26 | 11.84 | 11.96 |
| $Cr_2O_3$ | < MDL | < MDL | < MDL | 0.08 | 0.01 | 0.03 | 0.02 | 0.01 | < MDL | < MDL |
| NiO | 0.01 | < MDL | < MDL | < MDL | 0.01 | < MDL | < MDL | 0.03 | < MDL | < MDL |
| FeO | 12.92 | 13.86 | 15.46 | 17.64 | 12.68 | 11.84 | 12.40 | 11.77 | 14.96 | 11.53 |
| MnO | 0.17 | 0.24 | 0.33 | 0.46 | 0.16 | 0.16 | 0.18 | 0.16 | 0.20 | 0.20 |
| MgO | 12.32 | 11.95 | 13.31 | 11.01 | 12.49 | 12.50 | 12.32 | 12.61 | 10.37 | 13.29 |
| CaO | 11.54 | 11.23 | 10.85 | 10.79 | 11.27 | 11.21 | 11.52 | 11.41 | 11.25 | 11.68 |
| $Na_2O$ | 2.34 | 2.38 | 2.04 | 1.81 | 2.33 | 2.23 | 2.30 | 2.33 | 2.30 | 2.35 |
| $K_2O$ | 1.21 | 1.20 | 0.87 | 0.76 | 1.23 | 1.20 | 1.20 | 1.06 | 1.28 | 0.97 |
| F | NA | NA | NA | NA | 0.14 | 0.23 | 0.19 | 0.17 | 0.13 | 0.21 |
| Cl | NA | NA | NA | NA | 0.03 | 0.02 | 0.04 | 0.02 | 0.02 | 0.04 |
| Total | 97.10 | 96.96 | 97.13 | 96.68 | 97.11 | 96.06 | 96.46 | 96.36 | 96.37 | 96.29 |

NA not analyzed

The Method Detection Limit (MDL) for the routine analysis of common elements is ~0.02 wt.%

***Supplementary Table 10.*** *Continued*

| Sample | Amp 41 | Amp 42 | Amp 43 | Amp 44 | Amp 45 | Amp 46 | Amp 47 | Amp 48 | Amp 49 | Amp 50 |
|---|---|---|---|---|---|---|---|---|---|---|
| Unit | Lamp | Lamp | Lamp | Lamp | Lamp | Lamp | Lamp | Lamp | Lamp | Lamp |
| Type | Micr-dt | Micr-dt | Krs | Krs | Krs | Krs | Krs | Krs | Krs | Krs |
| $SiO_2$ | 39.27 | 40.09 | 39.34 | 39.83 | 39.91 | 40.38 | 40.05 | 40.31 | 41.54 | 42.21 |
| $TiO_2$ | 4.29 | 3.97 | 4.60 | 4.37 | 4.13 | 4.37 | 3.71 | 4.01 | 3.82 | 3.25 |
| $Al_2O_3$ | 11.70 | 11.44 | 12.96 | 13.54 | 13.24 | 13.20 | 12.24 | 12.48 | 11.60 | 10.69 |
| $Cr_2O_3$ | 0.02 | 0.01 | 0.01 | 0.01 | < MDL | < MDL | < MDL | < MDL | < MDL | < MDL |
| NiO | < MDL | 0.04 | < MDL | 0.01 | < MDL | 0.04 | < MDL | < MDL | < MDL | 0.01 |
| FeO | 14.69 | 14.28 | 11.95 | 10.23 | 11.67 | 10.06 | 13.21 | 11.30 | 11.02 | 13.09 |
| MnO | 0.25 | 0.26 | 0.16 | 0.14 | 0.09 | 0.11 | 0.13 | 0.11 | 0.14 | 0.15 |
| MgO | 11.27 | 11.45 | 12.35 | 13.52 | 13.03 | 13.98 | 12.39 | 13.60 | 14.36 | 13.09 |
| CaO | 10.81 | 11.28 | 11.26 | 11.52 | 11.42 | 11.64 | 11.41 | 11.32 | 11.51 | 11.47 |
| $Na_2O$ | 2.26 | 2.27 | 2.07 | 1.97 | 1.96 | 2.00 | 2.06 | 2.06 | 2.07 | 1.76 |
| $K_2O$ | 1.07 | 1.09 | 1.47 | 1.64 | 1.61 | 1.60 | 1.34 | 1.45 | 1.32 | 1.08 |
| F | 0.18 | 0.04 | 0.18 | 0.21 | 0.13 | 0.17 | 0.15 | 0.38 | 0.13 | 0.10 |
| Cl | 0.04 | 0.06 | 0.04 | 0.05 | 0.04 | 0.04 | 0.06 | 0.03 | 0.04 | 0.06 |
| Total | 95.84 | 96.28 | 96.40 | 97.06 | 97.24 | 97.60 | 96.75 | 97.06 | 97.56 | 96.97 |

NA not analyzed

The Method Detection Limit (MDL) for the routine analysis of common elements is ~0.02 wt.%

***Supplementary Table 11.*** *U–Pb isotope data (LA-ICP-MS) of apatites from the Sierra Bermeja Pluton*

| Spot name | Data for Wetherill plot | | | | | Elemental concentration (µg g-1) | | |
|---|---|---|---|---|---|---|---|---|
| | $^{207}Pb/^{235}U$ | 2s (abs) | $^{206}Pb/^{238}U$ | 2s (abs) | Rho | U | Th | Pb |
| Ap 1 | 18.8 | 1.1 | 0.463 | 0.025 | 0.87 | 1.9 | 7.9 | 1.8 |
| Ap 2 | 5.9 | 0.2 | 0.171 | 0.004 | 0.15 | 5.5 | 23.9 | 1.7 |
| Ap 3 | 9.6 | 0.6 | 0.256 | 0.016 | 0.93 | 5.4 | 23.7 | 2.7 |
| Ap 4 | 6.0 | 0.2 | 0.171 | 0.006 | 0.85 | 8.7 | 38.7 | 2.9 |
| Ap 5 | 8.2 | 0.3 | 0.228 | 0.007 | 0.79 | 7.9 | 57.9 | 3.7 |
| Ap 6 | 9.3 | 0.5 | 0.254 | 0.012 | 0.69 | 7.1 | 24.2 | 2.9 |
| Ap 7 | 17.2 | 0.6 | 0.424 | 0.014 | 0.90 | 7.7 | 30.9 | 7.0 |
| Ap 8 | 17.1 | 0.6 | 0.423 | 0.015 | 0.86 | 5.2 | 23.5 | 4.7 |
| Ap 9 | 7.2 | 0.4 | 0.204 | 0.010 | 0.97 | 5.8 | 24.5 | 2.4 |
| Ap 10 | 16.5 | 0.9 | 0.415 | 0.021 | 0.90 | 4.8 | 20.5 | 4.4 |
| Ap 11 | 4.0 | 0.2 | 0.133 | 0.009 | 0.43 | 6.4 | 21.2 | 1.2 |
| Ap 12 | 14.4 | 0.4 | 0.353 | 0.010 | 0.59 | 2.9 | 12.7 | 2.1 |
| Ap 13 | 26.9 | 1.1 | 0.617 | 0.021 | 0.85 | 7.6 | 31.9 | 9.9 |
| Ap 14 | 11.6 | 0.5 | 0.305 | 0.012 | 0.73 | 4.8 | 21.0 | 3.1 |
| Ap 15 | 7.4 | 0.5 | 0.217 | 0.014 | 0.72 | 6.2 | 22.3 | 2.1 |
| Ap 16 | 6.2 | 0.2 | 0.179 | 0.006 | 0.21 | 9.4 | 39.9 | 3.1 |
| Ap 17 | 10.0 | 0.3 | 0.263 | 0.007 | 0.58 | 4.4 | 19.0 | 2.4 |
| Ap 18 | 6.8 | 0.4 | 0.198 | 0.009 | 0.31 | 4.9 | 20.6 | 1.7 |
| Ap 19 | 9.3 | 0.5 | 0.242 | 0.010 | 0.53 | 0.8 | 3.0 | 0.4 |
| Ap 20 | 7.5 | 0.2 | 0.211 | 0.007 | 0.45 | 0.7 | 2.5 | 0.2 |
| Ap 21 | 16.1 | 1.0 | 0.389 | 0.021 | 0.88 | 0.7 | 2.6 | 0.5 |
| Ap 22 | 7.3 | 0.3 | 0.199 | 0.006 | 0.58 | 1.0 | 4.0 | 0.4 |
| Ap 23 | 7.8 | 0.5 | 0.205 | 0.009 | 0.36 | 0.5 | 1.7 | 0.2 |
| Ap 24 | 6.8 | 0.2 | 0.192 | 0.006 | 0.22 | 1.5 | 5.8 | 0.5 |
| Ap 25 | 9.1 | 0.5 | 0.246 | 0.012 | 0.69 | 1.5 | 6.2 | 0.6 |
| Ap 26 | 6.6 | 0.2 | 0.189 | 0.006 | 0.42 | 0.9 | 3.6 | 0.3 |
| Ap 27 | 7.9 | 0.3 | 0.212 | 0.006 | 0.47 | 1.0 | 3.3 | 0.4 |
| Ap 28 | 3.9 | 0.3 | 0.121 | 0.006 | 0.75 | 1.2 | 3.2 | 0.2 |
| Ap 29 | 5.4 | 0.2 | 0.163 | 0.005 | 0.54 | 1.0 | 3.5 | 0.2 |
| Ap 30a | 4.7 | 0.2 | 0.144 | 0.006 | 0.41 | 1.1 | 3.7 | 0.2 |
| Ap 30b | 5.6 | 0.3 | 0.164 | 0.008 | 0.26 | 0.9 | 3.3 | 0.3 |
| Ap 31 | 5.5 | 0.2 | 0.151 | 0.005 | 0.15 | 1.1 | 4.9 | 0.3 |
| Ap 32 | 8.0 | 0.4 | 0.225 | 0.008 | 0.71 | 1.6 | 5.2 | 0.6 |
| Ap 33 | 5.3 | 0.2 | 0.157 | 0.005 | 0.57 | 1.2 | 3.8 | 0.3 |
| Ap 34 | 6.3 | 0.2 | 0.188 | 0.006 | 0.56 | 0.9 | 3.0 | 0.3 |
| Ap 35 | 5.7 | 0.2 | 0.169 | 0.005 | 0.40 | 1.2 | 4.7 | 0.4 |
| Ap 36a | 8.1 | 0.4 | 0.224 | 0.009 | 0.65 | 1.1 | 4.2 | 0.4 |
| Ap 36b | 9.8 | 0.5 | 0.257 | 0.010 | 0.83 | 1.2 | 4.9 | 0.6 |
| Ap 37 | 6.0 | 0.2 | 0.173 | 0.006 | 0.28 | 0.9 | 3.6 | 0.3 |
| Ap 38 | 4.8 | 0.2 | 0.155 | 0.005 | 0.21 | 1.2 | 4.9 | 0.3 |
| Ap 39 | 5.2 | 0.2 | 0.169 | 0.006 | 0.29 | 0.8 | 3.2 | 0.2 |
| Ap 40 | 6.6 | 0.4 | 0.199 | 0.011 | 0.70 | 0.7 | 2.8 | 0.2 |
| Ap 41 | 3.8 | 0.2 | 0.120 | 0.004 | 0.46 | 0.8 | 2.9 | 0.2 |

***Supplementary Table 11.*** *Continued*

| Spot name | Data for Tera-Wasserburg plot | | | | |
|---|---|---|---|---|---|
| | $^{238}U/^{206}Pb$ | 2s (abs) | $^{207}Pb/^{206}Pb$ | 2s (abs) | Rho |
| Ap 1 | 2.16 | 0.12 | 0.293 | 0.009 | 0.05 |
| Ap 2 | 5.87 | 0.13 | 0.252 | 0.006 | 0.18 |
| Ap 3 | 3.91 | 0.24 | 0.265 | 0.006 | -0.07 |
| Ap 4 | 5.86 | 0.19 | 0.251 | 0.005 | 0.09 |
| Ap 5 | 4.38 | 0.14 | 0.260 | 0.005 | 0.31 |
| Ap 6 | 3.94 | 0.19 | 0.273 | 0.010 | 0.29 |
| Ap 7 | 2.36 | 0.08 | 0.287 | 0.005 | 0.05 |
| Ap 8 | 2.36 | 0.08 | 0.285 | 0.005 | 0.23 |
| Ap 9 | 4.91 | 0.23 | 0.254 | 0.005 | -0.03 |
| Ap 10 | 2.41 | 0.12 | 0.281 | 0.006 | 0.18 |
| Ap 11 | 7.50 | 0.49 | 0.227 | 0.019 | 0.52 |
| Ap 12 | 2.83 | 0.08 | 0.291 | 0.008 | 0.36 |
| Ap 13 | 1.62 | 0.06 | 0.301 | 0.004 | 0.04 |
| Ap 14 | 3.28 | 0.13 | 0.273 | 0.008 | 0.29 |
| Ap 15 | 4.61 | 0.30 | 0.254 | 0.012 | 0.36 |
| Ap 16 | 5.57 | 0.17 | 0.249 | 0.009 | 0.28 |
| Ap 17 | 3.80 | 0.09 | 0.268 | 0.007 | 0.26 |
| Ap 18 | 5.06 | 0.24 | 0.250 | 0.010 | 0.23 |
| Ap 19 | 4.13 | 0.17 | 0.285 | 0.010 | 0.03 |
| Ap 20 | 4.75 | 0.16 | 0.271 | 0.009 | 0.58 |
| Ap 21 | 2.57 | 0.14 | 0.304 | 0.009 | 0.04 |
| Ap 22 | 5.03 | 0.15 | 0.270 | 0.009 | 0.03 |
| Ap 23 | 4.87 | 0.21 | 0.277 | 0.016 | 0.27 |
| Ap 24 | 5.20 | 0.15 | 0.258 | 0.009 | 0.54 |
| Ap 25 | 4.07 | 0.20 | 0.267 | 0.011 | 0.26 |
| Ap 26 | 5.30 | 0.16 | 0.257 | 0.009 | 0.53 |
| Ap 27 | 4.71 | 0.14 | 0.271 | 0.009 | 0.42 |
| Ap 28 | 8.26 | 0.38 | 0.228 | 0.010 | -0.11 |
| Ap 29 | 6.13 | 0.18 | 0.248 | 0.008 | 0.33 |
| Ap 30a | 6.94 | 0.29 | 0.238 | 0.011 | 0.35 |
| Ap 30b | 6.11 | 0.28 | 0.249 | 0.015 | 0.52 |
| Ap 31 | 6.62 | 0.21 | 0.262 | 0.009 | 0.42 |
| Ap 32 | 4.45 | 0.16 | 0.262 | 0.009 | 0.16 |
| Ap 33 | 6.38 | 0.19 | 0.244 | 0.008 | 0.06 |
| Ap 34 | 5.32 | 0.18 | 0.249 | 0.008 | 0.41 |
| Ap 35 | 5.93 | 0.17 | 0.247 | 0.009 | 0.28 |
| Ap 36a | 4.46 | 0.18 | 0.266 | 0.010 | 0.25 |
| Ap 36b | 3.89 | 0.15 | 0.279 | 0.008 | 0.08 |
| Ap 37 | 5.80 | 0.21 | 0.262 | 0.011 | 0.49 |
| Ap 38 | 6.47 | 0.19 | 0.231 | 0.009 | 0.54 |
| Ap 39 | 5.92 | 0.19 | 0.238 | 0.010 | 0.61 |
| Ap 40 | 5.03 | 0.28 | 0.250 | 0.011 | 0.19 |
| Ap 41 | 8.31 | 0.30 | 0.233 | 0.008 | 0.39 |

***Supplementary Table 11.*** *Continued*

| Spot name | Data for Wetherill plot | | | | | Elemental concentration (µg g-1) | | |
|---|---|---|---|---|---|---|---|---|
| | $^{207}Pb/^{235}U$ | 2s (abs) | $^{206}Pb/^{238}U$ | 2s (abs) | Rho | U | Th | Pb |
| Ap 42 | 5.3 | 0.2 | 0.157 | 0.004 | 0.34 | 0.8 | 2.6 | 0.2 |
| Ap 43 | 22.6 | 0.7 | 0.544 | 0.016 | 0.56 | 1.1 | 4.4 | 1.2 |
| Ap 44 | 21.8 | 0.6 | 0.518 | 0.014 | 0.68 | 1.2 | 4.9 | 1.2 |
| Ap 45 | 15.5 | 0.7 | 0.391 | 0.017 | 0.75 | 0.5 | 1.9 | 0.4 |
| Ap 46 | 12.9 | 0.4 | 0.336 | 0.010 | 0.60 | 0.7 | 2.8 | 0.5 |
| Ap 47 | 10.7 | 0.8 | 0.273 | 0.018 | 0.05 | 0.6 | 2.2 | 0.3 |
| Ap 48 | 10.5 | 0.9 | 0.275 | 0.022 | 0.82 | 0.6 | 2.2 | 0.3 |
| Ap 49 | 8.0 | 0.3 | 0.222 | 0.008 | 0.50 | 0.7 | 2.9 | 0.2 |
| Ap 50 | 8.9 | 0.3 | 0.241 | 0.007 | 0.52 | 1.2 | 5.4 | 0.5 |
| Ap 51 | 6.4 | 0.2 | 0.178 | 0.005 | 0.16 | 1.4 | 5.2 | 0.4 |
| Ap 52 | 24.4 | 0.9 | 0.570 | 0.019 | 0.69 | 0.7 | 2.7 | 0.8 |
| Ap 53 | 5.5 | 0.2 | 0.161 | 0.004 | 0.46 | 1.3 | 4.0 | 0.3 |
| Ap 54 | 5.2 | 0.2 | 0.152 | 0.004 | 0.54 | 1.5 | 6.0 | 0.4 |
| Ap 55 | 3.7 | 0.1 | 0.119 | 0.003 | 0.12 | 1.3 | 4.9 | 0.2 |
| Ap 56a | 4.4 | 0.2 | 0.131 | 0.004 | 0.36 | 0.8 | 2.8 | 0.2 |
| Ap 56b | 6.1 | 0.3 | 0.167 | 0.007 | 0.69 | 0.8 | 2.6 | 0.2 |
| Ap 57 | 5.1 | 0.2 | 0.151 | 0.005 | 0.56 | 1.9 | 6.8 | 0.5 |
| Ap 58a | 4.0 | 0.1 | 0.124 | 0.003 | 0.28 | 1.3 | 4.3 | 0.3 |
| Ap 58b | 4.2 | 0.2 | 0.132 | 0.005 | 0.30 | 1.1 | 3.5 | 0.2 |
| Ap 59 | 4.6 | 0.4 | 0.140 | 0.009 | 0.47 | 1.8 | 5.6 | 0.4 |
| Ap 60a | 6.1 | 0.2 | 0.169 | 0.005 | 0.72 | 1.7 | 5.8 | 0.5 |
| Ap 60b | 5.0 | 0.2 | 0.147 | 0.005 | 0.65 | 1.7 | 6.1 | 0.4 |
| Ap 61a | 6.9 | 0.2 | 0.190 | 0.006 | 0.56 | 1.8 | 5.9 | 0.6 |
| Ap 61b | 6.6 | 0.3 | 0.184 | 0.008 | 0.85 | 2.1 | 7.1 | 0.7 |
| Ap 62 | 4.4 | 0.3 | 0.136 | 0.008 | 0.67 | 1.8 | 5.8 | 0.4 |
| Ap 63 | 4.8 | 0.2 | 0.142 | 0.005 | 0.29 | 0.7 | 2.2 | 0.2 |
| Ap 64 | 5.9 | 0.3 | 0.167 | 0.006 | 0.56 | 1.0 | 3.5 | 0.3 |
| Ap 65 | 9.4 | 0.6 | 0.254 | 0.014 | 0.53 | 0.9 | 3.6 | 0.4 |
| Ap 66a | 3.5 | 0.2 | 0.116 | 0.006 | 0.12 | 0.9 | 3.0 | 0.1 |
| Ap 66b | 3.1 | 0.2 | 0.107 | 0.004 | 0.32 | 0.9 | 3.0 | 0.1 |
| Ap 67 | 10.4 | 0.8 | 0.279 | 0.020 | 0.03 | 0.9 | 3.3 | 0.4 |
| Ap 68 | 16.6 | 0.9 | 0.409 | 0.022 | 0.55 | 0.6 | 2.5 | 0.5 |
| Ap 69a | 6.1 | 0.2 | 0.173 | 0.005 | 0.28 | 0.8 | 3.1 | 0.2 |
| Ap 69b | 4.9 | 0.3 | 0.146 | 0.007 | 0.68 | 0.7 | 2.8 | 0.2 |
| Ap 70a | 6.9 | 0.3 | 0.193 | 0.007 | 0.66 | 1.6 | 6.1 | 0.5 |
| Ap 70b | 7.6 | 0.8 | 0.208 | 0.016 | 0.68 | 2.1 | 6.5 | 0.6 |
| Ap 71 | 5.5 | 0.3 | 0.158 | 0.008 | 0.19 | 0.8 | 2.5 | 0.2 |
| Ap 72 | 4.0 | 0.2 | 0.131 | 0.005 | 0.43 | 0.6 | 2.2 | 0.1 |
| Ap 73 | 5.0 | 0.2 | 0.150 | 0.005 | 0.56 | 0.9 | 3.2 | 0.2 |
| Ap 74 | 9.7 | 0.4 | 0.249 | 0.009 | 0.58 | 2.4 | 7.1 | 1.0 |
| Ap 75 | 3.8 | 0.1 | 0.119 | 0.003 | 0.13 | 1.9 | 6.2 | 0.4 |
| Ap 76a | 5.1 | 0.2 | 0.151 | 0.004 | 0.48 | 0.9 | 3.0 | 0.2 |
| Ap 76b | 5.1 | 0.3 | 0.151 | 0.006 | 0.34 | 0.7 | 2.1 | 0.2 |
| Ap 77 | 4.1 | 0.1 | 0.129 | 0.003 | 0.27 | 1.7 | 5.4 | 0.4 |
| Ap 78 | 13.2 | 0.6 | 0.326 | 0.014 | 0.89 | 1.0 | 4.2 | 0.6 |

***Supplementary Table 11.*** *Continued*

| Spot name | Data for Tera-Wasserburg plot | | | | |
|---|---|---|---|---|---|
| | $^{238}U/^{206}Pb$ | 2s (abs) | $^{207}Pb/^{206}Pb$ | 2s (abs) | Rho |
| Ap 42 | 6.36 | 0.18 | 0.253 | 0.009 | 0.50 |
| Ap 43 | 1.84 | 0.05 | 0.308 | 0.007 | 0.34 |
| Ap 44 | 1.93 | 0.05 | 0.309 | 0.006 | 0.45 |
| Ap 45 | 2.56 | 0.11 | 0.296 | 0.009 | 0.12 |
| Ap 46 | 2.98 | 0.09 | 0.287 | 0.009 | 0.44 |
| Ap 47 | 3.66 | 0.24 | 0.296 | 0.020 | 0.06 |
| Ap 48 | 3.64 | 0.29 | 0.283 | 0.016 | 0.13 |
| Ap 49 | 4.50 | 0.15 | 0.268 | 0.009 | 0.40 |
| Ap 50 | 4.15 | 0.12 | 0.277 | 0.007 | 0.49 |
| Ap 51 | 5.62 | 0.15 | 0.270 | 0.008 | 0.51 |
| Ap 52 | 1.75 | 0.06 | 0.316 | 0.007 | 0.28 |
| Ap 53 | 6.21 | 0.16 | 0.254 | 0.007 | 0.46 |
| Ap 54 | 6.60 | 0.19 | 0.255 | 0.008 | 0.42 |
| Ap 55 | 8.42 | 0.24 | 0.226 | 0.009 | 0.65 |
| Ap 56a | 7.62 | 0.24 | 0.245 | 0.010 | 0.32 |
| Ap 56b | 5.98 | 0.23 | 0.265 | 0.009 | 0.30 |
| Ap 57 | 6.62 | 0.21 | 0.250 | 0.007 | 0.23 |
| Ap 58a | 8.08 | 0.22 | 0.237 | 0.009 | 0.29 |
| Ap 58b | 7.58 | 0.30 | 0.239 | 0.013 | 0.48 |
| Ap 59 | 7.16 | 0.44 | 0.243 | 0.019 | 0.17 |
| Ap 60a | 5.93 | 0.17 | 0.263 | 0.006 | 0.23 |
| Ap 60b | 6.79 | 0.22 | 0.247 | 0.007 | 0.33 |
| Ap 61a | 5.26 | 0.15 | 0.265 | 0.007 | 0.40 |
| Ap 61b | 5.42 | 0.24 | 0.258 | 0.007 | 0.02 |
| Ap 62 | 7.35 | 0.43 | 0.239 | 0.014 | 0.16 |
| Ap 63 | 7.07 | 0.26 | 0.250 | 0.012 | 0.33 |
| Ap 64 | 5.98 | 0.22 | 0.255 | 0.009 | 0.21 |
| Ap 65 | 3.94 | 0.22 | 0.268 | 0.008 | 0.07 |
| Ap 66a | 8.60 | 0.47 | 0.219 | 0.017 | 0.53 |
| Ap 66b | 9.33 | 0.33 | 0.218 | 0.011 | 0.41 |
| Ap 67 | 3.58 | 0.26 | 0.278 | 0.021 | 0.18 |
| Ap 68 | 2.44 | 0.13 | 0.300 | 0.015 | 0.41 |
| Ap 69a | 5.78 | 0.15 | 0.257 | 0.010 | 0.52 |
| Ap 69b | 6.84 | 0.31 | 0.248 | 0.011 | 0.29 |
| Ap 70a | 5.19 | 0.18 | 0.261 | 0.007 | 0.25 |
| Ap 70b | 4.81 | 0.37 | 0.268 | 0.016 | -0.04 |
| Ap 71 | 6.34 | 0.34 | 0.257 | 0.015 | 0.36 |
| Ap 72 | 7.63 | 0.30 | 0.226 | 0.012 | 0.01 |
| Ap 73 | 6.68 | 0.24 | 0.242 | 0.009 | 0.27 |
| Ap 74 | 4.01 | 0.14 | 0.289 | 0.010 | 0.38 |
| Ap 75 | 8.41 | 0.20 | 0.231 | 0.008 | 0.60 |
| Ap 76a | 6.62 | 0.19 | 0.250 | 0.010 | -0.04 |
| Ap 76b | 6.61 | 0.26 | 0.255 | 0.015 | 0.47 |
| Ap 77 | 7.76 | 0.19 | 0.232 | 0.008 | 0.44 |
| Ap 78 | 3.07 | 0.13 | 0.300 | 0.007 | 0.18 |

***Supplementary Table 12.*** *Location of the samples. Coordinates in Universal Transverse Mercator (UTM), Zone 29N*

| Nº in Fig 15 (#) and Tables 16 and 17 | Lithotype | Sample | UTM X | UTM Y |
|---|---|---|---|---|
| 1 | Mzgr (OU) | JE 15 26 | 744541 | 4326147 |
| 2 | Mzgr (OU) | JE 15 62 | 745497 | 4325842 |
| 3 | Mzgr (OU) | JE 15 68 | 742169 | 4322868 |
| 4 | Mzgr (OU) | JE 15 34 | 737743 | 4331143 |
| 5 | Mzgr (OU) | JE 15 35 | 738124 | 4330015 |
| 6 | Mzgr (OU) | JE 15 36 | 740387 | 4329223 |
| 7 | Mzgr (OU) | JE 15 38 | 738974 | 4330248 |
| 8 | Mzgr (OU) | JE 15 48 | 738874 | 4325065 |
| 9 | Mzgr (OU) | JE 15 60 | 732407 | 4327558 |
| 10 | Mzgr (OU) | SB 169 | 744420 | 4322738 |
| 11 | Mzgr (MU) | JE 15 30 | 745355 | 4324029 |
| 12 | Mzgr (MU) | JE 15 57 | 737554 | 4325752 |
| 13 | Mzgr (MU) | JE 16 23 | 743749 | 4324242 |
| 14 | Mzgr (MU) | JE 16 44 | 735392 | 4326569 |
| 15 | Mzgr (MU) | JE 15 04 | 738267 | 4326251 |
| 16 | Mzgr (MU) | JE 15 53 | 738784 | 4329086 |
| 17 | Mzgr (MU) | JE 15 56 | 740122 | 4324756 |
| 18 | Mzgr (MU) | JE 15 59 | 733946 | 4326935 |
| 19 | Mzgr (MU) | JE 15 65 | 742115 | 4327371 |
| 20 | Mzgr (MU) | JE 15 67 | 741863 | 4324895 |
| 21 | Mzgr (MU) | SB 160 | 737382 | 4327278 |
| 22 | Mzgr (MU) | SB 166 | 738433 | 4325769 |
| 23 | Mzgr (MU) | SB 171 | 745410 | 4324269 |
| 24 | Mzgr (MU) | SB 176 | 740589 | 4327073 |
| 25 | Mzgr (MU) | SB 179 | 740387 | 4325552 |
| 26 | Mzgr (IU) | JE 16 45 | 743934 | 4324996 |
| 27 | Mzgr (IU) | JE 15 28 | 734226 | 4328038 |
| 28 | Mzgr (IU) | JE 15 45 | 740107 | 4327089 |
| 29 | Mzgr (IU) | JE 15 51 | 738852 | 4327988 |
| 30 | Mzgr (IU) | JE 15 64 | 737868 | 4328334 |
| 31 | Mzgr (IU) | JE 15 66 | 742138 | 4325621 |
| 32 | Mzgr (IU) | SB 162 | 737536 | 4327690 |
| 33 | Mzgr (IU) | SB 180 | 735875 | 4328707 |
| 34 | Mzgr (IU) | SB 184 | 736439 | 4328590 |
| 35 | Mzgr (IU) | SB 186 | 737471 | 4328239 |
| 36 | MME | JE 15 01 | 744389 | 4322786 |
| 37 | MME | JE 16 30 | 745525 | 4323275 |
| 38 | MME | JE 16 33 | 745380 | 4323558 |
| 39 | Vaugneritic rock | JE 15 41 | 739195 | 4329241 |
| 40 | Vaugneritic rock | JE 16 03 | 737796 | 4327569 |
| 41 | Vaugneritic rock | JE 16 06 | 738848 | 4328912 |
| 42 | Vaugneritic rock | JE 16 41 | 737619 | 4327169 |
| 43 | Vaugneritic rock | JE 17 03 | 737660 | 4327333 |
| 44 | Micro-dt | JE 15 40 | 739433 | 4329438 |
| 45 | Vaugneritic rock | JE 16 42 | 738601 | 4328591 |
| 46 | Lamp (minette) | JE 15 22 | 741133 | 4327176 |
| 47 | Lamp (kersantite) | JE 15 39 | 738956 | 4329715 |
| 48 | Lamp (kersantite) | JE 15 70 | 743069 | 4326485 |
| 49 | Lamp (kersantite) | JE 16 12 | 740800 | 4326748 |
| 50 | Lamp (kersantite) | JE 16 18 | 743902 | 4324799 |
| 51 | Lamp (kersantite) | JE 16 24 | 742764 | 4324661 |
| 52 | Lamp (kersantite) | JE 16 38 | 742425 | 4323984 |
| 53 | Lamp (kersantite) | JE 16 43 | 740857 | 4327494 |

*Mzgr (Monzogranite); Micro-dt (micro-diorite); Lamp (lamprophyre); MME (mafic microgranular enclave)

***Supplementary Table 13.*** *Whole-rock termobarometric data for the Sierra Bermeja Pluton monzogranites*

| Sample name | Unit | TºC (Al/Ti) | | | TºC saturation | | | | |
|---|---|---|---|---|---|---|---|---|---|
| | | Psamite | Metaigneous | Pelite | Zrn | Mnz | Ap* | Ap** | Ap*** |
| JE 15 26 | OU | 872 | 871 | 950 | 769 | 778 | 963 | 659 | 890 |
| JE 15 62 | OU | 886 | 887 | 964 | 783 | 790 | 995 | 695 | 927 |
| JE 15 68 | OU | 893 | 894 | 970 | 800 | 764 | 981 | 917 | 972 |
| JE 15 34 | OU | 864 | 863 | 943 | 747 | 778 | 959 | 659 | 893 |
| JE 15 35 | OU | 868 | 867 | 946 | 743 | 777 | 988 | 683 | 926 |
| JE 15 36 | OU | 870 | 870 | 948 | 743 | 780 | 969 | 726 | 927 |
| JE 15 48 | OU | 845 | 843 | 925 | 739 | 783 | 971 | 682 | 911 |
| JE 15 60 | OU | 865 | 864 | 943 | 764 | 781 | 1002 | 674 | 928 |
| SB 169 | OU | 869 | 868 | 947 | 784 | 785 | 1001 | 601 | 887 |
| JE 15 38 | OU | 878 | 878 | 956 | 773 | 806 | 985 | 603 | 873 |
| JE 15 30 | MU | 832 | 829 | 913 | 726 | 787 | 992 | 647 | 901 |
| JE 15 57 | MU | 826 | 823 | 907 | 744 | 805 | 1012 | 601 | 875 |
| JE 16 23 | MU | 819 | 816 | 901 | 724 | 743 | 1004 | 739 | 958 |
| JE 16 44 | MU | 843 | 841 | 923 | 762 | 777 | 1021 | 624 | 917 |
| JE 15 59 | MU | 840 | 838 | 920 | 744 | 803 | 1013 | 602 | 872 |
| JE 15 65 | MU | 824 | 821 | 905 | 746 | 784 | 1014 | 630 | 897 |
| JE 15 53 | MU | 815 | 812 | 897 | 732 | 780 | 1031 | 626 | 901 |
| JE 15 67 | MU | 808 | 804 | 890 | 735 | 750 | 1015 | 773 | 970 |
| JE 15 56 | MU | 833 | 830 | 914 | 734 | 756 | 995 | 709 | 931 |
| JE 15 04 | MU | 826 | 823 | 907 | 746 | 794 | 988 | 569 | 824 |
| SB 171 | MU | 831 | 829 | 912 | 753 | 766 | 1022 | 596 | 877 |
| SB 166 | MU | 843 | 841 | 923 | 759 | 785 | 1017 | 573 | 835 |
| SB 176 | MU | 826 | 823 | 907 | 747 | 767 | 1040 | 610 | 885 |
| SB 179 | MU | 796 | 792 | 879 | 734 | 751 | 1030 | 605 | 887 |
| SB 160 | MU | 818 | 814 | 899 | 741 | 763 | 1036 | 604 | 885 |
| JE 15 66 | IU | 774 | 768 | 857 | 724 | 809 | 1063 | 576 | 791 |
| JE 15 45 | IU | 762 | 755 | 846 | 706 | 788 | 1051 | 585 | 844 |
| JE 15 51 | IU | 774 | 768 | 857 | 710 | 802 | 1052 | 576 | 807 |
| SB 180 | IU | 750 | 743 | 834 | 716 | 734 | 1036 | 591 | 879 |
| JE 15 64 | IU | 771 | 765 | 854 | 713 | 771 | 1057 | 614 | 882 |
| SB 184 | IU | 769 | 763 | 853 | 734 | 756 | 1051 | 612 | 890 |
| JE 15 28 | IU | 775 | 769 | 858 | 735 | 782 | 1016 | 537 | 773 |
| SB 162 | IU | 774 | 767 | 857 | 733 | 759 | 1034 | 578 | 861 |
| SB 186 | IU | 758 | 750 | 842 | 716 | 722 | 1039 | 592 | 872 |
| JE 16 45 | IU | 794 | 790 | 877 | 748 | 778 | 1045 | 589 | 866 |

Zircon (Zrn) saturation temperatures after Watson and Harrison (1983)

Monazite (Mnz) saturation temperatures based on Montel (1993)

Apatite (Ap) saturation temperatures based on Harrison and Watson (1984; Ap*), Pichavant *et al.* (1992; Ap**), and Bea *et al.* (1992; Ap***)

***Supplementary Table 14.*** *Distribution coefficients (Kds) used for the trace-element modelling of the Sierra Bermeja Pluton monzogranites*

| | Kfs | Pl | Bt | Mnz | Zrn | Ap | Xtm |
|---|---|---|---|---|---|---|---|
| La | 0.082 | 0.400 | 0.060 | 517 | 0.002 | 9.46 | 0.020 |
| Ce | 0.031 | 0.300 | 0.050 | 505 | 0.260 | 16.1 | 2.60 |
| Pr | 0.014 | 0.119 | 0.070 | 530 | 0.020 | 21.3 | 0.200 |
| Nd | 0.025 | 0.200 | 0.080 | 538 | 0.060 | 29.8 | 0.600 |
| Sm | 0.010 | 0.100 | 0.060 | 493 | 1.30 | 62.8 | 13.0 |
| Gd | 0.100 | 0.080 | 0.100 | 419 | 3.80 | 93.3 | 38.0 |
| Tb | - | - | 0.180 | 287 | 9.90 | 125 | 99.0 |
| Dy | 0.010 | 0.020 | 0.170 | 196 | 20.0 | 154 | 200 |
| Er | 0.010 | 0.010 | 0.220 | 100 | 77.0 | 145 | 770 |
| Yb | 0.030 | 0.010 | 0.120 | 40.0 | 219 | 116 | 2190 |
| Y | 0.100 | 0.011 | 0.100 | 130 | 47.0 | 141 | 470 |
| U | 0.010 | 0.019 | 0.260 | 22.0 | 148 | 54.1 | 7907 |
| Th | 0.010 | 0.010 | 0.010 | 589 | 27.4 | 1.47 | 274 |

Kfs: Bachmann *et al*. (2005) and Padilla and Gualda (2016)
Pl: Bachmann *et al.* (2005) and Padilla and Gualda (2016)
Bt: Bea *et al*. (1994b)
Mnz: Stepanov *et al.* (2012)
Zrn: Chapman *et al.* (2016) and Claiborne *et al.* (2018)
Ap: Data from this PhD Thesis; calculated dividing the average contents in analyzed apatites (Table 8) by the average contents in monzogranites of the three units of the Sierra Bermeja Pluton (Table 15)
Xtm: Zircon Kds x 10 (*e.g.* Merino Martínez *et al*., 2014); Kds for Uranium after Pérez-Soba *et al.* (2014)
Mineral abbreviations from Whitney and Evans (2010)

***Supplementary Table 15.*** *Inventory of Geological Points of Interest (GPI)*

| Nº GPI | Coord. (UTM zone 29N) | | Description |
|---|---|---|---|
| GPI-01 | 731396 | 4325975 | Neoproterozoic dioritoids |
| GPI-02 | 746042 | 4326709 | Paleozoic shales, slates and quartzites |
| GPI-03 | 744905 | 4322601 | Intrusive contact between monzogranites and host rocks |
| GPI-04 | 738040 | 4324332 | Andalusite spotted slates |
| GPI-05 | 735972 | 4330687 | Cenozoic cover |
| GPI-06 | 744877 | 4322668 | Intrusion of MU into the OU (the Rugidero Berrocal) |
| GPI-07 | 744594 | 4322852 | OU main type |
| GPI-08 | 744843 | 4322706 | K-feldspar phenocrysts large accumulations (the Rugidero Berrocal) |
| GPI-09 | 741257 | 4329021 | K-feldspar phenocrysts large accumulations |
| GPI-10 | 740854 | 4323779 | Microgranular mafic magmatic enclaves |
| GPI-11 | 745493 | 4325834 | OU local variety |
| GPI-12 | 745190 | 4325997 | Sheet-by-sheet intrusions between the main type of the OU and its local variety |
| GPI-13 | 744208 | 4326526 | Intrusion of MU into the OU |
| GPI-14 | 740364 | 4327181 | Mixing/mingling relations between the MU and IU |
| GPI-15 | 736734 | 4327626 | Mixing/mingling relations between the MU and IU |
| GPI-16 | 740774 | 4324875 | MU main type |
| GPI-17 | 741752 | 4325037 | MU main type |
| GPI-18 | 745440 | 4324368 | MU local variety |
| GPI-19 | 743868 | 4323997 | MU local variety |
| GPI-20 | 738828 | 4327985 | IU main type |
| GPI-21 | 735835 | 4328694 | IU main type |
| GPI-22 | 743934 | 4325161 | IU local variety |
| GPI-23 | 738380 | 4328360 | Vaugnerite series rocks |
| GPI-24 | 737667 | 4327343 | Vaugnerite series rocks |
| GPI-25 | 742425 | 4323984 | Lamprophyre dyke |
| GPI-26 | 743903 | 4324799 | Lamprophyre dyke |
| GPI-27 | 744399 | 4324809 | Aplite dyke |
| GPI-28 | 738511 | 4327836 | Quartz dyke |
| SI-01 | 741022 | 4327099 | Dehesa |
| SI-02 | 744843 | 4322706 | Berrocal |
| SI-03 | 745439 | 4326715 | Large granite boulder |
| SI-04 | 742361 | 4323560 | Large granite boulder |
| SI-05 | 744186 | 4320965 | Cornalvo Reservoir |

# Supplementary map – Geological map of the Sierra Bermeja Pluton

730000 735000 740000 745000

4330000 4325000

N

**Scale 1:10 000**

0 kilometres 2

UTM zone 29N, datum ETRS 89
Map accuracy: ± 5 m
Background hillshading
from 5 m LiDAR DTM (2010, IGN)

CÁCERES
BADAJOZ

**Topographical features**
- Village / Building
- Province boundary
- Highway
- Road
- Trail
- Reservoir
- River / Stream

**Cornalvo Natural Park**
- Nature trail
- Natural Park boundary
- Geological Point of Interest (GPI)

GPI-01 GPI-02 GPI-03 GPI-04 GPI-05 GPI-06 GPI-07 GPI-08 GPI-09 GPI-10 GPI-11 GPI-12 GPI-13 GPI-14 GPI-15 GPI-16 GPI-17 GPI-18 GPI-19 GPI-20 GPI-21 GPI-22 GPI-23 GPI-24 GPI-25 GPI-26 GPI-27 GPI-28
G-1 G-2 / GPI-08 G-3 G-4 G-5

Aljucén River
Fresneda River
Hinojosa River

Aljucén Village
Mirandilla Village
Cortijo de la Raposera de Arriba
Cortijo de la Raposera de Abajo
Casa del Bonatillo
Casa Lucas
Casa de la Encomienda del Moro
Casa de San Pablo
Casa del Huevo
Casa del Gamo
Casa de la Mezquita
Casa de Victor Martín
Casas Bajas de Valdelasyeguas
Casas Altas de Valdelasyeguas

## GEOLOGICAL LEGEND

*SIERRA BERMEJA PLUTON*

**Aplites and quartz dykes**
- Quartz dyke
- Aplite dyke
- Aplite mass

**Vaugnerite series rocks and lamprophyres**
- Calc-alkaline lamprophyres
- Vaugnerite series rocks

**Cordierite-bearing monzogranites**
- *INNER UNIT*
  - Cordierite-rich two-mica leucogranite
  - Cordierite-poor two-mica leucogranite
  - Mixing/mingling zone
- *MIDDLE UNIT*
  - Cordierite-rich monzogranite
  - Cordierite-poor monzogranite
- *OUTER UNIT*
  - Porphyritic coarse-grained monzogranite
  - Porphyritic fine-grained monzogranite

**Cenozoic cover**
- Alluvial and colluvial deposits

**Host rocks**
- Cadomian intrusive rocks
- Paleozoic metasedimentary sequence
- Contact metamorphism aureole

- Fault
- Intrusive contact
- Unconformity
- Contact metamorphism aureole limit
- Thrust